

CRANFIELD UNIVERSITY

MOHAMED MOSTAFA HASSAN TAWFIK

NUMERICAL AND EXPERIMENTAL STUDY OF A LENS-LENS
BEAM GENERATOR SOLAR CONCENTRATOR

SCHOOL OF AEROSPACE, TRANSPORT AND
MANUFACTURING
PhD in Manufacturing

PhD Thesis
Academic Year: 2017 - 2018

Supervisor: Assoc. Prof. Christopher Sansom
Associate Supervisor: Dr. Peter King
June 2018

CRANFIELD UNIVERSITY

SCHOOL OF AEROSPACE, TRANSPORT AND
MANUFACTURING
PhD in Manufacturing

PhD Thesis

Academic Year 2017 - 2018

MOHAMED MOSTAFA HASSAN TAWFIK

Numerical and Experimental Study of a Lens-Lens Beam Generator
Solar Concentrator

Supervisor: Assoc. Prof. Christopher Sansom

Associate Supervisor: Dr. Peter King

June 2018

This thesis is submitted in partial fulfilment of the requirements for
the degree of PhD degree

© Cranfield University 2018. All rights reserved. No part of this
publication may be reproduced without the written permission of the
copyright owner.

ABSTRACT

The increased risk of climate change, besides the rapid depletion of non-renewable sources, motivated researchers to replace non-renewable energy sources with renewable ones. Solar energy can be considered as the “mother” of all renewable energy sources. The research trend in concentrated solar power systems tends to study optimising the utilisation of such power source. However, most researches deal with building new facilities that uses solar thermal power efficiently. Although it is important to improve innovative designs for our energy future, parallel thinking in currently existing facilities is necessary.

The aim of this work is to lower the Carbon footprint of currently existing conventional power systems that uses fossil fuels through hybridisation with solar energy efficiently. This would encourage countries, especially developing ones, to move forward to solar technologies.

Therefore, an overview of different concentrated solar power (CSP) technologies is carried out. Among different CSP technologies, a two-stage lens system was used to generate a powerful and controllable concentrated solar beam, namely Lens-Lens Beam Generator (LLBG), is found to allow achieving the aim with minimum modifications requirements. The LLBG provides a unique flexibility in selecting the receiver location. This facilitates implementing solar energy in fossil-fuel systems which are currently in service and affording reduced land usage.

However, it was built on a small scale with a restricted concentration ratio (CR) of 6.25 to avoid overheating its rear lens, using two bi-convex lenses. As a relatively high efficiency of 82.65% was reported at this low CR, it has the potential to achieve high CR values and higher thermal efficiency using a dual-axis tracking system.

Building large aperture refractive-based solar concentrating systems tends to employ Fresnel lens geometry due to their cost and design advantages. Then, an evaluation of implementing Fresnel lenses in building such LLBG system became as the gap of knowledge for the current research. Covering this gap required investigating the front and rear lenses geometries and materials.

However, because of the UK location within a relatively low-DNI region with an average annual direct normal irradiation (DNI) of 400-1000 kWh/m², building a solar simulator for thermal testing arose as a critical need to achieve the required objectives within the limited research time-scale. Therefore, it became as one of the main research objectives of the present work. To fulfil this, different light sources have been reviewed and two of them are selected to be further studied. These selected light sources were metal halide and tungsten halogen. Metal halide lamps showed better match with solar spectrum over full spectral bandwidth compared to tungsten halogen light source. Despite that, utilising dimmable tungsten halogen lamp is more recommended for thermal testing, use as it provides controllable good output spectrum over the IR spectral zone.

For the front lens design, manufacturing and cost studies carried out within the present work indicated that using plastic Fresnel lenses is the most cost-effective option for large-scale aperture refractive systems. Based on optical study performed, PMMA has been selected as the best material due to its higher ideal optical efficiency, compared to polycarbonate. For the rear lens geometry, thermal study indicated that positive meniscus geometry can withstand higher CRs, compared to both plano- and bi-convex geometries. Combination of thermal and optical studies showed that SiO₂ represents the optimum material for the rear lens, allowing highest CRs with maximum transmittance.

Two Fresnel-based LLBG systems are designed and built to experimentally assess their performance. These systems were: prototype- and full-size systems, with results showing average field efficiencies of 17.30% and 17.65%, respectively, within 0.5m from the control mirror. By suppressing the influence of optical efficiencies due to different components used, a thermal conversion efficiency of 29.5% was obtained for both systems. These values showed that building a unit aperture area of an LLBG system can save up to 25.76 kg/year and 29.37m³/year of petroleum and natural gas, respectively. This can lead to annual CO₂ footprint reduction by 26.95 and 23.84 kgCO₂ for power generation systems that use combined cycles fuelled by petroleum and natural gas, respectively.

Further optical investigation of Fresnel-based LLBG system to study the effects of different parameters on its performance. Although this investigation showed that IR spectrum deviates less than VIS and UV spectra, it also indicated that using Fresnel geometry for the front lens causes increases in the generated beam deviation angle. This reduces the system efficiency dramatically and its ability to carry the beam efficiently over long distances.

Keywords: COMSOL, ANSYS, sun, simulator, tracking, Fresnel

ACKNOWLEDGEMENTS

First and foremost, I would like to take this opportunity to thank ALLAH who has the complete knowledge and guides me in every field of life. Without Him, I would not have endowed with health or knowledge to complete this thesis.

I would like to express my sincere gratitude to the Egyptian Government for supporting this project under the Egyptian Government External Missions Funding Program. The Egyptian Ministry of Higher Education, Cultural Affairs and Missions Sector, is represented in the UK by The Egyptian Cultural and Educational Bureau in London.

In addition, it is important to acknowledge the NERC Field Spectroscopy Facility, University of Edinburgh, Grant Institute, School of GeoSciences, for lending us the “SVC HR-1024i Field Spectroradiometer” which was used in measuring the output spectrum of the PHILIPS HPI-T 2000W and PHILIPS 6994Z 2000W lamps used in Cranfield University Solar Laboratory’s solar simulator.

I am extremely grateful to Assoc. Prof. Chris Sansom and my ex-supervisor Dr Xavier Tonnellier for their continuous support, advice and scientific contribution to my work. Special thanks to Dr. Peter King for his kind help through my study.

An honourable mention goes to my parents for their effort and encouragements throughout my life. Without their endless love and support to reach my full potential, I would have not been able to be here to even start my thesis.

My sincere thanks to my wife, Eman El-Shennawy, and my beloved children, Hossam and Haneen, for their support and sacrifices during the years I have been working on this thesis. Especially, for the great environment they provided me to discuss my project hurdles with them and to write-up the thesis. Without their continuous love and enduring hard times, this thesis could not be completed.

Last but not least, I would like to express my deep thanks to all the technicians and staff of the Precision Engineering Institute, Cranfield University, for the time they spent discussing, producing my design and helping during test setup and testing.

TABLE OF CONTENTS

ABSTRACT	i
ACKNOWLEDGEMENTS.....	iv
LIST OF FIGURES.....	ix
LIST OF TABLES	xvii
LIST OF ABBREVIATIONS.....	xx
NOMENCLATURE	xxii
LIST OF PUBLICATIONS.....	xxvii
1 RESEARCH BACKGROUND.....	1
1.1 Thermal Power Generation.....	1
1.1.1 Conventional Vs. Solar Thermal Power Systems.....	1
1.1.2 Power Cycles	2
1.2 Characteristics of Solar Radiation.....	3
1.2.1 Solar Spectrum	3
1.2.2 Solar Angular Aperture.....	5
1.3 CSP Terminology.....	5
1.3.1 Concentration Ratio.....	5
1.3.2 Efficiency.....	6
1.4 Solar Simulator Design Motivation	8
1.5 Thesis Structure.....	8
1.6 Summary	10
2 LITERATURE REVIEW	11
2.1 CSP Technology Overview	11
2.1.1 Reflection-based Concentrators.....	11
2.1.2 Refraction-based Concentrators	18
2.2 Review of Simulation Software	32
2.2.1 Discretisation Techniques	33
2.2.2 CSP Simulating Software Overview	34
2.3 Transparent Materials Review	43
2.3.1 Materials Physical Properties	43
2.3.2 Materials Transmittances	48
2.4 Fresnel Lens Review	52
2.4.1 Fresnel Lens Terminology.....	52
2.4.2 Fresnel Lens Manufacturing Methods	52
2.4.3 Fresnel Lens Optical Losses	53
2.5 Solar Simulator Review.....	57
2.5.1 Light sources.....	57
2.5.2 Trends in using light sources.....	62
2.5.3 Light sources characteristics	65
2.6 Summary	68
3 AIM OF STUDY	69

3.1 Aim.....	69
3.2 Objectives	69
3.3 Gap of Knowledge	70
3.4 Methodology	70
4 EXPERIMENTAL INSTRUMENTS & PRELIMINARY TESTS.....	72
4.1 Experimental Instruments	72
4.1.1 SVC HR-1024i Field Spectroradiometer.....	72
4.1.2 TESA-VISIO® 300 DCC Machine	72
4.1.3 PHILIPS Strand Portable Dimmer	73
4.1.4 SMP10 pyranometer	74
4.1.5 TC-08 Thermocouple Data Logger.....	74
4.1.6 TITAN MK7-15 Laser Distance Measurer	74
4.1.7 Condor Reflectometer	75
4.1.8 Leitz PMM-F Coordinate Measuring Machine	75
4.2 Preliminary Tests	75
4.2.1 Solar Simulator Back Reflector Measurement.....	75
4.2.2 Mirror Reflectivity	77
4.2.3 Front Lens Bending Measurement.....	78
5 SOLAR SIMULATOR DESIGN AND TESTING.....	80
5.1 Solar Simulator Design	80
5.1.1 Main Components	80
5.1.2 Ray Tracing Simulation	82
5.2 Solar Simulator Testing.....	85
5.2.1 Lamps Spectra Comparison Experiments	85
5.2.2 Fresnel Lens Transmittance Measurement Experiment.....	86
5.2.3 Irradiance Measurement Experiments.....	88
5.2.4 Thermal Response Evaluation Experiments	89
5.2.5 Lens Mount Model Validation Experiments	90
5.3 Summary	92
6 LLBG SYSTEM DESIGN AND TESTING.....	93
6.1 Theoretical Study Framework	93
6.1.1 System Working Principle	93
6.1.2 Front Lens Study	94
6.1.3 Rear Lens Study	99
6.1.4 LLBG System Optical Analysis.....	121
6.2 LLBG Design	135
6.2.1 LLBG System Description	135
6.2.2 The Pugh Matrix Components.....	137
6.2.3 The Pugh Matrix Discussion.....	139
6.2.4 Main Arm Profile Selection	146
6.2.5 Main Arm Motor Sizing.....	153
6.2.6 Azimuth Platform Motor Sizing	163

6.2.7 LLBG Tracking System Design	167
6.3 LLBG Testing.....	170
6.3.1 Optical Analysis Code Validation Test.....	170
6.3.2 Prototype-Size LLBG System Test.....	171
6.3.3 Full-Size System LLBG System Test	175
6.4 Summary	178
7 RESULTS AND DISCUSSION	180
7.1 Solar Simulator Testing Results.....	180
7.1.1 Lamps Spectra Comparison Experiments	180
7.1.2 Fresnel Lens Transmittance Measurement Experiment.....	181
7.1.3 Irradiance Measurement Experiments.....	182
7.1.4 Thermal Response Evaluation Experiments	183
7.1.5 Lens Mount Model Validation Experiments	184
7.2 LLBG Modelling Results	185
7.2.1 Rear Lens Thermal Modelling Validation.....	185
7.2.2 Rear Lens Detailed Numerical Model Results	190
7.2.3 Optical Analysis Code Results	196
7.3 LLBG Testing Results	210
7.3.1 Optical Analysis Code Validation Test.....	210
7.3.2 Prototype LLBG System Test.....	211
7.3.3 Full-Size LLBG System Test	212
7.4 Prototype-Size LLBG System Evaluation.....	213
7.4.1 System Efficiency Evaluation	213
7.4.2 Reduction in Carbon Footprint and Fuel Consumption.....	216
7.5 Full-Size LLBG System Evaluation	218
7.5.1 System Efficiency Evaluation	218
7.5.2 Reduction in Carbon Footprint and Fuel Consumption.....	221
7.6 Summary	222
8 CONCLUSIONS AND FURTHER WORK	224
8.1 Conclusions	224
8.1.1 Design and build a sun simulator device	224
8.1.2 Build and validate numerical models to design an LLBG solar concentrator	224
8.1.3 Design and build an LLBG solar concentrator.....	225
8.1.4 Assess the performance of this concentrating technology	225
8.1.5 Assess performance limitations and system implementation obstacles.....	225
8.2 Further Work.....	226
9 REFERENCES.....	227
APPENDICES	279
Appendix A Rear Lens Thermal Model MATLAB Cod	279
Appendix B Incident Heat Flux Boundary Condition	281

Appendix C TESA-VISIO 300 DCC Report.....	285
Appendix D LLBG Design	286
Appendix E Aluminium Profile Deflection Study.....	290
Appendix F Wood Cross-section Deflection Study	300
Appendix G Aluminium Extrusion Deflection Study	309
Appendix H Selecting Wind Speed	321
Appendix I Counter Wight Arm Length Effect	322
Appendix J Optical Analysis MATLAB Code.....	325
Appendix K Rear Lens Different Geometries	347

LIST OF FIGURES

Figure 1-1 Air Mass (AM)	4
Figure 1-2 Solar angular aperture	5
Figure 1-3 Energy flow through a CSP system.....	7
Figure 1-4 Direct Normal Irradiation (DNI) on UK (Solargis, 2015).....	8
Figure 2-1 Concentrating technologies classification	11
Figure 2-2 Ancient Chinese bronze solar igniters.....	11
Figure 2-3 Ancient inventors and scholars	12
Figure 2-4 Mouchot's solar concentrator	12
Figure 2-5 Shuman's solar plant in Egypt,.....	13
Figure 2-6 Parabolic trough power plant major components	14
Figure 2-7 Linear Fresnel reflector solar field major components.....	15
Figure 2-8 Power tower plant major components	16
Figure 2-9 Sun-tracking and target-aiming proposed method	17
Figure 2-10 Parabolic dish main components	17
Figure 2-11 Lavoisier combustion experiment in 1770s	19
Figure 2-12 Golmud 2 plant, Qinghai, China	21
Figure 2-13 Different FLFL collector mountings	23
Figure 2-14 Piszczor's group CPV refractive system and components	24
Figure 2-15 Proposed light-transmission system for CPV on spacecraft.....	25
Figure 2-16 TIR lens-concentrator details	26
Figure 2-17 Andreev's group two-stage refractive system main components ..	27
Figure 2-18 Schematic of concentrating optical system with ball lens.....	27
Figure 2-19 Compact CPV-hydrogen system for rooftop operation.....	28
Figure 2-20 O'Neill's proposed point focus system and components	28
Figure 2-21 LLBG proposed point focus system	29
Figure 2-22 Xie's group point-focus Fresnel lens solar concentrator test rig....	30
Figure 2-23 Han's group two-stage refractive system and components.....	30
Figure 2-24 Vu's group proposed modified optical fibre daylighting system.....	31

Figure 2-25 Transparent materials transmittances against solar spectrum (AM1.5).....	50
Figure 2-26 Materials transmittances over different spectral zones	51
Figure 2-27 Schematic of Fresnel lens cross-section.....	52
Figure 2-28 Geometric losses	54
Figure 2-29 Enlarged ideal and fabricated groove profiles in one groove	54
Figure 2-30 Enlarged representation of a blocked ray.....	55
Figure 2-31 Reflection losses	56
Figure 2-32 Schematic of vortex water-wall argon arc lamp.....	58
Figure 2-33 Metal halide lamp structure	59
Figure 2-34 Tungsten halogen lamp structure.....	60
Figure 2-35 Xenon arc lamp structure	60
Figure 2-36 Light sources spectra comparison against solar spectrum (AM1.5)	61
Figure 2-37 Light sources usage share in different eras	62
Figure 3-1 Methodology to achieve the aim and objectives.....	71
Figure 4-1 SVC HR-1024i Field Spectroradiometer	72
Figure 4-2 TESA-VISIO® 300 DCC machine	73
Figure 4-3 PHILIPS Strand portable dimmer.....	73
Figure 4-4 Kipp & Zonen Instruments SMP10 Pyranometer.....	74
Figure 4-5 TC-08 thermocouple data logger & K-type thermocouple used	74
Figure 4-6 TITAN MK7-15 laser distance measurer	75
Figure 4-7 Condor reflectometer	75
Figure 4-8 Leitz PMM-F coordinate measuring machine.....	76
Figure 4-9 Solar simulator back reflector measurement setup	76
Figure 4-10 Front lens bending measurement test setup	78
Figure 4-11 Front lens surface profile.....	79
Figure 5-1 Solar simulator optical system	82
Figure 5-2 Solar simulator schematic diagram	82
Figure 5-3 Tungsten halogen case.....	83

Figure 5-4 Metal halide lamp representation	84
Figure 5-5 Metal halide case	84
Figure 5-6 Spectrum measuring test setup	85
Figure 5-8 Fresnel lens transmittance measuring test setup	87
Figure 5-8 Irradiance measuring test setup	89
Figure 5-9 Thermal response measuring test setup	90
Figure 5-10 Lens mount model validation experimental setup layout	92
Figure 6-1 The LLBG optical configuration	93
Figure 6-2 Polymeric materials measured, CDE-6 coefficients, SDE-2 coefficients and SDE-6 coefficients refractive indices	97
Figure 6-3 Reflectance of polymeric transparent materials	97
Figure 6-4 Ideal and reflection efficiencies of polymeric transparent materials for solar concentration applications	98
Figure 6-5 Summary of front lens study results	98
Figure 6-6 Physical problem description	99
Figure 6-7 Energy balance through a semi-transparent sample	100
Figure 6-8 Thermal resistance circuit for the sample	102
Figure 6-9 Absorption, reflection, and transmission of incident radiation over a semi-transparent sample	106
Figure 6-10 Different lens geometries ray diagrams	106
Figure 6-11 Schematic of simulated lenses	107
Figure 6-12 Temperature distribution through lenses (Solar noon, CR=100, SiO ₂)	108
Figure 6-13 Maximum rear lens temperature for different geometries vs. CR	109
Figure 6-14 Comparison of COMSOL and ANSYS models results (Geometry Test)	109
Figure 6-15 Maximum rear lens temperature for different materials vs. CR ...	111
Figure 6-16 Comparison of COMSOL and ANSYS models results (Material Test)	112
Figure 6-17 Lens mount geometry	113
Figure 6-18 Rear lens positive meniscus lens geometry (Thorlabs, 2010d) ...	114
Figure 6-19 Maximum temperature achieved (ANSYS results)	115

Figure 6-20 Temperature distribution over the lens.....	116
Figure 6-21 Maximum temperature achieved with partial insulation of lens ...	118
Figure 6-22 Temperature distribution over the lens with partial insulation.....	119
Figure 6-23 Analysis of heat transfer through the gasket patches.....	120
Figure 6-24 Fresnel facets face configurations.....	121
Figure 6-25 Ray geometry for spot diameter derivation	122
Figure 6-26 Analogy between bended Fresnel lens and spherical aberration	124
Figure 6-27 Buckling direction effect	126
Figure 6-28 Configuration-buckling combined effect	127
Figure 6-29 Positive meniscus lens nomenclatures	129
Figure 6-30 The lens-lens optical configuration.....	129
Figure 6-31 Detailed geometry of the rear lens	130
Figure 6-32 Detailed geometry for negative deviation	132
Figure 6-33 Flowchart of optical analysis MATLAB code	134
Figure 6-34 The sun's path and solar angles	136
Figure 6-35 LLBG main components motions	137
Figure 6-36 Main arm deflection effect	146
Figure 6-37 Shifted beam and lost power.....	146
Figure 6-38 Concentrated power lost as a function of deflection.....	147
Figure 6-39 Causes of main arm deflection.....	148
Figure 6-40 Cross section of main arm Aluminium profile, 40x120L	149
Figure 6-41 General force affecting a cantilever beam.....	150
Figure 6-42 Nomenclature for moment of inertia for a rectangular cross-section	151
Figure 6-43 Nomenclature for moment of inertia of available Aluminium extrusions	151
Figure 6-44 Wind load on main arm	153
Figure 6-45 Wind load moment on main arm pivot as a function of altitude angle	155
Figure 6-46 Weight load on main arm	155
Figure 6-47 Weight load on main arm pivot as a function of altitude angle ...	156

Figure 6-48 Wind and weight loads on main arm pivot without a counter weight	156
Figure 6-49 Wind and weight combined load on main arm pivot without using a counter weight, as a function of altitude angle.....	157
Figure 6-50 Wind and weight loads on main arm pivot with a counter weight	157
Figure 6-51 Wind, weight and counter weight combined load on main arm pivot with using a counter weight, as a function of altitude angle.....	158
Figure 6-52 Combined moment range affecting on main arm pivot in absence/presence of wind load ($L_{cw}=0.5m$)	159
Figure 6-53 Absolute combined moment range affecting on main arm pivot in absence/presence of wind load ($L_{cw}=0.5m$)	159
Figure 6-54 Absolute combined moment range affecting on main arm pivot in absence/presence of wind load ($L_{cw}=1.0m$)	160
Figure 6-55 Relation between the optimum counter weight mass and length from the pivot point	160
Figure 6-56 Deflection due to static load on Aluminium profile end.....	161
Figure 6-57 Calculated deflection due to static load on Aluminium profile end	161
Figure 6-58 Bending stress on Aluminium profile	162
Figure 6-59 Azimuth platform	163
Figure 6-60 Moment at azimuth platform motor and total number of BUs vs. counter weight mass.....	165
Figure 6-61 Allowed BUs separations vs. counter weight mass.....	166
Figure 6-62 Flowchart of calculating solar angles algorithm based on GPS data	167
Figure 6-63 Flowchart of presented solar tracking control system	168
Figure 6-64 Solar tracking control system	169
Figure 6-65 Optical analysis code validation test setup.....	171
Figure 6-66 Graphite receiver geometry.....	172
Figure 6-67 Prototype-size LLBG system test setup	173
Figure 6-68 Receiver nomenclature (left) and inserted thermocouples (right)	175
Figure 6-69 Solar simple manual tracking indicator.....	175
Figure 6-70 Initial full-size LLBG test setup.....	176

Figure 6-71 The insulating gasket mask.....	177
Figure 6-72 Cracks in the float glass-based 45° mirror	177
Figure 6-73 Receiver window setup	178
Figure 7-1 Tungsten halogen lamp spectra comparison with solar spectrum.	180
Figure 7-2 Metal halide lamp spectrum comparison with solar spectrum	181
Figure 7-3 Measured transmittance of the front Fresnel lens	182
Figure 7-4 Irradiance distribution.....	183
Figure 7-5 Temperature over the black screen.....	184
Figure 7-6 Lens mount model validation tests results	184
Figure 7-7 Cross-section view of the packed-bed solar reactor (Piatkowski, Wieckert and Steinfeld, 2009).....	185
Figure 7-8 Schematic of the reactor upper cavity with boundary conditions... ..	186
Figure 7-9 Measured incident power and calculated power flux versus time .	187
Figure 7-10 Mathematical models validation against experimental data	188
Figure 7-11 ANSYS and COMSOL models validation against experimental data	190
Figure 7-12 Maximum allowable CR vs. latitude angle of set-up location	191
Figure 7-13 Maximum allowable CR vs. positive meniscus lens thickness	192
Figure 7-14 Maximum allowable CR vs. Transmittance	193
Figure 7-15 Maximum allowable CR vs. maximum working temperature	194
Figure 7-16 Maximum allowable CR vs. material density	194
Figure 7-17 Maximum allowable CR vs. heat capacity.....	195
Figure 7-18 Maximum allowable CR vs. material thermal conductivity.....	195
Figure 7-19 Maximum allowable CR vs. material thermal diffusivity.....	196
Figure 7-20 Case study Fresnel lenses prisms θ_s as a function of r (calculated)	197
Figure 7-21 Spectral spot diameter at ($x = 1.4\text{m}$) against solar spectrum (AM1.5)	198
Figure 7-22 Spectral spot diameter with different assumptions and models ..	198
Figure 7-23 Spectral deviation angle at different RLPFRs	200
Figure 7-24 Spectral beam diameter over distance, l , from the rear lens.....	200

Figure 7-25 Extended front lens radii of curvature effect study	202
Figure 7-26 Schematic diagram of the generated beam path.....	203
Figure 7-27 Sun's position calculator for Mansoura, Egypt on 24/06/2008	204
Figure 7-28 Spectral beam diameter over distance, l , from the rear lens.....	204
Figure 7-29 Spectral deviation angle for different rear lenses	206
Figure 7-30 Average beam deviation angles and reciprocal of RLPFR.....	206
Figure 7-31 Average deviation angle at different LLBG#s	209
Figure 7-32 Beam diameter against rear lens–screen distance	211
Figure 7-33 Receiver and ambient temperatures recorded (LLBG Prototype Test)	211
Figure 7-34 Receiver, window and ambient temperatures recorded	212
Figure 7-35 Energy flow within the LLBG system.....	213
Figure 7-36 Energy flow within the receiver.....	214
Figure 7-37 Prototype-size LLBG system field efficiency	215
Figure 7-38 Rear lens manufacturer spectral transmittance (280–2500nm) ..	216
Figure 7-39 Annual electric energy can be generated from 1m ² of LLBG aperture	217
Figure 7-40 Annual Carbon footprint reduction for 1m ² of LLBG aperture.....	218
Figure 7-41 Schematic diagram of geometry explaining equivalent diameter	219
Figure 7-42 MATLAB code output predicting spot diameter at x_1	219
Figure 7-43 Full-size LLBG system field efficiency.....	220
Figure 7-44 Annual electric energy can be generated from 1m ² of LLBG aperture	221
Figure 7-45 Annual Carbon footprint reduction for 1m ² of LLBG aperture.....	222
Figure B-1 Altitude angle range.....	283
Figure B-2 Azimuth angle definition.....	283
Figure B-3 Azimuth angle range.....	283
Figure B-4 Snap shot from solar angles calculator programme.....	284
Figure D-5 Aluminium profile used	287
Figure D-6 Free body diagram of the Main Arm	288
Figure D-7 Control Mirror stroke definition.....	289

Figure I-8 Absolute combined moment range affecting on main arm pivot in presence/absence of wind load ($L_{cw}=0.50m$)	322
Figure I-9 Absolute combined moment range affecting on main arm pivot in presence/absence of wind load ($L_{cw}=0.75m$)	322
Figure I-10 Absolute combined moment range affecting on main arm pivot in presence/absence of wind load ($L_{cw}=1.0m$)	323
Figure I-11 Absolute combined moment range affecting on main arm pivot in presence/absence of wind load ($L_{cw}=1.25m$)	323
Figure I-12 Absolute combined moment range affecting on main arm pivot in presence/absence of wind load ($L_{cw}=1.50m$)	324
Figure I-13 Absolute combined moment range affecting on main arm pivot in presence/absence of wind load ($L_{cw}=1.75m$)	324
Figure K-14 Schematic of bi-convex lens (Part number: LB4879).....	347
Figure K-15 Schematic of plano-convex lens (Part number: LA4052).....	347
Figure K-16 Schematic of positive meniscus lens (Part number: LE4173).....	348
Figure K-17 Schematic of positive meniscus lens (Part number: LE4197).....	348
Figure K-18 Schematic of positive meniscus lens (Part number: LE4467).....	348
Figure K-19 Schematic of positive meniscus lens (Part number: LE4329).....	349
Figure K-20 Schematic of positive meniscus lens (Part number: LE4484).....	349
Figure K-21 Schematic of positive meniscus lens (Part number: LE4950).....	349

LIST OF TABLES

Table 2-1 Reflection-based concentrators development	13
Table 2-2 Refraction-based concentrators development	20
Table 2-3 CPV power plants using linear Fresnel lenses	22
Table 2-4 CSP technologies comparison	32
Table 2-5 Discretisation techniques comparison	34
Table 2-6 Summary of optical design software codes	40
Table 2-7 Summary of thermal design software codes	43
Table 2-8 Summary of transparent materials properties	49
Table 2-9 Comparison of different thermal solar simulators (chronological order)	63
Table 2-10 Summary of main characteristics of different light sources	67
Table 4-1 Solar simulator back reflector measurement data	77
Table 4-2 Mirrors reflectance measurements	77
Table 4-3 Front lens surface characteristics	78
Table 5-1 Optical elements specifications	82
Table 6-1 CDE and SDE coefficients for polymeric transparent materials, based on fitting experimental data (Sultanova, Kasarova and Nikolov, 2009).....	96
Table 6-2 Boundary conditions assumptions.....	107
Table 6-3 Rear lens materials transmittances over (280–2500nm) bandwidth	110
Table 6-4 Model boundary conditions	114
Table 6-5 RMSE and MAPE values for tested samples	114
Table 6-6 Patches dimensions in investigated cases	117
Table 6-7 Gasket material properties (Flexitallic, 2018)	117
Table 6-8 Analogy between bended Fresnel lens and SA effect	125
Table 6-9 Pugh Matrix criteria and weighting	138
Table 6-10 Pugh Matrix ranking system explanation	139
Table 6-11 Main arm motion concepts description and comparison.....	140
Table 6-12 Azimuth platform motion concepts description and comparison...	142

Table 6-13 Control mirror motion concepts description and comparison.....	144
Table 6-14 Pugh Matrix for different motions.....	145
Table 6-15 Parameters values for Eq. (6-93)	149
Table 6-16 Properties of studied timbers.....	151
Table 6-17 Comparison between accepted cross-sections (mass and cost). 152	
Table 6-18 Modified specifications of the main arm	152
Table 6-19 Parameters values for equations (6-108) and (6-109).....	154
Table 6-20 Mechanical properties of the 100x100x2 Aluminium Extrusion beam	161
Table 6-21 Azimuth platform main assumptions.....	163
Table 6-22 ALWAYSSE 3-Hole Flange BU specifications	165
Table 6-23 LLBG design parameters	166
Table 6-24 Receiver material properties	174
Table 6-25 Insulating material properties	174
Table 6-26 BOROFLOAT® window properties.....	177
Table 7-1 Spectral properties of the quartz window	187
Table 7-2 Model input data.....	188
Table 7-3 RMSE and MAPE values for mathematical models	189
Table 7-4 RMSE and MAPE values for numerical and mathematical models	190
Table 7-5 Polynomial constants for CR_{max} –Latitude relation	191
Table 7-6 Polynomial constants for CR_{max} –lens thickness relation	192
Table 7-7 Technical details of studied front lenses.....	197
Table 7-8 Longest distance beam travel to reach the feasible beam limit	201
Table 7-9 Technical details of studied rear lenses	205
Table 7-10 Optimum rear lens position, RLPFR and average deviation angle	205
Table 7-11 Probable front–rear lenses combinations	208
Table 7-12 MATLAB code output for different investigated combinations	208
Table 7-13 Fourier series fits coefficients and evaluation.....	210
Table 7-14 Average HRs by fuel and prime mover (EIA, 2017).....	217
Table D-1 Front lens specifications	286

Table D-2 Rear lens specifications.....	286
Table D-3 Aluminium profile specifications.....	287
Table E-4 Profile deflection study for $N_{MA} = 2.0$	290
Table E-5 Summary of accepted profiles for $N_{MA}=2.0$	292
Table E-6 Profile deflection study for $N_{MA} = 4.0$	292
Table E-7 Summary of accepted profiles for $N_{MA}=4.0$	295
Table E-8 Profile deflection study for $N_{MA} = 6.0$	296
Table E-9 Summary of accepted profiles for $N_{MA}=6.0$	298
Table E-10 Comparison between accepted profiles for $N_{MA}= 4.0$ and 6.0	299
Table F-11 Wood cross-section deflection study for $N_{MA} = 2.0$	300
Table F-12 Summary of accepted cross-sections for $N_{MA}=2.0$	302
Table F-13 Wood cross-section deflection study for $N_{MA} = 4.0$	302
Table F-14 Summary of accepted cross-sections for $N_{MA}=4.0$	305
Table F-15 Wood cross-section deflection study for $N_{MA} = 6.0$	305
Table F-16 Summary of accepted cross-sections for $N_{MA}=6.0$	307
Table F-17 Comparison between accepted cross-sections (mass and cost) .	308
Table G-18 Aluminium extrusion deflection study for $N_{MA} = 2.0$	309
Table G-19 Summary of accepted extrusion cross-sections for $N_{MA}=2.0$	312
Table G-20 Aluminium extrusion deflection study for $N_{MA} = 4.0$	312
Table G-21 Summary of accepted extrusion cross-sections for $N_{MA}=4.0$	315
Table G-22 Aluminium extrusion deflection study for $N_{MA} = 6.0$	316
Table G-23 Summary of accepted extrusion cross-sections for $N_{MA}=6.0$	319
Table H-24 Wind speeds at different locations in Egypt and UK	321

LIST OF ABBREVIATIONS

AC	Alternating current
ALON	Aluminium Oxynitride
Al-SiO	Aluminium-Silicon Monoxide
AM	Air Mass coefficient
BK7	Borosilicate Crown (“Krone” <i>in German</i>) glass
BU	Ball transfer unit
CA	Chromatic aberration
CAD	Computer-aided design
CAE	Computer-aided engineering
CaF ₂	Calcium Fluoride
CCD	Charge-coupled device
CDE	Cauchy’s dispersion equation
CMM	Coordinate measuring machines
CPC	Compound parabolic concentrator
CPV	Concentrated photovoltaic
CR	Concentration ratio
CSI	Compact source iodide
CSP	Concentrated solar power
DC	Direct current
DNI	Direct normal irradiation
DSG	direct steam generation
EC	Experts committee
FEM	Finite element method
FLFL	Flat linear Fresnel lenses
FS	Factor of safety
FSF	Field Spectroscopy Facility
FVM	Finite volume method
GE	Governing equations
GI	Grooves-In configuration
GO	Grooves-Out configuration
GUI	Graphical user interface
HFSS	High-Flux Solar Simulator

HID	High-intensity discharge
HR	Heat rate
HTF	Heat transfer fluid
InGaAs	Indium gallium arsenide
IR	Infrared
LED	Light-emitting diode
LLBG	Lens-Lens Beam Generator
MAPE	Mean absolute percentage error
MSC	MacNeal-Schwendler Corporation
NCV	Net calorific value
NERC	Natural Environment Research Council
NOABL	Numerical Objective Analysis Boundary Layer
PC	Polycarbonate
PDE	Partial differential equations
PID	Proportional–integral–derivative
PMMA	Polymethyl methacrylate
PV	Photovoltaic
PVD	Physical vapor deposition
RLPFR	Rear lens position focal ratio
RMSE	Root mean square error
SA	Spherical aberration
SAA	Solar angular aperture
SAM	Solar advisor model
SDE	Sellmeier's dispersion equation
SiC	Silicon Carbide
SiO ₂	Fused Silica (Quartz)
STPV	Solar thermophotovoltaic
TIR	Total internal reflection
UK	United Kingdom
ULE	Ultra-Low Expansion glass
UV	Ultraviolet
VIS	Visible
Y ₂ O ₃	Yttrium Oxide (Yttria)

NOMENCLATURE

Symbol	Description	Unit
A	Area	m^2
a	Wave aberration function	m
AM	Air Mass coefficient	–
C	Pyranometer output current	mA
C_d	drag coefficient	–
C_f	Friction coefficient	–
C_p	Specific heat capacity	J/kg.K
CR	Geometric CR	–
D	Diameter	m
D_1	Front lens aperture diameter	m
D_2	Rear lens aperture diameter	m
D_B	Beam diameter (LLBG output)	m
DN	Day number	–
D_s	Spot diameter (at front lens focal plane)	m
e	Thickness	m
E	Modulus of elasticity	Pa
f	Focal length (design condition)	m
F	Force	N
f^{\wedge}	Focal length (considering SAA effect)	m
$f^{\wedge\wedge}$	Focal length (considering buckling effect)	m
\bar{f}	Average focal length (considering combined effect)	m
f_b	Back focal length	m
g	Gravity acceleration	m/s^2
h	Convective heat transfer coefficient	$W/m^2.K$
H	Hour angle	degree
I	Irradiation	W/m^2
I_c	Moment of inertia	m^4
k	Thermal conductivity	$W/m.K$
l	Distance	m
L	Latitude angle	degree

L_0	Longitude angle	degree
LA	Longitudinal aberration	m
L_{MA}	Main arm length	m
m	Mass	kg
M	Moment	N.m
n	Refractive index	–
N	Number of data points	–
NG	Number of grooves	–
N_{MA}	Number of main arm supporting rods	–
P	Power	W
Q	Total heat power	W
q	Heat transfer per unit area	W/m ²
r	Radius	m
R	Radius of clear aperture	m
R_1	Radius of curvature of rear lens front surface	m
R_2	Radius of curvature of rear lens back surface	m
R_C	Radius of curvature	m
s	Paraxial focal length	m
s'	Marginal focal length	m
T	Temperature	K
t	Time	s
T_∞	Ambient temperature	K
T_s	Surface temperature	K
U	Velocity	m/s
W	Weight	N
Z	Height	m
z	Zenith angle	degree
α	Ray deflection angle (design condition)	rad
α'	Ray deflection angle (considering SAA effect)	rad
α''	Ray deflection angle (considering buckling effect)	rad
$\bar{\alpha}$	Ray deflection angle (considering combined effect)	rad
α_d	Thermal diffusivity	m ² /s
α_l	Absorbance	–

γ	Solar altitude angle	degree
Γ	Main arm deflection	m
Δ	Change in incidence angle	rad
δ	Deviation angle	rad
δ_s	Declination angle	degree
ε	Emissivity	–
η	Efficiency	–
θ_a	Solar aperture cone-half angle	rad
θ_d	Draft angle of Fresnel prisms	rad
θ_i	Incidence angle	rad
θ_s	Slope angle of Fresnel prisms	rad
θ_t	Refraction angle	rad
λ	Wavelength	nm
ρ	Density	Kg/m ³
ρ_I	Reflectance	–
σ	Stefan-Boltzmann constant (5.67x10 ⁻⁸)	W/m ² .K ⁴
σ_b	Bending stress	Pa
τ_I	Transmittance	–
T_{MA}	Torque for main arm motor	N.m
φ	Solar azimuth angle	degree
ω	Mass per unit length	Kg/m
μ	dynamic viscosity	Pa.s

Subscripts

Symbol	Description
1	Front lens
2	Rear lens
a	Aperture
ab	Absorbed
acc	Accumulated
AP	Azimuth platform
av	Average

<i>B</i>	Beam
<i>c</i>	Centre
<i>cap</i>	Captured
<i>cg</i>	Centre of gravity
<i>CM</i>	Control mirror
<i>con</i>	Conversion
<i>cond</i>	Conduction
<i>conv</i>	Convection
<i>cr</i>	Critical
<i>cw</i>	Counter weight
<i>d</i>	Design
<i>D</i>	Direct
<i>DE</i>	Dispersion equation-based
<i>DL</i>	Dispersion losses
<i>e</i>	edge
<i>eq</i>	equivalent
<i>ex</i>	Experimentally measured
<i>f</i>	Friction
<i>F</i>	Field
<i>FL</i>	Front lens
<i>g</i>	Gained
<i>geom</i>	Geometric
<i>i</i>	Initial
<i>in</i>	Incident
<i>l</i>	Lost
<i>LF</i>	Lens frame
<i>m</i>	Material
<i>max</i>	Maximum
<i>mod</i>	Model
<i>o</i>	Original
<i>op</i>	Optimum
<i>opt</i>	Optical
<i>p</i>	Peak

<i>pp</i>	P-polarised
<i>r</i>	Receiver
<i>rad</i>	Radiation
<i>RL</i>	Rear lens
<i>sp</i>	S-polarised
<i>T</i>	Transmitted
<i>t</i>	Total
<i>th</i>	Thermal
<i>u</i>	Useful
<i>w</i>	Wind
<i>wt</i>	Weight
<i>z</i>	Zenith direction
λ	Spectral

Dimensionless Numbers

Symbol	Description
Nu	Nusselt number
Pr	Prandtl number
Ra	Rayleigh number
Re	Reynolds number

LIST OF PUBLICATIONS

1. **Journal article:** M. Tawfik, X. Tonnellier, C. Sansom, “*Light Source Selection for a Solar Simulator for thermal Applications: A Review*”, Published in **Renewable and Sustainable Energy Reviews**, Vol. 90, 2018 (**Status:** *Published*)
2. **Journal article:** M. Tawfik, X. Tonnellier, C. Sansom, “*Parameters Influencing the Output Precision of a Lens-Lens Beam Generator Solar Concentrator*”, Published in **International Journal of Electrical, Computer, Energetic, Electronic and Communication Engineering**, Vol. 11, No. 4, 2017 (**Status:** *Published*)
3. **Journal article:** M. Tawfik, X. Tonnellier, C. Sansom, “*Design and Evaluation of Fresnel-Based Solar Concentrator with Secondary Lens for Thermal Applications*”, to be submitted to **Applied Energy**. (**Status:** *Under internal revision*)
4. **Conference paper:** M. Tawfik, X. Tonnellier, C. Sansom, “*Numerical Study of Lens Geometry and Material Effects on Allowed Concentration Ratio of a Lens-Lens Beam Generator Solar Concentrator*”, in Proceedings of the 2nd Renewable Energy Sources - Research and Business (RESRB) Conference, June 2017, Wrocław, Poland. (**Status:** *Published*)

1 RESEARCH BACKGROUND

Mankind's increasing demand for energy raised the load on the limited fossil-fuel resources, as they supply more than 80% of the current world energy requirements (Kumar, 2013). This led to a rapid depletion of such non-renewable energy sources besides creating a negative environmental impact due to increasing greenhouse gas emissions levels. With a large power availability in sunlight, ranging from about 500 W/m² at 60°N latitude to 1000 W/m² at the equator measured on a cloudless midsummer's day at noon (Houghton, 2004), solar energy represents a reliable, inexhaustible and renewable energy source (Wilson, 2010).

Concentrated solar thermal power (CSP) systems can achieve higher conversion efficiencies than photovoltaic systems (PV). Although CSP global market has been expanded with an average rate of 40% per year during 2000s (REN21, 2016), more research is required to reduce the cost of CSP systems (Pitchumani, 2014).

1.1 Thermal Power Generation

Thermal power generation is based on using a heat engine which converts heat into mechanical work to drive a generator through a thermodynamic cycle. The working fluid used in such thermodynamic cycles may be gas or steam. In gas power cycles, heat is added to the working medium in a combustion chamber, while it is added through a boiler in steam cycles. The most common gas power cycles are Brayton (gas-turbine) and Stirling cycles, whereas Rankine cycle is the well-known steam power cycle (Çengel and Boles, 2010).

1.1.1 Conventional Vs. Solar Thermal Power Systems

Conventional thermal power systems are fossil-fuelled heat engines that have been used in supplying electric power. On the other hand, in solar thermal power systems case, thermal energy from the sun fuels the heat engines which drive electric power generators.

1.1.2 Power Cycles

a) Gas Power Cycles

In the 19th century, two gas power cycles were patented: Stirling (1816) and Brayton (1872) cycles (Sier, 1995; Cleveland and Morris, 2013). To maximize the output power and efficiency of Stirling engines, they were required to be run at very high temperatures. Consequently, such a requirement restricted Stirling engines development because of poor material properties of that era. In addition, working under such extreme conditions caused unacceptable frequent failures and raised engine explosion possibilities (Finkelstein and Organ, 2001).

On the other hand, the Brayton cycle was improved over decades. The early Brayton engines utilised reciprocating compressors to pressurise the working fluid. Recently, rotary compressors replaced the reciprocating ones. The compressor and turbine shafts became coupled. Therefore, this cycle is also known as the gas-turbine cycle (Balmer, 2011). These cycles are also used as thrust generators in modern aircraft propulsion systems (Dingle and Tooley, 2013). Modern gas-turbine cycles can achieve a thermal efficiency near 60% at a pressure ratio of 40.

However, by the last quarter of the twentieth century, the use of the Stirling cycle has been revived. This was thanks to a modern revolution in metallurgy (De Brey, Rinia and Van Weenen, 1974). It was employed in different applications including submarine propulsion systems (Erickson *et al.*, 2012). On the topic of electric power generation, Stirling engines became the heart of certain CSP systems that utilise parabolic dish concentrating technology. A thermal efficiency of about 20% can be achieved by such heat engines at an operating temperature of 142°C (Minassians, 2007).

b) Steam Cycles

Steam cycles have been utilised since the late 1880s to drive DC generators. At this early stage, coal was used to supply reciprocating piston steam engines with heat. However, these systems could not provide the market with commercial power generation (Flynn, 2003).

By the end of the nineteenth century, water-tube boilers were used to generate steam (Rippon, 1988). In such boilers, compressed water is circulated through tubes which are heated externally. In case of conventional water-tube boilers, hot gases from burning fossil fuels are used as a heat source to generate steam. These boilers are employed in heat engines that undergo Rankine cycles, which typically attained thermal efficiencies ranging from 30–40%. However, modern power plants tend to use heat recovery steam generators to recapture heat exhausted from gas-turbine cycles. This configuration is capable of achieving higher thermal efficiencies in the range of 50–60% (Flynn, 2003).

Steam power cycles can also be driven by the heat from the sun. It can be implemented in different CSP technologies, including: parabolic trough, linear Fresnel reflectors and power tower systems. However, each concentrating technology requires a distinctive design for the boiler (receiver) to handle solar thermal power efficiently. More information about different CSP systems are reviewed later in section 2.1.

1.2 Characteristics of Solar Radiation

1.2.1 Solar Spectrum

Despite the approximation of the sun as a blackbody radiator at a temperature of 5800K (Hu and Ding, 2011), the actual solar spectrum differs from such radiance as a result of the absorption in the cool peripheral solar gas (Fraunhofer lines) (Holweger, 1971; Chance and Spurr, 1997). Moreover, the solar spectrum is affected by passing through the earth's atmosphere as it is attenuated by scattering and absorption due to atmospheric gaseous molecules (Gates, 1966). Therefore, the solar spectrum standard conditions are defined by an Air Mass (AM) coefficient, which represents the ratio of solar radiation path length through the atmosphere, l , the atmosphere thickness in the zenith direction, l_z , and the incident at a zenith angle, z (Wurfel, 2009):

$$AM = \frac{l}{l_z} = \frac{1}{\cos z} \quad (1-1)$$

The air mass is typically expressed with the syntax "AM" followed by its value (Kwok, 2016). Hence the major solar installations and industry centres are located within mid-latitudes, and a zenith angle of 48.19° defines a specific standard AM number for terrestrial solar applications (Rhodes and Stone, 1981). Since the 1970s, AM1.5 has been used as a standard solar irradiance (Gonzalez and Ross, 1980; Bird, Hulstrom and Lewis, 1983; Gueymard, Myers and Emery, 2002). Comparison between different AM values, i.e. AM0, AM1.0 and AM1.5, is shown in Figure 1-1. Although the standard terrestrial solar spectrum (AM1.5) given by (ASTM Standard G173-03, 2012) includes spectral data up to 4000nm, data up to 2500nm is considered as sufficient to describe the incoming solar spectral energy flux (Da, Xuan and Li, 2016; Kumar and Babu, 2017; Kumar, Saboor and Babu, 2017) as they represent 99% of the total incoming solar energy flux. The plotted data in Figure 1-1 illustrates also the major solar spectral regimes: ultraviolet (UV), visible (VIS), and infrared (IR). The VIS-regime starts from 400nm, while the IR-zone is defined to start either from 700nm (Giacomoni, 2007) or from 760nm (Farage, Miller and Maibach, 2010). For PV applications, the typical spectral zone of interest lies in wavelengths between 380 and 1600 nm (Languy *et al.*, 2011), while in CSP applications the VIS and IR are the most desired spectral regime to be considered (Wang *et al.*, 2018).

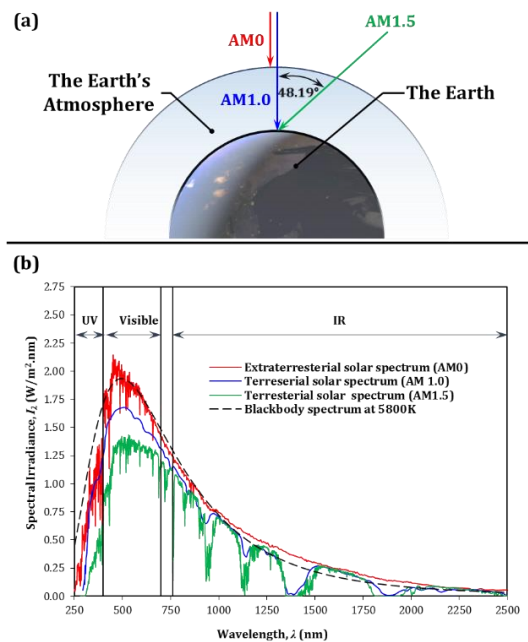


Figure 1-1 Air Mass (AM)

(a) definition (Agrawal and Tiwari, 2010) **(b) comparison between solar spectra;**
AM0 (ASTM Standard E490, 2000), **AM1.0** (2011 ASHRAE Handbook - Heating, Ventilating, and Air-Conditioning Applications. I-P Ed., 2011), **AM1.5** (ASTM Standard G173-03, 2012) and **5800K-black body radiator spectrum** (Masters, 2013)

1.2.2 Solar Angular Aperture

Considering the mean sun–earth distance of 149,597,870 km and the sun and earth diameters of 1,391,608 km and 12,742 km (Emilio *et al.*, 2012), respectively, then sunlight rays are found to be not perfectly collimated. They reach the earth as a cone with an angular aperture of about 9.3 mrad. This means that the solar aperture cone-half angle, θ_a , is 0.266° , as illustrated by Figure 1-2. For more accurate optical analysis of solar concentrating system, the solar angular aperture (SAA) effect must be taken into account, as the concentrated beams diverges with the length of their path (Abbas *et al.*, 2012).

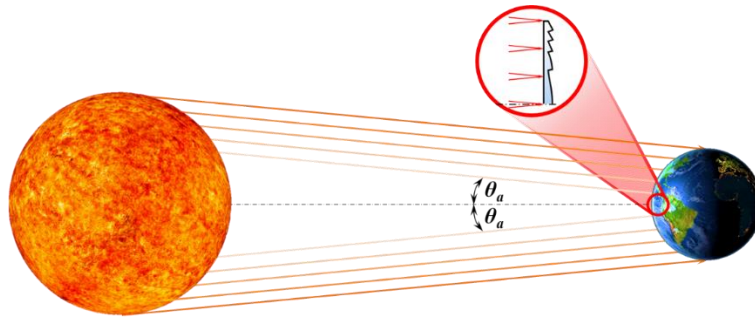


Figure 1-2 Solar angular aperture

1.3 CSP Terminology

To compare different CSP technologies, there are two critical parameters to be defined; concentration ratio (CR) and efficiency.

1.3.1 Concentration Ratio

There are two different definitions of this term; *Optical* and *Geometric* CR. They can be defined as follows (Stine and Harrigan, 1986):

- **Optical CR**

The optical CR, CR_{opt} , is the averaged power flux onto the receiver, I_r , integrated over receiver area, A_r , divided by incident irradiation on the collector aperture, I_{in} :

$$CR_{opt} = \frac{\frac{1}{A_r} \int I_r \cdot dA_r}{I_a} \quad (1-2)$$

- **Geometric CR**

Geometric CR, CR_{geom} , is defined as the ratio of collector aperture area, A_a , to receiver surface area A_r :

$$CR_{geom} \equiv CR = \frac{A_a}{A_r} \quad (1-3)$$

As receiver power flux and aperture insolation are uniform over the entire area, both terms are equal. In the present study, the term CR stands for geometric CR. Furthermore, there is a limit value of CR, known as “ideal CR”, based on collector’s tracking system. CR limit can be determined by the following formulae (Kalogirou, 2004):

$$CR_{ideal} = \frac{1}{\sin \theta_a} \quad (\text{For two – dimensional tracking})$$
$$CR_{ideal} = \frac{1}{(\sin \theta_a)^2} \quad (\text{For three – dimensional tracking})$$

(1-4)

Where, θ_a is the solar aperture cone-half. Then, the ideal CR will be 216 and 46,747 for single- and dual-axis tracking systems, respectively.

1.3.2 Efficiency

Converting solar to thermal energy passes through two stages. Firstly, solar energy passes through an optical element to concentrate its power. Then, it falls onto a thermal receiver where it can be converted into thermal energy. Each stage introduces some losses. The energy flow within a CSP system can be represented as Figure 1-3. It shows the energy amounts and types changes through different conversion stages.

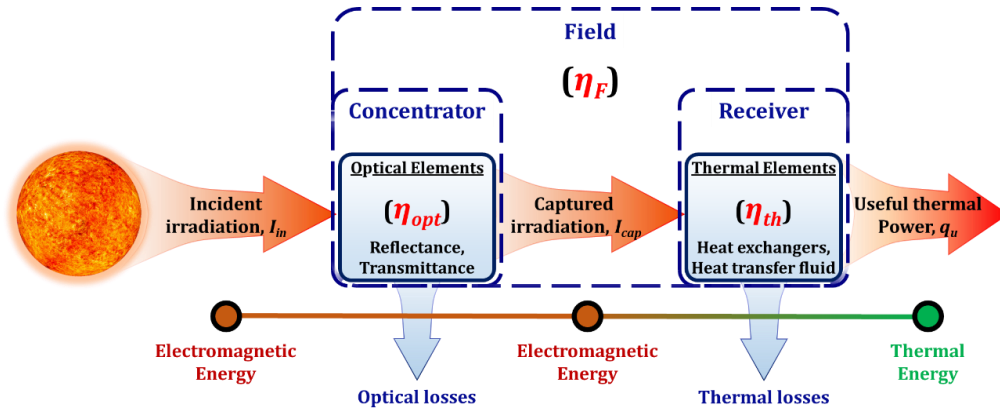


Figure 1-3 Energy flow through a CSP system

Therefore, different definitions of efficiency arise. For the first stage, part of the incident irradiation, I_{in} , can be captured and denoted as I_{cap} , then the ratio of captured to the incident irradiation can be expressed as “optical efficiency” (Collado, 2008), and calculated as follows:

$$\eta_{opt} = \frac{I_{cap}}{I_{in}} \quad (1-5)$$

This efficiency implements optical losses through the concentrator, such as reflectance/transmittance of the concentrator optical elements.

Through the thermal receiver, part of the captured solar irradiation, I_{cap} , can be converted into useful thermal power per unit area, q_u , while the rest is lost in the form of thermal losses. The ratio of the gained thermal power per unit area to the captured solar irradiation is the thermal (receiver) efficiency, which can be expressed as follows (Pacheco *et al.*, 2000):

$$\eta_{th} = \frac{q_u}{I_{cap}} \quad (1-6)$$

Finally, the field efficiency, η_F , can be defined as the product of the optical and thermal efficiencies at a given receiver aperture radius (Mancini, 1991) as:

$$\eta_F = \eta_{opt} \times \eta_{th} = \frac{q_u}{I_{in}} \quad (1-7)$$

In the present study, comparison between different CSP technologies is based on field efficiency definition.

1.4 Solar Simulator Design Motivation

Solar energy researchers require to perform in-field experiments during clear sunny days. Unfortunately, this is a time consuming and weather dependent job. In addition, the whole United Kingdom (UK) is located in a relatively low-DNI region with an average annual direct normal irradiation (DNI) of 400-1000 kWh/m² (Solargis, 2015), as shown in Figure 1-4.

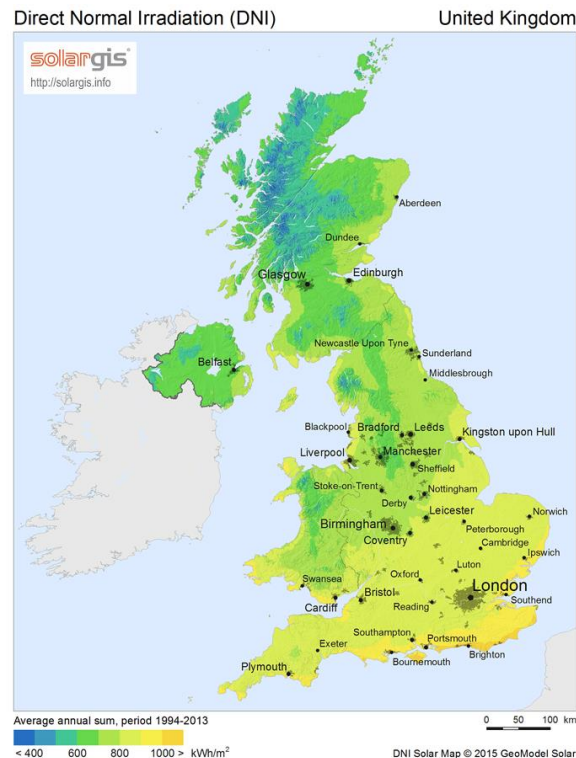


Figure 1-4 Direct Normal Irradiation (DNI) on UK (Solargis, 2015)

This makes it more difficult to carry out outdoors CSP experiments on UK land. Lead researchers travel to good-DNI locations such as North Africa (2400-2800 kWh/m² DNI), which increases the research cost significantly. Therefore, solar simulators were designed and built to ensure fast development of efficient ways to use solar power.

1.5 Thesis Structure

Chapter 1 presents an introduction of thermal power generation and CSP terminology. In addition, it covers different solar radiation characteristics such as solar spectrum and SAA.

Chapter 2 provides a literature review of different CSP technologies. Different transparent materials, simulation software codes and solar simulators have been reviewed within this chapter as well. Fresnel lens manufacturing methods and accompanying losses have been discussed.

Chapter 3 covers the aim and a list of the objectives of this research work, the covered gap of knowledge and the followed methodology have been also addressed in this chapter.

Chapter 4 displays specifications of instruments that are used in experimental study. It also shows the results of preliminary tests needed for further numerical and experimental study within the thesis.

Chapter 5 deals with designing, building and testing a solar simulator device, as an initial objective to be used in further LLBG numerical and experimental study. The design phase covers the main components, including detailed study of the light source as a key component in the system. While the testing phase includes both solar simulator calibration test as well as LLBG tests carried out using the solar simulator testing facility.

Chapter 6 covers the theoretical frame work, numerical study, design and testing of the Fresnel-based LLBG system. This includes manufacturing, optical, cost and thermal studies for determining the optimum front and rear lens geometries and materials. Moreover, an optical analysis of the LLBG system is provided within this chapter. The design and sizing steps to build the full-size LLBG system have been addressed. By the end of this chapter, experiments carried out to evaluate the system performance are described.

Chapter 7 shows the results of work discussed in Chapters 5 and 6. These results include both experimental and numerical results of solar simulator tests and LLBG theoretical study. Optical analysis and evaluation test results of the LLBG system are also displayed in this chapter. Moreover, discussion of obtained data has been addressed.

Chapter 8 discusses the conclusion of the presented work and an outline of the research future work suggestions.

Chapter 9 has a list of all reference cited in this thesis.

The final section of this thesis is the appendices which have all supportive tables for the presented work and results.

1.6 Summary

In this chapter, an introduction to thermal power generation through conventional and solar energy sources was presented. Characteristics of solar radiation, including solar spectrum description and SAA, are covered. In addition, basic CSP terms have been defined and explained, including: CR and efficiency. These definitions distinguished between optical and geometric CR besides showing the differences between field, optical and thermal efficiencies. These nomenclatures are going to be used later and throughout the thesis. Moreover, motivation behind the design of a solar simulator test rig is discussed. Finally, thesis structure is covered by the end of the chapter.

2 LITERATURE REVIEW

2.1 CSP Technology Overview

Concentrating solar power can be achieved either by reflecting or refracting the incident flux onto a smaller receiver/absorber area (Newton, 2007). In this section, the best known concentrating technologies will be reviewed briefly and classified into two main categories; reflection-based and refraction-based concentrators, as shown in Figure 2-1.

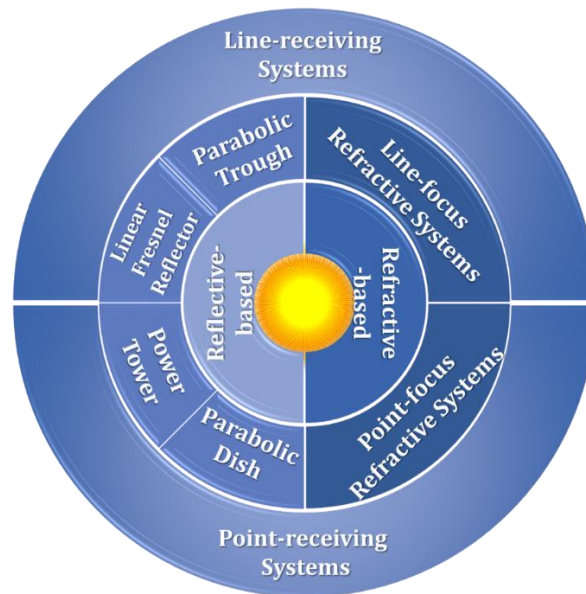


Figure 2-1 Concentrating technologies classification

2.1.1 Reflection-based Concentrators

2.1.1.1 Ancient Reflection-based CSP Systems

The first known use of mirrors for concentrating solar power was three thousand years ago, when the ancient Chinese used bronze burning mirrors, called *yang-sui*, to start fire by concentrating solar rays onto wood (Perlin, 2013), as shown in Figure 2-2.



Figure 2-2 Ancient Chinese bronze solar igniters (Perlin, 2013)

Thousands of years later, in 212 B.C., the Greek inventor Archimedes used mirrors to set fire on Roman ships attacking his city, as engraved in Figure 2-3 (Heath, 2013). By the 11th century, Ibn Al-Haytham, an Arab scholar and pictured in Figure 2-3, elaborated a detailed explanation and mathematical proof of the burning mirrors geometries (Perlin, 2013).

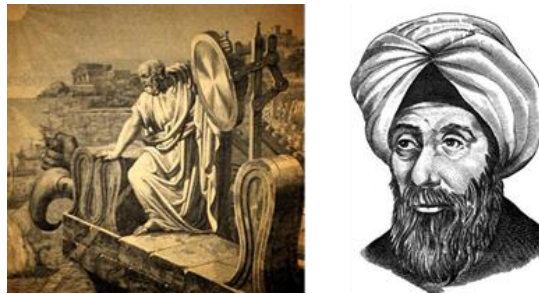


Figure 2-3 Ancient inventors and scholars

On left: Archimedes (287 – 212 B.C.) using a parabolic mirror to make his attack
(Krystek, 2010)

On right: Alhazen (Ibn AL Haytham) [965 – 1040 A.C.] (Gill and Williams, 2018)

By the 19th century, Augustin Mouchot built the first solar motor which was demonstrated at the Universal Exhibition in Paris of 1878, shown in Figure 2-4. It was used in the production of ice from solar power (Walker, 2013).

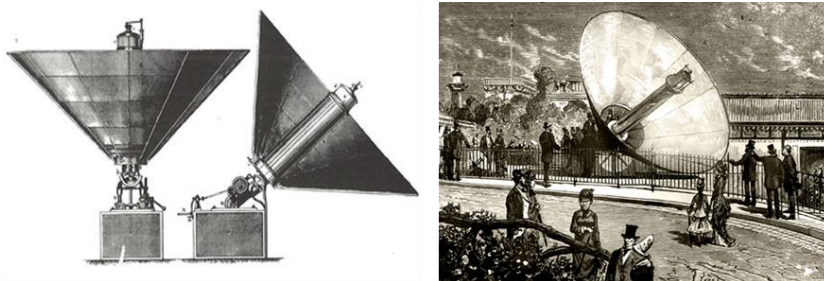


Figure 2-4 Mouchot's solar concentrator
(Land Art Generator, 2018)

Three decades later, in 1912 an American engineer and solar energy pioneer named Frank Shuman built the first practical and commercial solar plant in Maadi, Egypt based on the parabolic trough technology, as shown in Figure 2-5 (Stolten and Scherer, 2013). The plant was used to run steam engines to pump Nile river water with 6,000 gallons/min for irrigation purposes (Seba, 2009). Table 2-9 summarizes the development until the start of the 20th century.

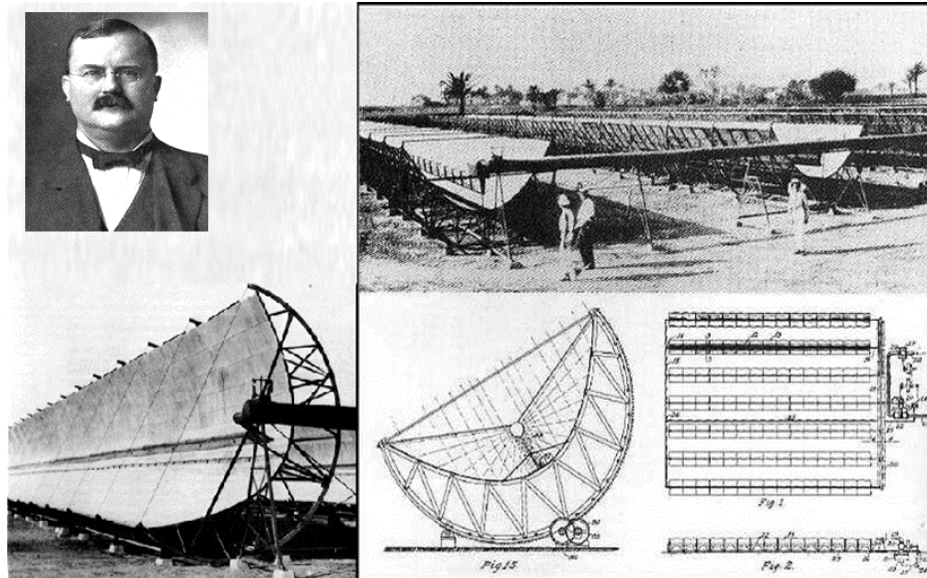


Figure 2-5 Shuman's solar plant in Egypt, Frank Shuman (pictured on top left) (Perlin, 2013)

Table 2-1 Reflection-based concentrators development

Era	Location	Application	Purpose
≈ 10 ³ B.C.	China	To start fire	Domestic
3 rd Century B.C.	Greece	To set fire to Roman ships	Defence
11 th Century A.C.	Egypt	Mathematical proof of mirrors geometries	Research
13 th – 18 th Century A.C.	Europe	Studied mirror geometries laws	Research
19 th Century A.C.	France	The first solar motor, for ice production	Cooling
20 th Century A.C.	Egypt	The first practical and commercial solar plant	Irrigation

2.1.1.2 Modern Reflection-based CSP Systems

Recently, reflection-based concentrators have been used in providing power plants with heat to generate electricity. This category includes concentrators which use mirrors to focus the incident solar power onto a receiver. The target receiver may be a line or a point.

- **Parabolic Trough**

A parabolic trough consists of a parabolic shaped reflective sheet which concentrates solar power onto a metal tube receiver positioned along the reflector's focal line and filled with the working fluid, as shown in Figure 2-6. For such type of concentrators, using a single-axis tracking system is sufficient, as the sun can be tracked from north to south (or east to west) only (Kalogirou, 2004). However, using single-axis tracking results in quite low concentration ratios ranging from 10 to 80 (Sukhatme and Nayak, 2008).

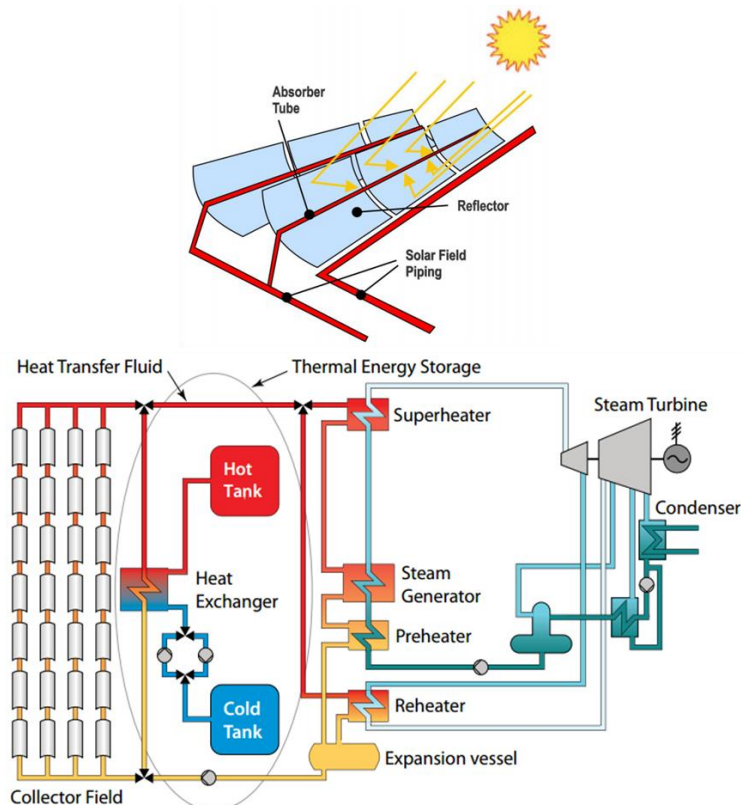


Figure 2-6 Parabolic trough power plant major components
(Chaanaoui, Vaudreuil and Bounahmidi, 2016)

The working fluid, usually oil, can be heated to temperatures between 50 and 400°C (Kalogirou, 2009). Using an oil-based working fluid restricts operating temperatures to 400°C (Sorenson and Breez, 2009). Therefore, (Eck and Zarza, 2006) investigated direct steam generation (DSG) in parabolic trough collectors using a steam cycle operated with saturated steam for the first time. They achieved a maximum thermal efficiency of 66.9%. A few years later, SkyFuel Company presented a new design, called the SkyTrough, in which glass mirror facets were replaced with high-reflectance silverised polymer film and a thermal efficiency of 73% was reported (Forsyth, 2011).

- **Linear Fresnel Reflector**

Linear Fresnel reflector technology is based on the principle of dividing the parabolic reflecting surface into thin segments to obtain an optical effect which is very like that obtained by the original reflecting surface (Günther, 2012). The reflected power is focused on a fixed absorber located at a common focal line of the mirror segments, as illustrated in Figure 2-7.

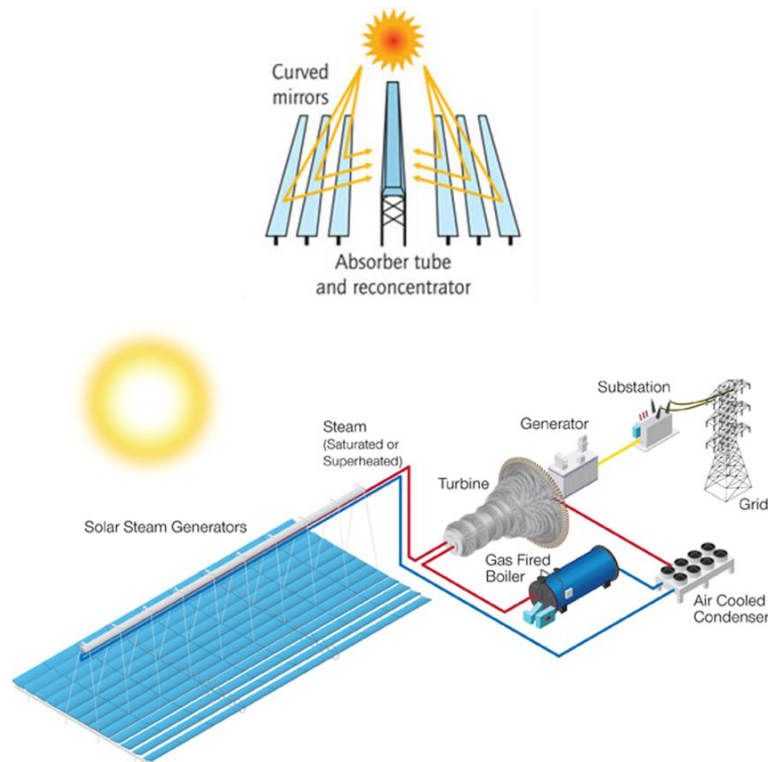


Figure 2-7 Linear Fresnel reflector solar field major components
(CSP-World, 2013; Chaanaoui, Vaudreuil and Bounahmidi, 2016)

This technology has a tracking flexibility advantage compared to parabolic trough technology, as the mirrors have a separate tracking device. This, in turn, leads to lower investment and operation cost than the parabolic trough system. In addition, mirrors are mounted close to the ground which minimizes structural requirements. These advantages have been confirmed by many researchers (Gharbi *et al.*, 2011; Morin *et al.*, 2012; Dostucok, Selbas and Şahin, 2014).

On the other hand, a linear Fresnel reflector system has a disadvantage of lower conversion efficiency, compared to parabolic trough systems (Österholm and Pålsson, 2014). The average efficiency of Fresnel reflector plants range between 18% and 20% with concentration ratios higher than 60 (Gianella, 2012; IRENA, 2012; Kalogirou, 2014). Although the maximum reported efficiency of this technology is 38% for the Puerto Errado 2, according to the operator, this value hasn't been confirmed by independent testing yet (Nixon and Davies, 2012; Candelaria, 2013; Novatec Solar, 2014).

- **Power Tower (Central Receiver Systems)**

In power tower systems, an array of dual-axis tracking heliostats is used to reflect and concentrate solar power onto a tower-mounted central receiver where the working fluid can be heated to a temperature of 500–1000°C (Martin and Goswami, 2005; Kesari *et al.*, 2015), as shown in Figure 2-8. This thermal energy can be converted into electrical energy either directly, throughout power-conversion systems, or indirectly, using energy storage systems. Although power tower technology is less advanced than parabolic trough systems, they produce high concentration ratios, ranging from 300 and 1500, and can minimize requirements for thermal-energy transport (Chu, 2011). This leads to a higher conversion efficiency, ranging from 86 to 88% (Pacheco *et al.*, 2000; Collado, 2008), as the solar power is concentrated directly on a single receiver. (Sorenson and Breez, 2009).

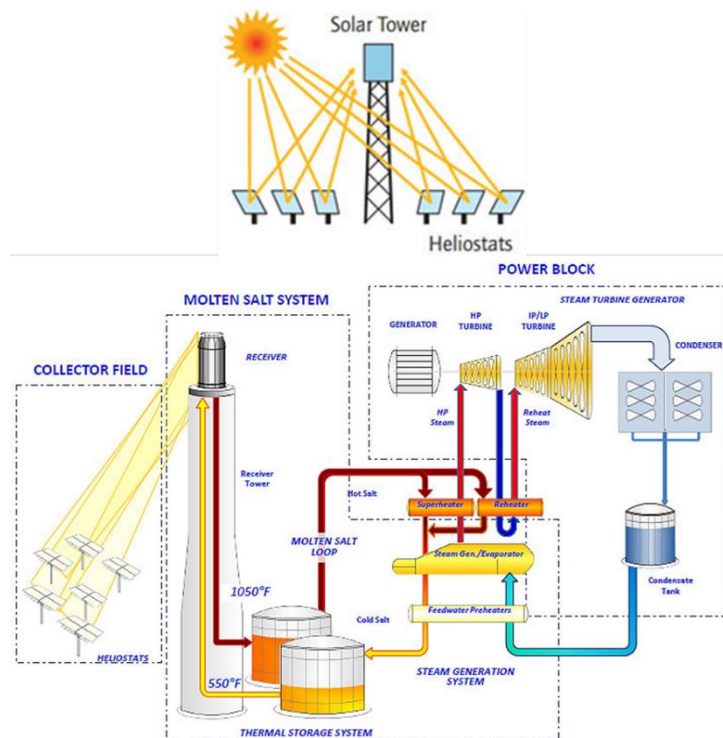


Figure 2-8 Power tower plant major components
(Paul Dvorak, 2009; Chaanaoui, Vaudreuil and Bounahmidi, 2016)

Shading and blocking, due to intercepting a part of the incident or reflected sunlight from a heliostat by another one in the field, are important losses in central receiver systems. Power tower systems show better capability for energy storage compared to parabolic trough and linear Fresnel reflector technologies.

In order to enhance the concentration efficiency of the central receiver system, (Hu, Shen and Yao, 2018) proposed a new sun-tracking and target-aiming method. It consisted of a paraboloidal mirror which uses a dual-axis sun tracking mechanism with a target-aiming device. The target-aiming device utilised a specifically designed lens to collimate the concentrated sun rays from the paraboloidal mirror. The collimated beam is reflected onto the fixed target (solar receiver) through a flat mirror with two degrees of freedom, as illustrated in in Figure 2-9. They constructed an optical model with TracePro software to simulate its concentration performance.

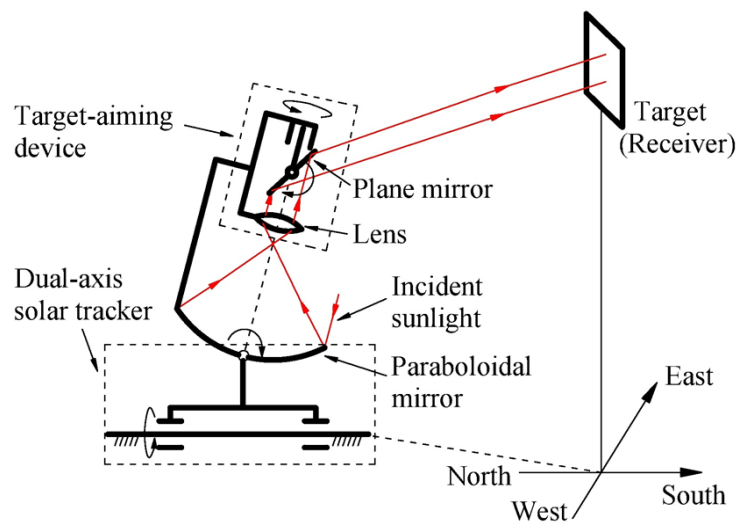


Figure 2-9 Sun-tracking and target-aiming proposed method
(Hu, Shen and Yao, 2018)

- **Parabolic Dish**

A parabolic dish is a point-focus, parabolic-shaped collector which concentrates solar energy onto a receiver located at its focal point, as illustrated in Figure 2-10.

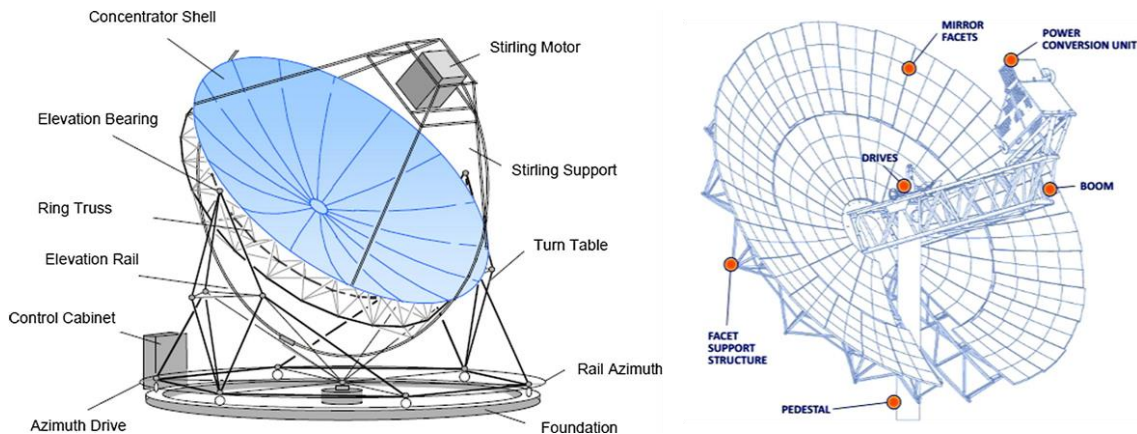


Figure 2-10 Parabolic dish main components
(Hafez *et al.*, 2016)

The thermal energy gained by the working fluid can then either be converted into electricity directly using a Stirling engine coupled with a generator (Martin and Goswami, 2005), or indirectly by piping the working fluid to a central power conversion system.

Such a type of concentrator requires a dual-axis tracking system, leading to achieving high temperatures of 1500°C (Sorenson and Breez, 2009) and high concentration ratios in the range of 600-3000 (Muller-Steinhagen, Tried and Trieb, 2004; Chu, 2011; Kesari *et al.*, 2015). In addition, this system can provide high conversion efficiency which can reach 91.7% as reported by Mancini (Mancini, 1991). However, this system lacks design simplicity because of the need to circulate the working fluid through the collector field.

2.1.2 Refraction-based Concentrators

2.1.2.1 Ancient Refraction-based CSP Systems

Using lenses in concentrating solar power dates back to antiquity. The *burning glasses*, which look like today's magnifying glasses, were known in ancient Greece. They were used by the public to start fire or light lamps. This was before 423 B.C., when the Greek playwright named Aristophanes wrote his play; *The Clouds*, in which the burning glasses were mentioned as a part of the author's knowledge (Perlin, 2013). By the end of the 3rd century B.C., the Greek mathematician and geometer, Diocles, knew about the burning glasses and he proposed to use them in temples (Dickey *et al.*, 2005).

Not only the Greeks used lenses for solar power concentration purposes, but also the Chinese used transparent rock crystals, known as '*fire-pearl*', between the 3rd century B.C. and the 1st century A.C. Fire-pearls were like biconvex lenses and were used for igniting tinder (Needham, 2004). Later, archaeologists proved that the Romans used burning glasses in medicine in the 1st century A.C. They healed their patients with transparent rock crystal balls (Andrews and Jones, 1956). In the 11th century, archaeologists found that the Vikings also used high-quality optical lenses made from crystallized rock (Helden *et al.*, 2010). Six centuries later, the German-Dutch lens maker, called Hans Lippershey, used lenses to

build the earliest version of a refractive telescope in 1608 (Eichler, 2014). One year later, Galileo Galilei and Johannes Kepler used lenses to improve the first refractive telescope designs (King, 2003).

By the eighteenth century, the French used a lens to mark the noon time every day by firing a cannon using focused solar energy (Perlin, 2013). In the same era, burning lenses were used in chemical processes to obtain oxides under elevated temperatures. They were used by Priestley and Lavoisier (Schofield, 2015). Lavoisier used burning glasses to determine melting or combustion points of different metals and minerals (Poirier, Gillispie and Balinski, 1998). He used large burning lenses mounted on a carriage, shown in Figure 2-10, to conduct his combustion experiments with flammable materials (Griffith, 2009). As shown in Figure 2-11, double lens were used in order to render the burning glass focus more efficient (Perlin, 2013).

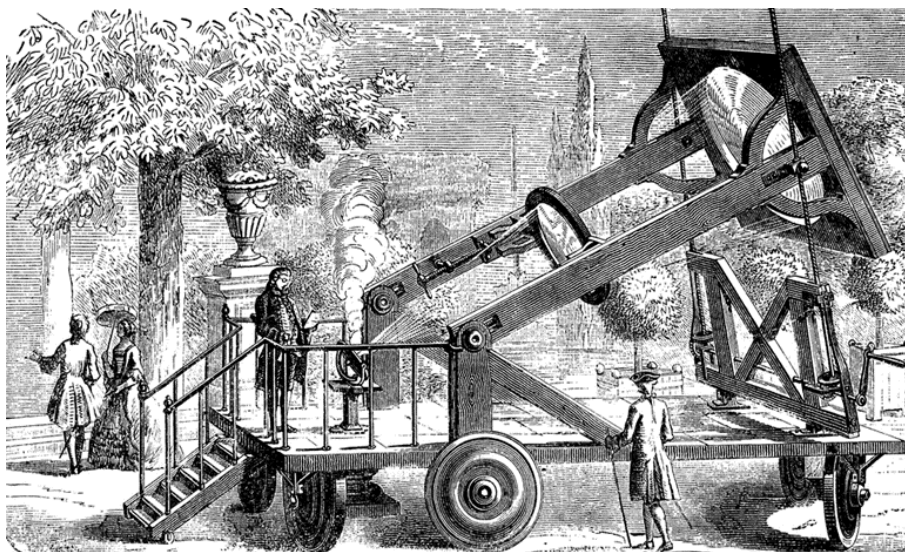


Figure 2-11 Lavoisier combustion experiment in 1770s
(Wikimedia, 2018)

In late of the eighteenth century, an idea of separating conventional lenses into sections mounted in a frame to create thinner, lighter lenses was firstly proposed by Georges-Louis Leclerc, Comte de Buffon (Miller, Vandome and McBrewster, 2010). This idea was carried out by the French physicist and engineer, named Augustin-Jean Fresnel, who developed a multi-part lens to be used for lighthouses. In 1822, the first Fresnel lens was used in the Cordouan lighthouse in France (Bruce, 1999). Fresnel lenses have reduced the amount of material

needed and lens weight compared to conventional lenses. Moreover, Fresnel lenses have produced a revolution in lenses manufacturing in the modern era. They are used in many applications, particularly in non-imaging applications, such as solar concentrators as will be explained in detail in the following section. Table 2-2 provides a summary of refraction-based solar concentrators up until the early 19th century.

Table 2-2 Refraction-based concentrators development

Era	Location	Application	Purpose
Before 3 rd Century B.C.	Greece	To start fire or light lamps	Domestic
3 rd – 1 st Century B.C.	China	To ignite tinder	Domestic
1 st Century A.C.	Europe	To heal patients	Medicine
11 th Century A.C.	Europe	Optical lenses	Medicine
17 th Century A.C.	Europe	Telescope designs	Research
18 th Century A.C.	France	To mark the noon time every day	Domestic
	France	Chemical & physical studies	Research
	UK	Chemical studies	Research
19 th Century A.C.	France	Development of Fresnel lenses	Lighting

2.1.2.2 Modern Refraction-based CSP Systems

Refraction-based concentrators are used nowadays to concentrate solar power either on PV cells to minimize the required area of the cells, or on a thermal absorber to convert solar electromagnetic energy into useful thermal energy for steam generation and cooking purposes. These concentrators represent a promising alternative to conventional reflection-based CSP systems, as they have potential to overcome their techno-commercial limitations. These limitations include installation, life cycle costs, as reflectors contribute 50% of installation total cost in addition to environmental impact and adverse service conditions that degrade such reflectors early, reducing their life cycle as well as system efficiency (Kumar, Shrivastava and Untawale, 2015).

Refraction-based concentrators are almost used in concentrated PV (CPV) systems. The largest solar power plant operated, since 2013, by lens-based concentrators is the Golmud 2 plant in the Qinghai, China, with 79.83 MW capacity (Kalogirou, 2018), shown in Figure 2-12.

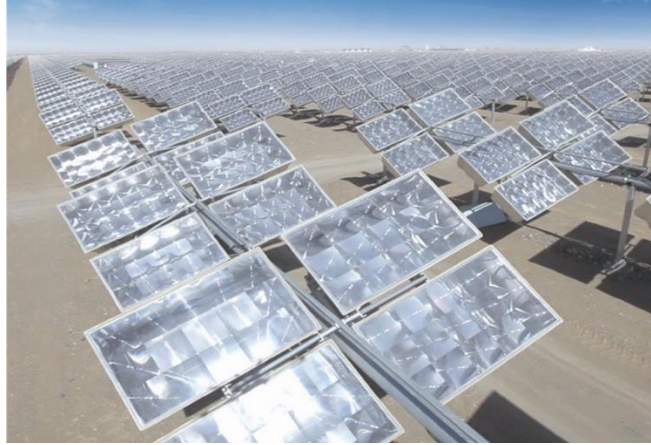


Figure 2-12 Golmud 2 plant, Qinghai, China
(The largest CPV plant since 2013) (CPV Consortium, 2018)

However, using lens-based solar concentrators for thermal purposes is still in the research phase, and there is no full-scale thermal power plant that is operated by lens concentrators (El-ladan *et al.*, 2013). In the following subsections, different techniques used in concentrating solar power will be reviewed.

- ***Line-focus refractive systems***

The line-focus refractive systems use linear lenses to convert the collimated solar rays into a line at its focal plane (Nelson, Evans and Bansal, 1975). Such a type of concentrator has an advantage of low tracking requirements, as only single-axis tracking is required (Tabor and Zeimer, 1962).

By the end of 1970s, using linear Fresnel lenses in concentrating solar power with high concentration ratios, near the ultimate limit of concentration ratio, was proposed by (Kritchman, Friesem and Yekutieli, 1979). In their work, the lens was designed with its smooth side up towards the sun. Although this position causes relatively high surface reflection losses and large off-axis aberrations, they used it to overcome the blocking effect, which reduces lens transmittance because of ineffective facet of the grooves, and to avoid dust accumulation on the grooves. Comparing their work with the ideal reflector, linear Fresnel lenses showed greater reliability and lower cost.

During the period between 1988 and 1993, researchers, (Piszczor *et al.*, 1987; O'Neill and Piszczor, 1988; O'Neill *et al.*, 1991; O'Neill and McDanal, 1993; Piszczor, O'Neill and Fraas, 1993), paid attention to study the enhanced PV

efficiency for space purposes using acrylic linear Fresnel lens concentrators. According to these studies, Fresnel lenses raised the PV efficiencies up to 29.3%.

For the subject of power generation using PV with linear Fresnel lens concentrators, the lenses are usually placed with the smooth surface upward and facing the sun while the Fresnel facets face the PV cells to protect the grooves from abrasion. Most Fresnel lens concentrators are made from acrylic due to its good transmittance, reliability and abrasion resistance (Johansson *et al.*, 1993).

Table 2-3 summarizes some of these projects.

Table 2-3 CPV power plants using linear Fresnel lenses

Project	Year	Location	Rated Power (kW)	CR	System Efficiency (%)	Reference
DFW Int'l Airport	1982	USA	24	25	?	(Johansson <i>et al.</i> , 1993)
Sandia National Labs	1985	USA	10	?	?	(O'Neill <i>et al.</i> , 2011)
ENTECH-3M Austin System	1989	USA	300	22	?	(Boes, 1990)
Pacific Gas & Electric Company	1991	USA	20	?	?	(Forn, 2009)
Commercial – Module Kits	1992	South Africa	40	?	?	(Forn, 2009)
Northern States Power Company	1995	USA	0.8	?	?	(O'Neill <i>et al.</i> , 2011)
Entech Inc	1995	USA	100	20	15	(O'Neill and McDanal, 1994)
NASA	1996	USA	2.4	?	?	(Forn, 2009)
Photovoltaics International, LLC	?	USA	30	10	12.7	(Muhammad-Sukki <i>et al.</i> , 2010)
Entech	?	?	0.52	20	?	(Forn, 2009)
NASA	2003	USA	1.3	?	?	(George <i>et al.</i> , 2004)

? = Unknown value

However, linear Fresnel lenses have also been investigated for heat generation. In 1979, (Collares-Pereira, 1979) designed and tested a non-evacuated collector with a linear Fresnel lens and a compound parabolic concentrator (CPC) as a second stage concentrator. A Fresnel lens was used to allow a height-to-aperture ratio close to 1. In addition, it protected the collector and played the role of a cover. They reached a concentration ratio of 15.56 and achieved 48% efficiency.

Several solar collectors with glass flat linear Fresnel lenses (FLFL) were built and their performance was tested by (Franc *et al.*, 1986), as shown in Figure 2-13. Their results showed that the collector efficiency varied between 61% and 69%, with collector exit temperature of 87°C. They also found that, in some cases, the thermal efficiency of the collector was higher than the lens optical efficiency. They attributed this to the greenhouse effect in the collector boxes.

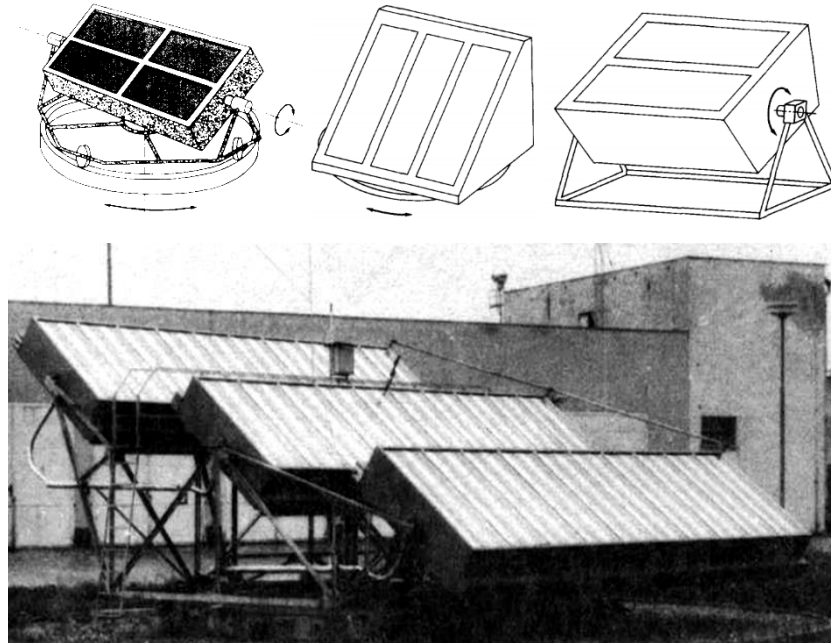


Figure 2-13 Different FLFL collector mountings
(Franc *et al.*, 1986)

By the end of the 1990s, (Al-Jumaily and Al-Kaysi, 1998) studied the thermal and optical losses of a solar collector which consisted of two FLFL and two absorbers connected in series. Their collector tracked the sun in two directions. An all-day collector efficiency of 58% was achieved with an outlet temperature of 37°C.

An optimum convex shaped Fresnel lens was designed by (Leutz *et al.*, 1999). The principle of the edge ray was followed in their design. The lens was used to concentrate solar energy on an evacuated tube to generate thermal energy for driving sorption cycles and providing heat for industrial processes. Leutz's group manufactured and tested a prototype of a linear Fresnel lens. They measured the radiation flux and concentration ratio and concluded that if the lens is convex shaped, then the outer surface must be smooth.

An experimental investigation of a concentrating solar collector based on FLFL was carried out by (Zhai *et al.*, 2010). The Fresnel lens grooves were placed downwards, facing the absorber tube. They observed a thermal efficiency of 52.1%, with an enhancement of 9% compared to the conventional evacuated tube collector, while the heat transfer fluid temperature (water) reached 90°C. The optical losses influenced the results significantly, with nearly 40% loss.

Moreover, (Soriga and Neaga, 2012) analysed a linear Fresnel lens solar collector with evacuated tubes in a cavity receiver. The smooth surface of the lens faced the sun. They achieved a maximum collector efficiency of 72.6% compared with 70.2% for the CPC at the same condition with the same receiver type.

- **Point-focus refractive systems**

The point-focus refractive systems use lenses to focus the solar beam into a point, where a PV cell can be located or a thermal absorber to convert solar energy into electrical or thermal energies. Point focus systems can also be utilised in transmission of sunlight for lighting purposes. Although such a type of concentrator suffers from complexity due to the requirement of dual-axis tracking, it has an advantage of achieving high concentration ratios which may exceed 1000 (Kurtz, 2012).

For the CPV field, an advanced CPV system was reported by (Piszczor *et al.*, 1987). It was designed for space applications and a dome-shaped Fresnel lens was used for solar radiation concentration, shown in Figure 2-14. They succeeded in eliminating metallisation losses as well as reducing the required area of the PV cells dramatically.

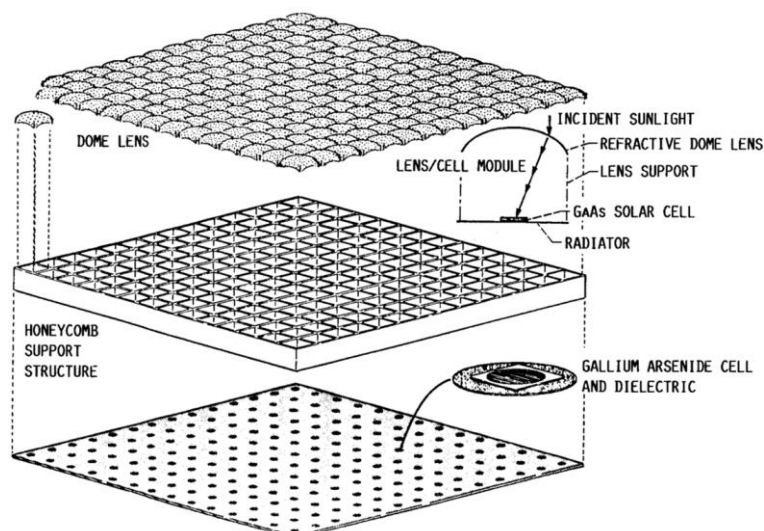


Figure 2-14 Piszczor's group CPV refractive system and components
(Piszczor et al., 1987)

As for space applications, exposure of photocells to high energy ionic, atomic and subatomic particles is responsible for continuous degradation of PV efficiency. Therefore (Nakamura, 1992) proposed a system to be used for power generation on spacecraft through conducting concentrated solar power to PV system in a protected enclosure to shield it from destructive radiation and particulate matter. The optical transmission means was a bundle of optical fibre waveguides whose input ends placed at the focal point of a reflective/refractive optical element used in concentrating solar radiation, as shown in Figure 2-15.

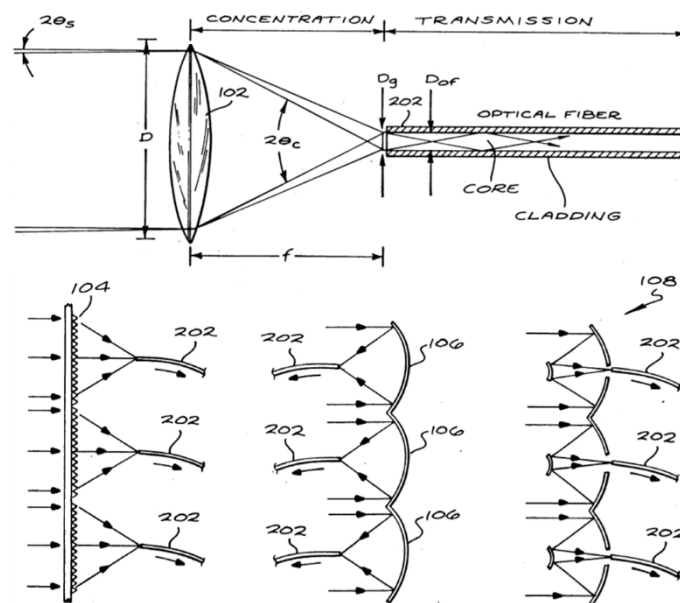


Figure 2-15 Proposed light-transmission system for CPV on spacecraft (Nakamura, 1992)

Optical fibres are again discussed as a means of transmission concentrated solar energy by (Jaramillo, Río and Huelsz, 1999). They developed a theoretical thermal study of a system in which an optical fibre tip is proposed to be positioned at the focus of a small paraboloidal mirror. Their calculations were based on using wavelength-dependent attenuation to study the ability of a 5-mm SiO₂ optical fibre to transmit 26 W of concentrated power for 10m.

By investigating the spectral solar flux through the optical fibre, (Jaramillo, Río and Huelsz, 1999) found that by the end of the transmission length the spectral solar flux is filtered by the optical fibre core, with a total optical efficiency of 85%. Through the first 0.5m of the transmission line, the core centre temperature is

found to reach the critical value of 400°C within 5 to 6 hours of transmission, while the cladding temperature did not reach 300°C.

Using two-stage refractive solar concentration systems has become more attractive for non-imaging concentrating system (Yeh, 2016). Using a second-stage optical element became a good candidate to build low-cost CPV systems (Fathabadi, 2016).

In 2000, (Terao *et al.*, 2000) designed and tested a novel flat-plate concentrator PV system to achieve a light-weight and low-cost PV module. They used a two-stage concentrating system. In the primary stage, an aspheric and TIR (Total Internal Reflection) lens was used, while a secondary conventional lens was used in the secondary stage, as shown in Figure 2-16. The use of the TIR lens in the primary stage helped in reducing the module thickness because of the focal length reduction.

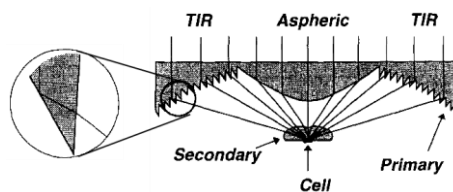


Figure 2-16 TIR lens-concentrator details
(Terao *et al.*, 2000)

Solar thermophotovoltaic (STPV) using a two-stage refraction system was developed and proposed by (Andreev *et al.*, 2006, 2007). In the primary stage, they used a commercially available Fresnel lens made of polymethyl methacrylate (PMMA), while the second-stage lens was a quartz meniscus lens, as illustrated in Figure 2-17. They achieved a concentration ratio of about 4000 and the emitter temperature was between 1100 to 1700°C. Their design was cost effective. Their module efficiency ranged between 19 and 20%, according to the emitter type, which is near the maximum theoretical efficiency of 22%. This high efficiency is attributed the high concentration ratio achieved.

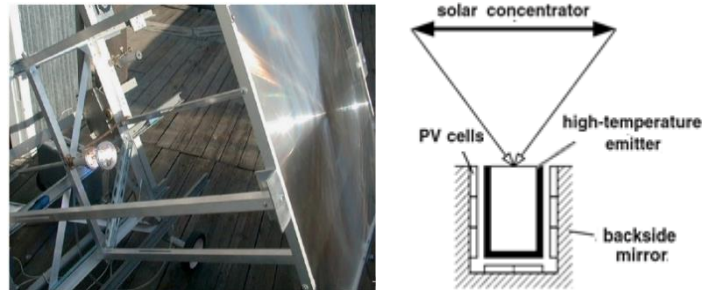


Figure 2-17 Andreev's group two-stage refractive system main components
(Andreev *et al.*, 2006, 2007)

Another two-stage concentrating system for CPV applications was presented and analysed later by (Huang and Xu, 2017). Their system consisted of a Fresnel lens as the first-stage optical element, followed by a ball lens as secondary optical element with a CR of 625, as schematically represented in Figure 2-18.

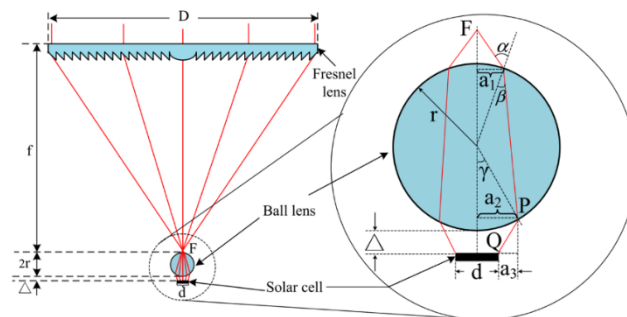


Figure 2-18 Schematic of concentrating optical system with ball lens
(Huang and Xu, 2017)

In their experimental system, the ball lens was coated with an anti-reflection layer and a solar cell with an efficiency of 40% was utilised. Their test results indicated that an electric power generation efficiency of 30.3% can be obtained with an acceptance angle of 0.72° for their proposed CPV system.

In order to expand the use of CPV technology, an in-house built compact CPV-Hydrogen system for the rooftop application in the urban regions was introduced by (Burhan, Shahzad and Ng, 2018). The developed system is a two-stage concentrating system which collimates the concentrated solar rays through an arrangement of convex–concave lenses, sharing same focal point. The convex lens concentrated the incident solar rays at its focal point, then the concave lens collimates these converging rays. Such collimated concentrated beam is then oriented to the centre of PV array, as illustrated in Figure 2-19. Then, the PV output power is used in electrolytic hydrogen production from water splitting.

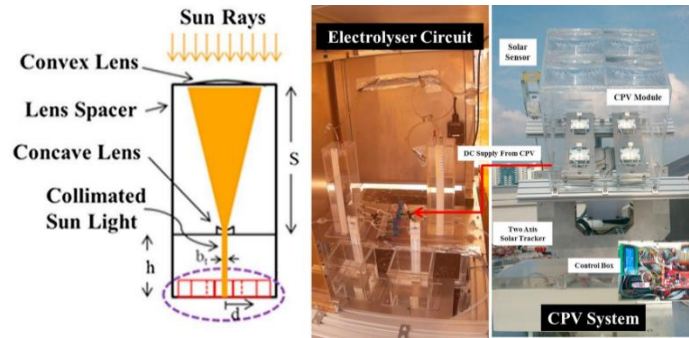


Figure 2-19 Compact CPV-hydrogen system for rooftop operation
(Burhan, Shahzad and Ng, 2018)

They have recorded a maximum sunlight-to-hydrogen efficiency of 18%, with a daily average efficiency of 15%. They found that in tropical regions, CPV systems have superior performance compared to conventional PV system.

Point-focus refractive systems are also used for thermal applications. A dome-shaped Fresnel lens, with short focal length and CR of 1500, was suggested and theoretically analysed by (O'Neill, 1984) for solar thermal energy applications, as illustrated in Figure 2-20. According to their analysis, the collector efficiency can achieve about 70% at a receiver operating temperature of 815°C.

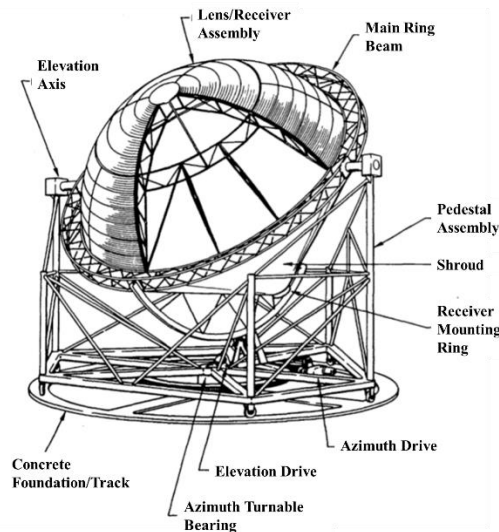


Figure 2-20 O'Neill's proposed point focus system and components
(O'Neill, 1984)

Recently, attention has been paid to the theoretical and experimental study of solar concentrators which implement point-focus lenses for thermal applications. A point-focus with a two-stage refraction concentrating system was introduced by (Salem, Tawfik and Hamed, 2010). They used double bi-convex lenses aligned with common focal points to generate a concentrated, nearly collimated solar

beam. It was called a lens-lens beam generator (LLBG). They achieved an experimental thermal efficiency of 82.65% at a concentration ratio of 6.25. Later, (Tawfik and Salem, 2014) carried out further investigations on the LLBG. They studied some parameters which affect the maximum allowed concentration ratio of the LLBG under different operating conditions. They assumed the melting point of the second-stage lens as its failure temperature. Based on their study, the rear lens should be intensively studied to select an appropriate shape, material and cooling mechanism.

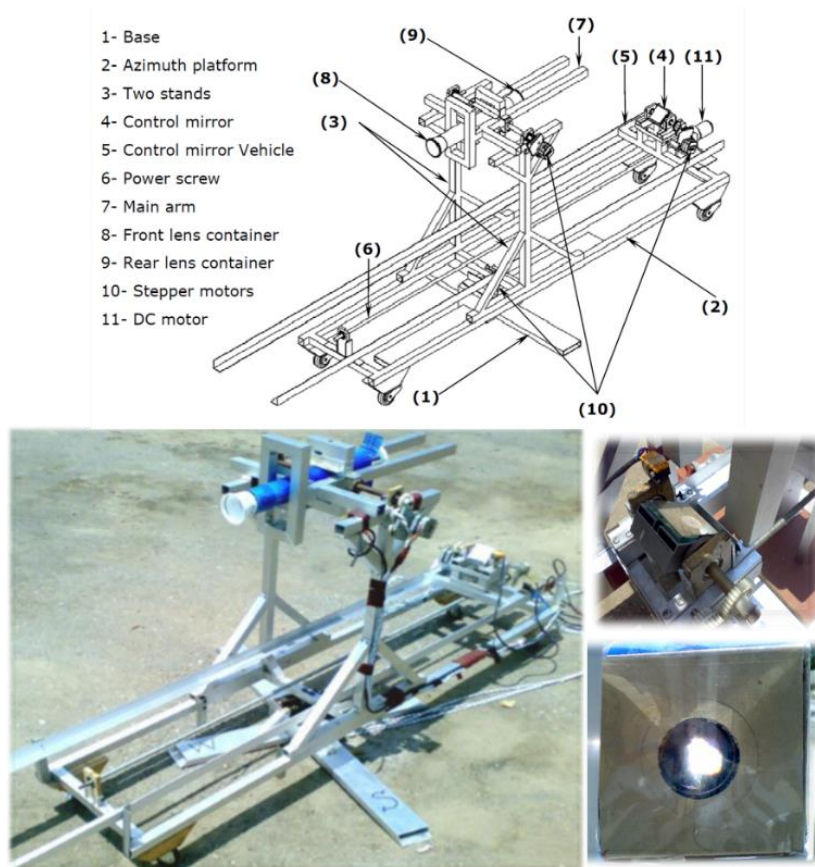


Figure 2-21 LLBG proposed point focus system
 (Salem, Tawfik and Hamed, 2010)

A cost-effective solar concentrator was designed and produced by (Xie, Dai and Wang, 2011, 2012). It consisted of a point-focus rectangular PMMA Fresnel lens which was used to concentrate solar power onto a cavity receiver, as shown in Figure 2-22. A synthetic heat transfer oil was used as a heat transfer fluid (HTF). They achieved a field efficiency of 86.6% at a HTF working temperature of 150°C at a concentration ratio of about 1148.



Figure 2-22 Xie's group point-focus Fresnel lens solar concentrator test rig
(Xie, Dai and Wang, 2012)

For the application of sunlight transmission for lighting applications, optical fibres were often used. A two-stage refractive system was proposed by (Han *et al.*, 2007; Han, Y., Dai, Y., and Wang, 2009). They investigated concentrated sunlight transmission through optical fibres for natural lighting and solar energy conversion, aiming to reduce solar concentrator cost. They used Fresnel lenses in both stages, as shown in Figure 2-23. The lenses were made of PMMA and BK7 glass materials and achieved a concentration ratio of 1000.

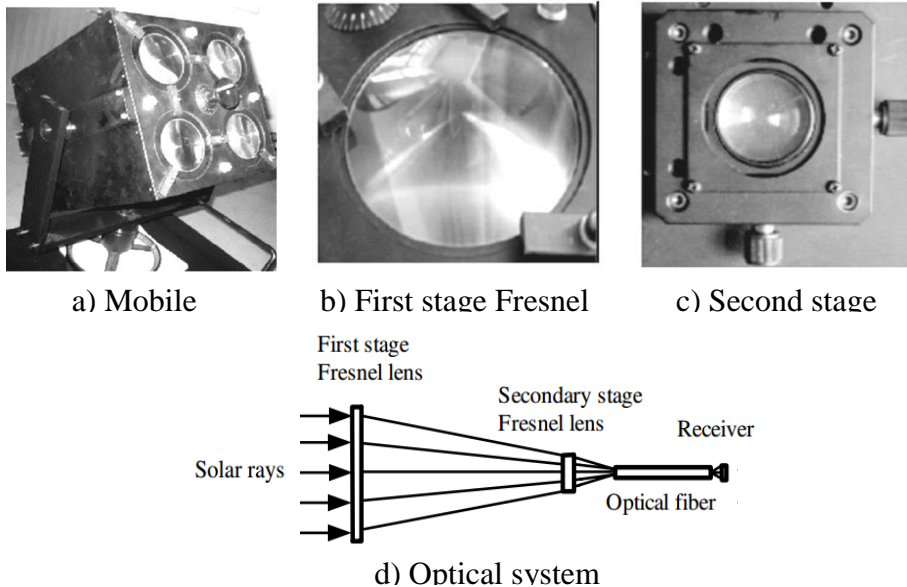


Figure 2-23 Han's group two-stage refractive system and components
(Han et al., 2007; Han, Y., Dai, Y., and Wang, 2009)

They found that the use of two lenses improved the system optical efficiency rather than using conventional thick lenses. Furthermore, they compared the performance of their design with other two-stage reflective designs. They

concluded that the optical efficiency of the reflective design is higher than refraction design, but on the other hand, using refraction concentrating systems required lower solar tracking accuracy than other reflection schemes.

A modified optical fibre daylighting system for indoor lighting was designed, optically simulated and experimentally investigated by (Vu, Pham and Shin, 2016). Their proposed system consisted of concentration, collimation, and distribution sub-systems. In the concentration sub-system, a Fresnel lens is coupled with a large-core plastic optical fibre, then the transmitted sunlight is collimated by the collimator part, which is a combination of a parabolic mirror and a convex lens. The distribution sub-system uniformly diffuses the guided collimated rays at the destination, as illustrated by Figure 2-24.

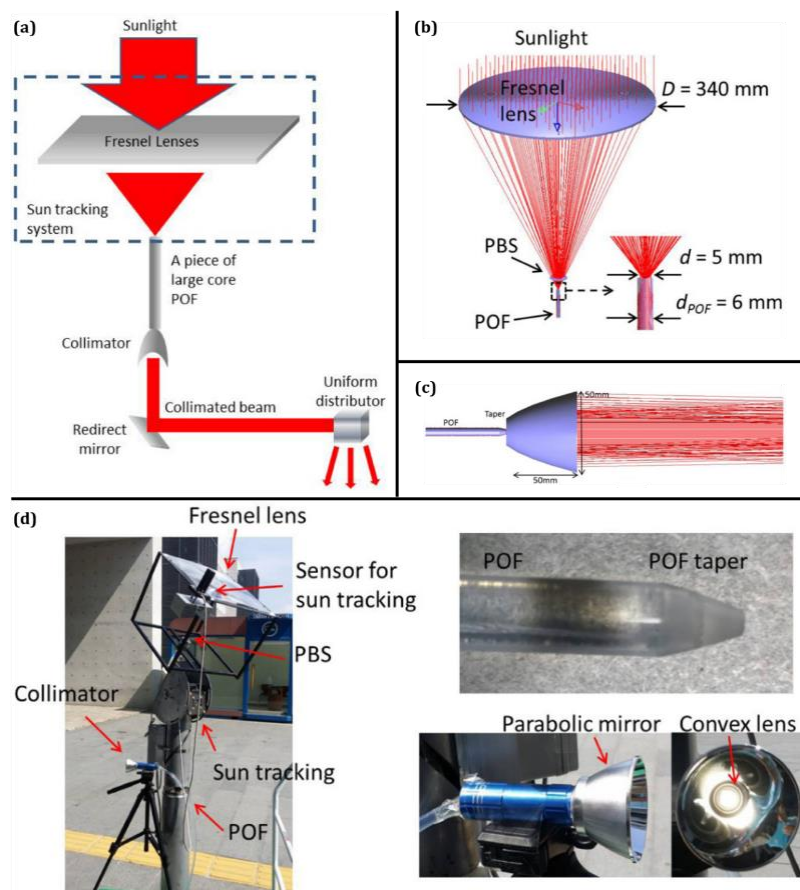


Figure 2-24 Vu's group proposed modified optical fibre daylighting system
(a) schematic diagram of the proposed system
(b) layout of the concentration part **(c) illustration of the collimator structure**
(d) prototype used in outdoor testing
 (Vu, Pham and Shin, 2016)

The simulation of their designed system demonstrated a maximum optical efficiency of 71% and indicated that it could transmit sunlight illumination to a destination at distance of 30m. Their results showed that using optical fibre daylighting system can be a strong candidate for cheap and highly efficient application of solar energy in buildings. Therefore, more research was carried out later on building daylighting systems either through refractive-based systems (Lighting, 2017; Pham, Vu and Shin, 2017) or reflective-based ones (Chong *et al.*, 2017; Song *et al.*, 2018).

A comparison between different solar power concentrating techniques is presented in Table 2-4.

Table 2-4 CSP technologies comparison

	Parabolic Trough	Linear Fresnel Mirror	Power Tower	Parabolic Dish	Line-focus refractive systems	Point-focus refractive systems
Concentration method	Reflection				Refraction	
Focus pattern	Line		Point	Line	Point	
Tracking axes	Single-axis		Dual-axes	Single-axis	Two-axes	
Working fluid temperature [°C]	50 – 400	500 – 1000	250 – 700	90	150	
Maximum reported thermal efficiency	73%	38%	88%	91.7%	69%	86.6%
CR range	10 – 80	> 60	300 – 1500	600 – 3000	80 – 200	500 – 4000
Advantages and disadvantages	Low operating cost	✓			✓	✓
	High conversion efficiency			✓	✓	✓
	Tracking simplicity	✓	✓			✓
	Achieving high CR capability			✓	✓	✓
	Energy storage capability			✓		✓
	Minimised thermal energy transport requirement			✓	✓	✓
	Land use intensity	✓	✓			✓

2.2 Review of Simulation Software

Conservation laws of mass, momentum, and energy are represented by a system of partial differential equations (PDEs) which are known as the “*governing equations*”. Therefore, numerical simulating software was developed to solve governing equations (GE) by replacing such PDE systems with a set of algebraic equations, so that they can be solved digitally using computers. This aim can be achieved through applying numerical methods, which require using discretisation techniques (Ferziger and Perić, 2002). In this section, a brief description of

different discretisation techniques will be introduced, then a subset of simulating software, which are used in the field of CSP, will be described.

2.2.1 Discretisation Techniques

There are several discretisation methods that can be applied, including: finite difference method (FDM), finite volume method (FVM), finite element method (FEM), spectral element method, and boundary element method and high-resolution discretisation schemes. However, the most popular discretisation techniques in use for the available commercial simulating software, which will be covered in this section, are FDM, FVM and FEM.

2.2.1.1 Finite Difference Method (FDM)

FDM is a numerical method that is used to replace PDEs, which are set in their differential forms, with a series of linear algebraic equations. In this replacement process, Taylor series expansion is usually used. Although FDM is simple in programming, it is used in few specialized codes. This may be attributed to its low accuracy when used in computer programming as well as dealing with complex geometry domains, as a result of round-off and truncation errors (LeVeque, 2007).

2.2.1.2 Finite Volume Method (FVM)

FVM is a popular numerical method that is used in approximating the integral form of PDEs. In this method, the domain is divided into a finite number of contiguous control volumes/cells. The centroid of each control volume/cell represents the computational node location. The solution is obtained through the integration of the PDEs over each control volume/cell. An advantage of the FVM, compared to the FDM, is its flexibility in meshing and solving irregular-shaped geometries with reduced geometric errors. In addition, FVM allows increasing resolution at particular regions of interest by redefining the mesh at such locations (Causon, Mingham and Qian, 2011). Moreover, FVM has the advantage of low memory usage and high speed solution speed, especially for large problems, when compared with FEM (Patankar, 1980).

2.2.1.3 Finite Element Method (FEM)

FEM is one of the numerical methods that is widely used in solving PDEs. It minimises errors in solutions by dividing the problem domain into a finite number of small parts, known as “*finite elements*”. FEM is based on multiplying the PDEs integral forms by a weight function, as it is based on Galerkin's method of weighted residuals, which then are integrated over each element. Although FEM is more complex, requires more memory and has slower solution speeds than FVM, it is more stable than the FVM (Surana *et al.*, 2007). In addition, FEM requires no more effort to deal with complex irregular-shaped geometries.

Table 2-5 summarises some of critical points characterising the discretisation methods mentioned above in a comparative form.

Table 2-5 Discretisation techniques comparison

		Discretisation Techniques		
		FDM	FVM	FEM
GE form		Differential	Integral	Integral * Weight function
Domain divisions		Grid	Finite number of control volumes/cells	Finite number of elements
Solving approach		PDEs → Set of linear algebraic equation (equation per grid node)	PDEs integrated over each control volume/cell	PDEs integrated over each element
Advantages and disadvantages	Complexity	Simplest	More complex	The most complex
	Domain geometry shape	Fits regular-shaped geometry	Requires more effort for irregular geometries	Suitable for any shaped geometry
	Stability & convergence	Low	Moderate	Maximum
	Computer memory requirement	Low	Moderate	Maximum
	Solving speed	Fastest	Fast	Slow

2.2.2 CSP Simulating Software Overview

A summarized overview of software tools that can be used in the analysis of different CSP technologies, including; optical design, HTF transport and thermal analysis, will be presented below.

2.2.2.1 Optical Design Software

In this section, different software used for optical simulation and design purposes which have been implemented in various optical applications will be briefly reviewed.

- **ASAB**

ASAB is a commercial software package that is used in rendering geometry, ray tracing and performing optical simulations of various systems. In addition, it can be used in optimization of optical systems. Its interface can import geometry from SolidWorks, while it is planned to be integrated directly within SolidWorks interface (Ho, 2008).

- **ATMOS**

ATMOS is a powerful, free software with a user-friendly interface which is used in designing telescopes. It allows its users to analyse, design and optimize different optical systems as well as being capable of performing Spot Diagrams for many wavelengths at the same time (Riccardi, 2016).

- **Biomimetic**

This is a software package that is used for heliostat field layout optimization based on a biomimetic pattern. It can perform annual average optical efficiencies calculations as well as determining different losses, including cosine, shading and blocking losses. In addition, it can calculate aberration atmospheric attenuation (Bode and Gauché, 2012).

- **CIRCE**

CIRCE is a computer software package which was developed by Sandia National Laboratories for the analysis of point-focus dish collector systems. In addition, it can be used in analysing the optics of parabolic trough and linear reflecting systems. The code was an improvement of the HELIOS software, which is used in evaluating solar flux density for heliostats fields. Its developers used statistical methods in estimating the directional distribution of reflected rays from various reflectors geometries, including: spherical, parabolic, flat, continuous and faceted shaped-reflectors. Moreover, CIRCE can model the angular distribution of the solar incident rays. It can also implement different reflector imperfections such as surface roughness and slope error as well as the impact of structural deformation caused by gravity and wind (Romero, 1994).

- **COMSOL**

COMSOL software is a Multiphysics simulation platform which applies FEM for modelling physics-based problems. It provides various modules allowing simulation of dedicated physics interfaces for electrical, mechanical, fluid flow, etc. One of its novel implemented modules is the Ray Optics Module, which can model electromagnetic wave propagation in systems where the wavelength is much smaller than the smallest geometric detail in the model. In this module, the electromagnetic waves are considered as rays propagating through homogeneous or graded media. To reduce computational cost, the module computations are based on the ray trajectories method, not the FEM.

- **CyberRay**

This optical simulation package can model various kinds of optical elements in arbitrary orientations. It is based on a photon kinetic model of light beams. It provides flexibility of positioning three dimensional optical elements. Its model implements dispersion and geometric aberrations (Informer Technologies, 2018).

- **DELSOL**

DELSOL is a software package which can design and predict the optical performance of a heliostat field in central receiver systems. Besides having optical simulating tools, it has an economic model tool allowing optimisation of field layout based on energy costs (Bode and Gauché, 2012). On the side of optical simulation, it considers insolation variations and atmospheric attenuation and different optical losses including: cosine effect, receiver reflectivity, shading and blocking (Falcone, 1986; Kistler, 1986).

- **HELIOS**

HELIOS is a software package which uses cone optics in evaluating the solar flux density for heliostats fields. It was improved to allow evaluation of other collector shapes, such as parabolic trough and dish, through the CIRCE software. HELIOS considers earth orbit eccentricity, atmospheric scattering, incident solar ray's angular distribution, error distributions in the surface curvature, aiming, and facet

orientation. In addition it calculates the shadowing and blocking losses in the central receiver field (Ho, 2008).

- **HFLCAL**

HFLCAL was developed for performing the calculation of the annual plant output at a given configuration as well as the optimization of the total heliostat field layout. To minimise the required computation times, HFLCAL is based on using a simplified mathematical concentrator optics model to simulate the reflected image of each heliostat rather than using ray tracing techniques. It provides automatic multi-aiming, secondary concentrator optics, tower reflector systems, various receiver models and the ability of least-cost optimization (Schmitz, Pitz-Paal and Schwarzbözl, 2009).

- **HFLD**

This is a MATLAB code which is developed for the design of a central receiver heliostat field layout, as HFLD stands for Heliostat Field Layout Design. It is based on the edge ray principal of non-imaging optics, which is explained by (Davies, 1994). It has a shorter computational time during design and optimization of the heliostat field when compared to DELSOL and HFLD. In addition, it allows evaluating the feasibility of crop growth on the land surface between heliostats throughout calculating the annual sunshine and duration on such land (Wei *et al.*, 2010).

- **ISOS**

This is a MATLAB based software package which was developed to improve the durability of power systems receivers. A numerical algorithm was used in calculating iso-surfaces, where flux was homogeneous. It can also generate a 3D flux map allowing its user to assess the flux at any height above the heliostat field (Riveros-Rosas, Sánchez-González and Estrada, 2008).

- **MATLAB**

Although sometimes confused with MATLAB, MATLAB is a ray-tracing software package, which is able to simulate the path of solar insolation and helps in calculating the proportion of solar energy that reaches the receiver (Reif and

Alhalabi, 2013). It is not a widely used software package and hasn't received updates since 2007.

- ***MIRVAL (SPRAY)***

MIRVAL is a ray-tracing software which is based on the Monte Carlo ray tracing methodology. It was developed in the 70's for central receiver systems aiming to carry out heliostat optical performance, as it can be used in calculating field efficiencies and flux maps for individual heliostats and the whole system (Leary and Hankins, 1979). The code includes three receiver configurations with four heliostat types. It takes into account different factors affecting the performance of the power tower system, including: shading, blocking, heliostat tracking, angular distribution of incoming solar rays, scattering, attenuation between the heliostats and receiver, reflectivity, aiming strategies, and random errors in heliostat tracking and conformation of the reflective surface (Ho, 2008). However, the original MIRVAL package is no longer available, but has been developed by DLR and re-named as SPRAY code (Bode and Gauché, 2012). SPRAY code has the same features as the original MIRVAL software as well as some additional features, such as having many built-in geometries.

- ***NS Code***

This is code which was developed by University of Houston, in 1978, and it was used in evaluating optical performance and performing optimization of heliostat fields in central receiver systems. It was used to plot flux maps for different receivers' types, based on a two-dimensional Hermite expansion method. In order to optimize the heliostat field layout, an allowable flux constraint was used in its improved versions (Dilip and Venkatraj, 2013).

- ***OpTaliX***

OpTaliX is a powerful software for design and simulation as well as ray tracing of optical systems, thin film multilayer coatings and illumination systems. It provides various features to design, optimize and analyse different optical systems. It was used successfully for the design of photographic and video lenses, space and

medical optics. Moreover, it was used in designing optical fibres, illumination devices, infrared and X-ray optics, and telescopes (Optenso, 2017).

- **OptGeo**

OptGeo is a free general optics simulation software. It is used in two-dimension geometric optics simulations. It allows creating geometric and wave optical models and displaying either refraction through lenses, or reflection on mirrors. It also provides the ability to show geometric and chromatic aberrations (Framatophe, 2017). Although its available resources are in French, its interface is now fully translated into English (Biansan, 2018).

- **Optica**

Optica is an optical design package which performs ray-tracing, energy calculations, and optimization of optical systems in three-dimensional space. In addition, it is capable of modelling diffraction, interference, wave-front, and Gaussian beam propagation calculations (Optica Software, 2018).

- **SolTrace**

SolTrace is a freeware ray tracing software with a user-friendly graphical user interface (GUI) and logical steps for the problem definition. It can be used in the design and simulation of different solar power optical systems including; parabolic trough, linear Fresnel reflectors, power tower and parabolic dish systems. SolTrace models the optical geometry as a series of stages composed of optical elements with certain attributes including shape, contour, and optical quality (Ho, 2008).

- **STRAL**

STRAL is a new ray tracing software used in simulation and design of heliostat fields in central receiver systems. It assumes generating rays on the surface of the heliostat, not in a plane above the heliostats. It is more efficient, computationally, than other software tools. It models the heliostat field in detail, as it resolves heliostat mirror geometry and surface data and blocking and shading problems (Belhomme *et al.*, 2009).

- **Tonatiuh**

Tonatiuh is a ray tracing freeware, based on the Monte Carlo method. It was developed for optical simulation and analysis of CSP systems, central receiver systems particularly. It has various geometric heliostat and receiver shapes. It is a direct access software as it allows free access to its source code to suit any application to meet different requirements. Tonatiuh was validated experimentally and the results by (Blanco *et al.*, 2011).

- **Zemax**

ZEMAX is an optical design software program which is one of the most widely used for illumination and laser design systems. In addition, it can be used in optical simulation for solar energy fields (Rugescu, 2014). It provides fast analysis and optimization tools.

Table 2-6 provides a summary of optical design software codes.

Table 2-6 Summary of optical design software codes

Code	Applied for*					Availability	Reference
	1	2	3	4	5		
ASAP	✓	✓	✓	✓		Commercial	(Ho, 2008)
ATMOS					✓	Free	(Riccardi, 2016)
Biomimetic			✓			Pending	(Bode and Gauché, 2012)
CIRCE	✓	✓		✓		Academic	(Romero, 1994)
COMSOL	✓	✓	✓	✓	✓	Commercial	(COMSOL, 2018)
CyberRay					✓	Commercial	(Informer Technologies, 2018)
DELSOL			✓			Academic	(Falcone, 1986; Kistler, 1986)
HELIOS			✓			Academic	(Ho, 2008)
HFLCAL			✓			Commercial	(Schmitz, Pitz-Paal and Schwarzbözl, 2009)
HFLD			✓			Commercial	(Davies, 1994; Wei <i>et al.</i> , 2010)
ISOS			✓			Academic	(Riveros-Rosas, Sánchez-González and Estrada, 2008)
MATLAB		✓			✓	Academic	(Reif and Alhalabi, 2013)
MIRVAL (SPRAY)			✓			Commercial	(Ho, 2008; Bode and Gauché, 2012)
NS Code			✓				(Dilip and Venkatraj, 2013)
OpTaliX					✓	Commercial	(Optenso, 2017)
OptGeo	✓	✓	✓	✓	✓	Free	(Framatophe, 2017; Biansan, 2018)
Optica					✓	Commercial	(Optica Software, 2018)
SolTrace	✓	✓	✓	✓		Free	(Ho, 2008)
STRAL			✓			Commercial	(Belhomme <i>et al.</i> , 2009)
Tonatiuh	✓	✓	✓	✓		Free	(Blanco <i>et al.</i> , 2011; Bode and Gauché, 2012)
Zemax					✓	Commercial	(Rugescu, 2014)

* 1= Parabolic trough 2= Linear Fresnel reflector 3= Power tower 4= Parabolic Dish 5= Other optical applications

2.2.2.2 Thermal Analysis Software

Different software packages used for thermal analysis, simulation and design of solar thermal receivers will be briefly reviewed in this section. In this review,

software codes that are no longer maintained, such as CAVITY and DRAC, are excluded.

- **ABAQUS**

ABAQUS is a FEA software suite which provides powerful solutions for either simple or sophisticated engineering problems, serving a wide spectrum of industrial applications. It can be employed to simulate the thermal characteristics of solar panels (Yang *et al.*, 2012).

- **ANSYS**

ANSYS is a comprehensive software suite which covers the entire range of physics. Fluent is a FVM-based software programme that works under the ANSYS suite, which allows modelling flow, turbulence, heat transfer and reactions for industrial applications. It also has the capability of modelling multiphase systems. ANSYS Fluent was employed to simulate heat transfer of various types of solar receivers by many researchers (Reddy and Satyanarayana, 2008; Reddy, Kumar and Satyanarayana, 2008; Xu, 2013; Ghasemi, Ranjbar and Ramiar, 2013; Tu, Wei and Fang, 2013; Wang *et al.*, 2013; Craig, Gauché and Kretzschmar, 2014; Fernández *et al.*, 2014; Frederickson, Dordevich and Miller, 2014; Prakash, 2014; Tijani and Roslan, 2014).

- **COMSOL**

As pointed to in Section 2.2.2.2, COMSOL software is a FEM-based simulation platform. It can be used for thermal simulation of diverse types of CSP receivers. It has features that allow flexibility to its users to define their own physics for any physical problem. Therefore, academia communities prefer using it rather than ANSYS, which is robust and more industry oriented. Many researchers used COMSOL in their thermal simulation in the field of solar thermal applications (Aichmayer, 2011; Lemcoff and Wyatt, 2012; Saung and Miller, 2014).

- **MSC NASTRAN**

MSC Nastran is FEM-based multi-discipline structural analysis software that can be used for performing static and dynamic thermal analysis across the linear and nonlinear domains, fatigue analysis as well as structural optimization. It was

developed by The MacNeal-Schwendler Corporation (MSC) in the late 1960s. MSC Nastran is widely used when it is a critical issue to study strength, stiffness, and life of a structural system (MSC Software, 2018).

- ***NX NASTRAN***

NX Nastran is an improvement of the MSC Nastran. Such improvement includes adding Computer-aided engineering (CAE) to NX Unigraphics' Computer-aided design (CAD) capabilities, creating a modern, multi-discipline environment to help in achieving high quality performance. NX Nastran can be employed for structural, thermal, flow and motion analysis. Moreover, engineering optimization, Multiphysics, simulation can be performed by NX Nastran under a single environment. In solar energy field, (Marcotte and Manning, 2014) used NX Nastran software for structural analysis of a large-aperture parabolic trough collector.

- ***RADSOLVER***

RADSOLVER was developed by Sandia National Laboratories in 1981 to calculate the radiation heat transfer within arbitrarily shaped solar cavity receivers (Dilip and Venkatraj, 2013). It neglects air convection within the cavity, while accounts for non-grey surfaces as well as wavelength-dependent radiative properties, such as emission and reflection, using an arbitrary number of wavelength bands. It also calculates heat transfer among cavity zones and to working fluids, and temperatures on adiabatic zone surfaces. This software has not been used in many years, and may be no longer maintained (Ho, 2008).

- ***SAM***

SAM stands for the “Solar Advisor Model” which is a freely distributed software. It was initially developed by NREL to predict the performance and economics of parabolic trough systems (Blair *et al.*, 2014). However, over the last few years, SAM was developed to include other CSP systems. It was used by (Casella, Casati and Colonna, 2014) for sizing a solar power tower plant and evaluating its economic performance.

- **TermoFluids**

This is a general purpose, parallel and unstructured object-oriented CFD software which is based on numerical simulations with advanced numerical methods to deal with and solve industrial flows (Lehmkuhl *et al.*, 2009). It was used by (Chiva Segura, Lehmkuhl Barba and Oliva Llana, 2012; Colomer *et al.*, 2014) to model solar tower receivers, numerically.

- **TRNSYS**

TRNSYS is a flexible graphically-based software which is employed in simulating transient systems behaviour to assess thermal and electrical energy systems performance. It can be used in other applications, such as traffic flow and biological processes simulations. Different authors (Jones *et al.*, 2001; Siangsukone and Lovegrove, 2003; Desai, 2013) used TRNSYS in assessment of the performance of their solar thermal projects.

Table 2-7 presents a summary of thermal analysis software codes.

Table 2-7 Summary of thermal design software codes

Code	Applied for*					Availability	Reference
	1	2	3	4	5		
ABAQUS				✓		Commercial	(Yang <i>et al.</i> , 2012)
ANSYS	✓	✓	✓	✓	✓	Commercial	(Reddy and Satyanarayana, 2008; Reddy, Kumar and Satyanarayana, 2008; Xu, 2013; Ghasemi, Ranjbar and Ramiar, 2013; Tu, Wei and Fang, 2013; Wang <i>et al.</i> , 2013; Craig, Gauché and Kretzschmar, 2014; Fernández <i>et al.</i> , 2014; Frederickson, Dordevich and Miller, 2014; Prakash, 2014; Tijani and Roslan, 2014)
COMSOL	✓	✓	✓	✓	✓	Commercial	(Aichmayer, 2011; Lemcoff and Wyatt, 2012; Saung and Miller, 2014)
MSC NASTRAN				✓		Commercial	(MSC Software, 2018)
NX NASTRAN	✓			✓		Commercial	(Marcotte and Manning, 2014)
RADSOLVER						Academic	(Ho, 2008)
SAM	✓					Free	(Blair <i>et al.</i> , 2014)
TermoFluids			✓	✓		Academic	(Lehmkuhl <i>et al.</i> , 2009; Chiva Segura, Lehmkuhl Barba and Oliva Llana, 2012; Colomer <i>et al.</i> , 2014)
TRNSYS	✓	✓	✓	✓		Commercial	(Jones <i>et al.</i> , 2001; Siangsukone and Lovegrove, 2003; Desai, 2013)

* 1= Parabolic trough 2= Linear Fresnel reflector 3= Power tower 4= Parabolic Dish 5= Other optical applications

2.3 Transparent Materials Review

2.3.1 Materials Physical Properties

There are several types of transparent materials used in manufacturing lenses including: glass, polymers and ceramics. They have various optical and physical properties. In this section, some of these materials will be reviewed. In addition, a comparison between their thermal and mechanical properties will be made.

2.3.1.1 ALON

ALON is an optical ceramic crystalline material which is composed of Aluminium Oxynitride ($\text{Al}_{23}\text{O}_{27}\text{N}_5$). It can be considered a high-performance material due to its excellent optical and mechanical properties (Zheng and Forslund, 1995). For optical properties, it has an approximate optical transparency of 85% over a wide range of wavelengths from 220 nm to 4000 nm (Goldman *et al.*, 2017). This covers the near ultraviolet, visible and infrared solar radiation spectrum. On the topic of its mechanical properties, ALON it has excellent properties as an isotropic cubic crystal structure. It can withstand high temperature, as it melts at 2050°C (McCAULEY and CORBIN, 1979).

2.3.1.2 BK7

BK7 is a glass material used in optical applications. Its designation is related to the German company, SchottTM, which stands for Borosilicate Crown (Krone in German) glass (Crystran, 2017). It can be used in a wide variety of visible applications such as optical imaging and Laser optics, as it has an excellent stable transmittance exceeding 90% over a bandwidth ranging from 350 nm to 2000 nm (SCHOTT, 2017).

2.3.1.3 Borosilicate

Borosilicate is a type of glass with silica (typically over 60%) and boron trioxide (5–20%) (El-Damrawi and Mansour, 2005). It has high resistance to thermal shock due to its low coefficient of thermal expansion ($3.25\text{E}-06^\circ\text{C}^{-1}$). Therefore, it represents a good choice for high heat and outdoor lighting applications (GrayGlass, 2013). For optical properties, Borosilicate has a transmittance range 85–92% over a wavelength range 350 nm–2000 nm (Sinclair Manufacturing, 2011).

2.3.1.4 Calcium Fluoride (CaF_2)

Calcium fluoride is one type of non-oxide optical glasses. It has a simple cubic crystal structure with fairly well known properties (Druon *et al.*, 2011). Its simple structure permits good thermal properties (Boudeile *et al.*, 2008). It has excellent optical properties with high transmission, exceeding 92%, from wavelengths of

250 nm to 7000 nm (Thorlabs, 2018b). Therefore, it is often chosen for excimer laser optics due to its low absorption and high damage threshold.

2.3.1.5 CLEARCERAM-Z

CLEARCERAM[®]-Z is an optical ceramic material which is developed by the Ohara Company. It has outstanding thermal, mechanical and chemical properties. For optical properties, its transmission is higher than 80% for wavelengths from 350 nm to 700 nm. However, its transmittance exceeds 90% for bandwidths ranging from 700 nm to 2200 nm (Ohara, 2013).

2.3.1.6 PMMA

PMMA is a transparent thermoplastic material. Although it is not a type of silica-based glass, it is historically considered as a type of non-crystalline glass and has often been known as acrylic glass. It has been used widely in various industrial applications due to stiffness, light weight and clarity (Elashmawi and Hakeem, 2008). In addition, it has good optical properties making it possible to be used in nonlinear optics (Tawansi *et al.*, 2002). It has a stable transmittance of more than 90% over a wavelength range from 400 nm to 1100 nm, while it drops down with unstable form over the rest bandwidth to 2200 nm (Thorlabs, 2018a).

2.3.1.7 Polycarbonate (PC)

Polycarbonate is a clear, colourless type of thermoplastic polymers. Compared with PMMA, it has lighter weight and higher strength. Therefore, it is extensively used in a wide range of engineering applications that require using lightweight transparent armour materials. This is attributed to its high yield strain and ductility; leading to achieving high impact and perforation resistance (Wright, Fleck and Stronge, 1993). On the subject of optical properties, Polycarbonate is commonly used for optical applications within the visible light range as it has approximately the same transmission behaviour as PMMA (Thorlabs, 2018a).

2.3.1.8 Fused Silica (SiO₂)

Quartz is a colourless and transparent material which is composed of silica, SiO₂, in crystalline form. It is a common mineral forming silica-oversaturated rocks

(Flem *et al.*, 2002). When silica has a non-crystalline form structure, it is known as fused silica or fused quartz. Pure quartz has extremely high transmittance, near 100%, over wavelengths from 200 nm to more than 2000 nm. While different types of fused quartz have slightly lower transmittance, but still over 90% for the same wavelength range (Advanced Research Systems, 2016).

2.3.1.9 Sapphire

Sapphire is a single crystal of Al_2O_3 with hexagonal crystalline structure. It has a unique combination of excellent physical and optical properties. This makes it withstand thermal shocks and water and sand erosion, and scratching. It also has a high glass transition temperature, near 790°C , so that it can resist high temperature (Yue and Angell, 2004). In addition, it has a stable transmittance near 85% over a large bandwidth ranging from 400 nm to 2000 nm (Precision Micro-Optics, 2016). Therefore, it is a superior material to be used under severe conditions of elevated temperature and pressure, or thermal shock.

2.3.1.10 Silicon Carbide (SiC)

Silicon Carbide is a non-oxide ceramic which has attracted the interest of many researchers recently as a promising material (Ferraro, García-Tuñón and Saiz, 2015). Transparent SiC has excellent mechanical and thermal properties as well as good resistance to thermal shock. In addition, it has excellent optical properties over the IR region, therefore it is recommended for use in extremely high temperature applications (Riza, Arain and Perez, 2005). Although transparent SiC is opaque for short wavelengths ranging from 350 nm to 500 nm, it has high optical transmittance over the wavelength region 500 nm to 6000 nm (Harris, 1999).

2.3.1.11 Spinel

Spinel is a hard-transparent ceramic material with a cubic crystal structure. It is composed of Magnesium Aluminium Oxide (MgAl_2O_4) that has been used as a gemstone. It possesses unique mechanical, thermal and optical properties. It resists high thermal shock due to its low coefficient of thermal expansion. In addition, it can withstand high temperatures up to its melting point of 2105°C ,

without any transition in phase (Molla *et al.*, 2014). It has a high transmittance of 70% and more over wavelengths from 350 nm to 5000 nm (Optocity, 2017).

2.3.1.12 ULE

ULE[®] is a binary glass composed of SiO₂ and TiO₂. It was developed by Corning Company. It has Ultra Low Expansion (ULE) coefficient of (0.03E-06°C⁻¹). According to its unique characteristics, it became the recommended material choice in various applications ranging from machine tools to space satellite applications (Corning Incorporated, 2008). It has high transmittance exceeding 95% over a large bandwidth from 350 nm to 2000 nm (Rathmann, Mann and Nordberg, 1968).

2.3.1.13 Yttria (Y₂O₃)

Yttria is a transparent polycrystalline ceramic which is composed of Yttrium Oxide (Y₂O₃). Due to its excellent mechanical and thermal properties, it has high ability to resist corrosion and high temperature environments (Huang *et al.*, 2010). Therefore, it has been used in various applications such as missile domes. In addition, it is a promising material in laser applications due to its high thermal conductivity. Moreover, it has good optical properties. It has a transmittance higher than 80% over wavelengths from 250 nm to 2500 nm (Basak and Sen, 1995; Fujita, 2008).

2.3.1.14 ZERODUR

ZERODUR is a lithium aluminium silicon oxide glass-ceramic material which was developed by the Schott Company. It has extremely low thermal expansion coefficient. Therefore, it is suitable for applications that require minimization of geometrical shape changes during shifts in temperature (SCHOTT AG, 2017). In addition, it has a transmittance of 70% near a wavelength of 400 nm and reaches about 90% at 700 nm to 5500 nm (Präzisions Glas & Optik, 2017).

Physical and thermal properties of the reviewed transparent materials are summarised in Table 2-8. The value of maximum working temperature property in Table 2-8 represent the melting point for ceramic materials, while in case of glass and thermoplastic materials it stands for glass transition temperature.

2.3.2 Materials Transmittances

Based on references listed in Table 2-8, the transmittance of all materials listed can be replotted as shown in Figure 2-25. For reference, standard terrestrial solar spectral irradiance (AM1.5) is also plotted.

Table 2-8 Summary of transparent materials properties

Material	Type	Transmittance ^a (%)	Density (kg/m ³)	Thermal Conductivity (W/m.K)	Specific Heat (J/kg.K)	Maximum Working Temperature ^b (°C)	Coefficient of Thermal Expansion ×10 ⁻⁶ (°C ⁻¹)	Elastic Modulus (GPa)	Poisson's Ratio	References
ALON	Ceramic	85	3700	9.50	0.77	2050	4.70	317	0.24	(Crystran, 2017)
BK7	Glass	90	2510	1.11	858	557	8.30	82	0.21	(El-Damrawi and Mansour, 2005; GrayGlass, 2013)
Borosilicate	Glass	85	2230	1.20	830	525	3.25	64	0.2	(Boudeile <i>et al.</i> , 2008; Druon <i>et al.</i> , 2011; Thorlabs, 2018b)
CaF ₂	Glass	92	3180	9.71	854	530	18.90	75.8	0.26	(Ohara, 2013)
CLEARCERAM-Z	Ceramic	80–90	?	1.51	777	650	0.02	90	0.25	(Tawansi <i>et al.</i> , 2002; Elashmawi and Hakeem, 2008; Thorlabs, 2018a)
PMMA	Thermoplastic	80–90 ^c	1880	1.93	1420	105	70.00	3.3	0.38	(Wright, Fleck and Stronge, 1993; Thorlabs, 2018a)
PC	Thermoplastic	80–90 ³	1220	0.20	1250	141	700.00	2.2	0.37	(Bendler, 1999; Thorlabs, 2018a)
Sapphire	Glass	80	3980	36.00	761	790	8.40	420	0.22	(Harris, 1999; Riza, Arain and Perez, 2005; Ferraro, Garcia-Tuñon and Saiz, 2015)
SiC	Ceramic	50–60 ^d	3210	120.00	750	2730	1.00	466	0.14	(Flem <i>et al.</i> , 2002; Advanced Research Systems, 2016)
SiO ₂	Glass	90–95	2210	1.40	730	1202	0.55	73	0.17	(Molla <i>et al.</i> , 2014; Optocity, 2017)
Spinel	Ceramic	70	3590	14.70	920	2105	9.17	268	0.26	(Corning Incorporated, 2008)
ULE	Glass	95	2210	1.31	767	890	0.03	67.6	0.17	(Basak and Sen, 1995; Huang <i>et al.</i> , 2010)
Y ₂ O ₃	Ceramic	80 ^e	5030	2.00	480	2,425	10.0	179	0.23	(Präzisions Glas & Optik, 2017; SCHOTT AG, 2017)
ZERODUR	Glass-ceramic	70–90 ^f	2530	1.46	800	600	0.40	90.3	0.24	(Ho, 2008)

^a Represents average value of transmittance percentage over a wavelength range from 350 nm to 2000 nm.

^b Represents: melting point (for ceramic materials), glass transition temperature (for glass and thermoplastic materials).

^c For wavelengths from 350 nm to 1100 nm, while it drops for longer wavelengths to 2000 nm.

^d For wavelengths from 500 nm to 4000 nm, while it is opaque for shorter wavelengths.

^e For wavelengths from 250 nm to 800 nm, with a drop to less than 40% at 300 nm.

^f For wavelengths from 400 nm to 2500 nm, while it is opaque for shorter wavelengths.

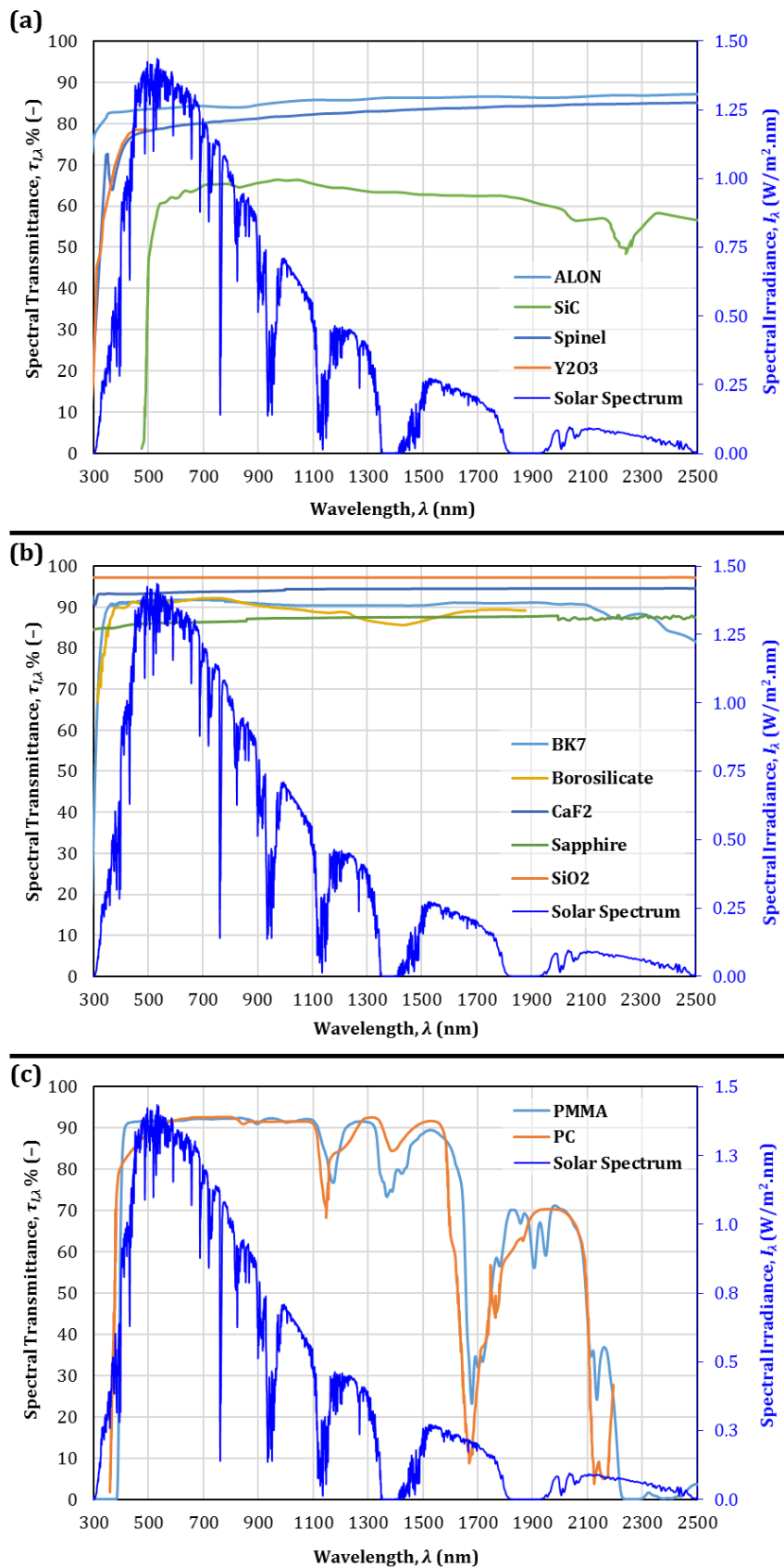


Figure 2-25 Transparent materials transmittances against solar spectrum (AM1.5)
 (a) Ceramics (b) Glass (c) Plastics

The optical efficiency of each material can be considered as a selection criterion to determine the best material candidate for using in the LLBG system. It represents the amount of transmittance. For solar thermal applications, Figure 2-25 shows that this value should be significantly high over a bandwidth ranging from 200 to 1700nm. The transmitted irradiation, I_T , over a bandwidth ranging from λ_1 to λ_2 , is calculated as follows:

$$I_T = \frac{1}{(\lambda_2 - \lambda_1)} \int_{\lambda_1}^{\lambda_2} I_{\lambda} \cdot \tau_{I,\lambda} \cdot d\lambda \quad (2-1)$$

With I_{λ} and $\tau_{I,\lambda}$ are solar spectral irradiation and transmittance of material at a wavelength λ , respectively. The average amount of incident irradiation, I_{in} , is calculated as:

$$I_{in} = \frac{1}{(\lambda_2 - \lambda_1)} \int_{\lambda_1}^{\lambda_2} I_{\lambda} \cdot d\lambda \quad (2-2)$$

Where, Equations (2-1) and (2-2) can be applied over a defined wavelength bandwidth. Then, material optical efficiency, η_{opt} , can be obtained using:

$$\eta_{opt} = \frac{I_T}{I_{in}} * 100 \quad (2-3)$$

The average transmittance over a spectral zone can express optical efficiency. Applying Equations (2-1), (2-2) and (2-3), materials transmittances can be plotted over various spectral zones, as illustrated in Figure 2-26.

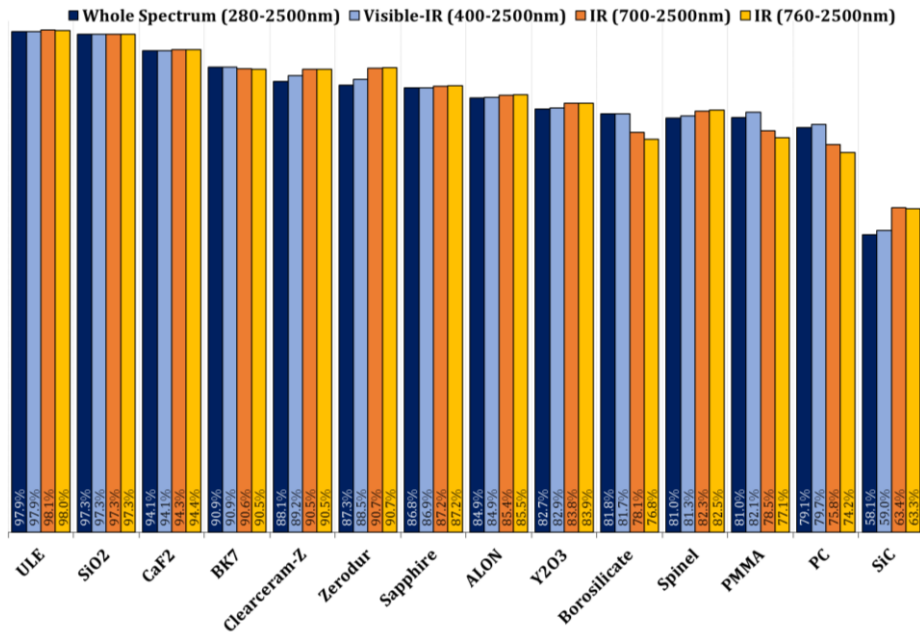


Figure 2-26 Materials transmittances over different spectral zones

2.4 Fresnel Lens Review

2.4.1 Fresnel Lens Terminology

The Fresnel lens is a type of compact lens which utilises portions of an aspherical lens, which work as prisms, to refract the light's rays (see Figure 2-27). The distance between two successive prisms is the “*pitch*”. Each prism has two main surfaces: slope and draft facets, which are inclined by *slope* and *draft angles* with respect to the plane of the lens and to its normal, respectively. These nomenclatures are illustrated in Figure 2-27.

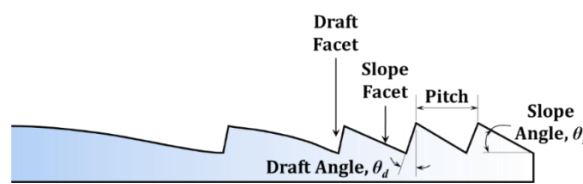


Figure 2-27 Schematic of Fresnel lens cross-section

2.4.2 Fresnel Lens Manufacturing Methods

Manufacturing Fresnel lenses can be carried out via several techniques including: injection moulding, compression moulding and diamond turning (Egger, 1979; Maekawa *et al.*, 2009).

2.4.2.1 Injection Moulding

Injection moulding is a cost-effective technique in which molten plastic is injected into a shaped mould. It is used for the mass production of high precision optical components including micro/nano-optical elements (Kang, 2004; Yoon *et al.*, 2006; Michaeli *et al.*, 2007). This advantage arises from the ability of using this method to produce several parts per individual cycle with optimised tooling complexity and precision level (Tribastone and Peck, 2001). This method usually uses polymeric materials substrates (Tosello *et al.*, 2012; Kuo and Liao, 2015).

2.4.2.2 Compression Moulding

The compression moulding or embossing process is one of the cheapest ways to produce high quality Fresnel lenses, in which heated plastic sheet material is pressed on a moulding die until curing. It is cheaper than the injection moulding method (Benitez *et al.*, 2014). It allows better control over the moulding

parameters to obtain sharp grooves. This technique is more appropriate for polymer materials especially in fabricating micro-optical elements (Becker and Heim, 2000; Hecke and Schomburg, 2004; Worgull, 2009). However, embossing using glass materials involves different technical problems. These problems include: requirement of higher temperatures for glass compared to polymers (Schulz *et al.*, 2000; Kujawa *et al.*, 2012), requirement of stabilising temperature to make glass malleable but not molten (Kasztelanic *et al.*, 2013).

2.4.2.3 Diamond Turning

Diamond turning is a modern technology that is used to turn optical surfaces directly to finished tolerances. It allows producing Fresnel lenses with curved prismatic grooves (Egger, 1979). There are some “diamond-turnable” materials that can be applied to this process without noticeable problems either for the turning tool or the specimen itself. These include: CaF₂, PMMA and PC (Rhorer and Evans, 2010). However, brittle materials are not recommended for diamond turning (Anderson and Burge, 2001).

2.4.3 Fresnel Lens Optical Losses

2.4.3.1 Geometric losses

These losses cause drifting of the refracted rays away from the desired focal point region. There are two types of such losses; chromatic dispersion and incident angle variation. Chromatic dispersion is caused by the chromatic aberration (CA) effect, caused by the refractive index variation with wavelength. From Snell’s law, such variation causes changing of refraction angles for different colours (Leutz and Fu, 2007), as represented in Figure 2-28a. These losses can also be caused because of manufacturing processes. Surface forming errors can deviate the refracted rays from their supposed path (Wallhead *et al.*, 2012). The variation of incidence angle caused by the SAA effect represents another source of geometric losses. As a solar collection lens has an angular input range of $\pm 0.266^\circ$, these losses increase with refraction angle, as illustrated by Figure 2-28b.

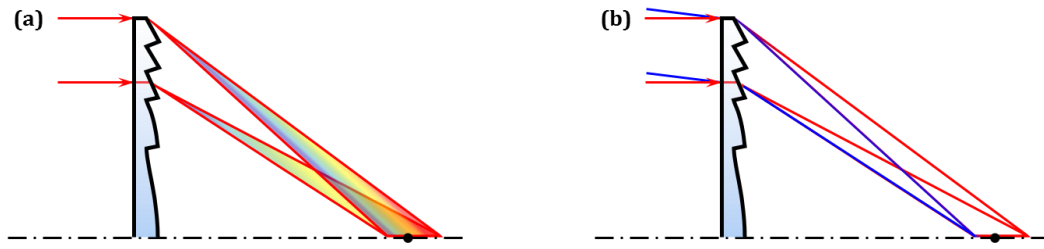


Figure 2-28 Geometric losses
 (a) CA effect (b) SAA effect

2.4.3.2 Dispersion Losses

When a refracted ray hits a tip groove peak, it disperses. To minimize such loss, it is required to keep them in the sharpest shape. However, this cannot be achieved due to manufacturing limitations which makes peak rounding always exist, as shown in Figure 2-29.

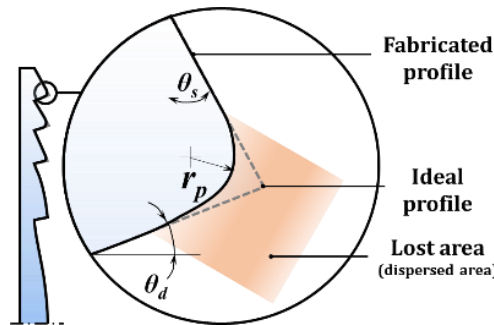


Figure 2-29 Enlarged ideal and fabricated groove profiles in one groove

The total area lost corresponding to dispersion losses, A_{DL} , for a lens with total number of grooves, NG , and draft and slope angles of each groove: θ_d and θ_s , respectively, can be determined from (Shim *et al.*, 2015):

$$A_{DL} = \frac{\pi}{4} \left[\sum_{i=1}^{NG} r_{p,i} (\cos \theta_{d,i} + \sin \theta_{s,i}) \right]^2 \quad (2-4)$$

Where, r_p is the peak rounding radius at each groove. From this equation, minimizing dispersion losses requires optimizing the number of grooves.

2.4.3.3 Blocking Losses

Blocking losses occur when refracted rays leaving a certain prism hits the back side of the adjacent prism (Leutz and Suzuki, 2001) as illustrated by Figure 2-30.

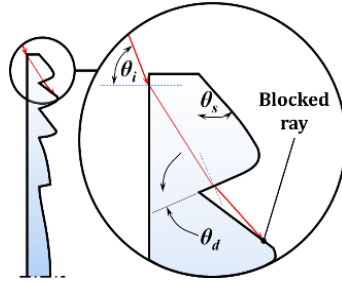


Figure 2-30 Enlarged representation of a blocked ray

From Figure 2-30, blocking losses depend on facet slope and draft angles besides the incident angle. To avoid blocking losses, the slope angle should be kept below the maximum slope angle, $\theta_{s,max}$, which can be determined for any incidence and draft angles, θ_i , θ_d , respectively, by (Yeh and Yeh, 2016):

$$\theta_{s,max} = \theta_d + \sin^{-1} \left\{ n \cos \left[\sin^{-1} \left(\frac{\sin \theta_i}{n} \right) + \theta_d \right] \right\} \quad (2-5)$$

Where n is the lens material refractive index when placed in air. Therefore, designing prisms angles requires paying attention to the combination of incidence and draft angles for a certain lens material.

2.4.3.4 Transmission Losses

Transmission is not only related to the lens material, but also depends on the direction the Fresnel lens facets face. The average material transmittances, $\tau_{I,m}$, over a certain wavelength range ($\lambda_1 - \lambda_2$) through the following formula:

$$\tau_{I,m} = \frac{\int_{\lambda_1}^{\lambda_2} I_{\lambda} \tau_{I,\lambda} d\lambda}{\int_{\lambda_1}^{\lambda_2} I_{\lambda} d\lambda} \quad (2-6)$$

Where I_{λ} is the incident irradiation at a certain wavelength, λ . Hence PMMA and PC are widely used in manufacturing Fresnel lenses, spectral transmittance, $\tau_{I,\lambda}$, of both materials (Thorlabs, 2018a), plotted in Figure 2-25, can be used to determine the average material transmittances. Considering incident solar radiation bandwidth from 280 to 2500nm, then the average material transmittances for PMMA and PC are 81.04% and 79.12%, respectively. While for the VIS-IR spectrum (400-2500nm), the average material transmittances for PMMA and PC are found to be 82.11% and 79.75%, respectively. Therefore, PMMA is widely used as a substrate material in Fresnel lenses production.

2.4.3.5 Reflection Losses

As the light reaches the boundary of two materials with different refractive indices, some of it will be reflected. Refractive index of lens material, incidence angle and lens design are responsible for such type of losses. These losses are represented by rays A and B in Figure 2-31.

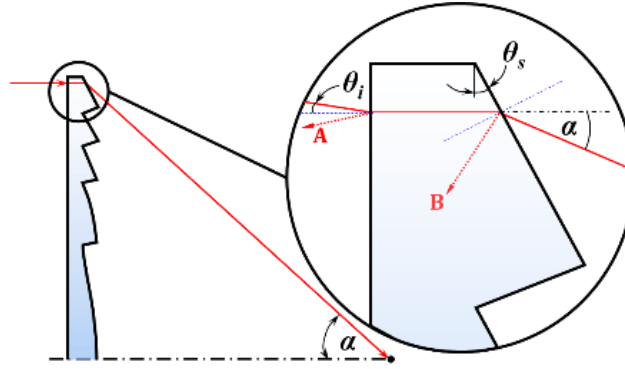


Figure 2-31 Reflection losses

Applying Fresnel formulae (Bennett, 2010), the amount of reflection loss can be calculated for both rays A and B for a known lens material. The reflectance of p-polarised, $\rho_{I,pp}$, and s-polarised, $\rho_{I,sp}$, and averaged, ρ_I , of the incident rays with an incidence angle, θ_i , from a medium to another one with refractive indices of n_1 and n_2 , respectively, can be then calculated by (Ruoduan, Yu and Xiaju, 2013; Lvovsky, 2015):

$$\rho_{I,pp} = \left| \frac{n_1 \sqrt{1 - \left(\frac{n_1}{n_2} \sin \theta_i\right)^2} - n_2 \cos \theta_i}{n_1 \sqrt{1 - \left(\frac{n_1}{n_2} \sin \theta_i\right)^2} + n_2 \cos \theta_i} \right|^2 \quad (2-7)$$

$$\rho_{I,sp} = \left| \frac{n_1 \cos \theta_i - n_2 \sqrt{1 - \left(\frac{n_1}{n_2} \sin \theta_i\right)^2}}{n_1 \cos \theta_i + n_2 \sqrt{1 - \left(\frac{n_1}{n_2} \sin \theta_i\right)^2}} \right|^2 \quad (2-8)$$

$$\rho_I = 0.5(\rho_{I,pp} + \rho_{I,sp}) \quad (2-9)$$

For ray B, the slope angle of the slope facet affects the amount of reflection loss besides the refractive index of the lens material. In order to control the amount of reflection loss in ray B, the phenomenon of total internal reflection (TIR) can be employed (Parkyn and Pelka, 1991; Brinksmeier *et al.*, 2004; Wang *et al.*, 2010). Moreover, double TIR design was proposed by (Wallhead *et al.*, 2012) to allow

more efficient light control. They found that Fresnel reflection loss in ray B is minimized at the design with a minimum final refraction angle which relies on the deflection angle. As the deflection angle is dependent on the prism location from the Fresnel lens major axis, designing a more efficient Fresnel lens comprises implementation of different prism sloping configurations over the Fresnel aperture.

2.5 Solar Simulator Review

A solar simulator is a device whose light source offers both an intensity level and a spectral composition close to that of natural sunlight (Wang, 2014). It is used to simulate either extra-terrestrial or terrestrial radiation (Meng, Wang and Zhang, 2011). Solar simulators are used for a wide range of applications including testing, calibrating and characterising photovoltaics (PV), sunscreens clinical testing, automotive industry for testing dashboards, steering wheels and air bags, materials and PV aging tests, agricultural cultivation for studying the effects of light on the growth of plants and algae and thermal/thermo-chemical devices, such as chemical reforming and production of chemical elements. However, this section focuses on solar simulators built for thermal applications. Such simulators have output fluxes ranging from a few suns (1 sun = 1 kW/m² (Luque and Hegedus, 2011; McEvoy and Markvart, 2011; Pérez-Higueras and Fernández, 2015)), to more than 30 suns, which are classified as low and high-flux solar simulators, respectively (Codd *et al.*, 2010).

2.5.1 Light sources

Light source selection is a principal step in designing a solar simulator with suitable simulated solar radiation. This light source is required to meet several criteria: spectral quality, illumination uniformity, collimation, flux stability and range of obtainable flux (Krusi and Schmid, 1983b). Various lamps types have been employed in solar simulators, including carbon arc lamps, metal halide lamps, tungsten halogen lamps, xenon arc lamps, mercury xenon lamps, high pressure sodium vapour lamps, argon arc lamps and light-emitting diode lamps (LED) (Sarwar *et al.*, 2014).

The choice can be narrowed down based on the field of application of the solar simulator. For solar simulators used in terrestrial thermal applications, the principal parameters determined are: the peak flux, the total beam power and the flux density distribution (Neumann and Groer, 1996). They are less sensitive to incident spectrum in the UV and visible spectrum parts compared to the IR spectrum part, as infrared represents most of the thermal radiation emitted by terrestrial objects (Ashcroft, 2016; Smith, 2016; Xu, 2016). Therefore, a mono-light source type is usually employed with single or multiple lamps configurations. Moreover, the low sensitivity to the light source output spectrum minimises lamps specifications requirements defined by standards related to solar thermal applications, including the International Standards (ISO 9806, ISO 19467) and British Standards (i.e. EN 12975-1, EN 12975-2, EN 12976-1 and EN 12976-2) (EN 12975-1, 2006; EN 12975-2, 2006; EN 12976-2, 2006; ISO 9806, 2013; ISO 19467, 2016; EN 12976-1, 2017). For these simulators, the type of lamps selected is usually argon arc, metal halide, tungsten halogen or xenon arc. These light types of light sources are reviewed in this section.

- **Argon arc lamp**

An Argon arc lamp is a free-burning DC powered device (Curtis and Decker, 1975). The pressurised argon gas (with approximate pressure of 7–10 bar (Decker and Pollack, 1972; Yan and Dawson, 1998; Halliop, 2008) enters at the cathode end, swirls along the central core until it exits at the anode end. In order to cool the arc edge, a sheet of water is created by swirling a high flow rate water vortex along the inside quartz tube wall with pressure over 60 bar at the inlet (Yan and Dawson, 1998; Grover *et al.*, 2015), as shown in Figure 2-32.

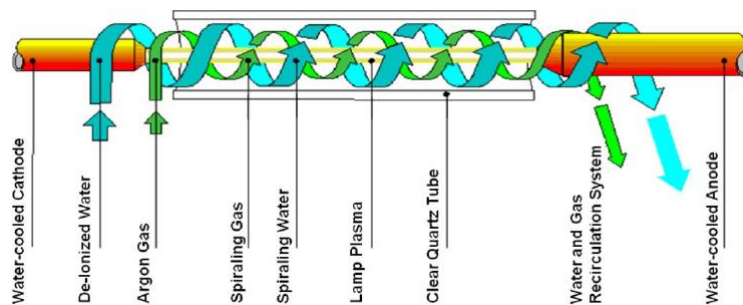


Figure 2-32 Schematic of vortex water-wall argon arc lamp (adapted from (Vortek Industries Ltd., 1999))

These lamps have been used since the 1970s (Richards and Albach, 1982; Barnes and Remelius, 1985; Yan and Dawson, 1998; Hirsch *et al.*, 2003) in the solar simulation field and in laser applications (Barnes and Remelius, 1985).

- **Metal halide lamp**

In a metal halide lamp, the light is produced by an electric arc which is generated through a gaseous mixture of vaporized mercury and metal halide compounds under a high pressure ranging from 10 to 35 bar (Osram, 2000; Dinklage, Klinger and Marx, 2005; Grondzik *et al.*, 2009). It is a type of high-intensity discharge (HID) gas lamp (Waymouth, 1971), as illustrated in Figure 2-33.

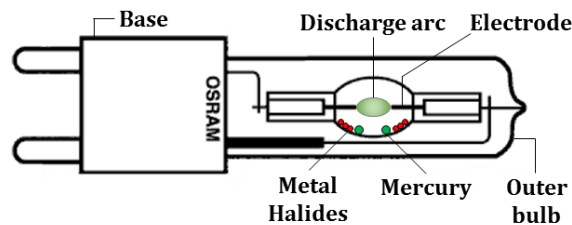


Figure 2-33 Metal halide lamp structure (adapted from (Osram, 2016a, 2016e))

Metal halide lamps were introduced as a light source option for solar simulation after the development of compact source iodide (CSI) metal halide lamps (Wang, 2014). Those CSI lamp types have high efficiency, a balanced spectral quality closely matching sunlight, long life time and relative low cost. Therefore, many researchers have selected them for their simulators (Ley, 1979; Geisheker, P.J. ; Putman, W.J. ; Bard, 1981; Dokos, 1982; Higashi, T., Umezit, 1982; Leiner and Altfeld, 1982; Ouden and Wijsman, 1982; Beghi, 1983; Gene A. Zerlaut, William T. Dokos, William J. Putman, 1983; Kenny, 1993; Kenny and Davidson, 1994). Other metal halide lamps types have also been tested (Gillet, 1977; Krusi and Schmid, 1983b, 1979; Brinkworth, 1980; Gillett, 1983; Codd *et al.*, 2010; Atlas Material Testing Technology, 2011; Meng, Wang and Zhang, 2011; Codd, 2011; Madsen, 2013; Pernpeintner *et al.*, 2015; Dong *et al.*, 2015; Ekman, Brooks and Akbar Rhamdhani, 2015; Ametek, 2016).

- **Tungsten halogen lamp**

A Tungsten halogen lamp is a type of incandescent lamp which contains halogen in the form of bromine or iodine surrounding a tungsten filament heated by an

electric current (Hill and Dolenga, 1977; Yoshizawa, 2015), as shown in Figure 2-34. While incandescent lamps have a maximum colour temperature of 3400K (Bickler, 1962), according to the Wien displacement law (Howell, Menguc and Siegel, 2015), these lamps radiate weaker in the ultraviolet and stronger in the infrared regions compared to the solar spectrum with its colour temperature of 5800K (Shu, 1982; Cicerone, 2000; Hu and Ding, 2011).

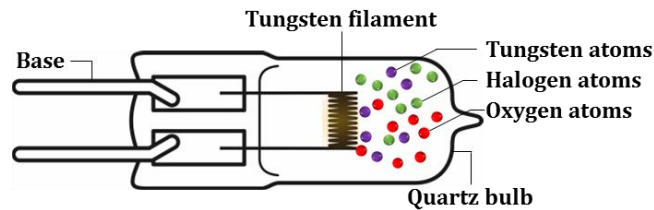


Figure 2-34 Tungsten halogen lamp structure (adapted from (Bommel, 2014; Osram, 2016b))

Despite this disadvantage, tungsten halogen lamps have been utilised in solar simulation (Yass and Curtis, 1975; Simon, 1976; Beeson, 1978; Humphries and George, 1978; Rueb, 1982; Beghi, 1983; Garg *et al.*, 1985; Kenny, 1993; Turner and Ash, 1994; Shatat, Riffat and Agyenim, 2013). This may be attributed to their excellent light output and relatively low cost (Beeson, 1978). They are widely used in less spectrum-sensitive applications such as concentrated solar collector testing and as an infrared light source in multi-source solar simulators (Wang, 2014).

- **Xenon arc lamp**

A Xenon arc lamp is a type of HID gas discharge lamp in which light is produced by passing an electric arc through ionized xenon gas under high pressure ranging from 10 to 40 bar (Wang, 2014; Osram, 2016f; Pedrotti and Pedrotti, 2016), as shown in Figure 2-35.

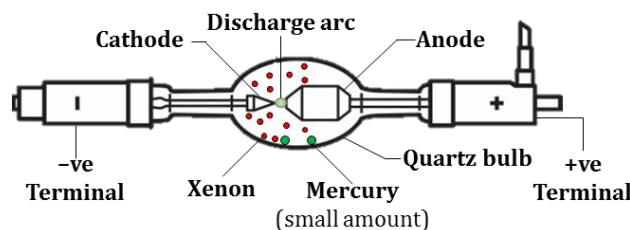


Figure 2-35 Xenon arc lamp structure (adapted from (Martini, 2014; Ahmadi, 2015; Osram, 2016f))

These lamps are preferred by manufacturers and researchers as a light source for solar simulators (Vaan, 1982; Beghi, 1983; Jaworske, Jefferies and Mason, 1996; Petrasch and Steinfeld, 2005; Petrasch *et al.*, 2007; Luque and Hegedus, 2010; Craig, 2010; Alxneit, Dibowski and Facilities, 2011; Li *et al.*, 2011, 2014; Krueger, Davidson and Lipiński, 2011; Erickson, 2012; Krueger, 2012; Krueger *et al.*, 2013; Wang, 2014, 2015; Wang *et al.*, 2014; Dibowski, 2014; Li, Gonzalez-Aguilar and Romero, 2015; Okuhara *et al.*, 2015; Horovitz *et al.*, 2016). They benefit from an excellent quality and stable spectrum in the UV and VIS bands. Their strong emission in the IR range can be filtered (Bickler, 1962) if required. Moreover, a collimated high intensity light beam can be generated as a result of a brighter point source than other light sources (Matson, Emery and Bird, 1984). However, operation of these lamps under high pressure creates an increased risk of explosion (Ma *et al.*, 2010). In addition, the UV radiation emitted by these types of lamps can generate ozone, which can create a respiratory hazard (Health and Safety Executive, 2014). Besides health and safety concerns, their high cost and output sensitivity to power supply instabilities represent significant drawbacks that need to be addressed before using them in solar simulators (Bickler, 1962; Matson, Emery and Bird, 1984; Codd *et al.*, 2010; Wang, 2014). Comparison between different spectra of the mentioned light sources is plotted in Figure 2-36.

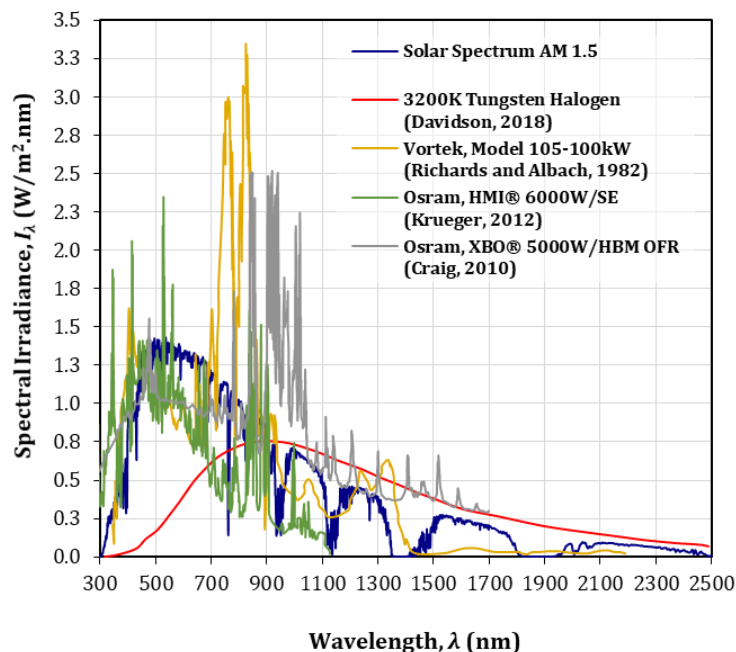
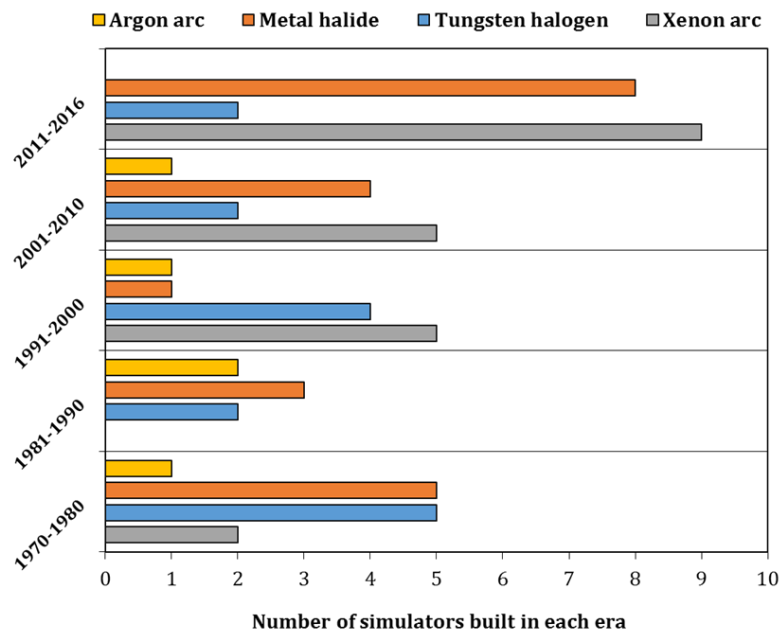


Figure 2-36 Light sources spectra comparison against solar spectrum (AM1.5)
(Richards and Albach, 1982; Craig, 2010; Krueger, 2012; Davidson, 2018)

2.5.2 Trends in using light sources

Table 2-9 summarises a list of thermal solar simulators details published in literature. Using data listed in Table 2-9, solar simulators were categorised based on their year of construction (ten-year era) and the lamp type selected (Figure 2-37). The number of simulators built in each era and usage percentages per era are shown in Figure 2-37a and Figure 2-37b respectively.

(a)



(b)

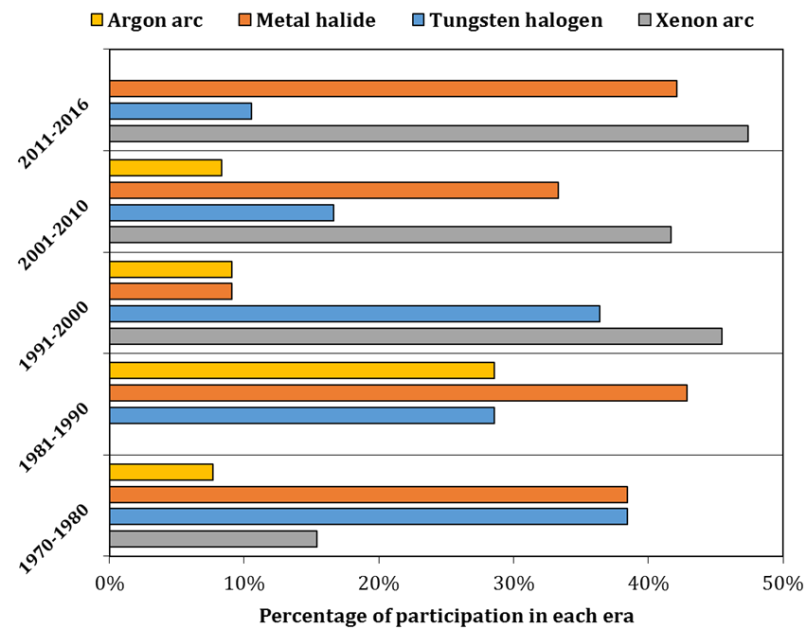


Figure 2-37 Light sources usage share in different eras

(a) Number of simulators built in each era (b) Percentage of usage in each era

Table 2-9 Comparison of different thermal solar simulators (chronological order)

Lamp type	Lamp power (kW _e)	Number of lamps	Total output flux (kW/m ²)	Spot dimensions (m)	Calculated conversion efficiency ^g (%)	Reference(s)
Argon-arc lamp	400 DC	2	1.21	4.6x9.2	6.42	(Decker and Pollack, 1972)
	100 DC	1	0.25–1.25	1.5x0.50	0.94	(Pullen, Albach and Harrison, 1982)
	100 DC	1	1	1.5x0.50	0.75	(Richards and Albach, 1982)
	150 DC	1	6680	Ø0.01905	1.27	(Choi <i>et al.</i> , 1996; Nguyen <i>et al.</i> , 1997)
	200 DC	1	4250	Ø0.06	6.01	(Hirsch <i>et al.</i> , 2003; Osinga <i>et al.</i> , 2004)
Metal halide lamp	1	19	0.4–0.9	Ø2.25	18.83	(Gillet, 1977; Brinkworth, 1980; Gillett, 1983)
	1	36	0.2–1.1	2x2	12.22	(Ley, 1979; Beghi, 1983)
	1	36	1–1.2	1.2x2.4	9.60	(Ley, 1979)
	1	27	0.6–1	1.5x1.8	10.00	(Ouden and Wijsman, 1982)
	1	55	0.865	2.5x2.3	9.04	(Geisheker, P.J.; Putman, W.J.; Bard, 1981; Dokos, 1982; Gene A. Zerlaut, William T. Dokos, William J. Putman, 1983)
	1	72	0.4–0.8	3x3	10.00	(Higashi, T., Umezit, 1982) ^h
	1	40	0.7–1	1.4x3	10.50	(Leiner and Altfeld, 1982)
	1	28	0.983–1.188	1.06x1.06	4.77	(Kenny, 1993; Kenny and Davidson, 1994)
	1	18	–	–	–	(Krusi and Schmid, 1979, 1983b)
	1.5	7	60	Ø0.38	64.81	(Codd <i>et al.</i> , 2010; Codd, 2011)
	1.2	1	0.8–1	–	–	(Atlas Material Testing Technology, 2011; Madsen, 2013)
	0.4	188	0.15–1.1	4.5x3.88	25.54	(Meng, Wang and Zhang, 2011)
	6	1	112	0.095x0.095	16.85	(Dong <i>et al.</i> , 2015)
	6	7	927	Ø0.175	53.09	(Ekman, Brooks and Akbar Rhamdhani, 2015)
	2.5	6	–	50x0.4	–	(Pernpeintner <i>et al.</i> , 2015)
	1.2	15	1	2.5x1.5	20.83	(Mei <i>et al.</i> , 2009)
	–	35	0.8	–	–	(Mondol <i>et al.</i> , 2009)
	0.575	35	1.2	1.8x2.2	23.61	(Zacharopoulos <i>et al.</i> , 2009; Kim <i>et al.</i> , 2016)
	0.4	88	0.15–1	1.6x1.6	7.27	(Guo <i>et al.</i> , 2016)
	1 & 2	6x1kW & 6x2kW	0.1–1	2.8x 2.7	42.00	(Sabahi <i>et al.</i> , 2016)
4	32	1	11x9.2	79.06	(Ametek, 2016)	
Tungsten halogen lamp	0.3	143	0.61–1.05	1.2x1.2	3.52	(Yass and Curtis, 1974, 1975; Simon, 1976)
	0.3	12	0.102–0.55	1.2x1.2	22.00	
	0.3	405	0.395–0.962	2x3	4.75	(Humphries and George, 1978)
	0.3	187	0.5–1.1	1.2x1.8	4.24	(Ley, 1979)
	0.3	200	0.5–1.46	(1.6 m2)	3.89	(Ley, 1979)

^g Energy conversion is defined and explained later in details in section 2.5.3.

^h Their measurements indicated that 143 klx is equivalent to 1kW/m², while it was reported that 139 klx corresponds 1kW/m² (Li *et al.*, 2011).

Lamp type	Lamp power (kW _e)	Number of lamps	Total output flux (kW/m ²)	Spot dimensions (m)	Calculated conversion efficiency ^g (%)	Reference(s)
	0.15	10	0.8	0.12x0.50	3.20	(Rueb, 1982)
	0.15	15	1.8	0.40x0.60	19.20	
	0.3	96	0.7–1	1.4x3	14.58	(Leiner and Altfeld, 1982)
	1	14	0.4–1.5	1x1	10.71	(Garg <i>et al.</i> , 1985)
	0.74	6	25	Ø0.1524	10.27	(Turner and Ash, 1994)
	0.3	45	0.6	1.2x2.4	12.80	(Sopian <i>et al.</i> , 1999)
	0.3	20	0.5–0.645	2x0.46	9.89	(Velmurugan and Kalaivanan, 2016)
	1	4	5.38–7.094	–	–	(Kongtragool and Wongwises, 2007, 2008)
	0.3	2	0.425–0.918	Ø0.12	1.73	(Njie and Rumsey, 1998)
	0.3 & 0.5	4x0.3kW & 12x0.5kW	0.63	1.9x0.55	9.14	(Mink <i>et al.</i> , 1998)
	0.4	30	0.2–1.2	1.45x1.6	23.20	(Shatat, Riffat and Agyenim, 2013)
Xenon-arc lamp	20	7	0.135–2.95	~ Ø3.05	15.40	(Ley, 1979)
	6.5	10	0.1–1.7	Ø1.6	5.26	(Ley, 1979; Kochan, Huebner and Sears, 1999)
	20	1	3,000	Ø0.015	2.65	(Kuhn and Hunt, 1991)
	6	10	4100	~ Ø0.11	64.94	(Neumann and Groer, 1996; Alxneit, Dibowski and Facilities, 2011; Dibowski, 2014)
	30	9	1.7	Ø4.8	11.39	(Jefferies, 1994; Jaworske, Jefferies and Mason, 1996)
	15	10	6800	Ø0.06	12.82	
	15	10	11,000	Ø0.003	0.05	(Petrasch and Steinfeld, 2005; Petrasch <i>et al.</i> , 2007; Schunk <i>et al.</i> , 2008; Schunk, Lipiński and Steinfeld, 2009)
	5	1	10	~ Ø0.20	6.28	(Craig, 2010)
	6.5	7	3250–3700	Ø0.06	22.99	(Krueger, Davidson and Lipiński, 2011; Krueger, 2012; Krueger <i>et al.</i> , 2013)
	7	1–12 ⁱ	54	Ø0.30	54.53	(Li <i>et al.</i> , 2011)
	6	7	4230	–	–	(Erickson, 2012)
	7	12	627	Ø0.20	23.45	(Wang <i>et al.</i> , 2014; Wang, 2015)
	7	1	43.2	Ø0.11	5.86	(Sarwar <i>et al.</i> , 2014)
	6	7	1860	Ø0.06	12.52	(Li <i>et al.</i> , 2014; Li, Gonzalez-Aguilar and Romero, 2015)
	7	19	735–1100	Ø0.2	25.98	(Nakakura <i>et al.</i> , 2016)
	7	1	329	0.06x0.06	16.92	(Gomez-Garcia <i>et al.</i> , 2016)
	3	1	100	0.06x0.06	12.00	
	3	1	1200	0.005x0.005	1.00	(Chow <i>et al.</i> , 2010; SpectroLab, 2010, 2016; Beal <i>et al.</i> , 2012)
	10	1	10,000	Ø0.01	7.85	(Andreev <i>et al.</i> , 2005, 2006)
	1	6	0.05–0.8	–	–	(Shaughnessy, Toplis and Wright, 2003)
30	9	1.8	Ø4.79	12.01	(Tolbert, 1994; Shaltens and Boyle, 1995; Kerslake, Mason and Strumpf, 1997; Mason, Shaltens and Espinosa, 1997)	
3	1	3.675	Ø0.91	79.67	(Lin and Stultz, 1995)	
5	20	18–24.3	0.4x0.07	0.68	(Okuhara <i>et al.</i> , 2015)	

ⁱ (Piatkowski and Steinfeld, 2011) carried out theoretical study based on 12 lamps, while experiments were reported on a single lamp.

The participation share over the period from 1970 to 2016, based on 62 cases listed in Table 2-9, showed that the most popular lamp types are metal halide and xenon arc lamps with usage share of 34% each, while 24% of listed cases used tungsten halogen lamps. It can be observed that in 1970-80s, researchers used principally low-cost and available tungsten halogen and metal halide lamps rather than xenon or argon arc lamps. In 1990-2000s, xenon arc lamps competed with other types because of their excellent performance and high-quality output spectrum. From 2000s, metal halide lamps have made a resurgence compared to tungsten halogen lamps. This may be attributed to receding argon arc lamps usage since 2005 as a result of the acquisition of Vortek Industries Ltd., the main historical supplier of argon arc lamps (Mattson Technology (MTSN), 2005).

2.5.3 Light sources characteristics

Selecting a light source for a solar simulator is a key process which requires considering some important aspects including: life time, internal pressure, additional requirements (e.g. required ballast and igniters). For example, in the case of metal halide and xenon arc lamps, ballast and an igniter are required to power the lamp. If one of these elements is incompatible, this may lead to a shift in colour temperature, a dramatically lower lamp life expectancy, and an increased risk of lamp or system failure. Moreover, safety concerns should be evaluated before using certain light sources. For example precautions have to be taken for HID lamps which carry risks associated with retinal damage, UV hazards, or lamp explosion hazards due to their high internal pressures (Sloney and Mellerio, 1980; Brennesholtz and Stupp, 2008). Table 2-10 summarises the main characteristics of different light sources, including cost and energy convergence efficiency comparison.

For the cost study, different light sources and any additional components required was addressed by selecting the same brand and lamp power. The Philips metal halide lamp (model: HPI-T), tungsten halogen lamp (model: 6994Z) and Xenon arc lamp (model: LTIX) with 2kW_e input power were selected for comparison. However, due to argon arc lamps unavailability, no data was collected. Although

costs listed in Table 2-10 fluctuate with time, power output and suppliers, this cost estimation can be used as an initial criterion in a light source selection. According to these data, tungsten halogen lamps are the cheapest light source, while a xenon arc lamp is the most expensive option.

The energy conversion efficiency of a system is defined as the ratio between the useful output and the input (Aldrich and Parello, 2010). A solar simulator can be considered as a system in which the electrical power supplying the light source is considered as input power, while the useful output power is represented by the radiative power reaching the target area, at which spot is detected. Hence, the energy conversion efficiency of a solar simulator, η_{con} , can be described by:

$$\eta_{con} = \frac{\textit{Total output radiative power}}{\textit{Total electric power consumed by lamps}} \quad (2-10)$$

By relating this definition to the target area, then it can be rewritten as:

$$\eta_{con} = \frac{\textit{Total output flux}}{\textit{Number of lamps} * \frac{\textit{Lamp power}}{\textit{Target area}}} \quad (2-11)$$

The reflector optical efficiency, which is the ratio between the flux reaching the target and the emitted global flux (Bortolini, Gamberi and Graziani, 2013), is already embedded in the energy conversion efficiency defined by Eq.(2-6) and Eq.(2-7). According to data listed in Table 2-9, the average conversion efficiencies of different light sources are listed in Table 2-10.

Table 2-10 Summary of main characteristics of different light sources

	Argon arc lamp	Metal halide lamp	Tungsten halogen lamp	Xenon arc lamp	Reference(s)
Life time (hours)	–	1000–6100	35–480	400–3500	(Hall, 1982; Leiner and Altfeld, 1982; Krusi and Schmid, 1983a; Philips, 2015a, 2015b, 2015c; GE product datasheet, 2016; Osram, 2016c, 2016d)
Internal pressure (bar)	7–10	10–35	–	10–40	(Decker and Pollack, 1972; Yan and Dawson, 1998; Osram, 2000; Dinklage, Klinger and Marx, 2005; Halliop, 2008; Grondzik <i>et al.</i> , 2009; Wang, 2014; Skoog, 2015; Pedrotti and Pedrotti, 2016)
Additional requirements	DC power supply, rectifier and DC choke	Ballast and igniter	–	Ballast and igniter	(Curtis and Decker, 1975; Rueb, 1982; Krusi and Schmid, 1983a; Yan and Dawson, 1998; Codd <i>et al.</i> , 2010; Codd, 2011; Meng, Wang and Zhang, 2011; Dong <i>et al.</i> , 2015; Osram, 2016a)
Lamp model	–	PHILIPS HPI-T 2000W	PHILIPS 6994Z 2000W	PHILIPS LTIX-2000W/H	(Philips, 2009, 2016a, 2016b)
Lamp cost (£)	–	96.07	32.65	634.68	(Any Lamp BV, 2016a; Get a Lamp S.C.P., 2016; Theatrical Bulb Supply, 2016)
Additional requirements cost (£)	–	178.2	0.00	2250	(Any Lamp BV, 2016b, 2017; Powergems Limited, 2017)
Total Cost (£)	–	274.27	32.65	2884.68	–
Average conversion efficiency (%)	3.08	24.59	10.21	18.77	All references listed in Table 2-9

2.6 Summary

In most reviewed concentrating technologies reported in literature, the receiver location is predetermined at the design phase. This is either for fixed-receiver cases, such as power tower and linear Fresnel reflectors, or moving-receiver situations, including the parabolic trough and dish cases. This constraint can be eliminated through employing multi-stage optical configurations in solar concentration, allowing generating a beam of concentrated radiation (Nakamura, 1992; Huang and Xu, 2017; Burhan, Shahzad and Ng, 2018; Hu, Shen and Yao, 2018). These proposed systems are used for PV or for lighting applications. For thermal applications, the LLBG system (Salem, Tawfik and Hamed, 2010) seems to be a promising system, in which the receiver location is controllable through generating and transferring the thermal beam to suitable location. This flexibility allows reducing land use intensity and provides the opportunity to modify conventional power plants which are already in service. In addition, the LLBG requires a dual-axis tracking system, leading to high CR values, which allows higher thermal efficiencies. However, the major current limitation of the LLBG system is represented in its scale, as it was built on a small scale to avoid overheating its rear lens. Consequently, this led to lower collector efficiency, compared to the maximum reported in literature. Therefore, this system needs to be investigated in more detail to scale it up allowing achievement of higher concentration ratios, hence achieving higher collector efficiency.

Using Fresnel lens geometry for refractive-based concentrating technologies secures low cost due to less material, mass and structure requirements needed. However, using Fresnel geometry leads to some limitations in selecting substrate materials due to manufacturing methods. In addition, some optical losses occur through Fresnel lenses, which have been reviewed in this chapter.

This chapter also reviewed different optical and thermal simulation software codes, as well as optical and physical properties of transparent materials. Moreover, building solar simulators for thermal testing applications has been reviewed.

3 AIM OF STUDY

3.1 Aim

The aim of this research is to reduce the Carbon footprint of currently existing fossil-fuelled power plants through hybridising them with solar energy. This requires reviewing different available CSP technologies to select and study the best option that achieves this target with minimum modifications.

3.2 Objectives

The literature review carried out in Chapter 2 led us to select the lens-lens beam generator (LLBG) solar concentrating technology as the best CSP technique that meets the aim requirements. To achieve the aim of this research, the following main objectives are listed as follows:

- ✓ Design and build a sun simulator device.
- ✓ Build and validate numerical models to design an LLBG solar concentrator.
- ✓ Design and build an LLBG solar concentrator.
- ✓ Assess the performance of this concentrating technology.
- ✓ Assess performance limitations and system implementation obstacles.

These objectives were divided in the following manageable sub-objectives and tasks:

- Investigate and select the front and rear lenses geometries,
- Investigate and select the front and rear lenses materials,
- Determine the maximum allowable CR of the LLBG in a certain location,
- Review sun simulators designs and currently used light sources,
- Design and build a sun simulator device,
- Calibrate and test the sun simulator output spectrum,
- Design and build a prototype of an LLBG concentrator,
- Design and build a solar thermal receiver,
- Perform experiments to assess the LLBG performance.
- Report obstacles facing the accomplishment of the previous objective,

3.3 Gap of Knowledge

The gap of knowledge is an evaluation of implementing Fresnel lenses in building LLBG systems. This evaluation starts with a detailed study of different parameters affecting the performance of the LLBG solar concentrator to achieve the optimum design point. Then, it extends to include real-field tests to assess a larger scale prototype compared to that found in the literature to date.

3.4 Methodology

The objectives can be achieved, through the following steps (see Figure 3-1):

1. Build up a numerical model of the rear lens using ANSYS and COMSOL software packages.
2. Create the mesh and perform the model convergence test.
3. Perform thermal analysis of the rear lens based on different operating conditions.
4. Design and build a sun simulator device for indoor testing purposes.
5. Measure and calibrating the sun simulator output spectrum and power density.
6. Validate the model results throughout comparing its results at a certain condition with experimental results.
7. Review materials monochromatic transmittances.
8. Calculate optical efficiencies of various materials.
9. Review large lenses availability.
10. Review low cost manufacturing techniques for large lenses.
11. Review materials suitable for processing in different manufacturing techniques for large lenses.
12. Select optimum materials and geometries for both front and rear lenses.
13. Design an LLBG prototype.
14. Carry out a design review.
15. Build the LLBG prototype.
16. Perform indoor and outdoor experimental tests to investigate the concentrator performance.

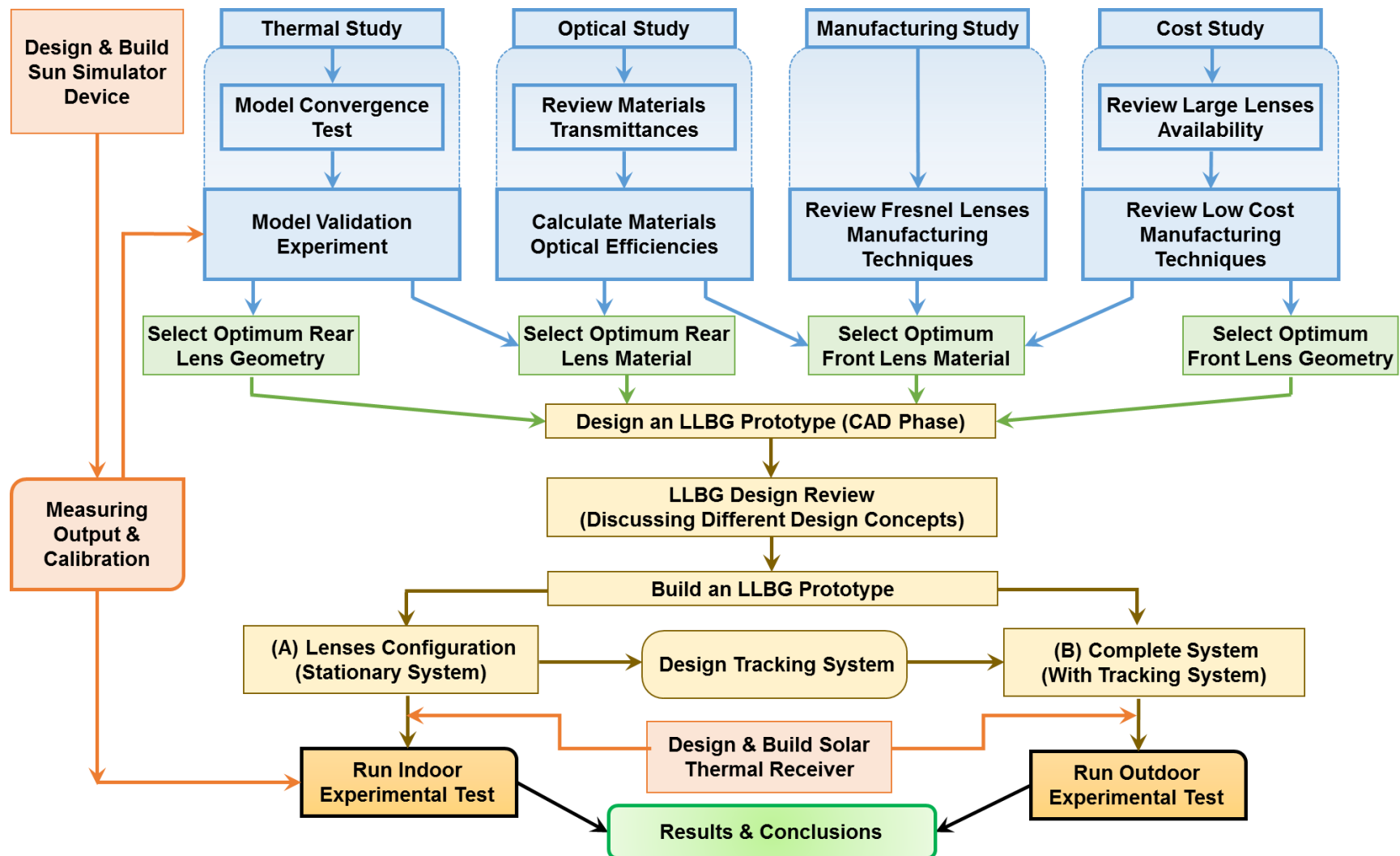


Figure 3-1 Methodology to achieve the aim and objectives

4 EXPERIMENTAL INSTRUMENTS & PRELIMINARY TESTS

TESTS

In this chapter, different equipment used in experimental testing in the following chapters are displayed, besides the preliminary tests carried out.

4.1 Experimental Instruments

4.1.1 SVC HR-1024i Field Spectroradiometer

The HR-1024i Field Spectroradiometer (Figure 4-1), from the Spectra Vista Corp.(SVC), is a compact, easy to set up and designed to collect solar reflectance, radiance and irradiance measurements. It has a high resolution over the VIS to short-wave infrared wavelength range with a spectral bandwidth from 350 to 2500 nm, as it includes 3 dispersion gratings spectrometers: Silicon photodiode array, Indium gallium arsenide (InGaAs) photodiode array and Extended InGaAs photodiode array. It operates through a Panasonic Toughbook computer with full graphic, data storage and functional control. For high precision irradiance measurements, the HR-1024i is configured with the Field Spectroscopy Facility (FSF) custom integrating sphere, as a sensing element, with a fibre optic light guide (National Centre for Earth Observation (NCEO), 2018).

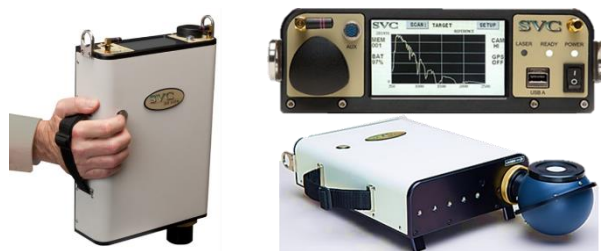


Figure 4-1 SVC HR-1024i Field Spectroradiometer
(Spectra Vista Corporation, 2016)

4.1.2 TESA-VISIO® 300 DCC Machine

The TESA-VISIO® (Figure 4-2) is automatic/manual non-contact measurement machine which inspects the tested object by an optical system fitted with a charge-coupled device (CCD) colour camera and additional zoom-like lenses.



Figure 4-2 TESA-VISIO® 300 DCC machine

As this measurement technology is based on image analysis, the inspected object is light illuminated by three different light illuminations: diascope illumination, ringlight and coaxial light. The diascope illumination allows the user to view the tested object profile, while the ringlight makes it possible to visualise the upper surface of the tested part. The coaxial light allows viewing inside a cavity or measuring cylindrical parts in upright position (TESA, 2011).

4.1.3 PHILIPS Strand Portable Dimmer

PHILIPS Strand dimmer (Figure 4-3) is a DMX512 controlled single channel, convection-cooled portable dimmer which provided with an external remote fader, allowing user to control the output of the attached fixture. It is rated for 10A and 2.3kW output (Philips Strand Lighting, 2015).



Figure 4-3 PHILIPS Strand portable dimmer
(Flashlight Ltd., 2018)

4.1.4 SMP10 pyranometer

SMP10 pyranometer (Figure 4-4) manufactured by Kipp & Zonen Instruments, which has a wide spectral range (285–2800nm) of response with an analogue output range of 0-4mA which corresponds irradiance range of 0–1600 W/m² (Kipp & Zonen Instruments, 2018b).



Figure 4-4 Kipp & Zonen Instruments SMP10 Pyranometer
(Kipp & Zonen Instruments, 2018a)

4.1.5 TC-08 Thermocouple Data Logger

TC-08 thermocouple data logger (Figure 4-5), manufactured by Pico Technology Ltd., is a data logger that measures and records up to 8 thermocouples with a temperature range of (–270°C to +1820°C). It has a built-in cold junction compensation and sampling rate up to 10 samples per second (Pico Technology Ltd., 2016). The data logger is connected to K-type thermocouples (Figure 4-5) to detect and record objects surface temperatures.



Figure 4-5 TC-08 thermocouple data logger & K-type thermocouple used
(Pico Technology Ltd., 2018)

4.1.6 TITAN MK7-15 Laser Distance Measurer

TITAN MK7-15 is a laser distance meter with digital point-finder (Figure 4-6), which emits 1mW class 2-Laser with wavelength bandwidth of 620–670nm. It has a measuring range of 0.05–15m and an accuracy of ± 2.0 mm. It displays results on a colour screen (Screwfix, 2018).



Figure 4-6 TITAN MK7-15 laser distance measurer

4.1.7 Condor Reflectometer

Condor reflectometer from Abengoa Solar (see Figure 4-7) measures mirrors reflectance in actual solar fields in working CSP. It tests the reflectivity in six wavelengths (435, 525, 650, 780, 940 and 1050 nm) across the solar spectrum which emitted from six LEDs and detected with six corresponding detectors. It has a resolution of 0.001 and repeatability is ± 0.002 (Abengoa Solar, 2014; Fernández-García *et al.*, 2017).



Figure 4-7 Condor reflectometer

4.1.8 Leitz PMM-F Coordinate Measuring Machine

The Leitz PMM-F-100 is a high-accuracy coordinate measuring machine (CMM) facility available in Precision Engineering Institute, Cranfield University, shown in Figure 4-8. It has a massive U-frame, completely made of granite and equipped with an integrated active vibration damping system (Hexagon, 2018).

4.2 Preliminary Tests

4.2.1 Solar Simulator Back Reflector Measurement

This test aims to measure the basic dimensions, i.e. the diameter and radius of curvature, of the solar simulator back reflector for running the ray-tracing software.

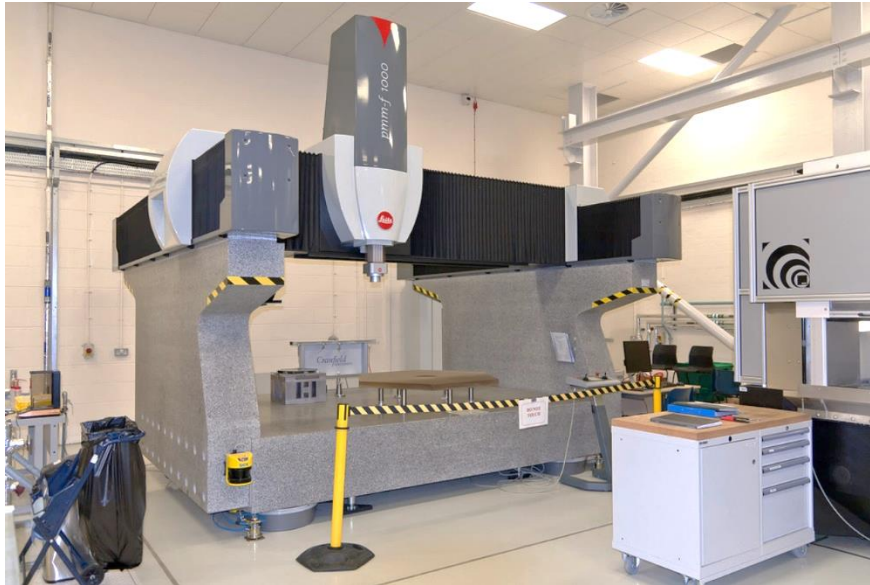


Figure 4-8 Leitz PMM-F coordinate measuring machine

- ***Instruments Required***

TESA-VISIO® 300 DCC machine (Figure 4-2)

- ***Experimental Setup and Procedure***

The back reflector is set over the glass plate support and then inspected with the optical system which employs CCD camera, as illustrated by Figure 4-9.

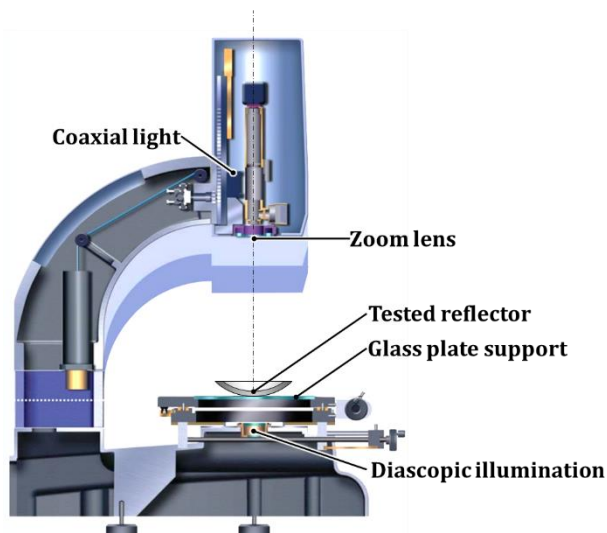


Figure 4-9 Solar simulator back reflector measurement setup

- ***Results***

The collected data of the tested reflector are listed in Table 4-1, and a scan of the full measurement report is available in Appendix C.

Table 4-1 Solar simulator back reflector measurement data

	Nominal	+Tol	-Tol	Mean	Deviation	OutTol
Radius of curvature (mm)	121.00	0.05	-0.05	121.33	0.33	0.28
Rim diameter (mm)	164.87	0.05	-0.05	164.87	0.00	0.00

4.2.2 Mirror Reflectivity

This test aims to measure LLBG mirrors reflectance. Mirrors tested are:

1. 2.0 mm-thick commercial float glass coated with Aluminium-Silicon Monoxide (Al-SiO) mirror, supplied by UQG Optics (UQG Optics, 1999).
2. 0.5 mm-thick “MIRO-SUN® weatherproof reflective 90”, supplied by Alanod-Solar. It is a multilayer material consisted of a main Aluminium strip sandwiched in anodised layers and coated with physical vapor deposition (PVD) and inorganic solar lacquer layers with a protective epoxy layer on the back (ALANOD, 2010).

- **Instruments Required**

Condor reflectometer (Figure 4-7).

- **Experimental Setup and Procedure**

The Condor reflectometer is left for 5 minutes for pre-heating and stabilisation, then it is calibrated using a provided standard mirror. To measure the reflectance of the mirror, the instrument is rested against the mirror and the measurements through the six LEDs and detectors are taken sequentially. Then the collected data are stored within the instrument and can be downloaded and copied into an Excel file. These steps are followed for each tested mirror.

- **Results**

The measured reflectance of the tested mirrors are available in Table 4-2.

Table 4-2 Mirrors reflectance measurements

		λ (nm)	435	525	650	780	940	1050	Solar Weighted
Reflectance (%)	Mirror #1 (Float glass)	Test #1	86.7	87.2	80.9	73.3	73.4	75.1	78.6
		Test #2	87.4	87.7	81.3	73.1	73.4	75.1	78.9
		Test #3	87.3	87.6	80.8	73.1	73.2	74.6	78.7
		Test #4	87.7	87.8	80.9	73.4	73.4	74.8	78.8
	Mirror #2 (MIRO-SUN®)	Test #1	94.8	94.5	88.5	79.8	84.3	89.7	87.7
		Test #2	94.7	94.6	88.3	80.5	83.6	89.7	87.7
		Test #3	95.2	94.7	88.5	80.4	84.3	89.4	87.8
		Test #4	94.7	93.9	88.7	79.6	84.5	89.2	87.5

4.2.3 Front Lens Bending Measurement

This test aims to measure the radius of curvature of the large front Fresnel lens at three distinct positions: vertical, 45° inclined and horizontal.

- **Instruments Required**

Leitz PMM-F CMM (Figure 4-8).

- **Experimental Setup and Procedure**

The lens frame structure is fixed over the CMM granite base and the lens angular position is adjusted to one of the required three positions through a swivel hinge, as illustrated in Figure 4-10, and then measurements are taken with approximately 100mm separation in both directions. After this, the lens is rotated to the next desired angular position and measurements are taken, as previous.

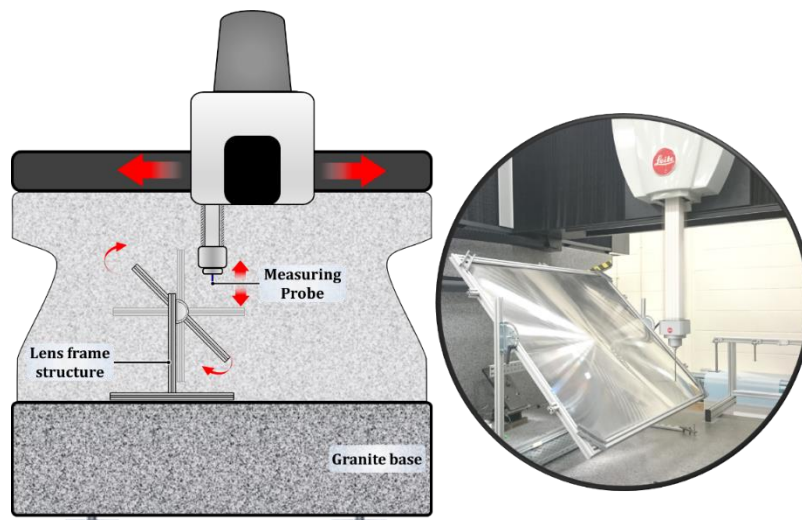


Figure 4-10 Front lens bending measurement test setup

- **Results**

The profile of the lens surface is plotted in Figure 4-11 for the three tested positions. The lens surface characteristics including, radius of curvature, form (i.e. the distance between the maximum and minimum deflection) and the maximum recorded deflection in lens surface in each tested position are listed in Table 4-3.

Table 4-3 Front lens surface characteristics

	Vertical	45° Inclination	Horizontal
Radius of curvature (m)	27.652	18.114	19.711
Form (m)	9.7006E-03	14.998E-03	14.443E-03
Maximum deflection (m)	10.980E-03	20.745E-03	22.836E-03

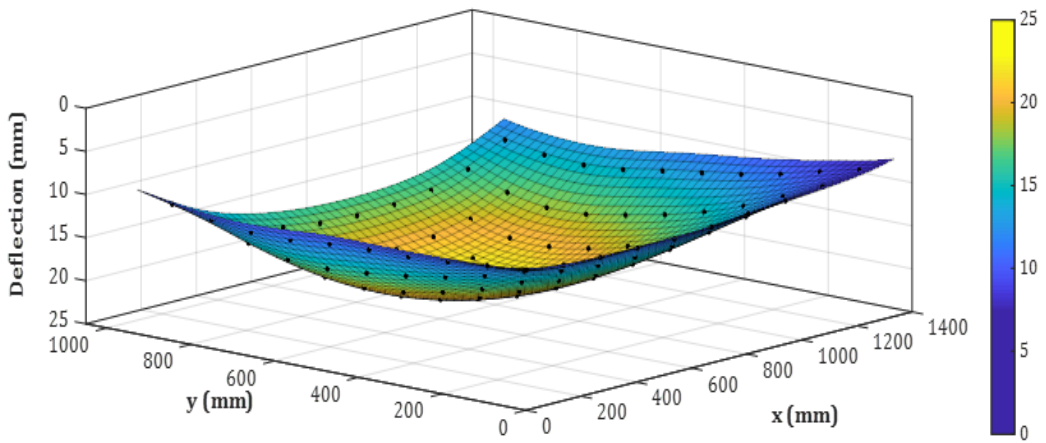
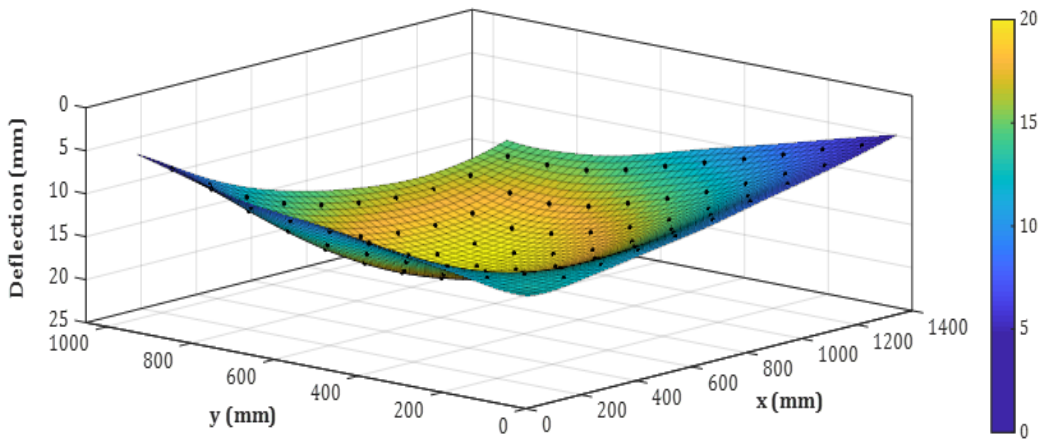
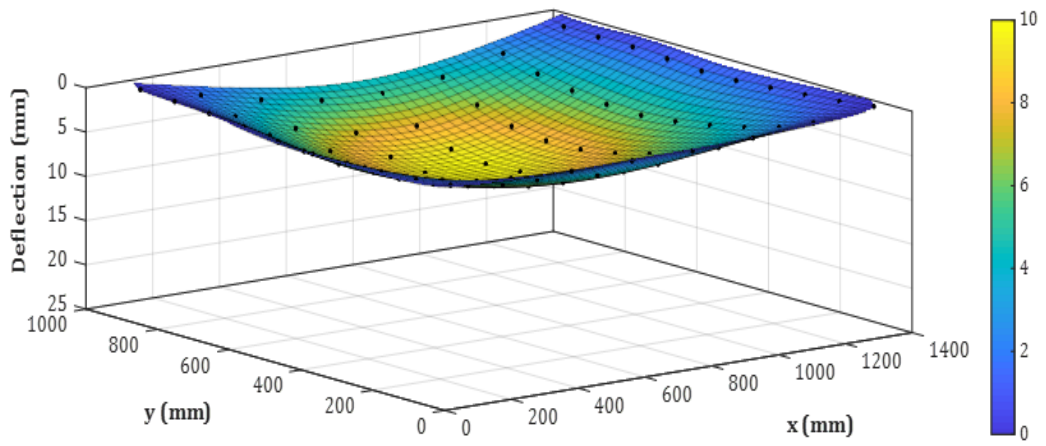


Figure 4-11 Front lens surface profile
(a) vertical (b) 45° inclination (c) horizontal

5 SOLAR SIMULATOR DESIGN AND TESTING

5.1 Solar Simulator Design

5.1.1 Main Components

To build a large-scale solar simulator facility for CSP tests, it is required to cover most of the solar spectrum (350-2500 nm). The aim is to get a collimated output beam with aperture area of minimum 1m^2 and output power of approximately one sun ($\approx 1\text{kW}/\text{m}^2$). In this section, the main required components required to build such system discussed.

- **Light Source**

Since 1960s, researchers paid attention to build large scale solar simulators for solar thermal applications. The common light sources for these simulators are: tungsten halogen, xenon arc, and metal halide arc lamps. In order to build inexpensive solar simulators, tungsten halogen lamps were selected as light sources (Yass and Curtis, 1974; Humphries and George, 1978; Ley, 1979). However, spectral composition of these lamps was shifted away from the solar one. They radiate stronger power in the IR bandwidth and weaker in the shorter wavelengths (Bickler, 1962). This is as a result of the difference between the colour temperature of such lamps, which is less than 3400K, compared to the AM0 colour temperature of approximately 5900K (Matson, Emery and Bird, 1984). Recently, researchers tended to use xenon arc lamps (Kuhn and Hunt, 1991; Jaworske, Jefferies and Mason, 1996; Hirsch *et al.*, 2003; Petrasch *et al.*, 2007). Although xenon arc lamps have an excellent continuum in UV and VIS band, they have strong emission lines in the infrared between 800-1000 nm, which requires filtrations (Bickler, 1962). In addition, these lamps show irradiance instabilities with time. Their output spectrum shifts slightly away from the UV to the IR with lamp aging (Wang, 2014). This output is also sensitive to the power supply instabilities (Matson, Emery and Bird, 1984). Furthermore, using xenon arc lamps implements high risk, as its approximate pressure is 10 bar and can increase during its operation up to 40 bar. However, in modern solar simulator designs, metal halide lamps are used to get closer to the spectral composition of

sun light (Zahler *et al.*, 2005, 2008; Codd *et al.*, 2010; Meng, Wang and Zhang, 2011). Besides having a balanced spectral output, metal halide lamps are relatively inexpensive (Beeson, 1978), compared to xenon arc lamps.

Based on the literature a PHILIPS 6994Z 2000W tungsten halogen lamp and a PHILIPS HPI-T 2000W metal halide lamp were selected to compare among them. In order to compare the output spectra from both lamps, The HR-1024i Field Spectroradiometer (Figure 4-1) was loaned from the Natural Environment Research Council (NERC), School of GeoSciences, University of Edinburgh, UK by writing a proposal.

- ***Power Supply***

For the tungsten halogen lamp, no special requirements are needed for its operation, as it can be plugged directly to a 230–240V AC power source. However, the metal halide one requires ballast and igniter compatible with the lamp to light it up. For this purpose, PHILIPS HID-High Power BHL 2000 ballast and a PHILIPS SI 52 igniter were fitted in an electrical circuit to supply the lamp with power needed.

- ***Optical System***

The light source, either the tungsten halogen or metal halide lamp, is placed in front of a spherical aluminium anodised reflector and behind a glass Fresnel lens. This system is enclosed in a housing coated with epoxy polyester powder. To test the LLBG indoor, it is required to receive a collimated beam. Therefore, a PMMA Fresnel lens is used as a collimating lens to receive a collimated beam for the testing section. The system for both tungsten halogen/metal halide lamps is illustrated in Figure 5-1. The full system configuration is illustrated schematically in Figure 5-2.

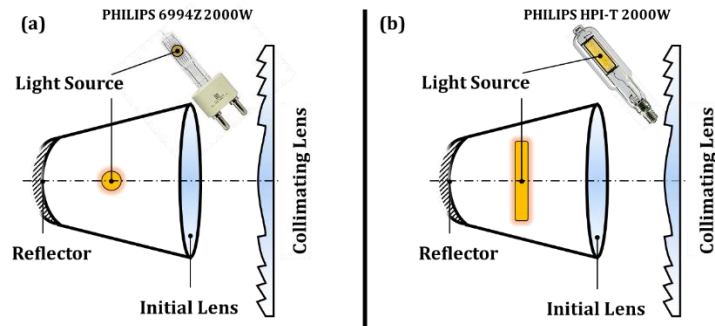


Figure 5-1 Solar simulator optical system
(a) Tungsten halogen lamp **(b) Metal halide lamp**

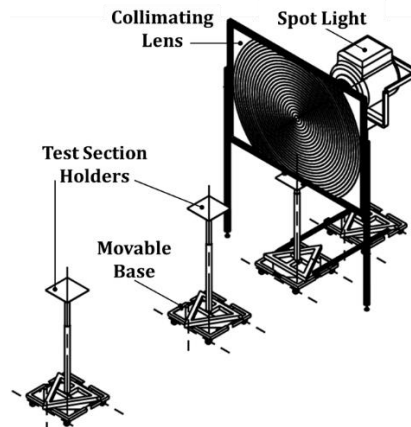


Figure 5-2 Solar simulator schematic diagram

Specifications of such optical elements are listed in Table 5-1. The values of reflector diameter and radius of curvature are measured using the TESA-VISIO[®] 300 DCC machine (Figure 4-2), available in Precision Engineering Laboratory, Cranfield University. The complete report is available in Appendix C.

Table 5-1 Optical elements specifications

Parameter	Value (mm)
Reflector diameter	164.86934
Reflector radius of curvature	121.32818
Distance between reflector tip to light source centreline	102.0
Distance between light source centreline to the initial lens	233.0
Initial lens diameter	480.0
Initial lens rear focal length (focal point at the light source side)	270.0
Initial lens front focal length (focal point at the collimating lens side)	385.0
Collimating lens focal length	1400.0
Length of the line source (in case of metal halide lamp only)	89.0

5.1.2 Ray Tracing Simulation

This section aims to predict the rays' behaviour in different cases. In such simulation, OptGéo, version 2.20 is used as an available freeware to fulfil the aim.

- **Tungsten Halogen Case**

In this case, a point line source is assumed with 250 rays output. Two options were investigated as illustrated in Figure 5-3. In the first case, shown in Figure 5-3a, the initial glass Fresnel lens was placed and the distance between it and the collimating lens was set to be 500mm. For shorter distances, no significant enhancement in the collimation output is achieved. In addition, the closer the collimating lens, the higher lens surface temperature is reached leading to higher risk of collimating lens damage.

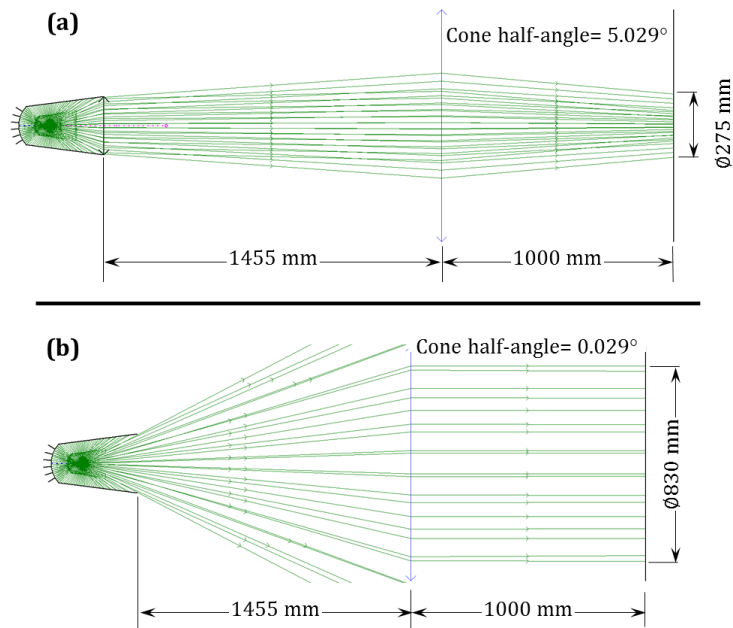


Figure 5-3 Tungsten halogen case
(a) with initial lens **(b) without initial lens**

In the second case, shown in Figure 5-3b, the initial glass Fresnel lens was removed and the distance between its plan and the collimating lens was set to be 1170mm. For closer distance, the output beam tends to diverge, while the larger distance causes beam convergence. At the set distance, the output cone half-angle is 0°.

- **Metal Halide Case**

In this, a line source is approximated by 9-point sources with output of 30 rays each as case shown in Figure 5-4. Two options were investigated as illustrated in Figure 5-5.

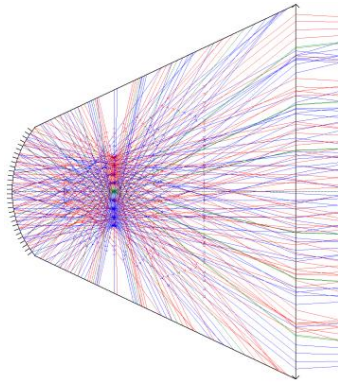


Figure 5-4 Metal halide lamp representation

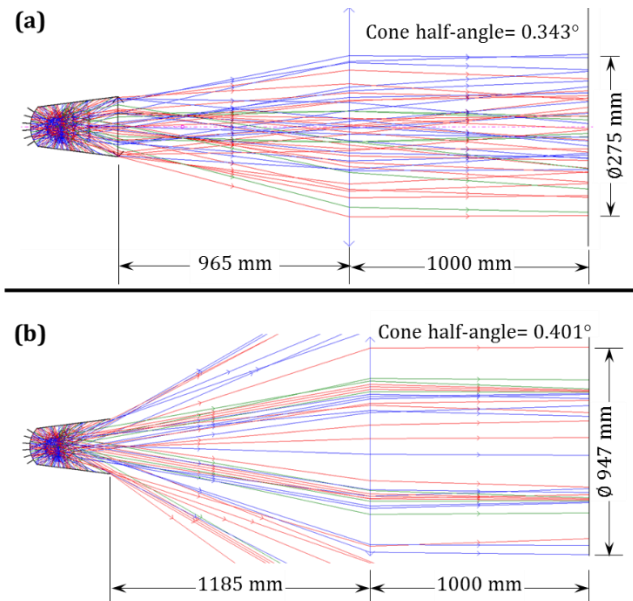


Figure 5-5 Metal halide case
(a) with initial lens **(b) without initial lens**

In the first case, shown in Figure 5-5a, the initial glass Fresnel lens was placed and the distance between it and the collimating lens was set to be 765mm with a beam diameter of 800mm. At this position, the output beam nearly achieves the full collimation with an approximate cone half-angle of 0° . For shorter distances, the beam shows more divergence while larger distances lead to beam convergence. In the second case, shown in Figure 5-5b, the initial glass Fresnel lens was removed and the distance between its plan and the collimating lens was set to be 1200mm. At such position, the output beam cone half-angle is approximately 1° and the beam maximum effective diameter reaches 890mm. For closer distance, the output beam tends to diverge, while the larger distance causes beam convergence.

5.2 Solar Simulator Testing

5.2.1 Lamps Spectra Comparison Experiments

These experiments aim to compare the spectral output of both tungsten halogen and metal halide lamp used in the system. Hence this experiment focuses on the light sources output spectra, the collimating lens would not participate in the setup of these experiment.

- **Instruments Required**

SVC HR-1024i Field Spectroradiometer (Figure 4-1) was used to measure the output spectrum in each case. Moreover, PHILIPS Strand single channel portable dimmer (Figure 4-3) is used to control the output power level from the tungsten halogen lamp.

- **Experimental Setup**

The testing setup for both tungsten halogen and metal halide cases are illustrated in Figure 5-6. The distance, l , is selected to be 1m from the spot light body to minimise the overheating risk for sensing element of the loaned equipment.

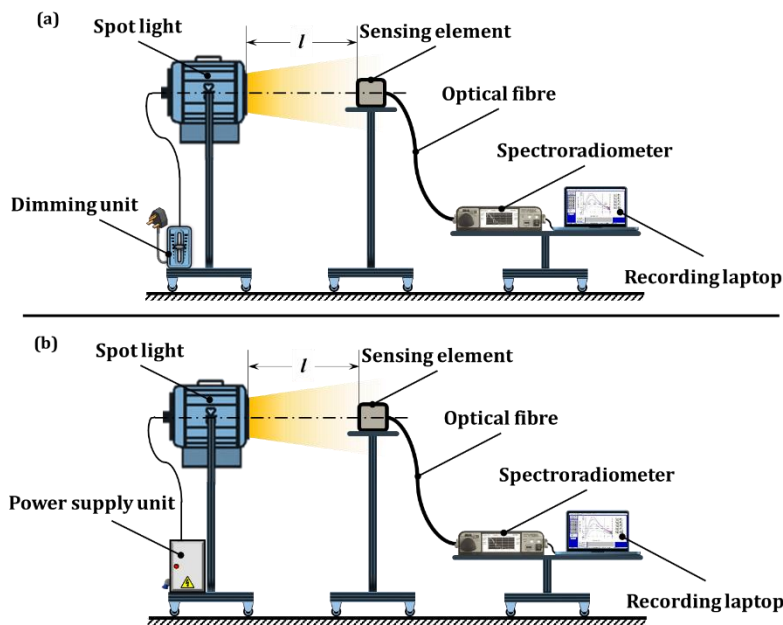


Figure 5-6 Spectrum measuring test setup
(a) Tungsten halogen case **(b) Metal halide case**

- ***Experimental Procedure***

(a) For Tungsten Halogen Case

To investigate the dimming effect on the output spectrum, data has been collected at 25, 50, 75 and 100% of lamp power. In each experiment, 10 data sets were recorded, separated with 5 seconds between each successive recording, and averaged to minimise the error in collected data (according to the recommendation of the NERC trainer). All tests are carried out in a completely dark room to avoid any unexpected spectra.

(b) For Metal Halide Case

Metal halide is not recommended to be dimmable (Benya and Leban, 2011), as they require special dimmers and dimmable ballasts (Grosslight, 1991) with very poor colour shift issues (Teicholz, 2001). Therefore, the dimmer in the tungsten halogen test setup is replaced with the power supply unit which include the ballast and the igniter. In each such experiment, 10 data sets were recorded, separated with 5 seconds between each successive recording, and averaged to minimise the error in collected data. Recording data starts after 15 minutes from the time of switching the lamp on, to reach the steady state condition. The time for reaching the steady state condition has been observed through running the lamp and displaying the output spectrum which has been found changing with time up to 10 minutes of lamp start-up. All tests are carried out in a completely dark room to avoid any unexpected spectra. Results of these experiments are plotted in Figure 7-1 and Figure 7-2.

5.2.2 Fresnel Lens Transmittance Measurement Experiment

This experiment aims to measure the actual transmittance of the already purchased PMMA Fresnel lens experimentally. It has been carried out with the metal halide lamp as it covers wider range of spectrum.

- ***Instruments Required***

SVC HR-1024i Field Spectroradiometer (Figure 4-1) was used to measure the output spectrum with/without the Fresnel lens.

- **Experimental Setup**

The testing setup for metal halide case with the PMMA Fresnel lens is illustrated in Figure 5-7. The distance, l , is selected to be 1m, as the previous set of experiments. The tested lens is then placed in midway between the light source and the sensing element.

- **Experimental Procedure**

In the first stage, the system setup as illustrated in Figure 5-7a, with no lens in the way between the light source and the sensing element. At this stage, 10 data sets were recorded, separated with 5 seconds between each successive recording, and then averaged. In the second stage, the tested Fresnel lens is placed in the midway between the lamp and the sensing element, as shown in Figure 5-7b. Then new 10 data sets were recorded, averaged and then compared with averaged data obtained from the first step. All data collected from both stages were recorded after at least 15 minutes from the lamp start-up. All tests are carried out in a completely dark room to avoid any unexpected spectra. Results are available in Figure 7-3.

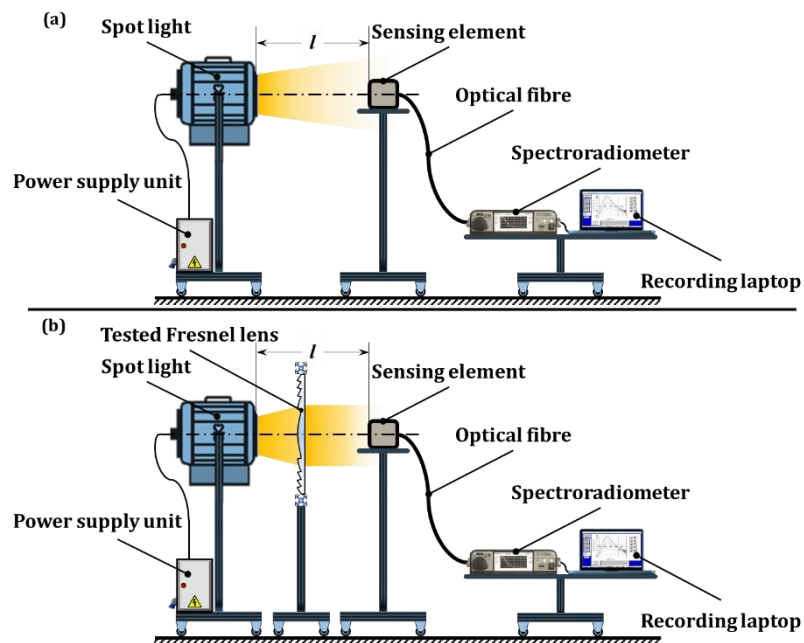


Figure 5-7 Fresnel lens transmittance measuring test setup
(a) first stage (b) second stage

5.2.3 Irradiance Measurement Experiments

These experiments aim to compare the irradiance of the solar simulator for both tungsten halogen and metal halide lamp cases. In these experiments, the collimating lens, which is identical to the tested one in section 5.2.2, is used.

- ***Instruments Required***

SMP10 pyranometer (Figure 4-4) is used to measure irradiance with an analogue output range of 0–1600 W/m².

- ***Experimental Setup***

The testing setup is illustrated in Figure 5-8. The collimating Fresnel lens is placed at distance l_0 from the spot light which obtained from the ray tracing model output. While the distance, l , is measured from the collimating lens plane to the sensing plane of the pyranometer, which is away from its base plane (the screen plane) by distance l_1 . The distance l is 1m, as the previous set of experiments, while the distance l_1 is 0.068m, as illustrated in Figure 5-8. Based on the ray tracing results in section 5.1.2, the tungsten halogen test is carried out without the initial glass Fresnel lens while it will be used in the metal halide test to ensure achieving the most amount of collimation.

- ***Experimental Procedure***

In the tungsten halogen lamp case, the test is run at full output power of the lamp. For the metal halide lamp case, the all measurements are recorded after at least 15 minutes from the lamp start-up to ensure reaching the steady state output power. In both tungsten halogen and metal halide lamp cases, the pyranometer is placed on different pre-marked patterned screen (Figure 5-8). These spots are separated horizontally by Δx and vertically by Δy , which correspond 0.2 and 0.14 m, respectively. The pyranometer output current (in mA) is detected by a multi-meter and recorded manually at each spot. Then the pyranometer datasheet correlation is applied to calculate the irradiance as follows:

$$I = 100(C - 4) \quad (5-1)$$

Where, I and C are the irradiation (W/m^2) and output current (mA), respectively. The output irradiance of both tungsten halogen and metal halide cases are illustrated in Figure 7-4.

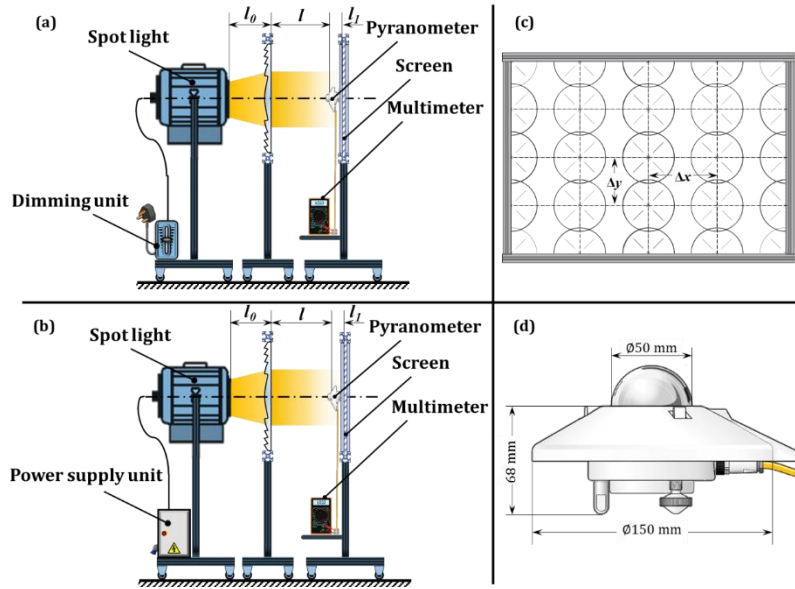


Figure 5-8 Irradiance measuring test setup
(a) Tungsten halogen case **(b) Metal halide case**
(c) patterned screen **(d) pyranometer dimension**

5.2.4 Thermal Response Evaluation Experiments

These experiments aim to evaluate and compare the thermal responses of an object irradiated by the simulator's output power in both tungsten halogen and metal halide lamp cases.

- **Instruments Required**

TC-08 thermocouple data logger is connected to thermocouples of K-type (Figure 4-5) to measure and record the screen's surface temperature.

- **Experimental Setup**

The testing setup is illustrated in Figure 5-9. The collimating Fresnel lens is placed at distance l_0 from the spot light which obtained from the ray tracing model output. While the distance, l , is measured from the collimating lens plane to the receiving black screen. The distance l is 1m, as the previous set of experiments. Seven thermocouples are attached, in equally-spaced form, to the black screen

wooden board. One is attached at the centre point of the output beam, and three are separated by 0.15m in the horizontal direction, while the rest are placed with the same separation but in the vertical direction.

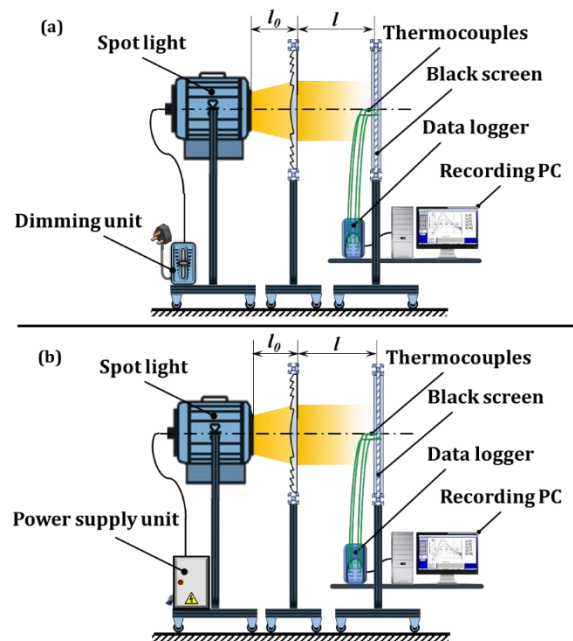


Figure 5-9 Thermal response measuring test setup
(a) Tungsten halogen case **(b) Metal halide case**

- **Experimental Procedure**

In the tungsten halogen lamp case, the test is run at full output power of the lamp. For the metal halide lamp case, the all measurements are recorded after at least 15 minutes from the lamp start-up to ensure reaching the steady state output power. In both tungsten halogen and metal halide lamp cases, the temperature at the seven points were detected and recorded with a sampling rate of 1 sample per second until the screen's surface temperature tends to stability. Results of these experimental results are displayed in Figure 7-5.

5.2.5 Lens Mount Model Validation Experiments

The aim of these experiments is to validate the numerical model developed (Section 6.1.3.4) for investigating the mounting effect on a transparent window subjected to radiative heat flux at one side.

- ***Instruments Required***

TC-08 thermocouple data logger (Figure 4-5) with K-type thermocouples to detect the mount temperature (Figure 4-5).

- ***Experimental Setup***

The testing setup is illustrated in Figure 5-10, is consisting a self-centring lens mount fixed over an adjustable stand which is used to hold a 25mm window between its clamps. It is adjusted so that the tested window lies at 1m from the collimating lens of the solar simulator and is located at the area of the output peak flux of 1600 W/m². As the mount is made of Delrin[®] acetal (Polyoxymethylene POM) which provides an operating temperature ranges from -40°C to 120°C, it has been masked with a 2mm-thick aluminium shield with a 25mm aperture holed coaxially with the sample's axis and separated from the mount by a 7.5mm air gap.

- ***Experimental Procedure***

The tungsten halogen lamp is run at the lamp full output power. The clamping fingers and the ambient temperatures have been recorded through K-type thermocouples connected to PC via a data logger. The data has been recorded for 30 minutes/sample to ensure reaching the steady-state temperatures in each case. Results of these tests are plotted in Figure 7-6.

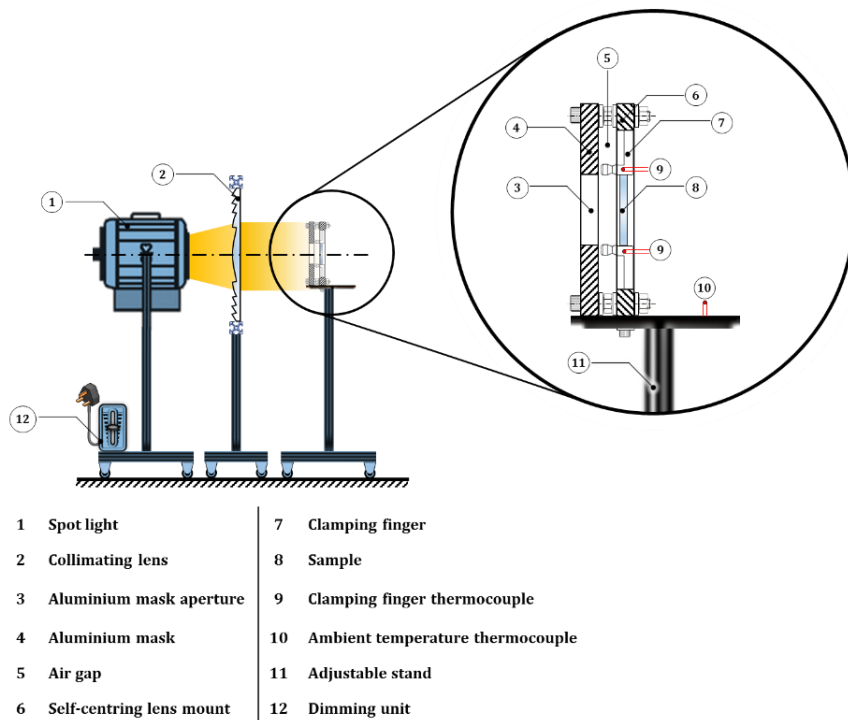


Figure 5-10 Lens mount model validation experimental setup layout

5.3 Summary

In this chapter, main components of solar simulator design have been discussed. This covered selection procedure of the suitable light sources for thermal testing applications. In addition, requirements to power up the selected light sources have been addressed as well as the design of an optical system that is able of producing nearly collimated rays to allow using the solar simulator in testing the LLBG system. Moreover, description of experiments that set up to calibrate solar simulator and that uses it for testing the LLBG has been discussed within this chapter.

6 LLBG SYSTEM DESIGN AND TESTING

6.1 Theoretical Study Framework

This chapter investigate the LLBG main parts from a numerical perspective. It describes the system main components and followed by various studies to select the optimum front and rear lens geometries and materials. These studies include: cost, manufacturing, optical and thermal investigations according the situation of each component. Then, an optical evaluation to the system configuration and different parameters affecting its optical performance has been investigated.

6.1.1 System Working Principle

The LLBG is a point-focus solar concentrating system, in which the sun rays refracted through the front lens focal point, F , which is coincident with the focal point of the rear lens. Such optical configuration is capable of generating a nearly-collimated and concentrated solar beam as illustrated by Figure 6-1. The system tracks the sun rays through a dual-axis tracking system. The generated beam direction is then controlled through a rotating flat mirror, shown in Figure 6-1.

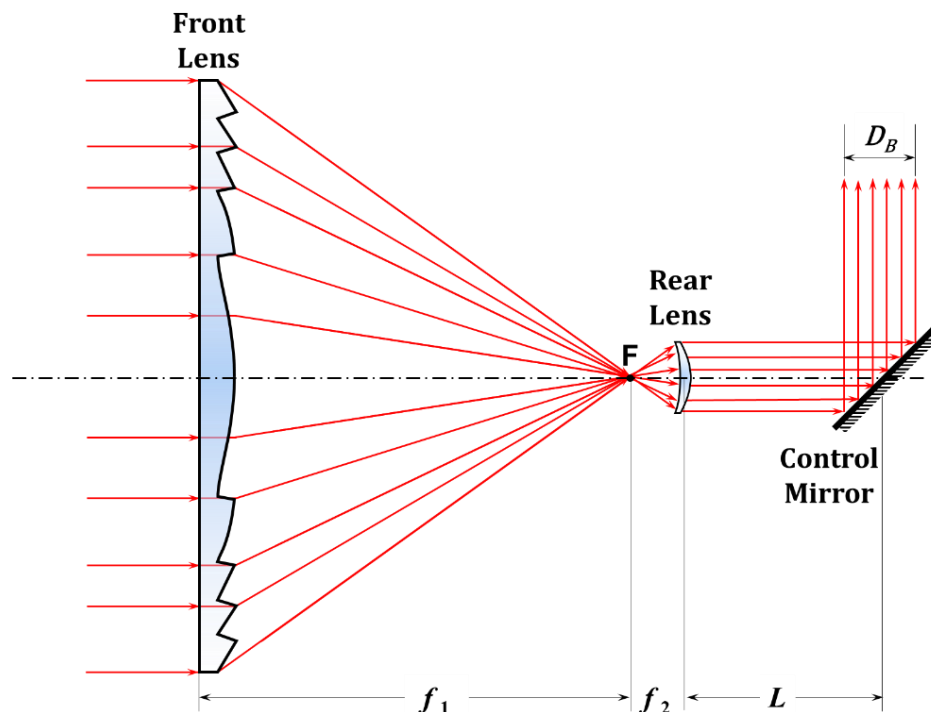


Figure 6-1 The LLBG optical configuration

6.1.2 Front Lens Study

6.1.2.1 Front Lens Geometry

The front lens has the largest surface area of all optical components in the LLBG. Therefore, design approach was to minimise its weight and cost. Based on this approach, Fresnel lens geometry is chosen for this part as it fulfils both aims by reducing the amount of material required to manufacture (Shim *et al.*, 2015). Fresnel lens terminology is discussed in Section 2.4.1.

6.1.2.2 Front Lens Material

In order to select the optimum material for the front lens, it is important to study Fresnel lenses manufacturing methods to identify a list of suitable materials. This list is refined according to the cost criterion. Then optical losses of Fresnel lenses are studied to determine the material which provides the maximum ideal optical efficiency.

A. Fresnel Lens Manufacturing Technologies

According to different manufacturing methods reviewed in Section 2.4.2, Fresnel lenses can be manufactured through several techniques: injection moulding, embossing and diamond turning. Polymeric materials (such as PMMA and PC) substrates can be used for all these manufacturing techniques, while CaF_2 can only be used with diamond turning technique. Based on this study, there are three materials candidates: CaF_2 , PMMA and PC.

B. Fresnel Lens Manufacturing Cost

From the previous section, injection moulding and embossing technologies are cheaper than diamond turning as they can be applied for mass production (Tribastone and Peck, 2001; Benitez *et al.*, 2014). These techniques can be applied for polymer materials such as PMMA and PC (Schulz *et al.*, 2000; Kujawa *et al.*, 2012; Tosello *et al.*, 2012; Kuo and Liao, 2015).

C. Fresnel Lens Optical Losses and Ideal Efficiency

Optical losses through Fresnel lenses include: geometric, dispersion, blocking absorption and reflection losses, as reviewed in Section 2.4.3. Based on such

review, it was found that some of them only depend on the lens material while the other relies on the facets design and lens set-up configuration. Therefore, ideal optical efficiency of plastic Fresnel lenses used for solar concentration is estimated. The estimation is restricted to the effect of spectral properties of lens materials over solar spectrum bandwidth. The calculation is based on considering materials transmittances, plotted in Figure 2-25, and the first-stage reflection losses, calculated from Eq. (2-9). Such first-stage reflection losses are found to be depending the material refractive index and the incidence angle, as indicated by Equations (2-7) and (2-8).

Refractive indices have been taken as values measured by (Sultanova, Kasarova and Nikolov, 2009) at $20 \pm 0.2^\circ\text{C}$ for wavelengths from 436.8 to 1052nm. For the rest of solar spectrum bandwidth (280–2500nm), spectral dependence of refractive index has been described via several models. Cauchy and Sellmeier dispersion equations have been widely used for many materials to fit the measured refractive index data. Cauchy's dispersion equation (CDE) is given by (Mistrik *et al.*, 2017):

$$n^2(\lambda) = A_1 + A_2\lambda^2 + \frac{A_3}{\lambda^2} + \frac{A_4}{\lambda^4} + \frac{A_5}{\lambda^6} + \frac{A_6}{\lambda^8} + \dots \quad (6-1)$$

while Sellmeier's dispersion equation (SDE) is stated in the following form (Mistrik *et al.*, 2017):

$$n^2(\lambda) = 1 + \frac{A_1\lambda^2}{\lambda^2 - A_2} + \frac{A_3\lambda^2}{\lambda^2 - A_4} + \frac{A_5\lambda^2}{\lambda^2 - A_6} + \dots \quad (6-2)$$

Where n is the refractive index and A_1, A_2, \dots, A_6 are the calculated dispersion coefficients, while λ represents the wavelength in (μm). The accuracy of CDE formula with respect to the number of dispersion coefficients has been studied by (Kasarova *et al.*, 2007). They achieved their best results, with precision of ± 0.001 , are obtained using six dispersion coefficients in CDE. The values of these coefficients which based on fitting data measured by (Sultanova, Kasarova and Nikolov, 2009). Although CDE has been used typically in the VIS region of the spectrum for various optical materials, recently it has been largely replaced by the SDE (Mistrik *et al.*, 2017). SDE with two dispersion coefficients has been used

to fit the same experimental data set (Sultanova, Kasarova and Nikolov, 2009) by (Polyanskiy, 2017). In the present work, six dispersion coefficients for SDE have been generated using MATLAB® curve fitting tool. In order to compare the accuracy between results (CDE-6, SDE-2 and SDE-6 coefficients), the root mean square error (RMSE) (Hyndman and Koehler, 2006) and mean absolute percentage error (MAPE) (Hyndman *et al.*, 2008) are calculated based on the following formulae:

$$RMSE = \sqrt{\left[\sum_{i=1}^N (n_{DE,i} - n_{ex,i})^2 \right] / N} \quad (6-3)$$

$$MAPE = (100/N) \sum_{i=1}^N |n_{DE,i} - n_{ex,i}| / n_{ex,i} \quad (6-4)$$

Where n_{DE} and n_{ex} are the model and experimentally measured values of refractive index at a certain step, i , while N represents the number of data points studied. Obtained dispersion coefficients for CDE and SDE and error values are listed in Table 6-1, while the refractive indices of PMMA and PC can be plotted in Figure 6-2 based on CDE and SDE against the experimental data. From Table 6-1, SDE-6 coefficients show the minimum error values; therefore, it will be selected in the present work to calculate the spectral dependence of refractive index. Then, the average values for PMMA and PC refractive indices are 1.483 and 1.575, respectively.

Table 6-1 CDE and SDE coefficients for polymeric transparent materials, based on fitting experimental data (Sultanova, Kasarova and Nikolov, 2009)

Material	Dispersion coefficients	Applied dispersion equation		
		CDE-6 coefficients (Kasarova et al., 2007)	SDE-2 coefficients (Polyanskiy, 2017)	SDE-6 coefficients
PMMA	A_1	2.39996400	1.1819	1.185
	A_2	-0.08308636	0.011313	0.01116
	A_3	-0.1919569	—	0.04079
	A_4	0.08720608	—	34.48
	A_5	-0.01.666411	—	-0.001914
	A_6	0.001169519	—	0.01895
		$RMSE$ (-)	2.98E-04	2.77E-04
	$MAPE$ (%)	1.78E-02	1.64E-02	1.44E-02
PC	A_1	2.633127	1.4182	1.107
	A_2	-0.07937823	0.021304	0.0223
	A_3	-0.1734506	—	1.533
	A_4	0.08609268	—	-166.2
	A_5	-0.01617892	—	0.3026
	A_6	0.001128933	—	0.02222
		$RMSE$ (-)	3.98E-04	5.60E-04
	$MAPE$ (%)	2.20E-02	3.12E-02	1.60E-02

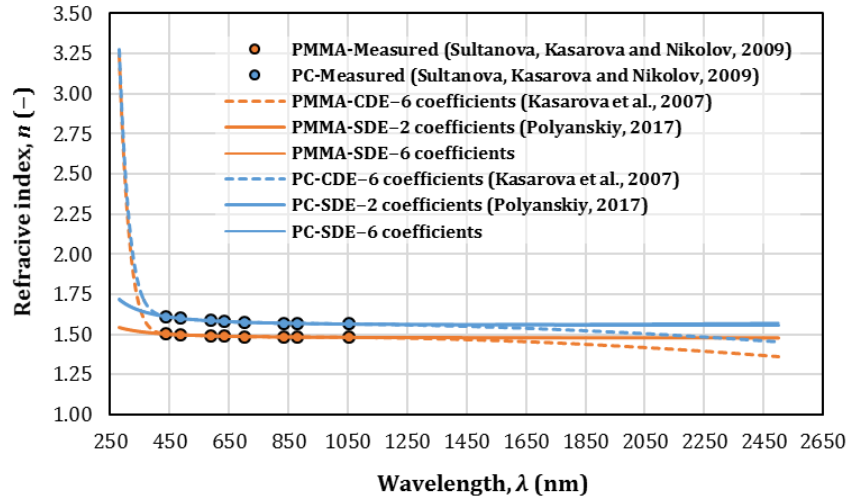


Figure 6-2 Polymeric materials measured, CDE-6 coefficients, SDE-2 coefficients and SDE-6 coefficients refractive indices

Applying Equations (2-7), (2-8) and (2-9), then the reflectance of Fresnel lenses made of PMMA and PC can be plotted in Figure 6-3.

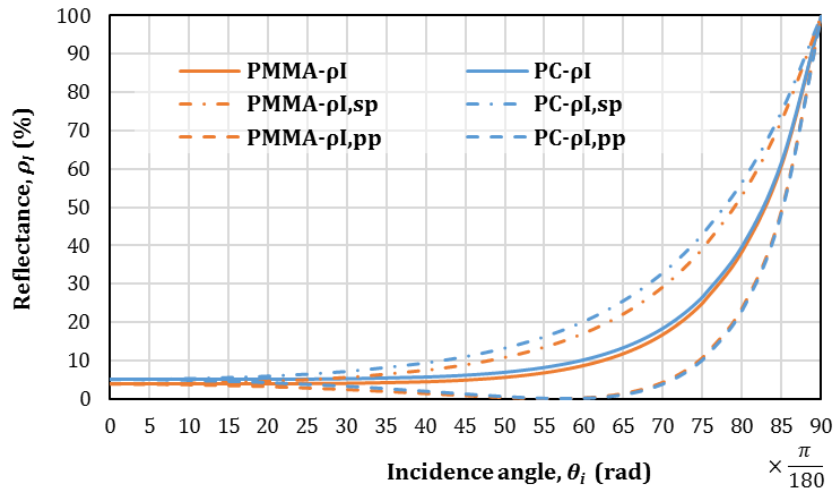


Figure 6-3 Reflectance of polymeric transparent materials

By restricting the incidence angle to the solar aperture cone-half angle, θ_a , of 0.266° , then the initial reflection losses will be 3.786% and 4.988% of the incident radiation on Fresnel lenses made of PMMA and PC, respectively. The ideal and reflection efficiencies of PMMA and PC are plotted in Figure 6-4. The average ideal efficiency, $\eta_{ideal,av}$, per material over wavelengths ranging from λ_1 to λ_2 can be obtained by:

$$\eta_{ideal,av} = \int_{\lambda_1}^{\lambda_2} \eta_{ideal} \cdot d\lambda / (\lambda_2 - \lambda_1) \quad (6-5)$$

Where the ideal efficiency, η_{ideal} is calculated from:

$$\eta_{ideal}(\lambda) = 100\tau_{I,\lambda}(1 - \rho_{I,\lambda,\theta_a}) \quad (6-6)$$

Where $\tau_{I,\lambda}$ is the spectral transmittance, while $\rho_{I,\lambda,\theta_a}$ represents the spectral reflectance at incidence angle equal to the solar aperture cone-half angle, θ_a .

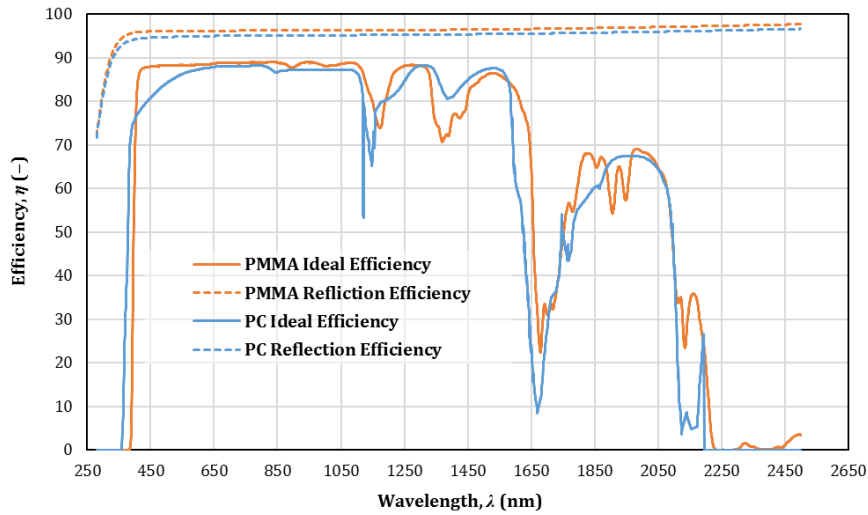


Figure 6-4 Ideal and reflection efficiencies of polymeric transparent materials for solar concentration applications

As a result of the limited data available for PC spatial transmittance, the average ideal efficiency is calculated over a wavelength range (360–2194nm) only. The results showed that PMMA and PC ideal efficiencies are 74.16 and 71.74%, respectively. According to this result, the final decision is to assign PMMA for the front lens. Figure 6-5 summarises the front lens study results.

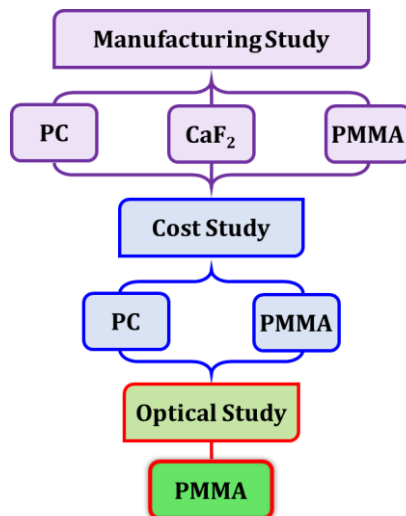


Figure 6-5 Summary of front lens study results

6.1.3 Rear Lens Study

Based on the geometry shown in Figure 6-1, the rear lens is subjected to a high-power flux. Therefore, it is important to simulate this lens thermally to select the best geometry and material that can withstand such severe operating conditions. Therefore, mathematical and numerical models have been developed and validated to simulate the thermal behaviour of such lens under high-radiative flux. The mathematical model is solved by MATLAB® (code in Appendix A), while two numerical models are solved by COMSOL Multiphysics 5.1 and ANSYS 16.0. Proposed mathematical and numerical models are validated in Section 7.2.1.

6.1.3.1 Rear Lens Thermal Modelling

A. Physical Model Description

As shown in Figure 6-6, a sample of a semi-transparent material is subjected to high-intensity radiative heat flux on one side. In reality, the sample may represent a solar receiver window, converging lens or a diverging lens with a diameter, D . To develop a generalised heat transfer model for similar cases, the sample geometry is simplified by assuming that it has a constant thickness, e .

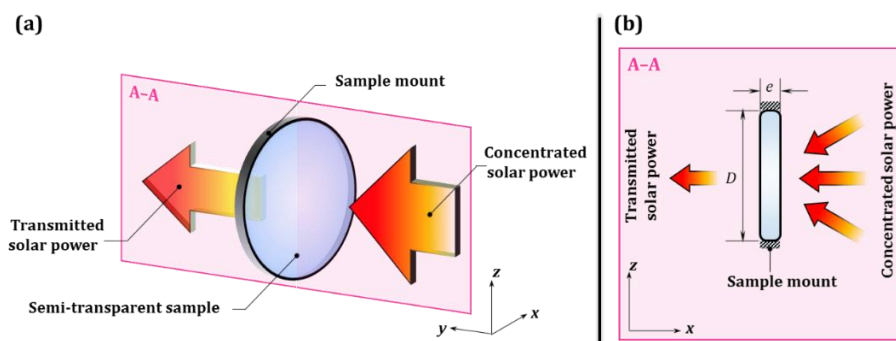


Figure 6-6 Physical problem description

(a) 3-D conceptual representation (b) 2-D simplified model with dimensions

The sample is assumed to be cooled down by natural convection only. Hence the sample thickness is very small compared to its diameter, the heat transfer in the radial direction can be neglected. The sample mounting types may be screw-threaded type, a bayonet-type, or a breech-lock (friction lock) type (Patnaik and Zhong, 2014). Each mounting type has different contacting nature with the optical part which affects the amount of heat transfer through the sample tip in the radial direction. To simulate the worst heat transfer case for the sample, heat dissipation

through its mount is neglected and its tip is assumed to be thermally insulated. However, the real mounting effect will be investigated by the end of this section.

B. Mathematical Model

In this section, progressive mathematical models to determine the sample temperature of a transparent material with a diameter, D , and thickness, e , are derived. All models are based on assuming that the sample surface and environmental conditions on the side facing the concentrated power is denoted by 1, while the other side is denoted by 2, as illustrated in Figure 6-7. In order to determine the most crucial assumptions to be taken into consideration, the modelling level has been developed from simplified form to an unsteady through a steady-state model.

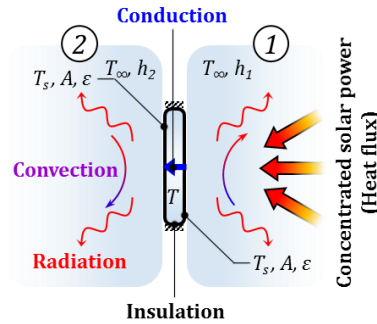


Figure 6-7 Energy balance through a semi-transparent sample

- **Simplified Model**

In this model, the thickness of sample is neglected by treating the sample as a thin surface, placed in an environment with an ambient temperature, T_{∞} . Consequently, temperature difference between both sides are neglected as well as heat transferred by conduction. Then the temperature of the sample on both sides are assumed to be equal to T_s . Then, the energy balance over the sample can be written as:

$$q_{ab} = q_{conv,1} + q_{conv,2} + q_{rad,1} + q_{rad,2} \quad (6-7)$$

Where, q_{ab} , q_{conv} and q_{rad} are representing the absorbed, convection and radiation heat transfer per unit area, respectively. This equation can be formulated in the form of 4th order polynomial as follows:

$$(2\varepsilon\sigma)T_s^4 + 0T_s^3 + 0T_s^2 + (h_1 + h_2)T_s - [(h_1 + h_2)T_{\infty} + 2\varepsilon\sigma T_{\infty}^4 + q_{ab}] = 0 \quad (6-8)$$

Where ε , σ and h are the sample emissivity, Stefan-Boltzmann constant (and the convective heat transfer coefficient. The sample surface temperature on both sides can be achieved through solving the last equation for T_s .

- **Steady-State Model**

For this model, the sample thickness and heat transfer by conduction between both sides are considered. This leads to solving the model for temperature on both sides, $T_{s,1}$, $T_{s,2}$. The accumulated heat in the sample is neglected in this model through assuming a steady-state condition. The energy balance on surface 1 can be expressed as:

$$q_{cond} = q_{ab} - q_{conv,1} - q_{rad,1} \quad (6-9)$$

And heat transferred by conduction, q_{cond} , is calculated from:

$$q_{cond} = k(T_{s,1} - T_{s,2})/e \quad (6-10)$$

From equations (6-9) and (6-10):

$$T_{s,2} = T_{s,1} - (e/k)[q_{ab} - h_1(T_{s,1} - T_\infty) - \varepsilon\sigma(T_{s,1}^4 - T_\infty^4)] \quad (6-11)$$

While the energy balance on surface 2 is:

$$q_{cond} = q_{conv,2} + q_{rad,2} \quad (6-12)$$

Combining equations (6-9)and (6-12) leads to:

$$q_{conv,1} + q_{conv,2} + q_{rad,1} + q_{rad,2} - q_{ab} = 0 \quad (6-13)$$

From Eq. (6-11) in (6-13) gives:

$$h_1(T_{s,1} - T_\infty) + h_2(T_{s,2} - T_\infty) + \varepsilon\sigma(T_{s,1}^4 - T_\infty^4) + \varepsilon\sigma(T_{s,2}^4 - T_\infty^4) - q_{ab} = 0 \quad (6-14)$$

To avoid the complexity resulting from substituting of Eq. (6-10) in Eq. (6-14), the last equation can be solved at an intermediate plane between the two surfaces to get the average temperature, T_{av} . The relation between T_{av} , $T_{s,1}$ and $T_{s,2}$ can be derived through the thermal resistance circuit as illustrated in Figure 6-8.

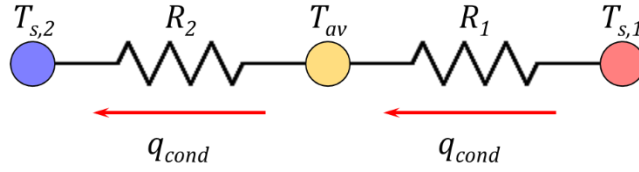


Figure 6-8 Thermal resistance circuit for the sample

$$q_{cond} = (T_{s,1} - T_{av})/R_1, \quad R_1 = e/2k \quad (6-15)$$

Then From Eq.(6-10),

$$T_{av} = T_{s,1} - (q_{cond}R_1) \quad (6-16)$$

Where

$$T_{av} = (T_{s,1} + T_{s,2})/2 \quad (6-17)$$

Equation (6-14) can be rewritten in terms of T_{av} as follows:

$$(2\varepsilon\sigma)T_{av}^4 + 0T_{av}^3 + 0T_{av}^2 + (h_1 + h_2)T_{av} - [(h_1 + h_2)T_\infty + 2\varepsilon\sigma T_\infty^4 + q_{ab}] = 0 \quad (6-18)$$

The last 4th degree polynomial equation can be solved for T_{av} . Based on the resulting value, the surfaces temperatures $T_{s,1}$ and $T_{s,2}$ can be determined by combining equations (6-11) and (6-16):

$$2T_{av} - T_{s,1} = T_{s,1} - (e/k)[q_{ab} - h_1(T_{s,1} - T_\infty) - \varepsilon\sigma(T_{s,1}^4 - T_\infty^4)] \quad (6-19)$$

This equation can be rearranged to a 4th degree polynomial form:

$$(e\varepsilon\sigma/k)T_{s,1}^4 + 0T_{s,1}^3 + 0T_{s,1}^2 + (2 + (eh_1/k))T_{s,1} - [(e/k)(T_\infty + \varepsilon\sigma T_\infty^4 + q_{ab}) + 2T_{av}] = 0 \quad (6-20)$$

This equation can be solved for $T_{s,1}$ and Eq. (6-18) can be applied to get $T_{s,2}$.

- **Unsteady-State Model**

In this model, the rate of change in energy within the sample due to heat accumulation is considered besides considering sample thickness. For this case, the physical properties of the sample, including: density, dimensions and heat capacity, as well as the time are considered. Following the same procedure of equations (6-9)–(6-12), the energy balance can be expressed as:

$$q_{conv,1} + q_{conv,2} + q_{rad,1} + q_{rad,2} + q_{acc} - q_{ab} = 0 \quad (6-21)$$

Where q_{acc} is the accumulated energy term within the sample which can be determined from:

$$q_{acc} = mC_p\Delta T/\Delta t, \quad m = 0.25\pi\rho_m eD^2 \quad (6-22)$$

Where m , C_p , Δt and ΔT are sample mass, specific heat capacity, the time step and the temperature difference at certain point between successive time steps, respectively. While ρ_m , e and D are the sample material density, thickness and diameter. However, Eq. (6-21) can be written in terms of T_{av} as follows:

$$(2\varepsilon\sigma)T_{av,j}^4 + 0T_{av,j}^3 + 0T_{av,j}^2 + [h_1 + h_2 + (mC_p/\Delta t)]T_{av,j} - [(h_1 + h_2)T_\infty + 2\varepsilon\sigma T_\infty^4 + q_{ab} + (mC_p/\Delta t)T_{av,j-1}] = 0 \quad (6-23)$$

Where $T_{av,j}$ and $T_{av,j-1}$ denote the average temperature, T_{av} , at the current and previous time steps. For the first-time step, the value of $T_{av,j-1}$ is taken equal to the sample initial temperature, T_i . Solving Eq. (6-23) for $T_{av,j}$ and substituting in Eq. (6-20) leads to get $T_{s,1,j}$ and by using Eq. (6-17), the value of $T_{s,2,j}$ can be obtained.

C. Numerical Model Governing Equations

Considering the semi-transparent sample as a thermal system, then concentrated solar radiation represents a source of energy entering the system, while the energy leaves the system via both of convection and radiation heat transfer to the surrounding environment. Internally, conduction heat transfer through the sample represents the change in internal energy of the sample. This kind of energy balance is illustrated by Figure 6-7. In this section, governing equations that applies for each term will be discussed.

• Conduction

The heat equation is used to analyse the pure heat transferred by conduction through the sample. Ignoring viscous heating, velocity and the internal heat generation, then the simplified form of heat equation can be expressed as follows (Incropera *et al.*, 2007):

$$\rho C_p (\partial T / \partial t) + \nabla \cdot (-k \nabla T) = 0 \quad (6-24)$$

Where ρ , C_p , T , t , and k are the density, specific heat capacity, the absolute temperature, time, and thermal conductivity, respectively.

- **Convection**

The total rate of heat transfer due to convection over one side, Q_{conv} , to the ambient environment with temperature, T_{∞} , can be determined from (Cengel, 2003):

$$Q_{conv} = \int_A Nu \left(\frac{k}{D} \right) (T_s - T_{\infty}) . dA, \quad Nu = Nu(Re, Pr, Ra) \quad (6-25)$$

Where, T_s , D and A are the side surface temperature, sample diameter and surface area of heat transfer, respectively. The Nusselt number, Nu , is a function of different dimensionless numbers: the Reynolds number, Re , the Prandtl number, Pr , and the Rayleigh number, Ra , which can be determined from the following expressions (Cengel, 2003):

$$Re = \rho U D / \mu \quad (6-26)$$

$$Pr = \mu C_p / k \quad (6-27)$$

$$Ra = \left[-(1/\rho_f) (\partial \rho_f / \partial T) \Big|_p \right] \rho^2 g C_p (T_s - T_{\infty}) D^3 / (\mu k) \quad (6-28)$$

Where ρ_f , U and μ are the ambient bulk fluid density, velocity and dynamic viscosity, respectively, while g , is the acceleration of gravity. The Nusselt number can be determined based on the convection type (i.e. natural or forced) and at the studied surface as well as the surface position. For natural convection over a flat sample inclined by an angle θ , measured from the vertical direction, the Nusselt number can be determined through applying a correlation (Churchill and Chu, 1975):

$$Nu = 0.68 + (0.67(\cos(\theta) Ra)^{1/4}) \left[1 + (0.492/Pr)^{9/16} \right]^{-4/9}, \quad \begin{array}{l} Ra \leq 10^9 \ \& \\ -\pi/3 < \theta < \pi/3 \end{array}$$

$$Nu = \left\{ 0.825 + (0.387 Ra^{1/6}) \left[1 + (0.492/Pr)^{9/16} \right]^{-8/27} \right\}^2, \quad \begin{array}{l} Ra > 10^9 \ \& \\ -\pi/3 < \theta < \pi/3 \end{array} \quad (6-29)$$

Where all fluid properties are evaluated at $(T_s + T_{\infty})/2$. In case of a horizontal surface subjected to natural convection, the Nusselt number can be calculated by applying the following correlation (McAdams, 1954):

$$\begin{array}{l}
\text{Nu} = 0.54\text{Ra}^{1/4}, \quad 10^4 \leq \text{Ra} \leq 10^7 \quad \& \quad T_s > T_\infty \\
\hline
\text{Nu} = 0.15\text{Ra}^{1/3}, \quad 10^7 \leq \text{Ra} \leq 10^{11} \quad \& \quad T_s > T_\infty \quad (6-30) \\
\hline
\text{Nu} = 0.14\text{Ra}^{1/3}, \quad \text{Ra} > 2 \times 10^8 \quad \& \quad T_s \leq T_\infty
\end{array}$$

When forced convection is in effect, the Nusselt number can be obtained from the correlation proposed by Churchill and Ozoe (Churchill and Ozoe, 1973):

$$\begin{array}{l}
\text{Nu} = (0.3387\text{Re}^{1/2}\text{Pr}^{1/3})[1 + (0.0468/\text{Pr})^{2/3}]^{-1/4}, \quad \text{Re} \leq 5 \times 10^5 \\
\hline
\text{Nu} = (0.037\text{Re}^{4/5} - 871)\text{Pr}^{1/3}, \quad 5 \times 10^5 \leq \text{Re} \leq 10^7 \quad (6-31) \\
\quad \quad \quad \& \quad 0.6 \leq \text{Pr} \leq 60
\end{array}$$

Where all fluid properties are evaluated at $(T_s + T_\infty)/2$.

- **Radiation**

Assuming the ambient surrounding as a blackbody at a constant temperature, T_∞ , then the total heat transfer from the sample surface, at a temperature T_s , to the ambient environment due to radiation, Q_{rad} , can be obtained from:

$$Q_{rad} = \varepsilon\sigma A(T_s^4 - T_\infty^4) \quad (6-32)$$

Where, ε is surface emissivity and σ is the Stefan–Boltzmann constant with a value of $(5.67 \times 10^{-8} \text{ W/m}^2\cdot\text{K}^4)$.

- **Solar Irradiance**

Solar irradiance represents a measure of the rate at which solar radiation is incident on a surface per unit surface area (Boxwell, 2017). As a result of intercepting the incident solar irradiation, I , by a semi-transparent medium, it is divided into three portions: reflected, absorbed and transmitted, as illustrated by Figure 6-9. The fraction of reflected irradiation is called the reflectance, ρ_I , the fraction of absorbed irradiation is known as absorbance, α_I , and the transmitted fraction is called transmittance, τ_I , (Incropera *et al.*, 2007). Then:

$$\rho_I + \alpha_I + \tau_I = 1 \quad (6-33)$$

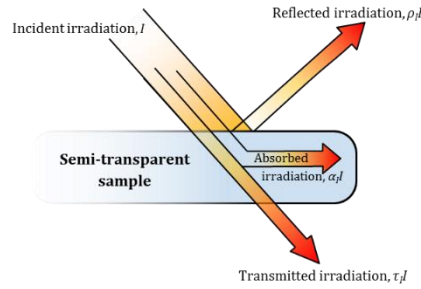


Figure 6-9 Absorption, reflection, and transmission of incident radiation over a semi-transparent sample

For the case of current study, the absorbed amount of solar irradiance represents the incoming energy to the system. This component is responsible for heating up the semi-transparent sample. Hence the solar irradiance is expressed in terms of power per unit area, it can be considered as a heat flux boundary condition as follows:

$$q_{ab} = \alpha_I I \quad (6-34)$$

Where q_{ab} is heat flux boundary condition which applies to the side facing the concentrated solar power.

6.1.3.2 Rear Lens Geometry

There are three geometries of converging lenses: bi-convex, plano-convex and positive meniscus lenses (Avison, 1989), as shown in Figure 6-10.

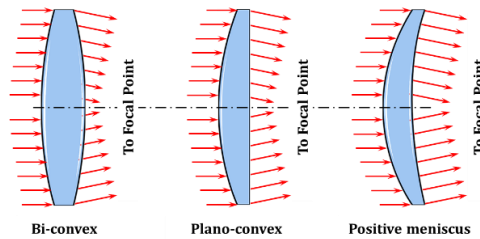


Figure 6-10 Different lens geometries ray diagrams (Serway and Jewett, 2010)

The followed sequence for geometry selection is to start with a randomly selected material and apply it to the available three geometrical options. The best geometry is selected via simulating each case under a progressive CR until the maximum working temperature of the lens material is reached. The corresponding CR is then defined as the maximum allowable concentration ratio, CR_{max} . The lens geometry which can resist the highest CR_{max} is then selected as the best geometry. The selected material was SiO_2 .

Boundary conditions applied to each surface are illustrated by Figure 6-7. Table 6-2 summarises the main assumptions used in these calculations. Hence keeping the focal length of the rear lens minimum is recommended for LLBG system (Salem, Tawfik and Hamed, 2010; Tawfik and Salem, 2014), lenses with the minimum available focal length have been selected over the available Thorlabs® stock for all cases (Thorlabs, 2017a, 2017b, 2017c). All simulated lenses are 25.4mm in diameter and other dimensions are illustrated by Figure 6-11. The glass transition point of 1200°C is assumed as damage criterion in simulation process.

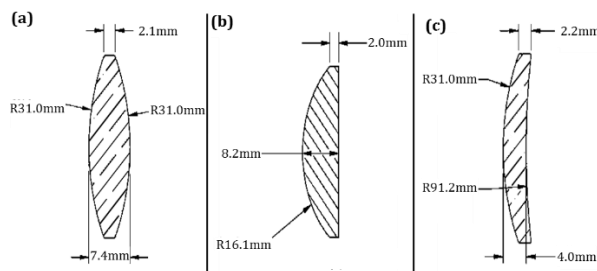


Figure 6-11 Schematic of simulated lenses
(a) bi-convex lens (Thorlabs, 2017b) (b) plano-convex lens (Thorlabs, 2017a)
(c) positive meniscus lens (Thorlabs, 2017c)

Table 6-2 Boundary conditions assumptions

Assumption	Value
Location	Cranfield, UK (52°N)
Day	June 21 st
Time	Daytime (08.25 hours)
Altitude from sea level	0 m
Solar insolation calculation safety factor	10%
Tracking system	2-axis
Front lens transmittance	100%
Rear lens transmittance (Geometry selection model)	90%
Rear lens emissivity	0.92
Rear lens initial temperature	25°C
Ambient temperature	25°C
Natural convective heat transfer coefficient (COMSOL / ANSYS)	Program controlled / 14 W/m ² .K
Model dimensions (COMSOL / ANSYS)	2D-Axisymmetric / 3D
Incident heat flux	Appendix A

Hence thermal behaviour of each case is independent of the CR value, a CR of 100 is assumed for estimating the best geometry. Figure 6-12 shows the temperature distribution through each lens at solar noon with a concentration ratio of 100. A comparison between maximum rear lens temperatures for the investigated geometries versus CRs applied is illustrated in Figure 6-13. While Figure 6-14 illustrates a comparison of COMSOL and ANSYS models results.

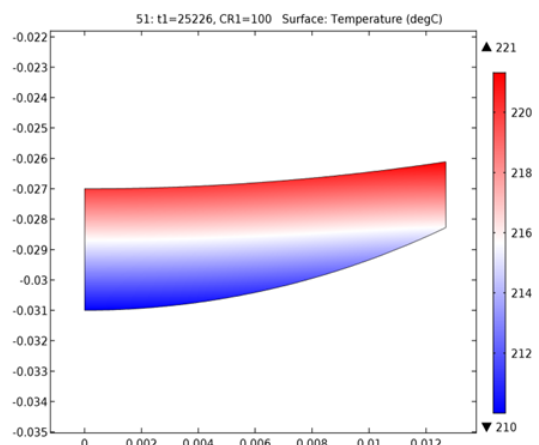
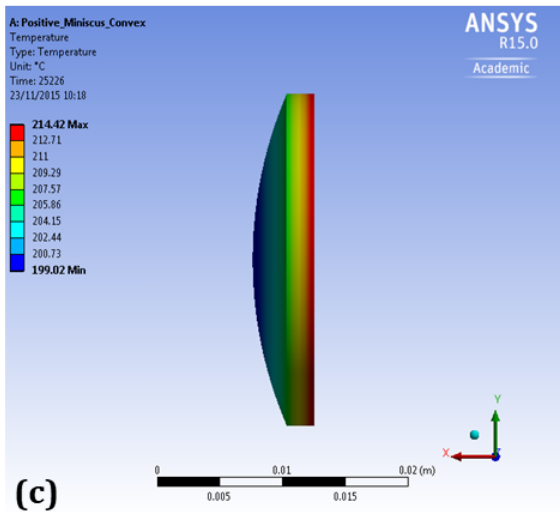
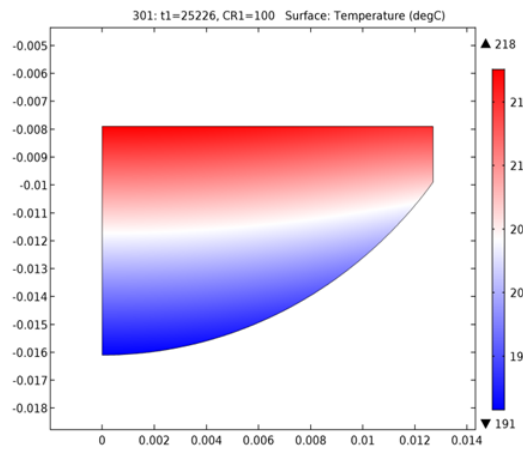
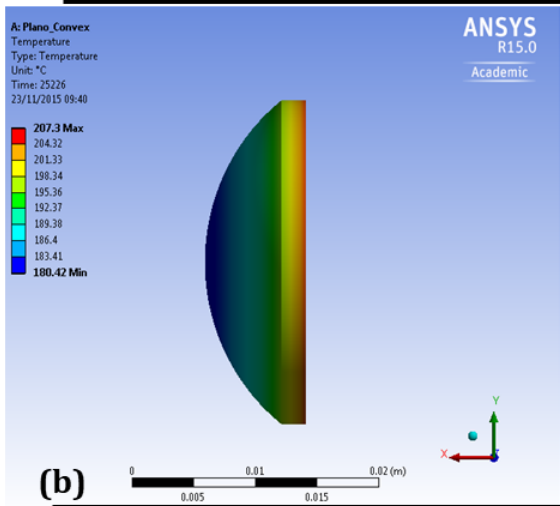
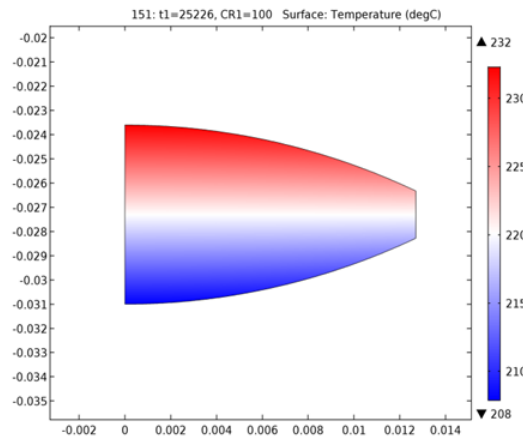
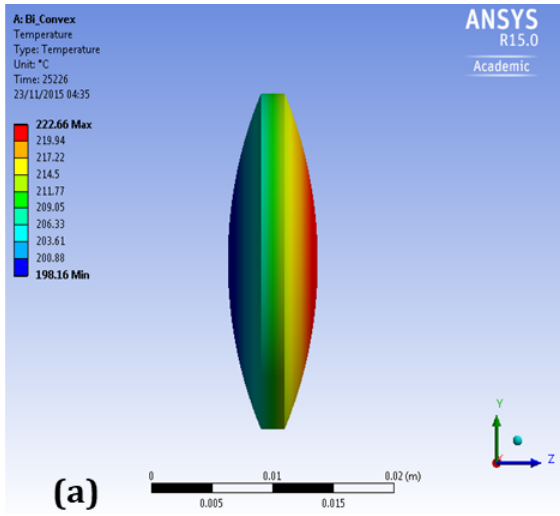


Figure 6-12 Temperature distribution through lenses (Solar noon, CR=100, SiO₂)
 (a) bi-convex lens (b) plano-convex lens (c) positive meniscus lens
 (ANSYS model to the left, COMSOL model to the right)

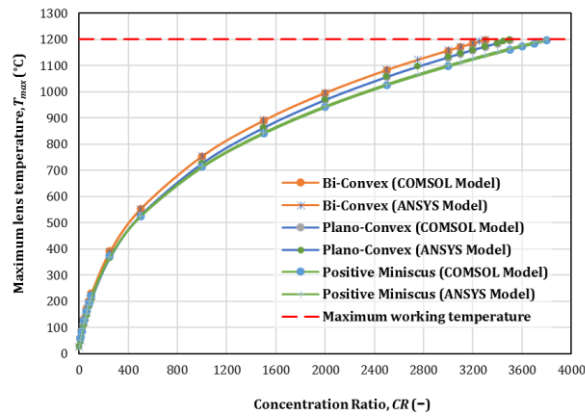


Figure 6-13 Maximum rear lens temperature for different geometries vs. CR

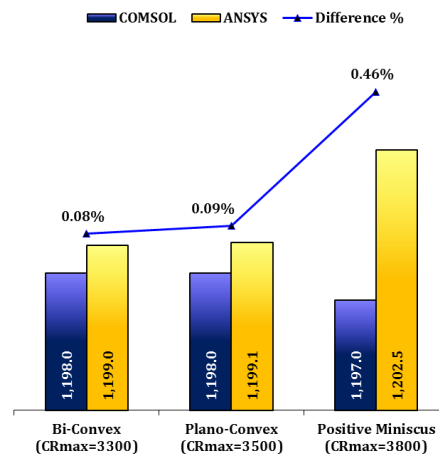


Figure 6-14 Comparison of COMSOL and ANSYS models results (Geometry Test)

From Figure 6-13, positive meniscus geometry withstood the highest CR compared to the other geometries. Therefore, positive meniscus geometry has been selected for further tests for material selection. Figure 6-14 indicated that COMSOL and ANSYS models results are in a good agreement. However, the difference between the results may be attributed to the assumption of the natural convection heat transfer coefficient. Hence it is assumed to be constant in the ANSYS model, while COMSOL allow the ability to evaluate its value during an iterative process, based on the lens surface temperature.

6.1.3.3 Rear Lens Material

There are 14 different materials reviewed in Section 2.3 with data listed in Table 2-8. These materials are investigated except CLEARCERAM-Z, as its density is unknown. The investigated materials are applied to the selected positive meniscus geometry. The selection criteria of selecting the optimum material is not only limited to the ability to withstand the highest CR, but they also include

the maximum transmittance of the material. The calculated transmittance, from section 2.3, of each material over the whole solar spectrum was taken into account as listed in Table 6-3, while the rest boundary conditions as listed in Table 6-2.

A comparison between maximum rear lens temperatures for the different studied materials, categorised based on materials types, versus applied CRs is illustrated in Figure 6-15. While Figure 6-16 shows a comparison of COMSOL and ANSYS models results. From Figure 6-15, ceramic materials show the highest resistance to CR, followed by glass-type materials and then the plastics. According to the followed methodology to select the optimum material, the material transmittance is required to be considered beside the highest CR_{max} . Getting back to their transmittances listed in Table 6-3, it has been found that glass-type materials including quartz, ULE, Calcium Fluoride and BK7 have transmittance over 90%. Among this particular group, quartz is found to fulfil both criteria of withstanding the allowable CR with the maximum transmittance. Therefore, quartz has been selected as the best rear lens material for the LLBG. Figure 6-16 indicated that COMSOL and ANSYS models results are in a good agreement. However, the difference between the results may be attributed to the same reason discussed previously in the lens geometry investigation model.

Table 6-3 Rear lens materials transmittances over (280–2500nm) bandwidth

Type	Material	Transmittance
Ceramics	ALON	84.90%
	SiC	58.14%
	Spinel	80.96%
	Y ₂ O ₃	82.70%
Glass	BK7	90.89%
	Borosilicate	81.78%
	CaF ₂	94.09%
	Sapphire	86.83%
	SiO ₂	97.27%
	ULE	97.85%
	Zerodur	87.34%
Plastics	PC	79.12%
	PMMA	81.04%

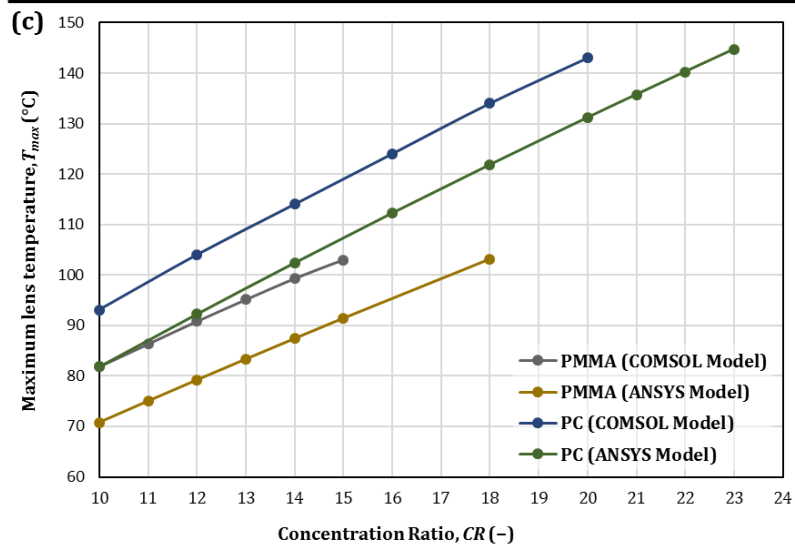
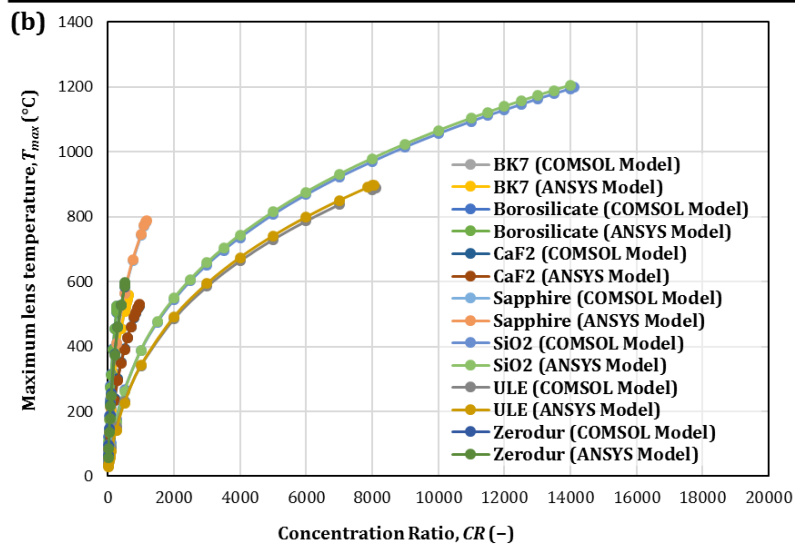
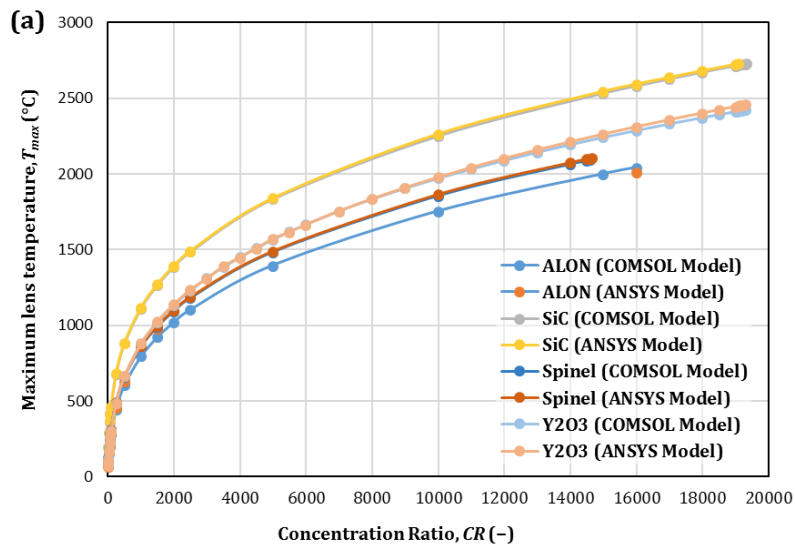


Figure 6-15 Maximum rear lens temperature for different materials vs. CR
(a) Ceramics (b) Glass (c) Plastics

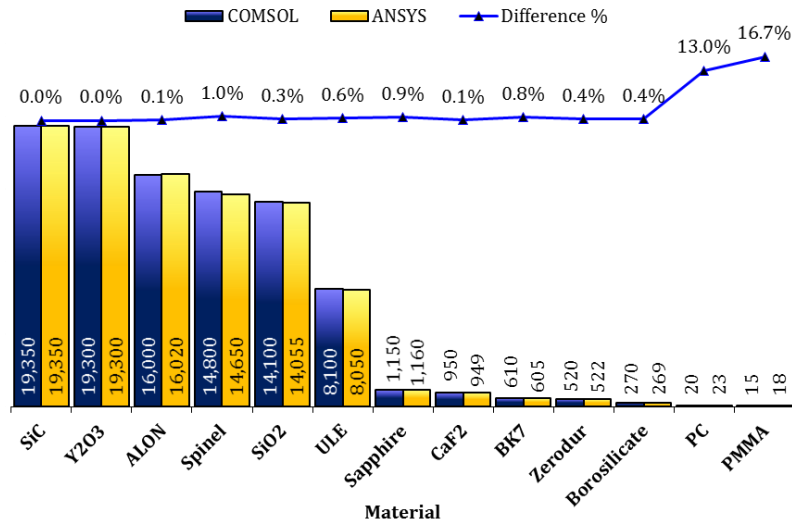


Figure 6-16 Comparison of COMSOL and ANSYS models results (Material Test)

6.1.3.4 Rear Lens Mount Study

Studying the rear lens model was based on assuming of severe working conditions through neglecting the lens mount influence. Therefore, in this section a study is carried out to develop and validate a numerical model simulating the rear lens under the real mounting conditions to investigate the thermal effect on such mounting system. The developed model is solved using ANSYS® Workbench as a heat transfer model through a semi-transparent material subjected to radiative heat flux at one side. To validate the proposed model, carried out experiments on transparent windows made from two different materials subjected to radiative heat flux from the tungsten halogen solar simulator, with designing and building details discussed in Chapter 5.

A. Model Description

The lens mount detailed geometry is illustrated in Figure 6-17a. As the present study focuses on the mounting effect on the sample, the mount parts contacting the sample, i.e. clamping fingers, will be considered in the numerical model while the rest parts of the mount will be neglected, as shown in Figure 6-17b. The numerical model has been applied to the simplified lens mount with the tested windows and solved using ANSYS Workbench 18.2 software as a transient thermal model. The boundary conditions for the numerical model are like those applied for the rear lens study with replacing the assumption of insulating sample tip with applying convection and radiation boundary conditions.

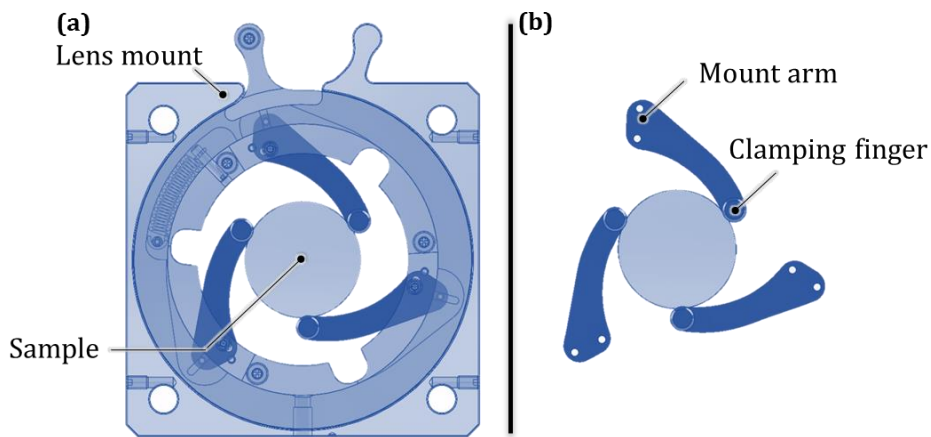


Figure 6-17 Lens mount geometry
(a) Detailed geometry description (b) Simplified modelled geometry

B. Model Validation

The model is validated against experimental results obtained from the setup described in Section 5.2.5. The tests carried out on IR fused quartz and BK7 windows, with applied boundary conditions for the numerical model are listed in Table 6-4. Comparison between the experimental and numerical model results are plotted in Figure 7-6. Error values are listed in Table 6-5. According to error comparison, the numerical model showed good agreement with experimental data for both samples materials.

C. Model Results

The model is applied for a fused silica, 50.8mm-diameter positive meniscus lens (see Figure 6-18) mounted in the self-centring mount made of Delrin® acetal (Polyoxymethylene POM). Different parameters have been investigated within this section.

Table 6-4 Model boundary conditions

Category	Property (unit)	Value	Unit
Geometry	Aperture diameter, D_a	0.025	m
	Window thickness, e	0.002	m
Mount Properties	Material	Delrin® acetal (Polyoxymethylene POM)	–
	Density, ρ	1420	kg/m ³
	Specific heat, C_p	1465	J/kg.K
	Thermal conductivity, k	0.37	W/m.K
	Maximum operating temperature, T_{max}	120	°C
	Coefficient of thermal expansion	110e-06	°C ⁻¹
Boundary Conditions	Initial temperature, T_i	From experimental data	°C
	Ambient temperature, T_∞		°C
	Convective heat transfer coefficient, h	5.0	W/m ² K
	Emissivity, ε	0.75	–
	Window transmittance, τ_l	From Table 6-3	–
	Window absorbance, α_l	$1 - \tau_l$	–
	Incoming irradiation, I	1600	W/m ²
	Input heat flux to the sample (effective), q_{ab}	$\alpha_l I$	W/m ²

Table 6-5 RMSE and MAPE values for tested samples

Model	IR fused quartz	BK7
RMSE (°C)	0.70	0.46
MAPE (%)	2.24	1.38

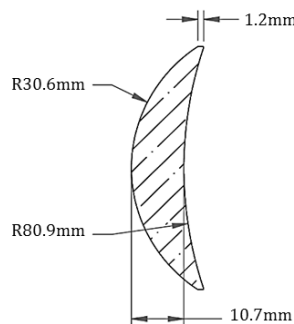


Figure 6-18 Rear lens positive meniscus lens geometry (Thorlabs, 2010d)

• **Perfect Insulation Assumption Influence**

In this part, a comparison between two modelling scenarios is held. In the first one, the lens tip is assumed to be perfectly insulated as assumed before in Section 6.1.3. In the second scenario, lens is mounted with direct contact with the mount clamping fingers. The maximum lens and mounting finger temperature values are plotted against daytime hours (Cranfield, 52°N on summer solstice) in Figure 6-19, while temperature distribution over the lens in both scenarios are shown in Figure 6-20.

The results show that perfect insulation assumption overestimates the maximum lens temperature to 447°C compared to 444°C with real mounting assumption, with an increment of 0.66%. This overestimation is an acceptable error in sizing and designing process of an LLBG as a kind of safety factor in terms of determining the maximum allowed temperature of the lens under certain operating conditions. However, real mounting assumption indicates generation of lower-temperature local spots in the lens around fixation points. These spots are quite important to be considered as they are responsible for creating local thermal stresses that may cause cracks or fractures in the lens.

On the other hand, Figure 6-19b indicates that the mount temperature will exceed its maximum operating temperature. Therefore, adding patches of an insulating material is found to be necessary.

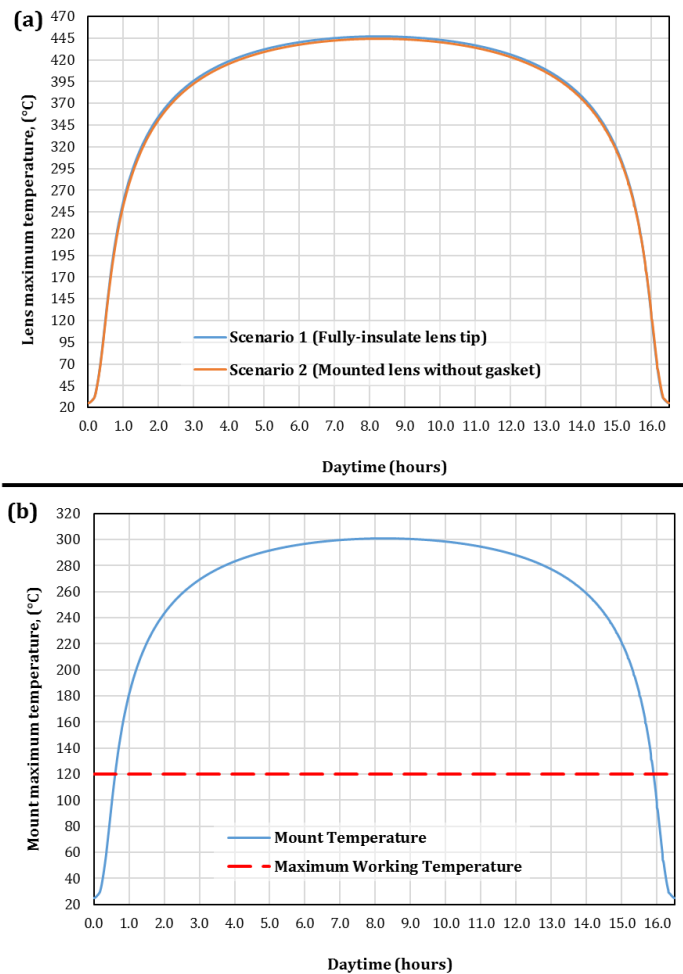


Figure 6-19 Maximum temperature achieved (ANSYS results)
(a) Over the lens **(b) Over the mounting finger**

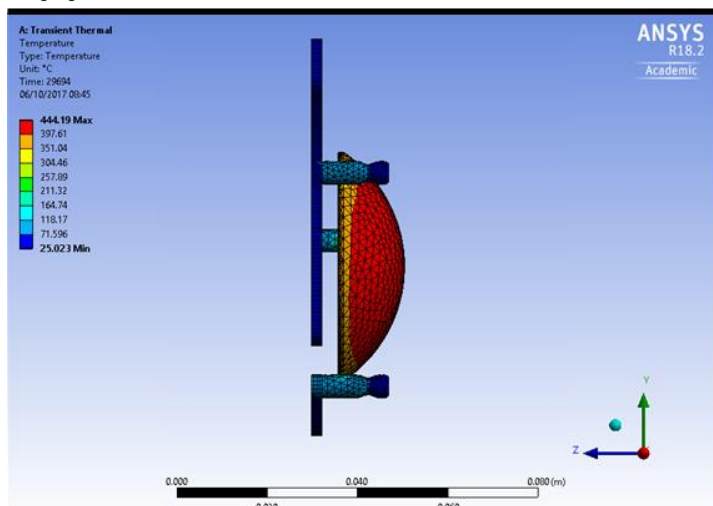
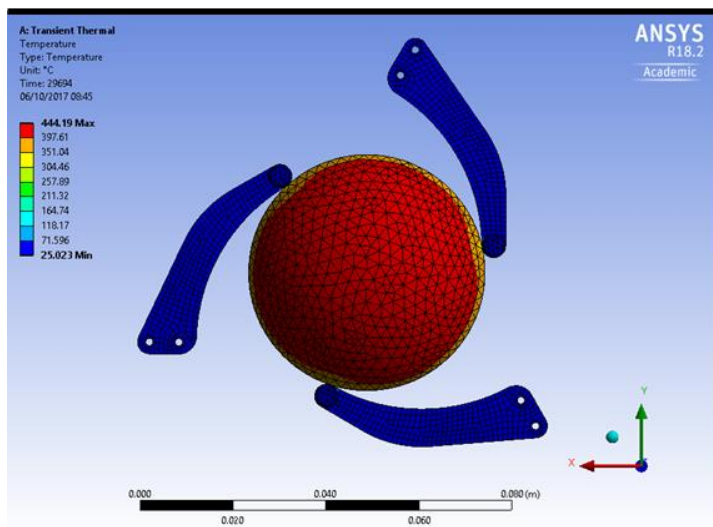
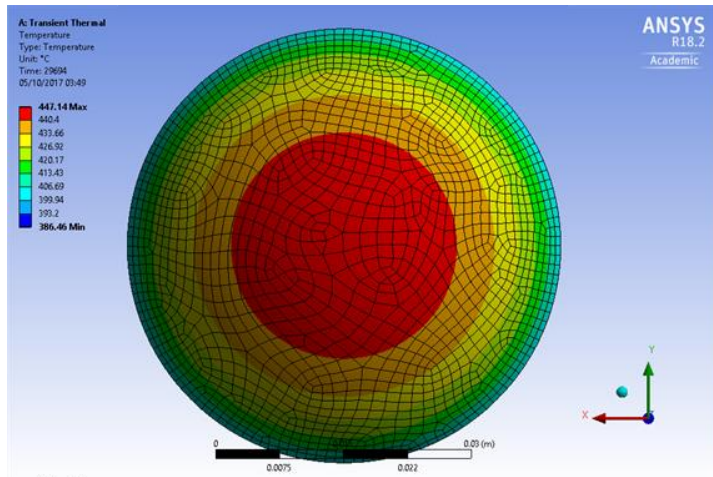


Figure 6-20 Temperature distribution over the lens
 (a) Perfect insulation scenario (b) Direct contact mounting scenario (Front View)
 (c) Direct contact mounting scenario (Side View)

- **Insulating Patch Shape Effect**

In this part, output results for three cases of insulating patches inserts, made of FLEXITALLIC THERMICULITE® 815 material, will be investigated and compared against direct contact case between the lens and its mount. The patches dimensions in the cases investigated are listed in Table 6-6, while their properties are listed in Table 6-7.

Table 6-6 Patches dimensions in investigated cases

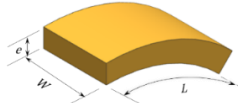
Geometry	Dimensions	Patch #1 (10x10mm)	Patch #2 (20x10mm)	Patch #3 (10x20mm)
	L (m)	10e-03	20e-03	10e-03
	W (m)	10e-03	10e-03	20e-03
	E (m)	03e-03	03e-03	03e-03

Table 6-7 Gasket material properties (Flexitallic, 2018)

Property (unit)	Value	Unit
Material	FLEXITALLIC THERMICULITE® 815	-
Density, ρ	1200	kg/m ³
Specific heat, C_p	500	J/kg.K
Thermal conductivity, k	0.18	W/m.K
Maximum operating temperature, T_{max}	982	°C

The maximum lens and mounting finger temperature values are plotted against daytime hours in Figure 6-21, while temperature distribution over the lens in all investigated cases are shown in Figure 6-22. From Figure 6-21, it is obvious that adding insulating material inserts between the lens and its mount leads to lowering down the mount's maximum temperature to an acceptable level under its maximum operating point temperature. The maximum lens temperature in both patches #1 and #3 is found to be nearly the same at 443°C which is found to be 0.4% exceeding its corresponding value for "patch #2" case while it was 0.3% less than the "no-gasket" case. Moreover, Figure 6-22 indicated that the temperature distribution through the lens and the gasket patches showed different patterns with different cases studied. In order to interpret this finding in addition to studying the influence of gasket material addition on both the lens and its mount, further investigation and thermal analysis is found to be required.

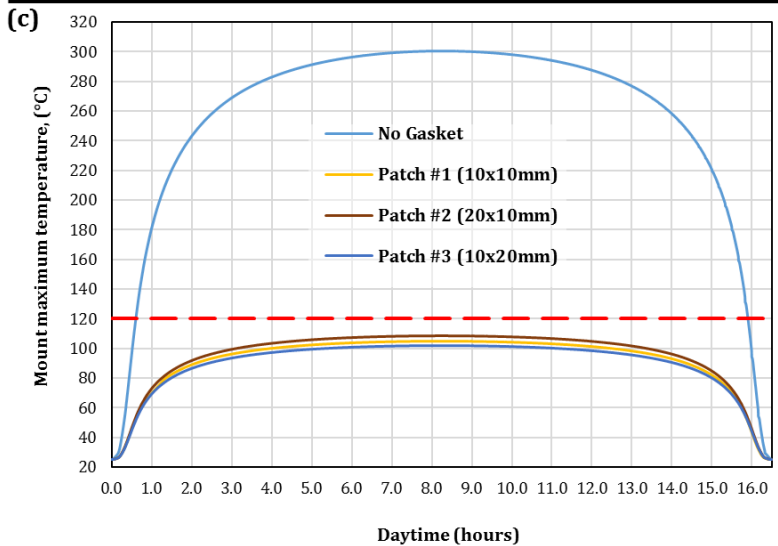
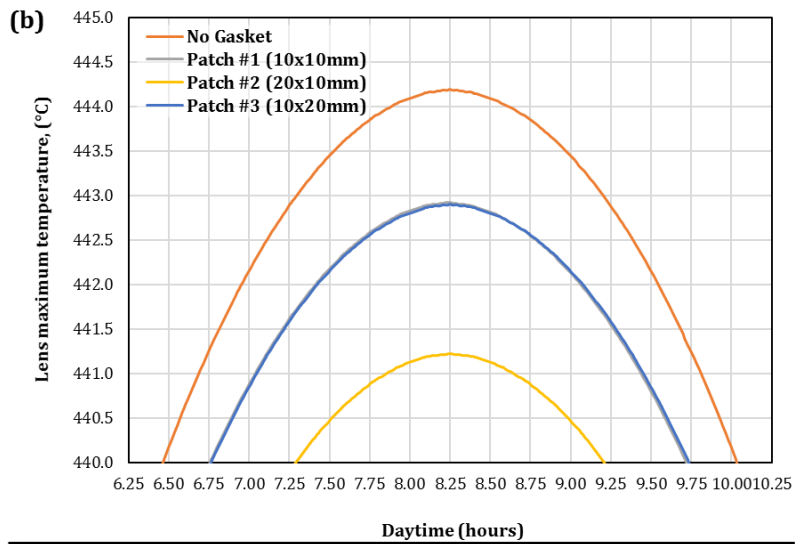
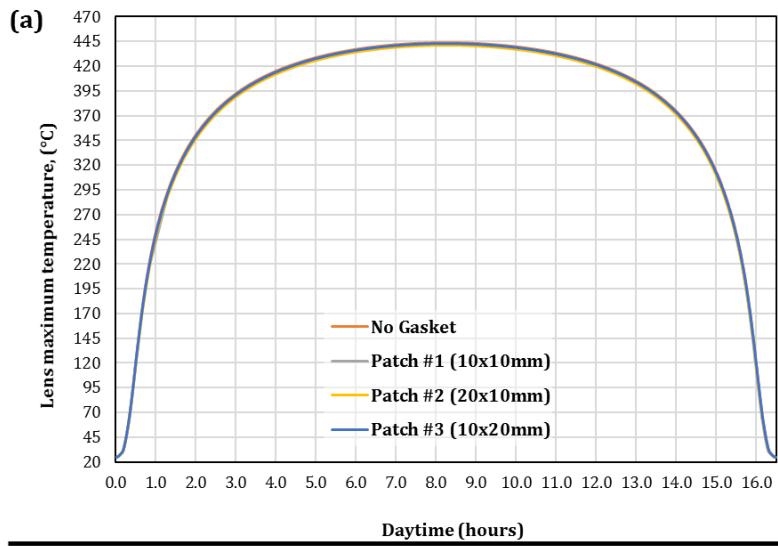


Figure 6-21 Maximum temperature achieved with partial insulation of lens
(a) Over the lens (in the full-daytime) (b) Over the lens (detailed around noon-time)
(c) Over the mounting finger

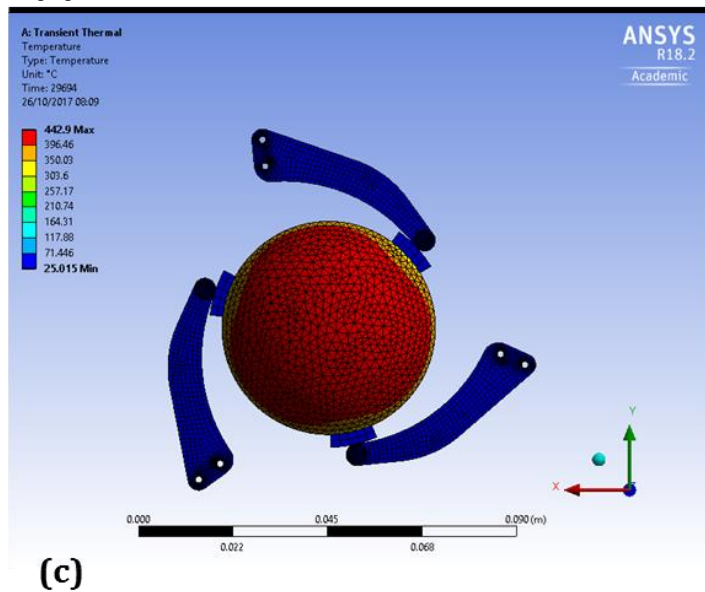
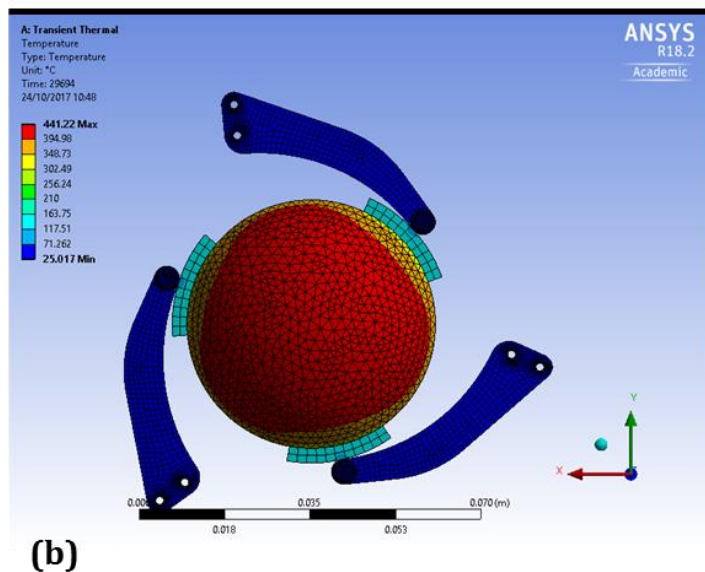
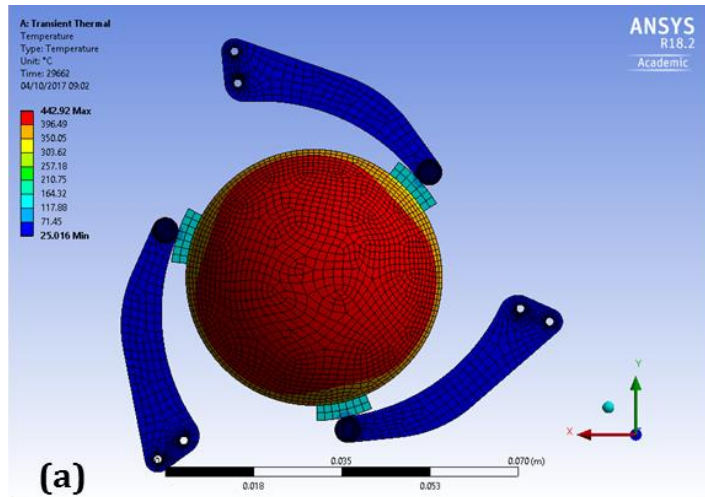


Figure 6-22 Temperature distribution over the lens with partial insulation
 (a) Patch #1 (10x10mm) (b) Patch #2 (20x10mm) (c) Patch #3 (10x20mm)

Data analysis for the conducted and absorbed heat through the 3-gasket patches for the cases listed in Table 6-6 is illustrated by Figure 6-23. Based on data plotted in Figure 6-23a, it is found that the amount of heat flowed by conduction is approximately the same in both “*patch #1*” and “*patch #3*” cases and less than it in the “*patch #2*” case. While data illustrated by Figure 6-23b indicated that patches #1 and #2 absorbed nearly the same amount of heat which is less than it in the “*patch #3*” case.

These achieved results may be attributed to energy balance over both the lens and its mount. From the lens side, the area of heat transfer by conduction is represented by the lens tip thickness multiplied by the gasket arc length, L . Then this area is maximum for “*patch #2*” case, leading to reducing its maximum temperature (Figure 6-21b) and tip temperature at the points of contact with gasket material (Figure 6-22) and maximising the amount of heat conducted from the lens (Figure 6-23a) compared to the other cases. This explain the similar behaviour of the lens under both patches #1 and #3 conditions.

On the mount side, “*patch #3*” case provides the maximum covering area which leads to minimising the mount temperature (Figure 6-21c). On the other hand, “*patch #3*” case shows the maximum absorbed amount of heat as a result of receiving the same amount of heat by conduction as the “*patch #1*” case but with less side temperature at the mount contact point (Figure 6-23b).

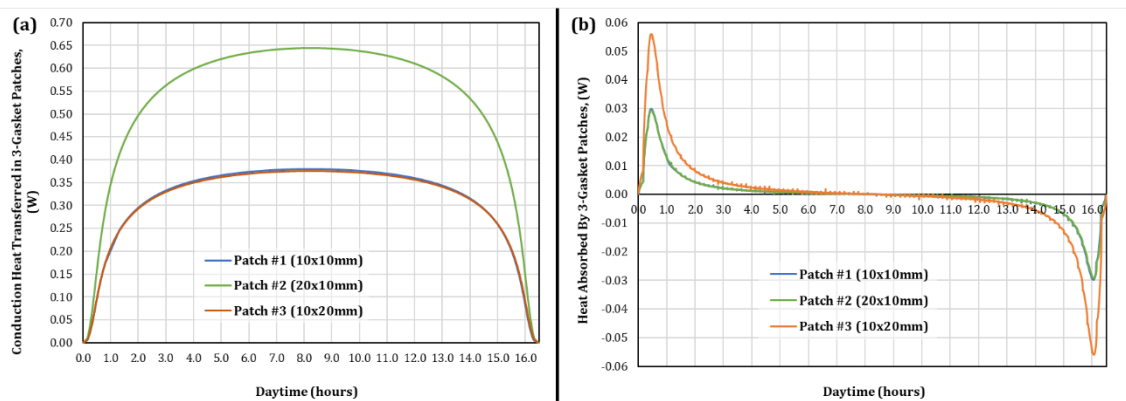


Figure 6-23 Analysis of heat transfer through the gasket patches
(a) Conducted heat flow through patches (b) Absorbed heat amount by the patches

6.1.4 LLBG System Optical Analysis

This section aims to investigate various optical parameters which influence the LLBG output beam.

6.1.4.1 Front Lens Configuration

For the facets face direction effect, there are two configurations which can be discussed; *grooves-in* (GI) and *grooves-out* (GO), as illustrated by Figure 6-24. In the GI configuration, the facets are oriented towards the lens focal point, which is called the short conjugate. While in the GO configuration, facets face is pointed towards the side of the collimated beam, which is also known as the long conjugate (Davis and Kühnlenz, 2007).

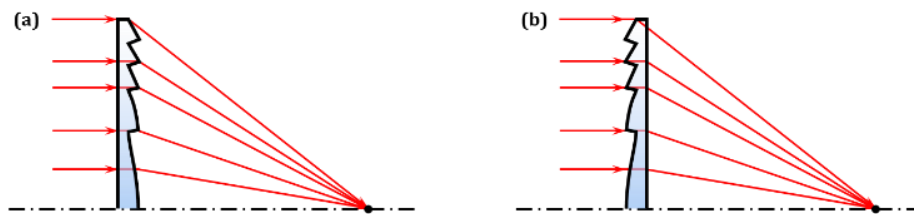


Figure 6-24 Fresnel facets face configurations
(a) grooves-in (GI) configuration **(b) grooves-out (GO) configuration**

Mathematical derivation to determine the transmittance due to the facet facing has been carried out by (Davis, 2004) and validated by (Davis, 2009). They found that using GO configuration enhances the lens transmittance when the incident rays are collimated. Approximating solar radiation as collimated rays leads to recommending the GO as the more efficient concentrating configuration. However, GI configuration practically in solar concentrators (Sierra and Vázquez, 2005; Xie *et al.*, 2011; Perini *et al.*, 2017) to avoid build-up of debris and dirt within the facets (Davis and Kühnlenz, 2007).

In order to evaluate each scenario, a mathematical derivation of spot diameter in each case is required. General geometry of rays refracted through a Fresnel prism at a radius, r , for both configurations is illustrated in Figure 6-25.

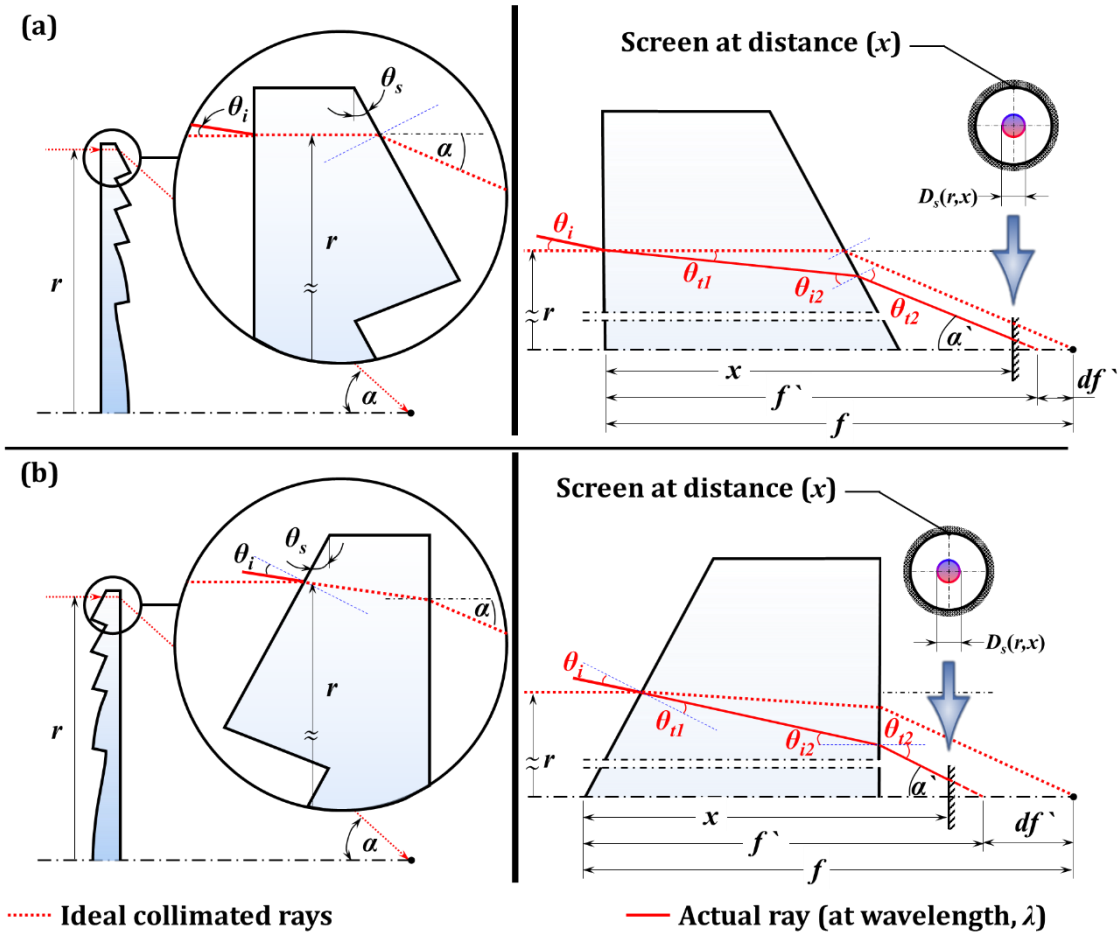


Figure 6-25 Ray geometry for spot diameter derivation with general geometry (on left) and magnified prism geometry (on right) (a) grooves-in (GI) configuration (b) grooves-out (GO) configuration

Generally, when an Ideal collimated ray hits the lens at normal incidence, it is deflected with a deflection angle, α , to reach the lens optical axis at the focal length, f distance from the lens plane (approximated to be the front lens plane). However, when the incident ray hits the plano-surface of the Fresnel at an incidence angle of, θ_i , it is refracted by angle, θ_{t1} . Then the refracted ray impinges the exit surface of the prism at an incidence angle, θ_{i2} , and refracted by angle, θ_{t2} . The refracted ray is deflected by an angel, α' . In the following derivation of these angles in both configurations is discussed, applying Snell's law for a lens with material refractive index, n , immersed in air. Both CA and SAA effects are considered in this derivation, with solar aperture cone-half angle, θ_α , of 0.266° .

A. For GI Configuration

$$\theta_i = \theta_a \quad (6-35)$$

$$\theta_{t1} = \sin^{-1} \left(\frac{\sin \theta_i}{n} \right) \quad (6-36)$$

$$\theta_{i2} = \theta_{t1} + \theta_s \quad (6-37)$$

$$\theta_{t2} = \sin^{-1}(n \sin \theta_{i2}) \quad (6-38)$$

$$\alpha' = \theta_{t2} - \theta_s \quad (6-39)$$

B. For GO Configuration

$$\theta_i = \theta_s - \theta_a \quad (6-40)$$

$$\theta_{t1} = \sin^{-1} \left(\frac{\sin \theta_i}{n} \right) \quad (6-41)$$

$$\theta_{i2} = \theta_s - \theta_{t1} \quad (6-42)$$

$$\theta_{t2} = \sin^{-1}(n \sin \theta_{i2}) \quad (6-43)$$

$$\alpha' = \theta_{t2} \quad (6-44)$$

Where θ_s is the slope angle of the Fresnel lens prisms.

C. For Both Configurations

Based on previous formulae, the actual refracted ray reaches the lens optical axis at a distance, f' , from the lens plane, which can be determined from:

$$f' = \frac{r}{\tan \alpha'} \quad (6-45)$$

$$df' = (f - f') = f - \frac{r}{\tan \alpha'} \quad (6-46)$$

Then the spot diameter, D_s , on a screen at any general distance, x , from the lens plane can be obtained by:

$$D_s(r, x) = 2|x - f'| \tan \alpha' \quad (6-47)$$

6.1.4.2 Front Lens Buckling

Since the front Fresnel lens is made of PMMA, it is more susceptible to buckling or under the influence of gravity, wind-load, thermal- or hydro-expansion (Miller and Kurtz, 2011). Lens buckling was found to shift its focal point (Goto *et al.*, 1995; Valette, 1995; Rai-Choudhury, 1997). In order to study the effect of the large Fresnel lens bending, rays can be traced at one prism of the lens which lies at a distance, r , from the lens centreline. The incident ray is assumed to be parallel with the lens major axis with an incidence angle, θ_i , with the prism surface. The prism deflects the ray to exit the lens with an angle of deflection, α , to be directed to the focal point. Assuming the Fresnel lens has been bent with a radius of curvature, R_c , and then the studied prism will rotate by an angle of $d\theta$, as shown in Figure 6-26a. Based on geometry of Figure 6-26a, it seems to be analogous to *spherical aberration* (SA) geometry shown in Figure 6-26b. Spherical aberration is produced by rotationally symmetrical surfaces centered and orthogonal in regard to the optical axis (Mahajan, 1991). In SA, paraxial rays (denoted by P in Figure 6-26b) are focused at a distance s from the lens (called paraxial focal length), while marginal rays (denoted by M in Figure 6-26b) are focused at a distance s' from the lens (called marginal focal length). The difference between paraxial and marginal focal lengths (is denoted by LA in Figure 6-26b) represents *longitudinal aberration*. In both lens buckling and SA cases, changing of the incidence angle, by either $d\theta$ or Δ , causes changing the focal point location.

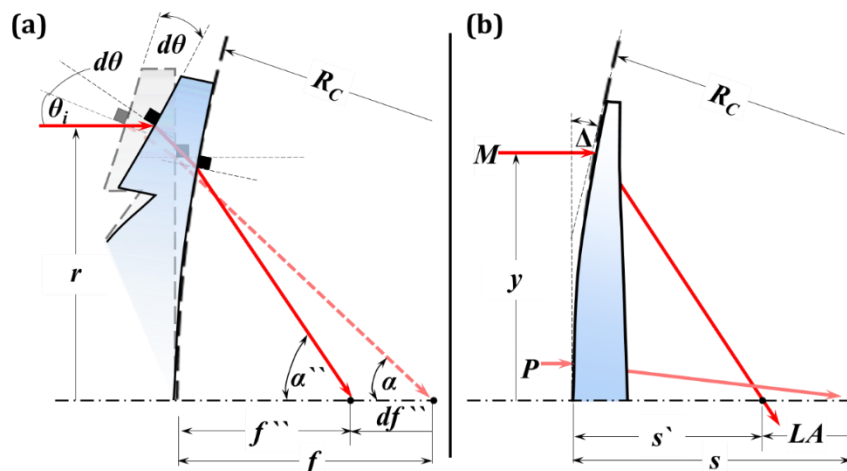


Figure 6-26 Analogy between bended Fresnel lens and spherical aberration
 (a) prism geometry of bended Fresnel lens (b) geometry describing SA (Smith, 2000a)

Table 6-8 lists and describes the analogous main parameters between lens buckling and SA geometries.

Table 6-8 Analogy between bended Fresnel lens and SA effect

Bended Fresnel lens (Figure 6-26a)		SA effect (Figure 6-26b)	
Symbol	Description	Symbol	Description
R_C	Radius of curvature	R_C	Radius of curvature
r	Distance from optical axis	y	Distance from optical axis
R	Fresnel lens aperture radius	R	Lens radius
f	Focal length (unbent lens)	s	Paraxial focal length
f''	New focal length (bent lens)	s'	Marginal focal length
df''	Focus position deviation	LA	Longitudinal aberration
$d\theta$	Change in incidence angle	Δ	Change in incidence angle

Applying the third order theory to a case similar to Figure 6-26b, then the spherical aberration can be determined from (Pedrotti, Pedrotti and Pedrotti, 2013):

$$|LA|_{y=R} = s^2 \frac{da/dy}{n \cdot y} \quad (6-48)$$

where n and s are the refractive index of the lens material and the paraxial focal length (see Figure 6-26b), respectively, while a is *wave aberration* function. The local curvature, (da/dy) , can be expressed as (Pedrotti, Pedrotti and Pedrotti, 2013):

$$\frac{da}{dy} = n \cdot \Delta \quad (6-49)$$

Where Δ represents the change in incidence angle, which can be determined from geometry of Figure 6-26b as:

$$\Delta = \sin^{-1} \left(\frac{R}{R_C} \right) \quad (6-50)$$

Where R and R_C are the lens radius and the radius of curvature of the lens. By substitution in Eq. (6-48) with $(y = R)$, then the longitudinal spherical aberration, LA , can be determined from:

$$|LA| = |s - s'| = s^2 \frac{\Delta}{R} \quad (6-51)$$

Where s' is the marginal focal length (see Figure 6-26b). Using analogy between spherical aberration and focal length deviation, then Eq. (6-51) can be re-written in terms of bent Fresnel lens case (Figure 6-26a) as follows:

$$|df''| = |f - f''| = f^2 \frac{d\theta}{R} \quad (6-52)$$

$$d\theta = \sin^{-1} \left(\frac{R}{R_C} \right) \quad (6-53)$$

The bending direction affects the location of the new focal point (see Figure 6-27).

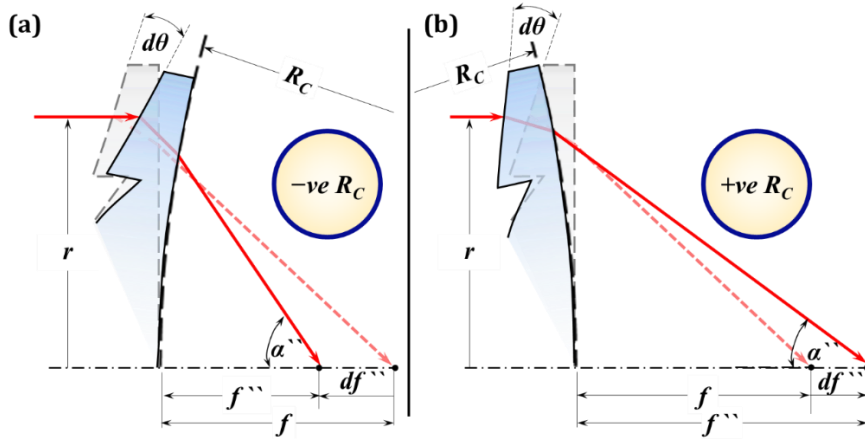


Figure 6-27 Buckling direction effect
(a) convex bending (pre-focus) (b) concave bending (post-focus)

From Figure 6-27, it is clear that bending the lens towards the original focal point in a convex-shape leads to shifting of the focal point nearer to the Fresnel lens (pre-focus). While bending in a concave-shape shifts the focal point away from the lens. Therefore, the new focal length achieved due to lens buckling effect, f'' , can be expressed as:

$$f'' = f \pm df'' \quad (6-54)$$

Which can be re-written as:

$$f'' = f \left[1 \pm \left(\frac{f}{R} \right) \sin^{-1} \left(\frac{R}{R_C} \right) \right] \quad (6-55)$$

Where the (-) sign is for the convex bending (pre-focus) and the (+) sign is for the concave bending (post-focus). For a generalised form of the last equation, it can be expressed as:

$$f'' = f \left[1 + \left(\frac{f}{R} \right) \sin^{-1} \left(\frac{R}{R_C} \right) \right] \quad (6-56)$$

Where R_C will be negative (-) for the convex bending (pre-focus) and positive (+) for the concave bending (post-focus). Then, in terms of df'' , equations (6-52) and (6-53) can be re-written according this sign rule as:

$$df'' = f - f'' = -\frac{f^2}{R} \sin^{-1} \left(\frac{R}{R_C} \right) \quad (6-57)$$

So that the positive value of df'' indicates that new focal point is nearer to the lens plane which corresponds substitution with a negative value of R_C (convex bending case, as shown in Figure 6-27a). The spot diameter, D_s , on a screen at any general distance, x , from the lens plane can be obtained by:

$$D_s(R_C, x) = 2|x - f''| \tan \alpha'' \quad (6-58)$$

6.1.4.3 Configuration-Buckling Combined Effect

The combined effect starts from the fact of shifting the focal point either by f' amount, in case of configuration effect, or by f'' , in case of buckling effect resulting in an average focal length, \bar{f} , as illustrated by Figure 6-28.

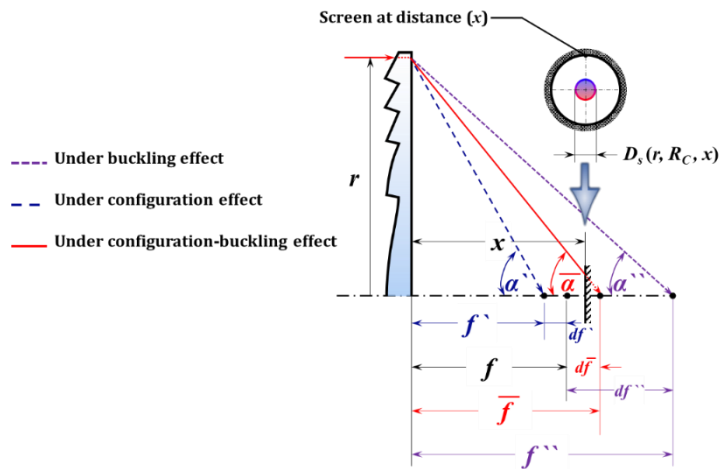


Figure 6-28 Configuration-buckling combined effect

The resulting focal length shift, $d\bar{f}$, can be approximated as:

$$d\bar{f} = df' + df'' = f - \bar{f} \quad (6-59)$$

Where the values of both df' and df'' are used according to their signs, leading to a value of $d\bar{f}$ with either positive or negative sign corresponding a new focal point nearer or further to the lens plane, respectively. This relation allows considering and neglecting either configuration or buckling effects. Then the rays' deflection angle can be obtained from:

$$\bar{\alpha} = \tan^{-1} \left(\frac{r}{|\bar{f}|} \right) = \tan^{-1} \left[\frac{r}{|f - 0.5(df' + df'')|} \right] \quad (6-60)$$

Then, the spot diameter, D_s , on a screen at any general distance, x , from the lens plane can be determined by:

$$D_s(r, R_C, x) = 2|x - \bar{f}| \tan \bar{\alpha} \quad (6-61)$$

Combining Equations (6-45), (6-55) and (6-60) and substituting in (6-61), then a more generalised form of spot diameter formula can be expressed as:

$$D_s(r, R_C, x) = 2r \left| \frac{x}{f - 0.5 \left[f - \frac{r}{\tan \alpha'} - \frac{f^2}{R} \sin^{-1} \left(\frac{R}{R_C} \right) \right]} - 1 \right| \quad (6-62)$$

Where, the negative and positive signs are for convex bending concave bending cases, respectively, while for GI configuration:

$$\alpha' = \sin^{-1} \left\{ n \sin \left[\sin^{-1} \left(\frac{\sin \theta_a}{n} \right) + \theta_s \right] \right\} - \theta_s \quad (6-63)$$

And for GO configuration:

$$\alpha' = \sin^{-1} \left\{ n \sin \left\{ \theta_s - \sin^{-1} \left[\frac{\sin(\theta_s - \theta_a)}{n} \right] \right\} \right\} \quad (6-64)$$

Equation (6-62) takes into account CA, SAA and buckling effects, based on assuming an average focal length combining configuration and buckling effects.

The minimum spot diameter, $D_{s,min}$, is achieved when the distance, x , reaches a critical value, x_{cr} , which can be obtained graphically or mathematically by solving the following equation for x :

$$\left. \frac{dD_s}{dx} \right|_{x=x_{cr}} = 0 \quad (6-65)$$

6.1.4.4 Generated Beam Diameter

In the previous sections, the front Fresnel lens has been optically investigated with different parameters that may influence its performance in converging incident solar rays. In this section, the rear positive meniscus lens, with nomenclatures illustrated in Figure 6-29, is included in the optical study of the LLBG system. The aim of this involvement is to give an estimation of the generated beam diameter.

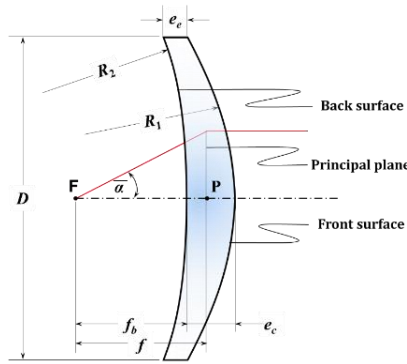


Figure 6-29 Positive meniscus lens nomenclatures
(Thorlabs, 2018c)

According to nomenclature shown in Figure 6-29, the focal length, f , is measured between the focal point (**F**) to the principal plane. The principal plane refers the plane defined by a set of intersection points between extended parallel rays the optical axis entering and emerging from the lens to its focal point (Smith, 2000b). The surface towards the parallel rays and the focal point are denoted as front and back surfaces, respectively. The back focal length, f_b , represents the distance between the point **F** and the back surface.

The lens-lens optical configuration is assumed to place the back surface of the rear positive meniscus lens at distance x_2 from the x -plane, which denotes a plane at distance $x_1 = x_{cr}$ from the front Fresnel lens, as shown in Figure 6-30. The deflection angle, $\bar{\alpha}$, is obtained from Eq. (6-60), which is a function of the distance, r , as the Fresnel prism slope angle, $\theta_s(r)$.

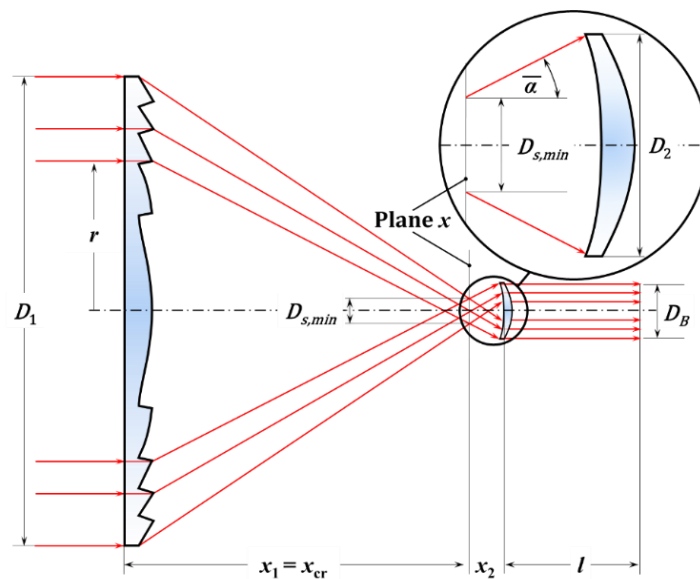


Figure 6-30 The lens-lens optical configuration

Detailed geometry of the rear lens and a ray tracing through it is illustrated in Figure 6-31. According to illustrated geometry, the ray hits the back surface of the rear lens at a vertical height from its optical axis of y with an incidence angle, θ_{i3} , which obtained by:

$$\theta_{i3} = |\bar{\alpha} - \beta_1| \quad (6-66)$$

Where β_1 is the angle between the normal to the lens surface tangent and the horizontal direction.

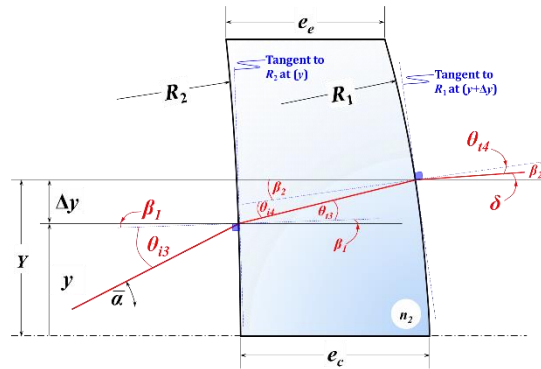


Figure 6-31 Detailed geometry of the rear lens

Hence the back surface of the lens represents a part of large sphere with a radius of R_2 , then applying the sphere's equation:

$$x^2 + y^2 = R_2^2 \quad (6-67)$$

Then

$$\frac{dy}{dx} = \frac{-x}{\sqrt{R_2^2 - x^2}} = \tan\left(\frac{\pi}{2} - \beta_1\right) \quad (6-68)$$

Which can be re-arranged as:

$$\beta_1 = \frac{\pi}{2} - \left| \tan^{-1}\left(\frac{-x}{\sqrt{R_2^2 - x^2}}\right) \right| \quad (6-69)$$

From Eq. (6-67), the previous can be expressed in terms of the distance, y , as:

$$\beta_1 = \frac{\pi}{2} - \left| \tan^{-1}\left(\frac{-1}{y} \sqrt{R_2^2 - y^2}\right) \right| \quad (6-70)$$

Then by substitution in (6-66):

$$\theta_{i3} = \left| \bar{\alpha} - \frac{\pi}{2} + \left| \tan^{-1}\left(\frac{-1}{y} \sqrt{R_2^2 - y^2}\right) \right| \right| \quad (6-71)$$

Where y can be approximated by applying Eq. (6-62) with $(x = x_{cr} + x_2)$ as:

$$y = \left. \frac{D_s(r, R_C, x)}{2} \right]_{x=x_{cr}+x_2}, \quad y \leq \frac{D_2}{2} \quad (6-72)$$

Then, applying Snell's law:

$$\theta_{t3} = \sin^{-1} \left(\frac{\sin \theta_{i3}}{n_2} \right) \quad (6-73)$$

Where n_2 is the refractive index of the rear lens material. The refracted ray within the rear lens hits its front surface at a vertical distance of $(Y = y + \Delta y)$ from its optical axis with an incidence angle, θ_{i4} . The distance Δy can be obtained by assuming an average constant lens thickness of $\left(\frac{e_c + e_e}{2}\right)$ as:

$$\Delta y = 0.5(e_c + e_e) \tan \theta_{t3} \quad (6-74)$$

Where e_c and e_e are centre and edge thicknesses, respectively. Similarly, to procedure followed at the back surface, then:

$$\theta_{i4} = |\theta_{t3} + \beta_1 - |\beta_2|| \quad (6-75)$$

Applying the sphere's equation for the front lens surface:

$$X^2 + Y^2 = R_1^2 \quad (6-76)$$

Then

$$\frac{dY}{dX} = \frac{-X}{\sqrt{R_1^2 - X^2}} = \tan \left(\frac{\pi}{2} - \beta_2 \right) \quad (6-77)$$

Which can be re-arranged as:

$$\beta_2 = \frac{\pi}{2} - \left| \tan^{-1} \left(\frac{-X}{\sqrt{R_1^2 - X^2}} \right) \right| \quad (6-78)$$

From Eq. (6-76), the previous can be expressed in terms of the distance, Y , as:

$$\beta_2 = \frac{\pi}{2} - \left| \tan^{-1} \left(\frac{-1}{Y} \sqrt{R_1^2 - Y^2} \right) \right| \quad (6-79)$$

Then by substitution in (6-75):

$$\theta_{i4} = \left| \theta_{t3} + \beta_1 - \frac{\pi}{2} + \left| \tan^{-1} \left(\frac{-1}{Y} \sqrt{R_1^2 - Y^2} \right) \right| \right| \quad (6-80)$$

Where Y can be approximated as:

$$Y = y + 0.5(e_c + e_e)\tan \theta_{t3}, \quad Y \leq \frac{D_2}{2} \quad (6-81)$$

Then, applying Snell's law:

$$\theta_{t4} = \sin^{-1}(n_2 \sin \theta_{i4}) \quad (6-82)$$

The deviation angle, δ , which represents the deviation of the output ray from perfect collimation, can be obtained from:

$$\delta = \beta_2 - \theta_{t4} \quad (6-83)$$

Therefore, beam diameter at any distance, l , from the rear lens can be determined from:

$$D_B = D_s(r, R_C, x)]_{x=x_{cr}+x_2} + 2l \tan \delta \quad (6-84)$$

This equation is valid only if ($\delta \geq 0$), as illustrated in Figure 6-31. In case of ($\delta < 0$), the beam shrinks with distance from the rear until the output refracted rays reaches the optical axis at the delay distance, l_{delay} , as represented in Figure 6-32.

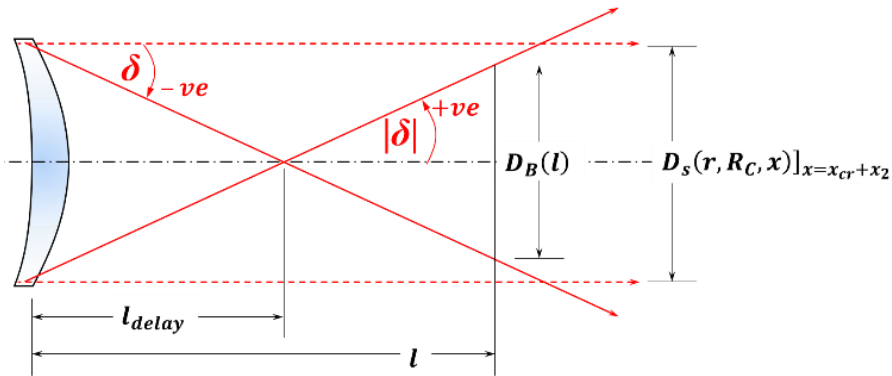


Figure 6-32 Detailed geometry for negative deviation

According to geometry of Figure 6-32, then the beam diameter calculating formula is depending on the target location with respect to the delay distance, as follows:

$$D_B = D_s(r, R_C, x)]_{x=x_{cr}+x_2} - 2l \tan|\delta|, \quad l \leq l_{delay} \quad (6-85)$$

$$D_B = 2(l - l_{delay}) \tan|\delta|, \quad l > l_{delay} \quad (6-86)$$

Where,

$$l_{delay} = [0.5 * D_s(r, R_C, x)]_{x=x_{cr}+x_2} / \tan|\delta| \quad (6-87)$$

6.1.4.5 Optical Analysis MATLAB Code

In order to further study of the generated beam diameter, equations from (6-35) to (6-84) are employed in a MATLAB code to calculate the beam diameter at certain wavelength bandwidth. Based on the front lens manufacturer focal length and GI/GO-configuration design recommendation, the code can estimate the Fresnel lens prisms slope angles as a function of front lens radius. The code is developed to consider the CA, SAA and front lens buckling and to calculate the beam diameter for both GI and GO-configurations. Moreover, the code gives estimation of the best location which represents the front lens focal plane and optimum position for the rear lens to achieve the minimum beam deviation angle. A flowchart of the code is illustrated in Figure 6-33. The code is available in Appendix J and validated with experimental test explained in Section 6.3.1, while the validation test results are plotted in Figure 7-32. Results of this model are displayed in detail through Section 7.2.3.

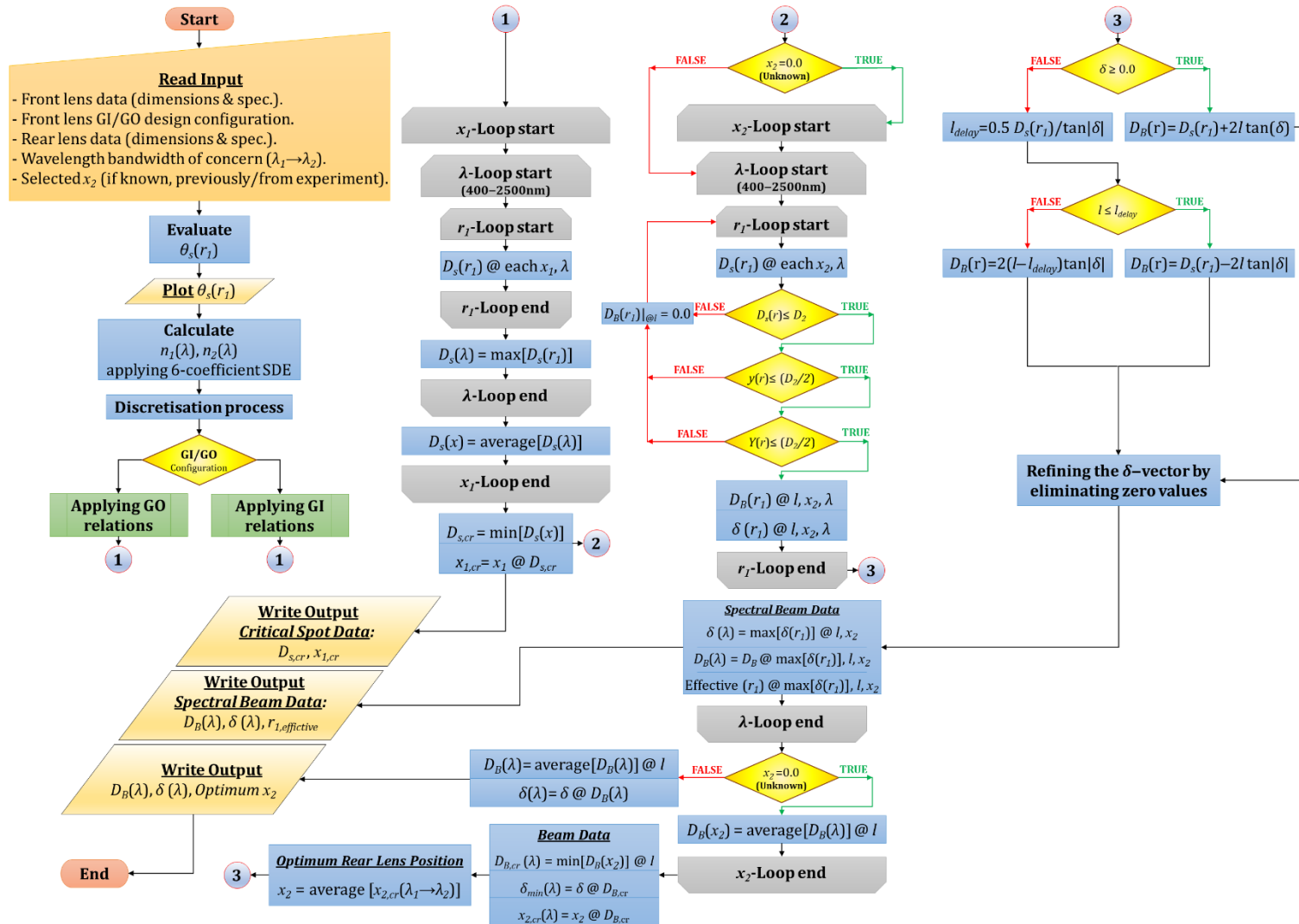


Figure 6-33 Flowchart of optical analysis MATLAB code

6.2 LLBG Design

The methodology followed to design and build the LLBG is to describe the system firstly and to introduce different design concepts for different major parts of the system to an experts committee (EC), a group of academic and technical experts in Precision Engineering Institute, Cranfield University. The discussion with the EC is carried out based on asking the members to fill in a Pugh Matrix based on their own opinions. The Pugh Matrix is an evaluation matrix that allows comparing the proposed design concepts against a number of design requirements, known as “criteria”. It also provides a degree of quantitative optimisation to select the optimum concept which meets a set of criteria. The background diversity of the EC members allows covering different academic/technical perspectives in making decision.

The selected design concepts out of the Pugh Matrix are then investigated in more details to specify the dimensions, materials and components specification to be purchased.

6.2.1 LLBG System Description

According to the LLBG system working principle discussed in section 6.1.1, a dual-axis tracking system is required to generate the beam. For the control mirror, the proposed previous model by (Salem, Tawfik and Hamed, 2010) introduced a linearly moving and rotating control mirror and their design required adding another mirror for complete control of the generated beam direction. However, the new system proposed now claims using only one control mirror which rotates around 2-axes to achieve the same target.

In dual-axis tracking, the system is required to follow the sun’s path in the sky, which is defined by two main angles: altitude, γ , and azimuth, φ , angles. The altitude angle is the angle between the horizontal and the line to the sun (Duffie and Beckman, 2013). It varies from 0° , at sunrise/sunset, to 90° or less, at noon. The azimuth angle is the angle between the South direction and the projection of solar beam radiation on the horizontal plane (Duffie and Beckman, 2013). The

clockwise direction is defined as the positive measurement direction. Figure 6-34 illustrates the sun's path and shows the solar angles limits.

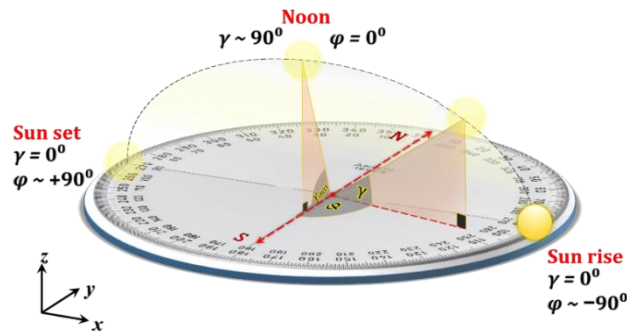


Figure 6-34 The sun's path and solar angles

Then, the LLBG can track the sun trough rotating the main arm, which holds the front and rear lenses, to track the angle γ over the range of $(0-90^\circ)^\diamond$, as shown in Figure 6-35a. In addition, the whole system is required to be rotated, with the azimuth platform, about the vertical (z -axis) to track the angle φ over an approximate range of $(\pm 90^\circ)^\diamond\diamond$, as illustrated by Figure 6-35b. Based on LLBG description, the basic system motions can be summarised in:

- Main arm rotational motion (about y -axis).
- Azimuth platform rotational motion (about z -axis).
- Control mirror rotational motion (about y –axis and z -axis).

Therefore, the Pugh Matrix introduces distinctive design concepts for each of these three motions.

[♦] The maximum range for Cranfield location (52°N) on the day of summer solstice is $(0-61.44^\circ)$

^{♦♦} The maximum range for Cranfield location (52°N) on the day of summer solstice is $(\pm 131.75^\circ)$.

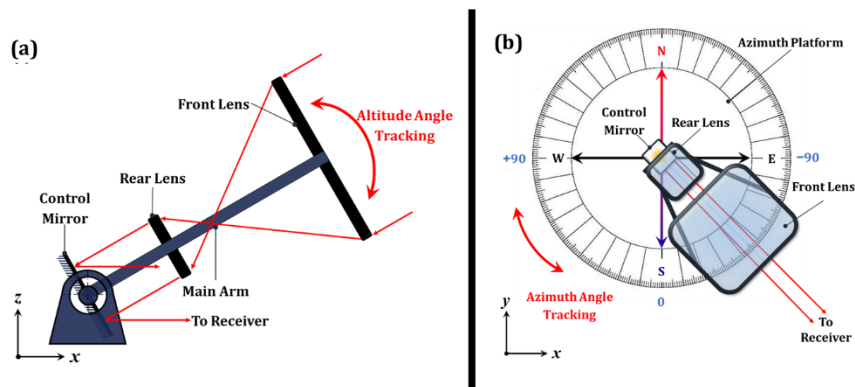


Figure 6-35 LDBG main components motions
(a) front view **(b) top view**

6.2.2 The Pugh Matrix Components

The criteria and their weighting were defined, based on their importance, and a ranking system was defined. Three main design problems and their concepts were investigated and the Pugh Matrix for each design problem was built to obtain the best concept in each case.

6.2.2.1 Design Criteria

Design requirements can be categorised in three main categories: construction, cost and time. Each category will be defined in the following:

A. Construction

- Complexity: Possible difficulties to build the system.
- System weight: The weight of the total system in case of shipping.
- Feedback requirement: Requiring of sensors to feedback the control system.
- Imprecise motion: Lack of system movements' precision in tracking process.
- System weakness: System instability under harsh environmental conditions, such as wind, sand storms and high ambient temperatures.
- Assembly problems: The difficulty of assembling and aligning system parts especially when considering installation in deserts and off-grid locations with the lack of available instruments.
- Number of elements: The number of required elements to build the system.

B. Cost

- Building cost: The required capital cost to build the system.
- Operating cost: Spent cost during the operation of the system, including power consumed to operate the system.
- Depreciation cost: The cost of the system over its lifetime. It implements system reliability and durability.
- Maintenance cost: The required cost for maintaining the system in harsh environmental conditions. It includes system cleaning and processing against corrosion and sand storms.

C. Time

- Design time: The time required to finalise the system design, depending on the system complexity.
- Building time: The time consumed through providing parts of the system. It depends on the number of elements and system complexity.
- Assembly time: The time to assembly system parts to start its function.

6.2.2.2 Weighting

Determining the weight of each criterion is required to allow a quantitative judging on different concepts based on their relative importance. Table 6-9 lists each criterion weighting. The higher weighting values the higher importance.

Table 6-9 Pugh Matrix criteria and weighting

Category	Criteria	Weighting (1–5)
Construction	Complexity	5
	System weight	2
	Feedback requirement	1
	Imprecise motion	4
	System weakness	3
	Assembly problems	2
	Number of elements	3
Cost	Building cost	5
	Operating cost	3
	Depreciation cost	3
	Maintenance cost	4
Time	Design time	1
	Building time	5
	Assembly time	3

6.2.2.3 Ranking

To compare each concept against all pre-defined criteria, the design concepts will be ranked from 1 to 5. The lower ranking values stand for the lower effect of the criterion on the design concept. Table 6-10 explains each rank value. It shows the effect of each criterion on the design concept.

Table 6-10 Pugh Matrix ranking system explanation

Rank	1	2	3	4	5
Criterion Effect	Extremely Low	Low	Medium	High	Extremely High

In the Pugh Matrix, summation of the products of rankings and criteria weights produces a total score for each concept. Good concepts produce lower scores.

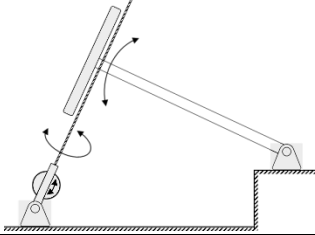
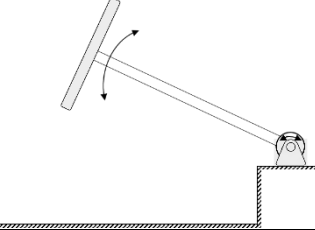
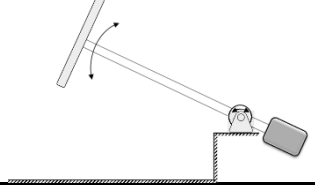
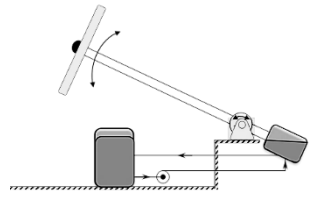
6.2.3 The Pugh Matrix Discussion

In this section, information about each motion concepts is displayed and the EC meeting outcomes are introduced.

Description and comparison between different concepts for the main arm motion is explained in Table 6-11. While for the azimuth platform and control mirror motions, different concepts described and compared in Table 6-12 and Table 6-13, respectively. The Pugh Matrix for different motions, as an outcome of the EC meeting, is displayed in Table 6-14.

According to values listed in Table 6-14, the second and third concepts for the main arm motion are found to be lower than the rest with very closing evaluation. Therefore, both of them will be considered in the system compononets sizing phase later to tip the best solution. For both azimuth platform and control mirror motions, the first concept in each case showed the minimum rank. Consequently, the first concept in both cases is adopted.

Table 6-11 Main arm motion concepts description and comparison

N°.	Schematic Diagram	Description	Benefits	Drawbacks
1		<p>Motor under the front lens, linked to driving power screws via bevel gears.</p>	<ul style="list-style-type: none"> - High stability against wind storms. - Low torque is required. 	<ul style="list-style-type: none"> - Large number of components. - Complex. - Mechanical losses in gearbox. - Needs regular maintenance. - Design complexity. - Long stroke.
2		<p>Motor linked directly to the main arm end.</p>	<ul style="list-style-type: none"> - Simple. - Low number of components. - Easy for installation. - Easy for maintenance. 	<ul style="list-style-type: none"> - High torque is required.
3		<p>Motor linked to the main arm end, with constant-mass balancing weights.</p>	<ul style="list-style-type: none"> - Low torque is required. - Low number of components. - Easy for installation. - Easy for maintenance. 	<ul style="list-style-type: none"> - Increased Main Arm weight. - Low stability of the Main Arm against wind storms. - Additional footprint.
4		<p>Motor linked to the main arm end, with variable-mass balancing weights.</p>	<ul style="list-style-type: none"> - High stability against wind storms. - Low torque is required. 	<ul style="list-style-type: none"> - Increased Main Arm weight. - Large number of components. - Complex. - Needs regular maintenance. - Additional footprint. - Pump cost.

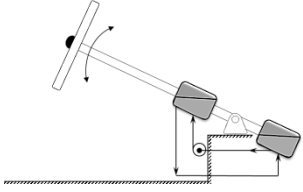
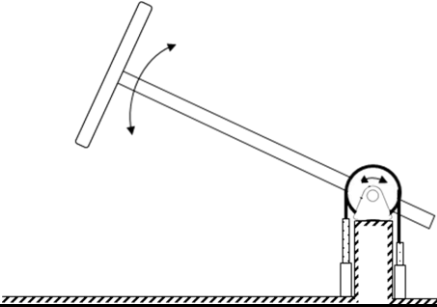
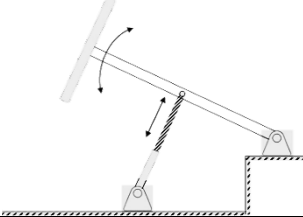
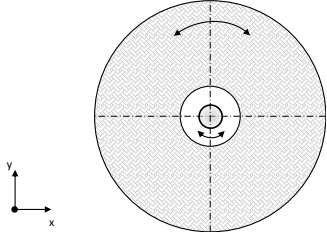
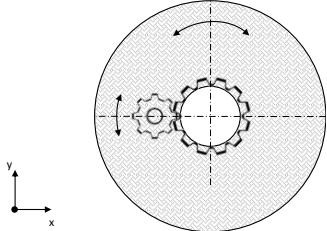
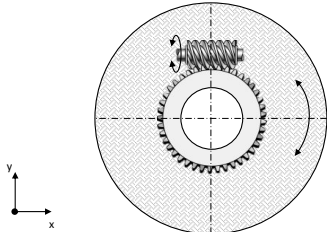
N°.	Schematic Diagram	Description	Benefits	Drawbacks
5		<p>Motor replaced with two variable-mass balancing weights.</p>	<ul style="list-style-type: none"> - No motor is required. 	<ul style="list-style-type: none"> - Increased Main Arm weight. - Large number of components. - Complex. - Needs regular maintenance. - Additional footprint. - Pump cost. - Instability against wind storms.
6		<p>Cylinders-chain-pulley mechanism employed.</p>	<ul style="list-style-type: none"> - High stability against wind storms. - Simple. - Easy for installation. - Easy for maintenance. 	<ul style="list-style-type: none"> - Higher cost compared to hydraulic motors. - Long stroke.
7		<p>Hydraulic cylinders used to push/pull the main arm.</p>	<ul style="list-style-type: none"> - Simple. - High stability against wind storms. - Low torque is required. 	<ul style="list-style-type: none"> - Higher cost compared to hydraulic motors. - Design complexity. - Long stroke.

Table 6-12 Azimuth platform motion concepts description and comparison

N°.	Schematic Diagram	Description	Benefits	Drawbacks
1		<p>A motor mounted at platform centre drives it directly.</p>	<ul style="list-style-type: none"> - Simple. - Easy for maintenance. - Low number of components. 	<ul style="list-style-type: none"> - High torque is required.
2		<p>Motor is linked to the platform via a gearbox.</p>	<ul style="list-style-type: none"> - Low torque is required. - High stability against wind storms. - Easy for maintenance. 	<ul style="list-style-type: none"> - Mechanical losses in gearbox.
3		<p>A slew drive (worm gear employing) is used to rotate the platform.</p>	<ul style="list-style-type: none"> - High stability against wind storms. - Smooth rotation with high precision. - Easy for maintenance. 	<ul style="list-style-type: none"> - Mechanical losses in gearbox.

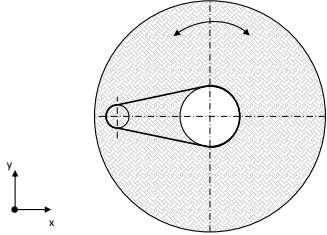
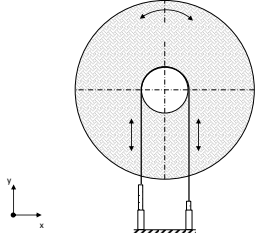
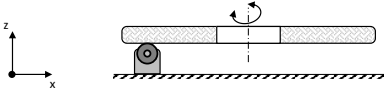
N°.	Schematic Diagram	Description	Benefits	Drawbacks
4		<p>Motor is linked to the platform via a belt.</p>	<ul style="list-style-type: none"> - Low torque is required. - High stability against wind storms. 	<ul style="list-style-type: none"> - Mechanical losses in belt. - Maintenance problems especially at high ambient temperature.
5		<p>Cylinders-chain-pulley mechanism is employed.</p>	<ul style="list-style-type: none"> - High stability against wind storms. - Easy for installation. - Easy for maintenance. 	<ul style="list-style-type: none"> - Higher cost compared to hydraulic motors. - Long stroke. - Additional footprint. - Large number of services required (for hydraulic system).
6		<p>Motor with a driving wheel is used to rotate the platform</p>	<ul style="list-style-type: none"> - Low number of components. - Easy for installation. 	<ul style="list-style-type: none"> - Mechanical losses in contact between wheel and platform. - Instability against wind storms, as the only mechanical stop for the platform is the friction between it & the driving wheels.

Table 6-13 Control mirror motion concepts description and comparison

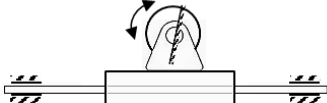
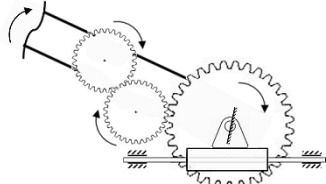
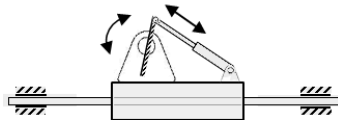
N°.	Schematic Diagram	Description	Benefits	Drawbacks
1		<p>Separate motor used to rotate the control mirror.</p>	<ul style="list-style-type: none"> - Easy for installation. - Easy for programming. 	<ul style="list-style-type: none"> - More power consumption. - Low precision. - Maintenance problems.
2		<p>Gearbox linked the Main Arm with the Control Mirror.</p>	<ul style="list-style-type: none"> - Low power consumption. - More precise. 	<ul style="list-style-type: none"> - Complex Design.
3		<p>Cylinder used to pull/push the control mirror.</p>	<ul style="list-style-type: none"> - Smooth motion. 	<ul style="list-style-type: none"> - Complex Design. - Higher cost compared to hydraulic motors.

Table 6-14 Pugh Matrix for different motions

Category	Criteria	Weight	Main arm motion concepts							Azimuth platform motion concepts						Control Mirror motion concepts		
			1	2	3	4	5	6	7	1	2	3	4	5	6	1	2	3
Construction	Complexity	5	4	3	3	5	5	4	4	2	3	3	2	5	2	2	5	4
	System weight	2	3	2	4	4	4	3	4	2	3	4	3	4	3	2	4	3
	Feedback requirement	1	3	3	3	5	5	3	3	2	4	3	4	3	3	4	3	4
	Imprecise motion	4	4	4	4	3	4	3	3	3	4	3	4	3	4	3	4	4
	System weakness	3	3	4	3	4	4	3	3	3	3	2	4	3	4	3	3	4
	Assembly problems	2	4	2	3	4	4	3	3	2	3	2	2	3	3	3	5	4
	Number of elements	3	4	2	3	4	4	4	3	2	3	3	3	4	2	2	4	3
Cost	Building cost	5	4	3	3	4	4	4	4	3	4	4	3	5	3	3	5	3
	Operating cost	3	3	3	2	3	3	3	3	3	3	4	3	4	3	3	2	2
	Depreciation cost	3	4	2	3	3	3	3	3	3	3	2	4	4	2	2	2	3
	Maintenance cost	4	4	3	3	4	4	4	3	3	3	3	3	5	3	3	4	4
Time	Design time	1	4	2	3	4	4	4	4	2	4	4	3	4	3	3	5	3
	Building time	5	4	3	2	4	4	3	3	3	4	4	3	4	3	3	4	3
	Assembly time	3	4	3	3	4	4	3	3	2	3	3	2	3	2	3	5	3
Total			167	128	130	172	176	150	145	115	148	140	133	177	125	120	176	148

6.2.4 Main Arm Profile Selection

It is important to select the appropriate profile with minimum deflection to avoid misaligning of the front lens focal point. Firstly, a deflection limit will be defined, and then a study of deflection values for different profiles will be carried out. Selection among acceptable profiles will be done based on the availability, weight and cost of the profile.

6.2.4.1 Acceptable Deflection Limit

Main arm deflection with an amount of Γ leads to shifting the generated beam centreline by d_B , as shown in Figure 6-36. The deflection is assumed to be occurring at the midpoint of the main arm with an angle θ . This shift results in losing an area of the beam generated as illustrated in Figure 6-37.

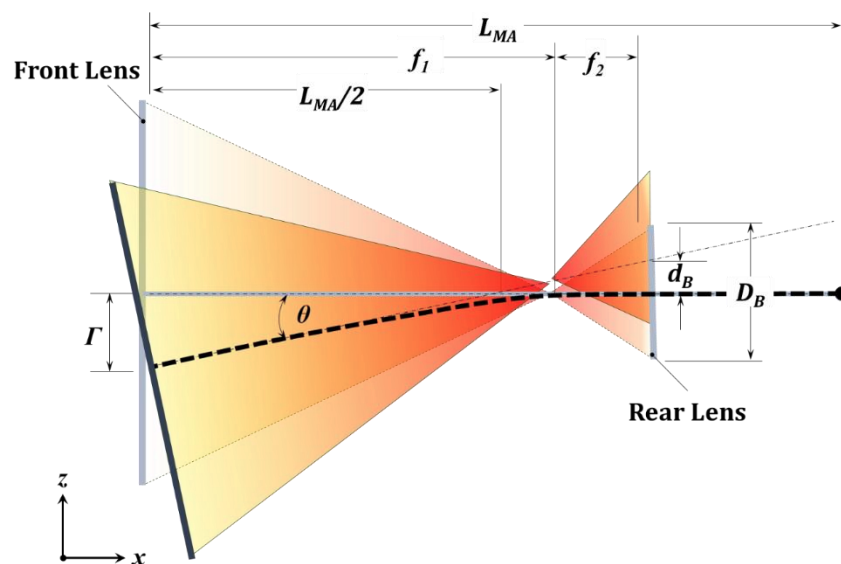


Figure 6-36 Main arm deflection effect

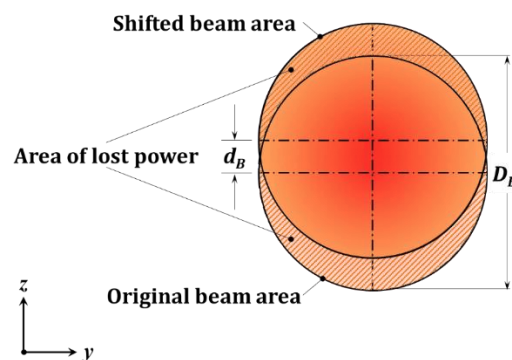


Figure 6-37 Shifted beam and lost power

Hence the power collected from input solar flux is directly proportional to the surface area, the beam area can be used as an indication of amount gained or lost from collected power. Assuming the shifted beam to keep its circular projected area with the same diameter of the original beam, D_B , then the gained (preserved) area of the beam, A_g , which represents the intersection area between the two circles of original and shifted beams, can be determined as follows (Ergenc, 2009):

$$A_g = 0.5 \left[\left(D_B^2 \cos^{-1} \left(\frac{d_B}{D_B} \right) \right) - d_B \sqrt{(D_B + d_B)(D_B - d_B)} \right] \quad (6-88)$$

Then the area of lost power, A_l , can be determined from:

$$A_l = A_o - A_g \quad (6-89)$$

Where, A_o is the original beam surface area. Then, the lost power is:

$$P_l \% = \left(1 - \frac{A_p}{A_o} \right) \times 100$$

Or (6-90)

$$P_l \% = \left\{ 1 - \left[\frac{2}{\pi} \cos^{-1} \left(\frac{d_B}{D_B} \right) \right] + \left(\frac{2d_B}{\pi D_B^2} \right) \sqrt{(D_B + d_B)(D_B - d_B)} \right\} \times 100$$

Where, d_B can be defined from geometry of Figure 6-36:

$$d_B = \frac{2\Gamma}{L_{MA}} [(f_1 + f_2) - 0.5L_{MA}] \quad (6-91)$$

Assuming that the values of D_B , L_{MA} and $(f_1 + f_2)$ are 5.0E-02m, 2.0m and 1.5m, respectively, then Eq. (6-91) can be plotted as shown in Figure 6-38.

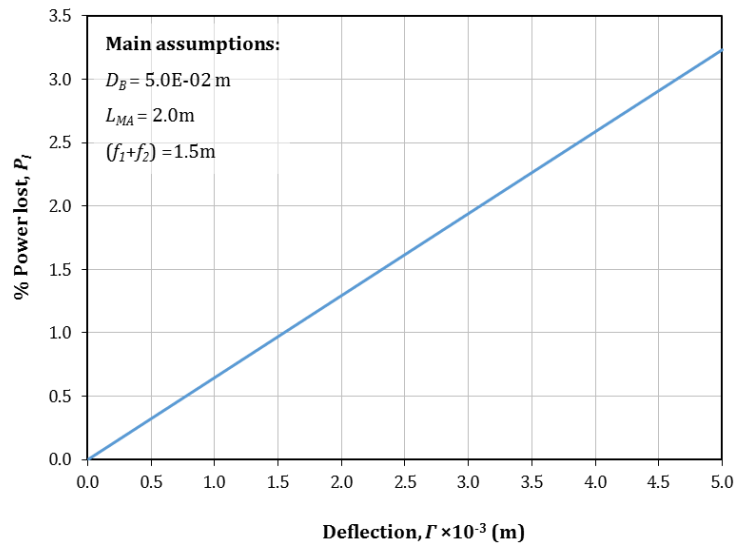


Figure 6-38 Concentrated power lost as a function of deflection

Assuming a power flux of 1000W/m² falling over the front lens with approximate aperture area of 1.5m² and neglecting the lens absorbance and reflectance, then the power of the concentrated beam at the rear lens can be estimated to be 1500W. To avoid damaging the LLBG structure or burning any surrounding operators or objects, the acceptable limit of power loss can be set to 1%. This leads to defining a maximum allowable deflection of **1.65E-03m**.

6.2.4.2 Aluminium Strut Profile Deflection Study

Deflection in profiles occurs due to the weight of the front lens and its frame. Moreover, the profile's own weight is another reason for deflection, as illustrated in Figure 6-39.

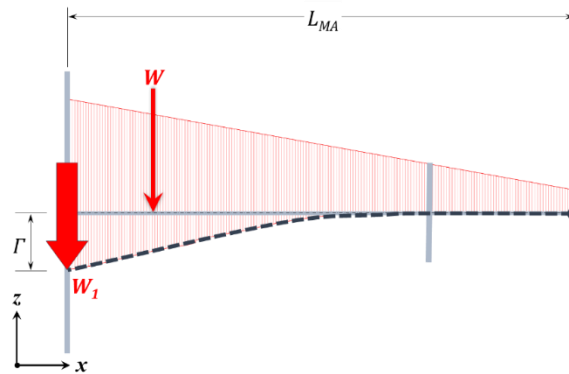


Figure 6-39 Causes of main arm deflection

In order to determine the total amount of deflection in an Aluminium profile, Γ , the following formula can be applied (Bosch Rexroth AG, 2015):

$$\Gamma = \left(\frac{\omega * g * L_{MA}^4}{8 * E * I_c} \right) + \left(\frac{W_1 * L_{MA}^3}{3 * E * I} \right) \quad (6-92)$$

Where, Γ is in (m), I_c is moment of inertia in (m⁴), ω is the profile mass per unit length in (kg/m), L_{MA} is the main arm length of 2.0m and E is the modulus of elasticity which equals 70E09 Pa. For the front lens weight, W_1 it can be calculated from:

$$W_1 = \frac{m_1 * g}{N_{MA}} * FS \quad (6-93)$$

Where, m_1 is front lens total mass including lens and its frame, N_{MA} is the number of rods used to support the front lens and its frame and FS is a factor of safety. The mass m_1 can be calculated based on data listed in Table 6-15.

Table 6-15 Parameters values for Eq. (6-93)

Parameter	Value	Unit
Profile for lens frame	0.030x0.030	m
Lens frame mass/length	0.9	Kg/m
Lens frame perimeter	4.9624	m
Lens Frame mass	4.46616	kg
Lens mass (PMMA)	5.2479	kg
Factor of safety	1.2	-
Front lens total mass	9.71406	kg

Then

$$W_1 = \frac{114.353208}{N_{MA}} \quad (6-94)$$

Values of the other parameters in Eq. (6-92) are considered as variables, as they are dependent on profile type. Appendix E shows these values and results of Eq. (6-92) for 95 Aluminium profiles at different number of front lens supporting rods, N_{MA} . Appendix E includes summarisation and comparison of accepted profiles in case of using two, four and six supporting rods, respectively. The comparison is based on the total mass of the main arm in each case, Nm_{MA} (neglecting rear lens supports), availability status for UK suppliers and price per meter for available profiles. Based on data listed in Appendix E, using two supporting rods will be rejected as a result of unavailability of profiles.

Aluminium profile (**40x120L**), illustrated in Figure 6-40 has been selected, with a total mass (including front lens and its frame mass) of **43.3kg**, with a deflection of **1.12E-03m** and total cost of **£200**.

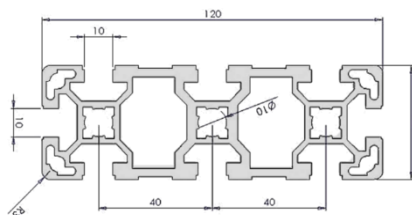


Figure 6-40 Cross section of main arm Aluminium profile, 40x120L
(Bosch Rexroth AG, 2015)

6.2.4.3 Wood Cross-section Deflection Study

As an alternative to Aluminium strut profiles, wood can insure a lighter and lower cost solution for the main arm part. In order to calculate deflection in wood cross-sections, general formula for deflecting cantilevers supported at one end, as shown in Figure 6-41, is applied. In that case the maximum amount of deflection can be calculated from (Wu, 2006):

$$\Gamma = \left(\frac{F a^2}{6EI_c} \right) (3L - l_{cg}) \quad (6-95)$$

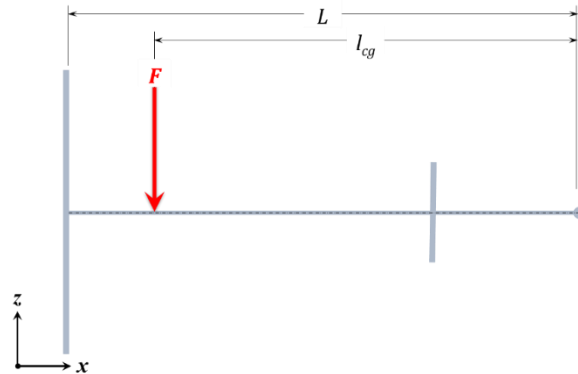


Figure 6-41 General force affecting a cantilever beam

Back to Figure 6-39, the deflection due to the weight of the front lens and its frame, W_1 , can be determined by substitution in Eq. (6-95) with W_1 for F and ($l_{cg_{W_1}} = L = L_{MA}$), then:

$$\Gamma_{W_1} = \left(\frac{W_1 * L_{MA}^3}{3 * E * I_c} \right) \quad (6-96)$$

For the deflection occurring due to arm's own weight, the resulting force for the triangular distribution of weight force can be determined from (Hall, Archer and Gilbert, 1999):

$$W = \left(\frac{\omega * g * L_{MA}^2}{2} \right) \quad (6-97)$$

This force acts at:

$$l_{cg_W} = \left(\frac{2 * L_{MA}}{3} \right) \quad (6-98)$$

From Equations (6-97) and (6-98) in Eq. (6-95), then:

$$\Gamma_W = \left(\frac{7}{81} \right) \left(\frac{\omega * g * L_{MA}^5}{E * I_c} \right) \quad (6-99)$$

Then the total deflection can be determined:

$$\Gamma = \left(\frac{W_1 * L_{MA}^3}{3 * E * I_c} \right) + \left[\left(\frac{7}{81} \right) \left(\frac{\omega * g * L_{MA}^5}{E * I_c} \right) \right] \quad (6-100)$$

Where, the moment of inertia for a rectangular cross section with dimensions of ($b \times h$), as illustrated in Figure 6-42, can be determined from (Gere and Goodno, 2012):

$$I_c = \left(\frac{bh^3}{12} \right) \quad (6-101)$$

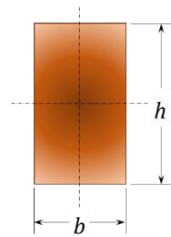


Figure 6-42 Nomenclature for moment of inertia for a rectangular cross-section

Considering the use of different types of timbers with properties listed in Table 6-16. Then, results of Eq. (6-100) are obtained and listed for 96 available cross-sections in Appendix F at different number of front lens supporting rods, N_{MA} .

Table 6-16 Properties of studied timbers

Timber Type	Density, ρ (kg/m ³)	Modulus of Elasticity, E (Pa)	Reference
American Ash	675	1.20E+10	(Britton Timbers, 2016a)
American Black Walnut	609	1.10E+10	(Britton Timbers, 2016b)
American Cherry	561	1.10E+10	(Britton Timbers, 2016c)
American White Oak	770	1.20E+10	(Britton Timbers, 2016d)
European Beech	725	1.30E+10	(Britton Timbers, 2016e)
European Oak	695	1.00E+10	(Britton Timbers, 2016f)

According to data listed in Appendix F, the optimum solution is using **European Beech Timber** with cross section of **19x222mm** with a total mass (including front lens and its frame mass) of **22kg**, a deflection of **0.85E-03m** and total cost of **£73**.

6.2.4.4 Aluminium Extrusion Cross-section Deflection Study

Aluminium extrusion represents also an alternative to Aluminium strut profiles and wood. In order to calculate deflection in Aluminium extrusions, Eq. (6-100) can be applied for different available extrusions shown in Figure 6-43 (L.A. Metals Ltd., 2016).

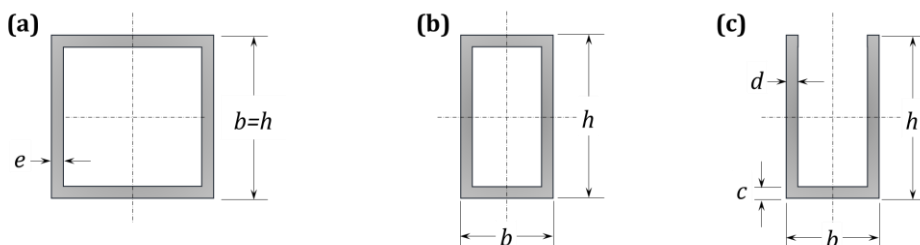


Figure 6-43 Nomenclature for moment of inertia of available Aluminium extrusions

(a) Square Tube

(b) Rectangular Tube

(c) U-Channel

Moment of inertia for square and rectangular tubes can be determined from Eq. (6-101), while it can be calculated for the U-Channel from (Gere and Goodno, 2012):

$$I_c = \left(\frac{hb^3 - (h - c)(b - 2d)^3}{12} \right) \quad (6-102)$$

The density and modulus of elasticity of Aluminium extrusions are 2700 Kg/m³ and 70 GPa (Aalco Metals Ltd, 2013).

However, the providing company did not allow prices of all accepted extrusions; a more specific quote was required. Therefore, the minimum mass solution was selected to be quoted. Based on that, the optimum solution is using **Square tube** with cross section of **100x100x2mm** with total mass (including front lens and its frame mass) of **18.2kg**, a deflection of **0.36E-03m** and total cost of **£52.6**. Comparing these results with Wood results obtained in Section 6.2.4.3 leads to rejecting the Wood solution for the main arm structure.

6.2.4.5 Front Lens Frame Re-design

Based on using timber for the main arm, there is no need any more to use the 30x30mm Aluminium profile for the front lens. It may be replaced by 20x20mm Aluminium profile or even employing the same timber profile used in the main arm. Table 6-17 shows comparison between these solutions.

Table 6-17 Comparison between accepted cross-sections (mass and cost)

Profile	Material	Perimeter (m)	Mass/length (Kg/m)	Total mass, m_f (kg)	Cost/length (£/m)	Total cost (£)
30x30	Aluminium	5	0.9	4.5	5.9	29.5
20x20	Aluminium		0.4	2.0	4.0	20.0

According to such comparison the front lens frame profile will be changed to be: 20x20 Aluminium profile. Then, the modified specifications of the main arm can be listed as shown in Table 6-18.

Table 6-18 Modified specifications of the main arm

Item	Material	Geometry	Mass (Kg)
Front lens	PMMA	Fresnel	5.25
Front lens frame	Aluminium Strut	20x20	2.0
Rear lens support	Aluminium Square tube	100x100x2	3.25
Main arm	Aluminium Square tube	100x100x2	8.5
Total Mass, m_{MA} (kg)			19.0

6.2.5 Main Arm Motor Sizing

6.2.5.1 Wind Load

Wind load acting on the front lens is a function of lens orientation, wind direction, and the lens dimensions (Peterka *et al.*, 1988). Generally, force load caused by an air flow can be determined from the aerodynamic loads theory as follows (Burisch *et al.*, 2015):

$$F_w = 0.5 * \rho_{air} * A * U^2 * C_d \quad (6-103)$$

Where, F_w is the wind force, ρ_{air} is air density, A is projected area, U is the wind speed and C_d is the drag coefficient.

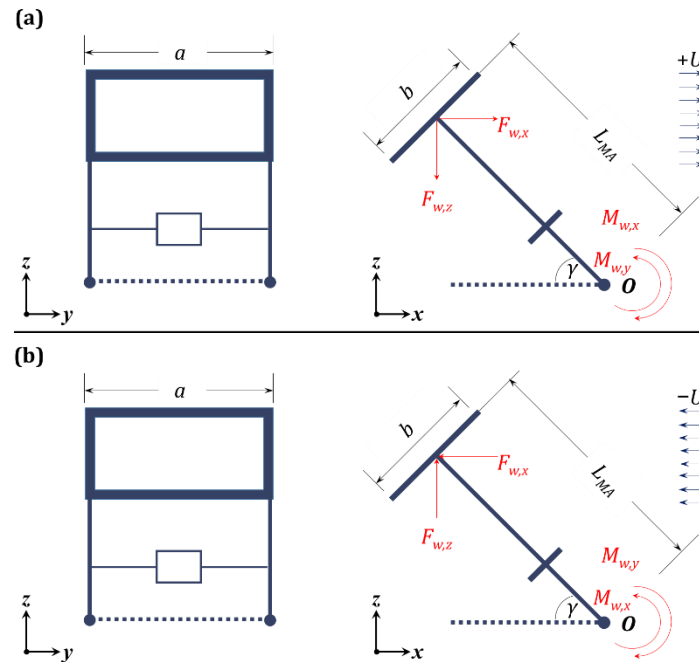


Figure 6-44 Wind load on main arm
(a) Wind speed is $+U$ **(b) Wind speed is $-U$**

At this stage, torque of the motor at pivot O , T_{MA} , to overcome wind effect is required to be calculated. Therefore, the wind is assumed to be blowing in the $x-z$ plan horizontally with a speed, U , as shown in Figure 6-44, in two different cases. In the first one wind is assumed to be blown in positive direction of the x -axis, Figure 6-44a, while in the second case it was in the opposite direction, Figure 6-44b. In both cases, two wind force components will generate moments at the main arm pivot O . Magnitudes of these components can be determined by applying the following equations:

$$F_{w,x} = 0.5 * \rho_{air} * A_x * U^2 * C_d \quad (6-104)$$

$$F_{w,y} = 0.5 * \rho_{air} * A_y * U^2 * C_d \quad (6-105)$$

Where, A_x and A_y are the projected area of the front lens on $y-z$ and $x-y$ plans, respectively. Then equations (6-104) and (6-105) can be re-written as function of altitude angle, γ , as follows:

$$F_{w,x} = 0.5 * \rho_{air} * a * b * \cos \gamma * U^2 * C_d \quad (6-106)$$

$$F_{w,y} = 0.5 * \rho_{air} * a * b * \sin \gamma * U^2 * C_d \quad (6-107)$$

Then, resulting moment loads can be determined from:

$$M_{w,x} = (0.5 * \rho_{air} * a * b * \cos \gamma * U^2 * C_d) * L_{MA} * \sin \gamma \quad (6-108)$$

$$M_{w,y} = (0.5 * \rho_{air} * a * b * \sin \gamma * U^2 * C_d) * L_{MA} * \cos \gamma \quad (6-109)$$

$$M_w = |(M_{w,x} - M_{w,y})| = 0 \quad (6-110)$$

Values of parameters in previous equations are listed in Table 6-19.

By substitution in equations (6-108)–(6-110), resulting moment due to wind load can be plotted as shown in Figure 6-45. Based on these results, the maximum wind load on main arm motor is **97.5 N.m**.

Table 6-19 Parameters values for equations (6-108) and (6-109)

Parameter	Value*
Air density, ρ_{air}	1.27 kg/m ³
Front lens frame length, a	1.5 m
Front lens frame width, b	1.1 m
Altitude angle, γ	0–90°
Wind speed, U	7.0 m/s
Drag coefficient, C_d	1.9
Main arm length, L_{MA}	2.0 m

* Assumed values of wind speed and drag coefficient are explained in Appendix H.

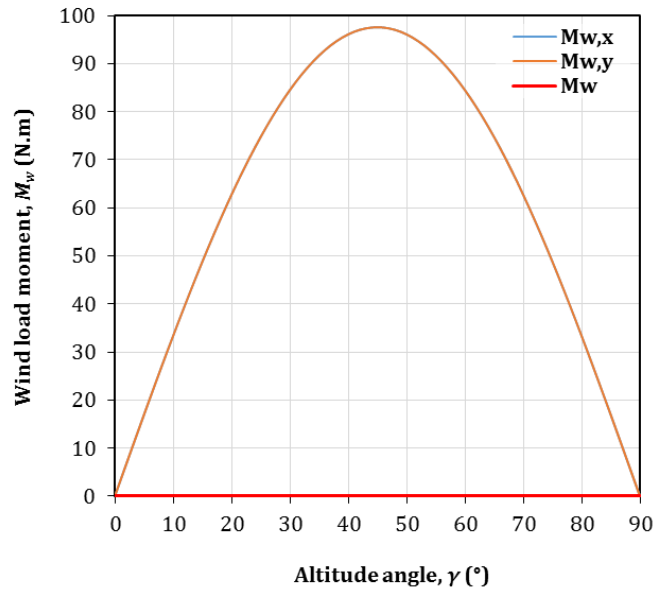


Figure 6-45 Wind load moment on main arm pivot as a function of altitude angle

6.2.5.2 Weight Load

In order to determine the moment at the main arm at pivot O due to its weight, the main arm centre of gravity is assumed to be located at the front lens centroid, as illustrated in Figure 6-46.

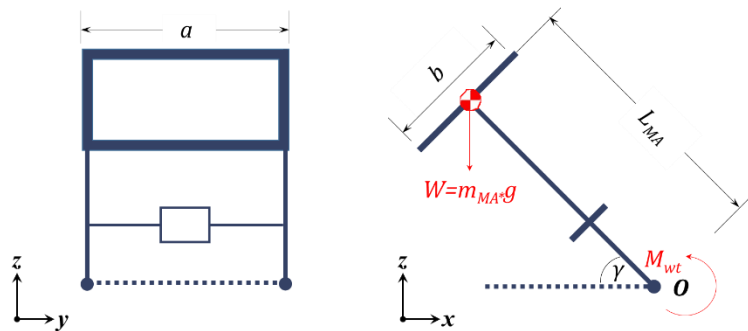


Figure 6-46 Weight load on main arm

Then:

$$M_{wt} = m_{MA} * g * L_{MA} * \cos \gamma \quad (6-111)$$

Where, M_{wt} is the moment at main arm pivot due to its weight, m_{MA} is the main arm mass and g is the gravitational acceleration. According to calculations carried out in Table 6-18, the main arm mass is 19.0 kg. Then, the moment at main arm pivot can be plotted as shown in Figure 6-47, with a maximum value of **373 N.m**.

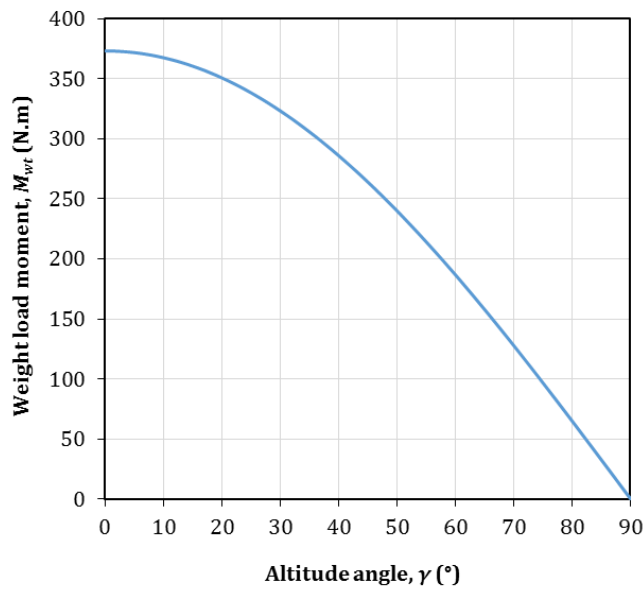


Figure 6-47 Weight load on main arm pivot as a function of altitude angle

6.2.5.3 Combined Load without Counter Weight

In order to get the maximum probable moment that may affect at the main arm pivot point, a superposition principle is applied. The combined loads due to wind force, F_w , and main arm weight force, W , are shown in Figure 6-48.

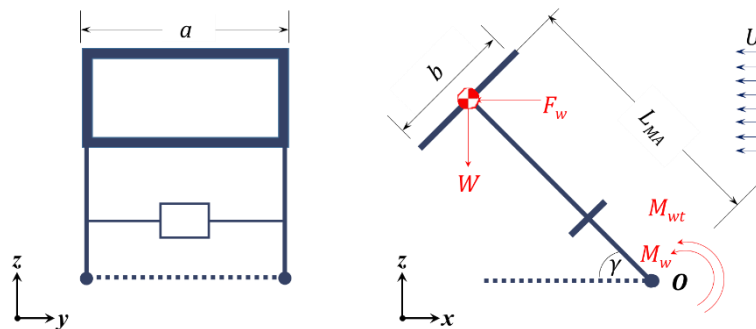


Figure 6-48 Wind and weight loads on main arm pivot without a counter weight

Therefore, the total combined moment, M_t , can be calculated as:

$$M_t = M_w + M_{wt} \quad (6-112)$$

The result of Eq. (6-112) is plotted in Figure 6-49. According to resulting data, the maximum affecting moment is **413.4 N.m**.

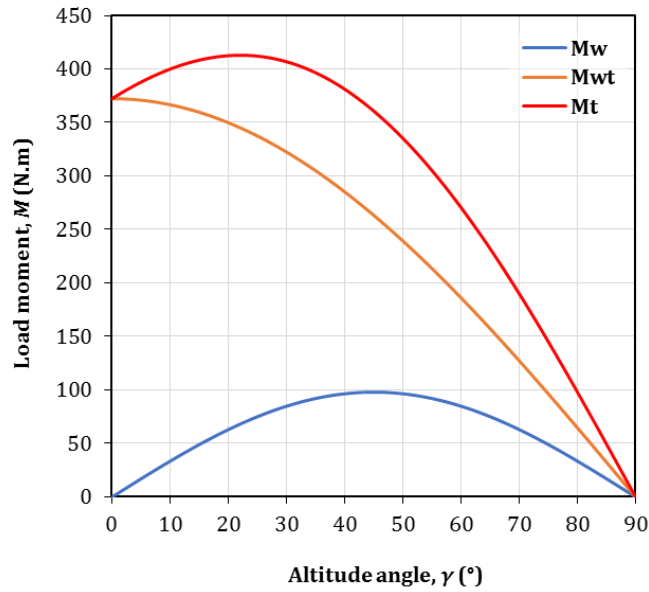


Figure 6-49 Wind and weight combined load on main arm pivot without using a counter weight, as a function of altitude angle

6.2.5.4 Combined Load with Counter Weight

In order to minimise the torque required for the main arm motor, a counter weight can be employed in the design, as shown in Figure 6-50.

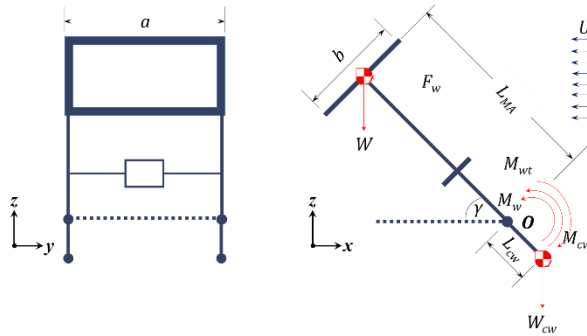


Figure 6-50 Wind and weight loads on main arm pivot with a counter weight

Based on geometry illustrated in Figure 6-50, the total combined moment, M_t , can be calculated as:

$$M_t = M_w + M_{wt} - M_{cw} \quad (6-113)$$

Which can be re-written as follows:

$$M_t = M_w + M_{wt} - (m_{cw} * g * L_{cw} * \cos \gamma) \quad (6-114)$$

Where, m_{cw} is the counter weight mass and L_{cw} is distance between the counter weight centroid and main arm pivot point with assumed values of 20 kg and 0.5 m, respectively. The result of Eq. (6-114) is plotted in Figure 6-51. According to resulting data, the maximum affecting moment is **323.75 N.m**.

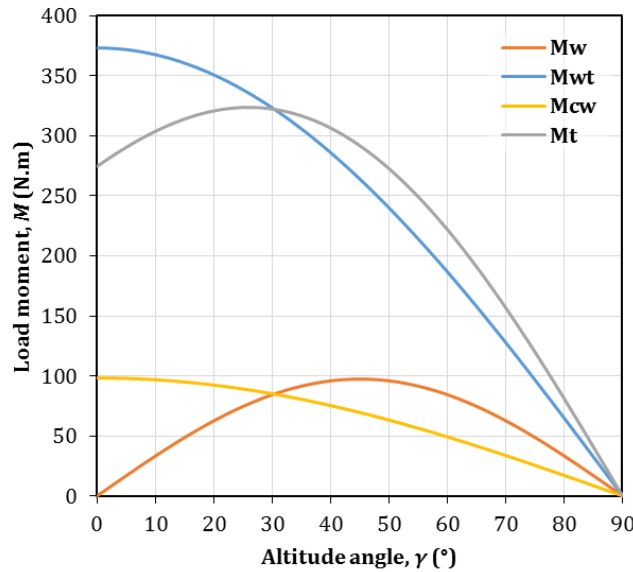


Figure 6-51 Wind, weight and counter weight combined load on main arm pivot with using a counter weight, as a function of altitude angle

According to obtained from Figure 6-51, it is clear that using a counter weight has a significant effect on total torque required for the main arm swivelling motor. Therefore, the effect of counter weight mass, m_{cw} , on the resulting moment at point O is studied in more details.

6.2.5.5 Counter Weight Effect on Combined Load

Although using a counter weight minimises the total combined load affecting on the main arm swivelling motor, this advantage is not absolute. The reason for this lies in Eq. (6-113), as the wind load, M_w , is variable. Accordingly, when wind load vanishes due to low wind speed, using a heavy counter weight will form additional load on the motor. Therefore, the torque range in case of wind load presence and absence are calculated and plotted in Figure 6-52. In all calculations, the value of L_{cw} is assumed to be fixed at 0.5m.

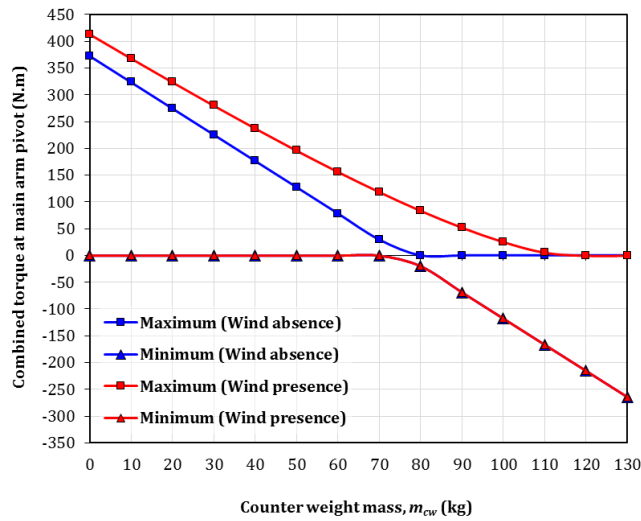


Figure 6-52 Combined moment range affecting on main arm pivot in absence/presence of wind load ($L_{cw}=0.5m$)

Negative moments appearing in Figure 6-52 represent torque load on the main arm motor in the opposite direction. Therefore, the absolute values of loads in Figure 6-52 are plotted in Figure 6-53.

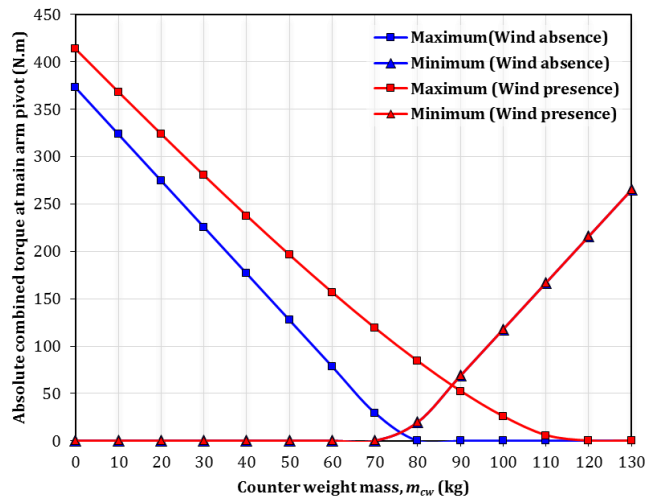


Figure 6-53 Absolute combined moment range affecting on main arm pivot in absence/presence of wind load ($L_{cw}=0.5m$)

According to Figure 6-53, it is found that optimum counter weight mass is **88.3kg** at **0.5m** from the pivot **O**. At this condition, the required torque will be **56 N.m**. However, heavy counter weight leads to overload the Aluminium structure as well as oversizing the azimuth platform swivelling motor. Therefore, further investigation to control the counter weight mass is carried out by calculating the absolute values of loads in case of L_{cw} is raised to 1m. Results are plotted in Figure 6-54.

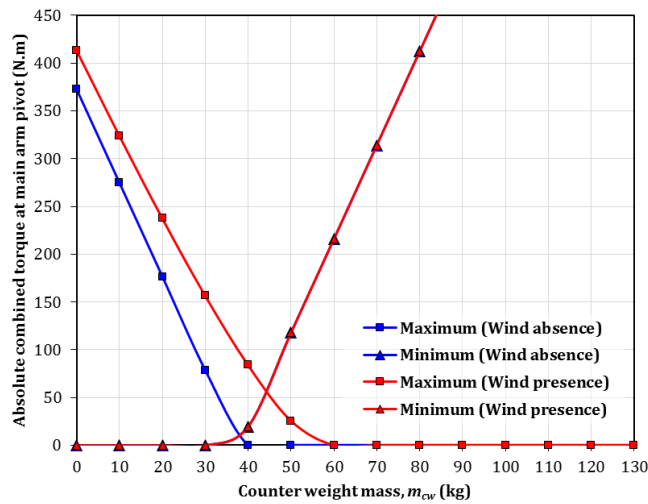


Figure 6-54 Absolute combined moment range affecting on main arm pivot in absence/presence of wind load ($L_{cw}=1.0m$)

Based on results shown in Figure 6-54, the optimum counter weight mass is reduced to **44.2kg** at a distance of **1.0m** from the pivot **O**, with exactly the same value of the required torque (**56 N.m**). Detailed plots of absolute values of loads in case of L_{cw} of 0.5, 0.75, 1.0, 1.25, 1.5 and 1.5m are displayed in Appendix I. Consequently, the relation between the optimum counter weight mass and length from the pivot point is plotted in Figure 6-55

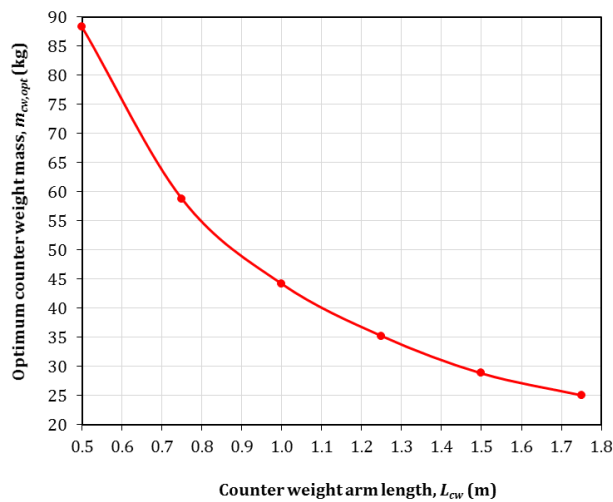


Figure 6-55 Relation between the optimum counter weight mass and length from the pivot point

In all cases, the optimum torque required at the pivot **O** is **56 N.m**. Applying a factor of safety (FS) of 1.2, the required torque of the motor to drive the main arm is **67.2 N.m**. The counter weight mass and arm length can be selected later, according to Figure 6-55 through studying its effect on the Aluminium structure.

6.2.5.6 Counter Weight Effect on Its Arm

Based on using Aluminium extrusion for the main arm part, it is preferred to use the same material as a counter weight arm with a certain length of L_{cw} . Figure 6-56 illustrates the effect of the counter weight force, W_{cw} , on the timber beam.

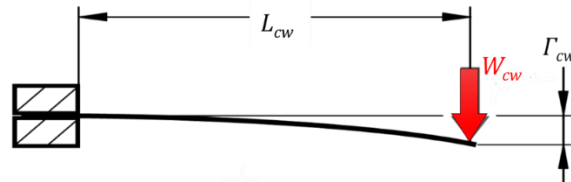


Figure 6-56 Deflection due to static load on Aluminium profile end

Then, total deflection can be determined through rewriting Eq. (6-100) as follows:

$$\Gamma = \left(\frac{W_{cw} * L_{cw}^3}{3 * E * I_c} \right) + \left[\left(\frac{7}{81} \right) \left(\frac{\omega * g * L_{cw}^5}{E * I_c} \right) \right] \quad (6-115)$$

By substitution in Eq. (6-115) using values listed in in Table 6-20, results can be plotted as shown in Figure 6-57.

Table 6-20 Mechanical properties of the 100x100x2 Aluminium Extrusion beam
(Bosch Rexroth AG, 2015; L.A. Metals Ltd., 2016)

Parameter	Value
Surface area, A (m ²)	7.84E-04
Moment of inertia, I_c (m ⁴)	8.33E-06
Mass per unit length, ω (kg/m)	2.12
Modulus of elasticity, E (Pa)	7.00E+10
Maximum permissible bending stress, $\sigma_{b,max}$ (Pa)	1.63E+08

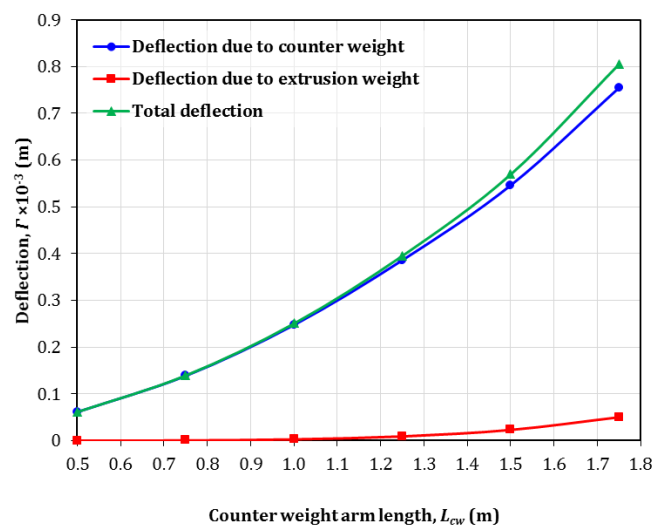


Figure 6-57 Calculated deflection due to static load on Aluminium profile end

However, deflection of the Aluminium profile results in bending stress. In order to avoid damaging the counter balance arm, the applied bending stress, σ_b , must be less than the maximum design bending stress, $\sigma_{b,d}$, which takes into account an *FS* of 1.2, as follows

$$\sigma_b < \sigma_{b,d} \quad (6-116)$$

Where

$$\sigma_{b,d} = \frac{\sigma_{b,max}}{FS} \quad (6-117)$$

According to Table 6-20 and Eq. (6-117), the applied bending stress must not exceed 135.42 MPa. Bending stress can be determined through the following formula (Beer *et al.*, 2012):

$$\sigma_b = \frac{M * y}{I_c} \quad (6-118)$$

Where, M is the moment about the neutral axis, y is the perpendicular distance to the neutral axis and I_c is the moment of inertia around the neutral axis. It can be rewritten as:

$$\sigma_b = \frac{(\omega * g * L_{cw} + W_{cw}) * L_{cw} * 6}{b * h^2} \quad (6-119)$$

Where, b and h for the selected cross section are equal to 100E-03 m. Results of Eq. (6-119) against different counter weight mass alternatives are plotted in Figure 6-58.

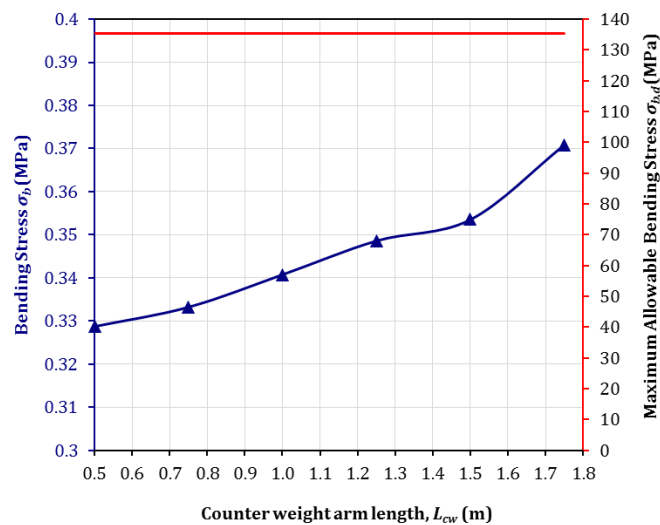


Figure 6-58 Bending stress on Aluminium profile

From Figure 6-58, it seems that none of the available alternatives of counter weight mass/arm length combinations will lead to structure damage. Although it is preferred to avoid either higher deflections or bending stresses, the higher mass of a counter weight will adversely affect the total load subjected to azimuth platform swivelling motor leading to overestimate its torque. Consequently, this may dramatically raise the total budget of building the LLBG device. Therefore, selection of the optimum counter weight mass/arm length combination will be postponed after studying the load on the azimuth platform motor.

6.2.6 Azimuth Platform Motor Sizing

To calculate the total required torque to rotate the azimuth platform, assume that the platform is consisting of four main arms, with N -ball transfer units (BUs) per arm as shown in Figure 6-59 . BUs are equally spaced with a step of ΔR . Assumed values are listed in Table 6-21.

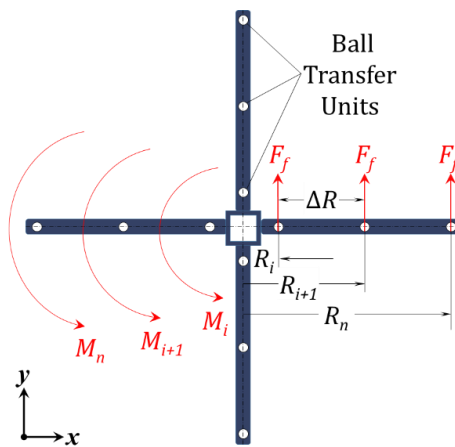


Figure 6-59 Azimuth platform

Table 6-21 Azimuth platform main assumptions

Parameter	Value
R_i (m)	0.3
R_n (m)	0.9
Number of base arms	4.0
Platform mass, m_{AP} (kg) ¹⁰	$40+m_{cw}$
Total number of BUs, N (-) ¹¹	$m_{AP}/3$

¹⁰ This includes the total mass of 19 kg for main arm (see Table 6-18) and 12kg as approximate mass of a slew drive (SKF, 2003; Always Engineering, 2015) with a FS of 1.2. All these masses are added the counter weight mass.

¹¹ (SKF, 2003; Shimoda *et al.*, 2004; Bosch Rexroth AG, 2006; Brancati *et al.*, 2013; Always Engineering, 2015)

Assuming that the LLBG mass has been distributed homogeneously over the total number of BUs, then friction force, F_f , at each BU can be determined as follows (Always Engineering, 2015):

$$F_f = \frac{(m_{AP} * 9.81) * C_f}{N} \quad (6-120)$$

Where m_{AP} is azimuth platform mass loaded on N of BUs rolling with friction coefficient, C_f . Then the total moment affecting at the azimuth platform swivelling motor is:

$$M = \sum_{i=1}^n M_i \quad (6-121)$$

Where n is the number of BUs per arm, which can be calculated from:

$$n = \frac{(m_{AP}/3)}{4} = \frac{m_{AP}}{12} \quad (6-122)$$

Equation (6-121) can be rewritten as follows:

$$M = \sum_{i=1}^n (4 * F_f * R_i)$$

Or

$$M = \sum_{i=1}^n \left(39.24 * \frac{(45 + m_{cw}) * C_f}{N} * R_i \right) \quad (6-123)$$

Where

$$R_i = R_1 + (i - 1) * \Delta R$$

Or

$$R_i = R_1 + \frac{i - 1}{n - 1} (R_n - R_1) \quad (6-124)$$

By substitution in Eq. (6-123) then:

$$M = \sum_{i=1}^n \left\{ \left[39.24 * \frac{(45 + m_{cw}) * C_f}{N} \right] * \left[R_1 + \frac{i - 1}{n - 1} (R_n - R_1) \right] \right\} \quad (6-125)$$

Based on data provided by Table 6-21 the total torque calculated from Eq. (6-125) is plotted in Figure 6-60, in which the minimum and maximum total moments are corresponding to friction factors of 0.01 and 0.06, respectively.

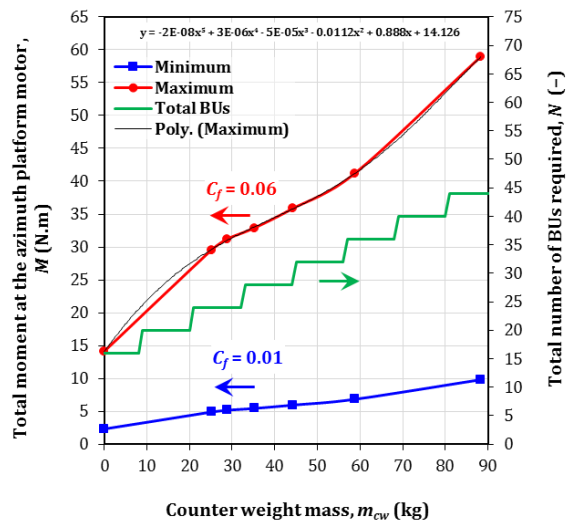


Figure 6-60 Moment at azimuth platform motor and total number of BUs vs. counter weight mass

Figure 6-60 indicates that using the minimum counter weight mass is recommended to minimise the total system weight and the required number of BUs. On the other hand, the minimum counter weight mass, the maximum deflection and bending stress over the counter weight supporting arm as illustrated in Figure 6-57 and Figure 6-58.

Another limit is the dimension of BU itself compared to the distance between two successive BUs, ΔR . Assuming the use of ALWAYSSE 3-Hole Flange BU with specifications listed in Table 6-22, then the limit can be defined as:

$$\Delta R \geq d_f \tag{6-126}$$

Table 6-22 ALWAYSSE 3-Hole Flange BU specifications
(Günther, 2012)

Parameter	Value
Part number	3006-13
Load Ball Diameter, d_b (m)	19E-03
Fixing Holes	3
Maximum dynamic loading (kg)	10.0
Maximum flange diameter, d_f (m)	61E-03
Pitch circle diameter of fixing holes centres, PCD (m)	44.5E-03
Required clearance under flange (m)	12E-03

Results of applying this limit is plotted in Figure 6-61, which indicates that the counter weight mass must not exceed 80.0 kg.

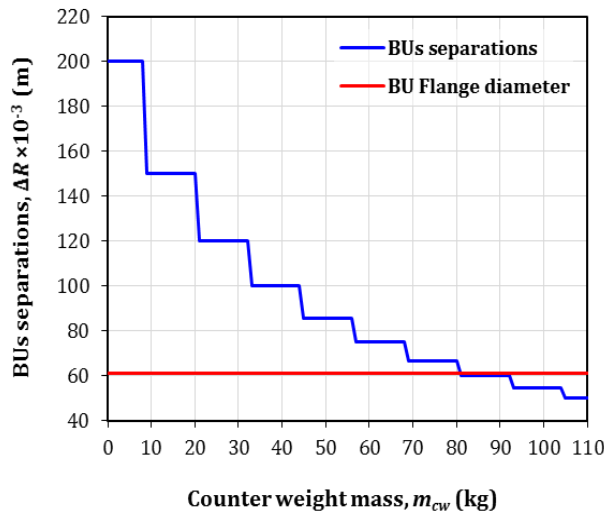


Figure 6-61 Allowed BUs separations vs. counter weight mass

Based on previous analysis, a point in midway was selected with a main arm counter weight mass of 40.0 kg as an optimum case. This alternative has a flexibility advantage in reacting to the actual carried out design. In other words, it allows increasing the counter weight mass up to 80.0 kg, in case of appearing unexpected problems during building phase, without affecting the required number of BUs. Considering a FS of 1.2, then the required torque for the azimuth platform swivelling motor is **40 N.m**. Then, the summarised design details of the LLBG system are listed in Table 6-23.

Table 6-23 LLBG design parameters

Part	Parameter	Value
Main arm	Mass, m_{MA} (kg)	19.0
	Length, L_{MA} (m)	2.0
	Counter weight mass, m_{cw} (kg)	40.0
	Counter weight arm length, L_{cw} (m)	1.09
	Approximate deflection in main arm, Γ_{MA} (m)	<0.36E-03
	Approximate deflection in counter weight arm, Γ_{cw} (m)	<0.25E-03
	Required torque for main arm motor, T_{MA} (N.m)	67.2
Azimuth platform	Distance for the 1 st BU, R_1 (m)	0.3
	Distance for the n^{th} BU, R_n (m)	0.9
	Number of base arms	4.0
	Total number of BUs, N (-)	28.0
	Mass on platform, m_{AP} (kg)	80.0
	Required torque for azimuth platform motor, T_{AP} (N.m)	40.0
Approximate LLBG mass (kg)		90.0

6.2.7 LLBG Tracking System Design

3-D tracking system is required to be designed to precisely track the sun's position of the full-size LLBG system. In this section, features of different tracking techniques is briefly described.

6.2.7.1 Astronomical Tracking Method

The astronomical method is based on defining the solar tracker location (longitude and latitude angles), date and time to determine and track the position of the sun using the astronomical equations. These data are usually provided through Global Positioning System (GPS) sensor. This method has an advantage high accuracy in addition to simple programming. However, this method requires fixing the tracker starting direction at sunrise every day. Details of solar angles calculations are available in Appendix B. A flowchart of calculating solar angles algorithm based on GPS data is displayed in Figure 6-62.

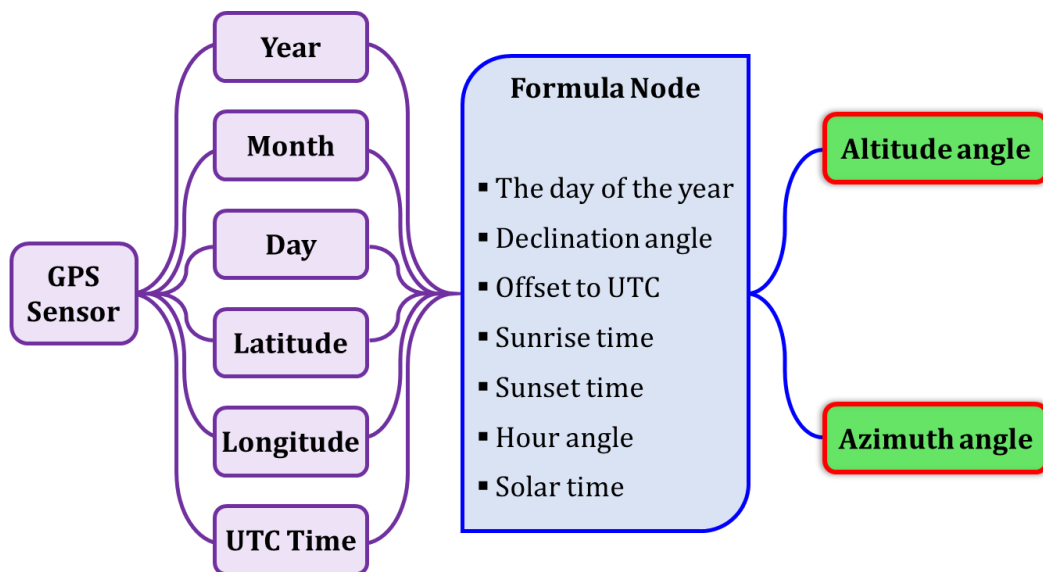


Figure 6-62 Flowchart of calculating solar angles algorithm based on GPS data

6.2.7.2 Optical Tracking Method

The optical method uses several light-intensity sensors, such as Light Dependent Resistors (LDRs). The sensors output signals are compared within a feedback loop of adjusting the tracker direction until the condition of minimum shadow on the sensors is fulfilled. The major drawback of this method is that it cannot effectively track the sun on a cloudy day without a robust algorithm.

6.2.7.3 Applied Tracking Design

The tracking system is designed to employ a hybrid technique which combines using the astronomical and the optical solar tracking methods (Oh *et al.*, 2012). Combining both methods aims to take the advantage of both methods and minimise the total drawbacks. In such design, the control system initialises all motors to their initial positions, then the GPS data is used to direct the system to the sun's position and the tracker uses the LDRs feedback for fine adjustment. Encoders are also used to send feedback of the actual position of the system. Motors controller deals with feedbacks from both LDRs and encoders through proportional–integral–derivative (PID) controller, which is a control loop feedback mechanism that continuously calculates error as the difference between a desired set-point and a measured process variable. The PID controller applies a correction based on proportional, integral, and derivative terms, as the controller output is proportional to the error, the amount of time that the error is present and the rate of change of the error (Wang, 2017). A flowchart describing the control process followed in the presented tracking system design is shown in Figure 6-63.

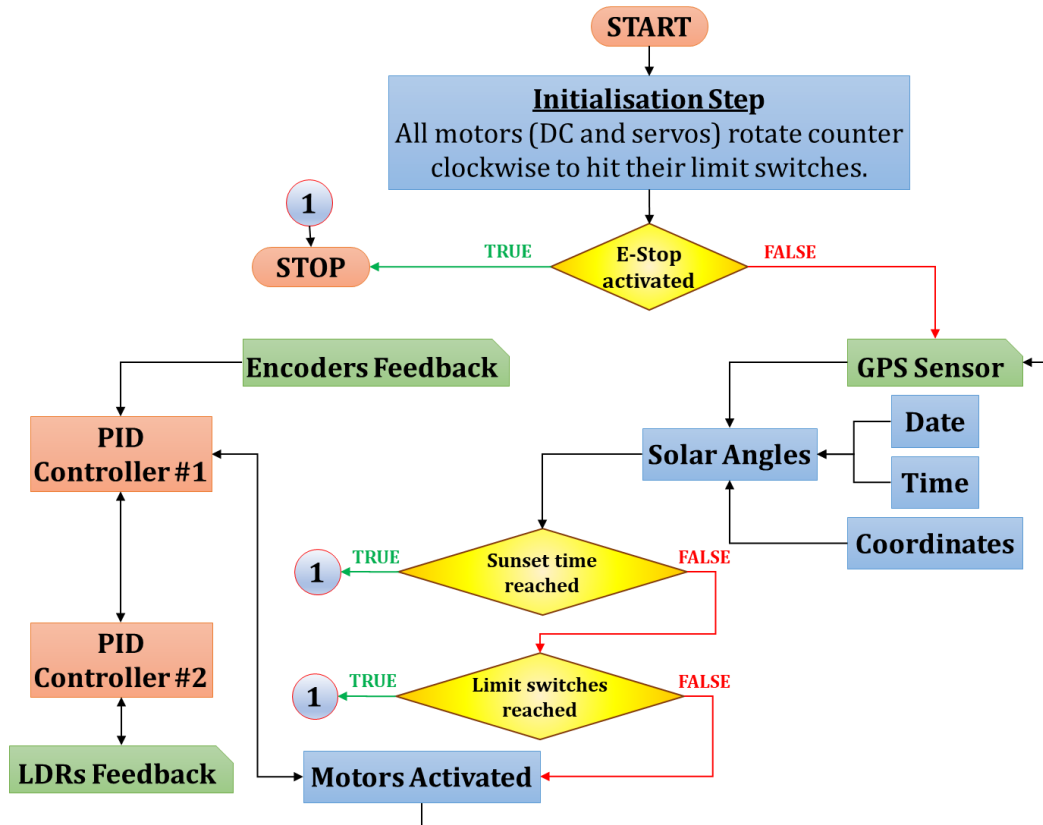


Figure 6-63 Flowchart of presented solar tracking control system

The system used Arduino MEGA[®] with an ATmega 2560 microcontroller as a core processor to drive and control the motors. In order to create user-friendly interface for the tracking system, a code developed by LabVIEW[®] platform to communicate with the Arduino microcontroller and to process the input and feedback data from the GPS module and feedback sensors (i.e. encoders, LDRs and limit switches). A photo of the designed system power block and a snapshot of the LabVIEW program interface are illustrated in Figure 6-64. However, during the indoor tracking tests, the safety relay (which is responsible for processing safety-related signals from the emergency stop) has been damaged. Accordingly, the tracking system tests have been paused for due to lack of available technicians within the limited time-scale of the experiments. Therefore, manual tracking has been employed for experimental testing in Section 6.3.

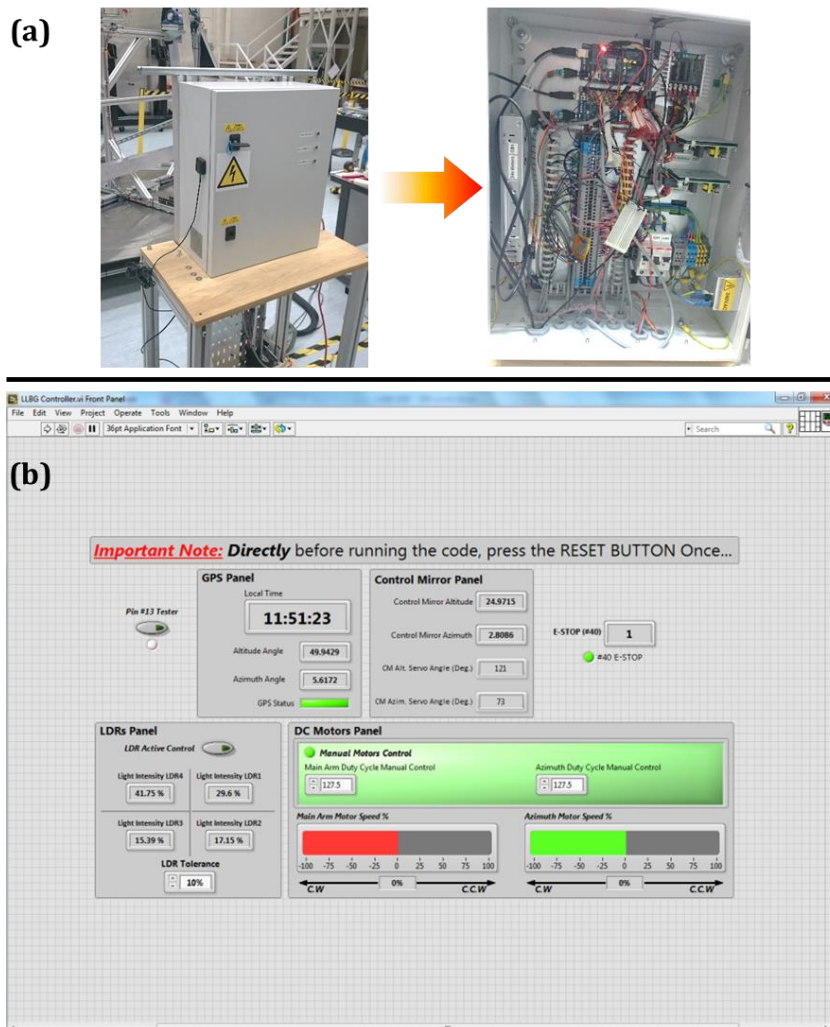


Figure 6-64 Solar tracking control system
 (a) photo of system power block (b) snapshot of LabVIEW interface

6.3 LLBG Testing

6.3.1 Optical Analysis Code Validation Test

The aim of this experiment is to validate the developed code (Section 6.1.3.4) for predicting the generated beam diameter out from an LLBG system.

- ***Instruments Required***

TITAN MK7-15 laser distance measurer (Figure 4-6) and metal measuring tape.

- ***Experimental Setup***

The testing setup is illustrated in Figure 6-65, is consisted of a wooden lens frame which tracks the sun manually. The used front lens is a PMMA Fresnel lens with a clear aperture diameter of 0.24m and focal length of 0.6096m, with GO configuration design (Edmund Optics, 2018a). The rear lens and the mirror are aligned with the front lens and separated by a distance, l_0 . The generated beam is then reflected on a screen, made of FLEXITALLIC THERMICULITE® 815 (properties listed in Table 6-7), separated by variable distance, l_1 .

- ***Experimental Procedure***

Two groups of tests have been carried out. In the first group, the distance, l_0 was set to be fixed to 0.135m, while the distance l_1 was varying as: 0.5, 1, 1.5, 2 and 3.5m. For the second test group, the 45° mirror was removed and the distance between the rear lens and the screen, $l = l_0$, was measured directly and was set to 0.075 and 0.12m. In each case, the generated beam diameter is recorded. All recorded data are displayed in Figure 7-32.

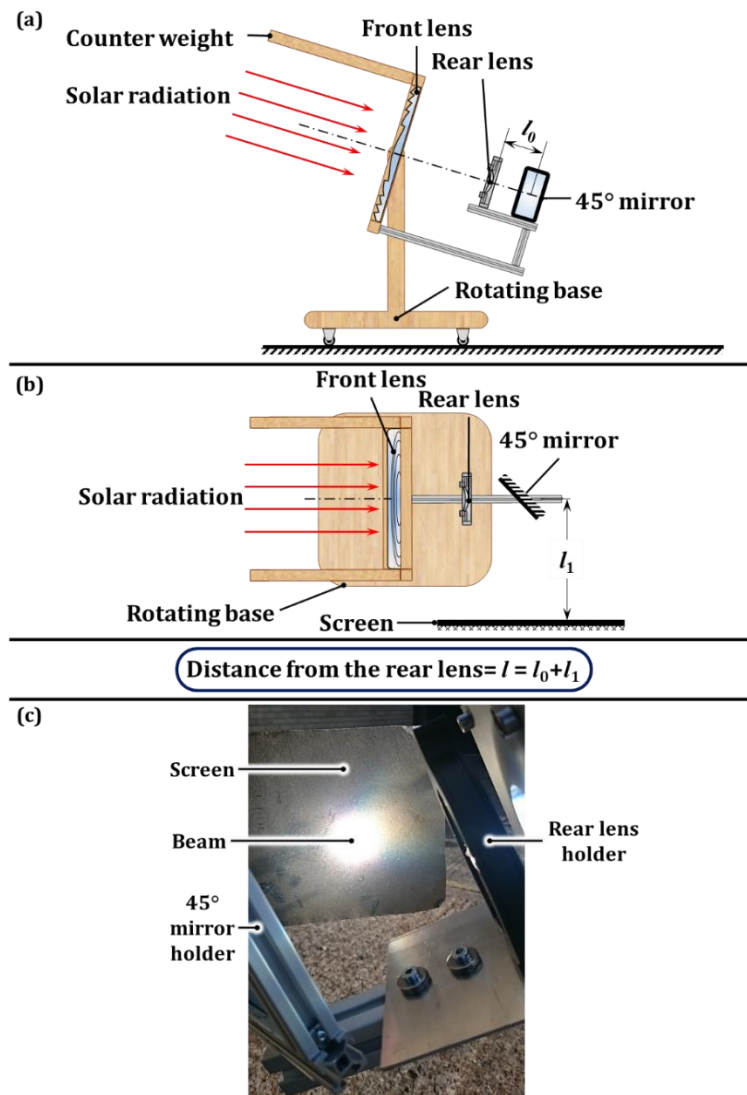


Figure 6-65 Optical analysis code validation test setup
 (a) side view (b) top view (c) photo of the beam

6.3.2 Prototype-Size LLBG System Test

This test has been carried out using a prototype-scale front lenses with manual control. This test aims to determine the amount of thermal energy can be obtained out of the LLBG system at different distances from the control mirror.

- **Instruments Required**

SMP10 pyranometer (Figure 4-4), TC-08 thermocouple data logger (Figure 4-5) which is connected to K-type thermocouples to detect the receiver's surface temperature (Figure 4-5). Four thermocouples utilised are miniature ones with a sheath diameter of 0.75mm, which can withstand up to 800°C.

- **Experimental Setup**

The testing setup consists of a wooden lens frame allowed to tilt with altitude angle and fixed to a rotating wooden base. The incident solar irradiance is measured by the pyranometer. The rear lens and the mirror are aligned with the front lens through an aluminium profile assembly. The generated beam is then reflected on an insulated graphite receiver with geometry drawing illustrated in Figure 6-66. The receiver has been placed on an adjustable-height table, as illustrated in Figure 6-67a. The ambient and the receiver temperatures are monitored through thermocouples connected to the data logger and recorded on a PC, as shown in Figure 6-67b. The receiver has been insulated with 25mm-thick Kaowool® Millboards with data listed in Table 6-25, which covers five faces of the receiver block. The properties of the receiver material are listed in Table 6-24. The front lens utilised is a PMMA Fresnel lens with a clear aperture of $0.24 \times 0.24 \text{m}^2$ and a focal length of 0.6096m, which is designed for set up with GO configuration (Edmund Optics, 2018a).

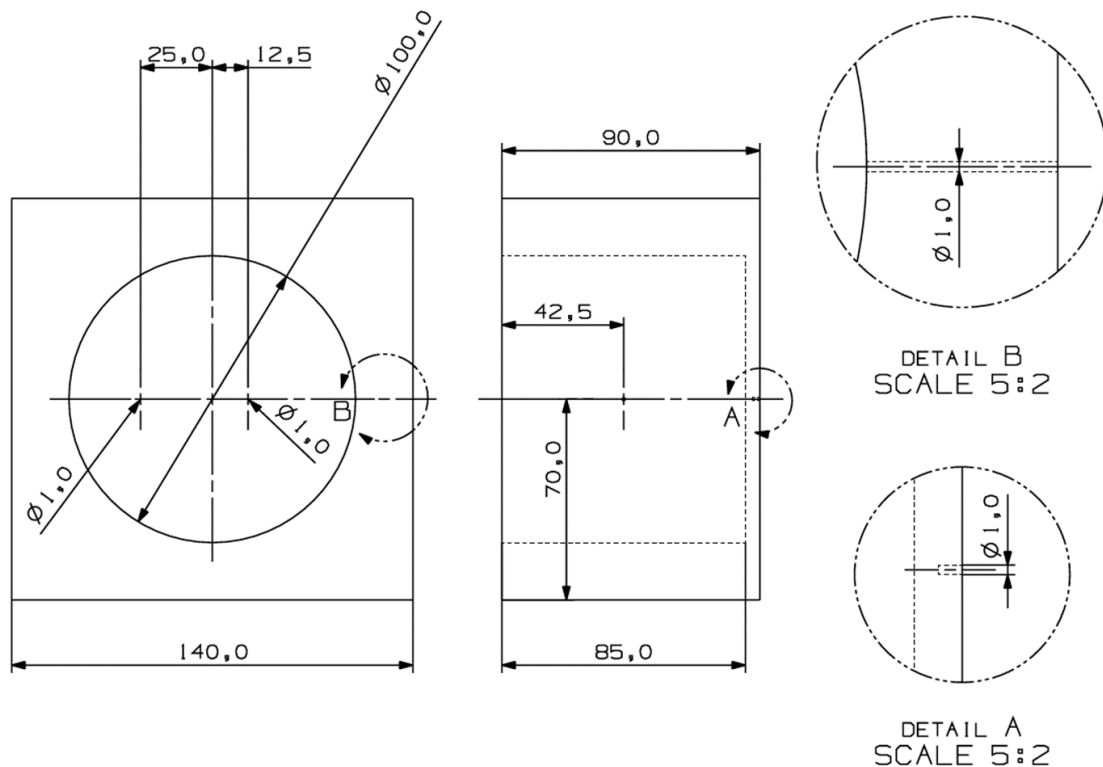


Figure 6-66 Graphite receiver geometry

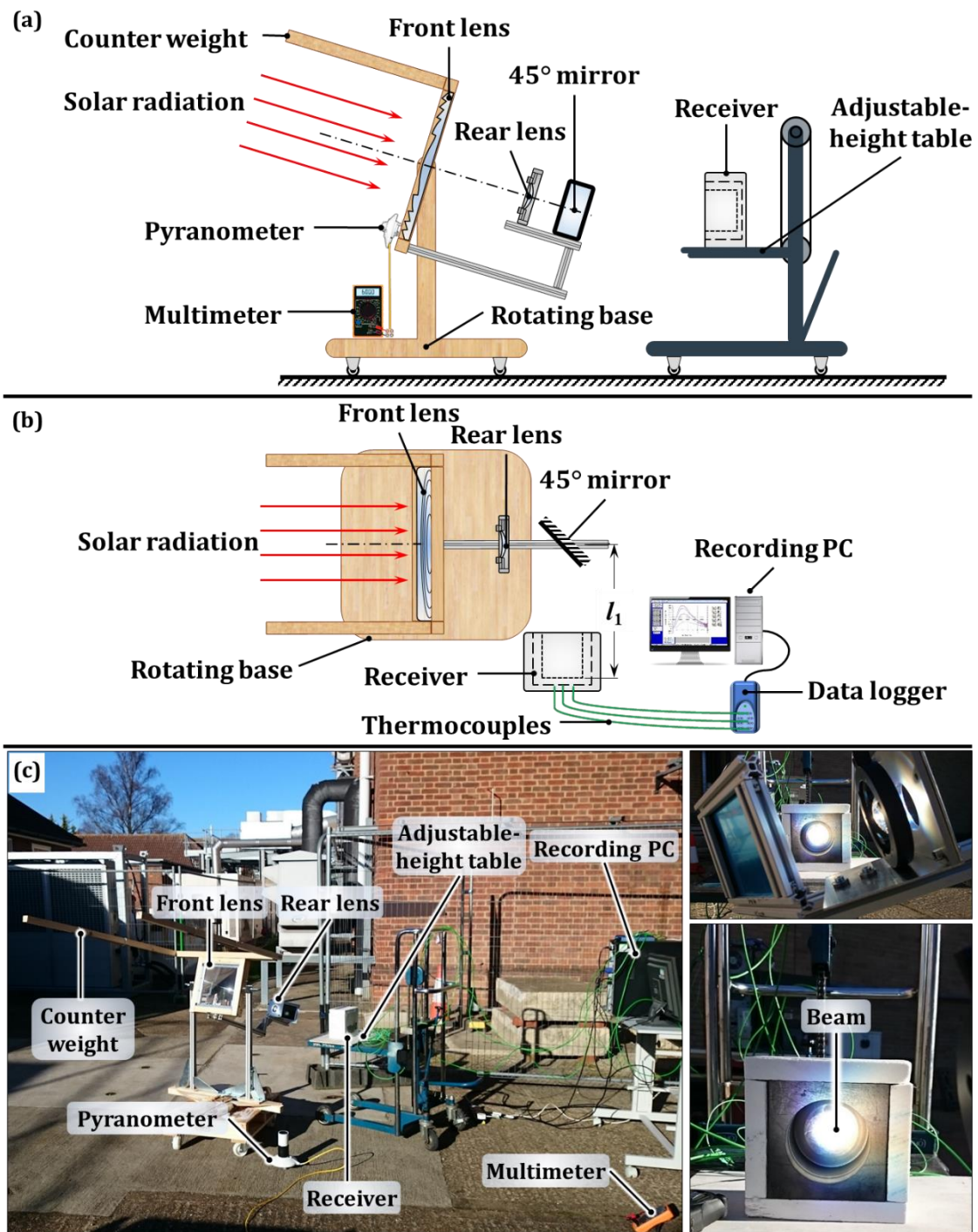


Figure 6-67 Prototype-size LLBG system test setup
 (a) side view (b) top view
 (c) photos of the test rig;
 (full system: on left, rear lens with mirror and receiver: top right, the receiver with the generated beam: bottom right)

Table 6-24 Receiver material properties

Parameter (unit)	Value	Reference
Material	Fine-Grain Graphite	—
Density (kg/m ³)	1897.861	Measured
Specific heat (J/kg.K)	586.1539	(SGL Group – The Carbon Company, 2015)
Thermal conductivity (W/m.K)	105	(SGL Group – The Carbon Company, 2015)
Emissivity (-)	0.85	(Ho, 1988)

Table 6-25 Insulating material properties

Parameter (unit)	Value	Reference
Material	Kaowool® Millboards	
Density (kg/m ³)	641	(Morgan Advanced Materials, 2016)
Thermal conductivity (W/m.K)	0.08	
Operating temperature (°C)	1093–1760	

- **Experimental Procedure**

The test has been carried out for three times with changing the distance from the 45° mirror to the receiver back surface, denoted as l_1 in Figure 6-67b. The distance, l_1 , sit to be 0.25, 0.5 and 1m. During each test, the incident solar irradiation is measured by the pyranometer, the ambient temperature is recorded. The receiver surface temperatures are monitored at the beam centre and at radii of 12.5 and 25mm, using three miniature K-type thermocouples inserted in the three 2.5mm-deep holes in the back of the graphite block (see Figure 6-66), as shown in Figure 6-68. Initial and final temperatures of the receiver front surface have been recorded for each test. The system tracks the sun path manually through adjusting a simple solar tracking indicator, which fixed to the front lens frame so that the sun image falls in its proper position (see Figure 6-69).

Between each test, the receiver is left to cool down to the initial temperature. However, the time required for cooling down is found to be long compared to the limited availability of the sun shine in the safe area used for testing. Therefore, the initial temperatures for each test are different from each other. All collected data are plotted in Figure 7-33.

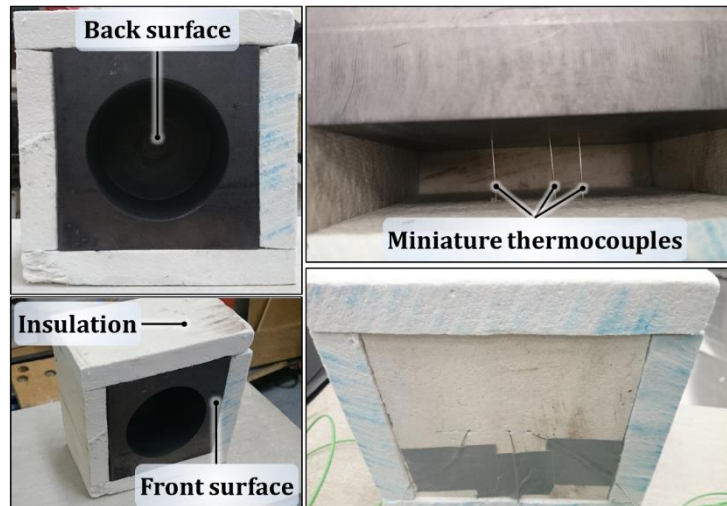


Figure 6-68 Receiver nomenclature (left) and inserted thermocouples (right)

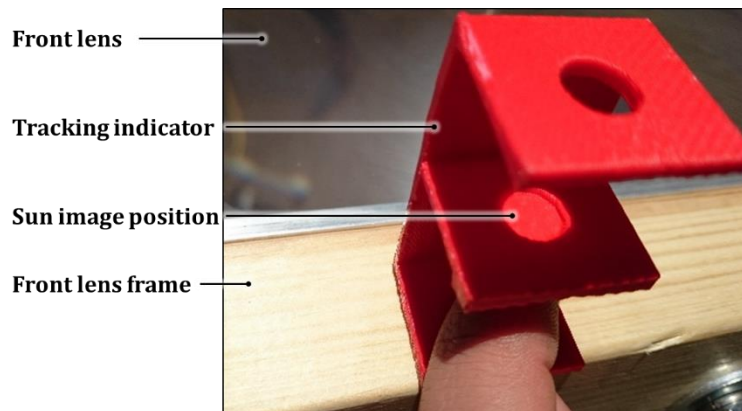


Figure 6-69 Solar simple manual tracking indicator

6.3.3 Full-Size System LLBG System Test

In this test, a full-scale front lens with manual control has been used. The aim of this test is to evaluate the output obtainable thermal energy from the LLBG system.

- ***Instruments Required***

SMP10 pyranometer (Figure 4-4), TC-08 thermocouple data logger (Figure 4-5) connected to K-type thermocouples to monitor the temperature of the receiver surface (Figure 4-5). Four miniature thermocouples with a sheath diameter of 0.75mm are used.

- **Experimental Setup**

In the first stage, the system was simply built similarly to the prototype-scale test rig described in detail in Section 6.3.2, with only replacement of the front lens to utilise the full-scale one, as shown in Figure 6-70. Based on initial tests in real environment, different issues have been arising and the system setup was modified to sort them out.

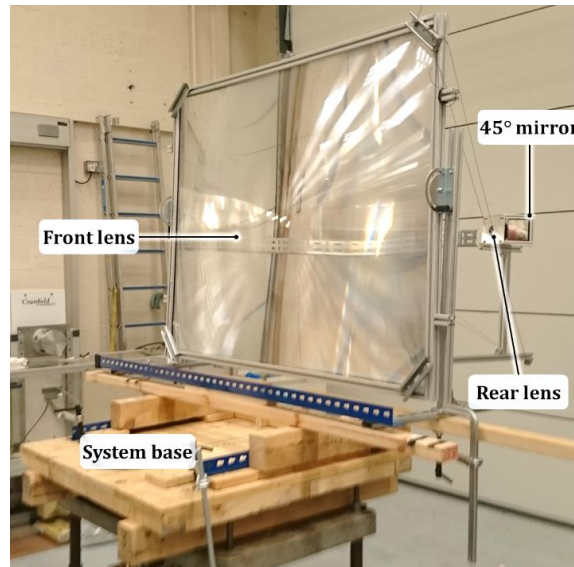


Figure 6-70 Initial full-size LLBG test setup

Initially, as the front lens had a larger size, the more collected power is focused at the rear lens plane. On the other hand, the design of the rear lens mount results in falling a part of the highly-concentrated rays on the edges of the mounting fingers, which have a maximum working temperature of 120°C. This caused initial signs of mount melting represented in emission of a small amount of smoke from it within seconds of exposure. In order to sort this out, the theoretical solution introduced in Section 6.1.3.4, in which insulating patches inserts made of FLEXITALLIC THERMICULITE® 815 material are assumed to be used at the point of contact between the rear lens and its mounting fingers. However, this solution is found to be unsuccessful practically, as the available insulating material is not providing enough friction force to grip the lens which in turn makes the lens tends to slip. Therefore, a mask of the same insulating material with an aperture hole diameter of 32mm is placed in front of the rear lens, as illustrated by Figure 6-71.

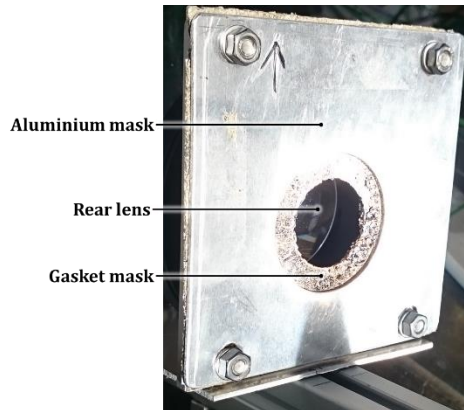


Figure 6-71 The insulating gasket mask

Secondly, after sorting out the previous issue and while the test which carried out in an ambient temperature of 0°C the 2.0mm thick float glass-based 45° mirror started to crack within approximately 3 minutes of the test as displayed in Figure 6-72. Therefore, the mirror is replaced with a 0.5mm thick Aluminium-based mirror with detailed description and reflectivity measured in Section 4.2.2.



Figure 6-72 Cracks in the float glass-based 45° mirror

For the receiver, the same design described in Section 6.3.2 is utilised as it is firstly and then with a 6.5mm-thick uncoated BOROFLOAT® window on its aperture with properties listed in Table 6-26. This setup is shown in Figure 6-73.

Table 6-26 BOROFLOAT® window properties

Parameter (unit)	Value	Reference
Material	BOROFLOAT® (Borosilicate)	
Density (kg/m ³)	2200	
Design wavelength (nm)	350–2000	(Edmund Optics, 2018b)
Transmittance (–)	90%	
Operating temperature (°C)	450°C (continuous)–500°C (1 hour)	

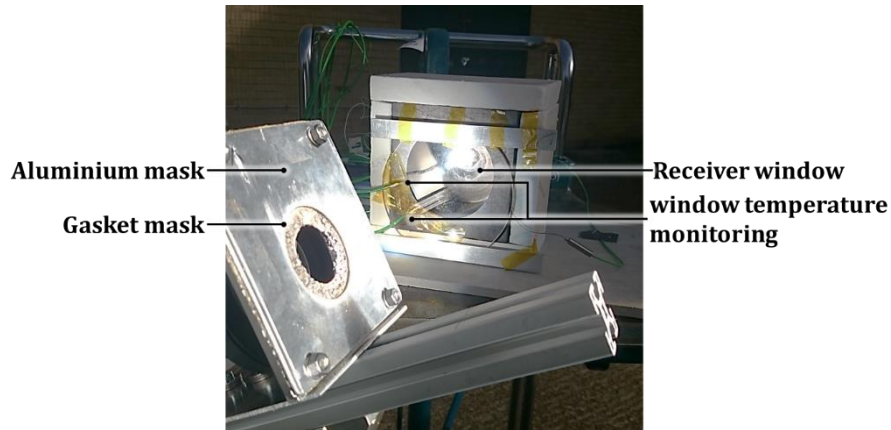


Figure 6-73 Receiver window setup

- ***Experimental Procedure***

The test has been carried out firstly without the use of the receiver window. In this case, the distance between the 45° mirror to the receiver back surface, l_1 , is set to 0.5m. Then, the BOROFLOAT® window is mounted to the receiver window and the test is repeated twice, at a distance, l_1 , set to 0.25 and 0.5m. Throughout each test, the pyranometer is used to measure the incident solar irradiation, while the ambient and receiver temperatures are recorded. As described in Figure 6-66, three miniature K-type thermocouples inserted in three 2.5mm-deep holes at the back of the receiver block to measure its back-surface temperatures at radii of 0.0, 12.5 and 25mm of the beam. As the system tracked the sun manually, the simple solar tracking indicator shown in Figure 6-69 is used to adjust the front lens altitude and azimuth angles. The initial temperatures for each test are different from each other, despite the receiver is left to cool down between each test, as it requires relatively long time to reach the original temperature.

6.4 Summary

Based on minimising cost criterion, Fresnel lens geometry was selected for the front lens. From the Fresnel lenses manufacturing methods review, CaF₂, PMMA and PC was selected initially as best material candidates to fabricate the front lens. Later, this list was refined by eliminating CaF₂ to keep down the cost. Then, PMMA was selected finally as the best material for the front lens through comparing its optical performance with its competitor, PC, as it showed higher

optical efficiency. For the rear lens, thermal simulation using a numerical model, which has been validated against a developed mathematical model and experimental work from literature, was carried out to select the best geometry. The simulations indicated that positive meniscus geometry can withstand higher CRs compared to either plano-convex or bi-convex geometries. For the rear lens material, the first stage was to run the thermal simulation on the positive meniscus geometry with 13 different transparent materials to prepare an initial list of preferred materials that can resist the highest CR. Secondly, materials transmittance played a role to optimise the selected material. Based on both stages, SiO₂ was found to be the optimum material for such component that allows reaching high CRs with maximum optical efficiencies. Finally, an optical assessment of the system has been carried out. In this study, the front lens direction (GI/GO-configuration) and the front lens buckling effects on the resulting concentrated spot were covered. Then the generated beam diameter has been calculated mathematically with considering the previously mentioned effects with considering both CA and SAA influences.

7 RESULTS AND DISCUSSION

7.1 Solar Simulator Testing Results

7.1.1 Lamps Spectra Comparison Experiments

For the tungsten halogen lamp, the measured output spectra of each case is plotted and compared to terrestrial solar spectrum (AM1.5), in Figure 7-1. It also shows a comparison with 3200K tungsten halogen light source spectrum (Davidson, 2018). The comparison shows that the used PHILIPS 6994Z 2kW tungsten halogen lamp delivers nearly the same spectrum given by a 3200K light source at 100% of its output. While, dimming the output lower down the output spectrum.

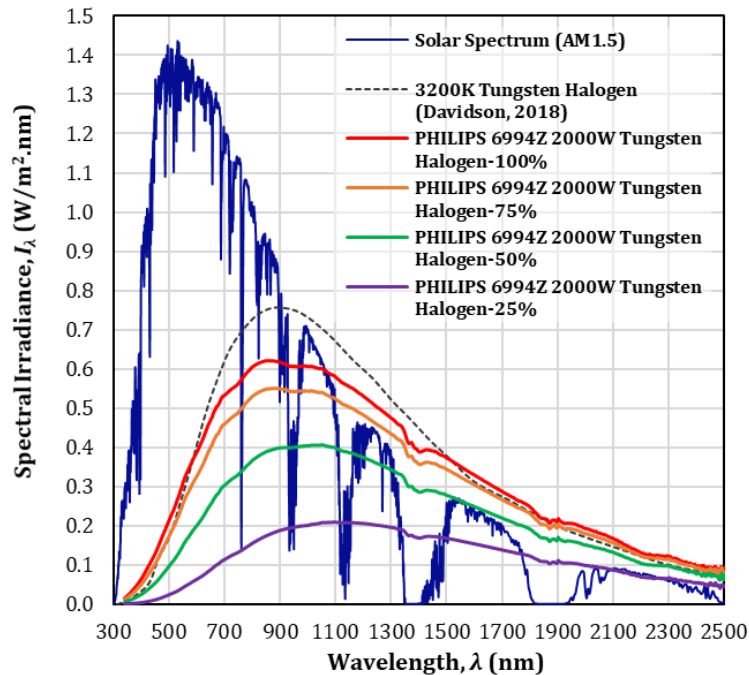


Figure 7-1 Tungsten halogen lamp spectra comparison with solar spectrum

Figure 7-2 shows the comparison of the measured PHILIPS HPI-T 2kW metal halide lamp output and Osram HMI® 6kW lamp (Krueger, 2012) and solar standard (AM1.5) spectra. According to this comparison, the used PHILIPS HPI metal halide lamp showed good match with solar spectrum over the full spectral bandwidth.

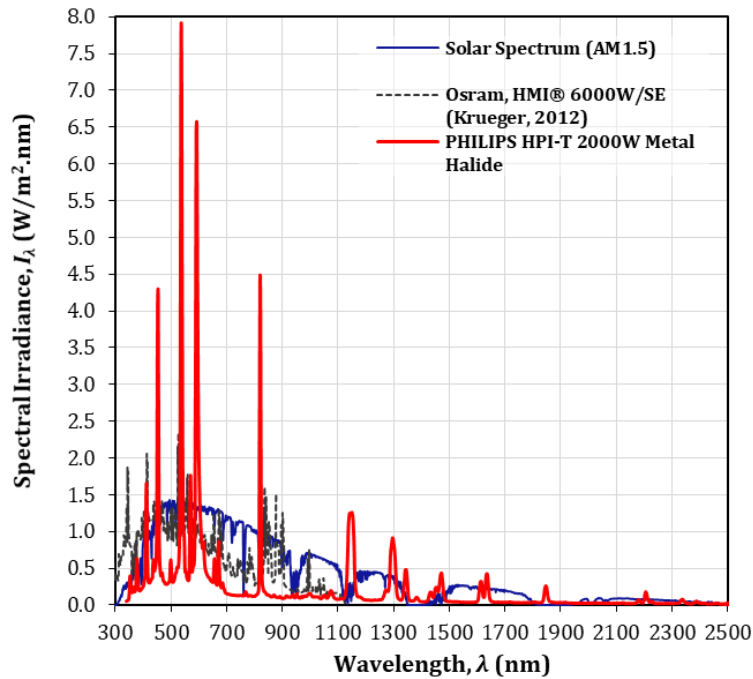


Figure 7-2 Metal halide lamp spectrum comparison with solar spectrum

7.1.2 Fresnel Lens Transmittance Measurement Experiment

The measured irradiance in both stages (without and with the tested PMMA lens) are plotted with the wavelength on the primary axis (to left) in Figure 7-3. Then the spectral transmittance of the tested lens, $\tau_{I,\lambda}$, can be obtained from:

$$\tau_{I,\lambda} = \frac{I_{\lambda,2nd\ stage}}{I_{\lambda,1st\ stage}} \quad (7-1)$$

Where $I_{\lambda,1st\ stage}$ and $I_{\lambda,2nd\ stage}$ are the measured irradiance in the first and second stages, respectively. The results of Eq. (7-1) are plotted against wavelength on the secondary axis (on right) in Figure 7-3. According to measured transmittance of the used PMMA full-size Fresnel lens, it showed much better behaviour compared to typical PMMA transmittance (plotted in Figure 2-25c) especially for the IR-zone spectrum. However, the measured values indicates that the PMMA full-size Fresnel lens has less average transmittance (74.18%) compared to 81.0% for typical PMMA material (Edmund Optics, 2018a).

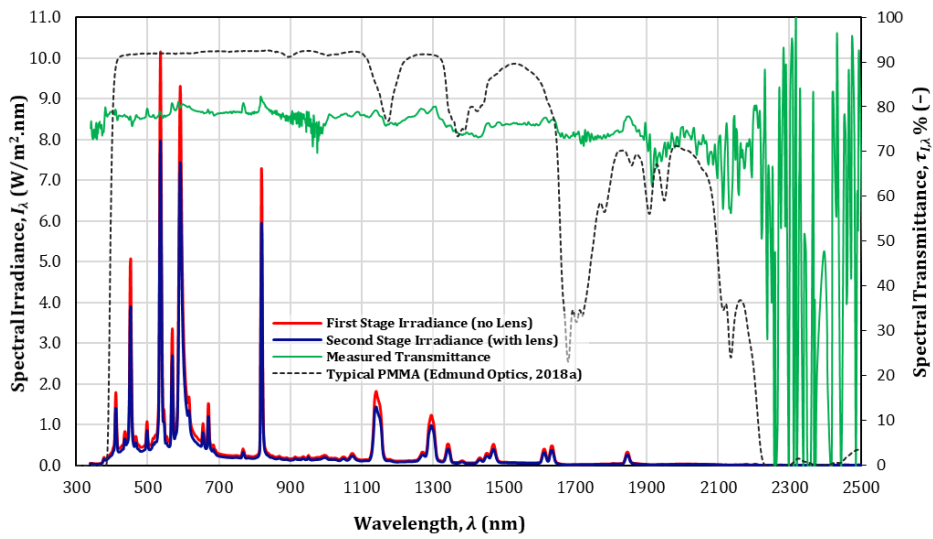


Figure 7-3 Measured transmittance of the front Fresnel lens

7.1.3 Irradiance Measurement Experiments

The measured irradiance in tungsten halogen case without participation of the initial glass Fresnel lens is plotted in Figure 7-4a. While the case of metal halide test results with using the initial glass Fresnel lens is shown in Figure 7-4b. The peak irradiation achieved was 255 W/m² and 479 W/m² for the tungsten halogen and metal halide cases, respectively. While the average irradiation over an area of 0.2*0.2 m² is 177.53 W/m² and 209.71 W/m² for the tungsten halogen and metal halide cases, respectively.

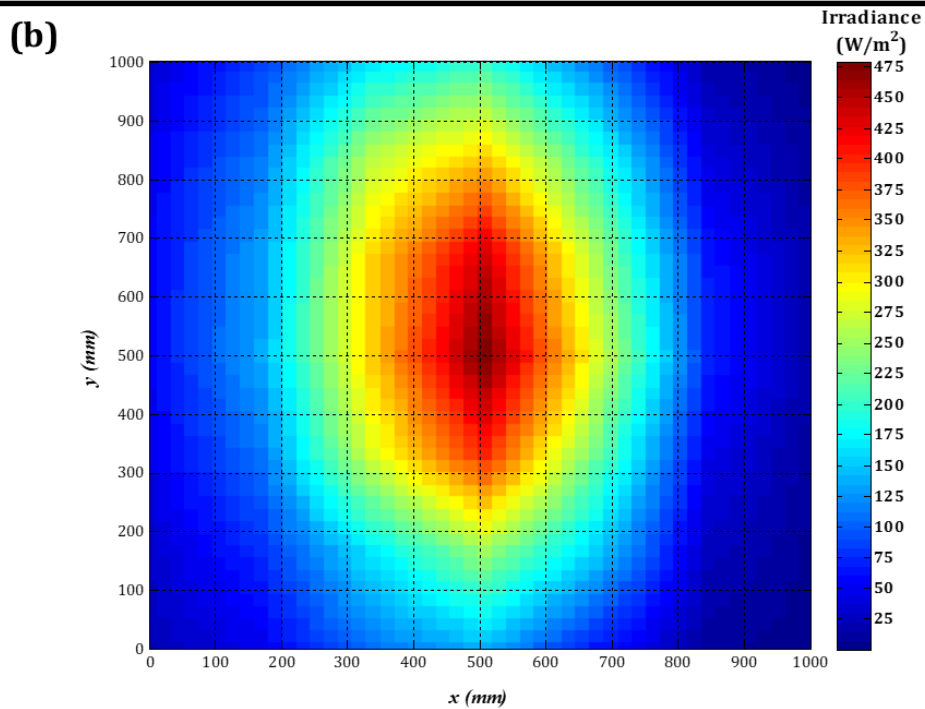
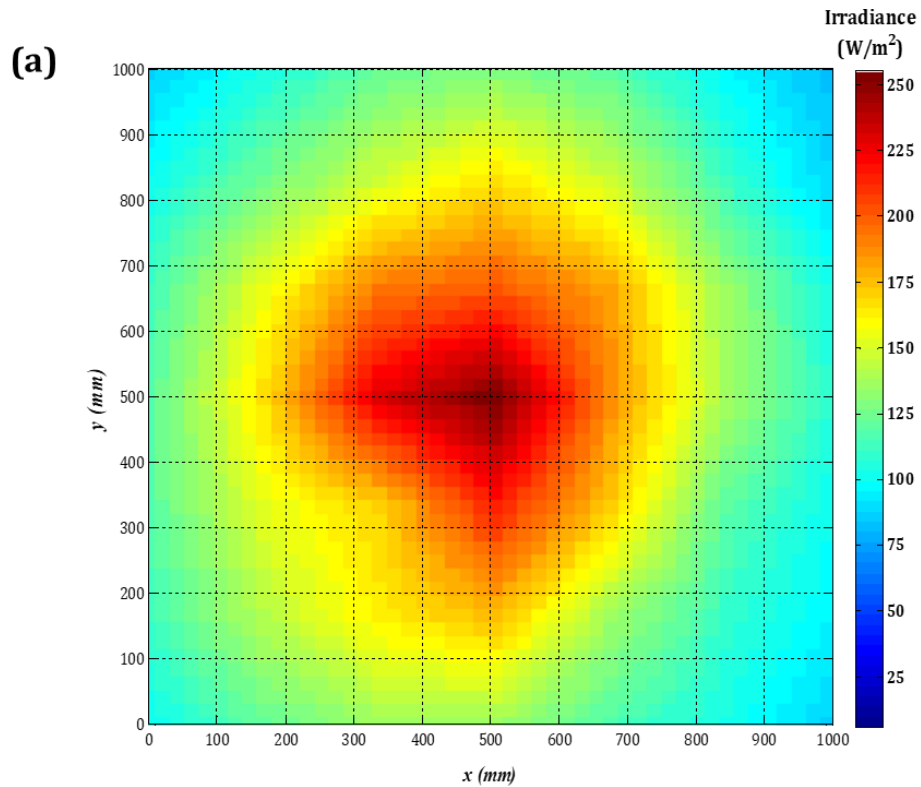


Figure 7-4 Irradiance distribution

(a) tungsten halogen case (without initial lens) (b) metal halide case (with initial lens)

7.1.4 Thermal Response Evaluation Experiments

The measured temperature over the black screen in cases of tungsten halogen and metal halide are plotted in Figure 7-5a and Figure 7-5b, respectively.

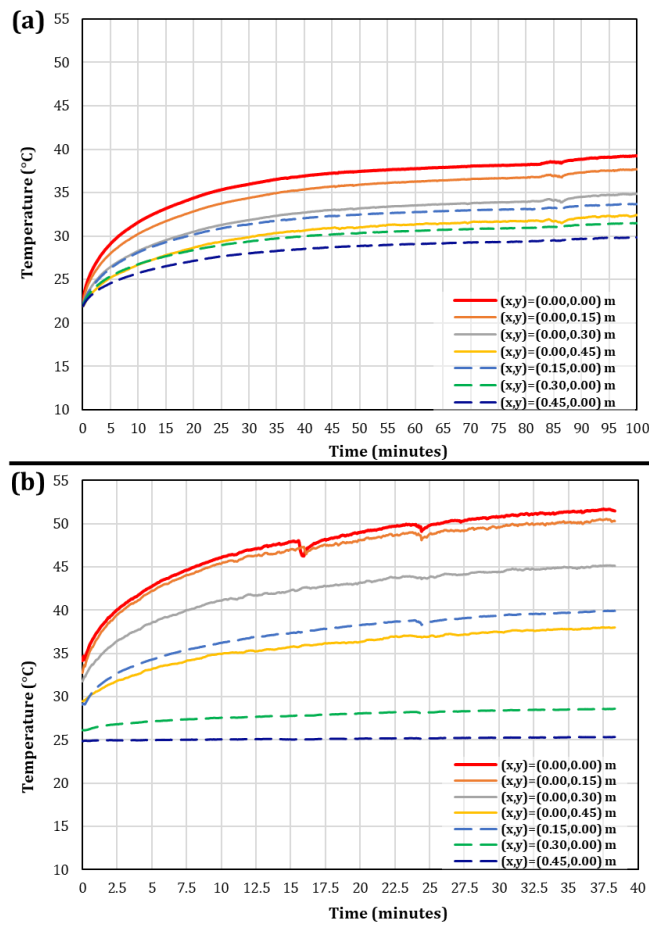


Figure 7-5 Temperature over the black screen
(a) tungsten halogen case **(b) metal halide case**

7.1.5 Lens Mount Model Validation Experiments

The measured clamping fingers average temperatures and changing ambient temperatures in each test are plotted in Figure 7-6.

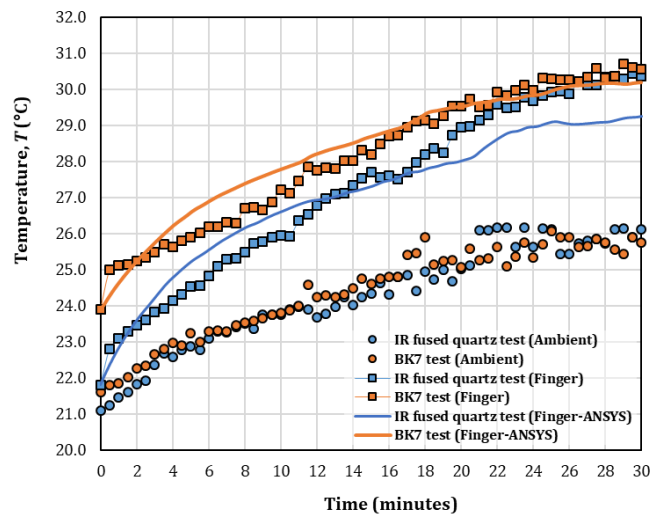


Figure 7-6 Lens mount model validation tests results

7.2 LLBG Modelling Results

7.2.1 Rear Lens Thermal Modelling Validation

In this section, the proposed mathematical and numerical models in Section 6.1.3 are validated against a selected experimental study carried out by (Piatkowski, Wieckert and Steinfeld, 2009; Piatkowski and Steinfeld, 2011). In their experiments, the temperature of a quartz window subjected to concentrated radiative power has been measured. The details of the experimental study and model input data are discussed.

7.2.1.1 Experiment Description

The experimental test was carried out on an 8-kW solar reactor used for thermochemical gasification of carbonaceous waste feedstock. It is designed for a “beam-down” optical configuration of solar towers (Yogev *et al.*, 1998). It consists of two successive cavities; the upper is used as solar absorber and sealed with a fused quartz aperture window facing the concentrated solar power, while the lower cavity represents the reaction chamber (Piatkowski and Steinfeld, 2011). The two cavities were separated by a SiC plate which functions as solar absorber and radiant emitter, as schematically shown in Figure 7-7.

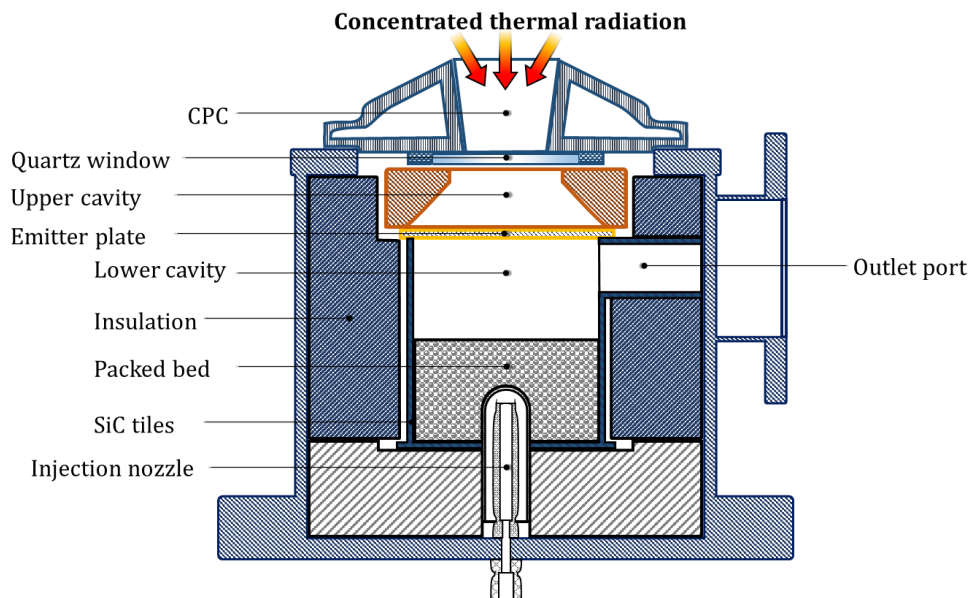


Figure 7-7 Cross-section view of the packed-bed solar reactor (Piatkowski, Wieckert and Steinfeld, 2009)

The upper cavity has an aperture diameter of 65mm purged with nitrogen flow at a flow rate of 2 litre/min. The quartz window has a 3mm thickness. The solar power has been simulated by a PSI's High-Flux Solar Simulator (HFSS), in which ten xenon-arc lamps with ellipsoidal reflectors were used to simulate highly concentrating solar systems. This resulted in subjecting the solar reactor to radiation fluxes up to 2560 kW/m^2 .

7.2.1.2 Models Boundary Conditions

As the point of the present work is to validate the modelling of a transparent material subjected to high-flux of radiative power, then it will focus on modelling the quartz window in the experiment carried out by Piatkowski's group (Piatkowski and Steinfeld, 2011). The basic boundary conditions affecting the quartz window are shown in Figure 7-8.

The upper and lower surfaces of the window are denoted by 1 and 2, respectively. The upper surface is subjected to free convection to the ambient air, while the lower surface is affected by forced convection due to the flow of nitrogen purging gas. The heat transfer coefficients were determined to be 15 and $6 \text{ W/m}^2\text{K}$ for the upper and lower window surfaces, respectively (Piatkowski and Steinfeld, 2011). The window was assumed as a semi-transparent disk with spectral absorbance, transmittance, and reflectance listed in Table 7-1.

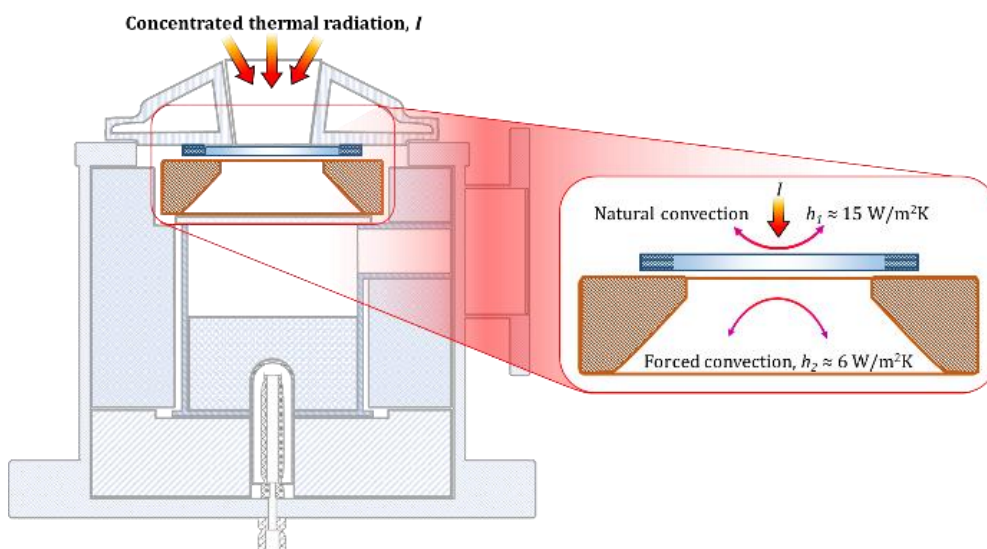


Figure 7-8 Schematic of the reactor upper cavity with boundary conditions

Table 7-1 Spectral properties of the quartz window¹²

Spectral Band	0–170nm	170–3500nm	3500 to ∞ nm
Transmittance, τ_t	0.0	0.835	0.0
Reflectance, ρ_r	0.094	0.136	0.134
Absorbance, α'	0.906	0.028	0.866

Hence the solar spectrum lies in spectral range 350–2500nm (ASTM Standard G173-03, 2012), the absorbance for the window has been assumed to be 0.028. The initial temperature of the plate was as same as the ambient temperature of 298 K. The emissivity of the window was assumed to be 0.85. The incident power, Q , is measured over the experiment time by Piatkowski's group (Piatkowski and Steinfeld, 2011). Whereas the absorbed irradiance represents the heat flux boundary condition affecting the upper surface of the quartz window, the incident Irradiation, I , has been calculated:

$$I = 4Q/(\pi D_a^2) \quad (7-2)$$

Where, D_a is the aperture diameter with a value of 0.065m. The measured and calculated data of incident power and radiative heat flux are plotted against the experiment time in Figure 7-9. Input data of numerical and mathematical models are summarised in Table 7-2.

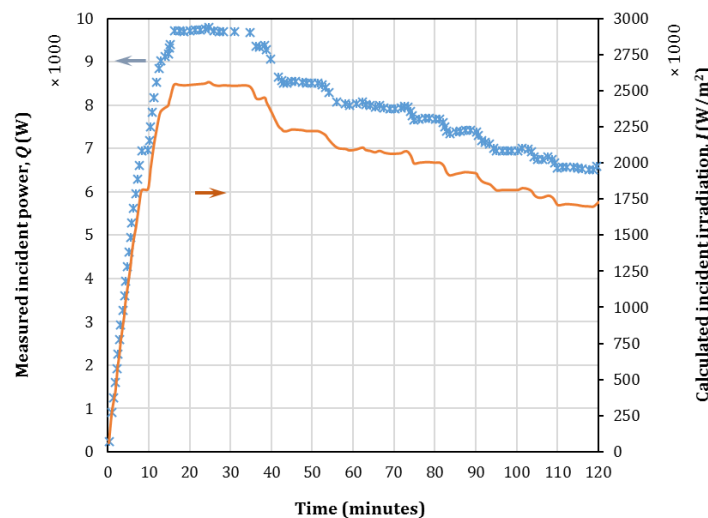


Figure 7-9 Measured incident power and calculated power flux versus time (Piatkowski and Steinfeld, 2011)

¹² According to data provided by (Kinematics Manufacturing, 2016).

Table 7-2 Model input data

Category	Property	Value	Unit
Geometry	Aperture diameter, D_a	0.065	m
	Window thickness, e	0.003	m
Material	Density, ρ	2210	Kg/m ³
	Thermal conductivity, k	1.4	W/mK
	Heat capacity, C_p	730	J/kgK
Boundary Conditions	Initial temperature, T_i	298	K
	Ambient temperature, T_∞	298	K
	Upper surface heat transfer coefficient, h_1	15	W/m ² K
	Lower surface heat transfer coefficient, h_2	6	W/m ² K
	Emissivity, ε	0.85	–
	Window absorbance, α_t	0.028	–
	Incoming irradiation, I	Figure 7-9	W/m ²
	Input heat flux to the upper surface (effective)	$\alpha_t I$	W/m ²

7.2.1.3 Mathematical Model Validation

This validation step aims to adjust the numerical model assumptions to minimise the time cost for calculation. Comparison between the proposed mathematical models results and the experimental data are held. In Figure 7-10, the calculated values of $T_{s,2}$ are plotted against the values obtained experimentally obtained by (Piatkowski and Steinfeld, 2011).

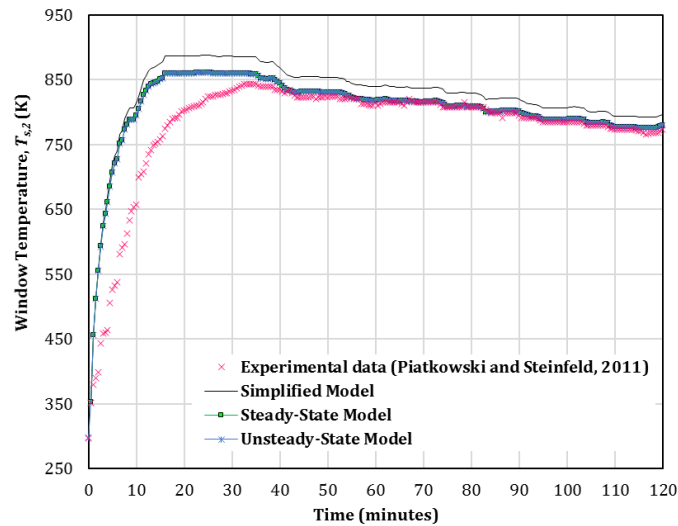


Figure 7-10 Mathematical models validation against experimental data

To evaluate the deviation between results, the RMSE and MAPE are calculated based on the following formulae:

$$RMSE = \sqrt{\left[\sum_{j=1}^N (T_{s,2,j,mod} - T_{s,2,j,ex})^2 \right] / N} \quad (7-3)$$

$$MAPE = (100/N) \sum_{j=1}^N |T_{s,2,j,mod} - T_{s,2,j,ex}| / T_{s,2,j,ex} \quad (7-4)$$

Where $T_{s,2,mod}$ and $T_{s,2,ex}$ are the model and measured values of window temperature at a certain time step, j , while N represents the number of data points studied. Error values are listed in Table 7-3.

Table 7-3 RMSE and MAPE values for mathematical models

Model	Simplified Model	Steady-state Model	Unsteady-state Model
RMSE (K)	66.139	54.273	54.244
MAPE (%)	6.918	4.350	4.347

According to error comparison, both steady- and unsteady-state models showed good agreement with experimental data obtained by (Piatkowski and Steinfeld, 2011). However, neglecting the window thickness in the simplified model led to larger deviation from the experimental data. On the other hand, steady- and unsteady-state models showed nearly the same results with a negligible difference. Therefore, steady-state model is used in COMSOL software calculations.

7.2.1.4 Numerical Model Validation

At this stage, a 2-D axisymmetric model with governing equations described in section 6.1.3.1.C has been solved using COMSOL Multiphysics® software. Steady-state solver has been applied with performing parametric sweep for the time variable so that the window temperature can be calculated at each time step. Numerical and mathematical (steady-state) models results for the lower surface temperature of the window are plotted against experimental results in Figure 7-11, while error values are listed in Table 7-4.

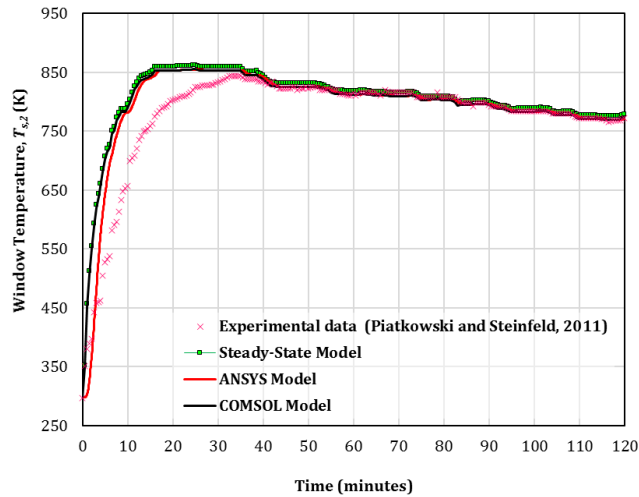


Figure 7-11 ANSYS and COMSOL models validation against experimental data

Table 7-4 RMSE and MAPE values for numerical and mathematical models

Model	COMSOL Model	ANSYS Model	Steady-state Model	Unsteady-state Model
<i>RMSE</i> (K)	51.486	40.232	54.273	54.244
<i>MAPE</i> (%)	3.939	3.077	4.350	4.347

The results shown in Figure 7-11 demonstrates a good agreement between the present numerical model and experimental data obtained by (Piatkowski and Steinfeld, 2011). Moreover, applying FEM in simulation, which is represented by using the COMSOL software, led to improving the obtained solution compared to mathematical models. However, the difference between the FEM-based and mathematical solutions is not significant. Therefore, the mathematical model can be applied for rough estimate calculations, while further adjusting can be performed using the COMSOL model solution.

7.2.2 Rear Lens Detailed Numerical Model Results

There are different parameters that may affect the maximum allowable CR that a lens can withstand. They can be categorised in three major categories: location, geometrical and material-based parameters. In this section numerical results obtained for simulating the rear lens using COMSOL software has been analysed to study the probable effects of parameters under each category. All simulations are based on assuming the day of Summer Solstice.

7.2.2.1 Location-based Parameters

Hence the location chosen for building the LLBG system affects the input power of solar radiation, the CR_{max} for the same lens can be varied. In this investigation, the simulation is carried on the positive meniscus lens with geometry described in Figure 6-11c, with quartz material. Simulation is carried out over latitude angles ranging from 0 to 60°N. Results shown in Figure 7-12, indicates a clear relationship between the latitude angle and CR_{max} which can be approximated by a fourth order polynomial as follows:

$$CR_{max} = a_1L^4 + a_2L^3 + a_3L^2 + a_4L + a_5 \quad (7-5)$$

The latitude angle, L , is in (degrees) and polynomial constants are listed in Table 7-5. Results shows that the minimum CR_{max} occurs at the maximum incident power on the Cancer Tropic on June 21.

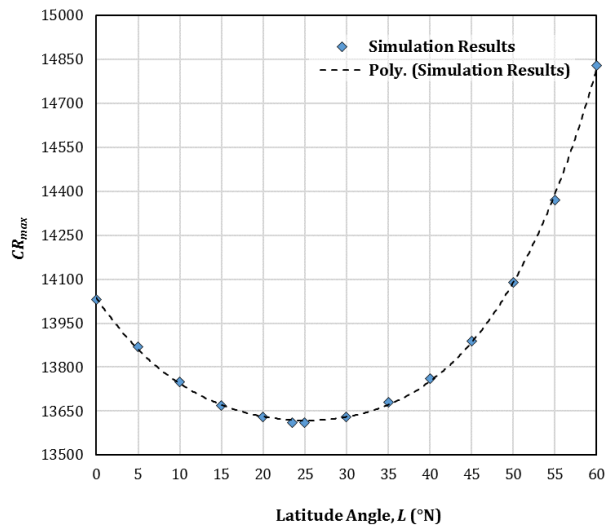


Figure 7-12 Maximum allowable CR vs. latitude angle of set-up location

Table 7-5 Polynomial constants for CR_{max} –Latitude relation

Constant	Value
a_1	3.38807E-04
a_2	-3.18869E-02
a_3	1.62184E+00
a_4	1.62184E+00
a_5	1.40370E+04

7.2.2.2 Geometrical-based Parameters

Positive meniscus lenses can be supplied in different thicknesses. The effect of lens thickness is to be investigated in this section through assuming lenses with different thicknesses ranging from 2.2 to 4.0 mm corresponding to available stock of Thorlabs®. The location is assumed to be at Cranfield, UK location (52°N) and the quartz material is assumed for all cases. Simulation results are shown in Figure 7-13, which can be fitted to a third order polynomial as:

$$CR_{max} = b_1e^3 + b_2e^2 + b_3e + b_4 \quad (7-6)$$

Where, lens thickness, e , is in meters and polynomial constants are listed in Table 7-6. Results indicate that the minimum lens thickness gives the maximum ability to withstand high CR values. This may be attributed to the better heat dissipation of heat through the lens thickness due to conduction as well as minimising the lens material.

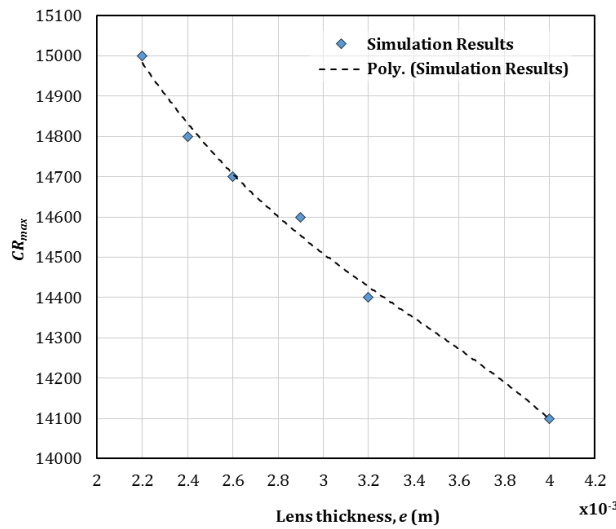


Figure 7-13 Maximum allowable CR vs. positive meniscus lens thickness

Table 7-6 Polynomial constants for CR_{max} –lens thickness relation

Constant	Value
b_1	-9.96896E+10
b_2	1.01728E+09
b_3	-3.84346E+06
b_4	1.95755E+04

7.2.2.3 Material-based Parameters

There are different optical and thermal materials properties that may influence thermal behaviour of the lens under the highly concentrated solar fluxes. These properties include: material transmittance, maximum working temperature, density, thermal conductivity and heat capacity. The investigation of these parameters is quite complex, as all of them can affect the thermal behaviour simultaneously. However, in the current study, individual relations for each property will be investigated separately through analysing the output data of the simulation process carried out in Section 6.1.3.3.

Material transmittance affects the amount of absorbed power, which is responsible for heating up the lens material. The simulation results of CR_{max} of the studied materials and their transmittances are plotted in Figure 7-14. However, the plotted data are not providing a clear relation between the parameters. The reason for this may be due to the influence of other parameters affecting CR_{max} .

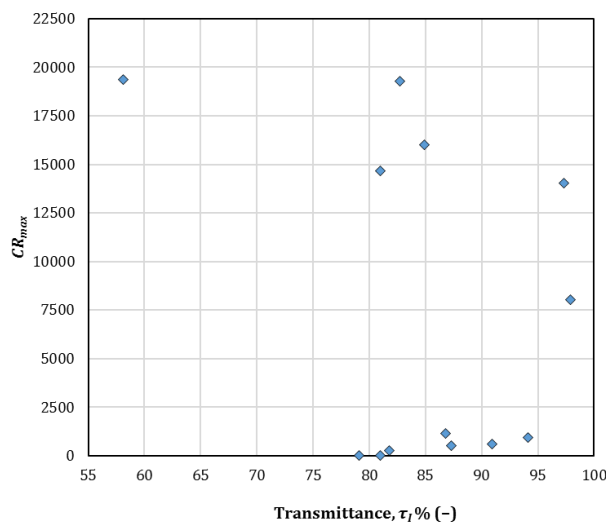


Figure 7-14 Maximum allowable CR vs. Transmittance

The effect of the maximum working temperature of materials on CR_{max} is shown in Figure 7-15. It indicates a direct relationship between the studied property and CR_{max} .

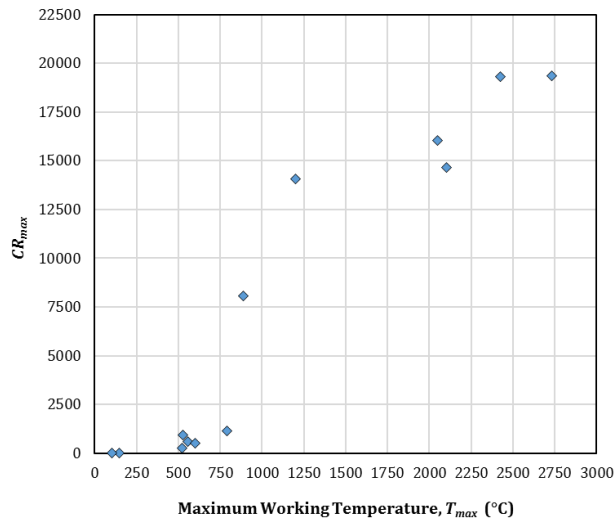


Figure 7-15 Maximum allowable CR vs. maximum working temperature

Material density can be used as a representation of the lens mass. Although the more material density indicates more mass of the lens and more heat capture, but data plotted in Figure 7-16 shows that it is not a general rule. The CR_{max} showed a random behaviour against applied materials densities.

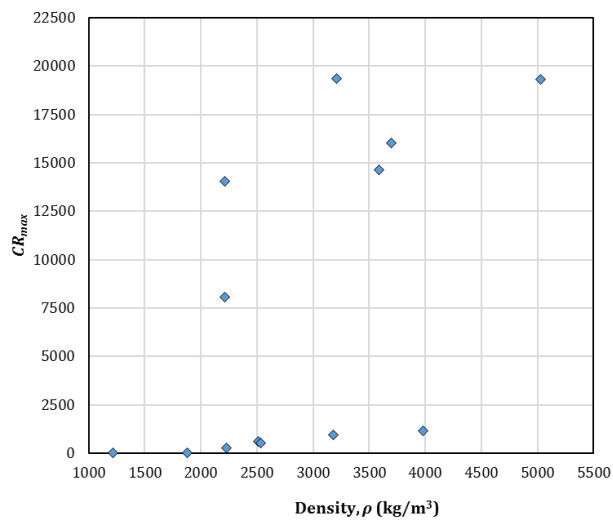


Figure 7-16 Maximum allowable CR vs. material density

Heat capacity is also a measure of heat captured by a certain material. The relation between heat capacity and CR_{max} has been showing a random behaviour as illustrated by Figure 7-17.

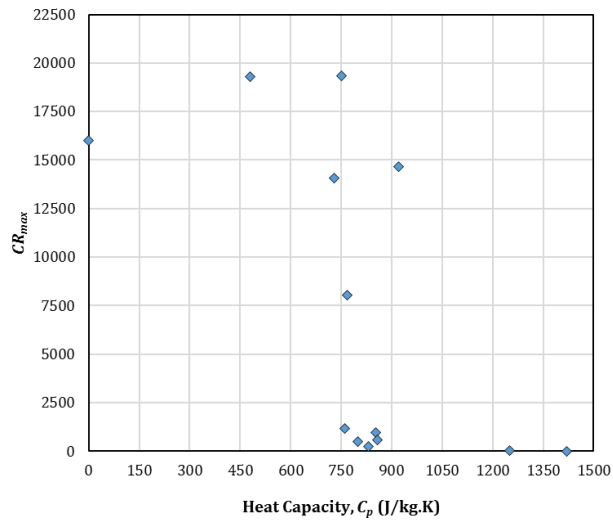


Figure 7-17 Maximum allowable CR vs. heat capacity

Thermal conductivity is responsible for minimising the temperature difference between the lens's surfaces. This effect may help in dissipating more heat from both sides of the lens. However, it is still unclear relationship between thermal conductivity of lens material and CR_{max} , based on data illustrated in Figure 7-18.

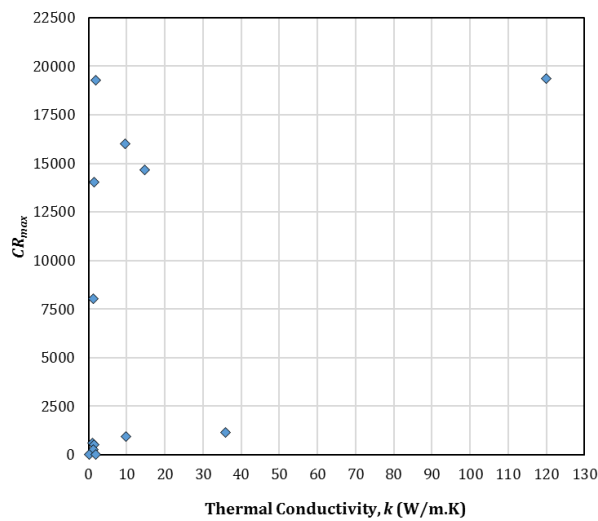


Figure 7-18 Maximum allowable CR vs. material thermal conductivity

The last three properties of materials can be combined under one property, known as thermal diffusivity, α_d , which can be defined as:

$$\alpha_d = k / (\rho C_p) \quad (7-7)$$

Thermal diffusivity relation with the CR_{max} is plotted in Figure 7-19. However, there is no clear relationship between maximum allowable CR and material thermal diffusivity.

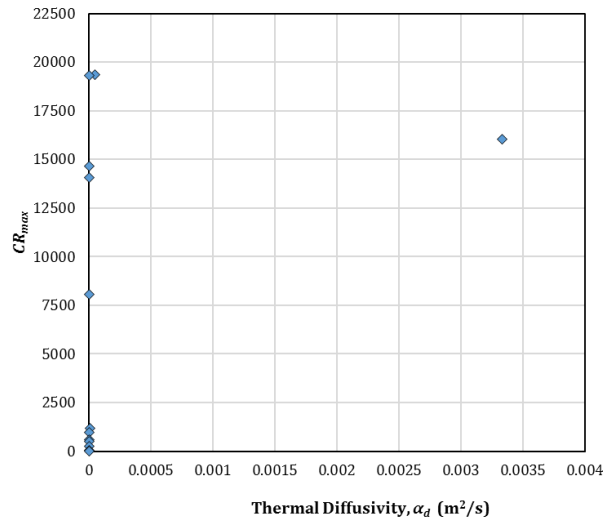


Figure 7-19 Maximum allowable CR vs. material thermal diffusivity

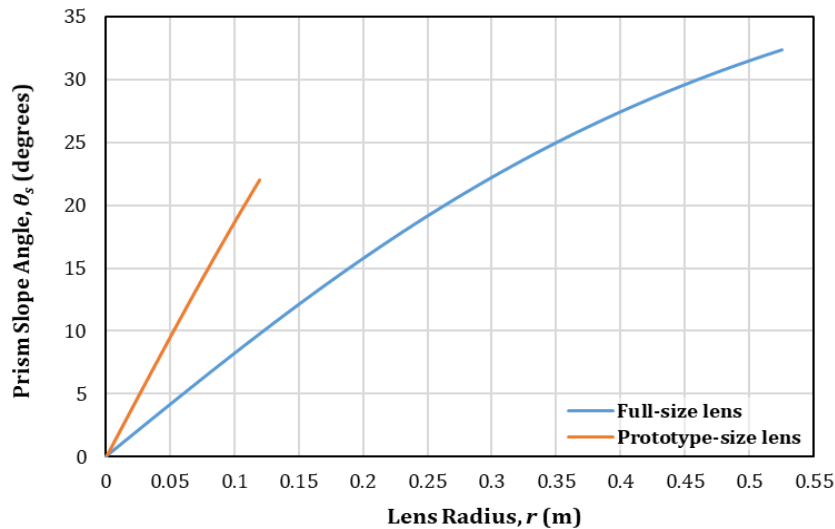
7.2.3 Optical Analysis Code Results

In this section, the mathematical formulae derived in Section 6.1.4.1 has been solved with a MATLAB[®] software, which is validated in Section 7.3.1, to investigate the influence of different assumptions and parameters on the LLBG performance. This investigation is carried on two major stages. In the first stage, the effects of CA and SAA assumptions on the front lens focal spot diameter. This study is applied to the full-size LLBG front lens as a case study. For the second stage, the performance of prototype- and full-size LLBG systems is studied. This study includes an optical study of the rear lens geometry and positioning effects as well as the front lens buckling effect on the output beam quality. Two different circular PMMA-Fresnel lenses are used as front lens for each system, with design details listed in Table 7-7.

Table 7-7 Technical details of studied front lenses

Property (unit)	Prototype-size system	Full-size system
Geometry	Fresnel	Fresnel
Material	PMMA	PMMA
Focal length, f (m)	0.6096	1.400
GI/GO design configuration	GO	GI
Aperture radius, R (m)	0.12	0.525
Refractive index, n_{st} (-)	1.49	1.491
Standard Wavelength, λ_{st} (nm)	586.0	586.0
Pitch, P (m)	?	0.33E-03
Slope angle, θ_s (°)	$\theta_s(r)=?$	$\theta_s(r)=?$
Draft angle, θ_d (°)	?	0.0
Reference	(Edmund Optics, 2018a)	(NTKJ, 2007)

As the slope angle of lens prisms are varying with lens aperture radius in an unknown function, the available data has been utilised to derive the function mathematically. To achieve this, collimated rays are assumed to fall at normal incidence, i.e. $\theta_i=0$, at a standard wavelength, n_{st} , to be refracted at the manufacturer focal length measured from the lens plane. The obtained function of slope angle, θ_s , (in degrees) as a function of the front lens radius, r , (in m) is plotted in Figure 7-20 for both front lenses studied.

**Figure 7-20 Case study Fresnel lenses prisms θ_s as a function of r (calculated)**

7.2.3.1 CA and SAA Effects on Focal Spot Diameter of Fresnel Lens

In this section, mathematical formulae derived in section 6.1.4.1 are applied for the full-size front full-size front Fresnel lens, with manufacturer data technical details listed in Table 7-7. Applying Eq. (6-47) using the previous data, the spectral spot diameter at distance (x) equal to the manufacturer focal length of 1.4m can be plotted as shown in Figure 7-21.

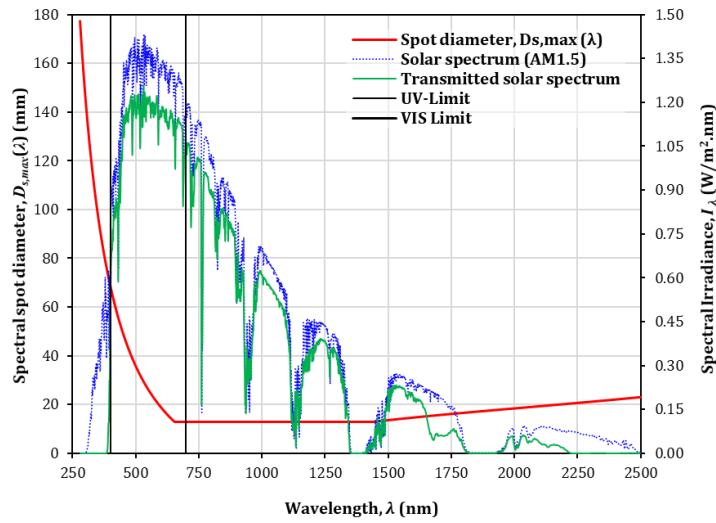


Figure 7-21 Spectral spot diameter at ($x = 1.4\text{m}$) against solar spectrum (AM1.5)

From Figure 7-21, it can be concluded that if the SAA and CA effects are considered, the spot has an extremely large diameter ranging from 177.2 to 68.7 mm over the whole UV-zone of solar spectrum. While the spot diameter remains constant at 13.02 mm over a wavelength ranges from 655 to 1439 nm, and starts to increase slightly through the IR- zone to reach 23.17 mm by the end of solar spectrum. In order to evaluate the influence of model assumptions on spectral spot diameter evaluation, Figure 7-22 shows a comparison between the current model with different assumptions and models proposed by (Cotal and Sherif, 2005) and (Bobkova *et al.*, 2006). For (Cotal and Sherif, 2005) model, the SAA has been neglected, while (Bobkova *et al.*, 2006) model neglected the CA effect.

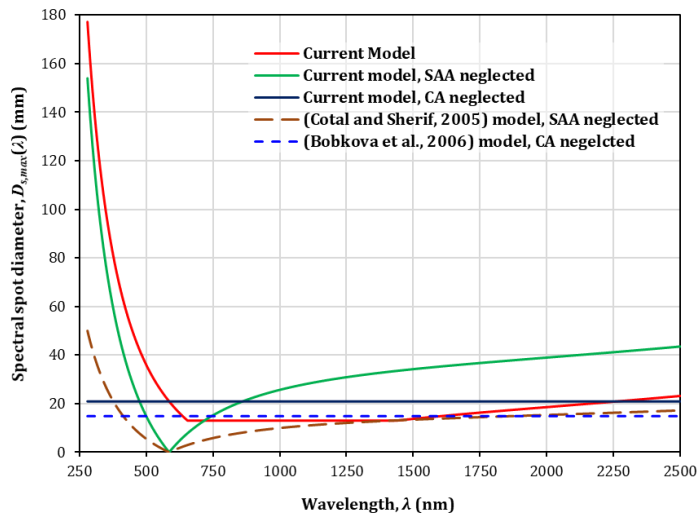


Figure 7-22 Spectral spot diameter with different assumptions and models

From Figure 7-22, neglecting SAA effect results in decreasing the predicted spot diameter in the UV-zone and through the VIS bandwidth until a minimum value is reached at the standard wavelength of 586nm. In the current model, neglecting the SAA, and (Cotal and Sherif, 2005) model, the spot diameter reaches 5.19E-07 and 0.0E00 mm, respectively, and tends to increase gradually beyond the point of standard wavelength. The difference between the results may be attributed to the neglect of lens geometry effect, including the prisms design and its aperture diameter.

When the CA is neglected, the spot diameter becomes independent of wavelength change. Therefore, both the current and (Bobkova *et al.*, 2006) models with this assumption showed constant spot diameter of 20.92 and 14.85 mm, respectively. The difference between the results can be interpreted as a result of neglecting the lens material properties in (Bobkova *et al.*, 2006) model. Results obtained from Figure 7-22 illustrates the importance in considering the SAA effect in optical designing of Fresnel lens-based solar concentrators.

7.2.3.2 Rear Lens Position Effect on Output Beam

In this section, the influence of rear lens position on spectral beam deviation angle, δ , is investigated for both prototype- and full-size systems with positive meniscus (LE4412). Figure 7-23 shows the effect of changing RLPFR around its optimum value for each system.

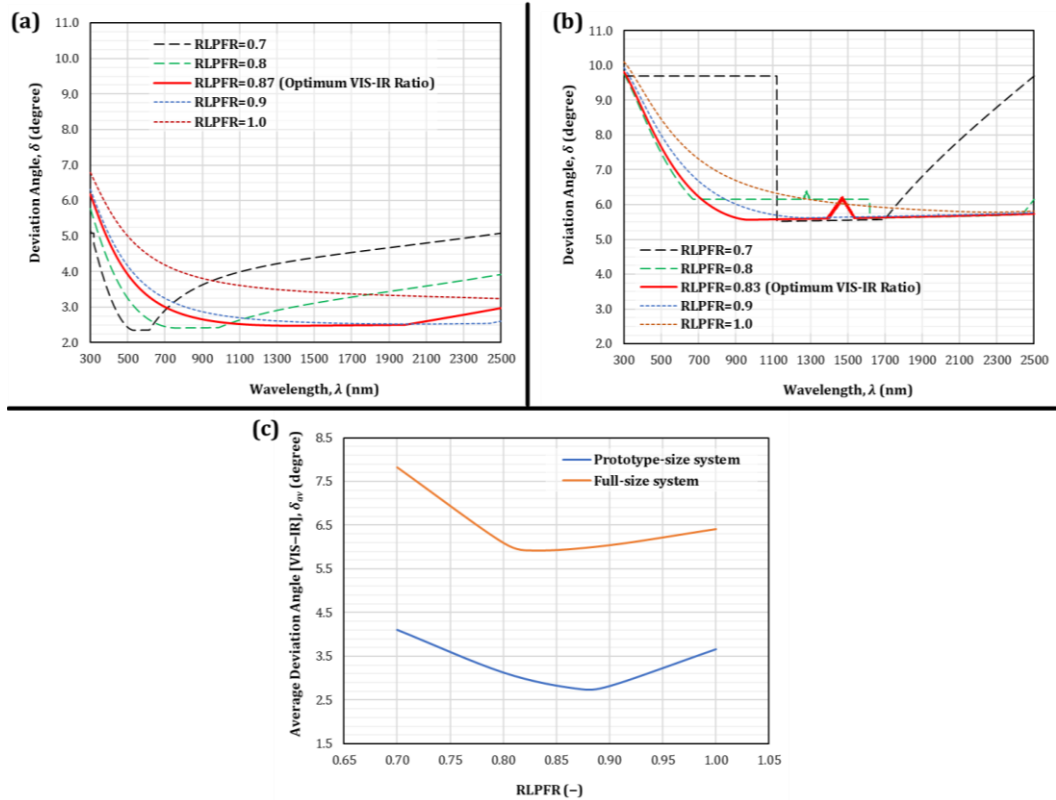


Figure 7-23 Spectral deviation angle at different RLPFRs
(a) prototype-size system (b) full-size system
(c) Average deviation angle (VIS-IR) for both systems

Figure 7-23 indicates that the optimum positioning of the rear lens with respect to the front lens focal length plays a significant role in minimising and stabilising the spectral deviation angle of the output beam. The obtained optimum RLPFRs are used in evaluating beam diameter in both system. The code is applied to wavelengths of [300, 350nm] (UV), [400, 550, 700nm] (VIS) and [1600, 2500nm] (IR). The evaluated beam diameter for both systems are illustrated in Figure 7-24.

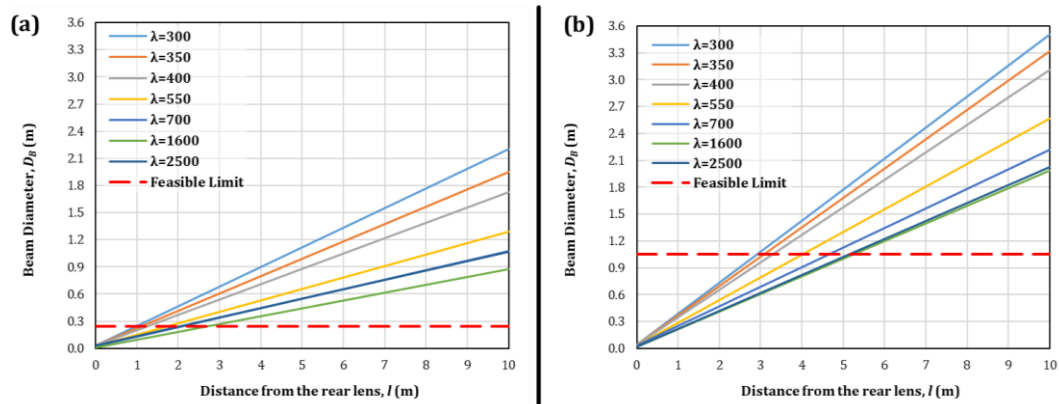


Figure 7-24 Spectral beam diameter over distance, l , from the rear lens
(a) prototype-size system (b) full-size system

The feasible limit plotted in Figure 7-24 is representing the maximum beam diameter at which it reaches the original aperture diameter. The longest distance that generated beam can travel to reach the feasible beam limit, $l_{feasible}$ in each system for different wavelengths are listed in Table 7-8. In order to normalise this distance, a relative value representing the ratio of the maximum feasible distance from the rear lens to the feasible beam limit is calculated and listed in Table 7-8.

Table 7-8 Longest distance beam travel to reach the feasible beam limit

Spectral Zone	Wavelength, λ (nm)	Prototype-size (Feasible Limit= 0.24m)		Full-size (Feasible Limit= 1.05m)	
		Maximum Distance (m)	Relative Distance (-)	Maximum Distance (m)	Relative Distance (-)
UV	300	0.942746386	3.928	2.919375643	2.780
	350	1.073784054	4.474	3.083592565	2.937
VIS	400	1.222979837	5.096	3.292877597	3.136
	550	1.682872769	7.012	4.01467442	3.823
	700	2.061001458	8.588	4.671115615	4.449
IR	1600	2.689966682	11.208	5.261668955	5.011
	2500	2.033252755	8.472	5.156891942	4.911

According to obtained results, positioning the rear lens at the optimum position leads to generate a more stable, collimated beam over IR-zone compared to VIS and UV region. This result is due to the less deviation angle for such bandwidth. In other words, under the optimum rear lens positioning condition, the generated thermal beam (IR) can be carried out for longer distance compared to shorter wavelengths.

However, this conclusion is contrary to (Jaramillo, Río and Huelsz, 1999) results, who found that thermal effect of concentrated solar rays in a 10m of SiO₂-optical fibre appears only within the first 0.5m of the transmission line compared to visible light. The main reason for this discrepancy is attributed to adding the rear lens to the optical configuration of the LLBG system which alternates the spectral distribution of the concentrated solar rays.

7.2.3.3 Front Lens Buckling Effect on Output Beam

The effect of buckled front lens with radius of curvature, R_C , has been investigated. Hence the full-size front lens has a larger aperture area compared to the prototype-size front lens, the buckling effect will be more significant.

Therefore, the lens buckling effect is studied for the full-size front lens. According to measured values of R_C , listed in Section 4.2.3, the code is applied for 4 different cases representing radii of curvature of 18.114, 19.711, 27.652m and ∞ (without buckling-case) with fixing the rear lens at the its optimum RLPFR of 0.833. For further investigation, two additional radii of curvature of 10 and 15m has been assumed. To facilitate representing the non-buckled front lens graphically, all studied cases are represented in terms of corresponding radius of curvature reciprocal, R_C^{-1} . The buckling effect on the spectral output beam deviation angle (for wavelengths selected in Section 7.2.3.1) is illustrated in Figure 7-25a, while the average deviation angle over the VIS–IR spectral zones are plotted against R_C^{-1} in Figure 7-25b.

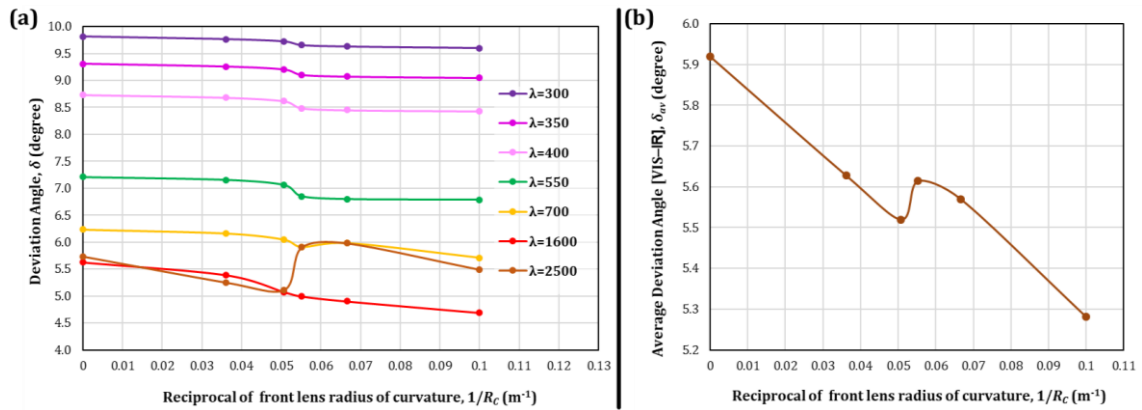


Figure 7-25 Extended front lens radii of curvature effect study
(a) spectral deviation angle (b) average deviation angle (VIS–IR)

Although Figure 7-25a shows low sensitivity of deviation angle with respect to front lens curvature, the results in IR zone tend to be more sensitive. For all investigated wavelengths, the more front lens curvature (less R_C), the less deviation angle occurs. However, a step in the 2500nm behaviour appears between radii of curvature of 19.711 and 15m. Within the same range of radii of curvature, a step is also observed in the average deviation angle (Figure 7-25b).

7.2.3.4 Front Lens Geometry Effect on Output Beam

In this section, the effect of using Fresnel geometry for the front lens on the output beam deviation is investigated through comparison with an experimental case study (Salem, Tawfik and Hamed, 2010). They introduced a small LLBG model using two bi-convex lenses of 50mm in diameter. Their front and rear lenses had

focal lengths of 0.2 and 0.1m, respectively. The generated beam had a diameter of 0.02m at receiver aperture. In the present investigation, a virtual Fresnel front lens is assumed to have a focal length and clear aperture diameter of 0.2 and 0.05m, respectively, while the rear lens is assumed to be the bi-convex lens LB4821 (Thorlabs, 2010b), with technical details listed in Table 7-9. Then the MATLAB code is applied for the Fresnel–bi-convex configuration to calculate and compare the output beam deviation angle and its diameter at the corresponding distance from the rear lens of Salem’s group case.

However, (Salem, Tawfik and Hamed, 2010) did not measure the ray path length from their rear lens to the receiver. Therefore, it has to be worked out through the available information provided by their raw data. A schematic diagram illustrating the path of the generated beam in their test rig is shown in Figure 7-26. The known values are Z , l_0 and l_3 corresponding 0.4, 0.15 and 0.85m, respectively. According to this, determining the initial altitude angle, γ_0 , is required to calculate the rest of unknowns. As (Salem, Tawfik and Hamed, 2010) took their measurements on June 24th by 10:50 AM (Egypt local time), then the altitude angle at this time for the given coordinates of 31.04°N and 31.36°E can be figured out. From sun’s position calculator (Figure 7-27), the altitude angle was 73.27°.

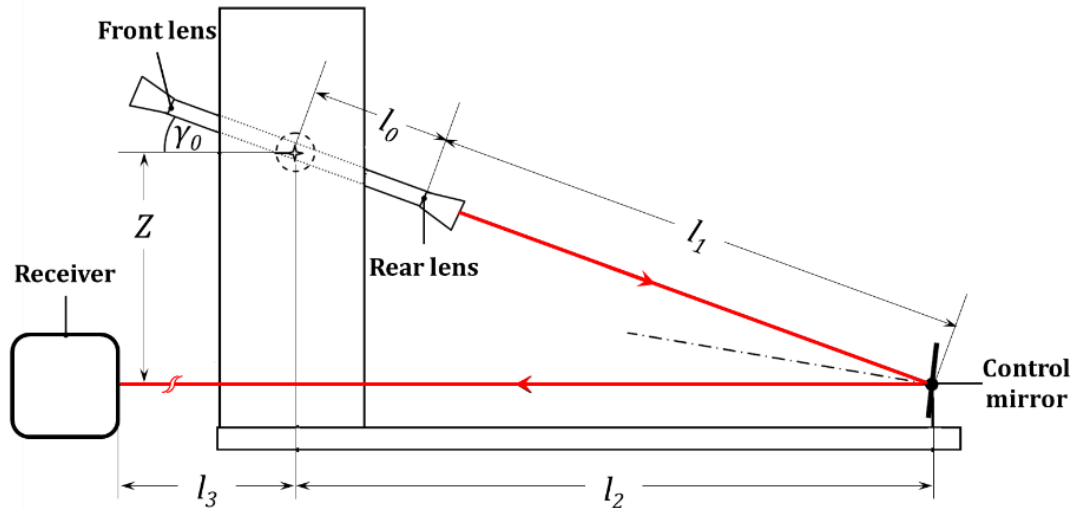


Figure 7-26 Schematic diagram of the generated beam path
(Salem, Tawfik and Hamed, 2010)

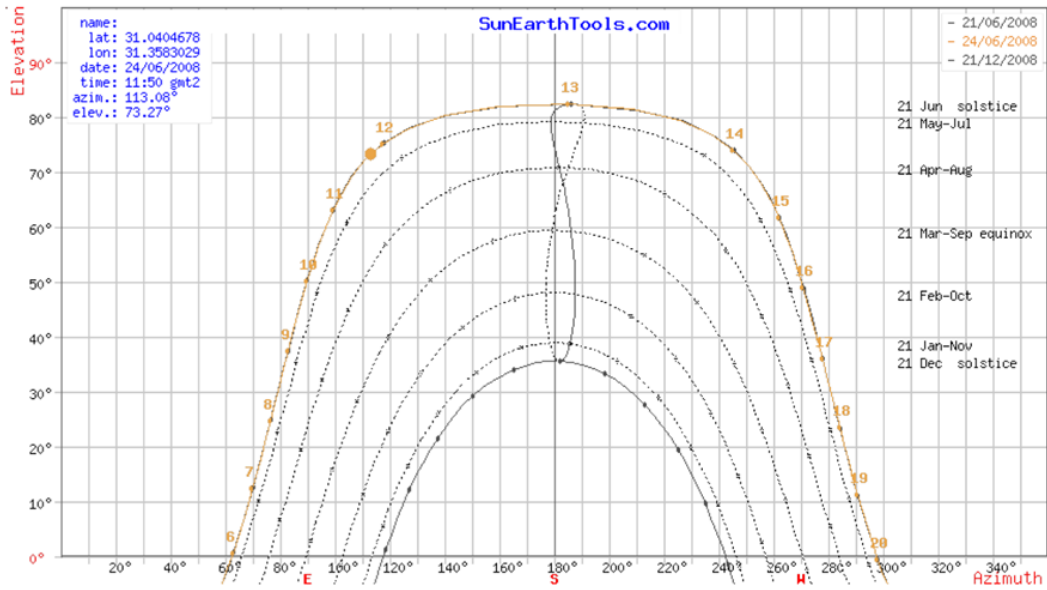


Figure 7-27 Sun's position calculator for Mansoura, Egypt on 24/06/2008 (SunEarthTools, 2018)

Based on that the total path travelled by the generated beam is 1.25m. Applying the MATLAB code for the Fresnel /bi-convex lenses configuration, then evaluated beam diameter for wavelengths of [300, 350nm] (UV), [400, 550, 700nm] (VIS) and [1600, 2500nm] (IR) are as plotted in Figure 7-28.

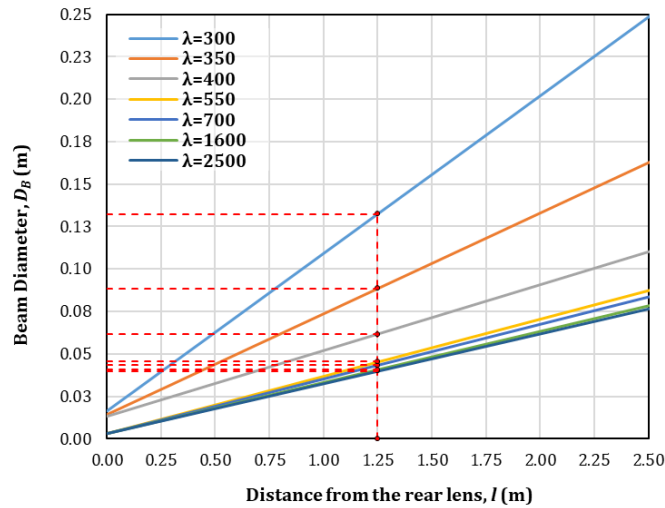


Figure 7-28 Spectral beam diameter over distance, l , from the rear lens

The obtained results show a beam diameter ranging from 0.0398 to 0.1323 m at wavelengths of 2500 and 300nm with an average visible beam diameter of 0.05m. This indicates that using Fresnel geometry for the front lens led to increasing the beam diameter by 150%.

7.2.3.5 Rear Lens Geometry Effect on Output Beam

The LLBG beam generation ability is evaluated by calculating the beam deviation angle for prototype- and full-size systems. For both systems, five different SiO₂– rear lenses have been employed, with technical details available in Table 7-9. For all studied rear lenses, the standard refractive index and wavelength are 1.458 and 587.6nm, respectively, and all have the same diameter of 0.0508m.

Table 7-9 Technical details of studied rear lenses

Property (unit)	Lens part number				
	LE4412	LE4125	LE4560	LA4545	LB4821
Geometry	Positive meniscus	Positive meniscus	Positive meniscus	Plano-convex	Bi-convex
Focal length, f (m)	0.100	0.150	0.200	0.100	0.100
Edge thickness, ee (m)	0.0012	0.0027	0.0030	0.0031	0.0030
Centre thickness, ec (m)	0.0107	0.0078	0.0066	0.0106	0.0103
Front surface radius of curvature, $R1$ (m)	0.0306	0.0465	0.0630	0.0460	0.0904
Back surface radius of curvature, $R2$ (m)	0.0809	0.1353	0.1934	∞	-0.0904
Reference	(Thorlabs, 2010d)	(Thorlabs, 2010c)	(Thorlabs, 2010e)	(Thorlabs, 2010a)	(Thorlabs, 2010b)

Most of the thermal radiation is carried by IR spectrum (Xu, 2016), therefore VIS and IR (400–2500nm) are chosen as the spectral zones of concern to evaluate the optimum location of the rear lens with respect to the front lens focal point. This location can be expressed in a nondimensionalised form as the rear lens position focal ratio (RLPFR), which is defined as the ratio of rear lens position, x_2 , to its focal length, f_2 . According to the applied code results, the optimum RLPFR is found to be as listed in Table 7-10. These values are obtained to match the minimum average deviation angle of the output beam over the spectral zone of concern (400–2500nm). The calculated average output beam deviation angle, δ_{av} , over the spectral zone of concern in each case is listed also in Table 7-10.

Table 7-10 Optimum rear lens position, RLPFR and average deviation angle

Lens part number	Prototype-size system			Full-size system		
	Optimum position, $x_{2,op}$ (m)	Optimum RLPFR (-)	Average deviation, δ_{av} (°)	Optimum position, $x_{2,op}$ (m)	Optimum RLPFR (-)	Average deviation, δ_{av} (°)
LE4412	0.0873333364	0.8733	2.76	0.0833333358	0.8333	6.08
LE4125	0.1389999986	0.9267	1.41	0.09099999815	0.6067	9.90
LE4560	0.02800000086	0.1400	3.68	0.03333333507	0.1667	9.20
LA4545	0.09399999678	0.9400	1.70	0.0886666700	0.8867	4.88
LB4821	0.04466666654	0.4467	2.59	0.0460000009	0.4600	7.17

The spectral beam deviation angle for both prototype- and full-size systems with different rear lenses is plotted in Figure 7-29.

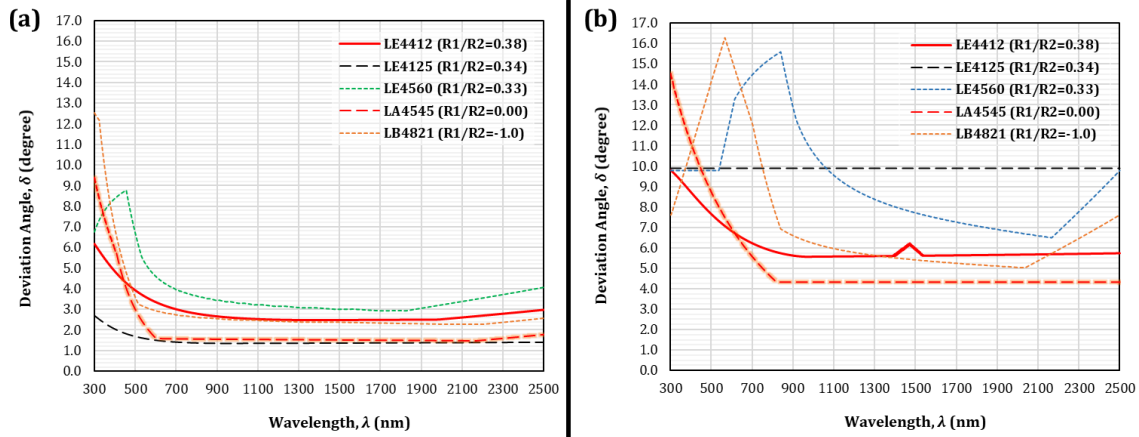


Figure 7-29 Spectral deviation angle for different rear lenses
(a) prototype-size system **(b) full-size system**

From Figure 7-29, it can be found that scaling-up the front lens aperture diameter by 338% led to the increase of the deviation angle by an average of 247% over all studied rear lenses. The prototype-size system has a larger front lens aperture by 380% compared to the system proposed by (Salem, Tawfik and Hamed, 2010). This may explain the ability of (Salem, Tawfik and Hamed, 2010) to generate and carry the beam efficiently over 1m, compared to the limited ability to the present experimental design with the positive meniscus rear lens. Hence the relation between the rear lens geometry and the LLBG output beam quality is still unclear to be inferred from Figure 7-29, further investigation is carried out from Figure 7-30.

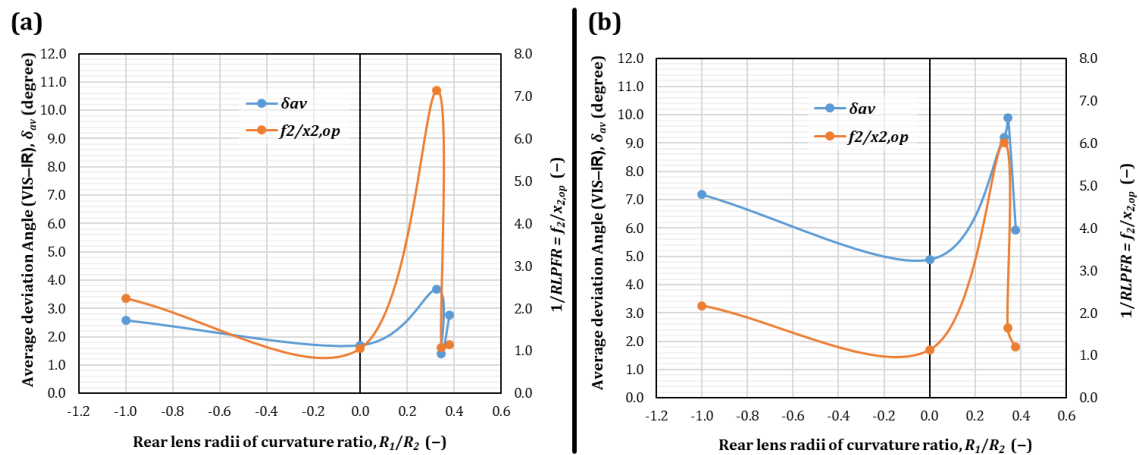


Figure 7-30 Average beam deviation angles and reciprocal of RLPFR
(a) prototype-size system **(b) full-size system**

7.2.3.6 Front–Rear Lenses Combination Effect on Output Beam Deviation

In this section, different combinations of front–rear lens have been examined to infer a relationship between the LLBG optical components specifications and the output beam average deviation angle, δ_{av} . To define a parameter that merge down different front–rear lenses geometrical details, a dimensionless number, called as LLBG#, is defined as follows:

$$LLBG\# = \left(\frac{D_1}{D_2}\right) \left(\frac{f_1 + f_2}{R_1 - R_2}\right) \quad (7-8)$$

Where, D_1, f_1, D_2, f_2 are the aperture diameter and focal length of the front and rear lenses, respectively, while R_1 and R_2 are the radii of curvature of the front and back surfaces of the rear lens, respectively. According to data provided by the manufacturer (Edmund Optics, 2018c), the specifications of different front PMMA-Fresnel lenses, which designed for GO configuration, can be combined with the 5 rear lenses studied in Section 7.2.3.4, with technical data available in Table 7-9. These combinations can create 110 LLBG#s, as listed in Table 7-11, ranging from 0 to 66.65.

In order to examine the relation between the LLBG# and average beam deviation angle, the first 6 front lenses among the list of Table 7-11 have been selected to generate a popularity of 30 cases, covering the full available range of LLBG# (0–66.65), to be studied. The MATLAB code is then applied for each combination to determine the optimum RLPFR and average deviation angle, δ_{av} , (over VIS–IR) corresponding to each LLBG#. Results obtained are listed in Table 7-12 and the relation between LLBG# and δ_{av} of the has been plotted and fitted with Fourier series formula with different number of terms to select the optimum fit, as illustrated in Figure 7-31.

Table 7-11 Probable front–rear lenses combinations

Front Lens #	Rear Lens #	LLBG #	Front Lens #	Rear Lens #	LLBG #	Front Lens #	Rear Lens #	LLBG #	Front Lens #	Rear Lens #	LLBG #	Front Lens #	Rear Lens #	LLBG #
32-691		40.41	32-691		66.65	32-691		0.00	32-691		29.33	32-691		18.54
32-690		33.66	32-690		54.72	32-690		0.00	32-690		24.73	32-690		15.22
43-019		32.30	43-019		52.33	43-019		0.00	43-019		23.81	43-019		14.56
43-018		26.63	43-018		42.31	43-018		0.00	43-018		19.95	43-018		11.77
32-598		20.41	32-598		31.34	32-598		0.00	32-598		15.71	32-598		8.72
32-597		19.06	32-597		28.96	32-597		0.00	32-597		14.79	32-597		8.06
32-681		3.90	32-681		5.64	32-681		0.00	32-681		3.13	32-681		1.57
32-682		5.92	32-682		8.97	32-682		0.00	32-682		4.61	32-682		2.49
32-590		3.65	32-590		4.95	32-590		0.00	32-590		3.06	32-590		1.38
43-011	LE4125	3.95	43-011	LE4412	5.48	43-011	LA4545	0.00	43-011	LE4560	3.26	43-011	LB4821	1.53
43-012		4.08	43-012		5.71	43-012		0.00	43-012		3.35	43-012		1.59
32-591		3.82	32-591		5.25	32-591		0.00	32-591		3.18	32-591		1.46
32-592		4.21	32-592		5.94	32-592		0.00	32-592		3.44	32-592		1.65
46-614		7.08	46-614		10.02	46-614		0.00	46-614		5.78	46-614		2.79
32-683		6.23	32-683		8.50	32-683		0.00	32-683		5.20	32-683		2.37
32-684		7.80	32-684		11.28	32-684		0.00	32-684		6.27	32-684		3.14
43-013		11.37	43-013		17.59	43-013		0.00	43-013		8.70	43-013		4.89
32-593		8.52	32-593		11.72	32-593		0.00	32-593		7.09	32-593		3.26
32-594		11.40	32-594		16.79	32-594		0.00	32-594		9.04	32-594		4.67
32-685		15.22	32-685		23.55	32-685		0.00	32-685		11.65	32-685		6.55
32-686		17.14	32-686		26.93	32-686		0.00	32-686		12.95	32-686		7.49
43-015		29.06	43-015		47.08	43-015		0.00	43-015		21.42	43-015		13.10

Table 7-12 MATLAB code output for different investigated combinations

Front Lens #	Rear Lens #	LLBG# (-)	Optimum RLPFR (-)	Average deviation, δ_{av} (°)
32-691	LE4125	40.41	0.9267	1.41
32-690	LE4125	33.66	0.7533	3.40
43-019	LE4125	32.30	0.7133	4.25
43-018	LE4125	26.63	0.1133	4.24
32-598	LE4125	20.41	0.1000	4.20
32-597	LE4125	19.06	0.1000	4.09
32-691	LE4412	66.65	0.8733	2.76
32-690	LE4412	54.72	0.8333	2.52
43-019	LE4412	52.33	0.8067	2.53
43-018	LE4412	42.31	0.7267	3.61
32-598	LE4412	31.34	0.1000	5.88
32-597	LE4412	28.96	0.1000	6.56
32-691	LA4545	0.00	0.9400	1.70
32-690	LA4545	0.00	0.9133	1.53
43-019	LA4545	0.00	0.8867	1.51
43-018	LA4545	0.00	0.7800	2.78
32-598	LA4545	0.00	0.1267	4.46
32-597	LA4545	0.00	0.1267	4.45
32-691	LE4560	29.33	0.1400	3.68
32-690	LE4560	24.73	0.1267	3.64
43-019	LE4560	23.81	0.1267	3.66
43-018	LE4560	19.95	0.1133	3.40
32-598	LE4560	15.71	0.1133	3.10
32-597	LE4560	14.79	0.1133	3.33
32-691	LB4821	18.54	0.4467	2.59
32-690	LB4821	15.22	0.4333	2.35
43-019	LB4821	14.56	0.4200	2.36
43-018	LB4821	11.77	0.4067	2.05
32-598	LB4821	8.72	0.3933	1.78
32-597	LB4821	8.06	0.3800	1.69

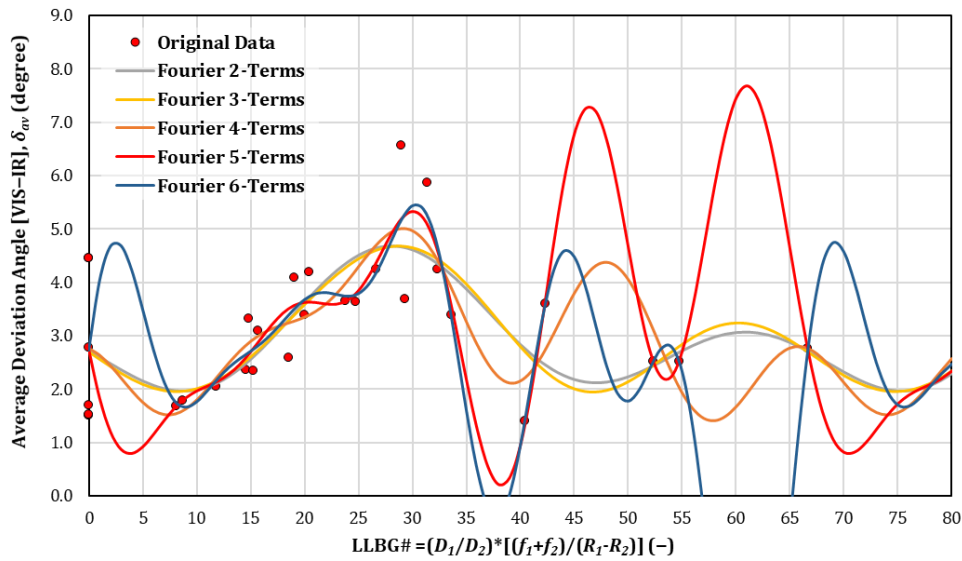


Figure 7-31 Average deviation angle at different LLBG#s

The applied Fourier series trigonometric form is (Serov, 2017):

$$\delta_{av} = \frac{\pi}{180} \left\{ a_0 + \sum_{i=1}^n [a_i \cos(i * w * LLBG\#) + b_i \sin(i * w * LLBG\#)] \right\} \quad (7-9)$$

Where δ_{av} in degrees, while a_0, a_i, b_i are constants, w is the frequency and n is the number of terms in the series. In order to check the accuracy of each fit is evaluated through determining the RMSE and MAPE for each fit. Moreover, a random combination is selected (32-686/LE4125, LLBG# =17.14) and studied through the MATLAB code and the resulting δ_{av} is compared against the predicted value from Eq. (7-9) for each fit. The obtained results are listed in Table 7-13. These results indicate that 5-term Fourier series best fits the studied data with a total MAPE of 17.86% and minimum error of the random combination studied of 3.92%. However, data listed and plotted in Table 7-12 and Figure 7-31 show that all combinations that use the plano-convex lens as a rear lens have LLBG# of 0.0. This fact leads to a relatively high MAPE of 50.15% for the corresponding 5 combinations. Therefore, the MAPE calculated over the rest 25 combinations of the studied popularity shows less MAPE of only 9.79% for the 5-term Fourier series fit. According to this, 5-term Fourier series fit, with coefficients available in Table 7-13, is valid for (LLBG#s > 0.0) to give an estimation of average beam deviation angel, δ_{av} , over VIS-IR spectrum of corresponding front-rear lenses combination, if the front lens is designed for GO-configuration.

Table 7-13 Fourier series fits coefficients and evaluation

		2-terms	3-terms	4-terms	5-terms	6-terms
Fourier series coefficients	a_0	0.052490	0.052520	0.051730	0.0629600	0.036850
	a_1	-0.012880	-0.012280	-0.017260	-0.0008480	-0.027880
	b_1	0.005681	0.005695	0.001730	-0.0170800	0.021640
	a_2	0.007783	0.008414	-0.001656	-0.0054850	-0.010230
	b_2	-0.012950	-0.013970	-0.007159	-0.0239100	0.012880
	a_3	—	-0.001506	0.006322	0.0105100	0.010550
	b_3	—	-0.001010	0.010060	-0.0016690	0.035910
	a_4	—	—	0.009078	-0.0002283	0.011990
	b_4	—	—	-0.008290	-0.0321800	0.008011
	a_5	—	—	—	-0.0190300	0.009034
	b_5	—	—	—	0.0018590	0.024780
	a_6	—	—	—	—	0.017460
	b_6	—	—	—	—	-0.002509
	w	0.094300	0.094270	0.094270	0.094270	0.094270
Evaluation	RMSE (°)	0.995	0.889	1.023	0.761	0.756
	MAPE (%)	24.59	24.71	23.80	17.86	17.89
	Error (%) @ LLBG# =17.14	11.56	11.13	7.02	3.92	8.81

7.3 LLBG Testing Results

7.3.1 Optical Analysis Code Validation Test

The measured beam diameters against different total distance from the rear lens to the screen, l , is plotted in Figure 7-32 and compared to the code output results. Hence the experimental measurement is taken by naked eyes covered with safety glasses, then the only VIS bandwidth (400–700nm) can be detected. Due to the lack of clarity of some certain wavelengths compared to others, the collected values may involve uncertainty. However, the experimental data is found to be in good agreement with the code results at some certain wavelengths with an average RMSE and MAPE of 2.52E-05m and 4.78% over 400–700nm bandwidth, which represents the clearest visible light can be observed.

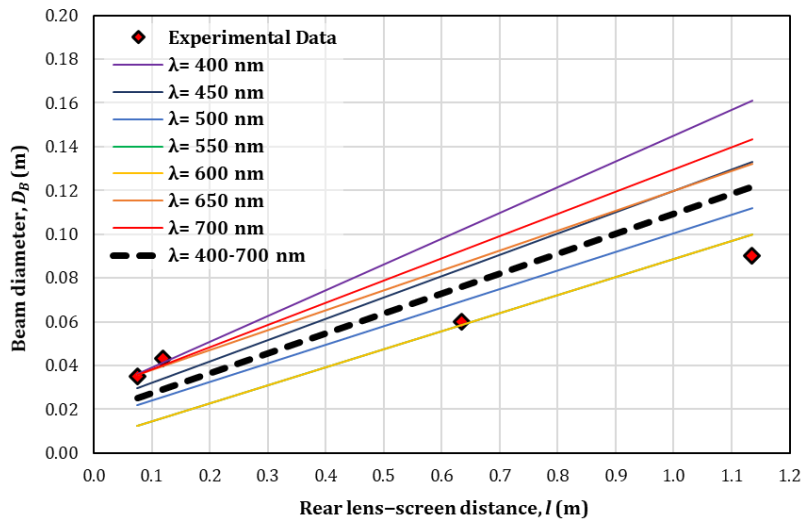


Figure 7-32 Beam diameter against rear lens-screen distance

7.3.2 Prototype LLBG System Test

The measured ambient temperature and the average receiver back surface temperatures are plotted in Figure 7-33 for the three tests carried out, with a sampling rate of one reading/second. The disturbance in readings collected in Figure 7-33 is attributed to system vibration during the rotation of the system over the extremely rough and bumpy ground during the tracking process. In addition to the time lag in recognising that the system is required to modify its position to follow the sun's path in the sky. The average incident irradiance over tests periods are 700, 1100 and 1000 W/m² for tests 1, 2 and 3, respectively.

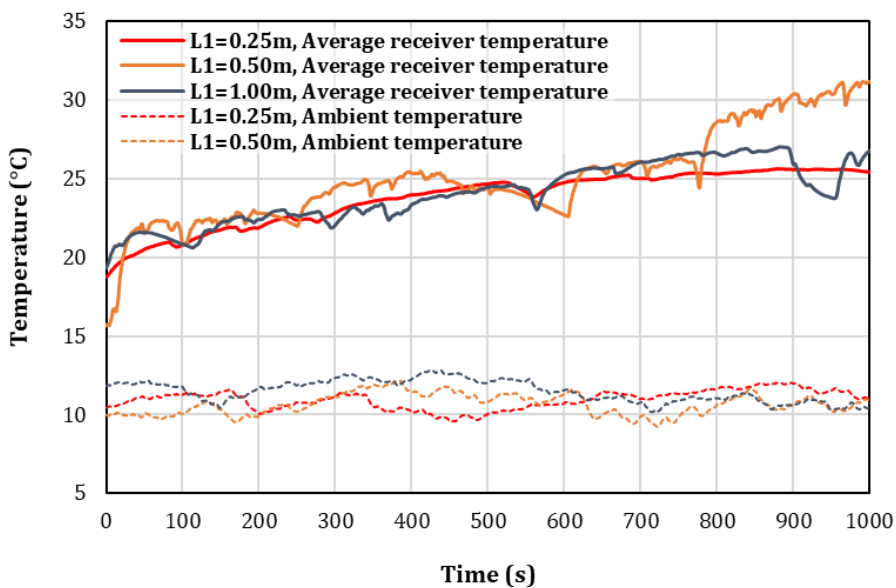


Figure 7-33 Receiver and ambient temperatures recorded (LLBG Prototype Test)

7.3.3 Full-Size LLBG System Test

The ambient temperature and the average receiver back surface temperature are recorded and plotted in Figure 7-34a for the receiver without window test, while for the receiver with the window they are plotted besides the average window temperature in Figure 7-34b. As the prototype-size test, instability in recorded readings is attributed to the lack of ability to trace the sun over the test period. The average measured solar irradiation for the receiver without window test is measured to be found to be 750 W/m^2 . While it has been recorded as 400 W/m^2 for the other two tests with windowed receiver tests.

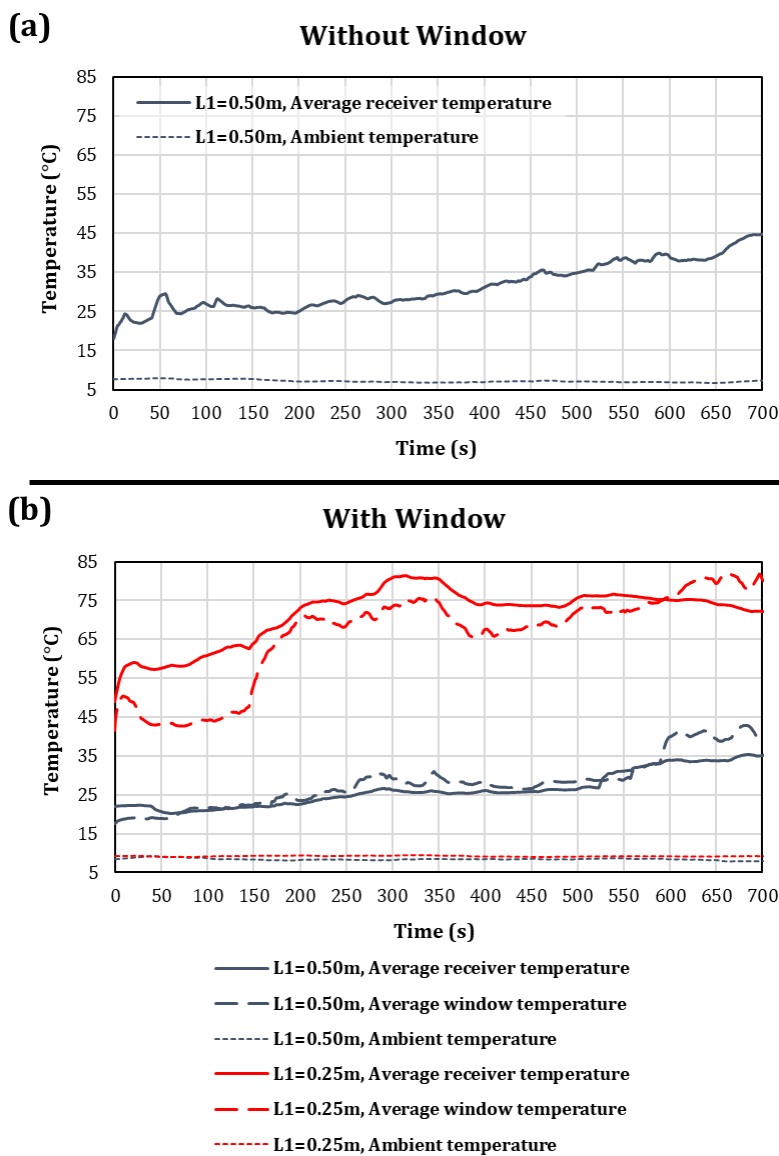


Figure 7-34 Receiver, window and ambient temperatures recorded (LLBG full-size Test)

(a) without window

(b) with window

7.4 Prototype-Size LLBG System Evaluation

The data obtained in Section 6.3.2 is analysed within this section to evaluate performance of the prototype-size LLBG system. This evaluation includes: determination of system efficiency, the amount of reduction in Carbon footprint and the amount of fuel saved due to utilising unit area of the system aperture.

7.4.1 System Efficiency Evaluation

The electromagnetic solar energy incident on the LLBG system passes through an optical system consisting of the front and rear lenses and the control mirror. Lenses transmittances and mirror reflectance represent the major components in calculating the optical efficiency of the LLBG system. In order to convert the electromagnetic energy passed through the optical system into thermal energy, thermal losses comprised within the system, e.g. heating up the lenses and the control mirror, causes a thermal efficiency. The total field efficiency of the LLBG system includes both optical and thermal efficiencies. The flow of the energy through the LLBG system can be illustrated as shown in Figure 7-35.

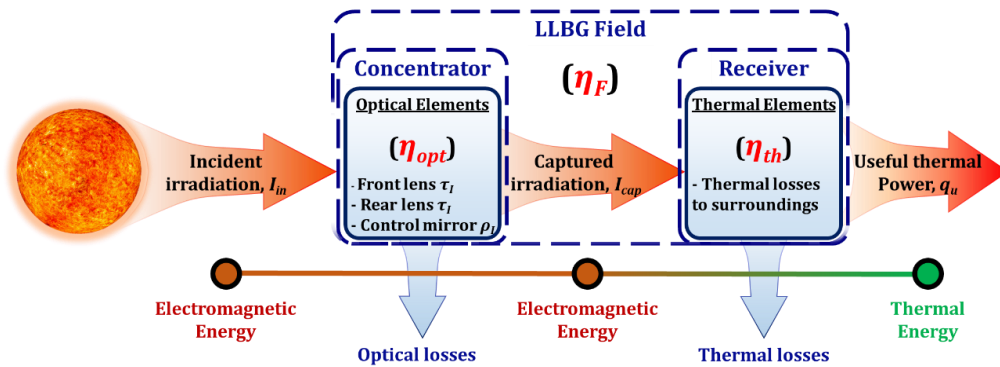


Figure 7-35 Energy flow within the LLBG system

The optical efficiency, η_{opt} , due to optical losses within the LLBG system can be determined from:

$$\eta_{opt} = \tau_{I,1} * \tau_{I,2} * \rho_{I,CM} \quad (7-10)$$

Where $\tau_{I,1}$, $\tau_{I,2}$ and $\rho_{I,CM}$ are the front and rear lens transmittances and control mirror reflectance, respectively, with neglecting lenses reflectance and mirror

absorbance. The total field efficiency, η_F , of the LLBG system can be calculated as follows:

$$\eta_F = \eta_{opt} * \eta_{th} = \frac{Q_u}{I_{in} * A_a} \quad (7-11)$$

Where I_{in} , Q_u and A_a are the input solar irradiation, the useful output thermal power and the front lens clear aperture area, respectively. Thermal efficiency, η_{th} , represents converging the captured electromagnetic energy into thermal energy. As the aim is to evaluate the LLBG ability to convert the incident solar energy into useful thermal energy, regardless the design of the receiver, the gained useful thermal power is monitored by including the receiver thermal losses to surroundings in different forms, as illustrated in Figure 7-36.

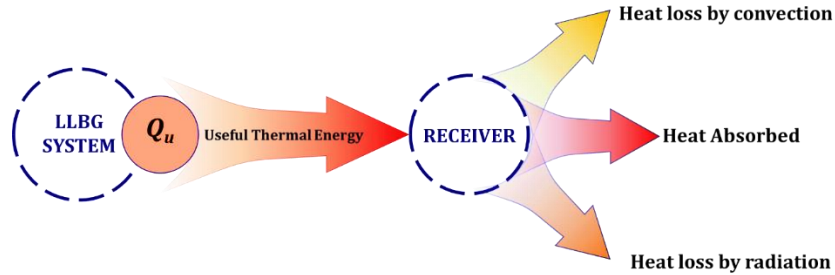


Figure 7-36 Energy flow within the receiver

From Figure 7-36, the useful thermal energy output from the LLBG system can be obtained from:

$$Q_u = [mC_p(T_f - T_i)/t] + [hA(T_s - T_\infty)] + [\varepsilon\sigma A(T_s^4 - T_\infty^4)] \quad (7-12)$$

Where m , C_p , T_i , T_f and t are the receiver mass, heat capacity, initial and final temperatures and the time, respectively. While h , ε , A , T_s and T_∞ are the convective heat transfer coefficient, receiver emissivity, surface area (uninsulated), surface and ambient temperatures, respectively. Applying Equations (7-11) and (7-12) with using experimental data collected in Section 6.3.2, then the LLBG system thermal can be determined and plotted as shown in Figure 7-37 indicating that increasing distance from the mirror is accompanied with decreasing field efficiency. This is due to distributing and attenuating the beam over a larger area, which increases the losses over the path from the mirror to the receiver.

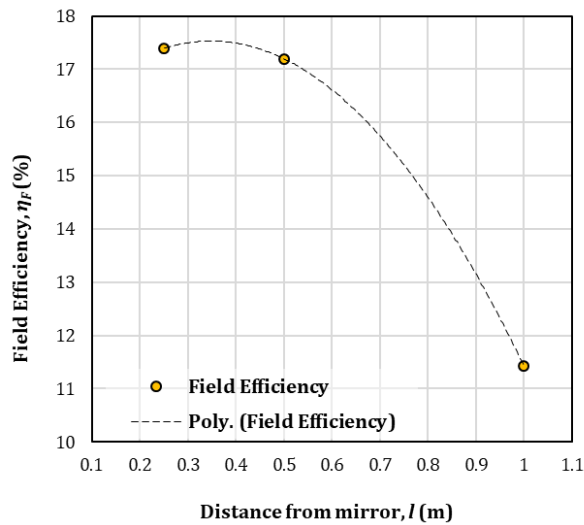


Figure 7-37 Prototype-size LLBG system field efficiency

The 2nd degree polynomial trend line that passes through field efficiency points indicates that the system field efficiency will reach 0.0% at 1.453m from the mirror, which means that after this distance, the beam is carrying only light without useful heat.

Assuming a limitation of keeping the receiver within 0.5m from the mirror, then the average field efficiency will be 17.30%. This value will be utilised later in evaluating process in the upcoming section. In order to investigate the reason behind this lower number, compared to literature, the system optical efficiency is calculated, and then thermal efficiency of the system can be derived.

For the front lens transmittance, it can be assumed to be 81.0%, as the spectral transmittance curve provided by the manufacturer is similar to the PMMA curve plotted in Figure 6-4 (Edmund Optics, 2018a). While the rear lens manufacturer spectral transmittance curve over solar spectral bandwidth (280–2500nm) is plotted in Figure 7-38, with an average LL transmittance of 91.83%. The mirror reflectance is measured using Condor Reflectometer (see Figure 4-7). The output data listed in Table 4-2. Then the average solar weighted reflectance is 78.75%. Based on these data, the prototype-scale LLBG optical efficiency, η_{opt} , is 58.58%, and then its thermal efficiency, η_{th} , is 29.53% within 0.5m from the mirror.

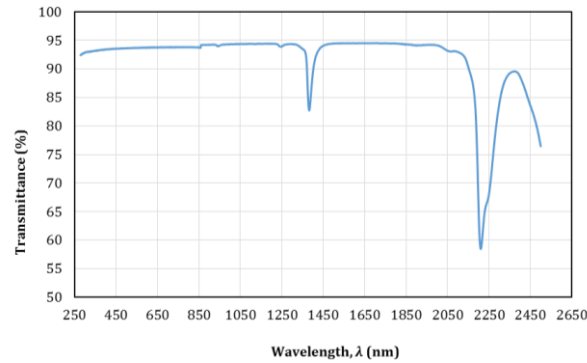


Figure 7-38 Rear lens manufacturer spectral transmittance (280–2500nm)

7.4.2 Reduction in Carbon Footprint and Fuel Consumption

In this section an evaluation model is developed out based on assuming 1m² of aperture is used to replace different prime movers (i.e. steam generator, gas turbine and combined cycle) working fossil fuels (i.e. natural gas and petroleum). The model assumes that the system is receiving an average incident power of 1000W/m² over 5-hours a day, with 330 days of operation per year. The LLBG average field efficiency of 17.30% is utilised to evaluate the amount of thermal energy gained annually for each 1m² of LLBG aperture, E_{th} . It has been calculated through:

$$E_{th} = Q_{th} * (3600s * 5h * 330days) = 5940000 * \eta_F * I_{in} * (1m^2) \quad (7-13)$$

Where Q_{th} is the thermal power gained from incident irradiation, I_{in} , with unit aperture area. It has been found to be 1027.62 MJ/year.

Net calorific value (NCV) of a fuel can be defined as “the quantity of heat evolved by the complete combustion of a unit mass (or unit volume) of the and the products of combustion are let off into the atmosphere” (Palanna, 2009). These values for natural gas and power station petroleum are 35.7 MJ/m³ and 40.7 MJ/kg, respectively (Department for Business Energy Strategy & Industrial, 2017). According to these values, building 1m² of LLBG aperture can save 28.78m³/year and 25.25kg/year of natural gas and petroleum, respectively.

To evaluate the equivalent amount of electrical energy can be produced out of thermal power gained from the LLBG, the Heat Rate term is required to be defined. Heat rate (HR) is a common measure of heat engines efficiency in

converting the energy content of the fuel into power. It can be defined as the amount of thermal energy needed to generate 1 kWh of electricity, which is expressed typically in Btu/kWh (Eydeland and Wolyniec, 2003). However, HR depends on both fuel and prime mover types (EIA, 2017), as listed in Table 7-14.

Table 7-14 Average HRs by fuel and prime mover (EIA, 2017)

Fuel		Natural Gas (Btu/kWh)	Petroleum (Btu/kWh)
Prime mover	Steam Generator	86.7	87.2
	Gas Turbine	87.4	87.7
	Combined Cycle	87.7	87.8

According to these data, the annual electric power can be substituted by utilising 1m² of LLBG aperture is as illustrated in Figure 7-39.

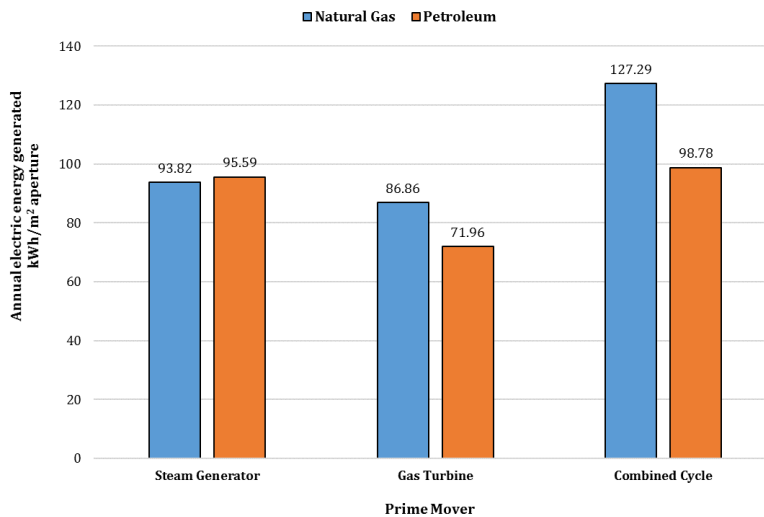


Figure 7-39 Annual electric energy can be generated from 1m² of LLBG aperture

Carbon footprint can be defined as: “the total amount of greenhouse gases produced to directly and indirectly support human activities, usually expressed in equivalent tons of carbon dioxide (CO₂)” (Idowu *et al.*, 2015). Considering Carbon footprints for natural gas and petroleum as 0.1836 and 0.2674 kgCO₂/kWh, respectively (Carbon Trust, 2011), then each unit area of LLBG aperture can reduce Carbon footprint annually by the amounts shown in Figure 7-40.

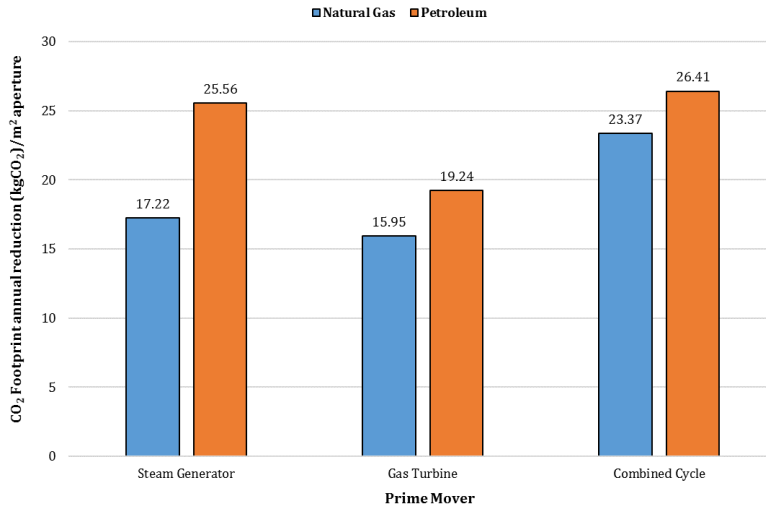


Figure 7-40 Annual Carbon footprint reduction for 1m² of LLBG aperture

7.5 Full-Size LLBG System Evaluation

In this section, the full-size LLBG system performance is evaluated through analysing experimental data to determine the field efficiency, reduction in Carbon footprint and saved amount of fuel per unit aperture area.

7.5.1 System Efficiency Evaluation

Following the same procedure in evaluating the prototype-size LLBG system, experimental data obtained in Section 6.3.3 are used in calculating the full-size LLBG system field efficiency applying Eq. (7-11). However, using the insulating gasket material (illustrated in Figure 6-71) affects the value of front lens clear aperture area, A_a , as part of the incident radiation on the front lens is already blocked by the mask before affecting the system. Therefore, it is required to evaluate the equivalent effective aperture diameter, D_{eq} , which indicates the diameter that receives all incident solar radiation that can pass through the masking material to the rear lens and generates the beam. According to geometry illustrated in Figure 7-41, D_{eq} , can be obtained from:

$$D_{eq} = D_{hole} + 2x_1 \tan \bar{\alpha} = D_{hole} + D_1 - D_s(x_1) \quad (7-14)$$

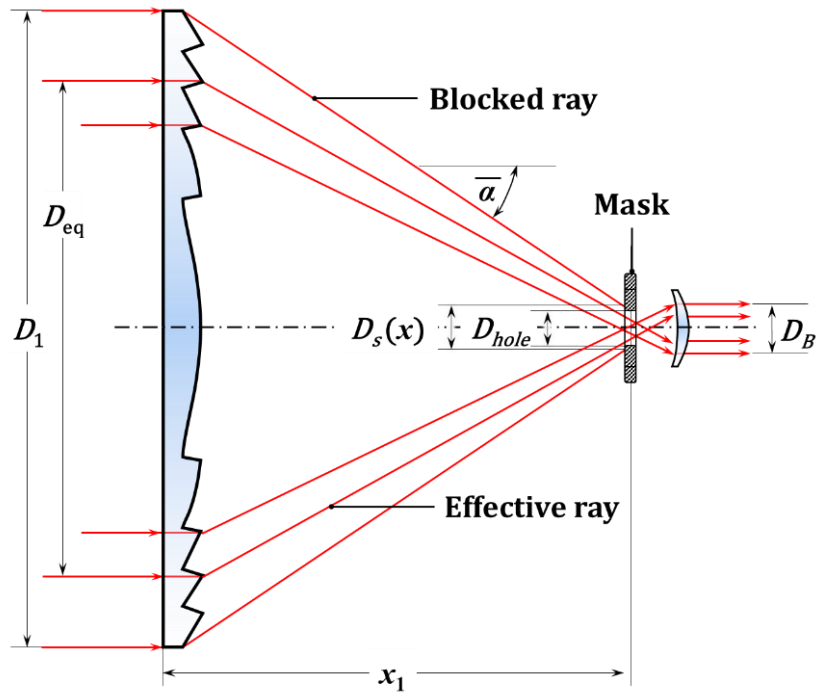


Figure 7-41 Schematic diagram of geometry explaining equivalent diameter

Where D_1 , D_{hole} and $D_s(x_1)$ are front lens, gasket mask hole diameters and spot diameter at certain distance, x_1 , respectively. To calculate spot diameter, $D_s(x_1)$, the MATLAB code developed in Section 6.1.4 is applied for the front lens, with an average R_C of 18.11m (corresponding measured 45°-inclined lens radius of curvature measured in Section 4.2.3). The results are illustrated in Figure 7-42, where the mask is placed at 1.22m from the front lens plane. From Eq. (7-14), the equivalent effective aperture diameter, D_{eq} , is found to be 0.890339m, leading to an effective clear aperture area, A_a , of 0.623m² to be used in Eq. (7-11).

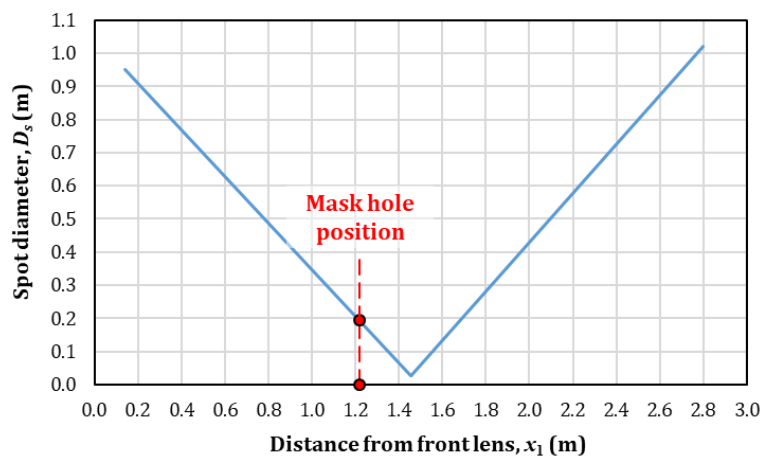


Figure 7-42 MATLAB code output predicting spot diameter at x_1

The system field efficiency is then calculated for each test, as plotted in Figure 7-43, which indicates higher efficiency of 26.14% for windowed receiver located at a 0.25m from the control mirror. While pushing the receiver further away drops down the field efficiency to record 17.65% at 0.5m. Moreover, using non-windowed receiver showed lower efficiency when placed at the same position, as it showed 12.89% for 0.5m away from the control mirror. The reason behind this may be attributed to unaccounted thermal losses within the receiver when the window is removed compared to the windowed case as more heat is captured and can be monitored.

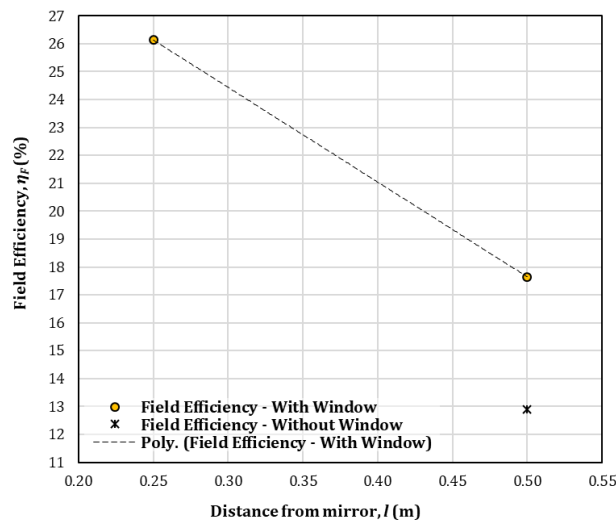


Figure 7-43 Full-size LLBG system field efficiency

To allow comparison with the prototype-size system, the receiver is assumed to be located at 0.5m from the control mirror, with field efficiency of 17.65%. This value will be used later in evaluating process in the upcoming section. In order to neutralise the effect of optical efficiency of the system components, thermal efficiency is required to be calculated for the full-size system and to be compared with the prototype-size case.

For the front lens transmittance, from measurements recorded in Section 7.1.2 which is found to be 74.18%, as the spectral transmittance curve provided by the manufacturer is similar to the PMMA curve plotted in Figure 6-4. While the rear lens manufacturer spectral transmittance curve over solar spectral bandwidth (280–2500nm) is plotted in Figure 7-38, with an average transmittance of 91.83%. The mirror reflectance is measured using Condor Reflectometer (see

Figure 4-7). The output data listed in Table 4-2. Then the average solar weighted reflectance is 87.68%. Based on these data, the prototype-scale LLBG optical efficiency, η_{opt} , is 59.73%, and then its thermal efficiency, η_{th} , is 29.54% within 0.5m from the mirror. This value is approximately the same as the one obtained for the prototype-size system (29.53%). This indicates that employing Fresnel geometry leads to internal thermal losses leading to lowering down the system thermal efficiency, regardless the system size.

7.5.2 Reduction in Carbon Footprint and Fuel Consumption

Using the same model applied in Section 7.4.2, using the same assumptions, an evaluation of using 1m² of aperture to replace different prime movers (i.e. steam generator, gas turbine and combined cycle) working fossil fuels. Considering LLBG having a field efficiency of 17.65% and by substitution in Eq. (7-13), then the amount of thermal energy gained annually for each 1m² of LLBG aperture, E_{th} , is found to be **1048.41 MJ/year**.

According to NCV values of considered fuels (i.e. natural gas and petroleum), building 1m² of LLBG aperture can save 29.37m³/year and 25.76kg/year of natural gas and petroleum, respectively. From values of HR listed in Table 7-14, the annual electric power can be substituted by utilising 1m² of LLBG aperture is as illustrated in Figure 7-44.

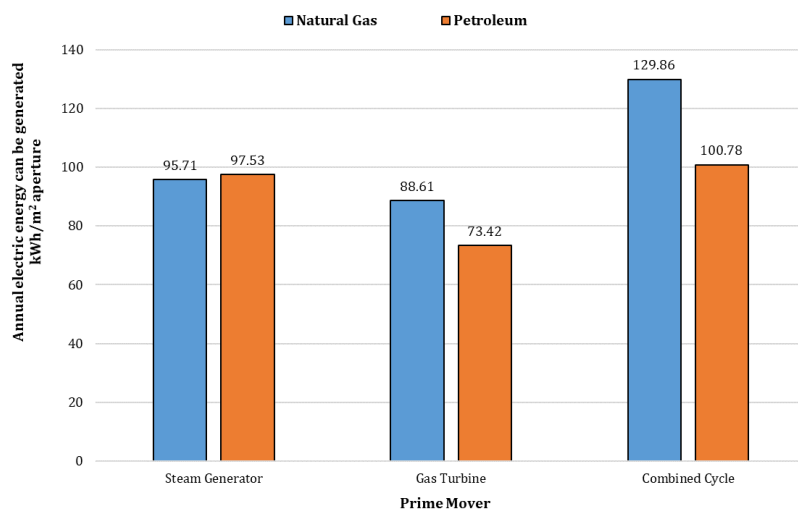


Figure 7-44 Annual electric energy can be generated from 1m² of LLBG aperture

Based on Carbon footprints of considered fuels, as mentioned in Section 7.4.2, then each unit area of LLBG aperture can reduce Carbon footprint annually by the amounts shown in Figure 7-45.

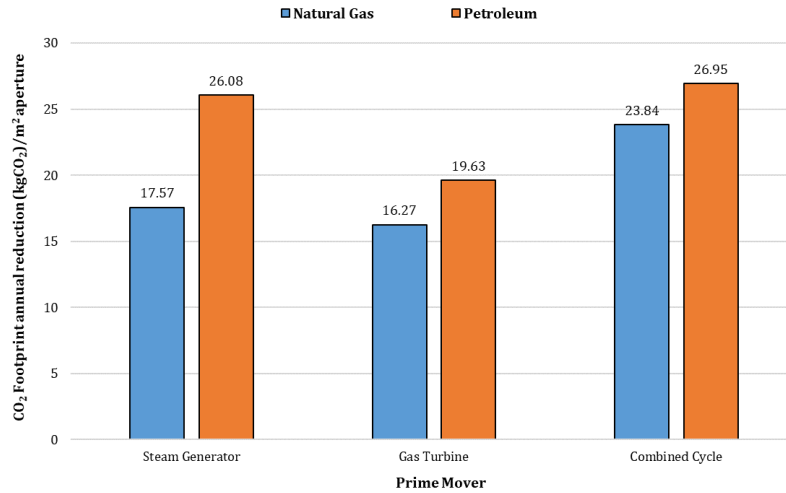


Figure 7-45 Annual Carbon footprint reduction for 1m² of LLBG aperture

7.6 Summary

Results of numerical and experimental work introduced in chapters 5 and 6 are displayed and discussed in this chapter. For solar simulators, using the metal halide lamp showed better match with solar spectrum over the full spectral bandwidth compared to tungsten halogen light source. Moreover, the average irradiation over an area of 0.2×0.2 m² is 209.71 W/m² and 177.53 W/m² for the metal halide and tungsten halogen cases, respectively. The solar simulator has been used to measure the full-size LLBG front lens transmittance and to validate the numerical model introduced in Chapter 6 of the rear lens mount in the LLBG system.

Tests on the LLBG system has been carried out to investigate the performance of both prototype- and full-size LLBG systems. Through these tests, the optical analysis code developed by MATLAB has been experimentally validated. This validated code is then applied for further investigation of the key parameters influencing the LLBG system performance. In both prototype- and full-size LLBG systems, field, optical and thermal efficiencies have been calculated and thermal conversion efficiency of both systems was around 29.5%. Thermal efficiency is used to compare the two systems as it neutralises the influence of optical

components efficiency in generating and transferring the beam. The reason behind such low conversion efficiency is attributed to using Fresnel geometry for the front lens of the system, according to results obtained in Section 7.2.3.4. These results indicated that a beam diameter is increased by 150% for identical case tested experimentally by (Salem, Tawfik and Hamed, 2010) but with replacing the front bi-convex lens in their experiment with an identical Fresnel lens geometry. Therefore, the beam generated with both prototype- and full-size LLBG systems is found to be thermally efficient within a short distance of approximately 0.5m. However, detailed investigation of Fresnel-based LLBG system has been carried out to determine different probable ways to minimise the deviation of the output generated beam. Positioning the rear lens at the optimum position is found to be critical in generating a more stable, collimated beam over IR-zone compared to VIS and UV region, due to less deviation angle for such bandwidth. Despite, beam deviation angle showed low sensitivity to front lens curvature due to its buckling effect, results indicated that the more front lens curvature, the less deviation angle occurs. Moreover, a dimensionless number, named as LLBG#, merging down front–rear lenses geometrical details, is defined in Section 7.2.3.6. A relation between this number and the beam deviation angle was developed, allowing estimation of average beam deviation angle for front–rear lenses combinations with LLBG#s > 0 over VIS–IR spectrum, if the front lens is designed for GO-configuration.

According to thermal performance tests carried out using the prototype- and full-size LLBG systems, it has been found that using such systems is more feasible in replacing combined cycles compared to steam generators or gas turbines. Each 1m² of LLBG aperture was found to save up to 26.95 and 23.84 kgCO₂ annually for combined cycle prime movers that are fuelled by petroleum and natural gas, respectively. In terms of annual fuel consumption savings, employing LLBG can save up to 25.76 kg/year and 29.37m³/year of petroleum and natural gas, respectively, for unit aperture area of the LLBG system. These values are based on assuming the LLBG system receiving an average incident power of 1kW/m² over 5-hours a day, with 330 days of operation per year.

8 CONCLUSIONS AND FURTHER WORK

The present study aimed to reduce the Carbon footprint of currently existing fossil-fuelled power plants through hybridising them with solar energy. The first section in this chapter covers conclusions related to each objective of the study.

8.1 Conclusions

In this section, the basic objectives discussed in Section 3.2 are displayed to explain how they covered within the thesis.

8.1.1 Design and build a sun simulator device

This objective is covered and tested in Chapter 5, and results are displayed in Chapter 7 (Section 7.1). Using a metal halide lamp shows better match with solar spectrum over full spectral bandwidth compared to tungsten halogen light source. However, for thermal testing, it is more recommended to use a dimmable tungsten halogen lamp as it gives a good controllable output spectrum over the IR zone.

8.1.2 Build and validate numerical models to design an LLBG solar concentrator

Chapter 6 dealt with this objective, while the numerical and experimental results are presented in Chapter 7 (Section 7.2). To achieve this objective, the LLBG design phase included investigation of different front and rear lenses geometries and materials through a series of studies, including thermal, optical, cost and manufacturing studies. According to these studies, PMMA-Fresnel geometry was approved to be used for the front lens as it represented the most cost-effective option for large-size aperture, with enhanced transmittance, compared to usage of PC. For the rear lens, based on thermal study, it has been found that using positive meniscus geometry allows higher CRs, compared to both plano- and bi-convex geometries. Based on both thermal and optical studies of transparent materials, it has been found that SiO₂ represents the optimum material for the rear lens.

8.1.3 Design and build an LLBG solar concentrator

The details of the procedure followed in designing and sizing the full-size LLBG system is introduced in Section 6.2. It showed how various design concepts are refined through a Pugh matrix and how components are sized. It also covers the tracking system design to control the full-size system.

8.1.4 Assess the performance of this concentrating technology

This objective was covered through a series of experiments designed and described in Section 6.3, while their results are discussed in Section 7.3. According to these results, the prototype- and full-size LLBG systems showed average field efficiencies of 17.30% and 17.65%, respectively, at 0.5m from the control mirror. By neutralising the effect of different optical efficiencies of systems components, it has been found that a thermal conversion efficiency of 29.5% was recorded for both systems. According to these values, that building unit aperture area of the LLBG system can save up to 25.76 kg/year and 29.37m³/year of petroleum and natural gas, respectively, which used in producing electric power through conventional power generation systems. This can lead to reducing annual Carbon footprint by 26.95 and 23.84 kgCO₂ for of such power generation systems that use combined cycles as prime movers powered by petroleum and natural gas, respectively.

8.1.5 Assess performance limitations and system implementation obstacles

Through building, testing and investigating the Fresnel-based LLBG, the following obstacles and limitations have been faced:

- Using large front Fresnel lens can lead to its buckling under either its weight load or due to thermal expansion (Section 4.2.3). This can cause changes in the front lens focal length position (Section 6.1.4.2). Using supporting ribs or dividing the aperture into sub-lenses is recommended.
- Using a glass-based control mirror is found to be a problem, especially in cold weather as it can be damaged due to thermal stresses (Section 6.3.3).

Therefore, it is recommended to replace it with Aluminium-based reflector which can withstand high thermal stress with acceptable level of reflectance.

- Material and design of the rear lens mount is found to be critical, as it can be targeted by the high concentrated power causing its damage (Section 6.3.3). Using more robust material (such as ceramic) and ensuring avoidance of blocking the concentrated rays' path are highly recommended.
- Using a Fresnel geometry for the front lens bounds the optical efficiency of the LLBG system due to its optical losses, such as reflection losses. For example, the ideal optical efficiency of a typical PMMA Fresnel lens is found to be 74.16%, considering only material transmittance and the first-stage reflection losses (Section 6.1.2.2).
- Another drawback of using a Fresnel front lens is the increase deviation angle of the generated beam, as beam diameter is increased by 150% at some stage compared to literature (Section 7.2.3.4). Consequently, this limits the distance that the generated beam can travel effectively. Moreover, this obstacle reduces the system efficiency.

8.2 Further Work

Based on current study, the following further work is recommended to be covered:

- Study the degradation of the front Fresnel lens in the real environment.
- Make a robust design for the rear lens mount.
- Make an optical design for the front Fresnel lens to minimise the generated beam deviation.

9 REFERENCES

2011 ASHRAE Handbook - Heating, Ventilating, and Air-Conditioning Applications. I-P Ed. (2011) American Society of Heating, Refrigerating and Air-Conditioning Engineers, Inc. American Society of Heating, Refrigerating and Air-Conditioning Engineers, Inc.

Aalco Metals Ltd (2013) *Aluminium Alloy 6082 - T6*. Available at: http://www.aalco.co.uk/datasheets/Aluminium-Alloy-6082-T6T651-Plate_148.ashx.

Abbas, R. *et al.* (2012) 'Solar radiation concentration features in Linear Fresnel Reflector arrays', *Energy Conversion and Management*, 54(1), pp. 133–144. doi: 10.1016/j.enconman.2011.10.010.

Abengoa Solar (2014) *Condor Reflectometer*. Available at: http://www.abengoasolar.com/web/en/Productos_y_Servicios/Equipos_OM/Reflectometro_Condor/ (Accessed: 15 February 2018).

Advanced Research Systems (2016) *Window Materials*-. Available at: <http://www.arscryo.com/Products/cryogenic-accessories/cryostat-window-materials.html> (Accessed: 9 April 2017).

Agrawal, B. and Tiwari, G. N. (2010) 'Solar Radiation and its Availability on Earth', in *Building Integrated Photovoltaic Thermal Systems: For Sustainable Developments*. Royal Society of Chemistry, pp. 1–49.

Ahmadi, H. (2015) *HV Igniter*. Available at: http://www.ece.ubc.ca/~hameda/igniter_for_xenon_short-arc_lamp.htm (Accessed: 9 November 2016).

Aichmayer, L. (2011) *Solar Receiver Design and Verification for Small Scale Polygeneration Unit*. KTH School of Industrial Engineering and Management, Sweden.

Al-Jumaily, K. E. J. and Al-Kaysi, M. K. A. (1998) 'The study of the performance and efficiency of flat linear Fresnel lens collector with sun tracking system in Iraq', *Renewable Energy*, 14(1–4), pp. 41–48. doi: 10.1016/S0960-

1481(98)00045-7.

ALANOD (2010) *MIRO-SUN®*. Available at: https://www.alanod.com/wp-content/uploads/2014/12/MIRO_SUN_engl_101112.pdf.

Aldrich, R. and Parello, J. (2010) *IP-Enabled Energy Management: A Proven Strategy for Administering Energy as a Service*. Indianapolis, Indiana: Wiley Publishing.

Always Engineering (2015) *Always Ball Transfer Units: Catalogue 14*. Birmingham, UK. Available at: <http://www.always.co.uk/brochures/CAT14August2015Revisions.pdf>.

Alxneit, I., Dibowski, G. and Facilities, S. (2011) *Solar Simulator Evaluation Report*. Project SFERA, PSI and DLR.

Ametek (2016) *Introduction to Atlas SolarConstant Series 4000 watt Sun Sources*. Available at: <http://www.lasermotion.com/atlassun.html#atlas1> (Accessed: 9 November 2016).

Anderson, D. and Burge, J. (2001) 'Optical Fabrication', in *Handbook of Optical Engineering*. 1st Ed. CRC Press.

Andreev, V. M. *et al.* (2005) 'Thermophotovoltaic Converters With Solar Powered', in *20th European Photovoltaic Solar Energy Conference*. Barcelona Spain, pp. 6–10.

Andreev, V. M. *et al.* (2006) 'Solar Thermophotovoltaic Converter with Fresnel Lens and GaSb Cells', in *2006 IEEE 4th World Conference on Photovoltaic Energy Conference*. Waikoloa, HI: IEEE, pp. 644–647. doi: 10.1109/WCPEC.2006.279537.

Andreev, V. M. *et al.* (2007) 'Solar Thermophotovoltaic Converters Based on Tungsten Emitters', *Journal of Solar Energy Engineering*, 129(3), pp. 298–303. doi: 10.1115/1.2734576.

Andrews, A. C. and Jones, W. H. S. (1956) *Natural History, Volume VII*. Harvard University Press.

Any Lamp BV (2016a) *Philips HPI-T 2000W 642 E40 220V*. Available at:

<https://www.any-lamp.co.uk/philips-hpi-t-2000w-646-e40-220v-crp-master>
(Accessed: 9 November 2016).

Any Lamp BV (2016b) *Philips SI 52 220-240V 50/60Hz*. Available at:
<https://www.any-lamp.co.uk/philips-si-52-220-240v-50-60hz> (Accessed: 9
November 2016).

Any Lamp BV (2017) *Philips HID-HighPower BHL 2000 L78*. Available at:
[https://www.any-lamp.co.uk/philips-hid-highpower-bhl-2000-l78-230-240v-50hz-
hp-317](https://www.any-lamp.co.uk/philips-hid-highpower-bhl-2000-l78-230-240v-50hz-hp-317) (Accessed: 25 October 2017).

Ashcroft, N. W. (2016) *Solid State Physics*. 1st Ed. Content Technologies, Inc.

ASTM Standard E490 (2000) *Standard Solar Constant and Zero Air Mass Solar Spectral Irradiance Tables*. West Conshohocken, Pennsylvania.

ASTM Standard G173-03 (2012) *Standard Tables for Reference Solar Spectral Irradiances: Direct Normal and Hemispherical on 37° Tilted Surface*. West Conshohocken, Pennsylvania.

Atlas Material Testing Technology (2011) *Network of Weathering Products & Services*.

Avison, J. (1989) *The World of Physics*. 2nd Ed. Oxford University Press.

Balmer, R. T. (2011) *Modern Engineering Thermodynamics*. Academic Press.

Barnes, N. P. and Remelius, D. K. (1985) 'Argon arc lamps', *Applied Optics*, 24(13), pp. 1947–1949.

Basak, D. and Sen, S. K. (1995) 'Determination of optical constants of Y2O3 films from reflectance and transmittance data using different approaches', *Materials Letters*, 25(1–2), pp. 9–12. doi: 10.1016/0167-577X(95)00146-8.

Beal, R. M. *et al.* (2012) 'High Intensity Light-Cycling of Hcpv Cell Assemblies Using the Xt-30 Solar Simulator', in *Photovoltaic Module Reliability Workshop 2012*. NREL. Available at:
http://www1.eere.energy.gov/solar/pdfs/pvmrw12_poster_cp_v_beal.pdf.

Becker, H. and Heim, U. (2000) 'Hot embossing as a method for the fabrication

- of polymer high aspect ratio structures', *Sensors and Actuators A: Physical*, 83(1–3), pp. 130–135. doi: 10.1016/S0924-4247(00)00296-X.
- Beer, F. P. *et al.* (2012) *Mechanics of Materials*. 6th Ed. McGraw-Hill Companies, Inc.
- Beeson, E. J. G. (1978) 'The CSI lamp as a source of radiation for solar simulation', *Lighting Research and Technology*, 10, pp. 164–166.
- Beghi, G. (1983) *Performance of Solar Energy Converters: Thermal Collectors and Photovoltaic Cells*. Dordrecht, Holland: D. Reidel Publishing Company. doi: 10.1007/978-94-011-9813-4.
- Belhomme, B. *et al.* (2009) 'A New Fast Ray Tracing Tool for High-Precision Simulation of Heliostat Fields', *Journal of Solar Energy Engineering*, 131(3), p. 31002. doi: 10.1115/1.3139139.
- Bendler, J. T. (1999) *Handbook of Polycarbonate Science and Technology*. 1st Ed. CRC Press.
- Benitez, P. *et al.* (2014) 'Fabrication and Tolerances of Optics for High Concentration Photovoltaics', in *Classical Optics 2014*. Hawaii, USA: OSA. doi: 10.1364/OFT.2014.OTu1B.3.
- Bennett, J. M. . (2010) 'Polarization', in *Handbook of Optics*. 3rd Ed. McGraw-Hill.
- Benya, J. R. and Leban, D. J. (2011) *Lighting Retrofit and Relighting: A Guide to Energy Efficient Lighting*. 1st Ed. Wiley.
- Biansan, J.-M. (2018) *OptGeo (in French)*. Available at: <http://jeanmarie.biansan.free.fr/optgeo.html> (Accessed: 11 March 2018).
- Bickler, D. (1962) 'The simulation of solar radiation', *Solar Energy*, 6(2), pp. 64–68.
- Bird, R. E., Hulstrom, R. L. and Lewis, L. J. (1983) 'Terrestrial Solar Spectral Data Sets', *Solar Energy*, 30(6), pp. 563–573.
- Blair, N. *et al.* (2014) *System Advisor Model, SAM 2014.1.14: General*

Description, NREL/TP-6A20-61019. doi: 10.2172/1126294.

Blanco, M. *et al.* (2011) 'Results of the empirical validation of Tonatiuh at Mini-Pegase CNRS-PROMES facility', in *SolarPACES*. Granada, Spain.

Bobkova, E. V. *et al.* (2006) 'Effect of chromatic aberration on the concentration of solar radiation by fresnel lenses', *Technical Physics Letters*, 32(12), pp. 1039–1042. doi: 10.1134/S1063785006120133.

Bode, S.-J. and Gauché, P. (2012) 'Review of optical software for use in concentrating solar power systems', in *The 1st Southern African Solar Energy Conference*. Technopark, Stellenbosch, pp. 1–8. Available at: <http://blogs.sun.ac.za/sterg/files/2012/06/CSP-06.pdf>.

Boes, E. C. (1990) 'Photovoltaic concentrator technology development', in *IEEE Conference on Photovoltaic Specialists*. IEEE, pp. 944–951. doi: 10.1109/PVSC.1990.111758.

Bommel, W. van (2014) 'Halogen Lamp', *Encyclopedia of Color Science and Technology*. Springer New York. doi: 10.1007/978-3-642-27851-8_126-8.

Bortolini, M., Gamberi, M. and Graziani, A. (2013) 'Ray-tracing model and Monte Carlo simulation for the design of the concentrating solar simulator reflector', *International Journal of Modern Engineering Research*, 3(1), pp. 13–15.

Bosch Rexroth AG (2006) *Rexroth Ball Transfer Units*. Schweinfurt, Germany. Available at: https://md.boschrexroth.com/modules/BRMV2PDFDownload-internet.dll/r310en_2910_2006_11.pdf?db=brmv2&lvid=117278&mvid=12235&clid=20&sid=20771C3D82014F508622E8F928C33B63.borex-tc&sch=M&id=12235,20,117278.

Bosch Rexroth AG (2015) *Basic Mechanic Elements*. Stuttgart, Deutschland. Available at: https://md.boschrexroth.com/modules/BRMV2PDFDownload-internet.dll/3842540392_2015-09_MGE_13_1_EN-US_web.pdf?db=brmv2&lvid=1193781&mvid=12235&clid=20&sid=79065F69341C4BD3FC8EECAF5BB4C3D3.borex-tc&sch=M&id=12235,20,1193781.

Boudeile, J. *et al.* (2008) 'Thermal behaviour of ytterbium-doped fluorite crystals under high power pumping', *Optics Express*, 16(14), p. 10098. doi: 10.1364/OE.16.010098.

Boxwell, M. (2017) *Solar Electricity Handbook: 2017 Edition: A simple, practical guide to solar energy - designing and installing solar photovoltaic systems*. Birmingham, UK: Greenstream Publishing.

Brancati, R. *et al.* (2013) 'Experimental Investigation of the Performances of a WRS-BTU Seismic Isolator', in *Proceedings of the World Congress on Engineering*. London, UK, pp. 1–6.

Brennesholtz, M. S. and Stupp, E. H. (2008) *Projection Displays*. 2nd Ed. Wiley-Blackwell.

De Brey, H., Rinia, H. and Van Weenen, F. (1974) 'Fundamentals for the Development of the Philips Air Engine', *Philips Technical Review*, 9, pp. 97–124.

Brinksmeier, E. *et al.* (2004) 'Design and Manufacture of Aspheric Lenses for Novel High Efficient Photovoltaic Concentrator Modules', in *the ASPE 19th Annual Meeting*. Orlando, USA. Available at: http://www.aspe.net/publications/Annual_2004/POSTERS/5PROC/2MACH/1575.PDF.

Brinkworth, B. J. (1980) 'Results of solar heating experiments', *Philosophical Transactions of the Royal Society of London A: Mathematical, Physical and Engineering Sciences*, 295(1414), pp. 361–373.

Britton Timbers (2016a) *American Ash*. Available at: <http://www.brittontimbers.com.au/timber/american-ash> (Accessed: 5 August 2016).

Britton Timbers (2016b) *American Black Walnut*. Available at: <http://www.brittontimbers.com.au/timber/american-black-walnut> (Accessed: 5 August 2016).

Britton Timbers (2016c) *American Cherry*. Available at:

<http://www.brittontimbers.com.au/timber/american-cherry> (Accessed: 5 August 2016).

Britton Timbers (2016d) *American White Oak*. Available at: <http://www.brittontimbers.com.au/timber/american-white-oak> (Accessed: 5 August 2016).

Britton Timbers (2016e) *European Beech*. Available at: <http://www.brittontimbers.com.au/timber/european-beech> (Accessed: 5 August 2016).

Britton Timbers (2016f) *European Oak*. Available at: <http://www.brittontimbers.com.au/timber/european-oak> (Accessed: 5 August 2016).

Bruce, W. (1999) 'Science Makes a Better Lighthouse Lens', *Smithsonian Magazine*, August, p. 30. Available at: <http://www.smithsonianmag.com/science-nature/science-makes-a-better-lighthouse-lens-170677431/?no-ist>.

Burhan, M., Shahzad, M. W. and Ng, K. C. (2018) 'Hydrogen at the rooftop : Compact CPV-hydrogen system to convert sunlight to hydrogen', *Applied Thermal Engineering*. Elsevier Ltd, 132, pp. 154–164. doi: 10.1016/j.applthermaleng.2017.12.094.

Burisch, M. *et al.* (2015) 'Experimental validation of theoretical heliostat wind loads', *Energy Procedia*, 69, pp. 50–59. doi: 10.1016/j.egypro.2015.03.007.

Candelaria, M. (2013) *Concentrating Solar Power: Mirrors or Fresnel Lenses*. Available at: http://www.novuslight.com/mirrors-vs-fresnel-lenses-for-concentrating-solar-power_N1760.html (Accessed: 2 May 2014).

Carbon Trust (2011) *Conversion Factors: Energy and carbon conversions*. Available at: https://www.carbontrust.com/media/18223/ctl153_conversion_factors.pdf.

Casella, F., Casati, E. and Colonna, P. (2014) 'Optimal Operation of Solar Tower Plants with Thermal Storage for System Design', *IFAC Proceedings*

Volumes. IFAC, 47(3), pp. 4972–4978. doi: 10.3182/20140824-6-ZA-1003.02622.

Causon, D. M., Mingham, C. G. and Qian, L. (2011) *Introductory Finite Volume Methods for PDEs*. 1st Ed. Bookboon.

Cengel, Y. A. (2003) *Heat Transfer: A Practical Approach*. 2nd edn. McGraw-Hill.

Çengel, Y. and Boles, M. (2010) *Thermodynamics: An Engineering Approach*. 7th Ed. McGraw-Hill Higher Education.

Chaanaoui, M., Vaudreuil, S. and Bounahmidi, T. (2016) 'Benchmark of Concentrating Solar Power Plants: Historical, Current and Future Technical and Economic Development', *Procedia Computer Science*. Elsevier Masson SAS, 83, pp. 782–789. doi: 10.1016/j.procs.2016.04.167.

Chance, K. V. and Spurr, R. J. D. (1997) 'Ring effect studies: Rayleigh scattering, including molecular parameters for rotational Raman scattering, and the Fraunhofer spectrum', *Applied Optics*, 36(21), pp. 5224–5230. doi: 10.1364/AO.36.005224.

Chiva Segura, J., Lehmkuhl Barba, O. and Oliva Llena, A. (2012) 'Detailed numerical model for the receiver of a solar power tower plant', in *Proceedings of SolarPACES 2012*. Marrakech, Morocco, pp. 1–6. Available at: <https://upcommons.upc.edu/handle/2117/111192#.WqUeLcqW9ol>.mendeley.

Choi, Y. *et al.* (1996) 'Installation and preliminary operation of a solar thermal-electric propulsion system', in *27th Plasma Dynamics and Lasers Conference*. New Orleans, USA: American Institute of Aeronautics and Astronautics, pp. 1–9. doi: 10.2514/6.1996-2321.

Chong, K. *et al.* (2017) 'Design and construction of active daylighting system using two-stage non-imaging solar concentrator', *Applied Energy*. Elsevier Ltd, 207, pp. 45–60. doi: 10.1016/j.apenergy.2017.05.188.

Chow, S. *et al.* (2010) 'Thermal test and simulation of alumina receiver with high efficiency multi-junction solar cell for concentrator systems', in Schriemer, H. P.

and Kleiman, R. N. (eds) *Photonics North 2010*. Niagara Falls, Canada: SPIE, p. 775035. doi: 10.1117/12.872894.

Chu, Y. (2011) *Review and Comparison of Different Solar Energy Technologies*, Global Energy Network Institute. Available at: <http://66.240.244.113/globalenergy/research/review-and-comparison-of-solar-technologies/Review-and-Comparison-of-Different-Solar-Technologies.pdf>.

Churchill, S. W. and Chu, H. H. S. (1975) 'Correlating equations for laminar and turbulent free convection from a vertical plate', *International Journal of Heat and Mass Transfer*, 18(11), pp. 1323–1329. doi: 10.1016/0017-9310(75)90243-4.

Churchill, S. W. and Ozoe, H. (1973) 'Correlations for Laminar Forced Convection with Uniform Heating in Flow over a Plate and in Developing and Fully Developed Flow in a Tube', *Journal of Heat Transfer*, 95(1), pp. 78–84. doi: 10.1115/1.3450009.

Cicerone, R. J. (2000) 'Human forcing of climate change: Easing up on the gas pedal', in *Proceedings of the National Academy of Sciences*, pp. 10304–10306. doi: 10.1073/pnas.97.19.10304.

Cleveland, C. J. and Morris, C. G. (2013) *Handbook of Energy: Chronologies, Top Ten Lists, and Word Clouds*. 1st Ed. Elsevier Science.

Codd, D. S. *et al.* (2010) 'A low cost high flux solar simulator', *Solar Energy*, 84(12), pp. 2202–2212. doi: 10.1016/j.solener.2010.08.007.

Codd, D. S. (2011) *Concentrated Solar Power on Demand by*. Massachusetts Institute of Technology.

Collado, F. J. (2008) 'Quick evaluation of the annual heliostat field efficiency', *Solar Energy*, 82(4), pp. 379–384. doi: 10.1016/j.solener.2007.10.007.

Collares-Pereira, M. (1979) 'High temperature solar collector with optimal concentration: Non-focusing fresnel lens with secondary concentrator', *Solar Energy*, 23(5), pp. 409–420. doi: 10.1016/0038-092X(79)90149-X.

Colomer, G. *et al.* (2014) 'Advanced CFD & HT numerical modeling of solar tower receivers', *Energy Procedia*, 49, pp. 50–59. doi:

10.1016/j.egypro.2014.03.006.

COMSOL (2018) *COMSOL Multiphysics: Release Notes*. Available at: <https://www.comsol.com/support/releasenotes/> (Accessed: 11 March 2018).

Corning Incorporated (2008) *ULE® Corning Code 7972 Ultra Low Expansion Glass, Corning Incorporated*. New York, USA. Available at: <http://www.corning.com/media/worldwide/csm/documents/D20FD2EA-7264-43DD-B544-E1CA042B486A.pdf>.

Cotal, H. and Sherif, R. (2005) 'The effects of chromatic aberration on the performance of GaInP/GaAs/Ge concentrator solar cells from Fresnel optics', in *Conference Record of the Thirty-first IEEE Photovoltaic Specialists Conference, 2005*. FL, USA: IEEE, pp. 747–750. doi: 10.1109/PVSC.2005.1488240.

CPV Consortium (2018) *Golmud 2*. Available at: <http://cpvconsortium.org/projects/21> (Accessed: 8 March 2018).

Craig, K., Gauché, P. and Kretzschmar, H. (2014) 'Optimization of Solar Tower Hybrid Pressurized Air Receiver Using CFD and Mathematical Optimization', *Energy Procedia*, 49, pp. 324–333. doi: 10.1016/j.egypro.2014.03.035.

Craig, R. A. (2010) *Investigating the use of Concentrated Solar Energy to Thermally Decompose Limestone*. The University of Adelaide.

Crystran (2017) *Optical Glass (N-BK7 and others)*. Available at: <https://www.crystran.co.uk/optical-materials/optical-glass-n-bk7-and-others> (Accessed: 9 April 2017).

CSP-World (2013) *Reliance Power begins pre-commissioning phase of 100 MW CSP Fresnel plant*. Available at: <http://csp-world.com/news/20131129/001265/reliance-power-begins-pre-commissioning-phase-100-mw-csp-fresnel-plant> (Accessed: 9 March 2018).

Curtis, H. B. and Decker, A. J. (1975) *Electrical characteristics of a free-burning direct-current argon arc operating between 90 and 563 kilowatts with two types of cathodes*. NASA-TN-D-8032.

Da, Y., Xuan, Y. and Li, Q. (2016) 'From light trapping to solar energy utilization:

- A novel photovoltaic–thermoelectric hybrid system to fully utilize solar spectrum’, *Energy*, 95, pp. 200–210. doi: 10.1016/j.energy.2015.12.024.
- Davidson, M. W. (2018) *Tungsten-Halogen Incandescent Lamps*, *Carl Zeiss Microscopy Online Campus*. Available at: <http://zeiss-campus.magnet.fsu.edu/articles/lightsources/tungstenhalogen.html> (Accessed: 31 March 2018).
- Davies, P. A. (1994) ‘Edge-ray principle of nonimaging optics’, *Journal of the Optical Society of America A*, 11(4), pp. 1256–1259. doi: 10.1364/JOSAA.11.001256.
- Davis, A. (2004) *Light Emitting Diode Source Modeling for Optical Design*, *Intertech-Pira LEDs 2004*.
- Davis, A. (2009) ‘Raytrace assisted analytical formulation of Fresnel lens transmission efficiency’, *Proceeding of SPIE*, 7429, p. 74290D. doi: 10.1117/12.823742.
- Davis, A. and Kühnlenz, F. (2007) ‘Optical Design using Fresnel Lenses’, *Optik & Photonik*, 2(4), pp. 52–55. doi: 10.1002/opph.201190287.
- Decker, A. J. and Pollack, J. L. (1972) ‘A 400 Kilowatt Argon Arc Lamp for Solar Simulation’, in *6th Space Simulation Conference*. New York, pp. 1–21.
- Department for Business Energy Strategy & Industrial (2017) *Digest of UK Energy Statistics (DUKES): calorific values*. Available at: <https://www.gov.uk/government/statistics/dukes-calorific-values>.
- Desai, R. (2013) *Thermo-Economic Analysis of a Solar Thermal Power Plant with a Central Tower Receiver for Direct Steam Generation*, *MSc. Thesis*. KTH Royal Institute of Technology.
- Dibowski, H.-G. (2014) *High-Flux Solar Furnace and Xenon-High-Flux Solar Simulator*. Available at: http://www.dlr.de/sf/en/desktopdefault.aspx/tabid-8558/14717_read-28267/ (Accessed: 25 February 2016).
- Dickey, F. M. *et al.* (2005) *Laser Beam Shaping Applications (Optical Science and Engineering)*. CRC Press.

- Dilip, J. S. and Venkatraj, V. (2013) 'Simulation of Solar Thermal Central Receiver Power Plants: A Review', *International Journal of Advanced Research*, 1(10), pp. 367–373.
- Dingle, D. and Tooley, M. (2013) *Aircraft Engineering Principles*. 2nd Ed. London, UK: Routledge.
- Dinklage, A., Klinger, T. and Marx, G. (2005) *Plasma Physics: Confinement, Transport and Collective Effects*. 2005 Ed. Springer.
- Dokos, W. (1982) 'Presentation of some U.S. solar simulator characteristics', in Commission, T. E., Aranovich, E., and Gillett, B. (eds) *Workshop on Solar Simulators*. Ispra; Italy, pp. 51–61.
- Dong, X. *et al.* (2015) 'Concentric multilayer model of the arc in high intensity discharge lamps for solar simulators with experimental validation', *Solar Energy*, 122, pp. 293–306. doi: 10.1016/j.solener.2015.09.004.
- Dostucok, I., Selbas, R. and Şahin, A. (2014) 'Experimental investigation of a linear Fresnel collector system', *Journal of Thermal Science and Technology*, 34, pp. 77–83.
- Druon, F. *et al.* (2011) 'On Yb:CaF₂ and Yb:SrF₂: review of spectroscopic and thermal properties and their impact on femtosecond and high power laser performance', *Optical Materials Express*, 1(3), p. 489. doi: 10.1364/OME.1.000489.
- Duffie, J. A. and Beckman, W. A. (2013) *Solar Engineering of Thermal Processes*. 4th Ed. Hoboken, New Jersey, USA: John Wiley and Sons, Inc. doi: 10.1115/1.2930068.
- Eck, M. and Zarza, E. (2006) 'Saturated steam process with direct steam generating parabolic troughs', *Solar Energy*, 80(11), pp. 1424–1433. doi: 10.1016/j.solener.2006.03.011.
- Edmund Optics (2018a) *11.0' x 11.0', 24" Focal Length, Fresnel Lens*. Available at: <https://www.edmundoptics.co.uk/optics/optical-lenses/fresnel-lenses/11.0quot-x-11.0quot-24quot-focal-length-fresnel-lens/#specs> (Accessed:

13 February 2018).

Edmund Optics (2018b) *150mm Diameter x 6.5mm Thickness, Uncoated, BOROFLOAT® Window*. Available at:

<https://www.edmundoptics.co.uk/optics/windows-diffusers/ultraviolet-uv-infrared-ir-windows/150mm-diameter-x-6.5mm-thickness-uncoated-borofloatreg-window/#specs> (Accessed: 28 March 2018).

Edmund Optics (2018c) *Fresnel Lenses*. Available at:

<https://www.edmundoptics.co.uk/optics/optical-lenses/fresnel-lenses/fresnel-lenses/> (Accessed: 28 April 2018).

Egger, J. R. (1979) 'Use of Fresnel lenses in optical systems: some advantages and limitations', in Yoder, Jr., P. R. (ed.) *SPIE 0193, Optical Systems in Engineering I*, pp. 63–69. doi: 10.1117/12.957873.

EIA (2017) *Electric Power Annual 2016, Eia.Doe.Gov*. Washington, D.C. Available at: http://www.eia.doe.gov/ask/electricity_faqs.asp#efficiency.

Eichler, H. M. (2014) *Characterisation studies on the optics of the prototype fluorescence telescope FAMOUS*. Rheinisch-Westfälischen Technischen Hochschule Aachen. Available at: https://web.physik.rwth-aachen.de/~hebbeker/theses/eichler_master.pdf.

Ekman, B. M., Brooks, G. and Akbar Rhamdhani, M. (2015) 'Development of high flux solar simulators for solar thermal research', *Solar Energy Materials and Solar Cells*, 141, pp. 436–446. doi: 10.1016/j.solmat.2015.06.016.

El-Damrawi, G. and Mansour, E. (2005) 'Electrical properties of lead borosilicate glasses', *Physica B: Condensed Matter*, 364(1–4), pp. 190–198. doi: 10.1016/j.physb.2005.04.012.

El-ladan, A. H. *et al.* (2013) 'The Prospects of a Promising Solar Thermal Concentrator (Fresnel Lens) for Cooking, Heating and Electricity Generation', in *7th International Conference on Renewable Energy Sources*. Kuala Lumpur, Malaysia: Wseas LLC, pp. 175–180.

Elashmawi, I. S. and Hakeem, N. A. (2008) 'Effect of PMMA addition on

characterization and morphology of PVDF', *Polymer Engineering & Science*, 48(5), pp. 895–901. doi: 10.1002/pen.21032.

Emilio, M. *et al.* (2012) 'Measuring the Solar Radius from Space during the 2003 and 2006 Mercury Transits', *The Astrophysical Journal*, 750(2), pp. 1–8. doi: 10.1088/0004-637X/798/1/48.

EN 12975-1 (2006) *Thermal solar systems and components — Solar collectors — Part 1: General requirements*. British Standards Institute.

EN 12975-2 (2006) *Thermal solar systems and components — Solar collectors — Part 2: Test methods*. British Standards Institute.

EN 12976-1 (2017) *Thermal solar systems and components — Factory made systems — Part 1: General requirements*. British Standards Institute.

EN 12976-2 (2006) *Thermal solar systems and components — Factory made systems — Part 2: Test methods, Test*. British Standards Institute.

Ergenc, A. F. (2009) *A Novel Method for ICSI: Rotationally Oscillating Drill: Design, Control and Monitoring*. VDM Verlag.

Erickson, A. *et al.* (2012) *China's Future Nuclear Submarine Force*. 1st Ed. Naval Institute Press.

Erickson, B. M. (2012) *Characterization of the University of Florida Solar Simulator and an Inverse Solution for Identifying Intensity Distributions from Multiple Flux Maps in Concentrating Solar Applications*, *PhD Thesis*. University of Florida. doi: 10.1017/CBO9781107415324.004.

Eydeland, A. and Wolyniec, K. (2003) *Energy and Power Risk Management: New Developments in Modeling, Pricing, and Hedging*. 1st Ed. John Wiley & Sons, Inc.

Falcone, P. K. (1986) *A handbook for solar central receiver design*. Springfield, VA, USA.

Farage, M. A., Miller, K. W. and Maibach, H. I. (2010) *Textbook of Aging Skin*. 2010 Ed. Springer Berlin Heidelberg.

- Fathabadi, H. (2016) 'Novel high accurate sensorless dual-axis solar tracking system controlled by maximum power point tracking unit of photovoltaic systems', *Applied Energy*. Elsevier Ltd, 173, pp. 448–459. doi: 10.1016/j.apenergy.2016.03.109.
- Fernández-García, A. *et al.* (2017) 'Equipment and methods for measuring reflectance of concentrating solar reflector materials', *Solar Energy Materials and Solar Cells*, 167, pp. 28–52. doi: 10.1016/j.solmat.2017.03.036.
- Fernández, P. *et al.* (2014) 'Design Space Exploration of a 5 MWth Small Particle Solar Receiver', *Energy Procedia*, 49, pp. 344–353. doi: 10.1016/j.egypro.2014.03.037.
- Ferraro, C., García-Tuñón, E. and Saiz, E. (2015) 'A silicon carbide lollipop', *Materials Today*, 18(2), pp. 117–118. doi: 10.1016/j.mattod.2015.01.020.
- Ferziger, J. H. and Perić, M. (2002) *Computational Methods for Fluid Dynamics*. Berlin, Heidelberg: Springer Berlin Heidelberg. doi: 10.1007/978-3-642-56026-2.
- Finkelstein, T. and Organ, A. J. (2001) *Air Engines: The History, Science, and Reality of the Perfect Engine*. 1st Ed. ASME Press.
- Flashlight Ltd. (2018) *PHILIPS STRAND single channel portable dimmer*. Available at: <http://www.flash-light.co.uk/product/selection-dim1-single-channel-portable-dimmer/> (Accessed: 16 January 2018).
- Flem, B. *et al.* (2002) 'In situ analysis of trace elements in quartz by using laser ablation inductively coupled plasma mass spectrometry', *Chemical Geology*, 182(2–4), pp. 237–247. doi: 10.1016/S0009-2541(01)00292-3.
- Flexitallic (2018) *Flexitallic thermiculite 815*. Available at: http://www.flexitallic-ae.co.uk/upload/datasheets/Thermiculite_815_Datasheet.pdf.
- Flynn, D. (2003) *Thermal Power Plant Simulation and Control*. London, UK: Institution of Engineering and Technology.
- Forn, X. S. (2009) *Industrial and Technological Transitions The Case of Concentrator Photovoltaic Technologies*, MSc. Thesis. Universitat Politècnica de Catalunya. Available at:

[https://upcommons.upc.edu/handle/2099.1/8752?locale-](https://upcommons.upc.edu/handle/2099.1/8752?locale-attribute=en#.WqN7ul4URRM.mendeley)

[attribute=en#.WqN7ul4URRM.mendeley](https://upcommons.upc.edu/handle/2099.1/8752?locale-attribute=en#.WqN7ul4URRM.mendeley) (Accessed: 10 March 2018).

Forsyth, R. (2011) 'Parabolic Trough Technology: Technical Advances Speed CSP toward Grid Parity', *New Energy Update*, August. Available at: <http://newenergyupdate.com/csp-today/technology/parabolic-trough-technology-technical-advances-speed-csp-toward-grid-parity>.

Framatophe (2017) *OptGeo (in French)*. Available at: <https://framalibre.org/content/optgeo> (Accessed: 11 March 2018).

Franc, F. *et al.* (1986) 'Concentrating collectors with flat linear fresnel lenses', *Solar & Wind Technology*, 3(2), pp. 77–84. doi: 10.1016/0741-983X(86)90017-2.

Frederickson, L., Dordevich, M. and Miller, F. (2014) 'Lab-scale Experimentation and CFD Modeling of a Small Particle Heat Exchange Receiver', *Energy Procedia*, 49, pp. 363–372. doi: 10.1016/j.egypro.2014.03.039.

Fujita, M. (2008) 'Making and Properties of Transparent YAG Ceramics', in *Advanced Solid-State Photonics*. Washington, D.C.: OSA, p. WC2. doi: 10.1364/ASSP.2008.WC2.

Garg, H. P. *et al.* (1985) 'Development of a simple low-cost solar simulator for indoor collector testing', *Applied Energy*, 21(1), pp. 43–54. doi: 10.1016/0306-2619(85)90073-X.

Gates, D. M. (1966) 'Spectral Distribution of Solar Radiation at the Earth's Surface', *Science*, 151(3710), pp. 523–529. doi: 10.1126/science.151.3710.523.

GE product datasheet (2016) *GE 300W ELH Model*. Available at: <http://catalog.gelighting.com/apac/lamp/showbiz-lamps/projection/f=multi-mirror-quartzline-projection-mr16/p=38476/?l=en&r=apac> (Accessed: 9 November 2016).

Geisheker, P.J. ; Putman, W.J. ; Bard, L. A. (1981) 'Development of facilities and methods for thermal performance tests of passive domestic hot water

- systems', in *6th National Passive Solar Conference*, Portland, OR, USA.
- Gene A. Zerlaut, William T. Dokos, William J. Putman, R. K. S. (1983) 'Solar simulator and method'. USA: U.S. Patent.
- George, I. S. *et al.* (2004) 'International Conference on Solar Power from Space', in *The 4th International Conference on Solar Power from Space*. Granada, Spain.
- Gere, J. M. and Goodno, B. J. (2012) *Mechanics of Materials, SI Edition*. 8th Ed. Cengage Learning.
- Get a Lamp S.C.P. (2016) *PHILIPS 6994Z 2000W G38 230V 1CT*. Available at: <https://www.getalamp.co.uk/philips-6994z-2000w-g38-230v-1ct.html> (Accessed: 9 November 2016).
- Gharbi, N. El *et al.* (2011) 'A comparative study between parabolic trough collector and linear Fresnel reflector technologies', *Energy Procedia*, 6, pp. 565–572. doi: 10.1016/j.egypro.2011.05.065.
- Ghasemi, S. E., Ranjbar, A. A. and Ramiar, A. (2013) 'Numerical Study on Thermal Performance of Solar Parabolic Trough Collector', 7, pp. 1–12.
- Giacomoni, P. U. (2007) *Biophysical and Physiological Effects of Solar Radiation on Human Skin*. 1st Ed. Edited by G. Jori and D.-P. Hader. Royal Society of Chemistry.
- Gianella, S. (2012) 'Porous Materials For High-Temperature Solar Absorbers', in *International Symposium on High Temperature Solar Materials*. Yeungnam University.
- Gill, K. and Williams, A. (2018) *The Original Invention*. Available at: <http://app.emaze.com/@AOZLLFWZ/cameras-by-kaitlyn-gill-and-alexis-williams#2> (Accessed: 9 March 2018).
- Gillet, W. B. (1977) 'Solar simulators and indoor testing', in *Testing of Solar Collectors and Systems: Proceedings of Conference (C11) at the the Sic. Royal Institution*. London: International Solar Energy Society, UK Section, pp. 30–48.
- Gillett, W. B. (1983) 'Performance Test Procedures for Thermal Collectors (2)

Solar Simulators', in Beghi, G. (ed.) *Performance of Solar Energy Converters: Thermal Collectors and Photovoltaic Cells*. Springer Netherlands, pp. 125–146.

Goldman, L. M. *et al.* (2017) *ALON® Optical Ceramic Transparencies for Sensor and Armor Applications*, Surmet Company. Available at: http://www.surmet.com/pdfs/news-and-media/Surmet_ALON_Paper_for_2010_EMWS_final.pdf (Accessed: 8 April 2017).

Gomez-Garcia, F. *et al.* (2016) 'A new laboratory-scale experimental facility for detailed aerothermal characterizations of volumetric absorbers', in *AIP Conference Proceedings*, p. 30018. doi: 10.1063/1.4949070.

Gonzalez, C. and Ross, R. (1980) 'Performance measurement reference conditions for terrestrial photovoltaics', in *Proceedings of the International Solar Energy Society Conference*. Phoenix, AZ, pp. 1–5.

Goto, H. *et al.* (1995) 'Micro focusing optical device using piezoelectric thin film actuator', in *Proceedings of SPIE - Micro-Optics/Micromechanics and Laser Scanning and Shaping*. San Jose, CA, pp. 136–143.

GrayGlass (2013) *Borosilicate*. Available at: <http://grayglass.net/glass.cfm/Lighting/Borosilicate/catid/3/conid/79> (Accessed: 9 April 2017).

Griffith, W. P. (2009) 'Melting the Platinum Group Metals', *Platinum Metals Review*, 53(4), pp. 209–215. doi: 10.1595/147106709X472507.

Grondzik, W. T. *et al.* (2009) *Mechanical and Electrical Equipment for Buildings*. Wiley.

Grosslight, J. (1991) *Light, light, light: effective use of daylight and electric lighting in residential and commercial spaces*. 2nd Ed. Crisp Publications Inc.

Grover, H. S. *et al.* (2015) 'Modelling of a Vortex Water-Wall Argon Arc Lamp for Rapid Thermal Annealing Applications', *IEEE Transactions on Industry Applications*, 51(6), pp. 4817–4823. doi: 10.1109/TIA.2015.2451099.

Gueymard, C. A., Myers, D. and Emery, K. (2002) 'Proposed reference

irradiance spectra for solar energy systems testing', *Solar Energy*, 73(6), pp. 443–467. doi: 10.1016/S0038-092X(03)00005-7.

Günther, M. (2012) 'Linear Fresnel Technology', in *Advanced CSP Teaching Materials*. Kassel, Germany: Enermena; German Aerospace Center (DLR).

Guo, P. *et al.* (2016) 'Experimental study on an indoor scale solar chimney setup in an artificial environment simulation laboratory', *Applied Thermal Engineering*, 107, pp. 818–826. doi: 10.1016/j.applthermaleng.2016.07.025.

Hafez, A. Z. *et al.* (2016) 'Solar parabolic dish Stirling engine system design, simulation, and thermal analysis', *Energy Conversion and Management*. Elsevier Ltd, 126, pp. 60–75. doi: 10.1016/j.enconman.2016.07.067.

Hall, A. S., Archer, F. and Gilbert, I. (1999) *Engineering Statics*. 2nd Ed. University of New South Wales Press.

Hall, R. (1982) 'Sealed beam discharge lamps for solar simulators', in Commission, T. E., Aranovich, E., and Gillett, B. (eds) *Workshop on Solar Simulators*. Ispra, Italy: Commission of the European Communities Joint Research Centre Ispra Establishment, pp. 11–19.

Halliop, B. (2008) *A Dynamic Model of a High Temperature Arc Lamp*. University of Toronto.

Han, Y., Dai, Y., and Wang, R. (2009) 'Schemes Optimization and Device Conformation of High Concentrating Solar Energy', *Journal of Shanghai Jiaotong University*, 43, pp. 261–265.

Han, Y. M. *et al.* (2007) 'Studies on the light permeance characteristic of a Fresnel lens group applied in high concentration solar energy', *Journal of Optics A: Pure and Applied Optics*, 9(11), pp. 988–997. doi: 10.1088/1464-4258/9/11/004.

Harris, D. C. (1999) *Materials for Infrared Windows and Domes: Properties and Performance*. 2nd Ed. Washington, DC, USA: SPIE.

Health and Safety Executive (2014) *Ozone : Health hazards and control measures, Guidance Note EH38*. Available at:

<http://www.hse.gov.uk/pubns/eh38.htm>.

Heath, S. T. (2013) *A History of Greek Mathematics, Volume II: From Aristarchus to Diophantus: 2*. 2nd Ed. Dover Publications Inc.

Heckele, M. and Schomburg, W. K. (2004) 'Review on micro molding of thermoplastic polymers', *Journal of Micromechanics and Microengineering*, 14, pp. 1–14. doi: 10.1088/0960-1317/14/3/R01.

Helden, A. Van *et al.* (2010) *The Origins of the Telescope*. Amsterdam University Press.

Hexagon (2018) *Leitz PMM-F*. Available at:

<http://www.hexagonmi.com/products/coordinate-measuring-machines/gantry-cmms/leitz-pmmf> (Accessed: 17 March 2018).

Higashi, T., Umezit, S. (1982) 'The conceptual design of a solar simulator for evaluating collectors', in Commission, T. E., Aranovich, E., and Gillett, B. (eds) *Workshop on Solar Simulators*. Ispra; Italy: Commission of the European Communities Joint Research Centre Ispra Establishment, pp. 36–39.

Hill, J. C. and Dolenga, A. (1977) 'Fluorine-cycle incandescent lamps', *Journal of Applied Physics*, 48(7), pp. 3089–3092. doi: 10.1063/1.324079.

Hirsch, D. *et al.* (2003) 'A New 75 kW High-Flux Solar Simulator for High-Temperature Thermal and Thermochemical Research', *Journal of Solar Energy Engineering*, 125(1), p. 117. doi: 10.1115/1.1528922.

Ho, C. K. (2008) *Software and Codes for Analysis of Concentrating Solar Power Technologies, SAND2008-8053*. Springfield, VA, USA.

Ho, F. H. (1988) *Graphite design handbook*. San Diego, CA. doi: 10.2172/714896.

Holweger, H. (1971) 'Damping and Solar Abundance of Sodium from NaI Fraunhofer Lines', *Astronomy and Astrophysics*, 10, pp. 128–133.

Horovitz, I. *et al.* (2016) 'Carbamazepine degradation using a N-doped TiO₂ coated photocatalytic membrane reactor: Influence of physical parameters', *Journal of Hazardous Materials*, 310, pp. 98–107. doi:

10.1016/j.actamat.2015.02.029.

Houghton, J. (2004) *Global Warming: The Complete Briefing*. 3rd Ed. Cambridge University Press.

Howell, J. R., Menguc, M. P. and Siegel, R. (2015) *Thermal Radiation Heat Transfer*. 6th edn. CRC Press.

Hu, Y. and Ding, F. (2011) 'Radiative constraints on the habitability of exoplanets Gliese 581 c and Gliese 581 d', in *Astronomy and astrophysics*, pp. 1–8. doi: 10.1051/0004-6361/201014880.

Hu, Y., Shen, H. and Yao, Y. (2018) 'A novel sun-tracking and target-aiming method to improve the concentration efficiency of solar central receiver systems', *Renewable Energy*. Elsevier Ltd, 120, pp. 98–113. doi: 10.1016/j.renene.2017.12.035.

Huang, Q. and Xu, L. (2017) 'Ball lens as secondary optical element for CPV system', *Solar Energy*, 148, pp. 57–62. doi: 10.1016/j.solener.2017.02.009.

Huang, Y. *et al.* (2010) 'Sintering of Transparent Ytria Ceramics in Oxygen Atmosphere', *Journal of the American Ceramic Society*, 93(10), pp. 2964–2967. doi: 10.1111/j.1551-2916.2010.03940.x.

Humphries, W. and George, C. (1978) *Use of the Marshall Space Flight Center solar simulator in collector performance evaluation*. NASA-TM-78165.

Hyndman, R. *et al.* (2008) *Forecasting with Exponential Smoothing*. Berlin, Heidelberg: Springer Berlin Heidelberg (Springer Series in Statistics). doi: 10.1007/978-3-540-71918-2.

Hyndman, R. J. and Koehler, A. B. (2006) 'Another look at measures of forecast accuracy', *International Journal of Forecasting*, 22(4), pp. 679–688. doi: 10.1016/j.ijforecast.2006.03.001.

Idowu, S. O. *et al.* (2015) *Dictionary of Corporate Social Responsibility*. Edited by S. O. Idowu *et al.* Springer International Publishing (CSR, Sustainability, Ethics & Governance). doi: 10.1007/978-3-319-10536-9.

Incropera, F. P. *et al.* (2007) *Fundamentals of Heat and Mass Transfer*. 6th Ed.

John Wiley & Sons.

Informer Technologies (2018) *CyberRay*. Available at:
<http://cyberray.software.informer.com> (Accessed: 11 March 2018).

IRENA (2012) *Cost Analysis of Concentrating Solar Power*.

ISO 19467 (2016) *Thermal performance of windows and doors — Determination of solar heat gain coefficient using solar simulator*. British Standards Institute.

ISO 9806 (2013) *Solar energy. Solar thermal collectors. Test methods*. British Standards Institute. Available at:
<https://bsol.bsigroup.com/Bibliographic/BibliographicInfoData/000000000030069106>.

Jaramillo, O. A., Río, J. A. del and Huelsz, G. (1999) 'A thermal study of optical fibres transmitting concentrated solar energy', *Journal of Physics D: Applied Physics*, 32(9), pp. 1000–1005.

Jaworske, D. A., Jefferies, K. S. and Mason, L. S. (1996) 'Alignment and Initial Operation of an Advanced Solar Simulator', 33(6), pp. 867–869. doi:
doi:10.2514/6.1996-102.

Jefferies, K. S. (1994) 'Solar Simulator for Solar Dynamic Space Power System Testing', in *ASME International Solar Energy Conference*. San Francisco, California, USA, pp. 1–8.

Johansson, T. B. *et al.* (1993) *Renewable Energy: Sources for Fuels and Electricity*. 2nd Ed. Island Press.

Jones, S. A. *et al.* (2001) 'TRNSYS Modeling of the SEGS VI Parabolic Trough Solar Electric Generating System', in *International solar energy conference*. Washington, DC: ASME, pp. 405–412.

Kalogirou, S. (2018) *McEvoy's Handbook of Photovoltaics: Fundamentals and Applications*. 3rd Ed. Academic Press.

Kalogirou, S. A. (2004) 'Solar thermal collectors and applications', *Progress in Energy and Combustion Science*, 30(3), pp. 231–295. doi:

10.1016/j.pecs.2004.02.001.

Kalogirou, S. A. (2009) *Solar Energy Engineering: Processes and Systems*. 1st Ed. Academic Press.

Kalogirou, S. A. (2014) *Solar Energy Engineering: Processes and Systems*. 2nd Ed. Elsevier Inc.

Kang, S. (2004) 'Replication Technology for Micro/Nano Optical Components', *Japanese Journal of Applied Physics*, 43(8B), pp. 5706–5716. doi: 10.1143/JJAP.43.5706.

Kasarova, S. N. *et al.* (2007) 'Analysis of the dispersion of optical plastic materials', *Optical Materials*, 29(11), pp. 1481–1490. doi: 10.1016/j.optmat.2006.07.010.

Kasztelanic, R. *et al.* (2013) 'Fresnel lens fabrication for broadband IR optics using hot embossing process', *Infrared Physics & Technology*, 60, pp. 1–6. doi: 10.1016/j.infrared.2013.03.010.

Kenny, S. P. (1993) *Design of an indoor solar simulator*. Colorado State University, Fort Collins,. CO.

Kenny, S. P. and Davidson, J. H. (1994) 'Design of a Multiple-Lamp Large-Scale Solar Simulator', *Journal of Solar Energy Engineering*, 116(4), pp. 200–205.

Kerslake, T. W., Mason, L. S. and Strumpf, H. J. (1997) 'High-flux, high-temperature thermal vacuum qualification testing of a solar receiver aperture shield', in *IECEC-97 Proceedings of the Thirty-Second Intersociety Energy Conversion Engineering Conference (Cat. No.97CH6203)*. Honolulu, Hawaii, USA: IEEE, pp. 440–445. doi: 10.1109/IECEC.1997.659230.

Kesari, J. P. *et al.* (2015) 'Review of the Concentrated Solar Thermal Technologies : Challenges and Opportunities in India', *International Journal of Research and Scientific Innovation*, 11(I), pp. 105–111.

Kim, S. in *et al.* (2016) 'Design, analysis and performance of a polymer–carbon nanotubes based economic solar collector', *Solar Energy*, 134, pp. 251–263.

doi: 10.1016/j.solener.2016.04.019.

Kinematics Manufacturing (2016) *SE Enclosed Slewing Drive*. Phoenix, AZ.

King, H. C. (2003) *The history of the telescope*. New York, USA: Dover Publications Inc.

Kipp & Zonen Instruments (2018a) *SMP10 Pyranometer*. Available at: http://www.kippzonen.com/Product/281/SMP10-Pyranometer#.WI8Q_XnLhph (Accessed: 17 January 2018).

Kipp & Zonen Instruments (2018b) *The SMP10 Pyranometer*. Delft, The Netherlands.

Kistler, B. L. (1986) *A user's manual for DELSOL3: A computer code for calculating the optical performance and optimal system design for solar thermal central receiver plants*. Springfield, VA, USA.

Kochan, H. W., Huebner, W. F. and Sears, D. W. G. (1999) 'Simulation Experiments with Cometary Analogous Material', in *Laboratory Astrophysics and Space Research*. Springer Netherlands, pp. 623–665.

Kongtragool, B. and Wongwises, S. (2007) 'Performance of a twin power piston low temperature differential Stirling engine powered by a solar simulator', *Solar Energy*, 81(7), pp. 884–895. doi: 10.1016/j.solener.2006.11.004.

Kongtragool, B. and Wongwises, S. (2008) 'A four power-piston low-temperature differential Stirling engine using simulated solar energy as a heat source', *Solar Energy*, 82(6), pp. 493–500. doi: 10.1016/j.solener.2007.12.005.

Kritchman, E. M., Friesem, A. A. and Yekutieli, G. (1979) 'Efficient Fresnel lens for solar concentration', *Solar Energy*, 22(2), pp. 119–123. doi: 10.1016/0038-092X(79)90095-1.

Krueger, K. R. (2012) *Design and Characterization of a Concentrating Solar Simulator*, PhD Thesis. The University of Minnesota.

Krueger, K. R. *et al.* (2013) 'Operational Performance of the University of Minnesota 45kWe High-flux Solar Simulator', *Journal of Solar Energy Engineering*, 135, pp. 44501-1-44501–4. doi: 10.1115/ES2012-91119.

- Krueger, K. R., Davidson, J. H. and Lipiński, W. (2011) 'Design of a New 45 kWe High-Flux Solar Simulator for High-Temperature Solar Thermal and Thermo-Chemical Research', *Journal of Solar Energy Engineering*, 133, pp. 0110131–0110138.
- Krusi, P. and Schmid, R. (1979) 'Design of an inexpensive solar simulator', in *Sun II; Proceedings of the Silver Jubilee Congress*,. Atlanta, Ga, pp. 417–421. Available at: <http://adsabs.harvard.edu/abs/1979sun2.conf..417K>.
- Krusi, P. and Schmid, R. (1983a) 'The CSI 1000 W lamp as a source for solar radiation simulation', *Solar Energy*, 30(5), pp. 455–462.
- Krusi, P. and Schmid, R. (1983b) 'The CSI lamp as a source of radiation for solar simulation', *Solar Energy*, 30(5), pp. 455–462. doi: 10.1177/096032717801000307.
- Krystek, L. (2010) *Archimedes and the Burning Mirror*. Available at: http://www.unmuseum.org/burning_mirror.htm (Accessed: 9 March 2018).
- Kuhn, P. and Hunt, A. (1991) 'A new solar simulator to study high temperature solid-state reactions with highly concentrated radiation', *Solar Energy Materials*, 24(1–4), pp. 742–750.
- Kujawa, I. *et al.* (2012) 'Development of glass microoptics for MidIR with hot embossing technology', in Thienpont, H. *et al.* (eds) *SPIE - The International Society for Optical Engineering*, p. 84281P. doi: 10.1117/12.922711.
- Kumar, A. (2013) 'Improvements in efficiency of solar parabolic trough', *IOSR Journal of Mechanical and Civil Engineering*, 7(6), pp. 63–75.
- Kumar, G. K. and Babu, T. P. A. (2017) 'Study of Various Glass Materials to Provide Adequate Day Lighting in Office Buildings of Warm and Humid Climatic Zone in India', *Energy Procedia*, 109, pp. 181–189. doi: 10.1016/j.egypro.2017.03.090.
- Kumar, G. K., Saboor, S. and Babu, T. P. A. (2017) 'Experimental and Theoretical Studies of Window Glazing Materials of Green Energy Building in Indian Climatic Zones', *Energy Procedia*, 109, pp. 306–313. doi:

10.1016/j.egypro.2017.03.072.

Kumar, V., Shrivastava, R. L. and Untawale, S. P. (2015) 'Fresnel lens: A promising alternative of reflectors in concentrated solar power', *Renewable and Sustainable Energy Reviews*, 44, pp. 376–390. doi: 10.1016/j.rser.2014.12.006.

Kuo, C.-C. K. and Liao, H.-Y. (2015) 'Dimensional accuracy optimization of the micro-plastic injection molding process using the Taguchi design method', *Materials Science*, 21(2). doi: 10.5755/j01.ms.21.2.5864.

Kurtz, S. R. (2012) *Opportunities and challenges for development of a mature concentrating photovoltaic power industry*.

Kwok, S. (2016) *Physics and Chemistry of the Interstellar Medium: Chemistry, Chemistry*. 1st edn. Content Technologies, Inc.

L.A. Metals Ltd. (2016) *L.A. Metals*. Available at: <http://www.lametals.co.uk/> (Accessed: 1 September 2016).

Land Art Generator (2018) *The 19th Century Solar Engines of Augustin Mouchot, Abel Pifre, and John Ericsson*. Available at: <http://landartgenerator.org/blagi/archives/2004> (Accessed: 9 March 2018).

Languy, F. *et al.* (2011) 'Flat Fresnel doublets made of PMMA and PC: combining low cost production and very high concentration ratio for CPV', *Optics Express*, 19(S3), pp. 280–294. doi: 10.1364/OE.19.00A280.

Leary, P. L. and Hankins, J. D. (1979) *User's guide for MIRVAL: a computer code for comparing designs of heliostat-receiver optics for central receiver solar power plants*. Albuquerque, NM, and Livermore, CA, USA. doi: 10.2172/6371450.

Lehmkuhl, O. *et al.* (2009) 'TermoFluids: A new Parallel unstructured CFD code for the simulation of turbulent industrial problems on low cost PC Cluster', in *Parallel Computational Fluid Dynamics 2007: Implementations and Experiences on Large Scale and Grid Computing*. Berlin, Heidelberg: Springer Berlin Heidelberg, pp. 275–282. doi: 10.1007/978-3-540-92744-0_34.

Leiner, W. and Altfeld, K. (1982) 'Design of a solar simulator with reduced

thermal radiation to be used as a component of a test facility for air heating collectors', in Commission, T. E., Aranovich, E., and Gillett, B. (eds) *Workshop on Solar Simulators*. Ispra, Italy: Commission of the European Communities Joint Research Centre Ispra Establishment, pp. 88–97.

Lemcoff, N. and Wyatt, S. (2012) 'Analysis of Superheater Tubes with Mutual Irradiation as Applied to a Solar Receiver Steam Generator', in *the 2012 COMSOL Conference*. Boston, USA.

Leutz, R. *et al.* (1999) 'Design of a nonimaging Fresnel lens for solar concentrators', *Solar Energy*, 65(6), pp. 379–387. doi: 10.1016/S0038-092X(98)00143-1.

Leutz, R. and Fu, L. (2007) 'Dispersion in tailored Fresnel lens concentrators', in *Proceedings of ISES Solar World Congress 2007: Solar Energy and Human Settlement*. Beijing, China, pp. 1366–1370.

Leutz, R. and Suzuki, A. (2001) *Nonimaging Fresnel Lenses: Design and Performance of Solar Concentrators*. Springer.

LeVeque, R. J. (2007) *Finite Difference Methods for Ordinary and Partial Differential Equations: Steady-State and Time-Dependent Problems*. Society for Industrial and Applied Mathematics.

Ley, W. (1979) *Survey of Solar Simulator Test Facilities and Initial Results of IEA Round Robin Tests Using Solar Simulators*. DFVLR, Cologne.

Li, J. *et al.* (2014) 'Optical Analysis of a Hexagonal 42kWe High-flux Solar Simulator', *Energy Procedia*, 57, pp. 590–596. doi: 10.1016/j.egypro.2014.10.213.

Li, J., Gonzalez-Aguilar, J. and Romero, M. (2015) 'Line-concentrating Flux Analysis of 42kWe High-flux Solar Simulator', *Energy Procedia*, 69, pp. 132–137. doi: 10.1016/j.egypro.2015.03.016.

Li, Z. *et al.* (2011) 'Study on the radiation flux and temperature distributions of the concentrator-receiver system in a solar dish/Stirling power facility', *Applied Thermal Engineering*, 31(10), pp. 1780–1789. doi:

10.1016/j.applthermaleng.2011.02.023.

Lighting, I. (2017) 'Flat Optical Fiber Daylighting System with Lateral Displacement Sun-Tracking Mechanism for Indoor Lighting', *Energies*, 10(10), pp. 1–13. doi: 10.3390/en10101679.

Lin, E. and Stultz, J. (1995) 'Cassini MLI blankets high-temperature exposure tests', in *33rd Aerospace Sciences Meeting and Exhibit*. Reno, USA: American Institute of Aeronautics and Astronautics, pp. 1–7. doi: 10.2514/6.1995-633.

Luque, A. and Hegedus, S. (2010) *Handbook of Photovoltaic Science and Engineering*. 2nd Ed. Wiley-Blackwell.

Luque, A. and Hegedus, S. (2011) *Handbook of Photovoltaic Science and Engineering*. 2nd edn. John Wiley & Sons, Ltd. doi: 10.1017/CBO9781107415324.004.

Lvovsky, A. I. (2015) 'Fresnel Equations', in Hoffman, C. and Driggers, R. (eds) *Encyclopedia of Optical Engineering*. 2nd Ed. Taylor and Francis: New York, pp. 1–6. doi: 10.1081/E-EOE-120047133.

Ma, Y. *et al.* (2010) 'Influencing factors of life of high power linear xenon-filled flash lamp', *Qiangjiguang Yu Lizishu/High Power Laser and Particle Beams*, 22(10), pp. 2483–2486. doi: 10.3788/HPLPB20102210.2483.

Madsen, M. V. (2013) *Lengthening the lifetime of roll-to-roll produced polymer solar cells*. Technical University of Denmark.

Maekawa, K. *et al.* (2009) 'JEM-EUSO lens manufacturing', in *the 31st International Cosmic Ray Conference (ICRC)*. Lodz, Poland, pp. 5–7.

Mahajan, V. N. (1991) 'Ray Spot Diagrams', in *Aberration Theory Made Simple*. Bellingham, WA, USA: SPIE, pp. 56–65. doi: 10.1117/3.43000.ch7.

Mancini, T. R. (1991) 'Analysis and Design of Two Stretched-Membrane Parabolic Dish Concentrators', *Journal of Solar Energy Engineering*, 113(3), pp. 180–187. doi: 10.1115/1.2930490.

Marcotte, P. and Manning, K. (2014) 'Development of an advanced large-aperture parabolic trough collector', *Energy Procedia*, 49, pp. 145–154. doi:

10.1016/j.egypro.2014.03.016.

Martin, C. L. and Goswami, D. Y. (2005) *Solar Energy Pocket Reference*. Routledge.

Martini, M. (2014) *Principles of Light Sources for Lithography*. Available at: <http://www.martini-tech.com/tag/light-sources/> (Accessed: 9 November 2016).

Mason, L. S., Shaltens, R. K. and Espinosa, W. D. (1997) 'Experimental data for two different alternator configurations in a solar Brayton power system', in *IECEC-97 Proceedings of the Thirty-Second Intersociety Energy Conversion Engineering Conference (Cat. No.97CH6203)*. Honolulu, Hawaii, USA: IEEE, pp. 454–459. doi: 10.1109/IECEC.1997.659232.

Massa, G. Di, Pagano, S. and Strano, S. (2014) 'Cabinet and Shelter Vibration Isolation : Numerical and Experimental Investigation', *Engineering Letters*, 22(4), pp. 149–157.

Masters, G. (2013) *Renewable and Efficient Electric Power Systems*. 2nd edn. Wiley.

Matson, R., Emery, K. A. and Bird, R. E. (1984) 'Terrestrial solar spectra, solar simulation and solar cell short-circuit current calibration: A review', *Solar Cells*, 11(2), pp. 105–145. doi: 10.1016/0379-6787(84)90022-X.

Mattson Technology (MTSN) (2005) *Acquisition of Vortek Industries Ltd*. Available at:

[http://www.wikinvest.com/stock/Mattson_Technology_\(MTSN\)/Acquisition Vortek Industries Ltd](http://www.wikinvest.com/stock/Mattson_Technology_(MTSN)/Acquisition_Vortek_Industries_Ltd) (Accessed: 9 November 2016).

McAdams, W. H. (1954) *Heat Transmission*. 3rd Ed. McGraw Hill.

McCAULEY, J. W. and CORBIN, N. D. (1979) 'Phase Relations and Reaction Sintering of Transparent Cubic Aluminum Oxynitride Spinel (ALON)', *Journal of the American Ceramic Society*, 62(9–10), pp. 476–479. doi: 10.1111/j.1151-2916.1979.tb19109.x.

McEvoy, A. and Markvart, T. (2011) *Practical Handbook of Photovoltaics: Fundamentals and Applications*. 2nd edn. Academic Press.

- Mei, L. *et al.* (2009) 'Equilibrium thermal characteristics of a building integrated photovoltaic tiled roof', *Solar Energy*, 83(10), pp. 1893–1901. doi: 10.1016/j.solener.2009.07.002.
- Meng, Q., Wang, Y. and Zhang, L. (2011) 'Irradiance characteristics and optimization design of a large-scale solar simulator', *Solar Energy*, 85, pp. 1758–1767. doi: 10.1016/j.solener.2011.04.014.
- Michaeli, W. *et al.* (2007) 'Geometrical Accuracy and Optical Performance of Injection Moulded and Injection-compression Moulded Plastic Parts', *CIRP Annals - Manufacturing Technology*, 56(1), pp. 545–548. doi: 10.1016/j.cirp.2007.05.130.
- Miller, D. C. and Kurtz, S. R. (2011) 'Durability of Fresnel lenses: A review specific to the concentrating photovoltaic application', *Solar Energy Materials and Solar Cells*. doi: 10.1016/j.solmat.2011.01.031.
- Miller, F. P., Vandome, A. F. and McBrewster, J. (2010) *Fresnel Lens: Physics, Augustin-Jean Fresnel, Lighthouse, Georges-Louis Leclerc, Comte de Buffon, Marquis de Condorcet, Burning Glass, Aperture, Focal Length, Lens (optics)*. Alphascript Publishing.
- Minassians, A. (2007) *Stirling Engines for Low-Temperature Solar-Thermal-Electric Power Generation*. University of California, Berkeley, USA.
- Mink, G. *et al.* (1998) 'Design parameters, performance testing and analysis of a double-glazed, air-blown solar still with thermal energy recycle', *Solar Energy*, 64(4–6), pp. 265–277. doi: 10.1016/S0038-092X(98)00076-0.
- Mistik, J. *et al.* (2017) 'Optical Properties of Electronic Materials: Fundamentals and Characterization', in Safa Kasap and Capper, P. (eds) *Springer Handbook of Electronic and Photonic Materials*. 2nd Ed. Springer International Publishing, pp. 47–83. doi: 10.1007/978-3-319-48933-9_3.
- Molla, A. R. *et al.* (2014) 'Microstructure, mechanical, thermal, EPR, and optical properties of MgAl₂O₄:Cr³⁺ spinel glass–ceramic nanocomposites', *Journal of Alloys and Compounds*, 583, pp. 498–509. doi: 10.1016/j.jallcom.2013.08.122.

- Mondol, J. D. *et al.* (2009) 'Experimental evaluation of a novel heat exchanger for solar water heating systems', in *the ISES Solar World Congress 2009: Renewable Energy Shaping Our Future*, pp. 499–507.
- Morgan Advanced Materials (2016) *Kaowool® Millboards*.
- Morin, G. *et al.* (2012) 'Comparison of Linear Fresnel and Parabolic Trough Collector power plants', *Solar Energy*, 86(1), pp. 1–12. doi: 10.1016/j.solener.2011.06.020.
- Mortensen, N. G. *et al.* (2006) 'Wind atlas for Egypt: Measurements, micro- and mesoscale modelling', in *In Proceedings (online)*. Brussels: European Wind Energy Association (EWEA), pp. 1–10. Available at: http://orbit.dtu.dk/files/106096924/Wind_atlas_for_Egypt_measurements_micro_and_mesoscale_modelling.pdf.
- MSC Software (2018) *MSC Nastran: Multidisciplinary Structural Analysis*. Available at: <http://www.mscsoftware.com/product/msc-nastran> (Accessed: 11 March 2018).
- Muhammad-Sukki, F. *et al.* (2010) 'Solar Concentrators', *International Journal of Applied Sciences*, 1(1), pp. 1–15.
- Muller-Steinhagen, H., Tried, F. and Trieb, F. (2004) 'Concentrating Solar Power – A review of the technology', *Ingenia, Royal Academy of Engineering*, 18, pp. 43–50.
- Nakakura, M. *et al.* (2016) 'Experimental demonstration and numerical model of a point concentration solar receiver evaluation system using a 30 kWth sun simulator', in *AIP Conference Proceedings*, p. 30026. doi: 10.1063/1.4949078.
- Nakamura, T. (1992) 'Survivable solar power-generating systems for use with spacecraft'. USA: U.S. Patent.
- National Centre for Earth Observation (NCEO) (2018) *SVC HR-1024i Field Spectroradiometer*. Available at: http://fsf.nerc.ac.uk/instruments/svc_hr-1024i.shtml (Accessed: 16 January 2018).
- Needham, J. (2004) *Science and Civilisation in China: Volume 4, Physics and*

Physical Technology. 6th Ed. Cambridge University Press.

Nelson, D. T., Evans, D. L. and Bansal, R. K. (1975) 'Linear Fresnel lens concentrators', *Solar Energy*, 17(5), pp. 285–289. doi: 10.1016/0038-092X(75)90045-6.

Neumann, A. and Groer, U. (1996) 'Experimenting with concentrated sunlight using the DLR solar furnace', *Solar Energy*, 58(4–6), pp. 181–190. doi: 10.1016/S0038-092X(96)00079-5.

Newton, C. C. (2007) *A Concentrated Solar Thermal Energy System*. Florida State University.

Nguyen, D. *et al.* (1997) 'Performance of thermal plume in solar thermal-electric propulsion system', in *33rd Joint Propulsion Conference and Exhibit*. Seattle, USA: American Institute of Aeronautics and Astronautics, pp. 1–6. doi: 10.2514/6.1997-3207.

Nixon, J. D. and Davies, P. A. (2012) 'Cost-exergy optimisation of linear Fresnel reflectors', *Solar Energy*, 86(1), pp. 147–156. doi: 10.1016/j.solener.2011.09.024.

Njie, D. N. and Rumsey, T. R. (1998) 'Influence of process conditions on the drying rate of cassava chips in a solar simulator', *Drying Technology*, 16(1–2), pp. 181–198. doi: 10.1080/07373939808917398.

Novatec Solar (2014) *Novatec Solar*. Available at: www.novatecsolar.com (Accessed: 1 May 2014).

NTKJ (2007) *Fresnel lens for solar concentrator*. Available at: http://www.ntkj.co.jp/product_fresnel_solar_en.html (Accessed: 24 December 2017).

O'Neill, M. J. (1984) 'A Transmittance-optimized, Point-focus Fresnel Lens Solar Concentrator', in *The proceedings of the Fifth Parabolic Dish Solar Thermal Power Program*. Indian Wells, CA: NASA, pp. 25–37.

O'Neill, M. J. *et al.* (1991) 'Recent developments in linear Fresnel lens concentrator technology, including the 300 kW 3M/Austin system, the 20 kW

PVUSA system, and the concentrator initiative', in *The Conference Record of the Twenty-Second IEEE Photovoltaic Specialists Conference*. Las Vegas, USA: IEEE, pp. 523–528. doi: 10.1109/PVSC.1991.169269.

O'Neill, M. J. *et al.* (2011) 'Low-Cost 20X Silicon-Cell-Based Linear Fresnel Lens Concentrator Panel', in *7th International Conference on Concentrating Photovoltaic Systems (CPV-7)*. AIP Conference Proceedings, pp. 120–124. doi: 10.1063/1.3658308.

O'Neill, M. J. and McDanal, A. J. (1993) 'Manufacturing technology improvements for a line-focus concentrator module', in *Conference Record of the Twenty Third IEEE Photovoltaic Specialists Conference*. Louisville, USA: IEEE, pp. 1082–1089. doi: 10.1109/PVSC.1993.346973.

O'Neill, M. J. and McDanal, A. J. (1994) 'Fourth-generation concentrator system: from the lab to the factory to the field', in *Proceedings of 1994 IEEE 1st World Conference on Photovoltaic Energy Conversion - WCPEC (A Joint Conference of PVSC, PVSEC and PSEC)*. Waikoloa, HI: IEEE, pp. 816–819. doi: 10.1109/WCPEC.1994.520085.

O'Neill, M. J. and Piszczor, M. (1988) 'An advanced space photovoltaic concentrator array using Fresnel lenses, gallium arsenide cells, and prismatic cell covers', in *Conference Record of the Twentieth IEEE Photovoltaic Specialists Conference*. Las Vegas, USA: IEEE. doi: 10.1109/PVSC.1988.105856.

Oh, S. J. *et al.* (2012) 'Development of an embedded solar tracker for the enhancement of solar energy utilization', *International Journal of Energy Research*, 36(2), pp. 249–258. doi: 10.1002/er.1813.

Ohara (2013) *Ultra-Low Expansion Glass-Ceramics: CLEARCERAM®-Z*. Available at: <http://www.oharacorp.com/pdf/ccz-2013-nav.pdf>.

Okuhara, Y. *et al.* (2015) 'A Solar Simulator for the Measurement of Heat Collection Efficiency of Parabolic Trough Receivers', *Energy Procedia*, 69, pp. 1911–1920. doi: 10.1016/j.egypro.2015.03.185.

Optenso (2017) *OpTaliX® Software for Optical Design, Thin-Films and Illumination*. Available at: <http://www.optenso.com/> (Accessed: 11 March 2018).

Optica Software (2018) *Optica*. Available at: [http://www.opticasoftware.com/store/index.php#Optica 3.0](http://www.opticasoftware.com/store/index.php#Optica%203.0) (Accessed: 11 March 2018).

Optocity (2017) *Transparent Ceramic Spinel*. Available at: <http://www.optocity.com/Spinel.htm> (Accessed: 9 April 2017).

Osinga, T. *et al.* (2004) 'Experimental Investigation of the Solar Carbothermic Reduction of ZnO Using a Two-cavity Solar Reactor', *Journal of Solar Energy Engineering*, 126(1), p. 633. doi: 10.1115/1.1639001.

Osram (2000) *Metal Halide Lamps Photo Optics: Technology and Application*. Osram Sylvania Inc. Available at: https://assets.sylvania.com/assets/documents/ENGR_BLTN7.13e279c9-3eba-4850-b60d-7347f23ab996.pdf.

Osram (2016a) *HMI 1800W/SE XS*. Available at: https://www.technilux.com/files/documents/bulbs/LHMI1800W-SE-O_spec-sheet.pdf (Accessed: 9 November 2016).

Osram (2016b) *Product datasheet: Low-voltage halogen lamps without reflector*. Available at: http://www.osram.com/osram_com/products/lamps/specialty-lamps/low-voltage-halogen-lamps/low-voltage-halogen-lamps-without-reflector/index.jsp?productId=ZMP_1006707 (Accessed: 9 November 2016).

Osram (2016c) *Product datasheet: XBO Xtreme Life, Xenon short-arc lamps for cinema projection*. Available at: http://www.osram.com/osram_com/products/lamps/specialty-lamps/xbo/xbo-xtreme-life/index.jsp (Accessed: 8 June 2017).

Osram (2016d) *Product datasheet: Xenon short-arc lamps without reflector*. Available at: http://www.osram.com/osram_com/products/lamps/specialty-lamps/xbo/xbo/index.jsp (Accessed: 8 June 2017).

Osram (2016e) *The operation principle: Generating light through gas discharge*. Available at: http://www.osram.com/osram_com/news-and-knowledge/high-pressure-discharge-lamps/professional-knowledge/operating-principle-high-pressure-discharge/index.jsp (Accessed: 22 March 2016).

Osram (2016f) *XBO HPN Xenon short-arc lamps for digital cinema projection*. Available at: https://www.osram.com/osram_com/products/lamps/specialty-lamps/xbo/xbo-hpn/index.jsp (Accessed: 9 November 2016).

Österholm, R. and Pålsson, J. (2014) 'Dynamic modelling of a parabolic trough solar power plant', in *Proceedings of the 10th International Modelica Conference*. Lund, Sweden, p. 1057. doi: 10.3384/ECP140961057.

Ouden, C. den and Wijsman, A. J. T. M. (1982) 'Lamp array design and simulator chamber design of the TNO-Solar-Simulator', in Commission, T. E., Aranovich, E., and Gillett, B. (eds) *Workshop on Solar Simulators*. Ispra, Italy: Commission of the European Communities Joint Research Centre Ispra Establishment, pp. 62–65.

Pacheco, J. E. *et al.* (2000) *Summary of the Solar Two: Test and Evaluation Program*. Available at: http://www.stratosolar.com/uploads/5/6/7/1/5671050/23_solar_2_test_and_evaluation_751185.pdf.

Palanna, O. G. (2009) *Engineering Chemistry*. New Delhi, India: Tata McGraw Hill Education Private.

Parkyn, W. A. and Pelka, D. G. (1991) 'Compact nonimaging lens with totally internally reflecting facets', in Winston, R. and Holman, R. L. (eds) *Nonimaging Optics: Maximum Efficiency Light Transfer*. SPIE, pp. 70–81. doi: 10.1117/12.49131.

Patankar, S. (1980) *Numerical Heat Transfer and Fluid Flow*. 1st Ed. CRC Press.

Patnaik, S. and Zhong, B. (2014) *Soft Computing Techniques in Engineering Applications*. Edited by J. Kacprzyk. Springer Switzerland. doi: 10.1007/978-3-

319-04693-8_2.

Paul Dvorak (2009) *Solar Reserve Signs Power Contract with NV Energy*. Available at: <https://www.designworldonline.com/solarreserve-signs-power-contract-with-nv-energy/> (Accessed: 9 March 2018).

Pedrotti, F. L. and Pedrotti, L. (2016) *Introduction to Optics*. 3rd edn. Content Technologies, Inc.

Pedrotti, F. L., Pedrotti, L. M. and Pedrotti, L. S. (2013) 'Aberration Theory', in *Introduction to Optics*. 3rd Ed. Pearson Prentice Hall.

Pérez-Higueras, P. and Fernández, E. F. (2015) *High Concentrator Photovoltaics: Fundamentals, Engineering and Power Plants*. Springer, Switzerland.

Perini, S. *et al.* (2017) 'Theoretical and experimental analysis of an innovative dual-axis tracking linear Fresnel lenses concentrated solar thermal collector', *Solar Energy*, 153, pp. 679–690. doi: 10.1016/j.solener.2017.06.010.

Perlin, J. (2013) *Let It Shine: The 6,000-Year Story of Solar Energy*. Revised Ed. New World Library.

Pernpeintner, J. *et al.* (2015) 'Linear Focus Solar Simulator Test Bench for Non-destructive Optical Efficiency Testing of Parabolic Trough Receivers', *Energy Procedia*, 69, pp. 518–522. doi: 10.1016/j.egypro.2015.03.060.

Peterka, J. A. *et al.* (1988) *Wind Loads on Heliostats and Parabolic Dish Collectors: Final Subcontract Report*. Fort Collins, Colorado. Available at: <http://www.nrel.gov/docs/legosti/old/3431.pdf>.

Petrasch, J. *et al.* (2007) 'A Novel 50 kW 11,000 suns High-Flux Solar Simulator Based on an Array of Xenon Arc Lamps', *Journal of Solar Energy Engineering*, 129(4), p. 405. doi: 10.1115/1.2769701.

Petrasch, J. and Steinfeld, A. (2005) 'A Novel High-Flux Solar Simulator Based on an Array of Xenon Arc Lamps: Optimization of the Ellipsoidal Reflector and Optical Configuration', in *ASME 2005 International Solar Energy Conference*. Orlando, Florida, pp. 175–180.

Pham, T. T., Vu, N. H. and Shin, S. (2017) 'Daylighting System Based on Novel Design of Linear Fresnel lens', *Buildings*, 7(4), pp. 1–16. doi: 10.3390/buildings7040092.

Philips (2009) *The Ultimate Experience with Philips Cinema Xenon Lamps*.

Available at:

http://www.lighting.philips.com/pwc_li/main/subsites/special_lighting/assets/Cinema_brochure_Febr_2011.pdf (Accessed: 8 June 2017).

Philips (2015a) *Product datasheet: Halogen High Voltage SE (Film/Studio)*.

Available at: http://download.p4c.philips.com/lfb/c/comf-2756/comf-2756_pss_en_aa_001.pdf (Accessed: 8 June 2017).

Philips (2015b) *Product datasheet: High Pressure Metal Halide Lamps - Double-Ended Metal Halide*. Available at:

http://download.p4c.philips.com/lfb/c/comf-1450/comf-1450_pss_en_aa_001.pdf (Accessed: 8 June 2017).

Philips (2015c) *Product datasheet: Xenon Entertainment (Follow Spots)*.

Available at: http://download.p4c.philips.com/lfb/c/comf-2128/comf-2128_pss_en_aa_001.pdf (Accessed: 8 June 2017).

Philips (2016a) *Philips Entertainment Lamps catalogue*.

Philips (2016b) *Product datasheet: HPI-T 2000W/646 E40 220V CRP/4*.

Available at: http://download.p4c.philips.com/lfb/f/fp-928073609231/fp-928073609231_pss_en_gb_001.pdf (Accessed: 8 June 2017).

Philips Strand Lighting (2015) *Dim 1: Single Channel Portable Dimmer*.

Piatkowski, N. and Steinfeld, A. (2011) 'Solar gasification of carbonaceous waste feedstocks in a packed-bed reactor-Dynamic modeling and experimental validation', *AIChE Journal*, 57(12), pp. 3522–3533. doi: 10.1002/aic.12545.

Piatkowski, N., Wieckert, C. and Steinfeld, A. (2009) 'Experimental investigation of a packed-bed solar reactor for the steam-gasification of carbonaceous feedstocks', *Fuel Processing Technology*, 90(3), pp. 360–366. doi: 10.1016/j.fuproc.2008.10.007.

Pico Technology Ltd. (2016) *TC-08 TC-08 Thermocouple Data Logger Data Sheet*.

Pico Technology Ltd. (2018) *TC-08 Thermocouple Data Logger*. Available at: https://www.picotech.com/data-logger/tc-08/thermocouple-data-logger?gclid=EAlalQobChMI6P6lw6Xg2AIVdCjTCh1YGQctEAYYBCABEGlW6vD_BwE (Accessed: 18 January 2018).

Piszczor, M. F. *et al.* (1987) 'Development of an advanced photovoltaic concentrator system for space applications', in *the 22nd Intersociety Energy Conversion Engineering Conference*. Philadelphia, PA, USA: NASA. Available at: <http://ntrs.nasa.gov/search.jsp?R=19880024585> (Accessed: 29 October 2016).

Piszczor, M. F., O'Neill, M. J. and Fraas, L. M. (1993) 'A novel space photovoltaic module using a linear Fresnel lens and a line-focus tandem cell receiver', in *Conference Record of the Twenty Third IEEE Photovoltaic Specialists Conference*. Louisville, USA: IEEE, pp. 1386–1391. doi: 10.1109/PVSC.1993.346914.

Pitchumani, R. (2014) *SunShot Initiative*. Washington D.C., USA.

Poirier, J.-P., Gillispie, C. C. and Balinski, R. (1998) *Lavoisier: Chemist, Biologist, Economist (Chemical Sciences in Society)*. University of Pennsylvania Press.

Polyanskiy, M. N. (2017) *Refractive index database*. Available at: <http://refractiveindex.info> (Accessed: 15 December 2017).

Powergems Limited (2017) *2000W Xenon Electronic Ballast*. Available at: <https://powergems.com/product/xm200-2000w-xenon-electronic-ballast/> (Accessed: 27 October 2017).

Prakash, M. (2014) 'Numerical Study of Natural Convection Heat Loss from Cylindrical Solar Cavity Receivers', *ISRN Renewable Energy*, 2014, pp. 1–7. doi: 10.1155/2014/104686.

Präzisions Glas & Optik (2017) *ZERODUR® Transmission*. Available at:

http://www.pgo-online.com/intl/katalog/curves/zerodur_tkurve.html (Accessed: 9 April 2017).

Precision Micro-Optics (2016) *Sapphire*. Available at:
<http://www.pmoptics.com/sapphire.html> (Accessed: 9 April 2017).

Pullen, H., Albach, G. and Harrison, S. (1982) 'The solar simulator at the Canadian National Solar Test Facility', in Commission, T. E., Aranovich, E., and Gillett, B. (eds) *Workshop on Solar Simulators*. Ispra, Italy: Commission of the European Communities Joint Research Centre Ispra Establishment, pp. 70–74.

Rai-Choudhury, P. (1997) *Handbook of Microlithography, Micromachining, and Microfabrication, Volume 2: Micromachining and Microfabrication*. Washington D.C., USA: SPIE.

Rathmann, C. L., Mann, G. H. and Nordberg, M. E. (1968) 'A New Ultralow-Expansion, Modified Fused-Silica Glass', *Applied Optics*, 7(5), p. 819. doi: 10.1364/AO.7.000819.

Reddy, K. S., Kumar, K. R. and Satyanarayana, G. V. (2008) 'Numerical Investigation of Energy-Efficient Receiver for Solar Parabolic Trough Concentrator', *Heat Transfer Engineering*, 29(11), pp. 961–972. doi: 10.1080/01457630802125757.

Reddy, K. S. and Satyanarayana, G. V. (2008) 'Numerical Study of Porous Finned Receiver for Solar Parabolic Trough Concentrator', *Engineering Applications of Computational Fluid Mechanics*, 2(2), pp. 172–184. doi: 10.1080/19942060.2008.11015219.

Reif, J. H. and Alhalabi, W. (2013) *Design and Analysis of a High-Efficiency, Cost-Effective Solar Concentrator*, *Journal of Solar Energy Engineering*. Available at:
<https://users.cs.duke.edu/~reif/paper/solar/SolarConcentrator/SolarConcentrator.pdf> (Accessed: 11 March 2018).

REN21 (2016) *Renewables 2016 Global Status Report*. Paris. Available at:
<http://www.ren21.net/wp->

content/uploads/2016/06/GSR_2016_Full_Report_REN21.pdf.

RenSMART (2016) *NOABL Wind Map*. Available at:

<http://www.rensmart.com/Weather/BERR> (Accessed: 28 July 2016).

Rhodes, F. H. T. and Stone, R. O. (1981) *Language of the Earth*. Pergamon Press Inc.

Rhorer, R. and Evans, C. (2010) 'Fabrication of optics by diamond turning', in *Handbook of Optics*. 3rd Ed. McGraw Hill.

Riccardi, M. (2016) *ATMOS: ATM Optical Design and Analysis Software*.

Available at: http://www.atmos-software.it/Atmos8_9.html (Accessed: 11 March 2018).

Richards, D. and Albach, G. (1982) 'A large area solar simulator construction and performance', in Commission, T. E., Aranovich, E., and Gillett, B. (eds) *Workshop on Solar Simulators*. Ispra, Italy: Commission of the European Communities Joint Research Centre Ispra Establishment, pp. 3–10.

Rippon, P. M. (1988) *Evolution of Engineering in the Royal Navy: Volume 1 1827-1939*. 1st Ed. Staplehurst, UK: Spellmount Publishers Ltd.

Riveros-Rosas, D., Sánchez-González, M. and Estrada, C. A. (2008) 'Three-Dimensional Analysis of a Concentrated Solar Flux', *Journal of Solar Energy Engineering*, 130(1), pp. 1–4. doi: 10.1115/1.2807212.

Riza, N. A., Arain, M. and Perez, F. (2005) '6-H single-crystal silicon carbide thermo-optic coefficient measurements for ultrahigh temperatures up to 1273 K in the telecommunications infrared band', *Journal of Applied Physics*, 98(10), p. 103512. doi: 10.1063/1.2133897.

Romero, V. J. (1994) *CIRCE2/DEKGEN2: A Software Package for Facilitated Optical Analysis of 3-D Distributed Solar Energy Concentrators*, SAND91-2238. Springfield, VA, USA.

Rueb, I. R. A. (1982) 'Quartz halogen dichroic mirror lamps for solar simulation', in Commission, T. E., Aranovich, E., and Gillett, B. (eds) *Workshop on Solar Simulators*. Ispra, Italy: Commission of the European Communities Joint

Research Centre Ispra Establishment, pp. 20–35.

Rugescu, R. D. (2014) *Solar Power*. InTech.

Ruoduan, S., Yu, M. and Xiaju, C. (2013) 'Effect of polarization to directional surface color measurement', in *ACA2013Thanyaburi: Blooming Color for Life*. Thanyaburi, Thailand, pp. 1–4.

Sabahi, H. *et al.* (2016) 'Design, construction and performance test of an efficient large-scale solar simulator for investigation of solar thermal collectors', *Sustainable Energy Technologies and Assessments*, 15, pp. 35–41. doi: 10.1016/j.seta.2016.03.004.

Salem, M. S., Tawfik, M. and Hamed, A. (2010) 'Analysis and Performance of Solar Concentrating-Tracking System', in *7th General International Engineering Conference*. Mansoura/Sharm El-Sheikh, Egypt.

Sarwar, J. *et al.* (2014) 'Description and characterization of an adjustable flux solar simulator for solar thermal, thermochemical and photovoltaic applications', *Solar Energy*, 100, pp. 179–194. doi: 10.1016/j.solener.2013.12.008.

Saung, E. and Miller, F. J. (2014) 'Dome Window and Mount Design for a 5 MWth Solar Receiver', *Energy Procedia*, 49, pp. 514–523. doi: 10.1016/j.egypro.2014.03.055.

Schmitz, M., Pitz-Paal, R. and Schwarzbözl, P. (2009) 'Visual HFLCAL - A software tool for layout and optimization of heliostat fields', in *SolarPACES*. Berlin, Germany.

Schofield, R. E. (2015) *Mechanism and Materialism: British Natural Philosophy in the Age of Reason*. Princeton University Press.

SCHOTT (2017) *N-BK7 Data Sheet*. Available at: http://www.amus.de/files/schott_datasheet_n-bk7.pdf (Accessed: 9 April 2017).

SCHOTT AG (2017) *ZERODUR® Extremely Low Expansion Glass Ceramic*. Available at: http://www.schott.com/advanced_optics/english/syn/advanced_optics/products/optical-materials/zerodur-extremely-low-expansion-glass-

- ceramic/zerodur/index.html?so=uk&lang=english (Accessed: 9 April 2017).
- Schulz, H. *et al.* (2000) 'Master replication into thermosetting polymers for nanoimprinting', *Journal of Vacuum Science & Technology B: Microelectronics and Nanometer Structures*, 18(6), pp. 3582–3585. doi: 10.1116/1.1319821.
- Schunk, L. O. *et al.* (2008) 'A Receiver-Reactor for the Solar Thermal Dissociation of Zinc Oxide', *Journal of Solar Energy Engineering*, 130(2), pp. 21009-21009–6. doi: 10.1115/1.2840576.
- Schunk, L. O., Lipiński, W. and Steinfeld, A. (2009) 'Heat transfer model of a solar receiver-reactor for the thermal dissociation of ZnO—Experimental validation at 10kW and scale-up to 1MW', *Chemical Engineering Journal*, 150(2–3), pp. 502–508. doi: 10.1016/j.cej.2009.03.012.
- Screwfix (2018) *TITAN MK715 Laser Distance Measurer*. Available at: https://www.screwfix.com/p/titan-mk715-laser-distance-measurer/5151p#product_additional_details_container (Accessed: 16 March 2018).
- Seba, T. (2009) *Solar Trillions: 7 Market and Investment Opportunities in the Emerging Clean-Energy Economy*. 1st Beta E. Tony Seba.
- Serov, V. (2017) *Fourier Series, Fourier Transform and Their Applications to Mathematical Physics*. 1st Ed. Springer International Publishing.
- Serway, R. A. and Jewett, J. W. (2010) *Physics for Scientists and Engineers with Modern Physics*. 8th Ed. Mary Finch.
- SGL Group – The Carbon Company (2015) *Specialty graphites for the photovoltaic industry*. Available at: http://www.sglgroup.com/cms/_common/downloads/products/product-groups/gb/brochures/Specialty_Graphites_for_the_Metal_Industry_e.pdf.
- Shaltens, R. K. and Boyle, R. V (1995) 'Initial Results From the Solar Dynamic (SD) Ground Test Demonstration (GTD) Project at NASA Lewis', in *30th Intersociety Energy Conversion Engineering Conference*. Orlando, Florida, USA: NASA, pp. 363–368.

- Shatat, M., Riffat, S. and Agyenim, F. (2013) 'Experimental testing method for solar light simulator with an attached evacuated solar collector', *International Journal of Energy and Environment*, 4(2), pp. 219–230.
- Shaughnessy, B. M., Toplis, G. M. and Wright, D. (2003) 'Thermal Testing of the Beagle 2 Mars Lander', in *33rd International Conference on Environmental Systems, ICES 2003*. Vancouver, BC; Canada, pp. 179–184. doi: 10.4271/2003-01-2462.
- Shim, J. *et al.* (2015) 'Design methodology accounting for fabrication errors in manufactured modified Fresnel lenses for controlled LED illumination', *Optics Express*, 23(15), p. 19743. doi: 10.1364/OE.23.019743.
- Shimoda, H. *et al.* (2004) 'Development of Seismic Isolation Table Supported by Ball Transfer Units and Circular Springs with Magnetic Damping', in *13th World Conference on Earthquake Engineering*. Vancouver, Canada, pp. 1–13.
- Shu, F. (1982) *The Physical Universe: An Introduction to Astronomy*. University Science Books.
- Siangsukone, P. and Lovegrove, K. (2003) 'Modelling of a 400m steam based Paraboloidal Dish concentrator for solar thermal power production', in *Destination Renewables – From Research to Market: 41st Annual Conference of the Australian and New Zealand Solar Energy Society, Australian and New Zealand Solar Energy Society*. ty, Australian and New Zealand Solar Energy, pp. 79–85.
- Sier, R. (1995) *Reverend Robert Stirling, D.D.: A Biography of the Inventor of the Heat Economiser and Stirling Cycle Engine*. 1st Ed. L.A.Mair.
- Sierra, C. and Vázquez, A. J. (2005) 'High solar energy concentration with a Fresnel lens', *Journal of Materials Science*, 40(6), pp. 1339–1343. doi: 10.1007/s10853-005-0562-6.
- Simon, F. (1976) 'Flat plate solar collector performance evaluation with a solar simulator as a basis for collector selection and performance prediction', *Solar Energy*, 18, pp. 451–466.

Sinclair Manufacturing (2011) *Technical Data-Optical Transmission Curves*. Available at: <http://www.sinclairmfg.com/datasheets/optical3.html> (Accessed: 9 April 2017).

SKF (2003) *SKF Ball Transfer Units*. Bethlehem, PA, USA. Available at: <http://www.skf.com/binary/30-97863/Ball-Transfer-units.pdf>.

Skoog, D. A. (2015) *Principles of Instrumental Analysis*. 6th edn. Content Technologies, Inc.

Sliney, D. H. and Mellerio, J. (1980) *Safety with Lasers and Other Optical Sources: A Comprehensive Handbook*. 1st Ed. Edited by M. Wolbarsht. Springer US.

Smith, J. (2016) *Organic Chemistry*. 4th Ed. Content Technologies, Inc.

Smith, W. J. (2000a) 'Aberrations', in *Modern optical engineering : the design of optical systems*. 3rd Ed. New York, USA: McGraw Hill, pp. 61–90.

Smith, W. J. (2000b) 'Image Formation', in *Modern Optical Engineering*. 3rd Ed. McGraw-Hill Companies, Inc., pp. 21–60.

Solargis (2015) *Solargis*. Available at: <https://solargis.com/assets/graphic/free-map/DNI/Solargis-United-Kingdom-DNI-solar-resource-map-en.png> (Accessed: 15 January 2018).

Song, J. *et al.* (2018) 'Application of heliostat in interior sunlight illumination for large buildings', *Renewable Energy*, 121, pp. 19–27. doi: 10.1016/j.renene.2018.01.011.

Sopian, K. *et al.* (1999) 'Technical note: Thermal performance of the double-pass solar collector with and without porous media.', *Renewable Energy*, 18(4), pp. 557–564.

Sorenson, B. and Breez, P. (2009) *Renewable Energy Focus Handbook*. Academic Press.

Soriga, I. and Neaga, C. (2012) 'Thermal analysis of a linear Fresnel lens solar collector with black body cavity receiver', *UPB Scientific Bulletin, Series D: Mechanical Engineering*, 74(4), pp. 105–116.

Spectra Vista Corporation (2016) *HR-1024i Field Spectroradiometer*. Available at: <http://www.spectravista.com/hr-1024i/> (Accessed: 16 January 2018).

SpectroLab (2010) *XT Series Continuous Wave Solar Simulator Product Description*. Sylmar, California, USA. Available at: <http://www.spectrolab.com/DataSheets/illumination/solarSim/XT RevB.pdf>.

SpectroLab (2016) *SpectroLab XT30 Solar Simulator*. Available at: <http://engineering.case.edu/centers/sdle/node/13> (Accessed: 9 November 2016).

Stine, W. and Harrigan, R. (1986) *Solar Energy Systems Design*. Hoboken, New Jersey, USA: John Wiley and Sons, Inc.

Stolten, D. and Scherer, V. (2013) *Transition to Renewable Energy Systems*. Weinheim, Germany: Wiley VCH.

Sukhatme, S. P. and Nayak, J. K. (2008) *Solar Energy: Principles of Thermal Collection and Storage*. 3rd Ed. New Delhi, India: Tata McGraw-Hill Education.

Sultanova, N., Kasarova, S. and Nikolov, I. (2009) 'Dispersion Properties of Optical Polymers', *Acta Physica Polonica A*, 116(4), pp. 585–587. doi: 10.12693/APhysPolA.116.585.

SunEarthTools (2018) *Sun Position*. Available at: https://www.sunearthtools.com/dp/tools/pos_sun.php?lang=en (Accessed: 2 May 2018).

Surana, K. S. *et al.* (2007) 'k-version of finite element method in gas dynamics: higher-order global differentiability numerical solutions', *International Journal for Numerical Methods in Engineering*. John Wiley & Sons, 69(6), pp. 1109–1157. doi: 10.1002/nme.1801.

Tabor, H. and Zeimer, H. (1962) 'Low cost Focusing Collector for solar power units', *Solar Energy*, 6, pp. 55–59.

Tawansi, A. *et al.* (2002) 'The effect of MnCl₂ filler on the optical window and the physical properties of PMMA films', *Polymer Testing*, 21(4), pp. 381–387. doi: 10.1016/S0142-9418(01)00100-3.

Tawfik, M. M. and Salem, M. S. (2014) 'Key parameters affecting concentration ratio of a solar concentrator based on lens-lens beam generator configuration', in *43rd ASES National Solar Conference 2014, SOLAR 2014*. San Francisco, CA, USA.

Teicholz, E. (2001) *Facility Design and Management Handbook*. McGraw-Hill Education.

Terao, A. *et al.* (2000) 'A mirror-less design for micro-concentrator modules', in *Conference Record of the Twenty-Eighth IEEE Photovoltaic Specialists Conference*. Anchorage, USA: IEEE, pp. 1416–1419. doi: 10.1109/PVSC.2000.916158.

TESA (2011) *TESA-VISIO Operating Principle*. Available at: http://www.conamaste.si/slo/oprema/Opticni_brezkontaktni_merilni_sistem.pdf.

Theatrical Bulb Supply (2016) *Philips LTIX-2000W/H Xenon Lamp*. Available at: <http://www.theatricalbulbsupply.com/xenon-short-arc-lamps/philips-lti/xenon-entertainment-follow-spots/philips-ltix-2000w-h-xenon-lamp/> (Accessed: 9 November 2016).

Thorlabs (2010a) *LA4545 - $f = 100.0$ mm, $\varnothing 2$ " UV Fused Silica Plano-Convex Lens, Uncoated*. Available at: <https://www.thorlabs.com/thorproduct.cfm?partnumber=LA4545>.

Thorlabs (2010b) *LB4821 - $f = 100.0$ mm, $\varnothing 2$ " UV Fused Silica Bi-Convex Lens, Uncoated*. Available at: <https://www.thorlabs.com/thorproduct.cfm?partnumber=LB4821>.

Thorlabs (2010c) *LE4125 - $\varnothing 2$ " UV Fused Silica, + Meniscus Lens, $f = 150.0$ mm, Uncoated*. Available at: <https://www.thorlabs.com/thorproduct.cfm?partnumber=LE4125>.

Thorlabs (2010d) *LE4412 - $\varnothing 2$ " UV Fused Silica, + Meniscus Lens, $f = 100.0$ mm, Uncoated*. Available at: <https://www.thorlabs.com/thorproduct.cfm?partnumber=LE4412>.

Thorlabs (2010e) *LE4560 - $\varnothing 2$ " UV Fused Silica, + Meniscus Lens, $f = 200.0$*

mm, Uncoated. Available at:

<https://www.thorlabs.com/thorproduct.cfm?partnumber=LE4560>.

Thorlabs (2017a) *LA4052-YAG - f = 35 mm, Ø1" UVFS Plano-Convex Lens*.

Available at: <https://www.thorlabs.de/thorproduct.cfm?partnumber=LA4052-YAG>.

Thorlabs (2017b) *LB4879 - f = 35.0 mm, Ø1" UV Fused Silica Bi-Convex Lens*.

Thorlabs (2017c) *LE4173 - f = 100.0 mm, Ø1" UV Fused Silica Positive Meniscus Lens*. Available at:

<https://www.thorlabs.de/thorproduct.cfm?partnumber=LE4173>.

Thorlabs (2018a) *Molded Plastic Aspheric Lenses*. Available at:

https://www.thorlabs.de/newgrouppage9.cfm?objectgroup_id=7027 (Accessed: 10 May 2018).

Thorlabs (2018b) *Optical Substrates-Calcium Fluoride Specifications*. Available at:

[https://www.thorlabs.de/newgrouppage9.cfm?objectgroup_id=6973&tabname=Calcium Fluoride](https://www.thorlabs.de/newgrouppage9.cfm?objectgroup_id=6973&tabname=Calcium%20Fluoride) (Accessed: 10 May 2018).

Thorlabs (2018c) *Positive Meniscus Lens Reference Drawing*. Available at:

https://www.thorlabs.com/images/TabImages/Positive_Meniscus_Lens_D1_350.jpg (Accessed: 13 January 2018).

Tijani, A. S. and Roslan, A. M. S. Bin (2014) 'Simulation Analysis of Thermal Losses of Parabolic trough Solar Collector in Malaysia Using Computational Fluid Dynamics', *Procedia Technology*, 15, pp. 841–848. doi:

10.1016/j.protcy.2014.09.058.

Tolbert, C. M. (1994) 'Selection of solar simulator for Solar Dynamic Ground Test', in *Proceedings of the Intersociety Energy Conversion Engineering Conference*.

Tosello, G. *et al.* (2012) 'Surface wear of TiN coated nickel tool during the injection moulding of polymer micro Fresnel lenses', *CIRP Annals - Manufacturing Technology*, 61(1), pp. 535–538. doi: 10.1016/j.cirp.2012.03.016.

Tribastone, C. and Peck, W. (2001) *An Introduction to the Design, Manufacture and Application of Plastic Optics*. Available at:

http://www.apollooptical.com/content/docs/photronics_article.pdf.

Tu, N., Wei, J. and Fang, J. (2013) 'Experimental and Numerical Study on the Thermal Performance of a Water/Steam Cavity Receiver', *Energies*, 6, pp. 1198–1216.

Turner, T. L. and Ash, R. L. (1994) 'Numerical and Experimental Analyses of the Radiant Heat Flux Produced by Quartz Heating Systems', (NASA Technical Paper 3387), p. 41.

UQG Optics (1999) *MFG-1002*. Available at: <http://www.uqgoptics.com/stock-product/MFG-1002.aspx> (Accessed: 18 March 2018).

Vaan, R. De (1982) 'Artificial light source for solar simulation', in Commission, T. E., Aranovich, E., and Gillett, B. (eds) *Workshop on Solar Simulators*. Ispra, Italy: Commission of the European Communities Joint Research Centre Ispra Establishment, pp. 75–82.

Valette, S. (1995) 'Micro-optics, a key technology in the race to microsystems', *Journal of Micromechanics and Microengineering*, 5(2), pp. 74–76. doi: 10.1088/0960-1317/5/2/005.

Velmurugan, P. and Kalaivanan, R. (2016) 'Energy and exergy analysis in double-pass solar air heater', *Sadhana*, 41(3), pp. 369–376. doi: 10.1007/s12046-015-0456-5.

Vortek Industries Ltd. (1999) *Model 201-200/200 200 kW Arc Lamp System*. Vancouver BC, V6P 6T7 Canada.

Vu, N.-H., Pham, T.-T. and Shin, S. (2016) 'Modified optical fiber daylighting system with sunlight transportation in free space', *Optics Express*, 24(26), pp. 1528–1545. doi: 10.1364/OE.24.0A1528.

Walker, A. (2013) *Solar Energy: Technologies and Project Delivery for Buildings*. 1st Ed. John Wiley & Sons.

Wallhead, I. *et al.* (2012) 'Design of an efficient Fresnel-type lens utilizing

- double total internal reflection for solar energy collection', *Optics Express*, 20(S6), p. A1005. doi: 10.1364/OE.20.0A1005.
- Wang, C.-M. *et al.* (2010) 'Single stage transmission type broadband solar concentrator', *Optics Express*, 18(S2), p. A118. doi: 10.1364/OE.18.00A118.
- Wang, F. *et al.* (2013) 'Thermal performance analysis of porous media receiver with concentrated solar irradiation', *International Journal of Heat and Mass Transfer*, 62, pp. 247–254. doi: 10.1016/j.ijheatmasstransfer.2013.03.003.
- Wang, H. *et al.* (2018) 'Design, fabrication and optical characterizations of large-area lithography-free ultrathin multilayer selective solar coatings with excellent thermal stability in air', *Solar Energy Materials and Solar Cells*, 174, pp. 445–452. doi: 10.1016/j.solmat.2017.09.025.
- Wang, J. (2017) *Real-Time Embedded Systems*. 1st Ed. John Wiley & Sons, Inc.
- Wang, W. *et al.* (2014) 'Design and validation of a low-cost high-flux solar simulator using Fresnel lens concentrators', *Energy Procedia*, 49, pp. 2221–2230. doi: 10.1016/j.egypro.2014.03.235.
- Wang, W. (2014) *Simulate a 'Sun' for Solar Research: A Literature Review of Solar Simulator Technology*. Stockholm, Sweden.
- Wang, W. (2015) *Development of an Impinging Receiver for Solar Dish-Brayton Systems*. Royal Institute of Technology. Available at: <http://kth.diva-portal.org/smash/get/diva2:873171/FULLTEXT01.pdf>.
- Waymouth, J. F. (1971) *Electric Discharge Lamps (Monographs in Modern Electrical Technology)*. The MIT Press.
- Wei, X. *et al.* (2010) 'A new code for the design and analysis of the heliostat field layout for power tower system', *Solar Energy*, 84(4), pp. 685–690. doi: 10.1016/j.solener.2010.01.020.
- Wikimedia (2018) *Berniere's Great Burning-Glass*. Available at: https://commons.wikimedia.org/wiki/File:Berniere%27s_Great_Burning-Glass.png?uselang=en-gb (Accessed: 8 March 2018).

- Wilson, L. R. (2010) *Luminescent Solar Concentrators : A Study of Optical Properties , and Device Optimisation*. Heriot-Watt University.
- Worgull, M. (2009) *Hot embossing, theory and technology of microreplication, Micro and Nano Technologies*. 1st Ed. William Andrew.
- Wright, S. C., Fleck, N. A. and Stronge, W. J. (1993) 'Ballistic impact of polycarbonate—An experimental investigation', *International Journal of Impact Engineering*, 13(1), pp. 1–20. doi: 10.1016/0734-743X(93)90105-G.
- Wu, T.-M. (2006) 'Computer-aided Deflection and Slope Analyses of Beams', *Journal of Applied Sciences*, 6(2), pp. 333–339.
- Wurfel, P. (2009) *Physics of Solar Cells: From Basic Principles to Advanced Concepts*. 2nd edn. Wiley-VCH.
- Xie, W. *et al.* (2011) 'Concentrated solar energy applications using Fresnel lenses: A review', *Renewable and Sustainable Energy Reviews*, 15(6), pp. 2588–2606. doi: 10.1016/j.rser.2011.03.031.
- Xie, W., Dai, Y. and Wang, R. (2011) 'Numerical and experimental analysis of a point focus solar collector using high concentration imaging PMMA Fresnel lens', *Energy Conversion and Management*, 52(6), pp. 2417–2426. doi: 10.1016/j.enconman.2010.12.048.
- Xie, W., Dai, Y. and Wang, R. (2012) 'Theoretical and experimental analysis on efficiency factors and heat removal factors of Fresnel lens solar collector using different cavity receivers', *Solar Energy*, 86(9), pp. 2458–2471. doi: 10.1016/j.solener.2012.05.017.
- Xu, H. (2013) *Numerical Study on the Thermal Performance of a Novel Impinging Type Solar Receiver for Solar Dish-Brayton System*. Royal Institute of Technology, Stockholm.
- Xu, X.-Y. (2016) *Applied Research of Quantum Information Based on Linear Optics*. 1st Ed. Springer-Verlag Berlin Heidelberg. doi: 10.1007/978-3-662-49804-0.
- Yan, W. and Dawson, F. P. (1998) 'Power supply design considerations for

maintaining a minimum sustaining current in a vortex water wall high-pressure argon arc lamp', *IEEE Transactions on Industry Applications*, 34(5), pp. 1015–1025. doi: 10.1109/28.720441.

Yang, D. J. *et al.* (2012) 'Simulation and experimental validation of heat transfer in a novel hybrid solar panel', *International Journal of Heat and Mass Transfer*, 55(4), pp. 1076–1082. doi: 10.1016/j.ijheatmasstransfer.2011.10.003.

Yass, K. and Curtis, H. B. (1974) *Low cost air mass 2 solar simulator*. NASA TM X-3059.

Yass, K. and Curtis, H. B. (1975) *Operational performance of a low-cost air mass 2 solar simulator*. NASA TM-X-71162.

Yeh, N. (2016) 'Illumination uniformity issue explored via two-stage solar concentrator system based on Fresnel lens and compound flat concentrator', *Energy*. Elsevier Ltd, 95, pp. 542–549. doi: 10.1016/j.energy.2015.12.035.

Yeh, N. and Yeh, P. (2016) 'Analysis of point-focused, non-imaging Fresnel lenses' concentration profile and manufacture parameters', *Renewable Energy*, 85, pp. 514–523. doi: 10.1016/j.renene.2015.06.057.

Yogev, A. *et al.* (1998) 'Solar "tower reflector" systems: A new approach for high-temperature solar plants', *International Journal of Hydrogen Energy*, 23(4), pp. 239–245. doi: 10.1016/S0360-3199(97)00059-1.

Yoon, S. *et al.* (2006) 'Critical factors for nanoscale injection molding', in Cullum, B. M. and Carter, J. C. (eds) *SPIE 6380, Smart Medical and Biomedical Sensor Technology IV*. SPIE, pp. K1–12. doi: 10.1117/12.686310.

Yoshizawa, T. (2015) *Handbook of Optical Metrology: Principles and Applications*. 2nd edn. Edited by T. Yoshizawa. CRC Press.

Yue, Y. and Angell, C. A. (2004) 'Clarifying the glass-transition behaviour of water by comparison with hyperquenched inorganic glasses', *Nature*, 427(6976), pp. 717–720. doi: 10.1038/nature02295.

Zacharopoulos, A. *et al.* (2009) 'State-of-the-art solar simulator with dimming control and flexible mounting', in *29th ISES Biennial Solar World Congress*

2009, *ISES 2009*. Johannesburg; South Africa, pp. 854–863.

Zahler, C. *et al.* (2005) 'Design, Manufacture and Installation of a Solar Simulator for the GREEN Laboratory at Pontifícia Universidade Católica de Minas Gerais in Brazil', in *the Solar World Congress 2005: Bringing Water to the World*. Orlando, Florida, USA, pp. 868–873.

Zahler, C. *et al.* (2008) 'Design, Manufacturing and Installation of a Combined Indoor and Outdoor Test Stand for Solar Thermal Collectors for the Centre for Solar Energy Studies (CSES) in Libya', in *1st International Conference on Solar Heating, Cooling and Buildings*. Lisbon, Portugal.

Zhai, H. *et al.* (2010) 'Experimental investigation and analysis on a concentrating solar collector using linear Fresnel lens', *Energy Conversion and Management*, 51(1), pp. 48–55. doi: 10.1016/j.enconman.2009.08.018.

Zheng, J. and Forslund, B. (1995) 'Carbothermal synthesis of Aluminium Oxynitride (ALON) powder: Influence of starting materials and synthesis parameters', *Journal of the European Ceramic Society*, 15(11), pp. 1087–1100. doi: 10.1016/0955-2219(95)00078-9.

APPENDICES

Appendix A Rear Lens Thermal Model MATLAB Cod

```
1 function [T2]=full_temperature(e,k,Ta,h1,h2,epsilon,qabsorb,D,roh
2 ,Cp,dt,Ti)
3 %This function is to calculate the lower surface temperature of
4 a window
5 %(the surface which is not subjected to concentrated solar
6 power)
7 %with diameter (D), thickness (e), density (roh), heat capacity
8 (Cp),
9 %emissivity (epsilon),thermal conductivity (k)
10 % h1,h2: are the convective heat transfer coefficients for the
11 upper (facing the sun)surface and the lower surface
12 % Ta: is the ambient temperature in (K)
13 % Ti: is the initial temperature in (K)
14 % dt: is the time step of calculations in (seconds)
15 % qabsorb: is the amount of absorbed solar power by the window
16 material
17 % which is calculated as: (qabsorb=absorbance*incident solar
18 flux)
19 % qabsorb is supplied to the function as a vector with values
20 corresponding
21 % the value of absorbed solar power at each time (t).
22
23 % In this code, all variables has been considered
24
25 % p is the polynomyal coefficients vector
26 % segma is Stefan-Boltzmann Const.
27
28 n=length(qabsorb);
29 m=roh*(pi*0.25*D^2*e);
30 C=m*Cp/dt;
31
32 Tav = zeros(n,1);
33 T1 = zeros(n,1);
34 T2 = zeros(n,1);
35
36 Tav(1)=Ti;
37 T1(1)=Ti;
38 T2(1)=Ti;
39
40 p = [0;0;0;0;0];
41 segma=5.67e-8;
42
43 p(1)=2*epsilon*segma;
44 p(4)=h1+h2+C;
45
46     for i=2:n
47         p(5)=-
48 (( (h1+h2) *Ta) + (2*epsilon*segma*(Ta^4)) +qabsorb(i) + (C*Tav(i-1)) );
```



```

49         T_full=roots(p);
50
51         T_real=real(T_full);
52         T_img=imag(T_full);
53         % scanning to select the real solution only
54         for j=1:4
55             if (T_img(j)==0)
56                 Tav(i)= T_real(j);
57             end
58         end
59     end
60     % Now the Average Temperature has been calculated
61     % Next step is to calculate T1
62
63     p(1)=e*epsilon*segma/k;
64     p(4)=2+(e*h1/k);
65     for i=2:n
66         p(5)=-
67         ((e/k)*(qabsorb(i)+Ta+(epsilon*segma*(Ta^4)))+(2*Tav(i)));
68         T_full=roots(p);
69
70         T_real=real(T_full);
71         T_img=imag(T_full);
72         % scanning to select the real solution only
73         for j=1:4
74             if (T_img(j)==0)
75                 T1(i)= T_real(j);
76             end
77         end
78     end
79     for i=2:n
80         T2(i)=(2*Tav(i))-T1(i);
81     end
82 end

```

Appendix B Incident Heat Flux Boundary Condition

B.1 Incident Heat Flux

Solar insolation calculations are based on assuming the location of Cranfield, UK at a latitude angle of 52°N and on the day of summer solstice. The sky is assumed to be clear for all the day time. The device is assumed to track the sun in three-dimension all the daytime. The transmittance of the front lens is assumed to be 100%. The solar irradiance can be determined by the empirical formula presented by **(Laue, 1970)**:

$$I_{in} = 1.353 \cdot [(1 - 0.14H)0.7^{AM^{0.678}} + (0.14Z/1000)] \quad (\text{B-1})$$

Where, I_D is direct solar irradiation in W/m^2 , Z is the location altitude above sea level and AM is the Air Mass and H is the hour angle. By neglecting the location altitude above sea level and including a calculation safety factor of 10%, then Eq. (B-1) can be rewritten as:

$$I_D = 1.1 * [1.353 \times (0.7^{AM})^{0.678}] \quad (\text{B-2})$$

Air Mass is the path length of solar light through the atmosphere normalized to the shortest possible path length. It quantifies the lost solar power dissipated through the atmosphere due to air and dust. This value can be calculated by the following equation which incorporates the curvature of the earth **(Kasten and Young, 1989)**:

$$AM = [\cos(z) + 0.50572(96.07995 - z)^{-1.6364}]^{-1} \quad (\text{B-3})$$

Where, z is the zenith angle, which can be determined from the following relation **(Jacobson, 2005)**:

$$\cos(z) = \sin(L) \sin(\delta) + \cos(L) \cos(\delta_s) \cos(H) \quad (\text{B-4})$$

Where, L is the location latitude angle, δ_s is the declination angle of the sun, while H is the hour angle.

B.2 Solar Angles

B.2.1 Declination angle, δ_s

There are simplified equations that can be applied to get the declination angle (Cooper, 1969; Perrin, 1975). These equations are quite accurate (Iqbal, 2012). In these equations, Earth's orbit is treated as being round rather than its true elliptical shape. In order to get more accurate results, the following equation takes into account the *eccentricity* of the Earth's orbit around the Sun and the true length of a year (365.24 days). This equation is introduced by (REUK, 2014) as follows:

$$\delta_s = \sin^{-1} \left[\sin(-23.44^\circ) \cdot \cos\left(\frac{360^\circ}{365.24}(DN + 10)\right) + \frac{360^\circ}{\pi} \cdot 0.0167 \sin\left(\frac{360^\circ}{365.24}(DN - 2)\right) \right] \quad (\text{B-5})$$

By evaluating constants, it can be simplified to:

$$\delta_s = -\sin^{-1} \{ 0.39779 \cos[0.98565(DN + 10)] + 1.914 \sin(0.98565(DN - 2)) \} \quad (\text{B-6})$$

Where, DN is the day of the year beginning with $N = 1$ on January 1st. Equation (B-6) is applied in calculation of declination angle in this thesis.

B.2.2 Hour angle, H

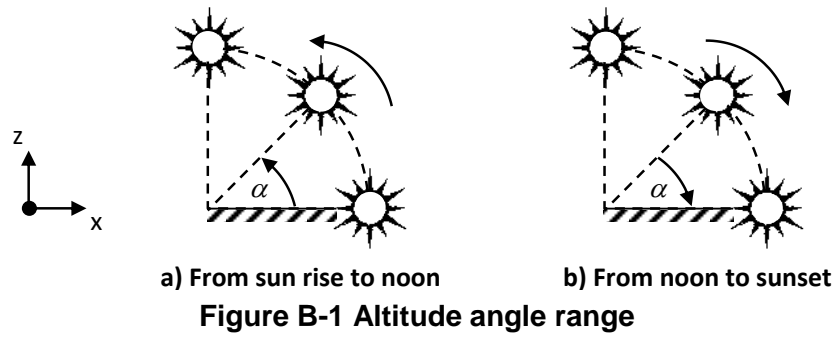
The following formula is applied to calculate the hour angle (Ballast, 1988):

$$H = \pm 0.25(\text{Number of minutes from local solar noon}) \quad (\text{B-7})$$

Where, + for PM and - for AM solar time.

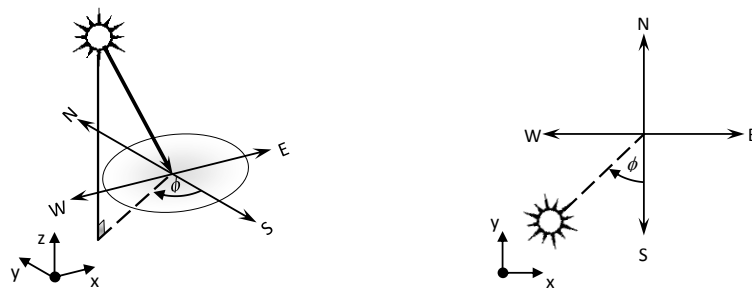
B.2.3 Altitude angle, γ

The altitude angle is the angle between the horizontal (x -axis) and the line to the sun (Duffie and Beckman, 2013). It varies from 0° , at sunrise/sunset, to 90° or less, at noon, as illustrated in Figure B-1.

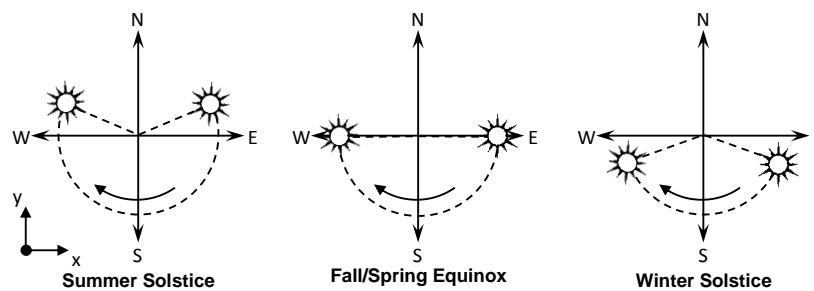


B.2.4 Azimuth angle, ϕ

The azimuth angle is the angle between the South direction and the projection of solar beam radiation on the horizontal ($x-z$) plane (Duffie and Beckman, 2013). The clockwise direction is defined as the positive measurement direction. Figure B-2 shows the azimuth angle definition.



Its range is more than $\pm 90^\circ$, at summer solstice, $\pm 90^\circ$, at fall/spring equinox, and less than $\pm 90^\circ$, at winter solstice, as illustrated in Figure B-3.



However, all of the previous solar angles are programmed in an Excel file to obtain a complete record of different angles at any time. Figure B-4 illustrates a snap shot from this program.

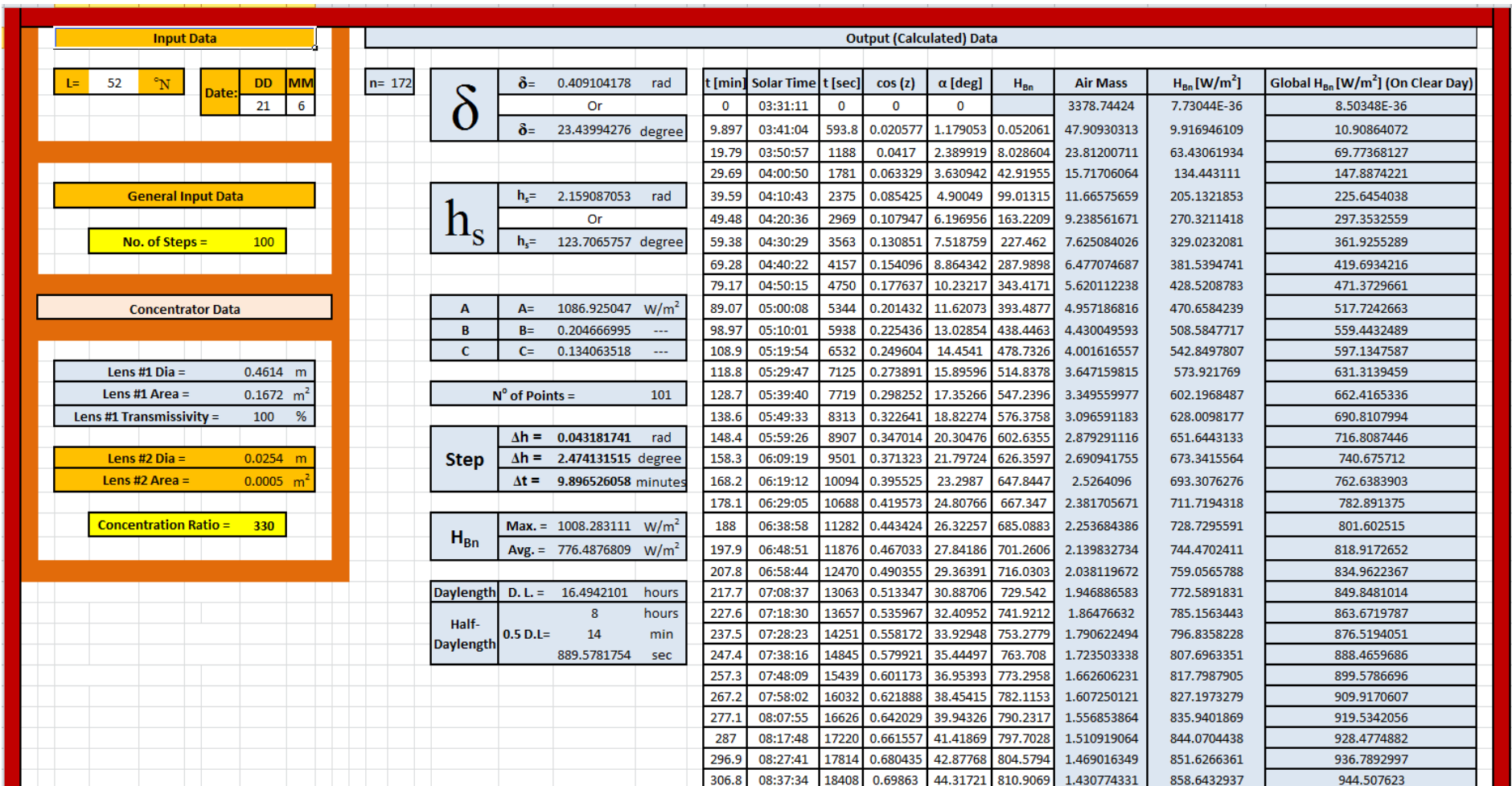


Figure B-4 Snap shot from solar angles calculator programme

Appendix C TESA-VISIO 300 DCC Report

This report for the solar simulator spot light back reflector diameter and radius of curvature:

pcdmis		PART NAME : Light Mirror		May 16, 2017	11:42			
		REV NUMBER :	SER NUMBER :	STATS COUNT : 1				
#	MM	LOC2 - SPH2 <i>Mirror</i>						
AX	NOMINAL	+TOL	-TOL	MEAS	DEV	OUTTOL		
X	0.00000	0.05000	-0.05000	-0.01066	-0.01066	0.00000		
Y	0.00000	0.05000	-0.05000	-0.10937	-0.10937	0.05937		
Z	79.50000	0.05000	-0.05000	79.16276	-0.33724	0.28724		
D	242.00000	0.05000	-0.05000	242.65636	0.65636	0.60636		
R	121.00000	0.05000	-0.05000	121.32818	0.32818	0.27818		
FEATURE	HITS	MEAS X	Y	Z	VECTOR I	J	K	DEV
SPH2 X	0	-0.01066	-0.10937	79.16276	1.00000	0.00000	0.00000	-0.01066
Y	0	-0.01066	-0.10937	79.16276	0.00000	1.00000	0.00000	-0.10937
Z	0	-0.01066	-0.10937	79.16276	0.00000	0.00000	1.00000	-0.33724
#	MM	LOC1 - CIR1 <i>Black Ring</i>						
AX	NOMINAL	+TOL	-TOL	MEAS	DEV	OUTTOL		
D	164.86934	0.05000	-0.05000	164.86934	0.00000	0.00000		
FEATURE	HITS	MEAS X	Y	Z	VECTOR I	J	K	DEV
CIR1 D	0	1.64428	-0.04694	-1.78883	0.00000	-0.00000	1.00000	0.00000
FCFCIRT...	MM	○ 0.01						
Feature	NOMINAL	+TOL	-TOL	MEAS	DEV	OUTTOL		
SPH2	0.00000	0.01000		0.57148	0.57148	0.56148		

Appendix D LLBG Design

D.1 Solar Angles

The sun path in the sky can be defined by two main angles: altitude, γ , and azimuth, φ , angles.

D.2 LLBG Design Assumptions

D.2.1 Main Arm Length

The Main Arm consists of two aluminium rails carrying front lens, its aluminium frame, and the rear lens at their ends. The front lens has specifications listed in Table D-1.

Table D-1 Front lens specifications

Parameter	Value
Lens Geometry	Fresnel
Supplier	Nihon Tokushu Kogaku Jushi Co., Ltd., Japan
Part Number	CF1200-B3
Focal length (f_1)	1.4 m
Dimensions	1.4 x 1.05 m
Thickness	3E-3 m
Perimeter (P)	4.9 m
Material	PMMA
Approximate mass (m_{L1})	8.3 kg

While the rear lens is a positive meniscus lens has specifications listed in Table D-2.

Table D-2 Rear lens specifications

Parameter	Value
Lens Geometry	Positive Meniscus
Supplier	Thorlabs Inc., USA
Part Number	LE4173
Focal length (f_2)	0.1 m
Diameter	0.0254 m
Thickness	4E-3 m
Material	UV Fused Silica
Approximate mass (m_{L2})	0.02 kg

Based on data provided in tables C-1 and C-2, the minimum Main Arm length, l_{MA} is:

$$l_{MA})_{min} = f_1 + f_2 \quad (\text{D-8})$$

From Eq. (D-8), the Main Arm Length total length can be assumed to be **1.5m**.

D.2.2 Front Lens Holder Weight

The aluminium profile used for the lens frame is shown in Figure D-5. All profile specifications are listed in Table D-3.

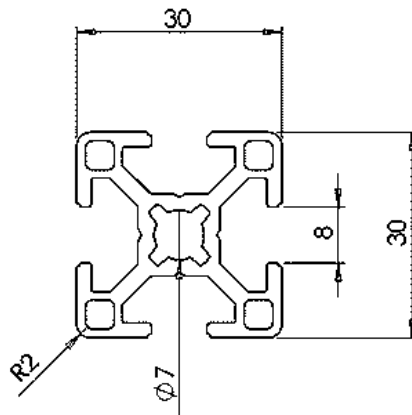


Figure D-5 Aluminium profile used

Table D-3 Aluminium profile specifications

Parameter	Value
Profile Geometry	30x30 Profile
Supplier	Bosch Rexroth Ltd., UK
Part Number	KJN990720
Maximum Length	6 m
Slot Size	8E-03 m
mass/l (w)	0.8 kg/m

The total mass of lens holder can be calculated as:

$$m_{LH1})_{total} = (P * \omega) + m_{L1} \quad (\text{D-9})$$

Substituting P with 5m, then the front Lens Holder weight including the lens will be 12.3 kg. It can be assumed to be **13 kg**.

D.2.3 Main Arm Weight

The main arm weight, excluding the front Lens Holder weight, is determined by:

$$m_{MA} = 2(l_{MA} * \omega) \quad (\text{D-10})$$

As the aluminium profile used as rails have the same specifications mentioned before in Table D-3, then the outcome of Eq. (D-10) is 2.4 kg. Therefore, the main arm weight can be assumed as **2.5 kg**.

D.2.4 Torque at Main Arm Hinge

Based on the free body diagram shown in Figure D-6, the torque at the Main Arm hinge can be calculated by:

$$T = (0.5 * l_{MA} * F_1) + (l_{MA} * F_2) \quad (\text{D-11})$$

Where

$$F_1 = m_{MA} * g \quad (\text{D-12})$$

$$F_2 = m_{LH} * g \quad (\text{D-13})$$

Then the torque outcoming is 228.1 N.m. So, it can be assumed to be **230 N.m**.

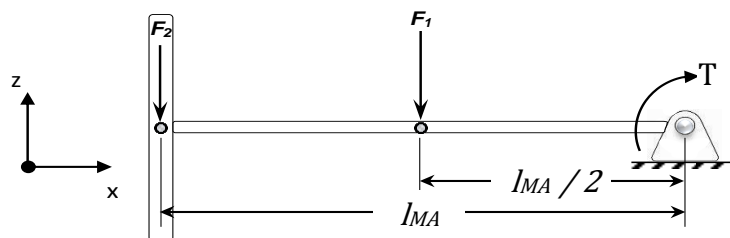


Figure D-6 Free body diagram of the Main Arm

D.2.5 Main Arm Angular Speed

As the Main Arm rotates to track the altitude angle, α , then it will rotate by a maximum angle of 90° within the half-day length. For rough calculations, let us assume that the day length* is 12 hours. In other words, the Main Arm will rotate 90° for 6 hours, which means an angular speed of $\pm 0.25^\circ/\text{min}$.

* Day length stands for the time from sunrise to sunset. This period is bisected by noon time into two equal halves.

D.2.6 Control Mirror Stroke

The LLBG do not start to collect and concentrate solar rays at sun rise. As this means that the concentrated beam will be received by the Control Mirror at a very far point at the infinity. Therefore, the altitude angle at which the LLBG starts to catch sunlight and generate the beam is called as catching altitude angle, γ_0 . Then, the Control Mirror stroke, l_{st} can be defined as the distance between the Control Mirror position at angle γ_0 to its position at the maximum altitude angle, γ_{max} . This definition is shown in Figure D-7, in which it can be noted that the distance l depends on the Main Arm hinge height, Z_0 , and the angle γ_0 .

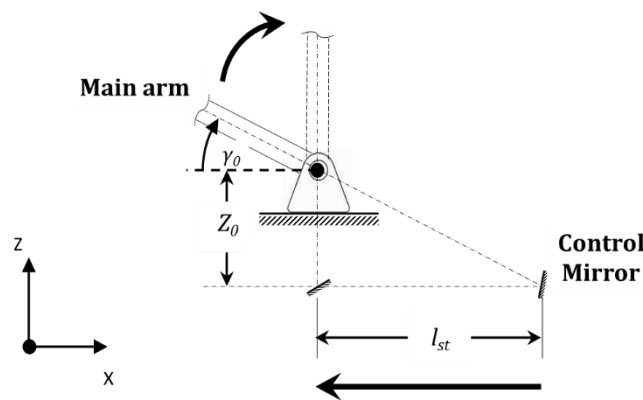


Figure D-7 Control Mirror stroke definition

From the geometry of Figure D-7, the Control Mirror stroke can be calculated as:

$$l_{st} = \frac{Z}{\tan \gamma_0} \quad (\text{D-14})$$

Assuming H to be 0.75m and α_0 to be 25° , then L_{st} will be 1.6m. Therefore, the stroke, l_{st} , can be assumed to be **2m**.

D.2.7 Control Mirror Linear Speed

The Control Mirror sweeps its stroke within the half-day length. Based on a day length of 12 hours, then the approximate Control Mirror will be $\pm 5.5\text{mm/min}$.

Appendix E Aluminium Profile Deflection Study

In this Appendix, the results of Eq. (6-92) are listed in tabular form for available Aluminium profile supplied by Bosch Rexroth® for different numbers of front lens supporting rods, N_{MA} . As derived in Section 6.2.4, a limiting deflection of 1.65×10^{-3} m has been applied. Deflections under this limit has been coloured in green fill.

Table E-4 Profile deflection study for $N_{MA} = 2.0$

$N_{MA} = 2.0$									
Profile	Slot	A (cm ²)	I_x (cm ⁴)	I_y (cm ⁴)	W_x (cm ³)	W_y (cm ³)	w (kg/m)	$\delta_x \times 10^{-03}$ (m)	$\delta_y \times 10^{-03}$ (m)
20x20	6	1.6	0.7	0.7	0.7	0.7	0.4	327.18	327.18
20x20 1N	6	1.9	0.8	0.8	0.8	0.8	0.5	289.79	289.79
20x20 2N	6	1.8	0.7	0.8	0.7	0.8	0.5	331.19	289.79
20x20 2NVS	6	1.8	0.7	0.7	0.7	0.7	0.5	331.19	331.19
20x20 3N	6	1.7	0.7	0.8	0.7	0.7	0.5	331.19	289.79
20x20 R	6	1.6	0.6	0.6	0.5	0.5	0.4	381.71	381.71
20x40	6	2.9	4.6	1.2	2.5	1.4	0.8	52.23	200.20
20x60	6	3.5	14.2	1.7	4.7	1.7	0.9	17.12	142.97
20x40x40	6	4.2	6	6	2.6	2.6	1.1	41.44	41.44
10x40	6	2.1	3.2	0.2	1.6	0.4	0.6	73.32	1173.17
30x30	8	3.1	2.8	2.8	1.8	1.8	0.9	86.80	86.80
30x30 1N	8	3.7	3.1	3.5	2	2.3	1	79.31	70.24
30x30 2N	8	3.5	2.8	3.5	2.1	2.7	1	87.80	70.24
30x30 2NVS	8	3.5	3.1	3.1	2	2	1	79.31	79.31
30x30 3N	8	3.3	3.1	2.8	2.3	2.2	0.9	78.40	86.80
30x30 _o	8	3.7	3.5	3.6	2	1.9	1	70.24	68.29
30x45 _o	8	4	3.6	5.1	2.1	2.3	1.1	69.07	48.75
30x60 _o	8	3.6	3.1	4.1	1.7	1.9	1	79.31	59.96
30x30 R	8	2.9	2.3	2.3	1.4	1.4	0.8	104.45	104.45
30x60	8	5.5	19.6	5.1	7	3.9	1.5	13.26	50.95
30x60 4N	8	5.8	20.2	5.5	6.7	3.8	1.6	13.00	47.76
30x60x60	8	8.2	26.2	26.2	7.6	7.6	2.2	10.67	10.67
30x90	8	7.7	60.7	7.3	13.5	4.9	2.1	4.56	37.90
30x120	8	9.9	136.3	9.6	22.7	6.4	2.7	2.15	30.57
30x45	8/10	4	8.1	3.9	3.9	2.9	1.1	30.70	63.76
60x60 8N	8	9.8	39.7	39.7	13.2	13.2	2.6	7.32	7.32
11x20	8	1	0.5	0.1	0.7	0.3	0.3	452.45	2262.26
15x120	8	9	110.4	2.2	18.4	2.7	2.4	2.58	129.58
40x40L	10	5.6	9.1	9.1	4.5	4.5	1.5	28.56	28.56
40x40L 0N	10	6.3	10.4	10.4	5.2	5.2	1.7	25.53	25.53
40x40L 1N	10	6.1	9.8	10.4	4.8	5.2	1.7	27.09	25.53
40x40L 2N	10	6	9	10.3	4.5	5.2	1.6	29.18	25.50
40x40L 2NVS	10	6	9.7	9.7	4.9	4.9	1.6	27.08	27.08

$N_{MA} = 2.0$									
Profile	Slot	A (cm ²)	I_x (cm ⁴)	I_y (cm ⁴)	W_x (cm ³)	W_y (cm ³)	w (kg/m)	$\delta_x \times 10^{-03}$ (m)	$\delta_y \times 10^{-03}$ (m)
40x40L 3N	10	5.8	9.7	9	4.8	4.5	1.6	27.08	29.18
40x30 _o	10	6.2	9.4	11.8	4.7	5.9	1.7	28.24	22.50
40x45 _o	10	6.8	9.9	16.6	5	8.3	1.8	27.10	16.16
40x60 _o	10	6.3	8.7	13.1	4.3	6.5	1.7	30.51	20.26
40x40L R	10	5	7.2	7.2	3.6	3.6	1.3	35.31	35.31
40x40 HR	10	5.5	8.1	7.6	4	3.6	1.5	32.08	34.19
40x80L	10	9.9	63.4	17.3	15.9	8.7	2.7	4.63	16.96
40x80L 4N	10	10.4	65.2	19.1	16.3	9.9	2.8	4.54	15.51
40x80L 3NVS	10	10.6	67.8	19	17	9.5	2.9	4.41	15.74
40x80x80L	10	15.4	96.6	96.6	24.2	24.2	4.2	3.47	3.47
40x120L	10	15.5	203.2	27.8	33.9	13.9	4.2	1.65	12.07
40x160L	10	20.5	466.7	37.2	58.3	18.6	5.5	0.80	10.00
80x80L	10	18.2	132.1	132.1	33	33	4.9	2.69	2.69
80x80L 4NVS	10	19.3	142.5	142.5	35.6	35.6	5.2	2.55	2.55
80x80L 6N	10	18.8	134.1	140.9	33.5	36.2	5.1	2.69	2.56
40x120x120L	10	24.6	318	318	42.2	42.2	6.7	1.28	1.28
80x120L	10	25.6	389.2	192.8	64.9	48.2	6.9	1.06	2.13
80x160L	10	32.9	850.7	253.4	106.3	63.4	8.9	0.55	1.84
45x45L	10	6	11.7	11.7	5.2	5.2	1.6	22.45	22.45
45x45L 0N	10	6.7	13.5	13.5	6	6	1.8	19.87	19.87
45x45L 1N	10	6.5	12.6	13.5	5.5	6	1.8	21.29	19.87
45x45L 2N	10	6.4	11.6	13.5	5.2	6	1.7	22.88	19.66
45x45L 2NVS	10	6.4	12.6	12.6	5.6	5.6	1.7	21.07	21.07
45x45L 3N	10	6.2	12.6	11.7	5.4	5.2	1.7	21.07	22.69
45x30 _o	10	6.9	12.7	15.2	5	5.3	1.9	21.34	17.83
45x45 _o	10	7.6	13.4	21.4	5.2	6.4	2	20.44	12.80
45x60 _o	10	6.8	11.4	16.9	4.4	5.2	1.8	23.53	15.87
45x45L R	10	4.9	8.6	8.6	5	5	1.3	29.56	29.56
45x45HR	10	6.6	11	10.7	4.4	4.8	1.8	24.39	25.07
45x45	10	7.5	13.8	13.8	6.1	6.1	2	19.85	19.85
45x60	10	11	37.2	22.7	12.4	10.1	3	8.12	13.30
45x90SL	10	9	73.4	18.1	16.3	8	2.4	3.88	15.75
45x90L	10	11.3	82	23.6	18.2	10.5	3	3.68	12.79
45x90L 2N	10	12	85.6	26.9	38.1	6	3.2	3.59	11.43
45x90L 3NVS	10	11.8	87.2	25.2	38.8	5.6	3.2	3.53	12.20
45x90	10	15.4	124.6	32.8	27.7	14.6	4.2	2.69	10.23
45x180	10	25.5	766.7	57.3	85.2	25.5	6.9	0.54	7.18
45x270	10	61.9	3962	118	300.2	61.6	16.7	0.17	5.81
45x90x90L	10	21.2	152.1	152.1	19.1	32.6	5.7	2.48	2.48
45x90x90L 4 N	10	22.1	160.8	160.8	30.6	30.6	5.95	2.39	2.39
90x90SL	10	14.1	130.2	130.2	28.9	28.9	3.8	2.49	2.49
90x90L	10	24.1	211.1	211.1	46.9	46.9	6.5	1.89	1.89
90x90L 4N	10	24.2	227.4	214.7	50.5	47.7	6.5	1.76	1.86

$N_{MA} = 2.0$									
Profile	Slot	A (cm ²)	I_x (cm ⁴)	I_y (cm ⁴)	W_x (cm ³)	W_y (cm ³)	w (kg/m)	$\delta_x \times 10^{-03}$ (m)	$\delta_y \times 10^{-03}$ (m)
90x90L 4NVS	10	24.2	220.9	220.9	49.2	49.2	6.5	1.81	1.81
90x90	10	38.4	299.8	299.8	66.7	66.7	10.4	1.70	1.70
90x180L	10	42.8	1380	401	153.3	89.1	11.6	0.39	1.35
90x180	10	63.6	2138.3	544.3	237.6	121	17.2	0.33	1.29
90x360	10	90.2	14065	710	781.4	157.7	24.4	0.06	1.27
15x22.5	10	1.3	0.8	0.3	0.9	0.6	0.3	282.78	754.09
15x180	10	11.6	321.7	3.2	35.7	4.2	3.1	0.95	95.22
22.5x45	10	4.7	7.1	2.9	3.2	2.6	1.3	35.81	87.67
22.5x180	10	21.6	581	11.8	66.8	14.7	5.8	0.65	32.24
50x50L	10	9.3	21.2	21.2	8.5	8.5	2.5	13.58	13.58
50x100L	10	17.2	162.8	42.6	32.6	17	4.6	2.13	8.14
50x150L	10	25.8	540	64.2	72	25.7	6.9	0.76	6.41
100x100L	10	29.9	318.3	318.3	63.7	63.7	8.1	1.40	1.40
100x200L	10	54	2133.1	602.1	213.3	120.4	14.6	0.29	1.04
60x60L	10	9.6	32.4	32.4	10.8	10.8	2.6	8.97	8.97
60x60	10	14.4	52.2	52.2	17.4	17.4	3.9	6.27	6.27
60x90	10	25.8	214.2	90.5	47.6	30.2	7	1.93	4.57
30x100 L/R Slotted plate	10	9.7	88.8	9.2	17.8	6	2.6	3.27	31.60
SP 4/R	10	26.1	222	95.5	84.9	16.4	3.5	1.42	3.31

Table E-5 Summary of accepted profiles for $N_{MA}=2.0$

Profile	Slot	$\delta_x \times 10^{-03}$ (m)	$\delta_y \times 10^{-03}$ (m)	m_{MA} (kg)	Availability (UK suppliers)	Price (£/m)
40x160L	10	0.8	10	31.71	✗	-
40x120x120L	10	1.28	1.28	36.51	✗	-
80x120L	10	1.06	2.13	37.31	✗	-
80x160L	10	0.55	1.84	45.31	✗	-
45x180	10	0.54	7.18	37.31	✗	-
45x270	10	0.17	5.81	76.51	✗	-
90x180L	10	0.39	1.35	56.11	✗	-
90x180	10	0.33	1.29	78.51	✗	-
90x360	10	0.06	1.27	107.31	✗	-
15x180	10	0.95	95.22	22.11	✗	-
22.5x180	10	0.65	32.24	32.91	✗	-
50x150L	10	0.76	6.41	37.31	✗	-
100x100L	10	1.4	1.4	42.11	✗	-
100x200L	10	0.29	1.04	68.11	✗	-
SP 4/R	10	1.42	3.31	23.71	✗	-

Table E-6 Profile deflection study for $N_{MA} = 4.0$

$N_{MA} = 4.0$									
Profile	Slot	A (cm ²)	I_x (cm ⁴)	I_y (cm ⁴)	W_x (cm ³)	W_y (cm ³)	w (kg/m)	$\delta_x \times 10^{-03}$ (m)	$\delta_y \times 10^{-03}$ (m)
20x20	6	1.6	0.7	0.7	0.7	0.7	0.4	171.60	171.60

$N_{MA} = 4.0$									
Profile	Slot	A (cm ²)	I_x (cm ⁴)	I_y (cm ⁴)	W_x (cm ³)	W_y (cm ³)	w (kg/m)	$\delta_x \times 10^{-03}$ (m)	$\delta_y \times 10^{-03}$ (m)
20x20 1N	6	1.9	0.8	0.8	0.8	0.8	0.5	153.65	153.65
20x20 2N	6	1.8	0.7	0.8	0.7	0.8	0.5	175.60	153.65
20x20 2NVS	6	1.8	0.7	0.7	0.7	0.7	0.5	175.60	175.60
20x20 3N	6	1.7	0.7	0.8	0.7	0.7	0.5	175.60	153.65
20x20 R	6	1.6	0.6	0.6	0.5	0.5	0.4	200.20	200.20
20x40	6	2.9	4.6	1.2	2.5	1.4	0.8	28.55	109.44
20x60	6	3.5	14.2	1.7	4.7	1.7	0.9	9.45	78.90
20x40x40	6	4.2	6	6	2.6	2.6	1.1	23.29	23.29
10x40	6	2.1	3.2	0.2	1.6	0.4	0.6	39.29	628.63
30x30	8	3.1	2.8	2.8	1.8	1.8	0.9	47.91	47.91
30x30 1N	8	3.7	3.1	3.5	2	2.3	1	44.17	39.12
30x30 2N	8	3.5	2.8	3.5	2.1	2.7	1	48.91	39.12
30x30 2NVS	8	3.5	3.1	3.1	2	2	1	44.17	44.17
30x30 3N	8	3.3	3.1	2.8	2.3	2.2	0.9	43.27	47.91
30x30 _o	8	3.7	3.5	3.6	2	1.9	1	39.12	38.04
30x45 _o	8	4	3.6	5.1	2.1	2.3	1.1	38.82	27.40
30x60 _o	8	3.6	3.1	4.1	1.7	1.9	1	44.17	33.40
30x30 R	8	2.9	2.3	2.3	1.4	1.4	0.8	57.10	57.10
30x60	8	5.5	19.6	5.1	7	3.9	1.5	7.70	29.60
30x60 4N	8	5.8	20.2	5.5	6.7	3.8	1.6	7.61	27.96
30x60x60	8	8.2	26.2	26.2	7.6	7.6	2.2	6.51	6.51
30x90	8	7.7	60.7	7.3	13.5	4.9	2.1	2.76	22.98
30x120	8	9.9	136.3	9.6	22.7	6.4	2.7	1.35	19.23
30x45	8/10	4	8.1	3.9	3.9	2.9	1.1	17.25	35.83
60x60 8N	8	9.8	39.7	39.7	13.2	13.2	2.6	4.58	4.58
11x20	8	1	0.5	0.1	0.7	0.3	0.3	234.63	1173.17
15x120	8	9	110.4	2.2	18.4	2.7	2.4	1.60	80.08
40x40L	10	5.6	9.1	9.1	4.5	4.5	1.5	16.59	16.59
40x40L 0N	10	6.3	10.4	10.4	5.2	5.2	1.7	15.05	15.05
40x40L 1N	10	6.1	9.8	10.4	4.8	5.2	1.7	15.98	15.05
40x40L 2N	10	6	9	10.3	4.5	5.2	1.6	17.08	14.93
40x40L 2NVS	10	6	9.7	9.7	4.9	4.9	1.6	15.85	15.85
40x40L 3N	10	5.8	9.7	9	4.8	4.5	1.6	15.85	17.08
40x30 _o	10	6.2	9.4	11.8	4.7	5.9	1.7	16.66	13.27
40x45 _o	10	6.8	9.9	16.6	5	8.3	1.8	16.10	9.60
40x60 _o	10	6.3	8.7	13.1	4.3	6.5	1.7	18.00	11.95
40x40L R	10	5	7.2	7.2	3.6	3.6	1.3	20.19	20.19
40x40 HR	10	5.5	8.1	7.6	4	3.6	1.5	18.64	19.86
40x80L	10	9.9	63.4	17.3	15.9	8.7	2.7	2.91	10.67
40x80L 4N	10	10.4	65.2	19.1	16.3	9.9	2.8	2.87	9.81
40x80L 3NVS	10	10.6	67.8	19	17	9.5	2.9	2.81	10.01
40x80x80L	10	15.4	96.6	96.6	24.2	24.2	4.2	2.35	2.35
40x120L	10	15.5	203.2	27.8	33.9	13.9	4.2	1.12	8.15

$N_{MA} = 4.0$									
Profile	Slot	A (cm ²)	I_x (cm ⁴)	I_y (cm ⁴)	W_x (cm ³)	W_y (cm ³)	w (kg/m)	$\delta_x \times 10^{-03}$ (m)	$\delta_y \times 10^{-03}$ (m)
40x160L	10	20.5	466.7	37.2	58.3	18.6	5.5	0.56	7.07
80x80L	10	18.2	132.1	132.1	33	33	4.9	1.86	1.86
80x80L 4NVS	10	19.3	142.5	142.5	35.6	35.6	5.2	1.79	1.79
80x80L 6N	10	18.8	134.1	140.9	33.5	36.2	5.1	1.88	1.79
40x120x120L	10	24.6	318	318	42.2	42.2	6.7	0.93	0.93
80x120L	10	25.6	389.2	192.8	64.9	48.2	6.9	0.78	1.57
80x160L	10	32.9	850.7	253.4	106.3	63.4	8.9	0.42	1.41
45x45L	10	6	11.7	11.7	5.2	5.2	1.6	13.14	13.14
45x45L 0N	10	6.7	13.5	13.5	6	6	1.8	11.80	11.80
45x45L 1N	10	6.5	12.6	13.5	5.5	6	1.8	12.65	11.80
45x45L 2N	10	6.4	11.6	13.5	5.2	6	1.7	13.50	11.60
45x45L 2NVS	10	6.4	12.6	12.6	5.6	5.6	1.7	12.43	12.43
45x45L 3N	10	6.2	12.6	11.7	5.4	5.2	1.7	12.43	13.38
45x30 _o	10	6.9	12.7	15.2	5	5.3	1.9	12.77	10.67
45x45 _o	10	7.6	13.4	21.4	5.2	6.4	2	12.31	7.71
45x60 _o	10	6.8	11.4	16.9	4.4	5.2	1.8	13.98	9.43
45x45L R	10	4.9	8.6	8.6	5	5	1.3	16.90	16.90
45x45HR	10	6.6	11	10.7	4.4	4.8	1.8	14.49	14.89
45x45	10	7.5	13.8	13.8	6.1	6.1	2	11.95	11.95
45x60	10	11	37.2	22.7	12.4	10.1	3	5.19	8.50
45x90SL	10	9	73.4	18.1	16.3	8	2.4	2.40	9.73
45x90L	10	11.3	82	23.6	18.2	10.5	3	2.35	8.18
45x90L 2N	10	12	85.6	26.9	38.1	6	3.2	2.32	7.38
45x90L 3NVS	10	11.8	87.2	25.2	38.8	5.6	3.2	2.28	7.88
45x90	10	15.4	124.6	32.8	27.7	14.6	4.2	1.82	6.91
45x180	10	25.5	766.7	57.3	85.2	25.5	6.9	0.39	5.28
45x270	10	61.9	3962	118	300.2	61.6	16.7	0.15	4.89
45x90x90L	10	21.2	152.1	152.1	19.1	32.6	5.7	1.77	1.77
45x90x90L 4 N	10	22.1	160.8	160.8	30.6	30.6	5.95	1.71	1.71
90x90SL	10	14.1	130.2	130.2	28.9	28.9	3.8	1.65	1.65
90x90L	10	24.1	211.1	211.1	46.9	46.9	6.5	1.38	1.38
90x90L 4N	10	24.2	227.4	214.7	50.5	47.7	6.5	1.28	1.36
90x90L 4NVS	10	24.2	220.9	220.9	49.2	49.2	6.5	1.32	1.32
90x90	10	38.4	299.8	299.8	66.7	66.7	10.4	1.34	1.34
90x180L	10	42.8	1380	401	153.3	89.1	11.6	0.31	1.08
90x180	10	63.6	2138.3	544.3	237.6	121	17.2	0.28	1.09
90x360	10	90.2	14065	710	781.4	157.7	24.4	0.06	1.12
15x22.5	10	1.3	0.8	0.3	0.9	0.6	0.3	146.65	391.06
15x180	10	11.6	321.7	3.2	35.7	4.2	3.1	0.61	61.19
22.5x45	10	4.7	7.1	2.9	3.2	2.6	1.3	20.47	50.12
22.5x180	10	21.6	581	11.8	66.8	14.7	5.8	0.47	23.01
50x50L	10	9.3	21.2	21.2	8.5	8.5	2.5	8.44	8.44
50x100L	10	17.2	162.8	42.6	32.6	17	4.6	1.46	5.58

$N_{MA} = 4.0$									
Profile	Slot	A (cm ²)	I_x (cm ⁴)	I_y (cm ⁴)	W_x (cm ³)	W_y (cm ³)	w (kg/m)	$\delta_x \times 10^{-03}$ (m)	$\delta_y \times 10^{-03}$ (m)
50x150L	10	25.8	540	64.2	72	25.7	6.9	0.56	4.71
100x100L	10	29.9	318.3	318.3	63.7	63.7	8.1	1.06	1.06
100x200L	10	54	2133.1	602.1	213.3	120.4	14.6	0.24	0.86
60x60L	10	9.6	32.4	32.4	10.8	10.8	2.6	5.61	5.61
60x60	10	14.4	52.2	52.2	17.4	17.4	3.9	4.18	4.18
60x90	10	25.8	214.2	90.5	47.6	30.2	7	1.42	3.37
30x100 L/R Slotted plate	10	9.7	88.8	9.2	17.8	6	2.6	2.05	19.76
SP 4/R	10	26.1	222	95.5	84.9	16.4	3.5	0.93	2.17

Table E-7 Summary of accepted profiles for $N_{MA}=4.0$

Profile	Slot	$\delta_x \times 10^{-03}$ (m)	$\delta_y \times 10^{-03}$ (m)	m_{MA} (kg)	Availability (UK suppliers)	Price (£/m)
30x120	8	1.35	19.23	31.31406	✗	–
15x120	8	1.6	80.08	28.91406	✗	–
40x120L	10	1.12	8.15	43.31406	✓	25
40x160L	10	0.56	7.07	53.71406	✗	–
40x120x120L	10	0.93	0.93	63.31406	✗	–
80x120L	10	0.78	1.57	64.91406	✗	–
80x160L	10	0.42	1.41	80.91406	✗	–
45x180	10	0.39	5.28	64.91406	✗	–
45x270	10	0.15	4.89	143.3141	✗	–
90x90L	10	1.38	1.38	61.71406	✓	37
90x90L 4N	10	1.28	1.36	61.71406	✗	–
90x90L 4NVS	10	1.32	1.32	61.71406	✗	–
90x90	10	1.34	1.34	92.91406	✗	–
90x180L	10	0.31	1.08	102.5141	✗	–
90x180	10	0.28	1.09	147.3141	✗	–
90x360	10	0.06	1.12	204.9141	✗	–
15x180	10	0.61	61.19	34.51406	✗	–
22.5x180	10	0.47	23.01	56.11406	✗	–
50x100L	10	1.46	5.58	46.51406	✓	26.55
50x150L	10	0.56	4.71	64.91406	✗	–
100x100L	10	1.06	1.06	74.51406	✗	–
100x200L	10	0.24	0.86	126.5141	✗	–
60x90	10	1.42	3.37	65.71406	✓	53.5
SP 4/R	10	0.93	2.17	37.71406	✗	–

Table E-8 Profile deflection study for $N_{MA} = 6.0$

$N_{MA} = 6.0$									
Profile	Slot	A (cm ²)	I_x (cm ⁴)	I_y (cm ⁴)	W_x (cm ³)	W_y (cm ³)	w (kg/m)	$\delta_x \times 10^{-03}$ (m)	$\delta_y \times 10^{-03}$ (m)
20x20	6	1.6	0.7	0.7	0.7	0.7	0.4	119.74	119.74
20x20 1N	6	1.9	0.8	0.8	0.8	0.8	0.5	108.27	108.27
20x20 2N	6	1.8	0.7	0.8	0.7	0.8	0.5	123.74	108.27
20x20 2NVS	6	1.8	0.7	0.7	0.7	0.7	0.5	123.74	123.74
20x20 3N	6	1.7	0.7	0.8	0.7	0.7	0.5	123.74	108.27
20x20 R	6	1.6	0.6	0.6	0.5	0.5	0.4	139.70	139.70
20x40	6	2.9	4.6	1.2	2.5	1.4	0.8	20.66	79.19
20x60	6	3.5	14.2	1.7	4.7	1.7	0.9	6.89	57.55
20x40x40	6	4.2	6	6	2.6	2.6	1.1	17.24	17.24
10x40	6	2.1	3.2	0.2	1.6	0.4	0.6	27.94	447.11
30x30	8	3.1	2.8	2.8	1.8	1.8	0.9	34.94	34.94
30x30 1N	8	3.7	3.1	3.5	2	2.3	1	32.46	28.75
30x30 2N	8	3.5	2.8	3.5	2.1	2.7	1	35.94	28.75
30x30 2NVS	8	3.5	3.1	3.1	2	2	1	32.46	32.46
30x30 3N	8	3.3	3.1	2.8	2.3	2.2	0.9	31.56	34.94
30x30 _o	8	3.7	3.5	3.6	2	1.9	1	28.75	27.95
30x45 _o	8	4	3.6	5.1	2.1	2.3	1.1	28.73	20.28
30x60 _o	8	3.6	3.1	4.1	1.7	1.9	1	32.46	24.54
30x30 R	8	2.9	2.3	2.3	1.4	1.4	0.8	41.32	41.32
30x60	8	5.5	19.6	5.1	7	3.9	1.5	5.85	22.48
30x60 4N	8	5.8	20.2	5.5	6.7	3.8	1.6	5.81	21.35
30x60x60	8	8.2	26.2	26.2	7.6	7.6	2.2	5.12	5.12
30x90	8	7.7	60.7	7.3	13.5	4.9	2.1	2.17	18.01
30x120	8	9.9	136.3	9.6	22.7	6.4	2.7	1.09	15.45
30x45	8/10	4	8.1	3.9	3.9	2.9	1.1	12.77	26.52
60x60 8N	8	9.8	39.7	39.7	13.2	13.2	2.6	3.66	3.66
11x20	8	1	0.5	0.1	0.7	0.3	0.3	162.03	810.14
15x120	8	9	110.4	2.2	18.4	2.7	2.4	1.27	63.58
40x40L	10	5.6	9.1	9.1	4.5	4.5	1.5	12.60	12.60
40x40L 0N	10	6.3	10.4	10.4	5.2	5.2	1.7	11.56	11.56
40x40L 1N	10	6.1	9.8	10.4	4.8	5.2	1.7	12.27	11.56
40x40L 2N	10	6	9	10.3	4.5	5.2	1.6	13.05	11.40
40x40L 2NVS	10	6	9.7	9.7	4.9	4.9	1.6	12.11	12.11
40x40L 3N	10	5.8	9.7	9	4.8	4.5	1.6	12.11	13.05
40x30 _o	10	6.2	9.4	11.8	4.7	5.9	1.7	12.79	10.19
40x45 _o	10	6.8	9.9	16.6	5	8.3	1.8	12.43	7.41
40x60 _o	10	6.3	8.7	13.1	4.3	6.5	1.7	13.82	9.18
40x40L R	10	5	7.2	7.2	3.6	3.6	1.3	15.14	15.14
40x40 HR	10	5.5	8.1	7.6	4	3.6	1.5	14.15	15.09
40x80L	10	9.9	63.4	17.3	15.9	8.7	2.7	2.34	8.57
40x80L 4N	10	10.4	65.2	19.1	16.3	9.9	2.8	2.32	7.91

$N_{MA} = 6.0$									
Profile	Slot	A (cm ²)	I_x (cm ⁴)	I_y (cm ⁴)	W_x (cm ³)	W_y (cm ³)	w (kg/m)	$\delta_x \times 10^{-03}$ (m)	$\delta_y \times 10^{-03}$ (m)
40x80L 3NVS	10	10.6	67.8	19	17	9.5	2.9	2.27	8.10
40x80x80L	10	15.4	96.6	96.6	24.2	24.2	4.2	1.97	1.97
40x120L	10	15.5	203.2	27.8	33.9	13.9	4.2	0.94	6.85
40x160L	10	20.5	466.7	37.2	58.3	18.6	5.5	0.49	6.10
80x80L	10	18.2	132.1	132.1	33	33	4.9	1.59	1.59
80x80L 4NVS	10	19.3	142.5	142.5	35.6	35.6	5.2	1.53	1.53
80x80L 6N	10	18.8	134.1	140.9	33.5	36.2	5.1	1.61	1.53
40x120x120L	10	24.6	318	318	42.2	42.2	6.7	0.82	0.82
80x120L	10	25.6	389.2	192.8	64.9	48.2	6.9	0.68	1.38
80x160L	10	32.9	850.7	253.4	106.3	63.4	8.9	0.38	1.27
45x45L	10	6	11.7	11.7	5.2	5.2	1.6	10.04	10.04
45x45L 0N	10	6.7	13.5	13.5	6	6	1.8	9.12	9.12
45x45L 1N	10	6.5	12.6	13.5	5.5	6	1.8	9.77	9.12
45x45L 2N	10	6.4	11.6	13.5	5.2	6	1.7	10.37	8.91
45x45L 2NVS	10	6.4	12.6	12.6	5.6	5.6	1.7	9.54	9.54
45x45L 3N	10	6.2	12.6	11.7	5.4	5.2	1.7	9.54	10.28
45x30.	10	6.9	12.7	15.2	5	5.3	1.9	9.91	8.28
45x45.	10	7.6	13.4	21.4	5.2	6.4	2	9.60	6.01
45x60.	10	6.8	11.4	16.9	4.4	5.2	1.8	10.79	7.28
45x45L R	10	4.9	8.6	8.6	5	5	1.3	12.68	12.68
45x45HR	10	6.6	11	10.7	4.4	4.8	1.8	11.19	11.50
45x45	10	7.5	13.8	13.8	6.1	6.1	2	9.32	9.32
45x60	10	11	37.2	22.7	12.4	10.1	3	4.21	6.90
45x90SL	10	9	73.4	18.1	16.3	8	2.4	1.91	7.73
45x90L	10	11.3	82	23.6	18.2	10.5	3	1.91	6.64
45x90L 2N	10	12	85.6	26.9	38.1	6	3.2	1.90	6.03
45x90L 3NVS	10	11.8	87.2	25.2	38.8	5.6	3.2	1.86	6.44
45x90	10	15.4	124.6	32.8	27.7	14.6	4.2	1.53	5.80
45x180	10	25.5	766.7	57.3	85.2	25.5	6.9	0.35	4.64
45x270	10	61.9	3962	118	300.2	61.6	16.7	0.14	4.58
45x90x90L	10	21.2	152.1	152.1	19.1	32.6	5.7	1.53	1.53
45x90x90L 4 N	10	22.1	160.8	160.8	30.6	30.6	5.95	1.49	1.49
90x90SL	10	14.1	130.2	130.2	28.9	28.9	3.8	1.38	1.38
90x90L	10	24.1	211.1	211.1	46.9	46.9	6.5	1.21	1.21
90x90L 4N	10	24.2	227.4	214.7	50.5	47.7	6.5	1.12	1.19
90x90L 4NVS	10	24.2	220.9	220.9	49.2	49.2	6.5	1.15	1.15
90x90	10	38.4	299.8	299.8	66.7	66.7	10.4	1.21	1.21
90x180L	10	42.8	1380	401	153.3	89.1	11.6	0.29	0.99
90x180	10	63.6	2138.3	544.3	237.6	121	17.2	0.26	1.02
90x360	10	90.2	14065	710	781.4	157.7	24.4	0.05	1.07
15x22.5	10	1.3	0.8	0.3	0.9	0.6	0.3	101.27	270.05
15x180	10	11.6	321.7	3.2	35.7	4.2	3.1	0.50	49.84
22.5x45	10	4.7	7.1	2.9	3.2	2.6	1.3	15.36	37.60

$N_{MA} = 6.0$									
Profile	Slot	A (cm ²)	I _x (cm ⁴)	I _y (cm ⁴)	W _x (cm ³)	W _y (cm ³)	w (kg/m)	$\delta_x \times 10^{-03}$ (m)	$\delta_y \times 10^{-03}$ (m)
22.5x180	10	21.6	581	11.8	66.8	14.7	5.8	0.40	19.93
50x50L	10	9.3	21.2	21.2	8.5	8.5	2.5	6.73	6.73
50x100L	10	17.2	162.8	42.6	32.6	17	4.6	1.24	4.73
50x150L	10	25.8	540	64.2	72	25.7	6.9	0.49	4.14
100x100L	10	29.9	318.3	318.3	63.7	63.7	8.1	0.94	0.94
100x200L	10	54	2133.1	602.1	213.3	120.4	14.6	0.23	0.80
60x60L	10	9.6	32.4	32.4	10.8	10.8	2.6	4.49	4.49
60x60	10	14.4	52.2	52.2	17.4	17.4	3.9	3.49	3.49
60x90	10	25.8	214.2	90.5	47.6	30.2	7	1.25	2.97
30x100 L/R Slotted plate	10	9.7	88.8	9.2	17.8	6	2.6	1.64	15.81
SP 4/R	10	26.1	222	95.5	84.9	16.4	3.5	0.77	1.79

Table E-9 Summary of accepted profiles for $N_{MA}=6.0$

Profile	Slot	$\delta_x \times 10^{-03}$ (m)	$\delta_y \times 10^{-03}$ (m)	m_{MA} (kg)	Availability (UK suppliers)	Price (£/m)
30x120	8	1.09	15.45	42.11	✗	-
15x120	8	1.27	63.58	38.51	✗	-
40x120L	10	0.94	6.85	60.11	✓	25
40x160L	10	0.49	6.1	75.71	✗	-
80x80L	10	1.59	1.59	68.51	✓	32
80x80L 4NVS	10	1.53	1.53	72.11	✗	-
80x80L 6N	10	1.61	1.53	70.91	✗	-
40x120x120L	10	0.82	0.82	90.11	✗	-
80x120L	10	0.68	1.38	92.51	✗	-
80x160L	10	0.38	1.27	116.51	✗	-
45x90	10	1.53	5.8	60.11	✓	25
45x180	10	0.35	4.64	92.51	✗	-
45x270	10	0.14	4.58	210.11	✗	-
45x90x90L	10	1.53	1.53	78.11	✗	-
45x90x90L 4 N	10	1.49	1.49	81.11	✗	-
90x90SL	10	1.38	1.38	55.31	✗	-
90x90L	10	1.21	1.21	87.71	✓	37
90x90L 4N	10	1.12	1.19	87.71	✗	-
90x90L 4NVS	10	1.15	1.15	87.71	✗	-
90x90	10	1.21	1.21	134.51	✗	-
90x180L	10	0.29	0.99	148.91	✗	-
90x180	10	0.26	1.02	216.11	✗	-
90x360	10	0.05	1.07	302.51	✗	-
15x180	10	0.5	49.84	46.91	✗	-
22.5x180	10	0.4	19.93	79.31	✗	-
50x100L	10	1.24	4.73	64.91	✓	26.55
50x150L	10	0.49	4.14	92.51	✗	-

Profile	Slot	$\delta_x \times 10^{-03}$ (m)	$\delta_y \times 10^{-03}$ (m)	m_{MA} (kg)	Availability (UK suppliers)	Price (£/m)
100x100L	10	0.94	0.94	106.91	✗	–
100x200L	10	0.23	0.8	184.91	✗	–
60x90	10	1.25	2.97	93.71	✓	53.5
30x100 L/R	10	1.64	15.81	40.91	✗	–
SP 4/R	10	0.77	1.79	51.71	✗	–

Table E-10 Comparison between accepted profiles for N_{MA} = 4.0 and 6.0

Profile	Slot	$\delta_x \times 10^{-03}$ (m)	$\delta_y \times 10^{-03}$ (m)	m_{MA} (kg)	N_{MA}	Price (£/m)	Total Price (£)
40x120L	10	1.12	8.15	43.31406	4	25	200
90x90L	10	1.38	1.38	61.71406	4	37	296
50x100L	10	1.46	5.58	46.51406	4	26.55	212.4
60x90	10	1.42	3.37	65.71406	4	53.5	428
80x80L	10	1.59	1.59	68.51	6	32	384
45x90	10	1.53	5.8	60.11	6	25	300

Appendix F Wood Cross-section Deflection Study

Table F-11 Wood cross-section deflection study for $N_{MA} = 2.0$

$N_{MA} = 2.0$					
Timber Type	Cross-section		I (m ⁴)	w (kg/m)	$\delta_{max} \times 10^{-03}$ (m)
	b(mm)	h(mm)			
European Oak	25	25	3.3E-08	4.34E-01	556.33
	25	32	6.8E-08	5.56E-01	270.61
	25	44	1.8E-07	7.65E-01	107.61
	25	70	7.1E-07	1.22E+00	28.62
	25	95	1.8E-06	1.65E+00	12.18
	25	121	3.7E-06	2.10E+00	6.26
	25	146	6.5E-06	2.54E+00	3.76
	25	171	1E-05	2.97E+00	2.47
	25	197	1.6E-05	3.42E+00	1.70
	25	222	2.3E-05	3.86E+00	1.24
	25	230	2.5E-05	4.00E+00	1.13
	32	32	8.7E-08	7.12E-01	216.74
	32	44	2.3E-07	9.79E-01	86.89
	32	70	9.1E-07	1.56E+00	23.47
	32	95	2.3E-06	2.11E+00	10.12
	32	121	4.7E-06	2.69E+00	5.26
	32	146	8.3E-06	3.25E+00	3.20
	32	171	1.3E-05	3.80E+00	2.11
	44	44	3.1E-07	1.35E+00	66.71
	44	70	1.3E-06	2.14E+00	18.46
	44	95	3.1E-06	2.91E+00	8.11
	44	121	6.5E-06	3.70E+00	4.29
	44	146	1.1E-05	4.46E+00	2.64
	57	57	8.8E-07	2.26E+00	26.79
	57	70	1.6E-06	2.77E+00	15.41
	57	95	4.1E-06	3.76E+00	6.89
	57	121	8.4E-06	4.79E+00	3.70
	70	70	2E-06	3.41E+00	13.49
	70	95	5E-06	4.62E+00	6.13
	70	121	1E-05	5.89E+00	3.33
	19	19	1.1E-08	2.78E-01	1624.48
	American White Oak	19	25	2.5E-08	3.66E-01
19		32	5.2E-08	4.68E-01	351.00
19		44	1.3E-07	6.44E-01	138.91
19		70	5.4E-07	1.02E+00	36.59
19		95	1.4E-06	1.39E+00	15.45
19		121	2.8E-06	1.77E+00	7.88
19		146	4.9E-06	2.14E+00	4.71
19		171	7.9E-06	2.50E+00	3.07

$N_{MA} = 2.0$					
Timber Type	Cross-section		I (m ⁴)	w (kg/m)	$\delta_{max} \times 10^{-03}$ (m)
	b(mm)	h(mm)			
	19	197	1.2E-05	2.88E+00	2.10
	19	222	1.7E-05	3.25E+00	1.53
	19	19	1.1E-08	2.20E-01	1608.47
American Black Walnut	19	25	2.5E-08	2.89E-01	714.47
	19	32	5.2E-08	3.70E-01	345.36
	19	44	1.3E-07	5.09E-01	135.93
	19	70	5.4E-07	8.10E-01	35.41
	19	95	1.4E-06	1.10E+00	14.81
	19	121	2.8E-06	1.40E+00	7.49
	19	146	4.9E-06	1.69E+00	4.44
	44	44	3.1E-07	1.18E+00	65.11
	44	70	1.3E-06	1.88E+00	17.83
	44	95	3.1E-06	2.55E+00	7.77
	44	121	6.5E-06	3.24E+00	4.08
	44	146	1.1E-05	3.91E+00	2.50
	19	19	1.1E-08	2.44E-01	1615.04
American Ash	19	25	2.5E-08	3.21E-01	718.27
	19	32	5.2E-08	4.10E-01	347.67
	19	44	1.3E-07	5.64E-01	137.15
	19	70	5.4E-07	8.98E-01	35.90
	19	95	1.4E-06	1.22E+00	15.07
	19	121	2.8E-06	1.55E+00	7.65
	19	146	4.9E-06	1.87E+00	4.55
	44	44	3.1E-07	1.31E+00	66.34
	44	70	1.3E-06	2.08E+00	18.31
	44	95	3.1E-06	2.82E+00	8.03
	44	121	6.5E-06	3.59E+00	4.24
	44	146	1.1E-05	4.34E+00	2.61
	19	19	1.1E-08	2.03E-01	1603.70
American Cherry	19	25	2.5E-08	2.66E-01	711.72
	19	32	5.2E-08	3.41E-01	343.68
	19	44	1.3E-07	4.69E-01	135.04
	19	70	5.4E-07	7.46E-01	35.06
	19	95	1.4E-06	1.01E+00	14.61
	19	121	2.8E-06	1.29E+00	7.37
	19	146	4.9E-06	1.56E+00	4.36
	44	44	3.1E-07	1.09E+00	64.22
	44	70	1.3E-06	1.73E+00	17.48
	44	95	3.1E-06	2.34E+00	7.58
	44	121	6.5E-06	2.99E+00	3.96
	44	146	1.1E-05	3.60E+00	2.42
	19	19	1.1E-08	2.62E-01	1620.01

$N_{MA} = 2.0$					
Timber Type	Cross-section		I (m ⁴)	w (kg/m)	$\delta_{max} \times 10^{-03}$ (m)
	b(mm)	h(mm)			
European Beech	19	25	2.5E-08	3.44E-01	721.14
	19	32	5.2E-08	4.41E-01	349.42
	19	44	1.3E-07	6.06E-01	138.08
	19	70	5.4E-07	9.64E-01	36.26
	19	95	1.4E-06	1.31E+00	15.27
	19	121	2.8E-06	1.67E+00	7.77
	19	146	4.9E-06	2.01E+00	4.63
	19	171	7.9E-06	2.36E+00	3.01
	19	197	1.2E-05	2.71E+00	2.06
	19	222	1.7E-05	3.06E+00	1.50
	44	44	3.1E-07	1.40E+00	67.26
	44	70	1.3E-06	2.23E+00	18.68
	44	95	3.1E-06	3.03E+00	8.23
	44	121	6.5E-06	3.86E+00	4.37
	44	146	1.1E-05	4.66E+00	2.69

Table F-12 Summary of accepted cross-sections for $N_{MA}=2.0$

Timber Type	Cross-section		I (m ⁴)	w (kg/m)	$\delta_{max} \times 10^{-03}$ (m)
	b(mm)	h(mm)			
American White Oak	19	222	1.7E-05	3.25E+00	1.53
European Beech	19	222	1.7E-05	3.06E+00	1.50
European Oak	25	222	2.3E-05	3.86E+00	1.24
	25	230	2.5E-05	4.00E+00	1.13

Table F-13 Wood cross-section deflection study for $N_{MA} = 4.0$

$N_{MA} = 4.0$					
Timber Type	Cross-section		I (m ⁴)	w (kg/m)	$\delta_{max} \times 10^{-03}$ (m)
	b(mm)	h(mm)			
European Oak	25	25	3.3E-08	4.34E-01	298.12
	25	32	6.8E-08	5.56E-01	147.49
	25	44	1.8E-07	7.65E-01	60.25
	25	70	7.1E-07	1.22E+00	16.85
	25	95	1.8E-06	1.65E+00	7.47
	25	121	3.7E-06	2.10E+00	3.98
	25	146	6.5E-06	2.54E+00	2.47
	25	171	1E-05	2.97E+00	1.66
	25	197	1.6E-05	3.42E+00	1.17
	25	222	2.3E-05	3.86E+00	0.87
	25	230	2.5E-05	4.00E+00	0.80
	32	32	8.7E-08	7.12E-01	120.55
	32	44	2.3E-07	9.79E-01	49.89

$N_{MA} = 4.0$						
Timber Type	Cross-section		$I \text{ (m}^4\text{)}$	$w \text{ (kg/m)}$	$\delta_{max} \times 10^{-03} \text{ (m)}$	
	b(mm)	h(mm)				
American White Oak	32	70	9.1E-07	1.56E+00	14.28	
	32	95	2.3E-06	2.11E+00	6.44	
	32	121	4.7E-06	2.69E+00	3.48	
	32	146	8.3E-06	3.25E+00	2.18	
	32	171	1.3E-05	3.80E+00	1.48	
	44	44	3.1E-07	1.35E+00	39.80	
	44	70	1.3E-06	2.14E+00	11.77	
	44	95	3.1E-06	2.91E+00	5.44	
	44	121	6.5E-06	3.70E+00	3.00	
	44	146	1.1E-05	4.46E+00	1.91	
	57	57	8.8E-07	2.26E+00	17.23	
	57	70	1.6E-06	2.77E+00	10.25	
	57	95	4.1E-06	3.76E+00	4.83	
	57	121	8.4E-06	4.79E+00	2.70	
	70	70	2E-06	3.41E+00	9.29	
	70	95	5E-06	4.62E+00	4.44	
	70	121	1E-05	5.89E+00	2.52	
	19	19	1.1E-08	2.78E-01	850.52	
	19	25	2.5E-08	3.66E-01	383.97	
	19	32	5.2E-08	4.68E-01	189.00	
	19	44	1.3E-07	6.44E-01	76.59	
	19	70	5.4E-07	1.02E+00	21.12	
	19	95	1.4E-06	1.39E+00	9.25	
	19	121	2.8E-06	1.77E+00	4.88	
	19	146	4.9E-06	2.14E+00	3.00	
	19	171	7.9E-06	2.50E+00	2.01	
	19	197	1.2E-05	2.88E+00	1.41	
	19	222	1.7E-05	3.25E+00	1.05	
	American Black Walnut	19	19	1.1E-08	2.20E-01	834.51
		19	25	2.5E-08	2.89E-01	374.72
		19	32	5.2E-08	3.70E-01	183.35
		19	44	1.3E-07	5.09E-01	73.61
19		70	5.4E-07	8.10E-01	19.94	
19		95	1.4E-06	1.10E+00	8.61	
19		121	2.8E-06	1.40E+00	4.49	
19		146	4.9E-06	1.69E+00	2.73	
44		44	3.1E-07	1.18E+00	38.20	
44		70	1.3E-06	1.88E+00	11.14	
44	95	3.1E-06	2.55E+00	5.10		

$N_{MA} = 4.0$						
Timber Type	Cross-section		$I \text{ (m}^4\text{)}$	$w \text{ (kg/m)}$	$\delta_{max} \times 10^{-03} \text{ (m)}$	
	b(mm)	h(mm)				
American Ash	44	121	6.5E-06	3.24E+00	2.79	
	44	146	1.1E-05	3.91E+00	1.76	
	19	19	1.1E-08	2.44E-01	841.07	
	19	25	2.5E-08	3.21E-01	378.51	
	19	32	5.2E-08	4.10E-01	185.67	
	19	44	1.3E-07	5.64E-01	74.83	
	19	70	5.4E-07	8.98E-01	20.42	
	19	95	1.4E-06	1.22E+00	8.88	
	19	121	2.8E-06	1.55E+00	4.65	
	19	146	4.9E-06	1.87E+00	2.84	
	44	44	3.1E-07	1.31E+00	39.42	
	44	70	1.3E-06	2.08E+00	11.63	
	44	95	3.1E-06	2.82E+00	5.36	
	44	121	6.5E-06	3.59E+00	2.95	
	44	146	1.1E-05	4.34E+00	1.87	
	American Cherry	19	19	1.1E-08	2.03E-01	829.74
19		25	2.5E-08	2.66E-01	371.97	
19		32	5.2E-08	3.41E-01	181.67	
19		44	1.3E-07	4.69E-01	72.72	
19		70	5.4E-07	7.46E-01	19.59	
19		95	1.4E-06	1.01E+00	8.42	
19		121	2.8E-06	1.29E+00	4.37	
19		146	4.9E-06	1.56E+00	2.65	
44		44	3.1E-07	1.09E+00	37.31	
44		70	1.3E-06	1.73E+00	10.79	
44		95	3.1E-06	2.34E+00	4.90	
44		121	6.5E-06	2.99E+00	2.67	
44		146	1.1E-05	3.60E+00	1.68	
European Beech		19	19	1.1E-08	2.62E-01	846.05
		19	25	2.5E-08	3.44E-01	381.39
		19	32	5.2E-08	4.41E-01	187.42
	19	44	1.3E-07	6.06E-01	75.76	
	19	70	5.4E-07	9.64E-01	20.79	
	19	95	1.4E-06	1.31E+00	9.08	
	19	121	2.8E-06	1.67E+00	4.77	
	19	146	4.9E-06	2.01E+00	2.93	
	19	171	7.9E-06	2.36E+00	1.95	
	19	197	1.2E-05	2.71E+00	1.36	
	19	222	1.7E-05	3.06E+00	1.01	

$N_{MA} = 4.0$					
Timber Type	Cross-section		I (m ⁴)	w (kg/m)	$\delta_{max} \times 10^{-03}$ (m)
	b(mm)	h(mm)			
	44	44	3.1E-07	1.40E+00	40.35
	44	70	1.3E-06	2.23E+00	11.99
	44	95	3.1E-06	3.03E+00	5.56
	44	121	6.5E-06	3.86E+00	3.07
	44	146	1.1E-05	4.66E+00	1.96

Table F-14 Summary of accepted cross-sections for $N_{MA}=4.0$

Timber Type	Cross-section		I (m ⁴)	w (kg/m)	$\delta_{max} \times 10^{-03}$ (m)
	b(mm)	h(mm)			
American White Oak	19	197	1.2E-05	2.88E+00	1.41
	19	222	1.7E-05	3.25E+00	1.05
European Beech	19	197	1.2E-05	2.71E+00	1.36
	19	222	1.7E-05	3.06E+00	1.01
European Oak	25	197	1.6E-05	3.42E+00	1.17
	25	222	2.3E-05	3.86E+00	0.87
	25	230	2.5E-05	4.00E+00	0.80
	32	171	1.3E-05	3.80E+00	1.48

Table F-15 Wood cross-section deflection study for $N_{MA} = 6.0$

$N_{MA} = 6.0$					
Timber Type	Cross-section		I (m ⁴)	w (kg/m)	$\delta_{max} \times 10^{-03}$ (m)
	b(mm)	h(mm)			
European Oak	25	25	3.3E-08	4.34E-01	212.05
	25	32	6.8E-08	5.56E-01	106.44
	25	44	1.8E-07	7.65E-01	44.46
	25	70	7.1E-07	1.22E+00	12.93
	25	95	1.8E-06	1.65E+00	5.90
	25	121	3.7E-06	2.10E+00	3.22
	25	146	6.5E-06	2.54E+00	2.03
	25	171	1E-05	2.97E+00	1.39
	25	197	1.6E-05	3.42E+00	0.99
	25	222	2.3E-05	3.86E+00	0.75
	25	230	2.5E-05	4.00E+00	0.69
	32	32	8.7E-08	7.12E-01	88.49
	32	44	2.3E-07	9.79E-01	37.55
	32	70	9.1E-07	1.56E+00	11.22
	32	95	2.3E-06	2.11E+00	5.21
	32	121	4.7E-06	2.69E+00	2.89
	32	146	8.3E-06	3.25E+00	1.85
	32	171	1.3E-05	3.80E+00	1.27
	44	44	3.1E-07	1.35E+00	30.83

$N_{MA} = 6.0$					
Timber Type	Cross-section		I (m ⁴)	w (kg/m)	$\delta_{max} \times 10^{-03}$ (m)
	b(mm)	h(mm)			
American White Oak	44	70	1.3E-06	2.14E+00	9.55
	44	95	3.1E-06	2.91E+00	4.55
	44	121	6.5E-06	3.70E+00	2.57
	44	146	1.1E-05	4.46E+00	1.66
	57	57	8.8E-07	2.26E+00	14.05
	57	70	1.6E-06	2.77E+00	8.53
	57	95	4.1E-06	3.76E+00	4.14
	57	121	8.4E-06	4.79E+00	2.37
	70	70	2E-06	3.41E+00	7.89
	70	95	5E-06	4.62E+00	3.88
	70	121	1E-05	5.89E+00	2.25
	19	19	1.1E-08	2.78E-01	592.53
	19	25	2.5E-08	3.66E-01	270.72
	19	32	5.2E-08	4.68E-01	134.99
	19	44	1.3E-07	6.44E-01	55.82
	19	70	5.4E-07	1.02E+00	15.96
	19	95	1.4E-06	1.39E+00	7.19
	19	121	2.8E-06	1.77E+00	3.89
	19	146	4.9E-06	2.14E+00	2.43
	19	171	7.9E-06	2.50E+00	1.65
	19	197	1.2E-05	2.88E+00	1.18
	19	222	1.7E-05	3.25E+00	0.88
American Black Walnut	19	19	1.1E-08	2.20E-01	576.52
	19	25	2.5E-08	2.89E-01	261.47
	19	32	5.2E-08	3.70E-01	129.35
	19	44	1.3E-07	5.09E-01	52.84
	19	70	5.4E-07	8.10E-01	14.78
	19	95	1.4E-06	1.10E+00	6.55
	19	121	2.8E-06	1.40E+00	3.49
	19	146	4.9E-06	1.69E+00	2.16
	44	44	3.1E-07	1.18E+00	29.23
	44	70	1.3E-06	1.88E+00	8.92
	44	95	3.1E-06	2.55E+00	4.20
	44	121	6.5E-06	3.24E+00	2.36
44	146	1.1E-05	3.91E+00	1.52	
American Ash	19	19	1.1E-08	2.44E-01	583.09
	19	25	2.5E-08	3.21E-01	265.26
	19	32	5.2E-08	4.10E-01	131.66
	19	44	1.3E-07	5.64E-01	54.06
	19	70	5.4E-07	8.98E-01	15.26
	19	95	1.4E-06	1.22E+00	6.81
19	121	2.8E-06	1.55E+00	3.65	

$N_{MA} = 6.0$					
Timber Type	Cross-section		I (m ⁴)	w (kg/m)	$\delta_{max} \times 10^{-03}$ (m)
	b(mm)	h(mm)			
American Cherry	19	146	4.9E-06	1.87E+00	2.27
	44	44	3.1E-07	1.31E+00	30.45
	44	70	1.3E-06	2.08E+00	9.40
	44	95	3.1E-06	2.82E+00	4.47
	44	121	6.5E-06	3.59E+00	2.52
	44	146	1.1E-05	4.34E+00	1.63
	19	19	1.1E-08	2.03E-01	571.75
	19	25	2.5E-08	2.66E-01	258.72
	19	32	5.2E-08	3.41E-01	127.67
	19	44	1.3E-07	4.69E-01	51.95
	19	70	5.4E-07	7.46E-01	14.43
	19	95	1.4E-06	1.01E+00	6.36
	19	121	2.8E-06	1.29E+00	3.37
	19	146	4.9E-06	1.56E+00	2.08
	44	44	3.1E-07	1.09E+00	28.34
	44	70	1.3E-06	1.73E+00	8.56
	44	95	3.1E-06	2.34E+00	4.01
	44	121	6.5E-06	2.99E+00	2.24
	44	146	1.1E-05	3.60E+00	1.44
	European Beech	19	19	1.1E-08	2.62E-01
19		25	2.5E-08	3.44E-01	268.14
19		32	5.2E-08	4.41E-01	133.42
19		44	1.3E-07	6.06E-01	54.99
19		70	5.4E-07	9.64E-01	15.63
19		95	1.4E-06	1.31E+00	7.01
19		121	2.8E-06	1.67E+00	3.78
19		146	4.9E-06	2.01E+00	2.36
19		171	7.9E-06	2.36E+00	1.60
19		197	1.2E-05	2.71E+00	1.13
19		222	1.7E-05	3.06E+00	0.85
44		44	3.1E-07	1.40E+00	31.38
44		70	1.3E-06	2.23E+00	9.77
44		95	3.1E-06	3.03E+00	4.67
44		121	6.5E-06	3.86E+00	2.64
44		146	1.1E-05	4.66E+00	1.71

Table F-16 Summary of accepted cross-sections for $N_{MA}=6.0$

Timber Type	Cross-section		I (m ⁴)	w (kg/m)	$\delta_{max} \times 10^{-03}$ (m)
	b(mm)	h(mm)			
American Ash	44	146	1.1E-05	4.34E+00	1.63
American Black Walnut	44	146	1.1E-05	3.91E+00	1.52
American Cherry	44	146	1.1E-05	3.60E+00	1.44

Timber Type	Cross-section		I (m ⁴)	w (kg/m)	$\delta_{max} \times 10^{-03}$ (m)
	b(mm)	h(mm)			
American White Oak	19	197	1.2E-05	2.88E+00	1.18
	19	222	1.7E-05	3.25E+00	0.88
European Beech	19	171	7.9E-06	2.36E+00	1.60
	19	197	1.2E-05	2.71E+00	1.13
	19	222	1.7E-05	3.06E+00	0.85
European Oak	25	171	1E-05	2.97E+00	1.39
	25	197	1.6E-05	3.42E+00	0.99
	25	222	2.3E-05	3.86E+00	0.75
	25	230	2.5E-05	4.00E+00	0.69
	32	171	1.3E-05	3.80E+00	1.27

Table F-17 Comparison between accepted cross-sections (mass and cost)

Timber Type	Cross-section		N_{MA}	$\delta_{max} \times 10^{-03}$ (m)	m_{MA} (kg)	Total Price (£)
	b(mm)	h(mm)				
American Ash	44	146	6	1.63	61.75	222.96
American Black Walnut	44	146	6	1.52	56.66	465.24
American Cherry	44	146	6	1.44	52.96	357
American White Oak	19	197	4	1.18	32.77	137.92
	19	222	2	0.88	35.70	621.12
	19	171	6	1.6	37.98	149.16
European Beech	19	197	4	1.13	31.42	124.32
	19	222	2	0.85	21.95	73
	25	171	6	1.39	45.37	168.36
European Oak	25	197	4	0.99	37.10	180
	25	222	2	0.75	25.14	101.68
	25	230	2	0.69	25.70	105.36
	32	171	4	1.27	40.14	167.04

Appendix G Aluminium Extrusion Deflection Study

Table G-18 Aluminium extrusion deflection study for $N_{MA} = 2.0$

$N_{MA} = 2.0$							
Extrusion Cross-section	Cross-section				$I (m^4)$	$w (kg/m)$	$\delta_{max} \times 10^{-03} (m)$
	h (mm)	b (mm)	t (or c) (mm)	d (mm)			
Square Bar	12.7	12.7	1.6	-	2.2E-09	1.92E-01	1.04E+03
	15.8	15.8	1.6	-	5.2E-09	2.45E-01	4.38E+02
	19	19	1.6	-	1.1E-08	3.01E-01	2.11E+02
	19	19	3.3	-	1.1E-08	5.60E-01	2.21E+02
	25.4	25.4	1.6	-	3.5E-08	4.11E-01	6.74E+01
	25.4	25.4	3.3	-	3.5E-08	7.88E-01	7.16E+01
	28.6	28.6	1.6	-	5.6E-08	4.67E-01	4.23E+01
	30	30	2	-	6.8E-08	6.05E-01	3.57E+01
	31.8	31.8	1.6	-	8.5E-08	5.22E-01	2.79E+01
	31.8	31.8	3.3	-	8.5E-08	1.02E+00	3.02E+01
	40	40	2	-	2.1E-07	8.21E-01	1.17E+01
	44.5	44.5	3.3	-	3.3E-07	1.47E+00	8.41E+00
	50	50	2	-	5.2E-07	1.04E+00	4.95E+00
	50.8	50.8	1.6	-	5.5E-07	8.50E-01	4.52E+00
	50.8	50.8	3.3	-	5.5E-07	1.69E+00	5.11E+00
	50.8	50.8	6.35	-	5.5E-07	3.05E+00	6.05E+00
	55	55	2	-	7.6E-07	1.14E+00	3.44E+00
	60	60	2	-	1.1E-06	1.25E+00	2.47E+00
	63.5	63.5	3.30	-	1.4E-06	2.15E+00	2.22E+00
	70	70	6	-	2E-06	4.15E+00	1.89E+00
76.2	76.2	3.3	-	2.8E-06	2.60E+00	1.13E+00	
76.2	76.2	6.35	-	2.8E-06	4.79E+00	1.44E+00	
89	89	3.6	-	5.2E-06	3.32E+00	6.63E-01	
100	100	2	-	8.3E-06	2.12E+00	3.60E-01	
101.6	101.6	3.3	-	8.9E-06	3.50E+00	3.98E-01	
101.6	101.6	6.35	-	8.9E-06	6.53E+00	5.30E-01	
150	150	3	-	4.2E-05	4.76E+00	9.54E-02	
150	150	4	-	4.2E-05	6.31E+00	1.10E-01	
Rectangular Tube	30	20	2	-	4.5E-08	6.05E-01	5.36E+01
	38.1	19	1.6	-	8.8E-08	6.31E-01	2.77E+01
	38.1	19	3.3	-	8.8E-08	1.24E+00	3.04E+01
	38.1	25.4	1.6	-	1.2E-07	6.31E-01	2.07E+01
	38.1	25.4	3.3	-	1.2E-07	1.24E+00	2.27E+01
	40	20	2	-	1.1E-07	8.21E-01	2.34E+01
	50.8	25.4	3.3	-	2.8E-07	1.69E+00	1.02E+01
	50.8	31.7	3.3	-	3.5E-07	1.69E+00	8.18E+00
	50.8	38.1	3.3	-	4.2E-07	1.69E+00	6.81E+00
	50	30	3	-	3.1E-07	1.52E+00	8.86E+00
	63.5	25.4	3.3	-	5.4E-07	2.15E+00	5.55E+00

$N_{MA} = 2.0$							
Extrusion Cross-section	Cross-section				$I (m^4)$	$w (kg/m)$	$\delta_{max} \times 10^{-03} (m)$
	h (mm)	b (mm)	t (or c) (mm)	d (mm)			
	63.5	38.1	3.3	-	8.1E-07	2.15E+00	3.70E+00
	76.2	25.4	3.3	-	9.4E-07	2.60E+00	3.40E+00
	76.2	38.1	3.3	-	1.4E-06	2.60E+00	2.27E+00
	76.2	44.5	3.3	-	1.6E-06	2.60E+00	1.94E+00
	76.2	50.8	3.3	-	1.9E-06	2.60E+00	1.70E+00
	76.2	50.8	6.35	-	1.9E-06	4.79E+00	2.15E+00
	101.6	50.8	6.35	-	4.4E-06	6.53E+00	1.06E+00
	101.6	50.8	3.3	-	4.4E-06	3.50E+00	7.96E-01
	101.6	25.4	3.3	-	2.2E-06	3.50E+00	1.59E+00
	101.6	44.5	3.3	-	3.9E-06	3.50E+00	9.09E-01
	101.6	76.2	3.3	-	6.7E-06	3.50E+00	5.31E-01
	114.3	44.4	3.2	-	5.5E-06	3.84E+00	6.64E-01
	120	60	4	-	8.6E-06	5.01E+00	4.77E-01
	127	44.5	3.3	-	7.6E-06	4.41E+00	5.12E-01
	152.4	44.5	3.3	-	1.3E-05	5.31E+00	3.23E-01
	152.4	50.8	3.3	-	1.5E-05	5.31E+00	2.83E-01
U-Channel	6.4	9.5	1.3	1.3	1.7E-10	0.080028	1.30E+04
	10	10	1.5	1.5	5.9E-10	0.10935	3.76E+03
	12.7	12.7	1.6	1.6	1.4E-09	0.150768	1.63E+03
	12.7	12.7	3.2	3.2	2E-09	0.273888	1.16E+03
	12.7	15.9	3.2	3.2	2.4E-09	0.329184	9.41E+02
	15.9	15.9	1.6	1.6	2.9E-09	0.19224	7.81E+02
	15.9	15.9	3.2	3.2	4.4E-09	0.356832	5.24E+02
	19	12.7	1.6	1.6	3.6E-09	0.177984	6.22E+02
	19	12.7	3.2	3.2	5.7E-09	0.32832	4.06E+02
	19	19	1.6	1.6	5.1E-09	0.232416	4.41E+02
	19	19	3.2	3.2	8.2E-09	0.437184	2.85E+02
	22.2	22.2	3.2	3.2	1.4E-08	0.520128	1.70E+02
	25.4	12.7	3.2	3.2	1.2E-08	0.383616	1.95E+02
	25.4	19	3.2	3.2	1.7E-08	0.49248	1.40E+02
	25.4	25.4	1.6	1.6	1.3E-08	0.31536	1.77E+02
	25.4	25.4	3.2	3.2	2.2E-08	0.603072	1.10E+02
	25.4	38.1	3.2	3.2	3.2E-08	0.822528	7.78E+01
	25.4	50.8	3.2	3.2	4.2E-08	1.041984	6.12E+01
	28.6	19	3.2	3.2	2.3E-08	0.520128	1.05E+02
	28.6	25.4	3.2	3.2	2.9E-08	0.63072	8.28E+01
	31.8	12.7	3.2	3.2	2.1E-08	0.438912	1.12E+02
	31.8	19	3.2	3.2	2.9E-08	0.547776	8.15E+01
	31.8	25.4	3.2	3.2	3.8E-08	0.658368	6.45E+01
	31.8	31.8	3.2	3.2	4.6E-08	0.76896	5.36E+01
	31.8	31.8	4.8	4.8	6.1E-08	1.111968	4.31E+01
	31.8	50.8	3.2	3.2	7.1E-08	1.09728	3.66E+01

$N_{MA} = 2.0$							
Extrusion Cross-section	Cross-section				$I (m^4)$	$w (kg/m)$	$\delta_{max} \times 10^{-03} (m)$
	h (mm)	b (mm)	t (or c) (mm)	d (mm)			
	34.9	25.4	3.2	3.2	4.7E-08	0.685152	5.18E+01
	38.1	12.7	3.2	3.2	3.3E-08	0.493344	7.11E+01
	38.1	19	3.2	3.2	4.6E-08	0.602208	5.29E+01
	38.1	25.4	3.2	3.2	5.8E-08	0.7128	4.22E+01
	38.1	38.1	3.2	3.2	8.3E-08	0.932256	3.06E+01
	38.1	38.1	4.8	4.8	1.1E-07	1.356912	2.43E+01
	38.1	38.1	6.4	6.4	1.3E-07	1.75392	2.15E+01
	44.5	25.4	3.2	3.2	8.4E-08	0.768096	2.94E+01
	44.5	44.5	3.2	3.2	1.4E-07	1.098144	1.91E+01
	50.8	12.7	3.2	3.2	6.9E-08	0.603072	3.47E+01
	50.8	19	3.2	3.2	9.2E-08	0.711936	2.66E+01
	50.8	25.4	3.2	3.2	1.2E-07	0.822528	2.16E+01
	50.8	25.4	4.8	4.8	1.6E-07	1.19232	1.68E+01
	50.8	25.4	6.4	6.4	1.9E-07	1.534464	1.45E+01
	50.8	38.1	3.2	3.2	1.6E-07	1.041984	1.60E+01
	50.8	38.1	6.4	6.4	2.7E-07	1.973376	1.08E+01
	50.8	50.8	3.2	3.2	2.1E-07	1.26144	1.28E+01
	50.8	50.8	6.4	6.4	3.5E-07	2.412288	8.85E+00
	57.2	31.8	4.8	4.8	2.5E-07	1.441152	1.08E+01
	63.5	25.4	3.2	3.2	2E-07	0.932256	1.29E+01
	63.5	38.1	4.8	4.8	3.8E-07	1.686096	7.48E+00
	76.2	25.4	3.2	3.2	3.1E-07	1.041984	8.40E+00
	76.2	38.1	3.2	3.2	4.2E-07	1.26144	6.42E+00
	76.2	38.1	6.4	6.4	7.3E-07	2.412288	4.26E+00
	76.2	50.8	3.2	3.2	5.2E-07	1.480896	5.25E+00
	76.2	50.8	6.4	6.4	9.3E-07	2.8512	3.53E+00
	88.9	38.1	6.4	7.9	1.2E-06	2.888514	2.75E+00
	101.6	25.4	3.2	3.2	6.2E-07	1.26144	4.28E+00
	101.6	50.8	3.2	3.2	1E-06	1.700352	2.79E+00
	101.6	50.8	4.8	4.8	1.5E-06	2.509056	2.17E+00
	101.6	50.8	6.4	6.4	1.8E-06	3.290112	1.87E+00
	101.6	50.8	6.4	7.9	2.1E-06	3.649752	1.71E+00
	127	50.8	6.4	6.4	3.2E-06	3.729024	1.15E+00
	152.4	50.8	6.4	7.9	5.6E-06	4.527576	7.08E-01
	152.4	76.2	6.4	9.5	8.7E-06	6.214212	5.29E-01
	152.4	76.2	9.5	12.7	1.1E-05	8.483346	4.93E-01

Table G-19 Summary of accepted extrusion cross-sections for $N_{MA}=2.0$

Extrusion Cross-section	Cross-section				$I (m^4)$	$w (kg/m)$	$\delta_{max} \times 10^{-03} (m)$
	h (mm)	b (mm)	t (or c) (mm)	d (mm)			
Square Tube	76.2	76.2	3.3	-	2.8E-06	2.60E+00	1.13E+00
	76.2	76.2	6.35	-	2.8E-06	4.79E+00	1.44E+00
	89	89	3.6	-	5.2E-06	3.32E+00	6.63E-01
	100	100	2	-	8.3E-06	2.12E+00	3.60E-01
	101.6	101.6	3.3	-	8.9E-06	3.50E+00	3.98E-01
	101.6	101.6	6.35	-	8.9E-06	6.53E+00	5.30E-01
	150	150	3	-	4.2E-05	4.76E+00	9.54E-02
	150	150	4	-	4.2E-05	6.31E+00	1.10E-01
Rectangular Tube	101.6	50.8	6.35	-	4.4E-06	6.53E+00	1.06E+00
	101.6	50.8	3.3	-	4.4E-06	3.50E+00	7.96E-01
	101.6	25.4	3.3	-	2.2E-06	3.50E+00	1.59E+00
	101.6	44.5	3.3	-	3.9E-06	3.50E+00	9.09E-01
	101.6	76.2	3.3	-	6.7E-06	3.50E+00	5.31E-01
	114.3	44.4	3.2	-	5.5E-06	3.84E+00	6.64E-01
	120	60	4	-	8.6E-06	5.01E+00	4.77E-01
	127	44.5	3.3	-	7.6E-06	4.41E+00	5.12E-01
	152.4	44.5	3.3	-	1.3E-05	5.31E+00	3.23E-01
152.4	50.8	3.3	-	1.5E-05	5.31E+00	2.83E-01	
U-Channel	127	50.8	6.4	6.4	3.2E-06	3.729024	1.15E+00
	152.4	50.8	6.4	7.9	5.6E-06	4.527576	7.08E-01
	152.4	76.2	6.4	9.5	8.7E-06	6.214212	5.29E-01
	152.4	76.2	9.5	12.7	1.1E-05	8.483346	4.93E-01

Table G-20 Aluminium extrusion deflection study for $N_{MA} = 4.0$

$N_{MA} = 4.0$							
Extrusion Cross-section	Cross-section				$I (m^4)$	$w (kg/m)$	$\delta_{max} \times 10^{-03} (m)$
	h (mm)	b (mm)	t (or c) (mm)	d (mm)			
Square Bar	12.7	12.7	1.6	-	2.2E-09	1.92E-01	5.37E+02
	15.8	15.8	1.6	-	5.2E-09	2.45E-01	2.28E+02
	19	19	1.6	-	1.1E-08	3.01E-01	1.11E+02
	19	19	3.3	-	1.1E-08	5.60E-01	1.20E+02
	25.4	25.4	1.6	-	3.5E-08	4.11E-01	3.60E+01
	25.4	25.4	3.3	-	3.5E-08	7.88E-01	4.02E+01
	28.6	28.6	1.6	-	5.6E-08	4.67E-01	2.28E+01
	30	30	2	-	6.8E-08	6.05E-01	1.96E+01
	31.8	31.8	1.6	-	8.5E-08	5.22E-01	1.52E+01
	31.8	31.8	3.3	-	8.5E-08	1.02E+00	1.74E+01
	40	40	2	-	2.1E-07	8.21E-01	6.60E+00
	44.5	44.5	3.3	-	3.3E-07	1.47E+00	5.07E+00
	50	50	2	-	5.2E-07	1.04E+00	2.86E+00

$N_{MA} = 4.0$							
Extrusion Cross-section	Cross-section				$I (m^4)$	$w (kg/m)$	$\delta_{max} \times 10^{-03} (m)$
	h (mm)	b (mm)	t (or c) (mm)	d (mm)			
	50.8	50.8	1.6	-	5.5E-07	8.50E-01	2.56E+00
	50.8	50.8	3.3	-	5.5E-07	1.69E+00	3.14E+00
	50.8	50.8	6.35	-	5.5E-07	3.05E+00	4.09E+00
	55	55	2	-	7.6E-07	1.14E+00	2.01E+00
	60	60	2	-	1.1E-06	1.25E+00	1.46E+00
	63.5	63.5	3.30	-	1.4E-06	2.15E+00	1.42E+00
	70	70	6	-	2E-06	4.15E+00	1.35E+00
	76.2	76.2	3.3	-	2.8E-06	2.60E+00	7.46E-01
	76.2	76.2	6.35	-	2.8E-06	4.79E+00	1.05E+00
	89	89	3.6	-	5.2E-06	3.32E+00	4.54E-01
	100	100	2	-	8.3E-06	2.12E+00	2.29E-01
	101.6	101.6	3.3	-	8.9E-06	3.50E+00	2.76E-01
	101.6	101.6	6.35	-	8.9E-06	6.53E+00	4.08E-01
	150	150	3	-	4.2E-05	4.76E+00	6.96E-02
	150	150	4	-	4.2E-05	6.31E+00	8.38E-02
Rectangular Tube	30	20	2	-	4.5E-08	6.05E-01	2.94E+01
	38.1	19	1.6	-	8.8E-08	6.31E-01	1.52E+01
	38.1	19	3.3	-	8.8E-08	1.24E+00	1.79E+01
	38.1	25.4	1.6	-	1.2E-07	6.31E-01	1.14E+01
	38.1	25.4	3.3	-	1.2E-07	1.24E+00	1.34E+01
	40	20	2	-	1.1E-07	8.21E-01	1.32E+01
	50.8	25.4	3.3	-	2.8E-07	1.69E+00	6.29E+00
	50.8	31.7	3.3	-	3.5E-07	1.69E+00	5.04E+00
	50.8	38.1	3.3	-	4.2E-07	1.69E+00	4.19E+00
	50	30	3	-	3.1E-07	1.52E+00	5.37E+00
	63.5	25.4	3.3	-	5.4E-07	2.15E+00	3.54E+00
	63.5	38.1	3.3	-	8.1E-07	2.15E+00	2.36E+00
	76.2	25.4	3.3	-	9.4E-07	2.60E+00	2.24E+00
	76.2	38.1	3.3	-	1.4E-06	2.60E+00	1.49E+00
	76.2	44.5	3.3	-	1.6E-06	2.60E+00	1.28E+00
	76.2	50.8	3.3	-	1.9E-06	2.60E+00	1.12E+00
	76.2	50.8	6.35	-	1.9E-06	4.79E+00	1.57E+00
	101.6	50.8	6.35	-	4.4E-06	6.53E+00	8.16E-01
	101.6	50.8	3.3	-	4.4E-06	3.50E+00	5.51E-01
	101.6	25.4	3.3	-	2.2E-06	3.50E+00	1.10E+00
	101.6	44.5	3.3	-	3.9E-06	3.50E+00	6.29E-01
	101.6	76.2	3.3	-	6.7E-06	3.50E+00	3.67E-01
114.3	44.4	3.2	-	5.5E-06	3.84E+00	4.66E-01	
120	60	4	-	8.6E-06	5.01E+00	3.51E-01	
127	44.5	3.3	-	7.6E-06	4.41E+00	3.68E-01	
152.4	44.5	3.3	-	1.3E-05	5.31E+00	2.40E-01	
152.4	50.8	3.3	-	1.5E-05	5.31E+00	2.10E-01	

$N_{MA} = 4.0$							
Extrusion Cross-section	Cross-section				$I (m^4)$	$w (kg/m)$	$\delta_{max} \times 10^{-03} (m)$
	h (mm)	b (mm)	t (or c) (mm)	d (mm)			
U-Channel	6.4	9.5	1.3	1.3	1.7E-10	0.080028	6.59E+03
	10	10	1.5	1.5	5.9E-10	0.10935	1.92E+03
	12.7	12.7	1.6	1.6	1.4E-09	0.150768	8.35E+02
	12.7	12.7	3.2	3.2	2E-09	0.273888	6.07E+02
	12.7	15.9	3.2	3.2	2.4E-09	0.329184	4.97E+02
	15.9	15.9	1.6	1.6	2.9E-09	0.19224	4.03E+02
	15.9	15.9	3.2	3.2	4.4E-09	0.356832	2.78E+02
	19	12.7	1.6	1.6	3.6E-09	0.177984	3.21E+02
	19	12.7	3.2	3.2	5.7E-09	0.32832	2.14E+02
	19	19	1.6	1.6	5.1E-09	0.232416	2.29E+02
	19	19	3.2	3.2	8.2E-09	0.437184	1.53E+02
	22.2	22.2	3.2	3.2	1.4E-08	0.520128	9.22E+01
	25.4	12.7	3.2	3.2	1.2E-08	0.383616	1.04E+02
	25.4	19	3.2	3.2	1.7E-08	0.49248	7.57E+01
	25.4	25.4	1.6	1.6	1.3E-08	0.31536	9.33E+01
	25.4	25.4	3.2	3.2	2.2E-08	0.603072	6.01E+01
	25.4	38.1	3.2	3.2	3.2E-08	0.822528	4.39E+01
	25.4	50.8	3.2	3.2	4.2E-08	1.041984	3.54E+01
	28.6	19	3.2	3.2	2.3E-08	0.520128	5.70E+01
	28.6	25.4	3.2	3.2	2.9E-08	0.63072	4.56E+01
	31.8	12.7	3.2	3.2	2.1E-08	0.438912	5.98E+01
	31.8	19	3.2	3.2	2.9E-08	0.547776	4.44E+01
	31.8	25.4	3.2	3.2	3.8E-08	0.658368	3.56E+01
	31.8	31.8	3.2	3.2	4.6E-08	0.76896	3.00E+01
	31.8	31.8	4.8	4.8	6.1E-08	1.111968	2.51E+01
	31.8	50.8	3.2	3.2	7.1E-08	1.09728	2.13E+01
	34.9	25.4	3.2	3.2	4.7E-08	0.685152	2.87E+01
	38.1	12.7	3.2	3.2	3.3E-08	0.493344	3.84E+01
	38.1	19	3.2	3.2	4.6E-08	0.602208	2.90E+01
	38.1	25.4	3.2	3.2	5.8E-08	0.7128	2.35E+01
	38.1	38.1	3.2	3.2	8.3E-08	0.932256	1.75E+01
	38.1	38.1	4.8	4.8	1.1E-07	1.356912	1.45E+01
	38.1	38.1	6.4	6.4	1.3E-07	1.75392	1.33E+01
	44.5	25.4	3.2	3.2	8.4E-08	0.768096	1.65E+01
	44.5	44.5	3.2	3.2	1.4E-07	1.098144	1.11E+01
	50.8	12.7	3.2	3.2	6.9E-08	0.603072	1.90E+01
	50.8	19	3.2	3.2	9.2E-08	0.711936	1.48E+01
	50.8	25.4	3.2	3.2	1.2E-07	0.822528	1.22E+01
	50.8	25.4	4.8	4.8	1.6E-07	1.19232	9.85E+00
	50.8	25.4	6.4	6.4	1.9E-07	1.534464	8.83E+00
50.8	38.1	3.2	3.2	1.6E-07	1.041984	9.23E+00	
50.8	38.1	6.4	6.4	2.7E-07	1.973376	6.83E+00	

$N_{MA} = 4.0$							
Extrusion Cross-section	Cross-section				$I (m^4)$	$w (kg/m)$	$\delta_{max} \times 10^{-03} (m)$
	h (mm)	b (mm)	t (or c) (mm)	d (mm)			
	50.8	50.8	3.2	3.2	2.1E-07	1.26144	7.59E+00
	50.8	50.8	6.4	6.4	3.5E-07	2.412288	5.75E+00
	57.2	31.8	4.8	4.8	2.5E-07	1.441152	6.51E+00
	63.5	25.4	3.2	3.2	2E-07	0.932256	7.34E+00
	63.5	38.1	4.8	4.8	3.8E-07	1.686096	4.60E+00
	76.2	25.4	3.2	3.2	3.1E-07	1.041984	4.86E+00
	76.2	38.1	3.2	3.2	4.2E-07	1.26144	3.80E+00
	76.2	38.1	6.4	6.4	7.3E-07	2.412288	2.77E+00
	76.2	50.8	3.2	3.2	5.2E-07	1.480896	3.17E+00
	76.2	50.8	6.4	6.4	9.3E-07	2.8512	2.36E+00
	88.9	38.1	6.4	7.9	1.2E-06	2.888514	1.84E+00
	101.6	25.4	3.2	3.2	6.2E-07	1.26144	2.53E+00
	101.6	50.8	3.2	3.2	1E-06	1.700352	1.72E+00
	101.6	50.8	4.8	4.8	1.5E-06	2.509056	1.42E+00
	101.6	50.8	6.4	6.4	1.8E-06	3.290112	1.28E+00
	101.6	50.8	6.4	7.9	2.1E-06	3.649752	1.19E+00
	127	50.8	6.4	6.4	3.2E-06	3.729024	8.02E-01
	152.4	50.8	6.4	7.9	5.6E-06	4.527576	5.12E-01
	152.4	76.2	6.4	9.5	8.7E-06	6.214212	4.03E-01
	152.4	76.2	9.5	12.7	1.1E-05	8.483346	3.95E-01

Table G-21 Summary of accepted extrusion cross-sections for $N_{MA}=4.0$

Extrusion Cross-section	Cross-section				$I (m^4)$	$w (kg/m)$	$\delta_{max} \times 10^{-03} (m)$
	h (mm)	b (mm)	t (or c) (mm)	d (mm)			
Square Tube	76.2	76.2	3.3	-	2.8E-06	2.60E+00	1.13E+00
	76.2	76.2	6.35	-	2.8E-06	4.79E+00	1.44E+00
	89	89	3.6	-	5.2E-06	3.32E+00	6.63E-01
	100	100	2	-	8.3E-06	2.12E+00	3.60E-01
	101.6	101.6	3.3	-	8.9E-06	3.50E+00	3.98E-01
	101.6	101.6	6.35	-	8.9E-06	6.53E+00	5.30E-01
	150	150	3	-	4.2E-05	4.76E+00	9.54E-02
	150	150	4	-	4.2E-05	6.31E+00	1.10E-01
Rectangular Tube	101.6	50.8	6.35	-	4.4E-06	6.53E+00	1.06E+00
	101.6	50.8	3.3	-	4.4E-06	3.50E+00	7.96E-01
	101.6	25.4	3.3	-	2.2E-06	3.50E+00	1.59E+00
	101.6	44.5	3.3	-	3.9E-06	3.50E+00	9.09E-01
	101.6	76.2	3.3	-	6.7E-06	3.50E+00	5.31E-01
	114.3	44.4	3.2	-	5.5E-06	3.84E+00	6.64E-01
	120	60	4	-	8.6E-06	5.01E+00	4.77E-01

Extrusion Cross-section	Cross-section				$I (m^4)$	$w (kg/m)$	$\delta_{max} \times 10^{-03} (m)$
	h (mm)	b (mm)	t (or c) (mm)	d (mm)			
	127	44.5	3.3	-	7.6E-06	4.41E+00	5.12E-01
	152.4	44.5	3.3	-	1.3E-05	5.31E+00	3.23E-01
	152.4	50.8	3.3	-	1.5E-05	5.31E+00	2.83E-01
U-Channel	127	50.8	6.4	6.4	3.2E-06	3.729024	1.15E+00
	152.4	50.8	6.4	7.9	5.6E-06	4.527576	7.08E-01
	152.4	76.2	6.4	9.5	8.7E-06	6.214212	5.29E-01
	152.4	76.2	9.5	12.7	1.1E-05	8.483346	4.93E-01

Table G-22 Aluminium extrusion deflection study for $N_{MA} = 6.0$

$N_{MA} = 6.0$							
Extrusion Cross-section	Cross-section				$I (m^4)$	$w (kg/m)$	$\delta_{max} \times 10^{-03} (m)$
	h (mm)	b (mm)	t (or c) (mm)	d (mm)			
Square Tube	12.7	12.7	1.6	-	2.2E-09	1.92E-01	3.69E+02
	15.8	15.8	1.6	-	5.2E-09	2.45E-01	1.58E+02
	19	19	1.6	-	1.1E-08	3.01E-01	7.76E+01
	19	19	3.3	-	1.1E-08	5.60E-01	8.68E+01
	25.4	25.4	1.6	-	3.5E-08	4.11E-01	2.55E+01
	25.4	25.4	3.3	-	3.5E-08	7.88E-01	2.97E+01
	28.6	28.6	1.6	-	5.6E-08	4.67E-01	1.63E+01
	30	30	2	-	6.8E-08	6.05E-01	1.42E+01
	31.8	31.8	1.6	-	8.5E-08	5.22E-01	1.09E+01
	31.8	31.8	3.3	-	8.5E-08	1.02E+00	1.31E+01
	40	40	2	-	2.1E-07	8.21E-01	4.89E+00
	44.5	44.5	3.3	-	3.3E-07	1.47E+00	3.96E+00
	50	50	2	-	5.2E-07	1.04E+00	2.17E+00
	50.8	50.8	1.6	-	5.5E-07	8.50E-01	1.90E+00
	50.8	50.8	3.3	-	5.5E-07	1.69E+00	2.49E+00
	50.8	50.8	6.35	-	5.5E-07	3.05E+00	3.44E+00
	55	55	2	-	7.6E-07	1.14E+00	1.53E+00
	60	60	2	-	1.1E-06	1.25E+00	1.12E+00
	63.5	63.5	3.30	-	1.4E-06	2.15E+00	1.15E+00
	70	70	6	-	2E-06	4.15E+00	1.17E+00
	76.2	76.2	3.3	-	2.8E-06	2.60E+00	6.17E-01
76.2	76.2	6.35	-	2.8E-06	4.79E+00	9.19E-01	
89	89	3.6	-	5.2E-06	3.32E+00	3.85E-01	
100	100	2	-	8.3E-06	2.12E+00	1.86E-01	
101.6	101.6	3.3	-	8.9E-06	3.50E+00	2.35E-01	

$N_{MA} = 6.0$							
Extrusion Cross-section	Cross-section				$I (m^4)$	$w (kg/m)$	$\delta_{max} \times 10^{-03} (m)$
	h (mm)	b (mm)	t (or c) (mm)	d (mm)			
	101.6	101.6	6.35	-	8.9E-06	6.53E+00	3.67E-01
	150	150	3	-	4.2E-05	4.76E+00	6.10E-02
	150	150	4	-	4.2E-05	6.31E+00	7.52E-02
Rectangular Tube	30	20	2	-	4.5E-08	6.05E-01	2.13E+01
	38.1	19	1.6	-	8.8E-08	6.31E-01	1.11E+01
	38.1	19	3.3	-	8.8E-08	1.24E+00	1.38E+01
	38.1	25.4	1.6	-	1.2E-07	6.31E-01	8.29E+00
	38.1	25.4	3.3	-	1.2E-07	1.24E+00	1.03E+01
	40	20	2	-	1.1E-07	8.21E-01	9.79E+00
	50.8	25.4	3.3	-	2.8E-07	1.69E+00	4.98E+00
	50.8	31.7	3.3	-	3.5E-07	1.69E+00	3.99E+00
	50.8	38.1	3.3	-	4.2E-07	1.69E+00	3.32E+00
	50	30	3	-	3.1E-07	1.52E+00	4.21E+00
	63.5	25.4	3.3	-	5.4E-07	2.15E+00	2.87E+00
	63.5	38.1	3.3	-	8.1E-07	2.15E+00	1.92E+00
	76.2	25.4	3.3	-	9.4E-07	2.60E+00	1.85E+00
	76.2	38.1	3.3	-	1.4E-06	2.60E+00	1.23E+00
	76.2	44.5	3.3	-	1.6E-06	2.60E+00	1.06E+00
	76.2	50.8	3.3	-	1.9E-06	2.60E+00	9.25E-01
	76.2	50.8	6.35	-	1.9E-06	4.79E+00	1.38E+00
	101.6	50.8	6.35	-	4.4E-06	6.53E+00	7.34E-01
	101.6	50.8	3.3	-	4.4E-06	3.50E+00	4.69E-01
	101.6	25.4	3.3	-	2.2E-06	3.50E+00	9.39E-01
	101.6	44.5	3.3	-	3.9E-06	3.50E+00	5.36E-01
101.6	76.2	3.3	-	6.7E-06	3.50E+00	3.13E-01	
114.3	44.4	3.2	-	5.5E-06	3.84E+00	4.01E-01	
120	60	4	-	8.6E-06	5.01E+00	3.09E-01	
127	44.5	3.3	-	7.6E-06	4.41E+00	3.21E-01	
152.4	44.5	3.3	-	1.3E-05	5.31E+00	2.12E-01	
152.4	50.8	3.3	-	1.5E-05	5.31E+00	1.86E-01	
U-Channel	6.4	9.5	1.3	1.3	1.7E-10	0.080028	4.45E+03
	10	10	1.5	1.5	5.9E-10	0.10935	1.30E+03
	12.7	12.7	1.6	1.6	1.4E-09	0.150768	5.71E+02
	12.7	12.7	3.2	3.2	2E-09	0.273888	4.22E+02
	12.7	15.9	3.2	3.2	2.4E-09	0.329184	3.48E+02
	15.9	15.9	1.6	1.6	2.9E-09	0.19224	2.77E+02
	15.9	15.9	3.2	3.2	4.4E-09	0.356832	1.96E+02
	19	12.7	1.6	1.6	3.6E-09	0.177984	2.20E+02

$N_{MA} = 6.0$							
Extrusion Cross-section	Cross-section				$I (m^4)$	$w (kg/m)$	$\delta_{max} \times 10^{-03} (m)$
	h (mm)	b (mm)	t (or c) (mm)	d (mm)			
	19	12.7	3.2	3.2	5.7E-09	0.32832	1.50E+02
	19	19	1.6	1.6	5.1E-09	0.232416	1.59E+02
	19	19	3.2	3.2	8.2E-09	0.437184	1.09E+02
	22.2	22.2	3.2	3.2	1.4E-08	0.520128	6.63E+01
	25.4	12.7	3.2	3.2	1.2E-08	0.383616	7.34E+01
	25.4	19	3.2	3.2	1.7E-08	0.49248	5.42E+01
	25.4	25.4	1.6	1.6	1.3E-08	0.31536	6.53E+01
	25.4	25.4	3.2	3.2	2.2E-08	0.603072	4.36E+01
	25.4	38.1	3.2	3.2	3.2E-08	0.822528	3.26E+01
	25.4	50.8	3.2	3.2	4.2E-08	1.041984	2.68E+01
	28.6	19	3.2	3.2	2.3E-08	0.520128	4.10E+01
	28.6	25.4	3.2	3.2	2.9E-08	0.63072	3.32E+01
	31.8	12.7	3.2	3.2	2.1E-08	0.438912	4.26E+01
	31.8	19	3.2	3.2	2.9E-08	0.547776	3.20E+01
	31.8	25.4	3.2	3.2	3.8E-08	0.658368	2.60E+01
	31.8	31.8	3.2	3.2	4.6E-08	0.76896	2.22E+01
	31.8	31.8	4.8	4.8	6.1E-08	1.111968	1.91E+01
	31.8	50.8	3.2	3.2	7.1E-08	1.09728	1.62E+01
	34.9	25.4	3.2	3.2	4.7E-08	0.685152	2.10E+01
	38.1	12.7	3.2	3.2	3.3E-08	0.493344	2.75E+01
	38.1	19	3.2	3.2	4.6E-08	0.602208	2.10E+01
	38.1	25.4	3.2	3.2	5.8E-08	0.7128	1.72E+01
	38.1	38.1	3.2	3.2	8.3E-08	0.932256	1.31E+01
	38.1	38.1	4.8	4.8	1.1E-07	1.356912	1.12E+01
	38.1	38.1	6.4	6.4	1.3E-07	1.75392	1.06E+01
	44.5	25.4	3.2	3.2	8.4E-08	0.768096	1.22E+01
	44.5	44.5	3.2	3.2	1.4E-07	1.098144	8.44E+00
	50.8	12.7	3.2	3.2	6.9E-08	0.603072	1.38E+01
	50.8	19	3.2	3.2	9.2E-08	0.711936	1.09E+01
	50.8	25.4	3.2	3.2	1.2E-07	0.822528	9.04E+00
	50.8	25.4	4.8	4.8	1.6E-07	1.19232	7.55E+00
	50.8	25.4	6.4	6.4	1.9E-07	1.534464	6.93E+00
	50.8	38.1	3.2	3.2	1.6E-07	1.041984	6.99E+00
	50.8	38.1	6.4	6.4	2.7E-07	1.973376	5.50E+00
	50.8	50.8	3.2	3.2	2.1E-07	1.26144	5.85E+00
	50.8	50.8	6.4	6.4	3.5E-07	2.412288	4.72E+00
	57.2	31.8	4.8	4.8	2.5E-07	1.441152	5.07E+00
	63.5	25.4	3.2	3.2	2E-07	0.932256	5.50E+00

$N_{MA} = 6.0$							
Extrusion Cross-section	Cross-section				$I (m^4)$	$w (kg/m)$	$\delta_{max} \times 10^{-03} (m)$
	h (mm)	b (mm)	t (or c) (mm)	d (mm)			
	63.5	38.1	4.8	4.8	3.8E-07	1.686096	3.65E+00
	76.2	25.4	3.2	3.2	3.1E-07	1.041984	3.68E+00
	76.2	38.1	3.2	3.2	4.2E-07	1.26144	2.92E+00
	76.2	38.1	6.4	6.4	7.3E-07	2.412288	2.27E+00
	76.2	50.8	3.2	3.2	5.2E-07	1.480896	2.48E+00
	76.2	50.8	6.4	6.4	9.3E-07	2.8512	1.97E+00
	88.9	38.1	6.4	7.9	1.2E-06	2.888514	1.54E+00
	101.6	25.4	3.2	3.2	6.2E-07	1.26144	1.95E+00
	101.6	50.8	3.2	3.2	1E-06	1.700352	1.36E+00
	101.6	50.8	4.8	4.8	1.5E-06	2.509056	1.17E+00
	101.6	50.8	6.4	6.4	1.8E-06	3.290112	1.08E+00
	101.6	50.8	6.4	7.9	2.1E-06	3.649752	1.02E+00
	127	50.8	6.4	6.4	3.2E-06	3.729024	6.87E-01
	152.4	50.8	6.4	7.9	5.6E-06	4.527576	4.47E-01
	152.4	76.2	6.4	9.5	8.7E-06	6.214212	3.62E-01
	152.4	76.2	9.5	12.7	1.1E-05	8.483346	3.62E-01

Table G-23 Summary of accepted extrusion cross-sections for $N_{MA}=6.0$

Extrusion Cross-section	Cross-section				$I (m^4)$	$w (kg/m)$	$\delta_{max} \times 10^{-03} (m)$
	h (mm)	b (mm)	t (or c) (mm)	d (mm)			
Square Tube	55	55	2	-	7.6E-07	1.14E+00	1.53E+00
	60	60	2	-	1.1E-06	1.25E+00	1.12E+00
	63.5	63.5	3.30	-	1.4E-06	2.15E+00	1.15E+00
	70	70	6	-	2E-06	4.15E+00	1.17E+00
	76.2	76.2	3.3	-	2.8E-06	2.60E+00	6.17E-01
	76.2	76.2	6.35	-	2.8E-06	4.79E+00	9.19E-01
	89	89	3.6	-	5.2E-06	3.32E+00	3.85E-01
	100	100	2	-	8.3E-06	2.12E+00	1.86E-01
	101.6	101.6	3.3	-	8.9E-06	3.50E+00	2.35E-01
	101.6	101.6	6.35	-	8.9E-06	6.53E+00	3.67E-01
	150	150	3	-	4.2E-05	4.76E+00	6.10E-02
	150	150	4	-	4.2E-05	6.31E+00	7.52E-02
Rectangular Tube	76.2	38.1	3.3	-	1.4E-06	2.60E+00	1.23E+00
	76.2	44.5	3.3	-	1.6E-06	2.60E+00	1.06E+00
	76.2	50.8	3.3	-	1.9E-06	2.60E+00	9.25E-01
	76.2	50.8	6.35	-	1.9E-06	4.79E+00	1.38E+00
	101.6	50.8	6.35	-	4.4E-06	6.53E+00	7.34E-01
	101.6	50.8	3.3	-	4.4E-06	3.50E+00	4.69E-01
	101.6	25.4	3.3	-	2.2E-06	3.50E+00	9.39E-01

Extrusion Cross-section	Cross-section				$I (m^4)$	$w (kg/m)$	$\delta_{max} \times 10^{-03} (m)$
	h (mm)	b (mm)	t (or c) (mm)	d (mm)			
	101.6	44.5	3.3	-	3.9E-06	3.50E+00	5.36E-01
	101.6	76.2	3.3	-	6.7E-06	3.50E+00	3.13E-01
	114.3	44.4	3.2	-	5.5E-06	3.84E+00	4.01E-01
	120	60	4	-	8.6E-06	5.01E+00	3.09E-01
	127	44.5	3.3	-	7.6E-06	4.41E+00	3.21E-01
	152.4	44.5	3.3	-	1.3E-05	5.31E+00	2.12E-01
	152.4	50.8	3.3	-	1.5E-05	5.31E+00	1.86E-01
U-Channel	88.9	38.1	6.4	7.9	1.2E-06	2.888514	1.54E+00
	101.6	50.8	3.2	3.2	1E-06	1.700352	1.36E+00
	101.6	50.8	4.8	4.8	1.5E-06	2.509056	1.17E+00
	101.6	50.8	6.4	6.4	1.8E-06	3.290112	1.08E+00
	101.6	50.8	6.4	7.9	2.1E-06	3.649752	1.02E+00
	127	50.8	6.4	6.4	3.2E-06	3.729024	6.87E-01
	152.4	50.8	6.4	7.9	5.6E-06	4.527576	4.47E-01
	152.4	76.2	6.4	9.5	8.7E-06	6.214212	3.62E-01
	152.4	76.2	9.5	12.7	1.1E-05	8.483346	3.62E-01

Appendix H Selecting Wind Speed

Wind speed depends on location to set up the LLBG test facility. Egypt and UK are the most probable candidates to test it. Therefore, wind speed data in different locations of both countries were collected based on the assesment of New and Renewable Energy Authority, the Egyptian Meteorological Authority, Risø National Laboratory (Mortensen *et al.*, 2006) and UK national wind speed database, which is known as Numerical Objective Analysis Boundary Layer (NOABL) (RenSMART, 2016). Based on data listed Table H-24, a wind speed of 7.0m/s is selected in calculating wid loads on the LLBG.

Table H-24 Wind speeds at different locations in Egypt and UK

Country	City	Latitude Angle	Longtude Angle	Wind Speed, U (m/s)
Egypt (Mortensen <i>et al.</i> , 2006)	Abu Simbel	22.336823°N	31.625532°E	4.8
	Alexandria	31.205753°N	29.924526°E	2.9
	Aswan	24.978548°N	32.875820°E	3.8
	Farafra	27.061529 °N	27.970091 °E	2.0
	Hurghada	27.192505°N	33.781710°E	5.4
	Mansoura	31.050000°N	31.383300°E	5.0
	Nuweiba	29.123453°N	34.899583°E	4.0
	Port Said	31.265300°N	32.301900°E	1.6
	Shark El-Ouinat	22.582900°N	28.707300°E	5.5
	Suez	29.964200°N	32.505600°E	3.9
	Zafarana	29.1152°N	32.6575°E	7.0
UK (RenSMART, 2016)	Aberdeen	57.155342°N	2.092676°W	6.1
	Blackpool	53.811225 °N	3.024646°W	5.8
	Cambridge	52.199533°N	0.118069°E	4.7
	Cardiff	51.469955°N	3.167908°W	4.7
	Cranfield	52.076407°N	0.628563°W	5.5
	Edinburgh	55.949661°N	3.181751°W	6.2
	Liverpool	53.388570°N	2.987293°W	4.8
	London	51.509159°N	0.130332°W	4.7
	Milton Kynes	52.024816°N	0.756848°W	5.1
	Oxford	51.740438°N	1.248081°W	4.6
	Plymouth	50.359276°N	4.142759°W	4.8
Maximum wind speed, U (m/s)				7.0

Appendix I Counter Wight Arm Length Effect

In this appendix, the effect of counter wight arm length, L_{cw} , is studied in different cases. The distance L_{cw} will be varied from 0.5m to 1.75m with a step of 0.25m forming six different alternatives. In each alternative, the optimum mass of the counter wight will be determined. It is the mass corresponding to the intersection point between maximum and minimum absolute combined torques in case of wind presence and absence, respectively.

I.1 Alternative #1

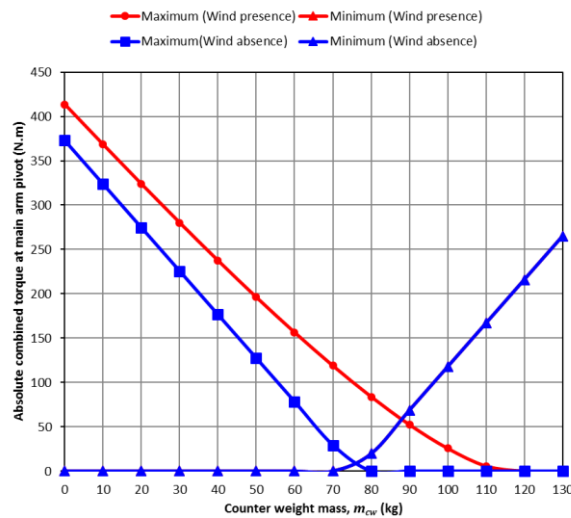


Figure I-8 Absolute combined moment range affecting on main arm pivot in presence/absence of wind load ($L_{cw}=0.50m$)

From Figure I-8, the optimum counter wight mass is **88.3 kg**.

I.2 Alternative #2

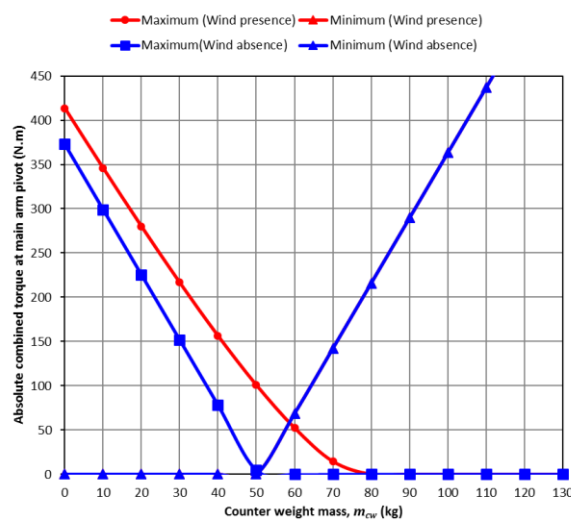


Figure I-9 Absolute combined moment range affecting on main arm pivot in presence/absence of wind load ($L_{cw}=0.75m$)

From Figure I-9, the optimum counter wight mass is **58.8 kg**.

I.3 Alternative #3

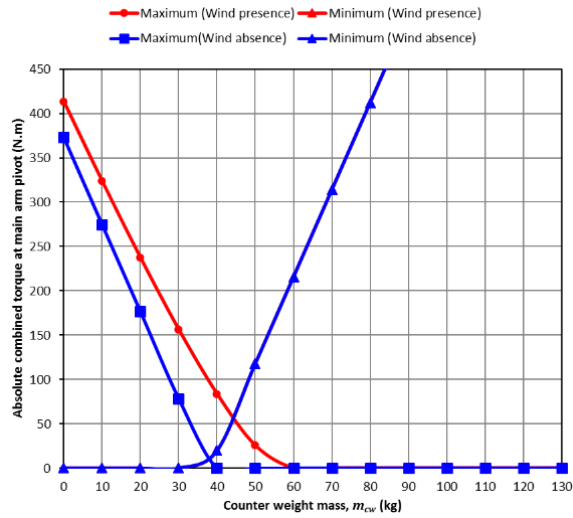


Figure I-10 Absolute combined moment range affecting on main arm pivot in presence/absence of wind load ($L_{cw}=1.0m$)

From Figure I-10, the optimum counter wight mass is **44.2 kg**.

I.4 Alternative #4

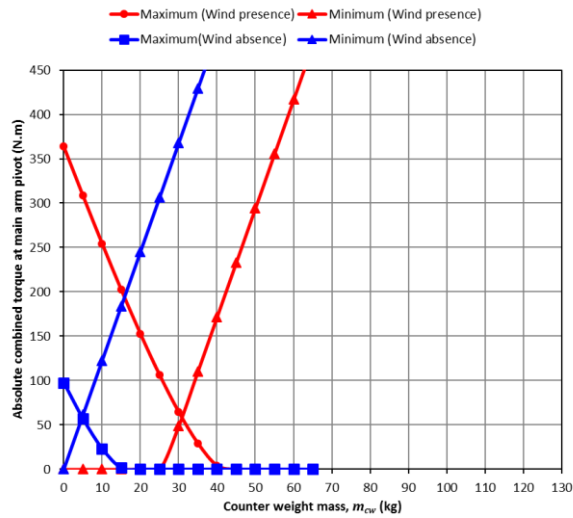


Figure I-11 Absolute combined moment range affecting on main arm pivot in presence/absence of wind load ($L_{cw}=1.25m$)

From Figure I-11, the optimum counter wight mass is **35.26 kg**.

I.5 Alternative #5

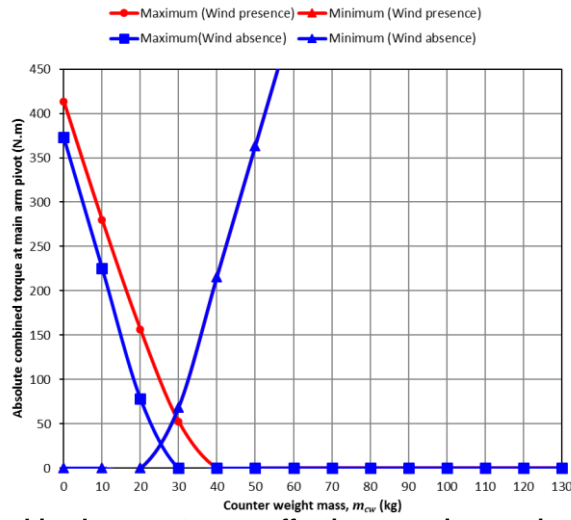


Figure I-12 Absolute combined moment range affecting on main arm pivot in presence/absence of wind load ($L_{cw}=1.50m$)

From Figure I-12, the optimum counter wight mass is **28.86 kg**.

I.6 Alternative #6

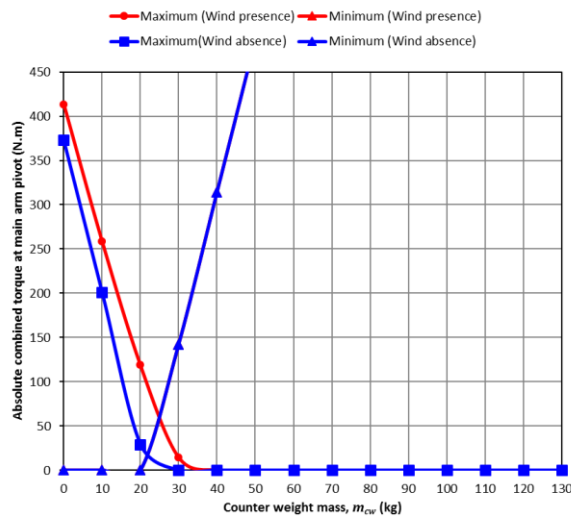


Figure I-13 Absolute combined moment range affecting on main arm pivot in presence/absence of wind load ($L_{cw}=1.75m$)

From Figure I-13, the optimum counter wight mass is **25.1 kg**.

Appendix J Optical Analysis MATLAB Code

```
1 function [T1,T2,T3,T4,T6,T7,T9,T16,T17,TEST] =
2 beam_diameter_GI_GO_complete(
3 lamda_concern,r,n_st,f,GIGOindicator,Rc_1,
4 D2,f2,tc,te,R12,R22,L22,x2 )
5 tic
6 %This function calculates the BEAM DIAMETER based on incident
7 wavelength (lamda),
8 % for PMMA-Fresnel FRONT LENS, with refractive index (n) as a
9 function of wavelength (lamda),
10 % and SiO2-Positive Meniscus REAR LENS, with refractive index
11 (n2) as a function of wavelength (lamda),
12
13 % Assuming solar rays coming with angular aperture of cone angle
14 9.3mrad, this angle is
15 % assumed to be between two "envelope RED and Blue rays"
16
17 %NOTE: The optimum position of the rear lens (x2cr) is selected
18 for both GI/GO configurations based on the MINIMUM DB_GI_avg or
19 MINIMUM DB_GO_avg, respectively, at (L=0), i.e. based on minimum
20 beam diameter if the screen is placed directly after the rear
21 lens.
22 %==== This distance is called (L2) and can be adjusted from
23 Line#52
24
25 %INPUTS:
26 %- lamda_concern= Wavelength bandwidth of concern[nm] (i.e. 400
27 to 2500nm for Visible & IR)
28 %- r= FRONT LENS radius (ranges from 0 to R1)[m]
29 %- n_st= Standard refractive index at which the manufacturer
30 calculated(f) for the FRONT LENS(-)
31 %- xf= Certain distance from the FRONT LENS plane [m]
32 %- f= Manufacturer focal length of the FRONT LENS (at
33 wavelength of "n_st") [m]
34 %- GIGOindicator= An integer indicator has a value of (0) if the
35 Fresnel is designrd for GI-configuration, or (1) if designed for
36 GO-configuration, according to the manufacturer data.
37 %- Rc_1= Reciprocal of the Bended FRONT LENS radius of
38 curvature, i.e. Rc_1=(Rc^-1)=(1/Rc)
39 % NOTE#1: Rc_1= -ve for the convex (pre-focus) bending (i.e.
40 bended around/towards its focal point)
41 % NOTE#2: Rc_1= +ve for the concave (post-focus) bending (i.e.
42 bended away from its focal point)
43
44 %- D2= REAR LENS diameter [m]
45 %- f2= Manufacturer focal length of the REAR LENS (at design
46 wavelength) [m]
47 %- tc= REAR LENS centre thickness [m]
48 %- te= REAR LENS edge thickness [m]
49 %- R12= REAR LENS radius of curvature, on the output beam side
50 [m]
```

```

51  %- R22=  REAR LENS radius of curvature, on the FRONT LENS side
52  [m]
53  %- L22=   Screen distance from the REAR LENS to receive the
54  beam [m]
55
56
57  %OUTPUTS:
58
59  %- T1=   Summary of critical values for FRONT LENS ONLY
60  %- T2=   Table of avergae/maximum/minimum spot diameters at
61  different (xfv) from the FRONT LENS ONLY
62  %- T3=   Table of slope angle (s) of Fresnel prisms (FRONT LENS)
63  as a function of lens radius(r)[rad]
64  %- T4=   Table of refractive indices (n1 and n2) of the FRONT
65  LENS (PMMA) and REAR LENS (SiO2) as a function of
66  wavelength(lamda)
67
68  %- T6=   Table of spectral Beam diameter (m) and deviation angle
69  (Delta)for each wavelength at each x2 (distance of the Rear lens
70  location measured from the focal length of the Front lens)
71  %- T7=   Table of critical data (i.e. minimum delat and
72  corresponding DB and x2 at each wavelength) deviation angle
73  (Delta)for each wavelength at the selected x2 (distance of the
74  Rear lens location measured from the focal length of the Front
75  lens)
76  %- T17=  Table of critical data (i.e. minimum delat and
77  corresponding DB and x2 at each wavelength) for optimum x2 of
78  concern
79
80  %- xfv=  Variable (xf) distance from the lens plane [m] (0 to
81  2*f)
82  lamda=lamda_concern;
83  %Defining the distance from REAR LENS to obtain (x2cr) (@which
84  minimum DB occurs)
85  L2=0.0;
86
87  xfv=(0.1*f):(2*f/500):(2*f);
88  xfv=xfv';
89
90  if (x2==0)
91      x2fv=(0.1*f2):(2*f2/150):(2*f2);
92      x2fv=x2fv';
93  else
94      x2fv=x2;
95  end
96
97  L= length(lamda);
98  R=length(r);
99  Xfv=length(xfv);
100 X2fv=length(x2fv);
101 KJ=X2fv*L;
102 TTT_STORE_GI=zeros(KJ,5);
103 TTT_STORE_GO=zeros(KJ,5);

```

```

104 R1=max(r);
105
106 % Calculating slope angle, s(r)*****
107 if (GIGOindicator==0)
108 for i=1:R
109
110     a(i)=atan(r(i)/f);
111     myfun = @(x,b,n_st) x-asin((sin(b+x))/n_st);
112     b=a(i);
113     fun=@(x)myfun(x,b,n_st);
114     x=fzero(fun,0.01);
115     s(i)=x;
116 end
117 end
118
119 if (GIGOindicator==1)
120 for i=1:R
121
122     a(i)=atan(r(i)/f);
123     myfun = @(x,b,n_st) asin(n_st*sin(x-asin(sin(x)/n_st)))-b;
124     b=a(i);
125     fun=@(x)myfun(x,b,n_st);
126     x=fzero(fun,0.01);
127     s(i)=x;
128 end
129 end
130 if (GIGOindicator~=0 && GIGOindicator~=1)
131     error('Error...GIGOindicator must be an integer indicator
132     has a value of (0) if the Fresnel is designrd for GI-
133     configuration, or (1) if designed for GO-configuration,
134     according to the manufacturer data')
135 end
136 s=s';
137 %*****
138 % Calculating refractive index, n(lamda) [for the FRONT LENS]
139 % Calculating refractive index, n2(lamda)[for the REAR
140 LENS]*****
141 % Using Sellmeier's Dispersion Equation (SDE)
142
143 for j=1:L
144
145 %as lamda in Sellmeier's Dispersion Equation in (microns), then:
146     l=lamda(j)/1000;
147
148 % Constants for SDE-6Coefficients for PMMA
149     A1=1.185;
150     A2=0.01116;
151     A3=0.04079;
152     A4=34.48;
153     A5=-0.001914;
154     A6=0.01895;
155 % Constants for SDE-6Coefficients for SiO2: source: raw data in
156 (https://refractiveindex.info/?shelf=main&book=SiO2&page=Malitso)

```



```

157 n) extracted from H. Malitson. "Interspecimen comparison of the
158 refractive index of fused silica", J. Opt. Soc. Am. 55, 1205-
159 1208 (1965)
160     A12=0.6962;
161     A22=0.004679;
162     A32=0.4079;
163     A42=0.01351;
164     A52=0.8975;
165     A62=97.93;
166
167 % For the FRONT LENS (PMMA)
168     n(j)=sqrt(1+((A1*1^2)/(1^2-A2))+((A3*1^2)/(1^2-
169 A4))+((A5*1^2)/(1^2-A6)));
170
171 % For the REAR LENS (SiO2)
172     n2(j)=sqrt(1+((A12*1^2)/(1^2-A22))+((A32*1^2)/(1^2-
173 A42))+((A52*1^2)/(1^2-A62)));
174
175 end
176 n=n';
177 n2=n2';
178 %*****
179
180 %===== GI = Grooves-In Configuration =====%
181
182 % Calculating Spot diameter at each lamda, Ds_GI(r)***
183
184 % Let solar aperture cone-half angle(?a=Theta_a)
185 Theta_a=9.3e-03/2; %In case of assuming SAA effect
186 %Theta_a=0; %In case of neglecting SAA effect
187 % Nomenclatures:
188 % ?t1_r_GI = Theta_t1_r_GI (For the red ray)
189 % ?i2_r_GI = Theta_i2_r_GI (For the red ray)
190 % ?t2_r_GI = Theta_t2_r_GI (For the red ray)
191 % ?`_r_GI = Alpha_r_GI (For the red ray)
192 % f`_r_GI = f_dash_r_GI (For the red ray)
193
194 % ?t1_b_GI = Theta_t1_b_GI (For the blue ray)
195 % ?i2_b_GI = Theta_i2_b_GI (For the blue ray)
196 % ?t2_b_GI = Theta_t2_b_GI (For the blue ray)
197 % ?`_b_GI = Alpha_b_GI (For the blue ray)
198 % f`_b_GI = f_dash_b_GI (For the blue ray)
199
200 h1 = waitbar(0, 'Step 1/7: Grooves In-Ds(x) Calculation
201 Progress....');
202 for k=1:Xfv
203 for j=1:L
204     nj=n(j);
205     for i=1:R
206         Theta_i_GI=Theta_a;
207
208         Theta_t1_r_GI=asin(sin(Theta_i_GI)/nj);
209

```

```

210     Theta_i2_r_GI=Theta_t1_r_GI+s(i);
211
212     if ((nj*sin(Theta_i2_r_GI))<1.0)
213         Theta_t2_r_GI=asin(nj*sin(Theta_i2_r_GI));
214
215         Alpha_r_GI=Theta_t2_r_GI-s(i);
216
217         f_dash_r_GI=r(i)/tan(Alpha_r_GI);
218
219         df_dash_r_GI=f- f_dash_r_GI;
220
221         %Front Lens Buckling/Bending Effect*****
222         % df_ddash_r_GI= df_double dash for GI configuration
223         % Alpha_ddash_GI= Alpha_double dash for GI
224 configuration
225         % df_bar_GI= Average shift of focal length for GI
226 configuration (combining configuration & buckling/bending
227 effects of the Front Lens)
228         % f_bar_GI= Average focal length for GI
229 configuration (combining configuration & buckling/bending
230 effects of the Front Lens)
231         df_ddash_r_GI=(-1*f^2)/(R1))*asin(R1*Rc_1);
232
233         df_bar_GI=(df_dash_r_GI+df_ddash_r_GI);
234         f_bar_GI= f-df_bar_GI;
235
236 %Average Spot Diameter at certain wavelength (j) an certain lens
237 radius (i) at distance (xf)
238 xf=xfv(k);
239
240         Dsr_GI(i)=2*r(i)*abs(xf-f_bar_GI)/abs(f_bar_GI);
241
242     else
243         Dsr_GI(i)=0;
244     end
245 end
246 Dsr_GI=Dsr_GI';
247 Ds_GI(j)=max(Dsr_GI);
248
249 end
250 % Then the list of (Ds_GI) at a certain (xfv) as a function of
251 wavelengths (lamda) can be listed as follows:
252 Ds_GI=Ds_GI';
253
254 Ds_GI_avg=mean(Ds_GI);
255 Ds_GI_max=max(Ds_GI);
256 Ds_GI_min=min(Ds_GI);
257
258 T_GI(k, :, :, :)= [xfv(k), Ds_GI_avg, Ds_GI_max, Ds_GI_min];
259
260 waitbar(k / Xfv)
261 end
262 close(h1)

```

```

263
264 [value_GI, index_GI]=min(T_GI(:,2,:,:),);
265 xcr_GI=xfv(index_GI);
266 Ds_cr_GI=value_GI;
267
268 toc;
269 time_Elapsed_Step_1 = toc;
270 TIME=['Time elapsed for step#1='
271 num2str(time_Elapsed_Step_1),'s'];
272 disp(TIME)
273 tic
274 %+++++++[Rear Lens on Configuration_GI]+++++++
275 h2 = waitbar(0,'Step 2/7: Grooves In-Beam Diameter [DB(x2+xcr)]
276 Calculation Progress....');
277 Beam_data_GI=zeros(R,3);
278 for k=1:X2fv
279     for j=1:L
280         nj=n(j);
281         n2j=n2(j);
282         % nj=1.490761121; %(refractive index at 586nm), activate
283         if chromatic aberration (CA) is wanted to be neglected
284         % n2j=1.460; %(refractive index at 588nm), activate if
285         chromatic aberration (CA) is wanted to be neglected
286         for i=1:R
287             Theta_i_GI=Theta_a;
288             Theta_t1_r_GI=asin(sin(Theta_i_GI)/nj);
289             Theta_i2_r_GI=Theta_t1_r_GI+s(i);
290
291             if ((nj*sin(Theta_i2_r_GI))<1.0)
292                 Theta_t2_r_GI=asin(nj*sin(Theta_i2_r_GI));
293                 Alpha_r_GI=Theta_t2_r_GI-s(i);
294                 f_dash_r_GI=r(i)/tan(Alpha_r_GI);
295                 df_dash_r_GI=f- f_dash_r_GI;
296                 %Front Lens Buckling/Bending Effect*****
297
298                 df_ddash_r_GI=(-1*f^2)/(R1))*asin(R1*Rc_1);
299                 df_bar_GI=(df_dash_r_GI+df_ddash_r_GI);
300                 f_bar_GI= f-df_bar_GI;
301
302                 if (r(i)==0)
303                     Alpha_bar_GI=0.0;
304                 else
305                     Alpha_bar_GI=atan(r(i)/abs(f_bar_GI));
306                 end
307
308                 xf=x2fv(k)+xcr_GI;
309
310                 Dsr_GI2(i)=2*r(i)*abs(xf-f_bar_GI)/abs(f_bar_GI);
311
312                 if (Dsr_GI2(i)<=D2)
313                     y(i)=Dsr_GI2(i)/2;
314
315                 beta_1(i)=(0.5*pi)-abs(atan((-1/y(i))*sqrt(R22^2-y(i)^2)));

```

```

316 Theta_i3(i)=abs(Alpha_bar_GI-beta_1(i));
317 Theta_t3(i)=asin(sin(Theta_i3(i))/n2j);
318 Y(i)=y(i)+(0.5*(tc+te)*tan(Theta_t3(i)));
319
320         if (Y(i)<=(D2/2))
321 beta_2(i)=(0.5*pi)-abs(atan((-1/Y(i))*sqrt(R12^2-Y(i)^2)));
322 Theta_i4(i)=abs(Theta_t3(i)+beta_1(i)-abs(beta_2(i)));
323 Theta_t4(i)=asin(n2j*sin(Theta_i4(i)));
324
325         % Deviation angle (Delta):
326 Delta(i)=beta_2(i)-Theta_t4(i);
327 Delta_Degrees(i)=Delta(i)*180/pi;
328 %Beam diameter for incident ray on FRONT LENS at(r)
329         if (Delta(i)>=0)
330 DBr_GI(i)=Dsr_GI2(i)+(2*L2*tan(Delta(i)));
331         else
332 L_delay=0.5*Dsr_GI2(i)/tan(abs(Delta(i)));
333         if(L2<=L_delay)
334             DBr_GI(i)=Dsr_GI2(i)-
335 (2*L2*tan(abs(Delta(i))));
336         else
337             DBr_GI(i)=2*(L2-
338 L_delay)*tan(abs(Delta(i)));
339         end
340         end
341
342 Beam_data_GI(i,:)=[DBr_GI(i),Delta_Degrees(i),r(i)];
343
344         else
345             Dsr_GI2(i)=0;
346             DBr_GI(i)=0;
347         end
348
349         else
350             DBr_GI(i)=0;
351             Delta(i)=0;
352         end
353     else
354         Dsr_GI2(i)=0;
355         DBr_GI(i)=0;
356     end
357 end
358 %Refining "Beam_data_GI" from (Zero delta's) rows
359 act=1;
360 active_Beam_data_GI=[0,0,0];
361 for i2=1:R
362     if(Beam_data_GI(i2,2)~=0)
363         active_Beam_data_GI(act,:)=Beam_data_GI(i2,:);
364         act=act+1;
365     end
366 end
367 %Refining "Beam_data_GI" from (Zero delta's) rows..END
368

```

```

369         Dsr_GI2=Dsr_GI2';
370         DBr_GI=DBr_GI';
371         Ds_GI2(j)=max(Dsr_GI2);
372         DB_GI(j)=max(DBr_GI);
373
374         [value_MAX_Delta_GI,
375 index_MAX_Delta_GI]=max(abs(active_Beam_data_GI(:,2)));
376         Spectral_delta_degrees_GI(j)=value_MAX_Delta_GI;
377
378 Spectral_beam_diameter_GI(j)=active_Beam_data_GI(index_MAX_Delta
379 _GI,1);
380
381 Spectral_effective_radius_GI(j)=active_Beam_data_GI(index_MAX_De
382 lta_GI,3);
383
384 Spectral_beam_data_GI(j,:)=[Spectral_beam_diameter_GI(j),Spectra
385 l_delta_degrees_GI(j),Spectral_effective_radius_GI(j)];
386         Wavelength_nm(j)=lamda(j);
387         X2(j)=x2fv(k);
388
389
390 TT_GI=table(X2',Wavelength_nm',Spectral_beam_diameter_GI',Spectr
391 al_delta_degrees_GI',Spectral_effective_radius_GI','VariableName
392 s',{'GI_x2_m' 'GI_lamda_nm' 'GI_DB_m' 'GI_Delta_degree'
393 'GI_Spectral_effective_Front_Lens_radius'});
394         TTT_GI=table2array(TT_GI);
395
396         Row_number=(k*L)-(L-j);
397         TTT_STORE_GI1(Row_number,:)=TTT_GI(j,:);
398
399 TTT_STORE_GI=array2table(TTT_STORE_GI1,'VariableNames',{'GI_x2_m
400 ' 'GI_lamda_nm' 'GI_DB_m' 'GI_Delta_degree'
401 'GI_Spectral_effective_Front_Lens_radius'});
402         T6_GI=single(table2array(TTT_STORE_GI));
403
404         end
405 Spectral_average_delta_degrees_GI(k,:)=x2fv(k),mean(Spectral_de
406 lta_degrees_GI)];
407 xf2(k)=x2fv(k)+xcr_GI;
408
409 waitbar(k / X2fv)
410 end
411     close(h2)
412
413     [value_GI2,
414 index_GI2]=min(Spectral_average_delta_degrees_GI(:,2));
415 x2cr_GI=Spectral_average_delta_degrees_GI(index_GI2,1);
416
417 toc;
418 time_Elapsed_Step_2 = toc;
419 TIME=['Time elapsed for step#2='
420 num2str(time_Elapsed_Step_2),'s'];
421 disp(TIME)

```

```

422 tic
423 %===== GO = Grooves-Out Configuration =====%
424 % Calculating Spot diameter at each lamda,
425 Ds_GO(r)*****
426
427 % Let solar aperture cone-half angle(?a=Theta_a)
428 Theta_a=9.3e-03/2; %In case of assuming SAA effect
429 %Theta_a=0; %In case of neglecting SAA effect
430 % Nomenclatures:
431 % ?t1_r_GO = Theta_t1_r_GO (For the red ray)
432 % ?i2_r_GO = Theta_i2_r_GO (For the red ray)
433 % ?t2_r_GO = Theta_t2_r_GO (For the red ray)
434 % ?`_r_GO = Alpha_r_GO (For the red ray)
435 % f`_r_GO = f_dash_r_GO (For the red ray)
436
437 % ?t1_b_GO = Theta_t1_b_GO (For the blue ray)
438 % ?i2_b_GO = Theta_i2_b_GO (For the blue ray)
439 % ?t2_b_GO = Theta_t2_b_GO (For the blue ray)
440 % ?`_b_GO = Alpha_b_GO (For the blue ray)
441 % f`_b_GO = f_dash_b_GO (For the blue ray)
442
443 h3 = waitbar(0, 'Step 3/7: Grooves Out-Ds(x) Calculation
444 Progress....');
445 for k=1:Xfv
446 for j=1:L
447 nj=n(j);
448 % nj=1.490761121; %(refractive index at 586nm), activate if
449 chromatic aberration (CA) is wanted to be neglected
450 for i=1:R
451 Theta_i_r_GO=s(i)-Theta_a;
452 Theta_t1_r_GO=asin(sin(Theta_i_r_GO)/nj);
453 Theta_i2_r_GO=s(i)-Theta_t1_r_GO;
454 if ((nj*sin(Theta_i2_r_GO))<1.0)
455 Theta_t2_r_GO=asin(nj*sin(Theta_i2_r_GO));
456 Alpha_r_GO=Theta_t2_r_GO;
457 f_dash_r_GO=r(i)/tan(Alpha_r_GO);
458 df_dash_r_GO=f- f_dash_r_GO;
459
460 %Front Lens Buckling/Bending Effect*****
461 % df_ddash_r_GO= df_double dash for GO configuration
462 % Alpha_ddash_GO= Alpha_double dash for GO Config.
463 % df_bar_GO= Average shift of focal length for GO config.
464 (combining configuration & buckling/bending effects of the Front
465 Lens)
466 % f_bar_GO= Average focal length for GO config. (combining
467 configuration & buckling/bending effects of the Front Lens)
468 df_ddash_r_GO=(-1*f^2)/(R1)*asin(R1*Rc_1);
469 df_bar_GO=(df_dash_r_GO+df_ddash_r_GO);
470 f_bar_GO=f-df_bar_GO;
471
472 %Average Spot Diameter at certain wavelength (j) an certain lens
473 radius (i) at distance (xf)

```

```

474   xf=xfv(k);
475   % In case of combined configuration & buckling/bending effects
476   of the Front Lens
477       Dsr_GO(i)=2*r(i)*abs(xf-f_bar_GO)/abs(f_bar_GO);
478
479       else
480           Dsr_GO(i)=0;
481       end
482   end
483   Dsr_GO=Dsr_GO';
484   Ds_GO(j)=max(Dsr_GO);
485
486   end
487   Ds_GO=Ds_GO';
488   Ds_GO_avg=mean(Ds_GO);
489   Ds_GO_max=max(Ds_GO);
490   Ds_GO_min=min(Ds_GO);
491   T_GO(k, :, :, :)= [xfv(k), Ds_GO_avg, Ds_GO_max, Ds_GO_min];
492   waitbar(k / Xfv)
493   end
494   close(h3)
495
496   [value_GO, index_GO]=min(T_GO(:, 2, :, :));
497   xcr_GO=xfv(index_GO);
498   Ds_cr_GO=value_GO;
499
500   toc;
501   time_Elapsed_Step_3 = toc;
502   TIME=['Time elapsed for step#3='
503   num2str(time_Elapsed_Step_3), 's'];
504   disp(TIME)
505   tic
506   %+++++[Rear Lens on
507   Configuration_GO]+++++
508   h4 = waitbar(0, 'Step 4/7: Grooves Out-Beam Diameter [DB(x2+xcr)]
509   Calculation Progress....');
510   Beam_data_GO=zeros(R, 3);
511   for k=1:X2fv
512       for j=1:L
513           nj=n(j);
514           n2j=n2(j);
515           %     nj=1.490761121;  %(refractive index at 586nm), activate
516           if chromatic aberration (CA) is wanted to be neglected
517           %     n2j=1.460;      %(refractive index at 588nm), activate
518           if chromatic aberration (CA) is wanted to be neglected
519               for i=1:R
520                   Theta_i_r_GO=s(i)-Theta_a;
521
522                   Theta_t1_r_GO=asin(sin(Theta_i_r_GO)/nj);
523
524                   Theta_i2_r_GO=s(i)-Theta_t1_r_GO;
525
526                   if ((nj*sin(Theta_i2_r_GO))<1.0)

```

```

527         Theta_t2_r_GO=asin(nj*sin(Theta_i2_r_GO));
528
529         Alpha_r_GO=Theta_t2_r_GO;
530
531         f_dash_r_GO=r(i)/tan(Alpha_r_GO);
532         df_dash_r_GO=f- f_dash_r_GO;
533
534         %Front Lens Buckling/Bending Effect*****
535         % df_ddash_r_GO= df_double dash for GO configuration
536         % Alpha_ddash_GO= Alpha_double dash for GO config.
537         % df_bar_GO= Average shift of focal length for GO config.
538         (combining configuration & buckling/bending effects of the Front
539         Lens)
540         % f_bar_GO= Average focal length for GO config. (combining
541         configuration & buckling/bending effects of the Front Lens)
542
543         df_ddash_r_GO=(-1*f^2)/(R1))*asin(R1*Rc_1);
544         df_bar_GO=(df_dash_r_GO+df_ddash_r_GO);
545         f_bar_GO= f-df_bar_GO;
546         if (r(i)==0)
547             Alpha_bar_GO=0.0;
548         else
549             Alpha_bar_GO=atan(r(i)/abs(f_bar_GO));
550         end
551         xf=x2fv(k)+xcr_GO;
552
553         Dsr_GO2(i)=2*r(i)*abs(xf-f_bar_GO)/abs(f_bar_GO);
554
555         if(Dsr_GO2(i)<=D2)
556             y(i)=Dsr_GO2(i)/2;
557             beta_1(i)=(0.5*pi)-abs(atan((-1/y(i))*sqrt(R22^2-y(i)^2)));
558             Theta_i3(i)=abs(Alpha_bar_GO-beta_1(i));
559             Theta_t3(i)=asin(sin(Theta_i3(i))/n2j);
560             Y(i)=y(i)+(0.5*(tc+te)*tan(Theta_t3(i)));
561             if (Y(i)<=(D2/2))
562                 beta_2(i)=(0.5*pi)-abs(atan((-1/Y(i))*sqrt(R12^2-Y(i)^2)));
563                 Theta_i4(i)=abs(Theta_t3(i)+beta_1(i)-abs(beta_2(i)));
564                 Theta_t4(i)=asin(n2j*sin(Theta_i4(i)));
565                 % Deviation angle (Delta):
566                 Delta(i)=beta_2(i)-Theta_t4(i);
567                 Delta_Degrees(i)=Delta(i)*180/pi;
568                 %Beam diameter for incident ray on FRONT LENS at (r)
569                 if (Delta(i)>=0)
570                     DBr_GO(i)=Dsr_GO2(i)+(2*L2*tan(Delta(i)));
571                 else
572                     L_delay=0.5*Dsr_GO2(i)/tan(abs(Delta(i)));
573                     if(L2<=L_delay)
574                         DBr_GO(i)=Dsr_GO2(i)-(2*L2*tan(abs(Delta(i))));
575                     else
576                         DBr_GO(i)=2*(L2-L_delay)*tan(abs(Delta(i)));
577                     end
578                 end
579

```



```

580
581 Beam_data_GO(i,:)=[DBr_GO(i),Delta_Degrees(i),r(i)];
582
583         else
584             Dsr_GO2(i)=0;
585             DBr_GO(i)=0;
586         end
587     else
588         DBr_GO(i)=0;
589         Delta(i)=0;
590     end
591 else
592     Dsr_GO2(i)=0;
593     DBr_GO(i)=0;
594 end
595 end
596 % Refining "Beam_data_GO" from (Zero delta's) rows
597     act=1;
598     active_Beam_data_GO=[0,0,0];
599     for i2=1:R
600         if(Beam_data_GO(i2,2)~=0)
601             active_Beam_data_GO(act,:)=Beam_data_GO(i2,:);
602             act=act+1;
603         end
604     end
605 %Refining "Beam_data_GI" from (Zero delta's) rows..END
606
607     Dsr_GO2=Dsr_GO2';
608     DBr_GO=DBr_GO';
609     Ds_GO2(j)=max(Dsr_GO2);
610     DB_GO(j)=max(DBr_GO);
611
612     [value_MAX_Delta_GO,
613 index_MAX_Delta_GO]=max(abs(active_Beam_data_GO(:,2)));
614     Spectral_delta_degrees_GO(j)=value_MAX_Delta_GO;
615
616     Spectral_beam_diameter_GO(j)=active_Beam_data_GO(index_MAX_Delta
617 _GO,1);
618
619     Spectral_effective_radius_GO(j)=active_Beam_data_GO(index_MAX_De
620 lta_GO,3);
621
622     Spectral_beam_data_GO(j,:)=[Spectral_beam_diameter_GO(j),Spectra
623 l_delta_degrees_GO(j),Spectral_effective_radius_GO(j)];
624     Wavelength2_nm(j)=lamda(j);
625     XX2(j)=x2fv(k);
626
627     TT_GO=table(XX2',Wavelength2_nm',Spectral_beam_diameter_GO',Spec
628 tral_delta_degrees_GO',Spectral_effective_radius_GO','VariableNa
629 mes',{'GO_x2_m' 'GO_lamda_nm' 'GO_DB_m' 'GO_Delta_degree'
630 'GO_Spectral_effective_Front_Lens_radius'});
631     TTT_GO=table2array(TT_GO);

```

```

632
633     Row_number=(k*L)-(L-j);
634     TTT_STORE_GO1(Row_number,:)=TTT_GO(j,:);
635
636     TTT_STORE_GO=array2table(TTT_STORE_GO1,'VariableNames',{'GO_x2_m
637     ' 'GO_lamda_nm' 'GO_DB_m' 'GO_Delta_degree'
638     'GO_Spectral_effective_Front_Lens_radius'});
639
640     T6_GO=single(table2array(TTT_STORE_GO));
641
642     end
643
644     Spectral_average_delta_degrees_GO(k,:)= [x2fv(k),mean(Spectral_de
645     lta_degrees_GO)];
646
647     xf2(k)=x2fv(k)+xcr_GO;
648     waitbar(k / X2fv)
649     end
650     close(h4)
651
652     [value_GO2,
653     index_GO2]=min(Spectral_average_delta_degrees_GO(:,2));
654     x2cr_GO=Spectral_average_delta_degrees_GO(index_GO2,1);
655     % PRINTING THE SUMMARY OUTPUT TABLE
656     *****
657     Rc=1/Rc_1;
658     T1=table(Rc,xcr_GI,Ds_cr_GI,xcr_GO,Ds_cr_GO,
659     'VariableNames',{'Front_Lens_radius_of_curvature_m'
660     'GI_Calculated_Front_Lens_focal_length_f1_m'
661     'GI_Min_Spot_Diameter_at_foca_point_m'
662     'GO_Calculated_Front_Lens_focal_length_f1_m'
663     'GO_Min_Spot_Diameter_at_foca_point_m'});
664     T2_array=horzcat(T_GI,T_GO);
665     T2=array2table(T2_array,'VariableNames',{'GI_Distance_from_Front
666     _Lens_x1_m' 'GI_Average_spot_diameter_m'
667     'GI_Maximum_spot_diameter_m' 'GI_Minimum_spot_diameter_m'
668     'GO_Distance_from_Front_Lens_x1_m' 'GO_Average_spot_diameter_m'
669     'GO_Maximum_spot_diameter_m' 'GO_Minimum_spot_diameter_m'});
670     T3=table(r,s,'VariableNames',{'Front_Lens_Radius_m'
671     'Prisms_Caluclated_Slope_Angle_rad'});
672     T4=table(lamda,n,n2,'VariableNames',{'Wavelength_nm'
673     'Front_Lens_PMMA_Refractive_index_n1'
674     'Rear_Lens_Quartz_Refractive_index_n2'});
675     T6_temp=horzcat(T6_GI,T6_GO);
676     T6=array2table(T6_temp,'VariableNames',{'GI_x2_m'
677     'GI_Wavelength_nm' 'GI_DB_m' 'GI_Delta_degree'
678     'GI_Spectral_effective_Front_Lens_radius_m' 'GO_x2_m'
679     'GO_Wavelength_nm' 'GO_DB_m' 'GO_Delta_degree'
680     'GO_Spectral_effective_Front_Lens_radius_m'});
681     T6_lamda_table = sortrows(T6,'GI_Wavelength_nm','ascend');
682     T6_lamda_array=table2array(T6_lamda_table);
683     T6_lamda_array(:, [1,2])=T6_lamda_array(:, [2,1]);
684     T6_lamda_array(:, [6,7])=T6_lamda_array(:, [7,6]);

```

```

685
686 KJ=L*X2fv;
687 spectral_critical_data_GI=zeros(L,5);
688 spectral_critical_data_GO=zeros(L,5);
689 T6_lamda_array_GI=T6_lamda_array(:,1:5);
690 T6_lamda_array_GO=T6_lamda_array(:,6:10);
691 spectral_critical_data_GI(1,:)=T6_lamda_array_GI(1,:);
692 spectral_critical_data_GO(1,:)=T6_lamda_array_GO(1,:);
693
694 %***** For GI-Configuration *****
695 jj=1;
696 for kj=2:KJ
697     if (T6_lamda_array_GI(kj,1)==T6_lamda_array_GI(kj-1,1))
698         jj=jj;
699         if
700 (abs(T6_lamda_array_GI(kj,4))<abs(spectral_critical_data_GI(jj,4
701 )))
702
703 spectral_critical_data_GI(jj,:)=T6_lamda_array_GI(kj,:);
704     end
705     else
706         jj=jj+1;
707         spectral_critical_data_GI(jj,:)=T6_lamda_array_GI(kj,:);
708     end
709 end
710 %***** For GO-Configuration *****
711 jj=1;
712 for kj=2:KJ
713     if (T6_lamda_array_GO(kj,1)==T6_lamda_array_GO(kj-1,1))
714         jj=jj;
715         if
716 (abs(T6_lamda_array_GO(kj,4))<abs(spectral_critical_data_GO(jj,4
717 )))
718
719 spectral_critical_data_GO(jj,:)=T6_lamda_array_GO(kj,:);
720     end
721     else
722         jj=jj+1;
723         spectral_critical_data_GO(jj,:)=T6_lamda_array_GO(kj,:);
724     end
725 end
726 T7_array_spectral=horzcat(spectral_critical_data_GI,spectral_cri
727 tical_data_GO);
728 T7_array_L=zeros(L,1);
729 T7_array_L(1:L,1)=L2;
730 T7_array=horzcat(T7_array_L,T7_array_spectral);
731 %T7_array=[1,T7_array];
732 T7=array2table(T7_array,'VariableNames',{
733 'Distance_from_the_rear_lens_m' 'GI_Wavelength_nm'
734 'GI_x2_Critical_m' 'GI_DB_Critical_m' 'GI_Delta_min_degree'
735 'GI_Spectral_effective_Front_Lens_radius_Critical_m'
736 'GO_Wavelength_nm' 'GO_x2_Critical_m' 'GO_DB_Critical_m'

```

```

737 'GO_Delta_min_degree'
738 'GO_Spectral_effective_Front_Lens_radius_Critical_m'}});
739 % PRINTING THE SUMMARY OUTPUT TABLE
740 *****
741 toc;
742 time_Elapsed_Step_4 = toc;
743 TIME=['Time elapsed for step#4='
744 num2str(time_Elapsed_Step_4), 's'];
745 disp(TIME)
746 tic
747 % Now it is required to fix the position of x2 to its optimum
748 position (according to "lamda_concern"
749
750 % To take the distance (L) into account to measure DB & Delta:
751 L2=L22;
752
753 jjj=1;
754 h5 = waitbar(0, 'Step 5/7: Defining Optimum x2 for Wavelength of
755 Concern Progress....');
756 x2_optimum_GI=x2cr_GI;
757 x2_optimum_GO=x2cr_GO;
758
759 if GIGOindicator==0
760     x2=x2_optimum_GI;
761 else
762     x2=x2_optimum_GO;
763 end
764 T9=table(x2,x2_optimum_GI,x2_optimum_GO,
765 'VariableNames',{'Optimum_x2_m' 'Optimum_x2_GI_m'
766 'Optimum_x2_GO_m'});
767 x2fv=x2;
768 X2fv=length(x2fv);
769 close(h5)
770 toc;
771 time_Elapsed_Step_5 = toc;
772 TIME=['Time elapsed for step#5='
773 num2str(time_Elapsed_Step_5), 's'];
774 disp(TIME)
775 tic
776 %VVVVVVVVVVVVVVVVVVVVVVVVVVVVVVVVVVVVVVVVVVVVVVVVVVVVVVVVVVVV
777 %+++++++[Rear Lens on Configuration_GI]++++++
778 h6 = waitbar(0, 'Step 6/7: Grooves In-Beam Diameter [DB(x2+xcr)]
779 Calculation Progress....');
780 Beam_data_GI=zeros(R,3);
781 for k=1:X2fv
782     for j=1:L
783         nj=n(j);
784         n2j=n2(j);
785         % nj=1.490761121; %(refractive index at 586nm), activate
786 if chromatic aberration (CA) is wanted to be neglected
787         % n2j=1.460; %(refractive index at 588nm), activate
788 if chromatic aberration (CA) is wanted to be neglected

```

```

789     for i=1:R
790         Theta_i_GI=Theta_a;
791         Theta_t1_r_GI=asin(sin(Theta_i_GI)/nj);
792         Theta_i2_r_GI=Theta_t1_r_GI+s(i);
793     if ((nj*sin(Theta_i2_r_GI))<1.0)
794         Theta_t2_r_GI=asin(nj*sin(Theta_i2_r_GI));
795         Alpha_r_GI=Theta_t2_r_GI-s(i);
796         f_dash_r_GI=r(i)/tan(Alpha_r_GI);
797         df_dash_r_GI=f- f_dash_r_GI;
798
799     %Front Lens Buckling/Bending Effect*****
800     % df_ddash_r_GI= df_double dash for GI configuration
801     % Alpha_ddash_GI= Alpha_double dash for GI config.
802     % df_bar_GI= Average shift of focal length for GI config.
803     (combining configuration & buckling/bending effects of the Front
804     Lens)
805     % f_bar_GI=Average focal length for GI configuration (combining
806     config. & buckling/bending effects of the Front Lens)
807     df_ddash_r_GI=(-1*f^2)/(R1))*asin(R1*Rc_1);
808     df_bar_GI=(df_dash_r_GI+df_ddash_r_GI);
809     f_bar_GI= f-df_bar_GI;
810     if (r(i)==0)
811         Alpha_bar_GI=0.0;
812     else
813         Alpha_bar_GI=atan(r(i)/abs(f_bar_GI));
814     end
815     xf=x2fv(k)+xcr_GI;
816
817     Dsr_GI2(i)=2*r(i)*abs(xf-f_bar_GI)/abs(f_bar_GI);
818
819     if(Dsr_GI2(i)<=D2)
820         y(i)=Dsr_GI2(i)/2;
821
822
823     beta_1(i)=(0.5*pi)-abs(atan((-1/y(i))*sqrt(R22^2-y(i)^2)));
824     Theta_i3(i)=abs(Alpha_bar_GI-beta_1(i));
825     Theta_t3(i)=asin(sin(Theta_i3(i))/n2j);
826
827     Y(i)=y(i)+(0.5*(tc+te)*tan(Theta_t3(i)));
828     if (Y(i)<=(D2/2))
829     beta_2(i)=(0.5*pi)-abs(atan((-1/Y(i))*sqrt(R12^2-Y(i)^2)));
830     Theta_i4(i)=abs(Theta_t3(i)+beta_1(i)-abs(beta_2(i)));
831     Theta_t4(i)=asin(n2j*sin(Theta_i4(i)));
832     % Deviation angle (Delta):
833     Delta(i)=beta_2(i)-Theta_t4(i);
834     Delta_Degrees(i)=Delta(i)*180/pi;
835     %Beam diameter for incident ray on FRONT LENS at (r)
836     if (Delta(i)>=0)
837     DBr_GI(i)=Dsr_GI2(i)+(2*L2*tan(Delta(i)));
838     else
839     L_delay=0.5*Dsr_GI2(i)/tan(abs(Delta(i)));
840     if(L2<=L_delay)
841     DBr_GI(i)=Dsr_GI2(i)-(2*L2*tan(abs(Delta(i))));

```

```

842         else
843     DBr_GI(i)=2*(L2-L_delay)*tan(abs(Delta(i)));
844         end
845     end
846     Beam_data_GI(i,:)=[DBr_GI(i),Delta_Degrees(i),r(i)];
847         else
848         Dsr_GI2(i)=0;
849         DBr_GI(i)=0;
850     end
851     else
852         DBr_GI(i)=0;
853         Delta(i)=0;
854     end
855     else
856         Dsr_GI2(i)=0;
857         DBr_GI(i)=0;
858     end
859 end
860 % Refining "Beam_data_GI" from (Zero delta's) rows
861     act=1;
862     active_Beam_data_GI=[];
863     for i2=1:R
864         if(Beam_data_GI(i2,2)~=0)
865     active_Beam_data_GI(act,:)=Beam_data_GI(i2,:);
866         act=act+1;
867     end
868     end
869 % Refining "Beam_data_GI" from (Zero delta's) rows.END
870     Dsr_GI2=Dsr_GI2';
871     DBr_GI=DBr_GI';
872     Ds_GI2(j)=max(Dsr_GI2);
873     DB_GI(j)=max(DBr_GI);
874     [value_MAX_Delta_GI,
875     index_MAX_Delta_GI]=max(abs(active_Beam_data_GI(:,2)));
876     Spectral_delta_degrees_GI(j)=value_MAX_Delta_GI;
877     Spectral_beam_diameter_GI(j)=active_Beam_data_GI(index_MAX_Delta
878     _GI,1);
879     Spectral_effective_radius_GI(j)=active_Beam_data_GI(index_MAX_De
880     lta_GI,3);
881     Spectral_beam_data_GI(j,:)=[Spectral_beam_diameter_GI(j),Spectra
882     l_delta_degrees_GI(j),Spectral_effective_radius_GI(j)];
883     Wavelength_nm(j)=lamda(j);
884     X2(j)=x2fv(k);
885     TT_GI=table(X2',Wavelength_nm',Spectral_beam_diameter_GI',Spectr
886     al_delta_degrees_GI',Spectral_effective_radius_GI','VariableName
887     s',{'GI_x2_m' 'GI_lamda_nm' 'GI_DB_m' 'GI_Delta_degree'
888     'GI_Spectral_effective_Front_Lens_radius'});
889     TTT_GI=table2array(TT_GI);
890     Row_number=(k*L)-(L-j);
891     TTT_STORE_GI1_2(Row_number,:)=TTT_GI(j,:);

```

```

892 TTT_STORE_GI_2=array2table(TTT_STORE_GI1_2,'VariableNames',{'GI_
893 x2_m' 'GI_lamda_nm' 'GI_DB_m' 'GI_Delta_degree'
894 'GI_Spectral_effective_Front_Lens_radius'});
895     T66_GI=single(table2array(TTT_STORE_GI_2));
896     end
897 % Then the list of (Ds_GI) at a certain (x2fv) as a function of
898 wavelengths
899 % (lamda) can be listed as follows:
900 Ds_GI2=Ds_GI2';
901 Ds_GI_avg2=mean(Ds_GI2);
902 DB_GI=DB_GI;
903 DB_GI_avg=mean(DB_GI);
904 Delta_GI_degree=(180/pi)*atan(abs(DB_GI_avg-Ds_GI_avg2)/(2*L2));
905 TB_GI22(k,:)=[x2fv(k),DB_GI_avg,Delta_GI_degree];
906 Ds_GI_avg2=mean(Ds_GI2);
907 Ds_GI_max2=max(Ds_GI2);
908 Ds_GI_min2=min(Ds_GI2);
909 xf22(k)=x2fv(k)+xcr_GI;
910 waitbar(k / X2fv)
911 end
912
913 [value_GI2, index_GI2]=min(TB_GI22(:,2));
914 x2cr_GI=x2fv(index_GI2);
915 DB_cr_GI=value_GI2;
916 Delta_cr_GI_degree=TB_GI22(index_GI2,3);
917
918     close(h6)
919     toc;
920     time_Elapsed_Step_6 = toc;
921     TIME=['Time elapsed for step#6='
922     num2str(time_Elapsed_Step_6),'s'];
923     disp(TIME)
924     tic
925
926 %===== GO = Grooves-Out Configuration =====%
927 %+++++[Rear Lens on Configuration_GO]+++++
928 h7 = waitbar(0,'Step 7/7: Grooves Out-Beam Diameter [DB(x2+xcr)]
929 Calculation Progress....');
930 Beam_data_GO=zeros(R,3);
931 for k=1:X2fv
932     for j=1:L
933         nj=n(j);
934         n2j=n2(j);
935         % nj=1.490761121; %(refractive index at 586nm), activate
936         if chromatic aberration (CA) is wanted to be neglected
937         % n2j=1.460; %(refractive index at 588nm), activate
938         if chromatic aberration (CA) is wanted to be neglected
939             for i=1:R
940                 Theta_i_r_GO=s(i)-Theta_a;
941
942                 Theta_t1_r_GO=asin(sin(Theta_i_r_GO)/nj);
943                 Theta_i2_r_GO=s(i)-Theta_t1_r_GO;

```

```

944         if ((nj*sin(Theta_i2_r_GO))<1.0)
945             Theta_t2_r_GO=asin(nj*sin(Theta_i2_r_GO));
946             Alpha_r_GO=Theta_t2_r_GO;
947             f_dash_r_GO=r(i)/tan(Alpha_r_GO);
948             df_dash_r_GO=f- f_dash_r_GO;
949             %Front Lens Buckling/Bending Effect*****
950             % df_ddash_r_GO= df_double dash for GO config.
951             % Alpha_ddash_GO= Alpha_double dash for GO config.
952             % df_bar_GO= Average shift of focal length for GO config.
953 (combining configuration & buckling/bending effects of the Front
954 Lens)
955             % f_bar_GO=Average focal length for GO configuration
956 (combining config. & buckling/bending effects of the Front Lens)
957             df_ddash_r_GO=(-1*f^2)/(R1)*asin(R1*Rc_1);
958             df_bar_GO=(df_dash_r_GO+df_ddash_r_GO);
959             f_bar_GO= f-df_bar_GO;
960             if (r(i)==0)
961                 Alpha_bar_GO=0.0;
962             else
963                 Alpha_bar_GO=atan(r(i)/abs(f_bar_GO));
964             end
965             xf=x2fv(k)+xcr_GO;
966             Dsr_GO2(i)=2*r(i)*abs(xf-f_bar_GO)/abs(f_bar_GO);
967             if(Dsr_GO2(i)<=D2)
968                 y(i)=Dsr_GO2(i)/2;
969                 beta_1(i)=(0.5*pi)-abs(atan((-1/y(i))*sqrt(R22^2-y(i)^2)));
970                 Theta_i3(i)=abs(Alpha_bar_GO-beta_1(i));
971                 Theta_t3(i)=asin(sin(Theta_i3(i))/n2j);
972                 Y(i)=y(i)+(0.5*(tc+te)*tan(Theta_t3(i)));
973                 if (Y(i)<=(D2/2))
974                     beta_2(i)=(0.5*pi)-abs(atan((-1/Y(i))*sqrt(R12^2-Y(i)^2)));
975                     Theta_i4(i)=abs(Theta_t3(i)+beta_1(i)-abs(beta_2(i)));
976                     Theta_t4(i)=asin(n2j*sin(Theta_i4(i)));
977                     % Deviation angle (Delta):
978                     Delta(i)=beta_2(i)-Theta_t4(i);
979                     Delta_Degrees(i)=Delta(i)*180/pi;
980
981                     %Beam diameter for incident ray on FRONT LENS at (r)
982                     if (Delta(i)>=0)
983                         DBr_GO(i)=Dsr_GO2(i)+(2*L2*tan(Delta(i)));
984                     else
985                         L_delay=0.5*Dsr_GO2(i)/tan(abs(Delta(i)));
986                         if(L2<=L_delay)
987                             DBr_GO(i)=Dsr_GO2(i)-
988 (2*L2*tan(abs(Delta(i))));
989                         else
990                             DBr_GO(i)=2*(L2-
991 L_delay)*tan(abs(Delta(i)));
992                         end
993                     end
994                     Beam_data_GO(i,:)=[DBr_GO(i),Delta_Degrees(i),r(i)];
995                 else

```



```

996             Dsr_GO2(i)=0;
997             DBr_GO(i)=0;
998         end
999     else
1000         DBr_GO(i)=0;
1001         Delta(i)=0;
1002     end
1003 else
1004     Dsr_GO2(i)=0;
1005     DBr_GO(i)=0;
1006 end
1007 end
1008 % Refining "Beam_data_GI" from (Zero delta's) rows
1009     act=1;
1010     active_Beam_data_GO=[];
1011     for i2=1:R
1012         if(Beam_data_GO(i2,2)~=0)
1013             active_Beam_data_GO(act,:)=Beam_data_GO(i2,:);
1014             act=act+1;
1015         end
1016     end
1017 %Refining "Beam_data_GI" from (Zero delta's) rows..END
1018     Dsr_GO2=Dsr_GO2';
1019     DBr_GO=DBr_GO';
1020     Ds_GO2(j)=max(Dsr_GO2);
1021     DB_GO(j)=max(DBr_GO);
1022     [value_MAX_Delta_GO,
1023     index_MAX_Delta_GO]=max(abs(active_Beam_data_GO(:,2)));
1024     Spectral_delta_degrees_GO(j)=value_MAX_Delta_GO;
1025     Spectral_beam_diameter_GO(j)=active_Beam_data_GO(index_MAX_Delta
1026     _GO,1);
1027     Spectral_effective_radius_GO(j)=active_Beam_data_GO(index_MAX_De
1028     lta_GO,3);
1029     Spectral_beam_data_GO(j,:)=[Spectral_beam_diameter_GO(j),Spectra
1030     l_delta_degrees_GO(j),Spectral_effective_radius_GO(j)];
1031     Wavelength2_nm(j)=lamda(j);
1032     XX2(j)=x2fv(k);
1033     TT_GO=table(XX2',Wavelength2_nm',Spectral_beam_diameter_GO',Spec
1034     tral_delta_degrees_GO',Spectral_effective_radius_GO','VariableNa
1035     mes',{'GO_x2_m' 'GO_lamda_nm' 'GO_DB_m' 'GO_Delta_degree'
1036     'GO_Spectral_effective_Front_Lens_radius'});
1037     TTT_GO=table2array(TT_GO);
1038     Row_number=(k*L)-(L-j);
1039     TTT_STORE_GO1_2(Row_number,:)=TTT_GO(j,:);
1040     TTT_STORE_GO_2=array2table(TTT_STORE_GO1_2,'VariableNames',{'GO_
1041     x2_m' 'GO_lamda_nm' 'GO_DB_m' 'GO_Delta_degree'
1042     'GO_Spectral_effective_Front_Lens_radius'});
1043     T66_GO=single(table2array(TTT_STORE_GO_2));
1044     end
1045
1046 % Then the list of (Ds_GO) at a certain (x2fv) as a function of
1047 wavelengths

```

```

1048 % (lamda) can be listed as follows:
1049 Ds_GO2=Ds_GO2';
1050 Ds_GO_avg2=mean(Ds_GO2);
1051 DB_GO=DB_GO;
1052 DB_GO_avg=mean(DB_GO);
1053
1054 Delta_GO_degree=(180/pi)*atan(abs(DB_GO_avg-Ds_GO_avg2)/(2*L2));
1055 TB_GO22(k,:)=[x2fv(k),DB_GO_avg,Delta_GO_degree];
1056
1057 Ds_GO_avg2=mean(Ds_GO2);
1058 Ds_GO_max2=max(Ds_GO2);
1059 Ds_GO_min2=min(Ds_GO2);
1060 xf22(k)=x2fv(k)+xcr_GO;
1061 waitbar(k / X2fv)
1062 end
1063
1064
1065 [value_GO2, index_GO2]=min(TB_GO22(:,2));
1066 x2cr_GO=x2fv(index_GO2);
1067 DB_cr_GO=value_GO2;
1068 Delta_cr_GO_degree=TB_GO22(index_GO2,3);
1069
1070 close(h7)
1071
1072 % PRINTING THE SUMMARY OUTPUT TABLE
1073 *****
1074 T16_temp=horzcat(T66_GI,T66_GO);
1075 T16=array2table(T16_temp,'VariableNames',{'GI_x2_m'
1076 'GI_Wavelength_nm' 'GI_DB_m' 'GI_Delta_degree'
1077 'GI_Spectral_effective_Front_Lens_radius_m' 'GO_x2_m'
1078 'GO_Wavelength_nm' 'GO_DB_m' 'GO_Delta_degree'
1079 'GO_Spectral_effective_Front_Lens_radius_m'});
1080 T16_lamda_table = sortrows(T16,'GI_Wavelength_nm','ascend');
1081 T16_lamda_array=table2array(T16_lamda_table);
1082 T16_lamda_array(:,[1,2])=T16_lamda_array(:,[2,1]);
1083 T16_lamda_array(:,[6,7])=T16_lamda_array(:,[7,6]);
1084
1085 KJ=L*X2fv;
1086 spectral_critical_data_GI=zeros(L,5);
1087 spectral_critical_data_GO=zeros(L,5);
1088
1089 T16_lamda_array_GI=T16_lamda_array(:,1:5);
1090 T16_lamda_array_GO=T16_lamda_array(:,6:10);
1091 spectral_critical_data_GI(1,:)=T16_lamda_array_GI(1,:);
1092 spectral_critical_data_GO(1,:)=T16_lamda_array_GO(1,:);
1093 %***** For GI-Configuration *****
1094 jj=1;
1095 for kj=2:KJ
1096     if (T16_lamda_array_GI(kj,1)==T16_lamda_array_GI(kj-1,1))
1097         jj=jj;
1098         if
1099             (abs(T16_lamda_array_GI(kj,4))<abs(spectral_critical_data_GI(jj,
1100 4)))

```

```

1101
1102 spectral_critical_data_GI(jj,:)=T16_lamda_array_GI(kj,:);
1103     end
1104     else
1105         jj=jj+1;
1106 spectral_critical_data_GI(jj,:)=T16_lamda_array_GI(kj,:);
1107     end
1108 end
1109 %***** For GO-Configuration *****
1110 jj=1;
1111 for kj=2:KJ
1112     if (T16_lamda_array_GO(kj,1)==T16_lamda_array_GO(kj-1,1))
1113         jj=jj;
1114         if
1115 (abs(T16_lamda_array_GO(kj,4))<abs(spectral_critical_data_GO(jj,
1116 4)))
1117
1118 spectral_critical_data_GO(jj,:)=T16_lamda_array_GO(kj,:);
1119     end
1120     else
1121         jj=jj+1;
1122 spectral_critical_data_GO(jj,:)=T16_lamda_array_GO(kj,:);
1123     end
1124 end
1125 T17_array_spectral=horzcat(spectral_critical_data_GI,spectral_cr
1126 itical_data_GO);
1127 T17_array_L=zeros(L,1);
1128 T17_array_L(1:L,1)=L2;
1129 T17_array=horzcat(T17_array_L,T17_array_spectral);
1130 %T17_array=[1,T17_array];
1131 T17=array2table(T17_array,'VariableNames',{
1132 'Distance_from_the_rear_lens_m' 'GI_Wavelength_nm' 'GI_x2_m'
1133 'GI_DB_Critical_m' 'GI_Delta_min_degree'
1134 'GI_Spectral_effective_Front_Lens_radius_Critical_m'
1135 'GO_Wavelength_nm' 'GO_x2_m' 'GO_DB_Critical_m'
1136 'GO_Delta_min_degree'
1137 'GO_Spectral_effective_Front_Lens_radius_Critical_m'});
1138 % PRINTING THE SUMMARY OUTPUT TABLE
1139 *****
1140 toc;
1141 time_Elapsed_Step_7 = toc;
1142 TIME=['Time elapsed for step#7='
1143 num2str(time_Elapsed_Step_7),'s'];
1144 disp(TIME)
1145
1146 Total_time_Elapsed_Step_minutes =
1147 (time_Elapsed_Step_1+time_Elapsed_Step_2+time_Elapsed_Step_3+tim
1148 e_Elapsed_Step_4+time_Elapsed_Step_5+time_Elapsed_Step_6+time_EL
1149 apsed_Step_7)/60;
1150 TIME=['Total Time elapsed='
1151 num2str(Total_time_Elapsed_Step_minutes),'minutes'];
1152 disp(TIME)

```

Appendix K Rear Lens Different Geometries

Dimensions of all geometries below are derived from Thorlabs' web site. The part number of each lens is shown in figures captions.

K.1 Bi-Convex Geometry



Figure K-14 Schematic of bi-convex lens (Part number: LB4879)

K.2 Plano-Convex Geometry

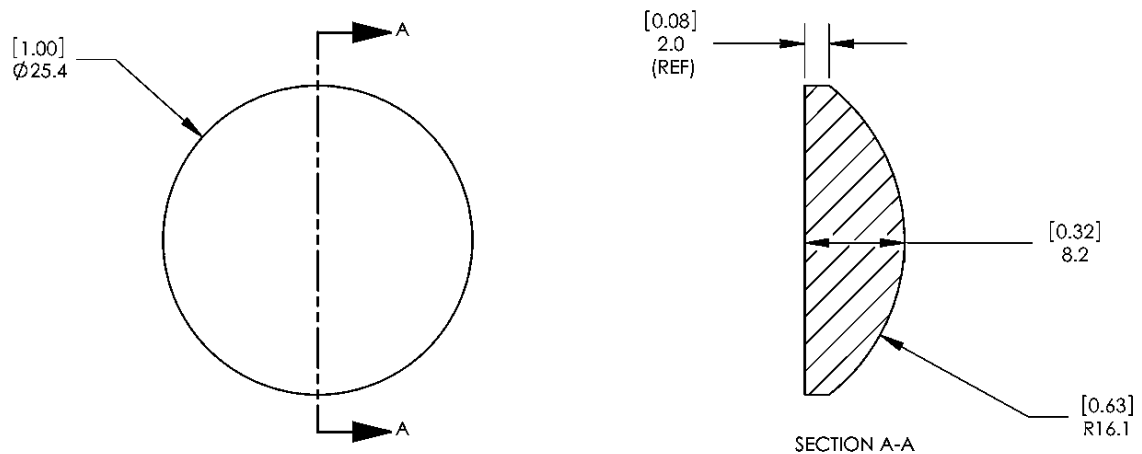


Figure K-15 Schematic of plano-convex lens (Part number: LA4052)

K.3 Positive Meniscus Geometry

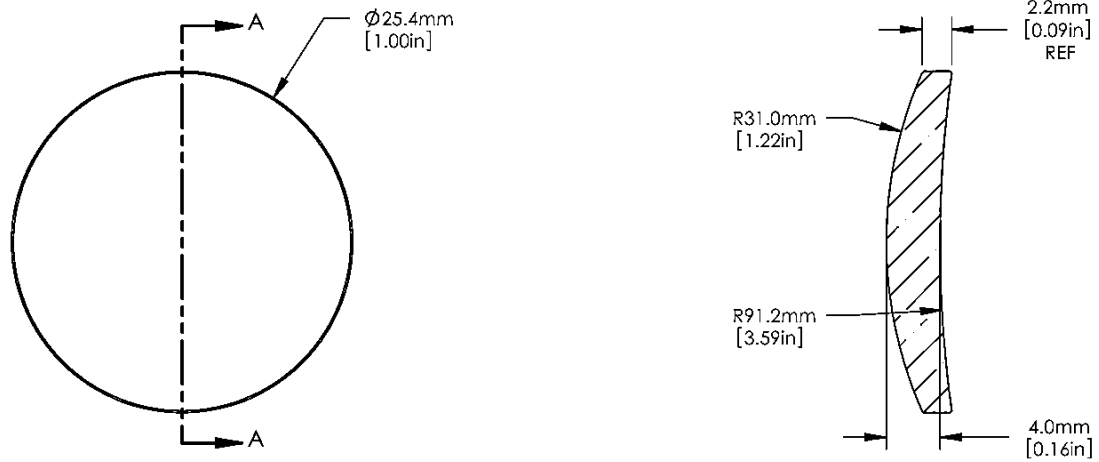


Figure K-16 Schematic of positive meniscus lens (Part number: LE4173)

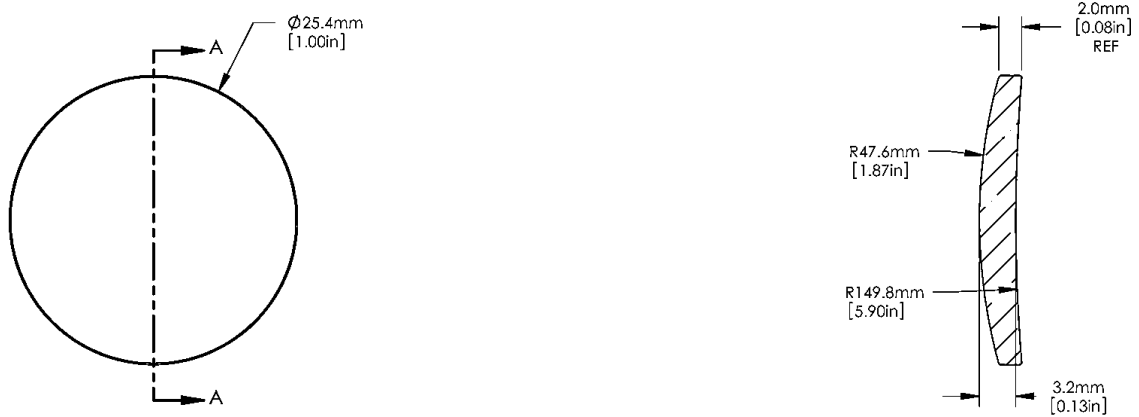


Figure K-17 Schematic of positive meniscus lens (Part number: LE4197)

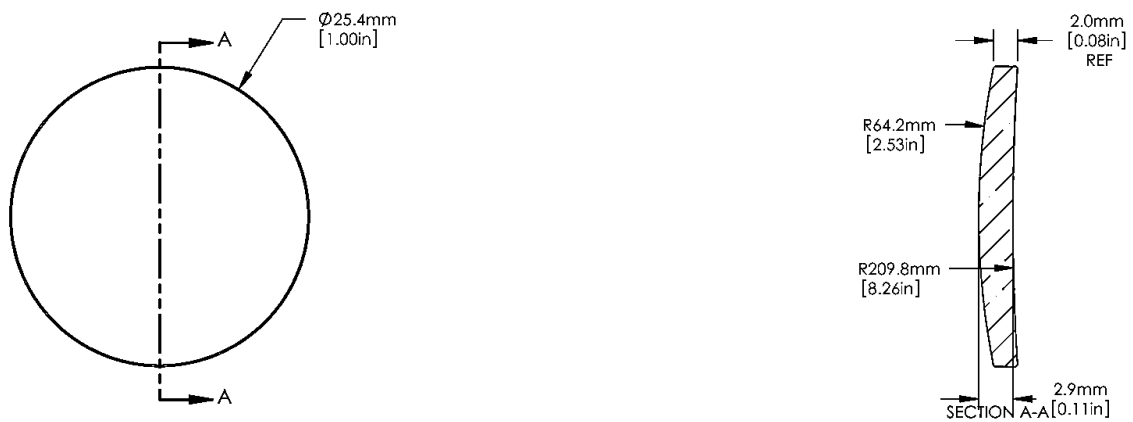


Figure K-18 Schematic of positive meniscus lens (Part number: LE4467)

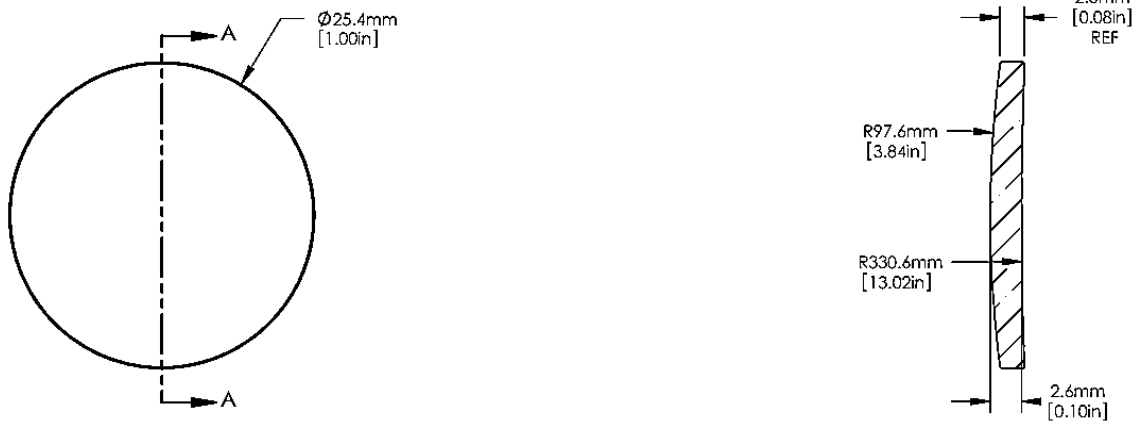


Figure K-19 Schematic of positive meniscus lens (Part number: LE4329)

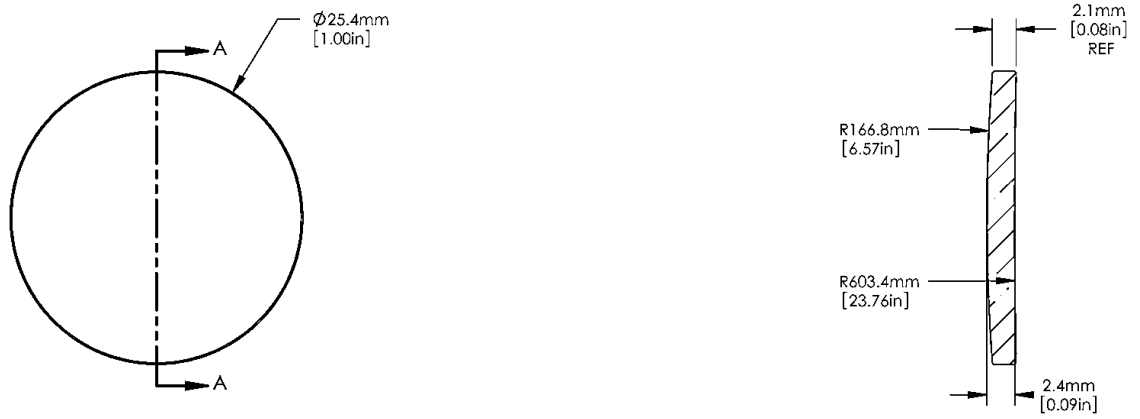


Figure K-20 Schematic of positive meniscus lens (Part number: LE4484)

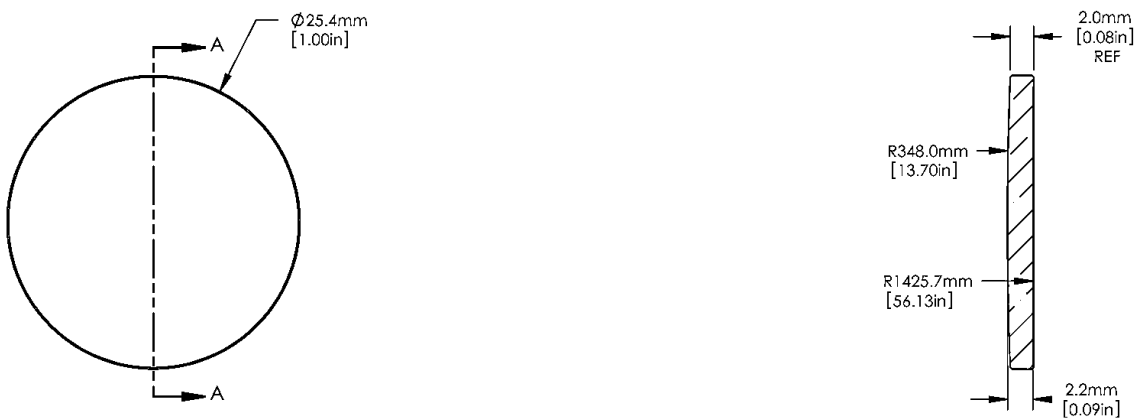


Figure K-21 Schematic of positive meniscus lens (Part number: LE4950)